

DES PETITS SEISMES POUR COMPRENDRE ET PREVOIR LES PLUS GROS

Françoise Courboulex

▶ **To cite this version:**

Françoise Courboulex. DES PETITS SEISMES POUR COMPRENDRE ET PREVOIR LES PLUS GROS. Géophysique [physics.geo-ph]. Université Nice Sophia Antipolis, 2010. ⟨tel-00519967⟩

HAL Id: tel-00519967

https://theses.hal.science/tel-00519967v1

Submitted on 23 Sep 2010

HAL is a multi-disciplinary open access archive for the deposit and dissemination of scientific research documents, whether they are published or not. The documents may come from teaching and research institutions in France or abroad, or from public or private research centers.

L'archive ouverte pluridisciplinaire **HAL**, est destinée au dépôt et à la diffusion de documents scientifiques de niveau recherche, publiés ou non, émanant des établissements d'enseignement et de recherche français ou étrangers, des laboratoires publics ou privés.



HAL Authorization

UNIVERSITE DE NICE-SOPHIA ANTIPOLIS, UFR SCIENCES
Ecole doctorale Sciences Fondamentales et Appliquées

Habilitation à diriger des recherches

FRANÇOISE COURBOULEX

DES PETITS SEISMES POUR COMPRENDRE ET PREVOIR LES PLUS GROS

Soutenue le 1er Avril 2010 devant le jury composé de :

Hideo Aochi	**BRGM, Orléans**	**Rapporteur**
Nicole Béthoux	**Géoazur, Université de Nice Sophia Antipolis**	**Présidente du jury**
Catherine Berge	**CEA, centre de Saclay, Gif sur Yvette**	**Rapporteur**
Massimo Cocco	**INGV, Rome, Italie**	**Examinateur**
Fabrice Cotton	**LGIT, Université de Grenoble**	**Rapporteur**
Philippe Guéguen	**LGIT, LCPC, Grenoble**	**Examinateur**
Isabelle Manighetti	**LGIT, Observatoire de Grenoble**	**Examinateur**

Géoazur, UMR 6526, OCA,
UNS-CNRS-IRD-UPMC
250 Av. Einstein,
06560 Valbonne

Remerciements

Un grand merci tout d'abord aux membres du jury qui ont très gentiment accepté de relire ce travail et d'assister à ma soutenance malgré leurs emplois du temps chargés.

Je tiens tout de suite à remercier les personnes directement impliquées dans le travail collectif qui est présenté dans ce mémoire :

- les étudiants et post-doctorants qui ont travaillé avec moi. Je pense particulièrement à Carine Kohrs-Sansorny, Céline Gélis, Julien Converset, Jérome Salichon et Laetitia Honoré. Certains ont changé de voie depuis mais tous ont apporté une pierre à l'édifice.
- Christophe Larroque pour nos fructueuses collaborations pluridisciplinaires, pour son énergie et aussi pour ses doutes scientifiques indispensables.
- Anne-Marie Duval du CETE Méditerranée qui m'a initiée au monde du risque sismique et a piloté avec moi le projet 'Passerelle', qui avait pour but de créer un pont entre les chercheurs et les gestionnaires opérationnels du risque. Etienne Bertrand qui a suivi le travail de Carine Kohrs et qui coordonne à présent le module risque sismique du master.
- Anne Deschamps qui a toujours été à mes cotés et dont les conseils sont précieux. Je la remercie tout particulièrement pour son investissement indéfectible pour l'obtention de données sismologiques de qualité.
- David Baumont (IRSN) pour nos collaborations passées sur la source sismique et nos collaborations futures sur la simulation des mouvements du sol. J'en profite pour saluer toute l'équipe du BERSIN (IRSN) : Oona Scotti, Catherine Berge, Fabian Bonilla, Céline Gélis … pour leur professionnalisme et leur gentillesse.
- Céline Beauval qui m'a fait toucher du doigt le monde probabiliste.
- Shri Krishna Singh et Javier Pacheco qui m'ont permis lors de mon séjour au Mexique de vivre une aventure passionnante en travaillant sur les gros séismes de subduction.
- Nicholas Deichmann pour l'étude délicate que nous avons réalisée ensemble sur le séisme d'Annecy.
- Bertrand Delouis et Martin Vallée qui proposent sans cesse de nouvelles méthodes pour mieux connaitre la source des séismes. Jean-Mathieu pour le pilotage du projet scientifique en l'Equateur.
- Je remercie toute l'équipe du 'Sismo à l'Ecole' et du projet européen O3E (Observation de l'Environnement à but éducatif à l'Ecole) : Jessica Leputh, Emmanuel Baroux (qui a joué le rôle d'interprète auprès de Massimo Cocco pour la soutenance de mon HDR), sans oublier Magali et tous les enseignants et référents du réseau. Je salue en particulier Jean-Luc Bérenguer qui mène avec brio ces projets depuis plusieurs années.

Dans le laboratoire, je tiens également à remercier tous ceux qui œuvrent pour que le travail de recherche puisse avancer : je pense particulièrement à Reine Saighi qui sans jamais s'énerver nous épaule et nous dirige dans la gestion des contrats, à Lionel et Caroline qui ont la tâche ingrate de s'occuper du réseau informatique et bien entendu à Christophe et Didier qui font tourner le réseau sismologique. Je n'ai cité ici que les plus anciens dans le laboratoire (comme moi) mais les nouveaux (ou moins anciens) le méritent aussi. Merci en particulier à Jenny de faire chantouiller nos systèmes d'informations géographiques …

Merci à Tony Monfret pour sa bonne humeur qui perdure malgré les responsabilités qu'il a accepté d'endosser et à toutes les personnes qui font avancer les choses positivement dans ce laboratoire, et il y en a heureusement beaucoup.

TABLE DES MATIERES

Remerciements **1**
INTRODUCTION **5**
CHAPITRE 1 Etudes des sources :
DES PETITS SEISMES POUR COMPRENDRE LES GROS **7**

1.1 Introduction 7
1.2 Pourquoi et quand utiliser des fonctions de Green empiriques 7
1.3 Méthodes 8
1.4 Limitations et précautions 14
1.5 Etude de grands séismes de subduction au Mexique 15
1.6 Etude du séisme d'Annecy (Mw 4.9) 34
1.7 Etude du séisme d'Athènes de 1999 (Mw 5.9) 46
1.8 Conclusions 59

CHAPITRE 2 Etudes de la sismicité :
DES PETITS SEISMES POUR IMAGER LES FAILLES ACTIVES **61**

2.1 Introduction 61
2.2 Méthodes de localisation et relocalisations relatives 61
2.3 La crise sismique de Colfiorito 63

2.3.1 Imagerie des failles et distribution spatio-temporelle de la sismicité 65
2.3.2 Etude des effets de site lithologiques et topographiques 66
2.3.3 L'analyse des surfaces de rupture activées 67

2.4 La jonction Alpes-Bassin Ligure 97

2.4.1 Contexte et questionnement 97
2.4.2 Etude de quelques petits séismes de la région 102
2.4.3 La campagne SALAM (Sismologie et Aléas dans Les Alpes Maritimes) 106
2.4.4 Le séisme de Nice 109

2.5 Conclusions 124

CHAPITRE 3 : Simulation des mouvements du sol :
DES PETITS SEISMES POUR PREVOIR LES GROS **125**

3.1 Introduction 125
3.2 Simulation des mouvements du sol 126
3.3 La méthode stochastique SIMULSTOC 127
3.4 Validation sur des données réelles 143

3.4.1 Objectifs 143
3.4.2 La crise des Saintes de 2004 145

3.5 Simulation d'un séisme futur 160
3.6 Méthode hybride probabiliste-déterministe 182
3.7 Conclusion 195

CHAPITRE 4 : DES SEISMES POUR PETITS ET GRANDS **197**

4.1 Sismos à l'Ecole 197
4.2 Le projet européen O3E 199
4.3 Et la suite ? 200

ELEMENTS DE PERSPECTIVE 205
Bibliographie citée dans le texte (hors articles) **208**
ANNEXE 213

INTRODUCTION

Les petits séismes ne font pas parler d'eux dans la presse : ils n'engendrent en général pas de destruction et surtout … ne tuent pas. Les petits séismes ne laissent pas de traces en surface, ils ne se détectent pour le moment pas sur les mesures GPS ni les images interférométriques. Ils sont parfois ressentis, parfois même pas. Pourtant, ces événements qui libèrent une énergie très faible si on la compare aux séismes majeurs sont d'une grande utilité.

J'ai choisi de bâtir ce mémoire d'HDR autour de l'utilisation que j'ai faite de ces petits séismes dans ma recherche pour comprendre et anticiper les gros. Le plan que je propose commence par l'étude des processus de la source, passe par la détection des failles actives pour déboucher sur la simulation des mouvements du sol en surface. Chaque partie est donc une composante de la détermination de l'aléa sismique.

Le chapitre 1 est consacré à l'étude de la source sismique. J'y explique comment, en se servant des petits séismes, on peut remonter au processus de rupture des plus gros. Les signaux des petits séismes sont utilisés comme des fonctions de Green pour représenter la fonction de propagation des ondes. Cette approche est particulièrement utile lorsque l'on travaille à des fréquences élevées (pour des séismes modérés par exemple) ou à des distances hypocentrales qui rendent la modélisation de la fonction de Green difficile.

Le chapitre 2 se concentre sur les études de sismicité, en particulier des études de crises sismiques comme celles de Colfiorito (Italie centrale) ou de Blausasc (Sud-est de la France). Là , les petits séismes nous aident à imager les surfaces de rupture simplement par leur position dans l'espace. En fait, la problématique de la localisation absolue ou relative des séismes n'est pas simple, mais quand les réseaux appropriés sont en place, il est possible d'obtenir une image des failles actives irremplaçable. J'ai appris en travaillant dans ce domaine que l'approche pluridisciplinaire était indispensable pour étudier les failles actives.

Le troisième chapitre est dédié à la simulation des mouvements du sol et à un test de mise au point d'une méthode déterministe-probabiliste. Ce chapitre est bien entendu lié aux précédents puisque lorsqu'on réalise des simulations, il faut savoir sur quelle faille et avec quelle source sismique. Les résultats présentés ici sont le fruit des recherches de plusieurs étudiants et post-doc qui ont travaillé avec moi sur le sujet mais aussi des interactions avec des chercheurs du BRGM, de l'IRSN (Institut de radioprotection et de sureté nucléaire) et du CETE (Centre d'études techniques de l'équipement) Méditerranée.

Dans chaque chapitre, je présente le contexte de l'étude ainsi qu'une introduction simple aux méthodes utilisées. C'est dans les articles insérés dans le texte que vous trouverez les détails des méthodes et des résultats. Certains travaux bien sûr sont transverses, en particulier le travail sur la crise de Blausasc que vous trouverez dans le chapitre 2.

Le quatrième chapitre ne concerne pas mon activité de recherche mais présente mon implication dans les réseaux de mesures environnementales en milieu scolaire et en particulier le « Sismos à l'Ecole » dont j'ai la responsabilité scientifique depuis quelques années.

Vous trouverez dans l'annexe le détail de mes publications, présentations à des colloques, encadrement d'étudiants et participation à l'enseignement.

CHAPITRE 1

Etudes des sources :
DES PETITS SEISMES POUR COMPRENDRE LES GROS

1.1 Introduction

L'étude des sources sismiques, c'est-à-dire du fonctionnement des failles au moment ou elles génèrent des tremblements de terre a toujours occupé une partie importante de mes recherches.
Pendant ma thèse je me suis penchée sur les mécanismes de la rupture des séismes de faible magnitude et mis en évidence des processus de rupture complexe et des effets de directivité même pour les petits séismes (magnitude < 4) [Courboulex et al., 1996a], ce qui est à présent régulièrement observé en différents endroits du monde [*Boatwright*, 2007; *Frez et al.*, 2010; *Wang and Rubin*, 2009]. Durant le post-doc que j'ai effectué à l'Instituto de Geofisica de l'Université Autonome de Mexico, j'ai travaillé cette fois sur de très gros événements liés à la subduction (magnitude 7 à 8) pour imager le processus de rupture dans le temps et dans l'espace. De retour en France, j'ai étudié principalement des séismes intermédiaires de magnitude 4.9 à 6 en Europe : Séisme d'Annecy de 1999, séismes de Colfiorito de 1997, séisme d'Athènes de 1999, séisme de Nice de 2001. Les recherches que je mène dans le domaine de la simulation des ondes sismiques (chapitre 3) m'amènent également à me pencher sur les sources sismiques et leur complexité (crise des Saintes de 2004, séismes de Pyrénées de 2006 et 2007, séisme de l'Aquila de 2009).

J'ai utilisé selon les cas les ondes de volume P et S ou les ondes de surface Rayleigh et Love. Dans la plupart des cas, l'approche par fonctions de Green empiriques était la seule qui permettait de s'affranchir correctement des effets de propagation et des effets de site. Ceci est particulièrement vrai pour les distances d'observation régionales et pour les petits événements où il est nécessaire de travailler à des fréquences élevées. C'est donc cette approche que j'ai souvent adoptée dans les inversions de source.

Je présenterai tout d'abord dans ce chapitre le principe de l'approche par fonctions de Green empiriques ainsi que les méthodes que j'ai utilisées (ou développées) pour obtenir des informations sur la fonction source. Les différentes inversions de séismes que j'ai réalisées seront regroupées par zone géographique, avec à chaque fois une introduction qui rappelle le contexte du travail, puis le ou les articles scientifiques qui présentent les méthodes et les résultats.

1.2 Pourquoi et quand utiliser des fonctions de Green empiriques

Un sismogramme en champ lointain peut s'écrire comme la convolution temporelle des effets de la source, de la propagation des ondes (la fonction de Green) et de la réponse instrumentale.

$$S(t) = s(t) * G(t) * I(t)$$

Si l'on souhaite isoler le signal dû à la source dans un sismogramme il est indispensable d'éliminer aussi efficacement que possible les autres effets.

La réponse instrumentale d'une station s'élimine en général assez facilement lorsqu'elle est bien connue. Il faut cependant toujours garder à l'esprit que c'est à travers le filtre de la station que l'on va pouvoir entrevoir le phénomène physique et que l'on n'a jamais accès au phénomène directement. Il est important par exemple de bien connaitre la partie du spectre qui va pouvoir être étudiée sans distorsion pour ne pas interpréter des fréquences qui ne sont pas correctement enregistrées par exemple. Les erreurs d'interprétation dues à la distorsion d'une station sont nombreuses. On peut citer notamment le célèbre effet FIR [Scherbaum and Bouin, 1997] qui a fait croire aux sismologues dans

les années 1990 que l'on observait des phases de nucléation au tout début de la rupture d'un séisme alors qu'il ne s'agissait que d'un effet numérique dû à l'utilisation d'un filtre dans la station. Notons à l'opposé, que des effets qui ont souvent été considérés comme purement instrumentaux comme les 'tilts', trouvent à présent une explication physique [Pillet and Virieux, 2007].

La fonction de propagation comprend ici les effets de la propagation des ondes à différentes distances : télésismiques, régionales ou locale selon les cas. La propagation dans les couches superficielles est souvent appelée 'effet de site'.
La fonction de propagation peut être modélisée. Une partie des chercheurs en sismologie et dans le domaine de l'industrie pétrolière travaille d'ailleurs sur des méthodes de plus en plus performantes pour calculer le champ d'onde à des fréquences de plus en plus élevées dans un temps de plus en plus court. Il est pour l'instant difficile de calculer des sismogrammes à plus de 2Hz sur des zones relativement restreintes (un bassin par exemple) dans un temps de calcul raisonnable (< 2 jours), mais il est certain que ces méthodes vont s'améliorer et permettre d'atteindre des fréquences plus élevées. Le problème viendra alors de la connaissance du sous sol pour atteindre ces fréquences.

Il est important lorsque l'on travaille sur la source d'un séisme de savoir quelle est la fréquence maximale que l'on cherche à atteindre. Cette fréquence dépend tout d'abord de la magnitude du séisme. Pour un séisme de magnitude 8, dont la rupture sera certainement de durée supérieure à 60 secondes, il reste intéressant de travailler à des fréquences relativement basses (0.1 Hz). Par contre pour un petit séisme dont la rupture dure 1 seconde, cela n'aura pas de sens.

En pratique, dans la plupart des cas, la modélisation de la fonction de propagation des ondes (fonction de Green) reste efficace si l'on travaille sur des séismes de magnitude assez élevée (supérieure à 6) à des distances télésismiques. A des distances régionales, la complexité du milieu de propagation rend cette modélisation difficile. A des distances locales, la modélisation reste possible uniquement si le milieu de vitesse est bien connu ou relativement simple et si l'on ne cherche pas à décrire les fréquences supérieures à 2Hz.

La fonction qui décrit l'effet de site devra prendre en compte l'effet de couches superficielles (effet de site lithologique), l'effet des reliefs (effet de site topographique) et les effets complexes dus à des structures 3D (bassins pas exemple). L'effet de site est intensément étudié par une partie de la communauté sismologique depuis le séisme de Mexico de 1885. Si l'effet de site lithologique peut être assez correctement approximé par une fonction de transfert 1D, l'effet de site topographique est encore très mal connu et des effets 3D doivent être étudiés au cas par cas. La variabilité observée des mouvements du sol rend la prévision des mouvements difficiles (nous en reparlerons dans le chapitre 3). Très souvent, les sismologues qui travaillent sur la source préfèrent ne pas utiliser les stations dont l'effet de site est important afin de ne pas perturber leurs modèles. Les sites « au rocher » sont alors sélectionnés préférentiellement.

Le pire cas de figure serait de vouloir étudier un séisme de magnitude faible (4 ou 5) à une centaine de kilomètres (la propagation des ondes devient complexe) en utilisant des stations au rocher et des stations sur sol mou. Dans ce cas (et dans bien d'autres) une solution subsiste : utiliser la méthode des fonctions de Green empiriques.

1.3 Méthodes

La méthode des fonctions de Green empiriques a tout d'abord été proposée par *Hartzel* en 1978 pour la simulation des mouvements forts puis utilisée par *Mueller* dès 1985 pour l'inversion des sources sismiques. Depuis, de très nombreuses études se basent sur cette méthode pour étudier la source sismique (par exemple : [*Dreger*, 1985], [*Fukuyama and Irikura*, 1986], [*S Hartzell*, 1989], [*Hutchings*, 1991], [*Jim Mori*, 1996; *Velasco et al.*, 1994], [*Ihmlé*, 1996], [*Hough*, 2001], [*Vallée*, 2007], [*Nozu and Irikura*, 2008], [*Mendoza and Hartzell*, 2009]).

Le principe est simple. Tous les séismes émis en un point donné et enregistrés sur une station donnée ont en commun : l'effet de propagation, l'effet de site et la réponse instrumentale. Seule la source des séismes va être différente (Nous verrons dans le chapitre 3 que cette hypothèse de linéarité n'est pas toujours valable pour des mouvements forts et en champ proche).
Nous allons alors considérer que la source d'un petit séisme est négligeable par rapport à celle d'un séisme plus important. Cela implique que la source du petit séisme doit être considérée comme ponctuelle et de durée négligeable. Le sismogramme du petit séisme à la station va donc pouvoir être pris comme la réponse impulsionnelle du système. On pourra considérer qu'il ne contient que l'effet de la propagation, du site et de l'instrument … tout ce que l'on souhaite éliminer du sismogramme du séisme à étudier. L'enregistrement du petit séisme sera appelé la fonction de Green empirique et pourra être utilisé comme une fonction de Green numérique (ou presque). Je désignerai souvent la fonction de Green empirique par le sigle EGF (Empirical Green's Function) couramment employé.

Bien entendu, ce raisonnement n'est que relatif puisque le petit séisme a bel et bien une fonction source qui peut également être complexe. La fréquence de coupure du petit séisme pris comme fonction de Green empirique (EGF) sera notre limite de résolution à haute fréquence. Une petite correction sera parfois effectuée sur la durée obtenue de la fonction source relative.

On peut ensuite utiliser cette fonction de Green empirique dans une inversion en une étape ou en deux étapes. L'approche en deux étapes ayant le mérite de stabiliser l'inversion, c'est celle que j'ai le plus couramment utilisée.

***Déconvolution* :**
La première étape consiste à déconvoluer le signal du séisme à étudier par celui du petit séisme pour retrouver sa fonction source. Il s'agira en fait d'une fonction source relative qui sera appelée dans la bibliographie « Relative source Time Function (RSTF) » ou « apparent source time function (ASTF)» puisqu'elle pourra être différente d'une station à l'autre à cause de la directivité de la rupture. On trouve parfois aussi « relative apparent source time function (RASTF) » qui est le terme le plus correct. C'est ce sigle que j'utiliserai par la suite.

Lors de cette déconvolution, il est important de chercher à isoler un seul type d'onde. En effet la durée apparente de la rupture à une station donnée dépend du rapport entre la vitesse de la rupture et la vitesse de propagation des ondes autour de la source. En toute rigueur, il faut donc travailler sur l'onde P seule, l'onde S seule ou bien toute phase réfléchie ou réfractée bien individualisée. Dans la pratique, et en particulier à des distances régionales, il est courant de ne pas pouvoir individualiser proprement les ondes. On travaille alors avec un « paquet d'onde » dont on doit estimer la vitesse moyenne.
On peut aussi travailler sur les ondes de surface de Rayleigh ou Love. Si le séisme a une magnitude très élevée, il est même possible d'envisager les trains R2 et L2 qui correspondent aux ondes de surfaces qui viennent de l'autre coté de la Terre. Les ondes de surface ont l'avantage de mieux mettre en évidence l'effet de directivité car elles ont des vitesses plus faibles, donc plus proches de la vitesse de propagation de la rupture. Par contre, leur nature dispersive ne nous aide pas à choisir une seule vitesse pour définir leur propagation. Ce point sera traité dans les articles sur les séismes de Colima-Jalisco et d'Athènes.

L'opération de déconvolution n'est pas la plus aisée car ce processus est instable. Plusieurs auteurs ont proposé des méthodes avec des avantages et des inconvénients. J'ai pour ma part utilisé différentes méthodes de déconvolution :

- Une méthode de déconvolution dans le domaine temporel que j'ai développée dans ma thèse basée sur une inversion par recuit simulé [*Courboulex et al.*, 1996a] que j'ai appliquée à des petits séismes en Grèce [*Courboulex et al.*, 1996c], en mer Ligure [*Courboulex et al.*, 1998] et au séisme de Copala [*Courboulex et al.*, 1997] pour les données régionales. Cette méthode était longue à mettre en œuvre, manquait de souplesse et n'apportait pas de résultats significativement plus fiables que les autres (résultats d'un Benchmark sur la déconvolution lors d'un congrès IASPEI), je l'ai donc laissée tomber assez rapidement après ma thèse.

- Une méthode simple de division spectrale avec « water level » [*Ammon et al.*, 1993; *Helmberger and Wiggins*, 1971] qui a le mérite d'être instantanée et de permettre de traiter un grand nombre de stations. Cette méthode cependant ne permet pas d'imposer une contrainte de positivité à la fonction source obtenue. J'ai utilisé cette méthode simple pour analyser le séisme de Colima-Jalisco (Figure 1. 1) de magnitude 8 ainsi que le séisme de Copala pour les données télésismiques uniquement (voir paragraphe 1.5).
- Une méthode de déconvolution dans le domaine temporel avec contrainte de positivité implémentée par C. Ammon (communication personnelle). Nous avons utilisé cette méthode, légèrement modifiée par David Baumont, pour l'étude du séisme d'Athènes de 1999 [*Baumont et al.*, 2002], (voir paragraphe 1.6).
- La méthode de projection de Lambert introduite en sismologie par Bertero *et al.*, [1997] et modifiée par Vallée [2004] pour ajouter une contrainte de stabilité sur les trois composantes. J'ai tout récemment tenté avec L. Honoré (doctorante Géoazur) d'utiliser cette méthode sur de petits séismes dans les Pyrénées. Même si cette tentative n'a pas été couronnée de succès (surement à cause d'une différence de mécanisme au foyer entre le gros et le petit séisme), c'est certainement la méthode que j'utiliserai dans le futur si j'en ai le besoin.

Il est important chaque fois que cela est possible, de réaliser la déconvolution avec plusieurs EGF possibles. Cette précaution permet d'obtenir des RASTF qui dépendront moins du séisme choisi comme EGF.

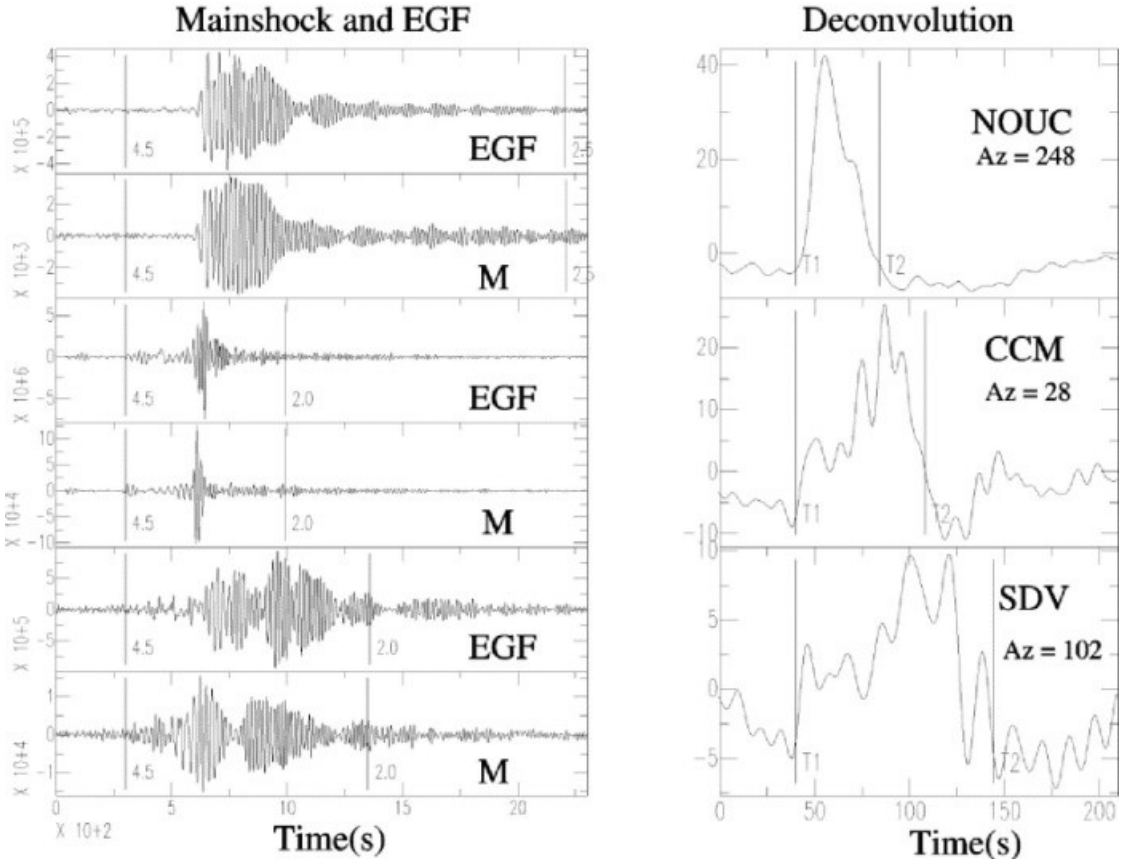


Figure 1. 1 : Séisme de Colima-Jalisco (Mw 8) : exemple de déconvolution entre le sismogramme du choc principal et celui d'une réplique de magnitude Mw 5.9 utilisée comme EGF. La fonction source relative apparente (RASTF) est présentée à droite. Elle montre très clairement l'effet de directivité de la rupture.

Inversion de la rupture :
La deuxième étape consiste à utiliser les informations temporelles contenues dans les différentes RASTF pour obtenir des résultats sur la propagation de la rupture. Elle n'est possible que si l'on dispose de stations bien distribuées en azimut autour de la source, quelque soit la distance épicentrale (il faut s'assurer de rester en champ lointain). Il s'agira alors d'inverser les RASTF pour reconstituer le processus de rupture sur le plan de faille dans le temps et dans l'espace. Plusieurs niveaux de résultats peuvent être obtenus :

Directivité de la rupture :
Il s'agit de retrouver la directivité dominante de la rupture. Pour l'obtenir, on cherche l'azimut du vecteur qui est en meilleure adéquation avec les données. Par exemple une directivité très marquée a été obtenue sur le séisme de Colima-Jalisco de 1995 de magnitude Mw=8 (Figure 1. 2).

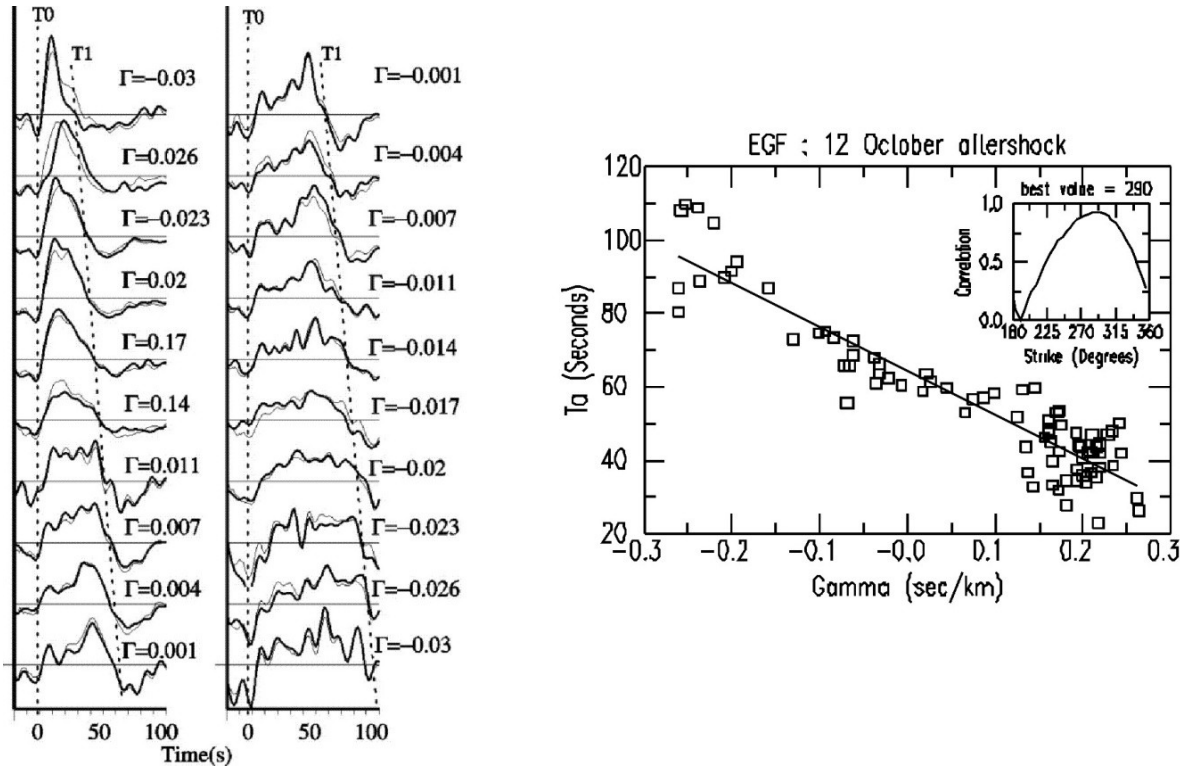


Figure 1. 2 : La directivité de la rupture du séisme de Jalisco de magnitude 8 est particulièrement marquée. La durée de la fonction source apparente Ta va de 25 sec pour la station la plus directive à 110 sec pour la station la plus anti-directive. A gauche les fonctions source apparentes obtenues , à droite l'analyse de la directivité [*Courboulex et al.*, 1996b].

Cette directivité peut permettre de discriminer dans certains cas le plan de faille actif parmi les deux plans nodaux obtenus avec le mécanisme au foyer. C'est ce que nous avons proposé pour le séisme de magnitude 4.7 au large de Vintimille [*Courboulex et al.*, 1998]. Pour le séisme d'Annecy de magnitude Mw 4.9, nous avons pu ainsi proposer deux scénarios de rupture probable (voir l'article paragraphe 1.6). Pour obtenir la direction maximale de directivité, il s'agit de trouver l'angle de directivité (angle formé entre l'azimut de la faille et celui de la direction préférentielle de la rupture) qui permet le mieux d'expliquer les données. On fait souvent l'hypothèse d'une vitesse de rupture constante (mais pas toujours).

Taille de la zone activée :
En utilisant le croisement des isochrones sur le plan de faille correspondant aux durées de RASTF, il est possible d'individualiser la zone de faille maximale qui a pu jouer ainsi que sa forme [*Bernard*

and Madariaga, 1984; *Spudich and Frazer*, 1984; *Zollo and Bernard*, 1991]. J'ai appliqué cette méthode à chaque fois que cela était possible et notamment pour les principales répliques des séismes de Colfiorito (Figure 1. 3) et pour un séisme au Mexique qui a eu lieu dans la zone intermédiaire du slab (séisme de Zihuatanejo). Cette méthode a permis dans ce dernier cas de sélectionner le plan de faille pseudo-vertical comme le seul possible [*Cocco et al.*, 1997].

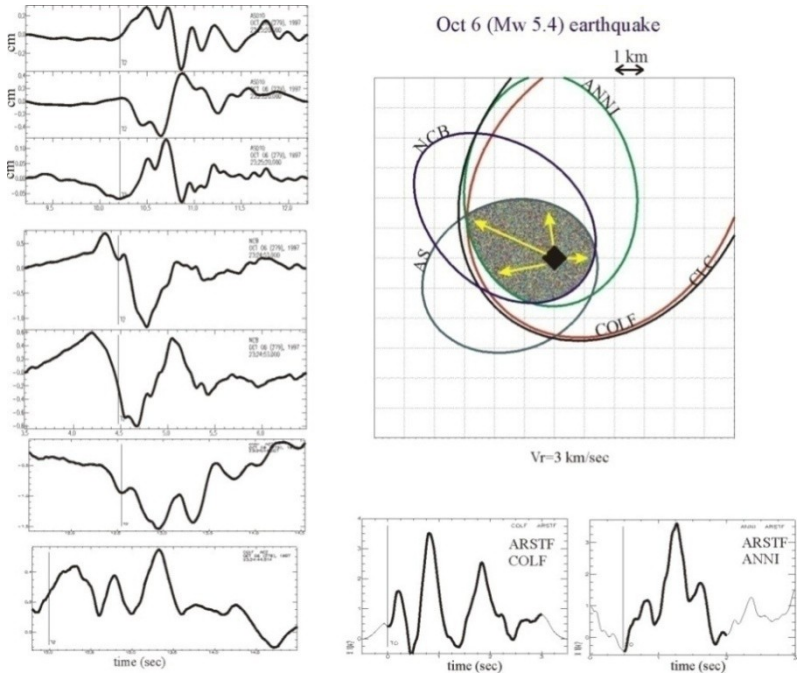


Figure 1. 3 : Détermination de la surface maximale de faille activée durant le séisme du 6 Oct 1997 de la crise de Colfiorito en Italie (zone grisée). Non publié.

Localisation des sous événements de la fonction source **:**

Lorsque la fonction source est complexe, et en particulier lorsqu'elle est constituée de plusieurs sous événements bien individualisés, il est possible de reconstruire grâce au tracé des isochrones la position relative des différents chocs. J'ai utilisé cette méthode dans l'analyse du séisme d'Annecy (Figure 1. 4).

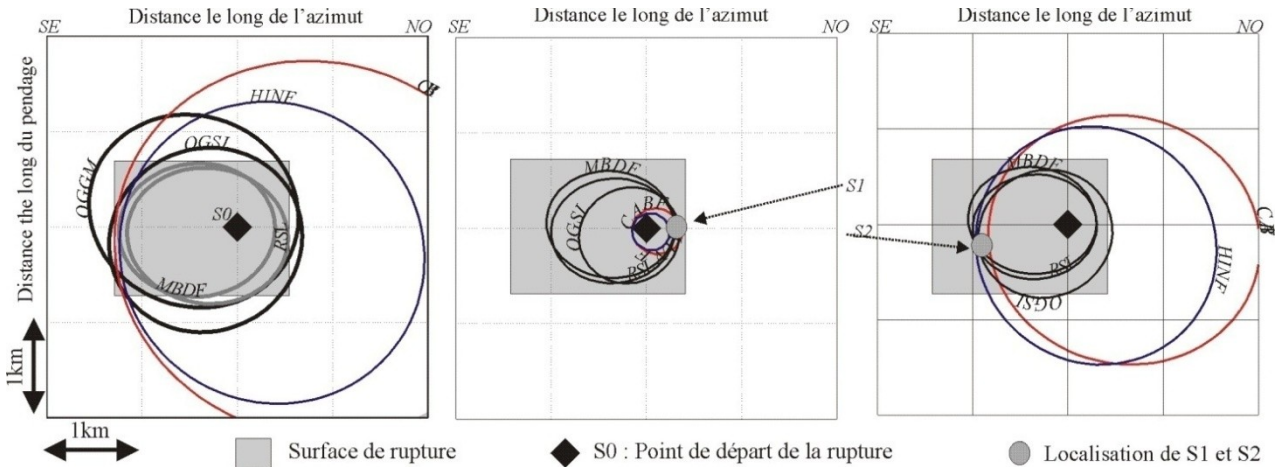


Figure 1. 4 : Détermination de la localisation de l'événement secondaire par rapport à l'hypocentre (séisme d'Annecy, Mw 5.9).

Inversion 1D le long de la direction de propagation de la rupture :
J'ai expérimenté dans le cas du séisme de Colima-Jalisco la transformée de Radon pour inverser les RASTF. Cette inversion a permis de mieux préciser la vitesse de la rupture de ce séisme ainsi que les zones ou la propagation n'était plus majoritairement latérale.

Inversion statique du glissement sur le plan de faille :
J'ai collaboré avec B. Hernandez durant sa thèse (Il est à présent chercheur au CEA) pour réaliser une inversion du glissement des séismes principaux de la crise de Colfiorito [*Hernandez et al.*, 2004]. Le processus en deux étapes consistait cette fois à inverser d'abord le glissement statique à partir des données géodésiques uniquement (Figure 1. 5), puis à inverser dans un second temps les données sismologiques pour obtenir des informations temporelles. Ce processus a l'avantage de stabiliser l'inversion mais a l'inconvénient de prendre la partie non-cosismique du glissement dans l'inversion.

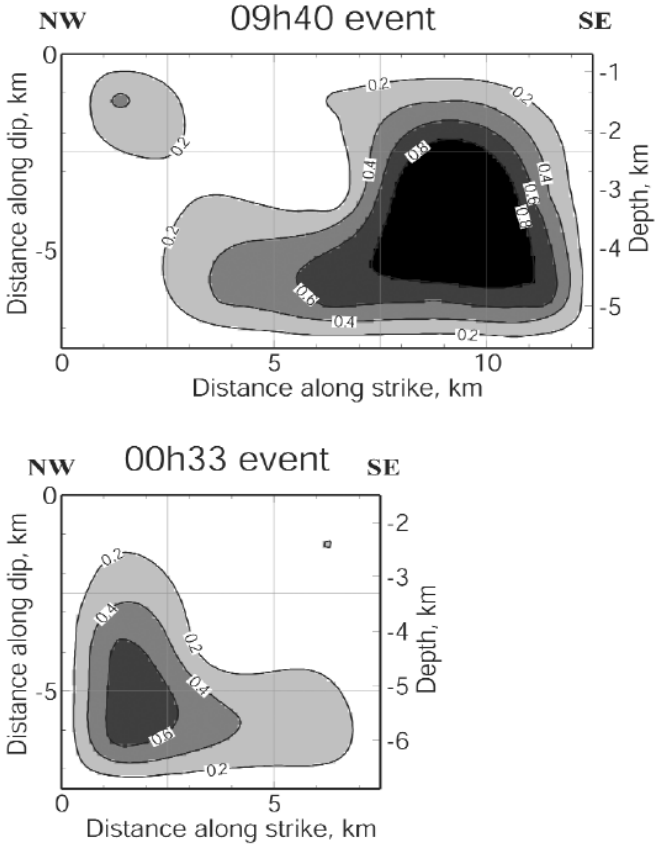


Figure 1. 5 : Inversion du glissement cosismique pour les séismes de Colfiorito à partir de données géodésiques (SAR et GPS), [*Hernandez et al.*, 2004].

Répartition du glissement en chaque point de la faille en fonction du temps :
Il est possible d'inverser les RASTF pour obtenir la distribution du glissement sur le plan de faille. Pour cette inversion, j'ai utilisé des méthodes linéaires (« damped least square ») par exemple pour l'inversion du séisme de Copala et d'Athènes ou non linéaires (recuit simulé) par exemple pour l'inversion de la source des séismes grecs étudiés dans ma thèse ou du séisme d'Annecy. Bien entendu de nombreux travaux proposent d'inverser les fonctions source temporelles avec des méthodes diverses.

1.4 Limitations et précautions

L'inversion de la source utilisant des fonctions de Green empiriques marche bien en général mais il y a des limitations à cette approche et des précautions à prendre.
Il sera impossible de travailler sur les stations trop proches de la rupture (en général on dit qu'il faut se situer à une distance supérieure ou égale à la longueur de la rupture). Les raisons de cette limitation sont les suivantes :

- La fonction source du gros séisme doit être vue dans sa globalité par la station pour pouvoir être inversée. Lorsqu'une station est au dessus de la faille, elle enregistre la propagation de la rupture de manière particulière.

- L'enregistrement du petit séisme doit être représentatif de l'effet de propagation du gros. Cela est forcement faux lorsque l'on se situe trop près de la faille.

- L'effet du champ proche et du champ intermédiaire est très important lorsque la distance source-station est faible ([*Aki and Richards*, 1980], chap 4.3). Cet effet existe également dans l'enregistrement du petit séisme mais il sera certainement plus vite masqué par le niveau de bruit.

- Lors d'un séisme important, des effets non linéaires peuvent se produire sur les stations soumises à une forte accélération (on peut lire notamment le chapitre 1 de l'HDR de Fabian Bonilla [2007] sur ce sujet). Si la-non linéarité de la réponse du sol n'est plus assurée, l'hypothèse des fonctions de Green empiriques n'est plus valide. Ce sujet de la non-linéarité sera particulièrement important dans le troisième chapitre de ce manuscrit.

L'utilisation des fonctions de Green empiriques n'est pas toujours facile. Alors que l'on sait ce que l'on injecte dans les fonctions de Green numériques, on ne sait pas toujours tout de notre fonction de Green empirique. Trois paramètres sont particulièrement importants : le mécanisme au foyer, la profondeur et la directivité éventuelle du petit séisme choisi. Lorsque le mécanisme au foyer du petit séisme est légèrement différent de celui du gros, il sera en général possible de travailler mais les stations proches des plans nodaux de l'onde considérée seront forcement fortement affectées par les différences et ainsi, la déconvolution ne va pas bien fonctionner. J'ai plusieurs fois cherché à corriger ces différences de mécanisme au foyer mais ne suis jamais parvenue à une solution satisfaisante. De la même manière, la profondeur du petit séisme ne devra pas être trop différente de celle du séisme principal, en particulier lorsque l'on travaille sur les ondes de surface. Enfin, il arrive que le petit séisme ait lui-même une source complexe. Si cette source a une directivité marquée, cela va se retrouver dans les résultats de la déconvolution et entrainer des erreurs parfois difficiles à déceler.

Il est important de rappeler également que cette méthode nécessite d'avoir des stations large bande et à grande dynamique afin d'enregistrer le signal du gros séisme sans saturation ainsi que celui du petit séisme avec un bon rapport signal sur bruit. Ces conditions sont de nos jours de plus en plus souvent réunies.

1.5 Etude de grands séismes de subduction au Mexique

Après ma thèse, j'ai ressenti le besoin de travailler dans un pays où le mot « sismologue » voulait dire quelque chose. Cette recherche du sens de mon travail et de son utilité est toujours présente à mon esprit d'ailleurs.

Mon arrivée au Mexique en Septembre 1995 coïncidait avec la commémoration du séisme de 1985. Cet événement terrible avait causé la mort de plus de 15 000 personnes dans la ville de Mexico. On connait maintenant assez bien la cause de cette catastrophe due à un effet d'amplification extraordinaire des ondes émises à plus de 300 km de la ville par un séisme majeur. Les recherches sur l'effet de site ont été stimulées de manière importante par les effets de ce fort séisme. Je suis donc arrivée à ce moment là, alors que depuis 10 ans, la terre avait cessé de trembler, mais que la catastrophe était encore bien présente dans toutes les mémoires.

Le lendemain de mon arrivée, le 14 septembre, un séisme de magnitude 7.4 se produisait dans la zone de Guerrero (séisme de Copala). Mon décalage horaire pas encore « avalé », je partais sur le terrain avec mes futurs collègues mexicains en balbutiant un espagnol sommaire appris rapidement avec quelques cassettes avant mon départ.
J'ai donc arpenté les routes vertigineuses et magnifiques de la zone de Guerero, rencontré les gens de villages touchés par l'événement qui hébergeaient nos stations dans leur jardin. Pour la première fois, j'ai vu tourner des stations analogiques dites « noirs de fumée ». J'ai découvert chaque matin les signaux que j'avais ressenti la nuit avec angoisse (angoisse légitime vu l'état des hôtels ou nous dormions) et découvert avec les villageois en palpitant chaque jour les soubresauts de la terre dessinés sur le papier. En quelques jours, je passais du virtuel au réel. C'est bien ce métier que je voulais faire ! Moins d'un mois plus tard, le 9 Octobre, un séisme de magnitude 8 avait lieu au nord du pays cette fois ci dans l'état de Colima (séisme de Jalisco).

Ma réputation de « déclencheuse de séisme » étant faite, j'ai pu travailler rapidement avec les équipes de sismologues de l'Institut et en particulier Shri Krishna Singh et Javier Pacheco mais aussi avec des sismologues américains (Charles Ammon) et italiens (Massimo Cocco) qui collaboraient avec l'institut.
La situation était idéale : j'avais pendant ma thèse essentiellement travaillé sur des méthodes (déconvolution et inversion) mais n'avait pas réellement pu adapter ces méthodes à des données adéquates (malgré plusieurs tentatives). J'ai donc immédiatement cherché à adapter mes méthodes aux données disponibles pour ces deux forts séismes. J'ai travaillé sur des données locales du réseau accélérométrique, régionales du réseau large bande (déjà fort bien développé à cette époque) et pour la première fois pour moi, sur des données télésismiques.

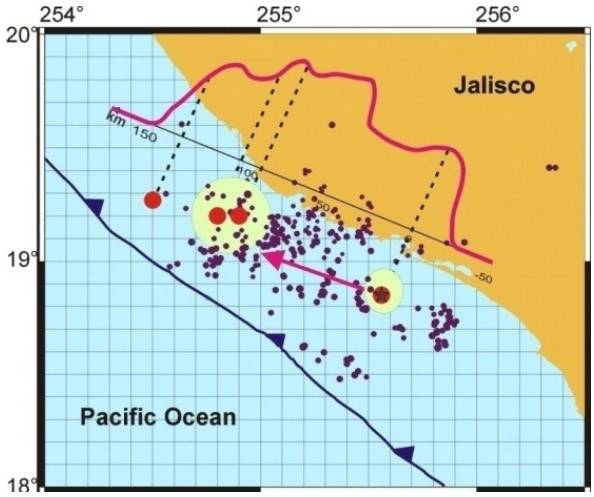


Figure 1. 6 : Distribution du glissement pendant le séisme de Jalisco (la valeur maximale est de 2.8 mètres). La flèche indique la direction de la directivité de la rupture, les ronds jaunes correspondent aux deux zones de glissement maximal. Les petits ronds violets représentent les répliques du séisme (1 mois), qui semblent se répartir autour le la zone de glissement maximal.

Le premier article qui est présenté ici résume l'étude du séisme de Jalisco (la partie sur les données télésismiques). Ce travail a été réalisé en partie à l'université de Saint Louis dans le Missouri où j'ai été accueillie chaleureusement par Chuck Ammon. Les excellentes données récoltées nous ont permis de mettre en évidence une directivité spectaculaire durant la rupture de cet événement (Figure 1. 6 et Figure 1. 7).

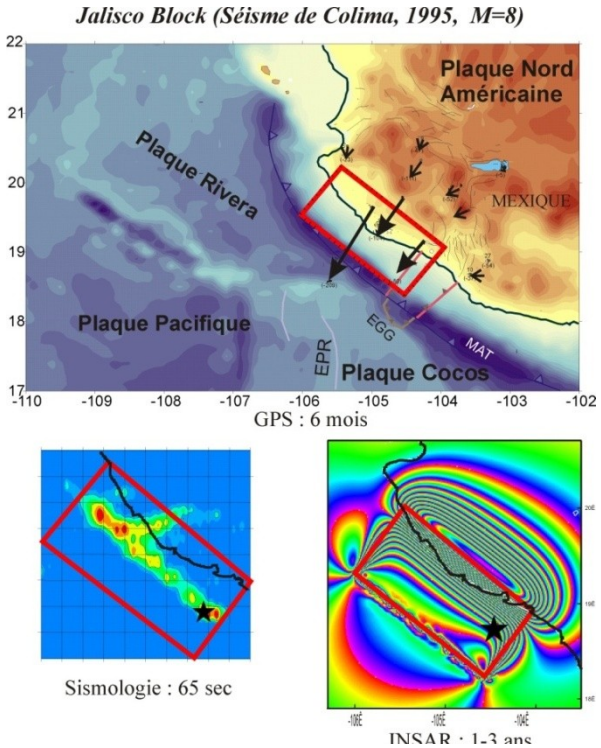


Figure 1. 7 : Le séisme de Jalisco vu par le GPS (en haut) et la sismologie (en bas à gauche). Modélisation de l'interférogramme que ce séisme aurait pu engendrer (en bas à droite). Les données SAR n'ont malheureusement pas permis de calculer un interférogramme réel (perte de cohérence due à la végétation).

Le second article propose une étude complète du séisme de Copala en utilisant séparément les stations à des distances télésismiques, les stations régionales et les accéléromètres proches. En utilisant ces données, nous avons obtenu une description fine du processus de rupture dans le temps et dans l'espace de ce séisme. Ces résultats sont en bon accord avec les dommages causés par cet événement.

Alors que ces deux séismes ont eu lieu à faible profondeur sur la zone d'interface entre les plaques avec un mécanisme au foyer en faille inverse, le séisme de Zihuatanejo, de magnitude plus faible (Mw 6.6) a été enregistré à 50 km de profondeur dans la plaque plongeante avec un mécanisme au foyer normal (Figure 1. 8). L'étude de ce séisme intermédiaire réalisée en collaboration avec Massimo Cocco fait l'objet d'un article dans le Geophysical Journal International [*Cocco et al.*, 1997]

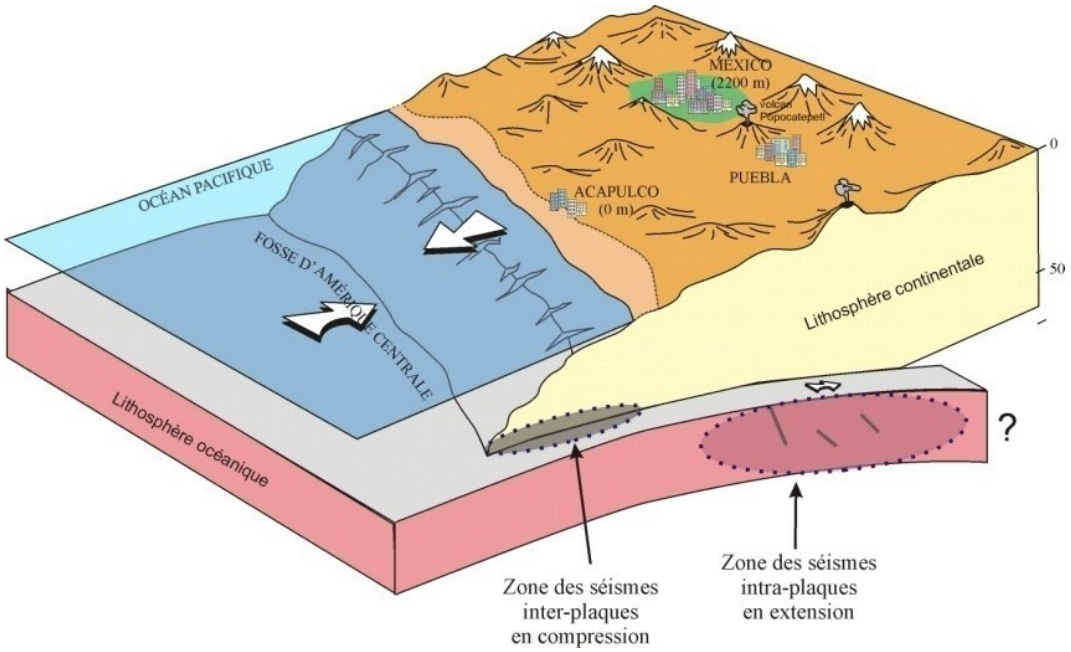


Figure 1. 8 : Vue 3D de la zone de subduction dans la zone de Guererro-Mexico (d'après le bloc 3D de J. Bourgois).

A mon retour en France, j'ai conservé une collaboration avec les équipes Mexicaines jusqu'en 2001 à peu près. Je suis notamment retournée au Mexique en 1999 juste au moment du séisme intraplaque de Puebla. J'ai écrit pour le magazine 'La Recherche' un article de divulgation sur ce séisme [*Courboulex et al.*, 1999].

J'ai également encadré les travaux de plusieurs étudiants (en licence et DEA) pour l'étude des sources de séismes mexicains (séisme de Puebla, séisme de Huatulco, de Oaxaca) et pour tester la variabilité des résultats en fonction des types d'ondes utilisés.

J'ai aussi co-encadré un étudiant avec Eric Calais qui a tenté de réaliser un interférogramme avec les données SAR (Synthetic Aperture radar) pour contraindre la rupture. Malheureusement, la zone de Colima étant trop boisée, nous n'avons pas pu obtenir de cohérence suffisante entre les deux images.

GEOPHYSICAL RESEARCH LETTERS, VOL. 24, NO. 9, PAGES 1019-1022, MAY 1, 1997

The 1995 Colima-Jalisco, Mexico, earthquake (Mw 8): A study of the rupture process

Françoise Courboulex, Shri K. Singh, Javier F. Pacheco
Instituto de Geofísica, UNAM, CU, 04510 México, D.F.
Charles J. Ammon
Saint Louis University, St Louis, Missouri

Abstract. In this study we map rupture characteristics of the great, shallow, thrust earthquake of October 9, 1995 which caused extensive damage to the coastal towns of Colima and Jalisco. To isolate the earthquake rupture details, we deconvolve surface waves with two empirical Green's functions, the aftershock of October 12, 1995 (Mw 5.9) and the foreshock of October 6, 1995 (Mw 5.8), from the corresponding mainshock records. Specifically, we use a spectral water-level deconvolution to obtain 80 Apparent Source Time Functions (ASTF) at 62 stations (Rayleigh and Love waves). Durations of the ASTF, as a function of azimuth indicate that the rupture propagated toward N70°W. The duration of the Source Time Function (STF) is around 62 s with a large pulse at 45 s. To map the main characteristics of the rupture, we use an inverse Radon transform of the ASTFs, assuming a ribbon fault-model aligned in the direction of the rupture propagation. Our analysis indicates that the rupture initiated about 20 km offshore of Manzanillo and propagated almost unilaterally for 150 km towards N70°W, with an average rupture velocity of approximately 2.8 km/s. The earthquake was a composite of three significant subevents, the largest occurred 45 s after the initiation of the rupture and was located about 100 km away. This result is in good agreement with the inversion of deformation data, measured with GPS [Melbourne *et al.*, 1997].

Introduction

On October 9, 1995, a great earthquake (Mw = 8.0) struck the coast of the states of Colima and Jalisco, Mexico, and caused extensive damage to the city of Manzanillo and coastal towns of both states. Many small fishing villages along the coast were affected by the tsunami that followed, which reached a runup height between 2 and 5 meters. Shaking was perceptible in Mexico City, located about 600 km from the epicenter. This earthquake was the largest to occur in Mexico since the great 1985 Michoacan earthquake. Previous large events along the Colima-Jalisco coast occurred on June 3 and 18, 1932 (Ms 8.2, Ms 7.8, respectively). The sum of the rupture lengths of these two events, estimated by Singh *et al.* [1985], who analyzed the aftershocks and some teleseismic P-wave recordings, is 280 km (Figure 1).

The 1995 Colima-Jalisco event occurred near the diffuse-triple junction between the North-American, Cocos, and Rivera plates (Figure 1). Because of the tectonic complexity of this region, it is not clear whether this earthquake is related to the subduction of the Rivera and/or Cocos plate beneath North America. The boundary between Rivera and Cocos plates as well as the Rivera-North American plate convergence rate are poorly known, and are topics of controversy and current research [Eissler and McNally, 1984; Kostoglodov and Bandy, 1995; DeMets and Wilson, 1997]. Estimates of the convergence rate vary between 2 and 5 cm/yr near the Cocos-Rivera boundary. Plate ages at the triple junction are estimated as 10 Ma and 12 Ma for the Rivera and Cocos plates, respectively [Kostoglodov and Bandy, 1995].

We use teleseismic data and an empirical Green's function (EGF) approach to study the rupture process of the 1995 earthquake. This approach, first proposed by Hartzell [1978], permits removal of the unknown effects of path, attenuation and site response. We first deconvolve the mainshock records using EGFs to isolate a relative apparent source time function (called ASTF or RSTF) at each station. Then we use the ASTFs to reconstruct the rupture history. In this study, we use surface waves as their low phase velocities enhance the directivity effect and also because at teleseismic distances surface waves are better recorded than body waves. This is especially important for the recording of the small event used as EGF. We follow a proce-

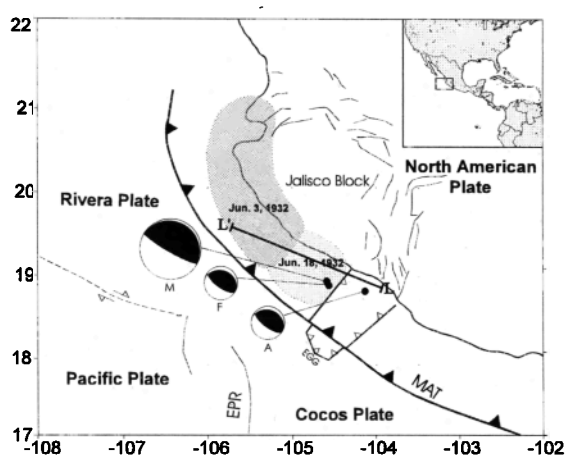


Figure 1. Plate tectonic framework of the Jalisco-Colima region. The 1995 Colima-Jalisco earthquake occurred close to the diffuse triple junction point between Rivera, Cocos and North American Plates. Aftershock areas of the June 3 (Ms 8.2) and the June 18 (Ms 7.8) 1932 earthquakes from Singh *et al.* (1985). M: October 9 Mainshock; A: October 12 aftershock; F: October 6 foreshock; EPR: East pacific rise; MAT: Middle Atlantic Trench; EGG: El Gordo graben. LL' shows the length of the rupture during the 1995 earthquake, estimated in this study.

Copyright 1997 by the American Geophysical Union.

Paper number 97GL00945.
0094-8534/97/97GL-00945$05.00

Table 1. Source parameters of the mainshock and the events used EGFs.

Date	Time*	Lat. °N*	Long. °W*	Depth *	Mw†	Strike†	Dip†	Rake†
1995/10/09	15:35:51.4	18.79	104.47	17	8.0	302	9	92
1995/10/06	05:13:22.8	18.77	104.51	10	5.8	285	25	70
1995/10/12	16:52:54.2	18.71	104.19	20	5.9	286	23	70

†determined from from Harvard CMT solution; * determined from local data.

dure developed by Ammon *et al.* [1993] and Velasco *et al.* [1994] in which deconvolutions are performed in the frequency domain using a water-level technique, and spatio-temporal characteristics of the rupture process is obtained by an inverse Radon transform (IRT).

Directivity Analysis

We chose the October 6 (Mw 5.8) foreshock and the October 12 (Mw 5.9) aftershock as empirical Green's functions (EGF). These two earthquakes occurred close to the mainshock epicenter and have almost the same focal mechanism (see Table 1; Figure 1). Although their depth is a little different, it may not be significant in our source analysis. The estimated duration of the source time function of these events is most likely less than or equal to 10 s. For this reason, this value represents the smallest periods of the mainshock source process that can be recovered from the analysis.

In the analysis of this large event, we deconvolve short-period surface waves (Rayleigh and Love waves) at 10-150 s. We first compared results of spectral division and time-domain deconvolution with positivity constraint at a couple of stations, and found that the differences were insignificant. For this reason, we opted for water-level deconvolution which permits a faster analysis of large datasets than a time-domain method.

Differences in path length and intrarupture dispersion in very long faults can cause distortion in the ASTFs obtained from surface waves. However, Velasco *et al.* [1994] demonstrated that these effects are small for a 100 km fault length for periods longer than 10 s, when the EGF is located at one end of the rupture. The two events chosen as EGFs occurred close to the mainshock epicenter (Figure 1) and near the SE end of the aftershock area which is about 130 km in length from the epicenter to the North-West end [Pacheco *et al.*, 1996]. The primary effect of intra-rupture dispersion discussed in Velasco *et al.* [1994] was the development of side lobes on the estimated ASTFs. At periods $T >= 20s$ the side-lobe effects for a moderate length rupture (100 km) are negligible [Velasco *et al.*, 1994]. We focus our discussion on rupture images obtained using observations containing periods up to 10 seconds. Caution is necessary when interpreting the rapidly varying features in the rupture model. We only interpret features that are robust in the imaging results using both 10- and 20-second period cut offs.

We use 66 broadband stations from the IRIS dataset, from which we retrieve 82 ASTFs using the aftershock as the EGF, and 42 ASTFs using the foreshock as the EGF, with a water-level value of 0.001 %. Differences in the number of stable ASTFs obtained come from the fact that the records of the foreshock were perturbed at

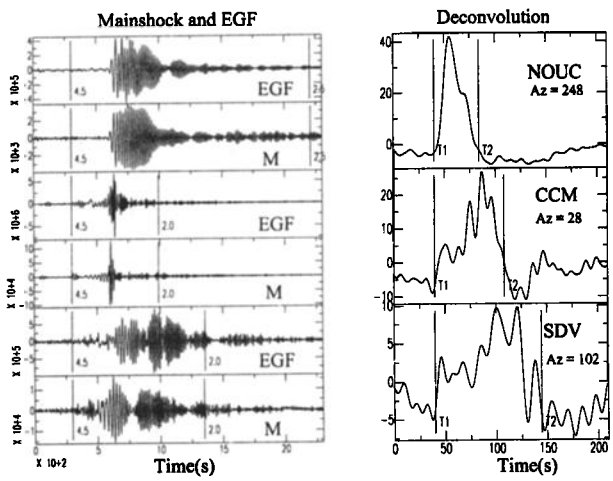


Figure 2. Examples of mainshock and aftershock (EGF) velocity seismograms of the vertical component, low-pass filtered at 10 s. The time windows used in the deconvolution and the corresponding phase velocities are marked by vertical bars. Right side of the figure represents the apparent source time functions (ASTF). T1 and T2 illustrate the beginning and the end of the ASTF, respectively.

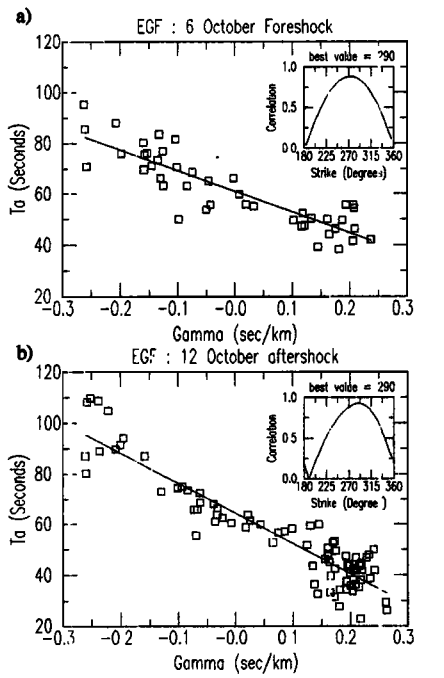


Figure 3. Directivity analysis using the Oct. 12 aftershock (a) and the Oct. 6 foreshock (b) as EGF. Inset shows the variation of the linear correlation coefficient as a function of azimuth of rupture propagation. The figure shows T_a of each ASTF as function of Γ, for the azimuth that gives the best linear regression.

several stations by the occurrence of another earthquake in Peru less than one minute later. For this reason, the foreshock will be used only to confirm the directivity estimation given by the aftershock analysis.

In Figure 2 we show the mainshock and the aftershock records at three stations situated at different azimuths, as well as the respective ASTFs. Azimuthal variation in pulse width of the ASTFs is due to directivity of the rupture process. The duration of the ASTF, T_a, can be expressed as : $T_a = T_0 - \Gamma\Delta$, where T_0 is the true duration of the rupture process and Δ the horizontal rupture length. The directivity factor Γ is given by: $\Gamma = \cos(\theta - \theta_0) / c$, where c is the phase velocity, θ is the azimuth of the station, and θ_0 the azimuth of direction of the rupture propagation. The phase velocity is taken as 3.8 km/sec for Rayleigh waves and 4.5 km/sec for Love waves. These are approximate values for the dispersive surface waves, but are sufficient for recovering first-order features of large ruptures. Each azimuth θ_0 is investigated systematically to estimate Δ and T_0. The preferred azimuth corresponds to the rupture direction producing the best linear correlation coefficient (see Figure 3, insets). Figure 3 shows T_a for each ASTF as a function of Γ, for the value of θ_0 which gives the best linear regression. Results are extremely clear : both the aftershock and the foreshock show a predominant unilateral rupture, propagating toward $280-290°$. Larger variation in the foreshock results is due to a lower signal-to-noise ratio. Using the aftershock results, the duration corresponding to $\Gamma = 0$, i.e. the STF duration without directivity effect T_0, is 62 ± 4 s. The slope of the regression line gives us a rough estimation of the rupture length of about 125 km.

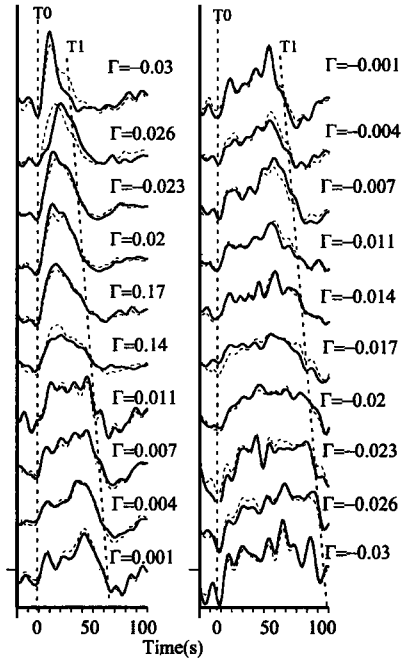


Figure 4. Stacked STF in bins of 0.03 sec/km (continuous line). Dashed lines represents the predicted ASTF obtained by IRT. T_0 and T_1 show beginning and end of the ASTF. Positive and negative Γ correspond to the station azimuths less than and more than 90° from the direction of rupture propagation, respectively.

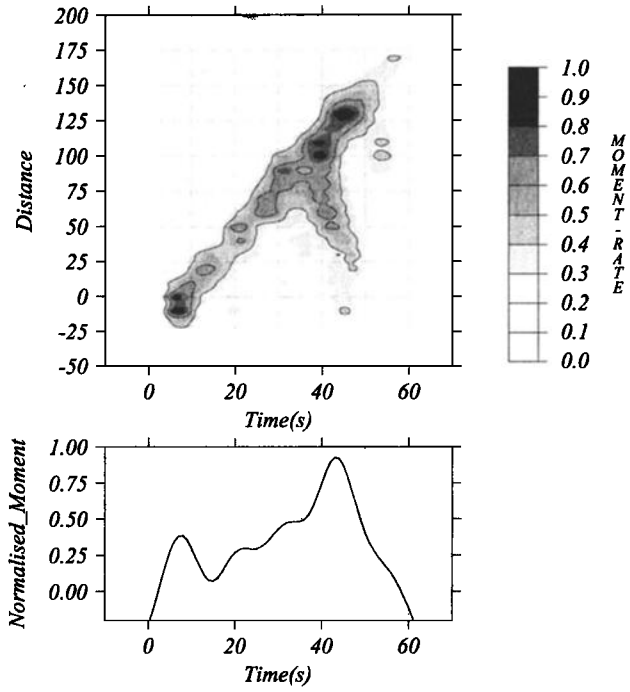


Figure 5. Moment rate density distribution in time and space obtained by an inverse Radon transform (IRT) at 10 sec. Values of the moment rate density larger than 0.2 are shaded and the ones larger or equal to 0.4 are contoured.

Spatio temporal imaging of the Rupture Process

The observed apparent source time functions are the Radon transform of the moment rate density [Ruff, 1987]. In order to image the rupture process in space and time, we follow Velasco *et al.* [1996] and perform an inverse Radon transformation (IRT) of the ASTFs using a conjugate gradient approach to invert a discretized version of the Radon Transform. Although we impose a 1D rupture propagation along the direction of main directivity, we make no assumption about the rupture velocity.

Apparent source time functions are low-pass filtered at 10 s and stacked in Γ bins of 0.03 s/km. In order to minimize local effects due to small differences in the focal mechanism of the mainshock and the EGF, the signals are normalized by the total moment at each Γ bin. Figure 4 shows the predicted ASTFs (dashed lines), at each Γ bin, after applying an IRT on the observed ASTF (continuous lines) assuming an azimuth of 290°.

The normalized moment rate, obtained from the IRT, is plotted in Figure 5 as a function of distance from the epicenter and time after the rupture initiation. Only positive amplitudes are shown, the side-lobes in the time functions produce troughs in the image, but for clarity, we show only the positive values in the reconstruction. Three regions that contribute highly to the moment rate (larger than 0.8) can be identified: near the epicenter, and at distances of 100 km and 130 km from the epicenter. The total rupture length is estimated as 150 ± 10km (marked LL' on Figure 1). This length is slightly larger than that estimated from the discrete directivity analysis described in the previous section. Two reasons may explain this minor

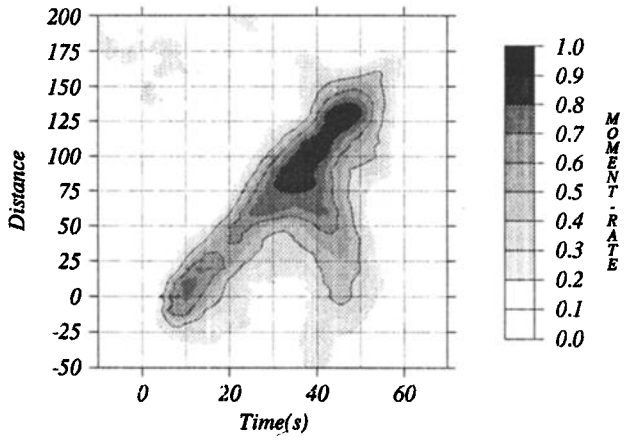


Figure 6. Moment rate density distribution obtained by IRT at 20 sec.

discrepancy. First, the IRT, like all tomographic methods, tends to streak and broaden features in the image. The more likely cause in this case is that the IRT results are less sensitive to picking problems associated with side-lobes in the time functions that can produce large uncertainties, especially for broad, long-duration ASTFs observed in directions opposite the rupture direction.

The regions of high moment rate show a linear trend and suggest a predominant unilateral rupture propagation. The rupture velocity obtained from the slope of this main feature gives an average value of 2.8 km/s. A region of relatively high moment rate deviates from the linear trend between 25 km and 80 km. This may indicate a significant updip or downdip rupture propagation, or a second episode of slip along that segment of the fault. A 2D inversion is needed to clarify this point. The predicted source time function, perpendicular to the rupture direction, is also presented in Figure 5. It shows two main temporal episodes of energy release, the first one immediately after the initiation of the rupture, and a larger one, 45 s later. Figure 6 represents the IRT obtained from data low-pass filtered at 20 s. Note that the main features of the rupture are similar to those shown in Figure 5.

Discussion and Conclusion

Our analysis shows that the rupture during the 1995 Colima-Jalisco earthquake propagated unilaterally towards N70°W for a length of about 150 km. We note that this rupture direction differs by about 20° from the azimuth of the trench, which is about N50°W. The estimated rupture length is in rough agreement with the total length of about 170 km of the aftershock area, mapped from data provided by portable and permanent local seismic networks [Pacheco *et al.*, 1996].

The retrieved source-time function shows two main pulses of moment release. The first pulse occurs soon after the rupture initiation and is located near the epicenter, while the second pulse, which is larger, acts about 45 s later and is situated at a distance of 100 to 130 km. The duration of the source is $\sim$ 62 s. This shape of the source time function is somewhat similar to those reported by M. Kikuchi (personal communication, 1995) and the University of Michigan Group, with the difference that, in the latter two studies, the larger moment release occurs at the beginning of the rupture rather than later. The fact that both studies were based on body waves instead of surface waves could explain the difference with our result which may extract better the low-frequency content of the source. Our source time function is in better agreement with the results of Melbourne *et al.* [1997] who inverted GPS measurements carried out in the states of Jalisco and Colima seven month before and one week after the earthquake. They too report two distinct patches of slip: one near the epicenter and another one, with much larger slip, occurring about 100 km NW of the epicenter.

Acknowledgments. We thank IRIS Data Management Center and GEOSCOPE for access to their data. We also thank H. Houston and two anonymous reviewers for their suggestions. The research was partially funded by DGAPA, UNAM projects IN100795 and IN102494, and by European Union (grant CI1-CI92-0036).

References

Ammon, C.J., A.A. Velasco, and T. Lay, Rapid estimation of rupture directivity: Application to the 1992 Landers (Ms=7.4) and Cape Mendocino (Ms=7.2) California earthquakes, *Geophys. Res. Lett.*, 20, 97–100, 1993.

DeMets, C., and D.S. Wilson, Relative motions of the Pacific, North American, and Cocos plates since 0.78 Ma, *J. Geophys. Res.*, 102, , 1997.

Eissler, H.K., and K.C. McNally, Seismicity and tectonics of the Rivera plate and implications for the 1932 Jalisco, Mexico earthquake, *J. Geophys. Res.*, 89, 4520–4530, 1984.

Hartzell, S., Earthquakes aftershocks as Green's functions, *Geophys. Res. Lett.*, 5, 1–4, 1978.

Kostoglodov, V., and W. Bandy, Seismotectonic constraints on the rate between the Rivera and North American plates, *J. Geophys. Res.*, 100, 977–990, 1995.

Melbourne, T., I. Carmichael, C. DeMets, K. Hudnut, O. Sanchez, J. Stock, G. Suarez, and F. Webb, The geodetic signature of the M8.0 Oct. 9, 1995, Jalisco subduction earthquake, *Geophys. Res. Lett.*, 24, 715–718, 1997.

Pacheco, J.F., S.K. Singh, G. Reyes, J. Domíngez, A. Hurtado, C. Ramírez, L. Quintanar, Z. Jiménez, J. Yamamoto, C. Gutiérrez, M.A. Santoyo, M. Guzmán, The October 9, 1995, Colima-Jalisco, Mexico earthquake (Mw 8) : An aftershock study and a comparison of this earthquake with those of 1932, *Geophys. Res. Lett.*, accepted, 1997.

Ruff, L., 1987, Tomographic imaging of seismic sources, *in* Nollet, G., Ed., Seismic Tomography: D. Reidel, Norwell, Mass., 339–366.

Singh, S.K, L. Ponce, and S.P. Nishenko, The great Jalisco Mexico, earthquake of 1932: Subduction of the Rivera plate, *Bull. Seism. Soc. Am.*, 75, 1301–1313, 1985.

Velasco, A.A., C.J. Ammon, and T. Lay, Empirical Green's function deconvolution of broadband surface waves: rupture directivity of the 1992 Landers, California (Mw=7.3), earthquake, *Bull. seism. Soc. Am.*, 84, 735–750, 1994.

Velasco, A.A., C.J. Ammon, T. Lay, and M. Hagerty, Rupture process of the 1990, Luzon, Philippines (Mw=7.7) earthquake, *J. Geophys. Res.*, in press, 1996.

F. Courboulex , S.K. Singh and J.F. Pacheco, Instituto de Geofísica, UNAM, CU, Coyoacan, 04510 México, D.F., Mexico. (e-mail: courboul@faille.unice.fr; krishna@ollin.igeofcu.unam.mx;javier@ollin.igeofcu.unam.mx

C.J. Ammon, Department of earth and atmospheric sciences, St Louis University, 3507 Laclede Ave., St. Louis, MO 63103.(e-mail:ammon@mantle.slu.edu)

(Received November 6, 1996; accepted January 24, 1997.)

Bulletin of the Seismological Society of America, Vol. 87, No. 4, pp. 999–1010, August 1997

The 14 September 1995 (M = 7.3) Copala, Mexico, Earthquake: A Source Study Using Teleseismic, Regional, and Local Data

by F. Courboulex, M. A. Santoyo, J. F. Pacheco, and S. K. Singh

Abstract We analyze source characteristics of the 14 September 1995, Copala, Mexico, earthquake (M = 7.3) using teleseismic, regional, and local seismograms. In the analysis of the teleseismic and the regional seismic waves, we apply the empirical Green's function (EGF) technique. The recording of an appropriate aftershock is taken as the EGF and is used to deconvolve the mainshock seismogram, thus obtaining an apparent far-field source-time function at each station. The deconvolution has been done using surface waves. For teleseismic data, we apply a spectral deconvolution method that enables us to obtain 37 apparent source-time functions (ASTFs) at 29 stations. In the analysis of the regional broadband seismograms, we use two different aftershocks as EGF, and the deconvolution is performed in the time domain with a nonlinear method, imposing a positivity constraint, and the best azimuth for the directivity vector is obtained through a grid-search approach.

We also analyze two near-source accelerograms. The traces are inverted for the slip distribution over the fault plane by applying a linear inversion technique. With the aid of a time-window analysis, we obtain an independent estimation of the source-time function and a more detailed description of the source process.

The analysis of the three datasets permits us to deduce the main characteristics of the source process. The rupture initiated at a depth of 16 km and propagated in two directions: updip along the plate interface toward 165° N and toward 70° N. The source duration was between 12 and 14 sec, with the maximum of energy release occurring 8 sec after the initiation of the rupture. The estimated rupture dimension of 35 × 45 km is about one-fourth of the aftershock area. The average dislocation over the fault was 1.4 m (with a maximum dislocation of 4.1 m located 10 km south of the hypocenter), which gives roughly 1 MPa as the average static stress drop.

Introduction

Along the Mexican subduction zone, the plate boundary between 98.2° W and 99.5° W, called the Ometepec segment, has been the site of frequent large earthquakes (Nishenko and Singh, 1987a). In the last 100 years, large earthquakes have occurred here in 1890 (M 7.2), 1937 (M 7.5), 1950 (M 7.3), and 1982 (M 6.9 and 7.0). Recently, two large earthquakes occurred in the region: the Copala earthquake of 14 September 1995 (M 7.3) and the Pinotepa Nacional earthquake of 25 February 1996 (M 7.1). The location of these events are shown in Figure 1.

The Ometepec segment is bracketed by the Oaxaca segment to the SE and the Guerrero segment to the NW (Fig. 1, inset). The seismicity of Oaxaca is characterized by the occurrence of characteristic earthquakes of magnitude close to 7.6 (Singh *et al.,* 1983), with relatively short and, apparently, quasi-periodic recurrences (Singh *et al.,* 1981). The Guerrero segment, which is presently a mature seismic gap (Singh *et al.,* 1982; Anderson *et al.,* 1989), has been the site of large/great earthquakes (e.g., 1845, M 7.9; 1907, M 7.7; 1957, M 7.5; 1989, M 6.9). Note that the 1907 earthquake seems to have ruptured parts of both the Guerrero and the Ometepec segments.

Earthquakes in Ometepec have been studied by Nishenko and Singh (1987a, 1987b), Beroza *et al.* (1984), Gonzalez-Ruiz and McNally (1988), Astiz and Kanamori (1984), and Zuñiga *et al.* (1993). Based on the seismicity of the region, a variable rupture mode has been suggested for this segment (Nishenko and Singh, 1987a). It should be noted, however, that the locations of the mainshocks and their aftershocks are poorly known with the exception of the 1982 doublet. Because of the relatively small expected rupture areas of the events in the Ometepec segment and the errors in their locations, we only have a blurred view of the rupture process in the region. In this context, the analysis of the source process of the recent earthquakes becomes important.

Since the deployment of the Guerrero Accelerograph

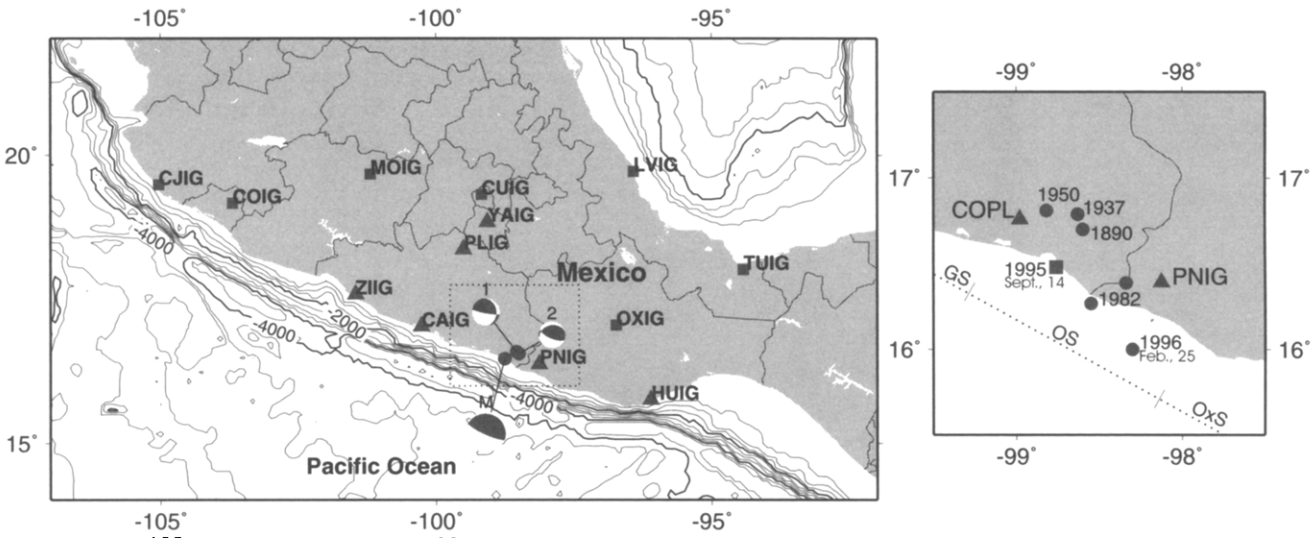


Figure 1. Map showing locations and focal mechanisms of the 14 September Copala earthquake (M) and two of its aftershocks (1,2) used as empirical Green's functions. Filled squares and triangles are broadband seismic network of Mexico. The data from stations marked by solid triangles were used in this study. Inset shows locations of large earthquakes in the region during the last 100 years. Triangles are stations whose strong-motion recordings are used in this study. GS, the Guerrero segment; OS, the Ometepec segment; OxS, the Oaxaca segment.

Array in 1985, all significant earthquakes along the Guerrero and Michoacan coast of the Mexican subduction zone have produced strong-motion recordings. Analyses of these data have greatly improved our knowledge of the source characteristics of Mexican earthquakes. The 14 September 1995 Copala earthquake is the first large event in Mexico that was well recorded not only by the various accelerometric networks of Mexico (see Anderson *et al.,* 1995) but also by the newly installed broadband seismological network (Fig. 1). The location of the mainshock from local and regional data (16.48° N, 98.76° W, H = 16 km) and its focal mechanism, as reported in the Harvard CMT catalog (strike 289°, dip 11°, slip 85°), is consistent with a shallow, reverse faulting interplate earthquake along the Mexican subduction zone.

In this study, we use the teleseismic and the regional broadband data, as well as two near-source strong-motion recordings to study the source process of the Copala earthquake. In the analysis of the teleseismic and the regional broadband data, the characteristics of the source are studied by deconvolution of the mainshock with one or more empirical Green's functions (EGFs). The two near-source recordings are inverted to obtain the slip history on the fault plane.

Source Analysis Using Empirical Green's Functions

Empirical Green's Function Method

Since Hartzell (1978) showed the feasibility of using small earthquakes as EGFs, this approach has gained increasing acceptance in the analysis and simulation of earthquake records (Irikura, 1983; Wennerberg, 1990; Mori and Hartzell, 1990). The advantage of the use of an EGF as compared to a theoretical Green's function comes from the fact that path and site effects in the propagation of seismic waves, which are often poorly known, are automatically included.

The method consists of deconvolving the mainshock seismogram by the recording of a smaller event chosen as EGF, thereby obtaining the far-field signature of the source process (Mueller, 1985). This signal, which depends on the azimuth of the station with respect to the directivity of the rupture, and the wave type selected for deconvolution, is called the apparent source-time function (ASTF). It is also called the relative source-time function (RSTF), because its amplitude is relative to the seismic moment of the small event.

We pursue this approach to study the 14 September 1995 Copala event using separately teleseismic and regional broadband data. In this analysis, we use only the information contained in surface waves. Because of their low speed, the directivity effect is more pronounced in the surface waves than in the body waves. One advantage of the EGF deconvolution method is that it extends the study of teleseismic surface waves to periods of about 5 to 10 sec, whereas classic surface-wave analysis is limited to periods larger than about 135 sec (Velasco *et al.,* 1994).

Teleseismic Data Study

Among the aftershocks of the 1995 Copala event (C. Gutierrez, personal comm., 1996), we chose the largest one as an empirical Green's function. It was located, using local

data, 28 km from the mainshock hypocenter (Table 1), and its focal mechanism is similar to that of the main event (Fig. 1). Many other aftershocks of smaller magnitude may have qualified as empirical Green's functions, but they were not well recorded at teleseismic distances.

Our analysis follows the method developed by Ammon *et al.* (1993) and Velasco *et al.* (1994). We window Rayleigh (R1) and Love (G1) waves on the vertical and the transverse components using group velocities between 4.5 and 2.0 km/sec for R1 and 5.3 to 2.1 km/sec for G1. The mean of each seismogram is removed and a Hanning window is applied to taper the seismogram near the ends. The deconvolutions are performed in the frequency domain using a water level method (Helmberger and Wiggins, 1971; Ammon *et al.,* 1993). Although the spectral deconvolution technique does not always give results that are easy to analyze in terms of source-time function (Sipkin and Lerner-Lam, 1992; Zollo *et al.,* 1995; Courboulex *et al.,* 1996), the method is fast, and this is an advantage when analyzing a large dataset.

Because of the relatively small magnitude of the available EGF ($M = 5$), the signal-to-noise ratio was low at some stations. Before the analysis, we visually examined the records and discarded the noisy ones. We selected the best 29 stations (Fig. 2), which provided us with 36 ASTFs. These ASTFs show a simple unipolar shape with different durations (Table 2).

For a unilateral rupture propagation, the duration Ta of the ASTF at a given station can be written in a linear form:

$$Ta = T_0 - \Gamma\Delta, \tag{1}$$

where T_0 represents the real duration of the source process, Δ the horizontal length of the rupture, and Γ the directivity factor, defined as

$$\Gamma = \cos(\theta - \theta_0)/c, \tag{2}$$

where c is the phase velocity of the wave type and θ and θ_0 are the azimuth of the station and the rupture propagation, respectively. Each azimuth θ_0 is investigated systematically to estimate Δ and T_0. The value of θ_0 that gives the best linear correlation coefficient is taken as the direction of rupture propagation. In our case, this value of θ_0 is N160°E (see top right of Fig. 3). The correlation coefficient of 0.65 is rather low as compared to the values reported in some other studies (e.g., Colombian earthquake of 1992 by Ammon *et al.,* 1994; Colima-Jalisco event of 1995 by Courboulex *et al.,* 1997). This can be due to the fact that the EGF is relatively small for teleseismic studies, with low signal-to-noise ratio, and/or due to the inadequacy of unilateral rupture propagation as the best model for this event.

ASTF duration, Ta, is plotted in Figure 3 as a function of Γ (with θ_0 = N160°E). From this figure, we obtain the length of the rupture Δ (which is given by the slope of the regression line) of 13 ± 3 km and the duration of the source-time function, Ta at $\Gamma = 0$ (i.e., without directivity effect), of about 12 sec. Because of the large dispersion in the data, our slope estimate of the regression line, and hence Δ, is not reliable. The estimate of the source duration, however, is less sensitive to the uncertainty in the slope and can be taken as a first approximation of the source duration.

Regional Broadband Data Analysis

In order to obtain more information about the source process, we use regional data from the new Mexican broadband seismic network (Fig. 1). Regional seismograms are well known to present large complexities due to path effects. To avoid these propagation problems, we again use the empirical Green's function approach.

The 14 September 1995 event gave rise to many aftershocks with $M \geqq 4.5$. We selected those aftershocks as possible EGFs that met the following desirable requirements:

1. Large signal-to-noise ratio.
2. Roughly the same location and focal mechanism as the mainshock.

Additionally, we required that the selected EGFs be recorded at station HUIG. This is important since HUIG is the only regional station in the SE quadrant (Fig. 1). Only two aftershocks, both of which occurred on 16 September, fulfilled these requirements. These two aftershocks, henceforth called EGF1 and EGF2, have magnitudes of 5.0 and 4.8, respectively. We note that EGF1 is the event used in the teleseismic study of the mainshock. The epicenters of these two events were determined using near-source strong-motion and nearby broadband recordings (Table 1). The moment tensor and centroid depths of the aftershocks were obtained from

Table 1
Event Source Parameters

Event	Date	Time (GMT)	Latitude* (deg)	Longitude* (deg)	Depth* (km)	Moment† (N.m)	Magnitude M_w
Mainshock	14 Sept. 1995	14:04:30.1	16.48	−98.76	16.	$8.9\ 10^{19}$	7.3
EGF1	16 Sept. 1995	3:30:5.2	16.61	−98.54	20.	$3.37\ 10^{16}$	5.
EGF2	16 Sept. 1995	22:19:1.3	16.57	−98.49	25.	$1.75\ 10^{16}$	4.8

*Epicenters and depths from focal and regional data.

†Moment of the mainshock from Harvard CMT catalog. Moment of the aftershocks determined from CMT inversion of regional broadband seismograms (see text).

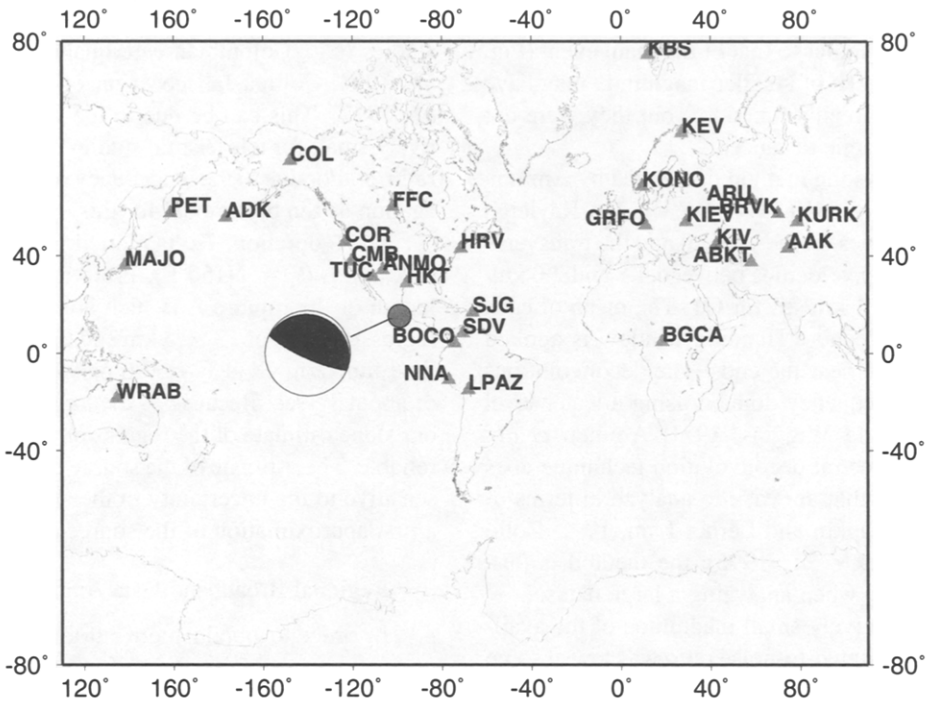


Figure 2. Location of the 14 September 1995 Copala earthquake and its focal mechanism reported in the Harvard CMT catalog. Teleseismic stations whose data are used in the study are shown by triangles.

the inversion of the regional broadband records (Table 1) using an algorithm developed by Randall *et al.* (1995). For this inversion, observed seismograms were filtered between 20 and 100 sec, as the long-period waves are less sensitive to unknown details of the crustal structure. The crustal structure was taken from Campillo *et al.* (1996). The moment tensor solutions were obtained for a suite of depths. The lowest rms residuals were found for depths close to those reported in the hypocenter locations, between 15 and 25 km. Both events show a shallow-angle reverse fault, striking parallel to the Middle American trench, similar to the reported mechanism of the mainshock in the Harvard CMT catalog. Small differences in the mechanisms of these two aftershocks as compared to the main event (Fig. 1) may partly be real and partly due to unknown crustal structure, lateral variations of wave velocities in the crust, surface-wave multipathing, and noise in the records.

Apparent Source-Time Functions from the Regional Data

Ideally, the deconvolution should be performed independently on *P*, *S*, and surface waves, as it increases the amount of information. In our case, however, the stations along the coast are almost nodal for *P* waves and close to the nodal plane for Rayleigh waves. Moreover, the *S* wave is difficult to isolate since it arrives very close to the arrival of surface waves. For these reasons, we only study surface waves and focus on Love waves for the stations that are nodal for Rayleigh waves. The five available stations we use are shown on Figure 1 by triangles (PLIG, YAIG, ZIIG, CAIG, and HUIG). An example of a displacement seismogram is shown in Figure 4 for the mainshock and the two aftershocks at station PLIG.

In the analysis, we first window seismograms around the Airy phase for Rayleigh and Love waves (Campillo *et al.,* 1996; Shapiro *et al.,* 1997) and then deconvolve the mainshock signal successively by the two EGFs. As the number of stations is small and we seek accurate ASTFs, we use a time-domain deconvolution with positivity constraint based on simulated annealing (Courboulex *et al.,* 1996). The time discretization used in the deconvolution is 1 sec, which is close to the corner frequency of the EGFs. We deconvolve both Love and Rayleigh waves at stations PLIG, HUIG, and YAIG. The ASTFs obtained are very similar for both types of waves. For simplicity, in Figure 5, we only show the ASTFs obtained from the analysis of Love waves. In this figure, the signals have been smoothed with B_splines. The ASTFs show a strong directivity effect. This effect is most spectacular at HUIG where we obtain a simple ASTF with a duration of 9 sec. At YAIG and PLIG, the ASTF duration is close to 17 sec, and the shape of the signal suggests two different episodes of rupture in time. We note that the ASTFs obtained using the two different EGFs are very similar.

Integrating the pulses under the ASTFs, we obtain an average value of 1350 for EGF1 and 3600 for EGF2. As the seismic moments of EGF1 and EGF2 are 3.37×10^{16} and 1.75×10^{16} N-m, respectively, the corresponding estimates for the moment of the mainshock are 4.55×10^{19} and 6.3

Table 2
Duration of the ASTFs Obtained by Spectral Deconvolution

Station Name	Type of Wave	Azimuth (deg)	Distance (deg)	Duration of the ASTF (sec)
AAK	R1	5.7606	120.84	18.83
ABKT	R1	21.364	121.68	19.66
ADK	R1	319.76	69.740	14.33
ANMO	G1	340.96	19.613	16.9
ANMO	R1	340.96	19.613	15.39
ARU	R1	12.785	104.91	17.2
BGCA	G1	76.383	114.32	17.6
BGCA	R1	76.383	114.32	13.92
BOCO	R1	113.26	26.940	11.87
BRVK	R1	6.9921	110.10	15.97
CMB	G1	322.70	28.654	15.56
CMB	R1	322.70	28.654	19.65
COL	G1	337.80	58.417	14.33
COL	R1	337.80	58.417	18.84
COR	R1	328.72	34.795	14.33
FFC	G1	357.02	38.232	15.56
FFC	R1	357.02	38.232	15.97
GRFO	R1	37.602	89.927	13.92
HKT	R1	10.928	13.677	17.2
HRV	R1	36.327	34.846	11.05
KBS	R1	10.659	77.809	17.2
KEV	R1	16.438	86.034	16.79
KIEV	R1	30.498	99.088	14.74
KIV	R1	28.654	110.30	17.2
KONO	R1	28.934	84.875	14.33
KURK	R1	1.7828	113.04	17.2
LPAZ	R1	135.62	44.453	11.87
MAJO	R1	315.71	104.68	15.15
NNA	R1	141.14	35.671	12.69
PET	R1	323.66	84.322	14.74
SDV	G1	101.95	28.475	13.51
SDV	R1	101.95	28.475	9.82
SJG	R1	82.180	31.192	9.41
TUC	G1	327.56	19.130	14.76
TUC	R1	327.56	19.130	17.73
WRAB	R1	257.57	129.56	13.1

$\times 10^{19}$ N-m. These values are lower than the mainshock moment reported in the Harvard CMT catalog (8.9×10^{19} N-m). This may be due to the small difference in the focal mechanisms of the two EGFs and the mainshock or due to an underestimation of the moments of the EGFs. When the ASTFs are reconvolved with the EGFs and compared with the observed seismograms of the mainshock, an excellent agreement between the synthetic and the observed records is found (Fig. 6).

Directivity Analysis

Knowing the ASTF duration at the five stations using Love waves, we perform a systematic search of the best directivity vector for all the possible strikes along the fault plane. We take an average value of 3.6 km/sec for the Love waves phase velocity (Gomberg *et al.*, 1988). The rupture velocity is varied between 2 and 3 km/sec (step 0.1 km/sec) and the rupture length between 20 and 60 km (step of 1 km). Only a unilateral rupture propagation is allowed. We obtain

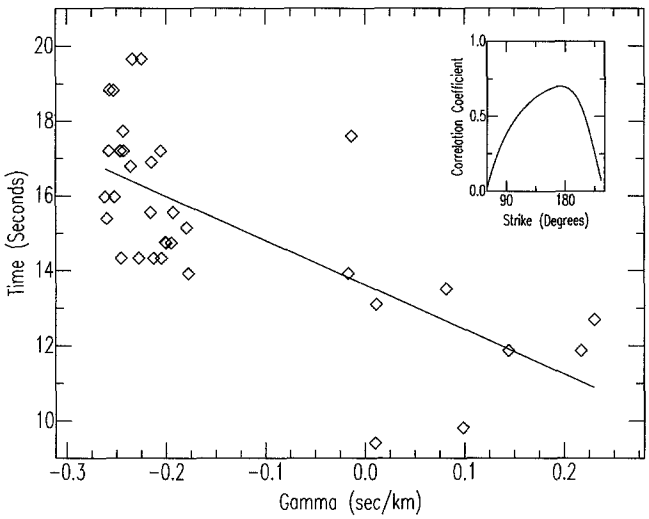


Figure 3. Directivity analysis from the teleseismic data. The figure shows a plot of ASFT duration (diamonds) as a function of the directivity factor Γ, for the best value of the directivity (165° N). Top-right part of the figure shows that the best correlation value is obtained for a directivity toward 165° N.

the best fit with a rupture propagation direction of N165°E, a length of 25 km, and a rupture velocity of 2.2 km/sec. If we reconstruct the STF using those parameters and the ASTF obtained on stations PLIG and YAIG, we obtain a STF duration of about 12 sec with two episodes of energy release as shown in Figure 7. It is important to note that a length of 25 km represents a lower bound. The upper bound would be the double of this value, that is, 50 km, corresponding to a pure bilateral rupture propagation. The strong directivity observed in the regional data, however, shows that this hypothesis is not viable for this earthquake. Even so, a fault length greater than 25 km is likely.

Source Inversion for the Slip Distribution Using Near-Source Data

In this section, we compliment the study of the source-time function and the directivity, presented above, by mapping the slip distribution on the fault plane through a linear inversion of near-source strong-motion data.

Data

We only use the data recorded by the two near-source accelerographs, located at Copala (COPL, $\Delta = 26$ km, $\phi = 302°$) and Pinotepa Nacional (PNIG, $\Delta = 68$ km, $\phi = 98.7°$) (Fig. 1, inset). The earthquake was recorded by many other accelerographs (see Anderson *et al.*, 1995). Although several of these were located at epicentral distances between 60 and 200 km, their azimuth was similar to COPL. For this reason, we ignored data from stations other than COPL and PNIG.

The accelerograms from the two stations were integrated to obtain the velocity and displacement seismograms.

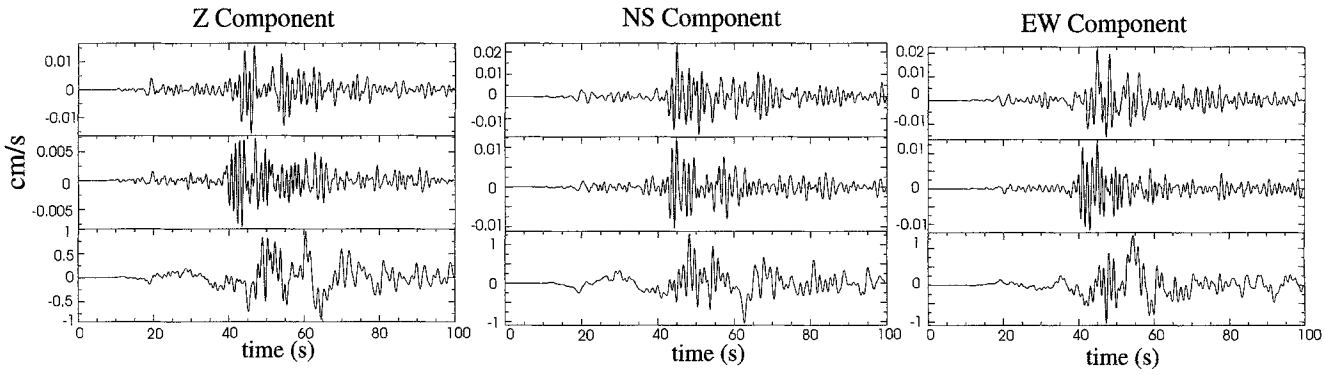


Figure 4. Regional seismograms of mainshock and two aftershocks used as empirical Green's functions (EGF1 and EGF2) recorded at station PLIG (Fig. 1). Traces are low-pass filtered at 1 sec.

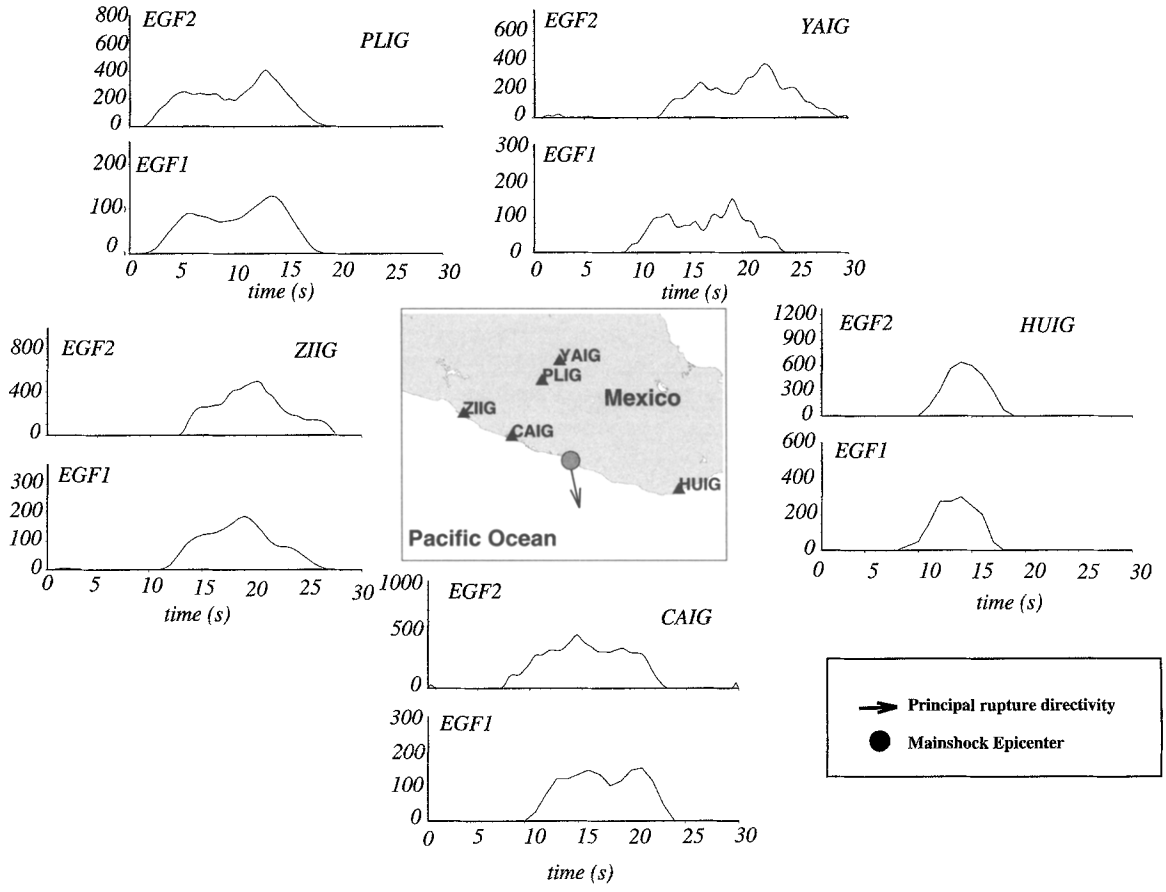


Figure 5. Result of deconvolutions of the mainshock seismogram by two different aftershocks used as empirical Green's function (EGF1 and EGF2) at five broadband regional stations. Deconvolution has been performed in the time domain with positivity constraint. Love-wave results are shown. Solid arrow indicates main rupture directivity (N165°E) obtained by a grid-search method. Mainshock is represented by a black dot.

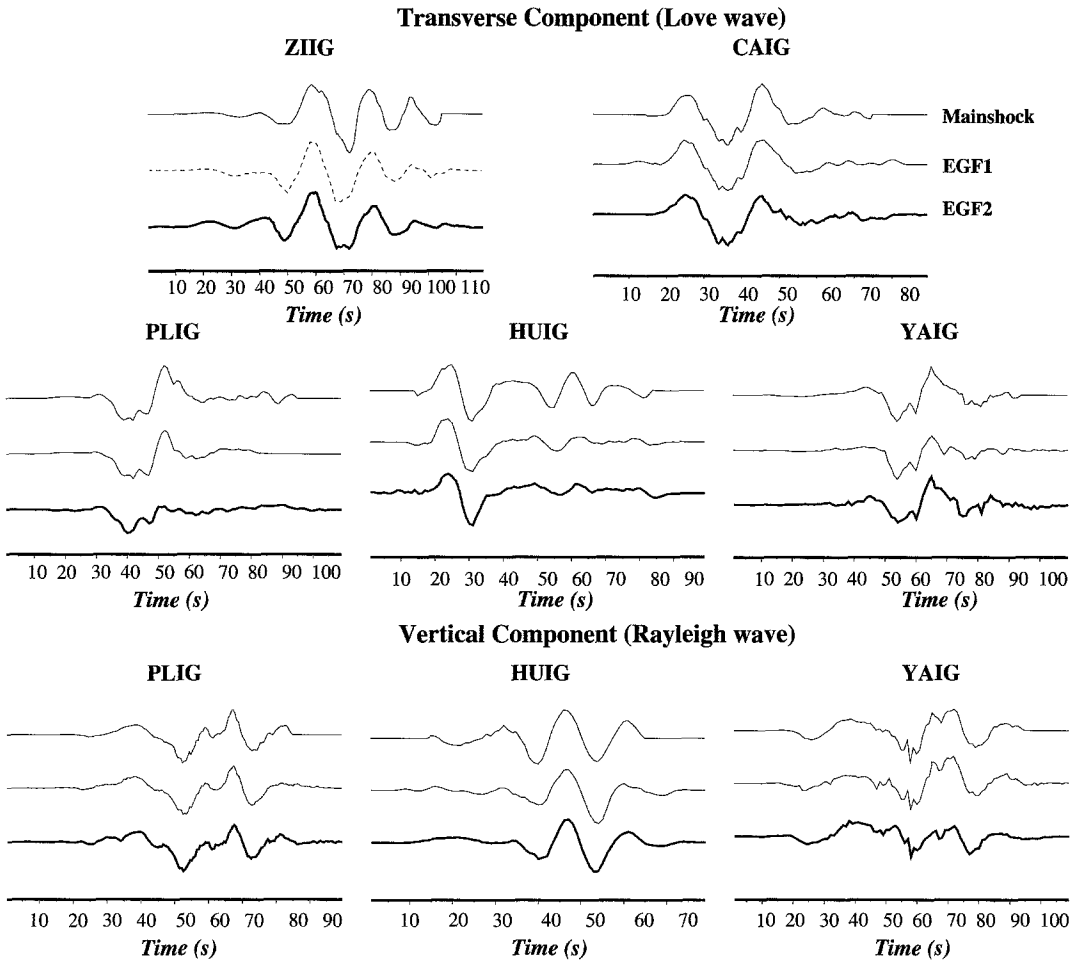


Figure 6. Comparison of observed seismograms of the mainshock (thin lines) with synthetic seismograms obtained by the convolution of the ASTF time series with the two EGFs (dashed lines for EGF1 and bold line for EGF2).

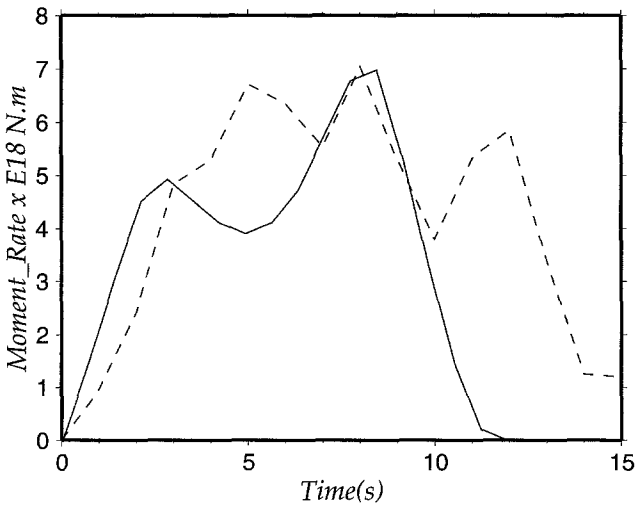


Figure 7. Source-time functions obtained from the analysis of regional broadband data (continuous line) and near-source strong-motion data (dashed line).

For the integrations, we applied a modified version of the technique proposed by Iwan *et al.* (1985). The integrated time series were lowpass filtered using a Butterworth filter, at 0.5 Hz, thereby, in the case of the displacements, maintaining the static field. In all inversions, we use the first 40 sec of the signal; this duration is sufficient to retrieve the total source process characteristics.

Inversion Method

We represented the fault by a rectangular dipping plane embedded in a horizontally layered structure. The strike (289°) and dip (11°) of the fault plane was taken to be the same as that of the mainshock focal mechanism reported in the Harvard CMT catalog. However, the Harvard mechanism was not consistent with the polarities of two of the displacement components at COPL, and at PNIG. After some tests, we found that by changing the rake of 85° reported in the Harvard CMT solution to 75°, the polarities at these stations could be fit. In all further computations, we took the rake as

75°. The fault plane was subdivided into 165 subfaults of equal size (5 × 5 km), setting a point source in the center of each subfault. The crustal structure used in modeling the near-source data, given in Table 3, is one that was found adequate for the nearby region of San Marcos (Santoyo, 1994).

We computed synthetic seismograms using the discrete wavenumber method (Bouchon and Aki, 1977; Bouchon 1979). The effect of rupture velocity was included by giving a time lag to the synthetic Green's functions. We assumed a circular rupture propagation with a constant rupture velocity V_R. In the inversion, we tested different values of V_R between 2.3 and 2.8 km/sec. The best-fit solution was found for $V_R = 2.5$ km/sec. Given this value of V_R, the size of the subfaults, $\Delta x = 5$ km, and the maximum frequency, f_{eff}, of 0.5 Hz that we aim to resolve, we chose for each subfault a trapezoidal source-time function with a duration of 3 sec with an equivalent moment release of a 2-sec boxcar. This allows us to generate a continuous, smooth rupture, in accordance with the equation $1/f_{\text{eff}} \geqq T_i \geqq \Delta x/V_R$.

Synthetic and observed seismograms constitute an overdetermined system of linear equations of the form $\mathbf{Ax} = \mathbf{b}$, where $\mathbf{A}$ is a 2D matrix of synthetics, $\mathbf{b}$ is a vector containing the observed seismograms, and $\mathbf{x}$ is a vector of the subfault dislocation weights required to reproduce the observed data vector $\mathbf{b}$. We solve $\mathbf{x}$ using a non-negative least-squares inversion scheme (Lawson and Hanson, 1974) that imposes a positivity constraint on the solution. We impose additional stability to the solution by setting a smoothly varying spatial distribution, as explained by Mendoza and Hartzell (1988).

Resolution Analysis

With data from only two stations, COPL and PNIG, how well can we retrieve the slip history on the fault? To answer this question, we performed two synthetic tests for the same configuration of the fault plane and the station locations as used in the inversion of near-source data. In the first one, we computed synthetic seismograms using a constant slip distribution over a rectangular area of 20 × 30 km centered at the hypocenter and zero slip over the rest of the fault. We added a white noise of 20% of the maximum amplitude to the signals of each seismogram and filtered it with a 2-sec low-pass Butterworth filter. These seismograms were then inverted for slip distribution using the same space discretization as in the real case. Whereas the inversion without noise gave us a perfect result, that is, a constant patch of slip over the 20 × 30 km area, the inversion of the data contaminated with the noise created some artificial high and low slip zones. These zones, however, were located over those parts of the fault plane that were more than 35 km away from COPL. Because PNIG is relatively far from the epicenter (68 km), this station provides a poor constraint to the source. Only COPL, which is 25 km from the epicenter, is sensitive to the details of the slip, especially in the regions close to the fault. This synthetic test shows that we may expect a good resolution over the fault plane up to 30 to 35 km away from COPL. At farther distances, care is warranted in interpreting the results of the inversion.

In the second test, we generated synthetic seismograms corresponding to the slip distribution obtained from the inversion of the real data. We inverted these synthetic seismograms (a) without adding any noise and (b) after adding 20% noise. As expected, the inversion (a) gave back the same slip distribution that was used in the generation of the synthetics. Inversion (b) resulted in a slightly different pattern of slip distribution, with a difference in the amplitudes of about 20% to 30%. The moment release also did not change appreciably. The changes were smaller than the changes found in the first test. We believe that the first test is less biased than the second one because the slip obtained from the inversion of the real data is already affected by the station distribution. It is, therefore, not surprising that the inversion based on synthetics from this slip distribution, along with 20% noise, returns nearly the same slip.

Slip Inversion

Inversions were performed on velocity as well as displacement records. Although the sense and the amplitude of the static displacements at the two stations, obtained from the integration, are reasonable for shallow-dipping reverse faulting, we cannot be certain of their accuracy. For this reason, we performed the inversion of these traces, including the static field in one case and filtering it in another. We also inverted velocity waveforms. The general pattern of the slip history on the fault plane were similar in all inversions. Below we present results from the inversion of displacement traces including the zero-frequency component.

Table 3
Crustal Structure*

Depth (km)	*P*-wave velocity (km/sec)	*S*-wave velocity (km/sec)	Density (g/cm^3)	*Q* for *P*	*Q* for *S*
0.0	5.0	2.88	2.50	400	200
5.0	6.1	3.57	2.76	400	200
20.0	6.8	4.03	2.84	400	200
25.0	7.4	4.25	2.90	400	200
35.0	7.9	4.40	3.31	800	400

*From Santoyo (1994).

We first performed the inversion without any spatial smoothness constraint. Then, we searched for a value of smoothness that resulted in a smooth distribution of the slip and, at the same time, in a good agreement between the observed and synthetic traces. This is illustrated in Figure 8, which shows that the fit is good, except for the static level, which is not entirely reproduced by the synthetics.

The final slip distribution (Fig. 9) shows two branches: one aligned toward the south-southeast and the other in the east direction. It covers an area of about 35 × 45 km. It is clear from this figure that the area covered by the aftershocks is much bigger than the one described by the mainshock high-slip zone. There is another patch SW of the hypocenter that also contributes to the total moment release of 7.31×10^{19} N-m. The maximum slip on the fault of 4.12 m occurs 10 km south (updip) of the hypocenter in the southern branch, approximately 8 sec after nucleation. The average slip is 1.4 m, and the average static stress drop, $\Delta\sigma$, obtained

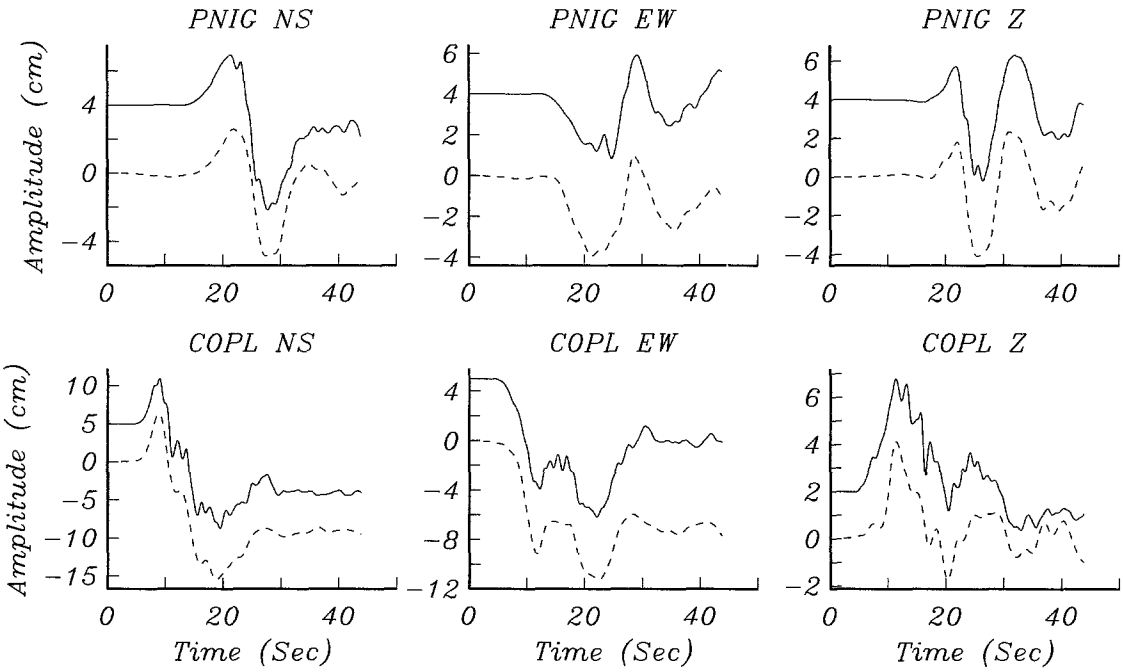


Figure 8. Displacement seismograms, including static component (continuous line), are compared with synthetic seismograms (dashed lines) obtained from linear inversion for the slip distribution.

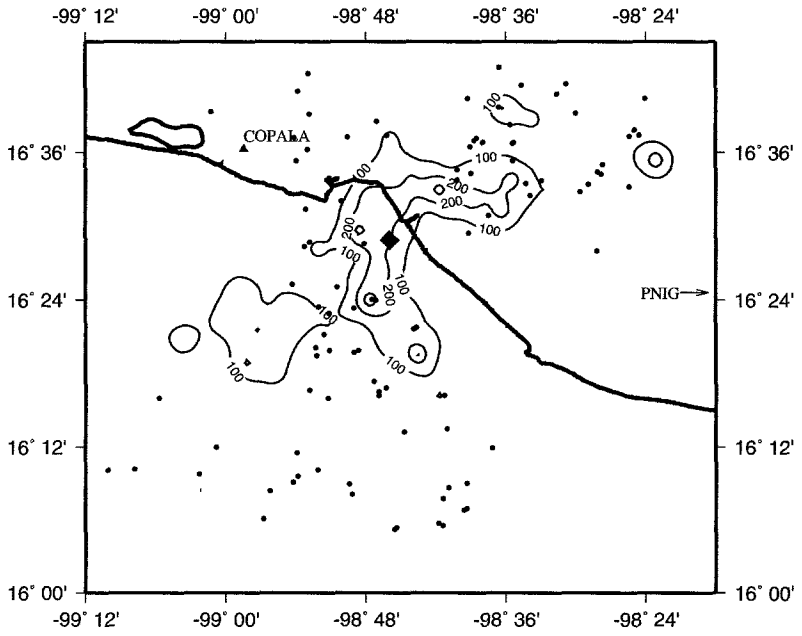


Figure 9. Final dislocation pattern, obtained from linear inversion of near-source displacement traces, projected on the surface. Contour values are in centimeters. Bold line indicates the coast. Diamond, mainshock epicenter; dots, aftershocks.

from the relation $\Delta\sigma = 8M_0/(3\pi L^2 W)$, where $L = 45$ km and $W = 35$ km, is around 1 MPa. The rupture dimension of 35 × 45 km is in rough agreement with the minimum length estimate of 25 km obtained in the previous section.

To map the rupture directivity, we performed a time-window analysis with a snapshot every 2 sec (Fig. 10). These snapshots suggests rupture propagating in two directions: one toward 160° ± 10° N, in agreement with the analysis of teleseismic and regional data presented earlier, and another toward 70° ± 10° N. This latter direction of rupture may explain the large damage observed to the towns of Igualapa, Acatlán, Azoyu, and Ometepec, which lie toward this azimuth. We then reconstruct the source-time function from the final slip distribution by taking the derivative of

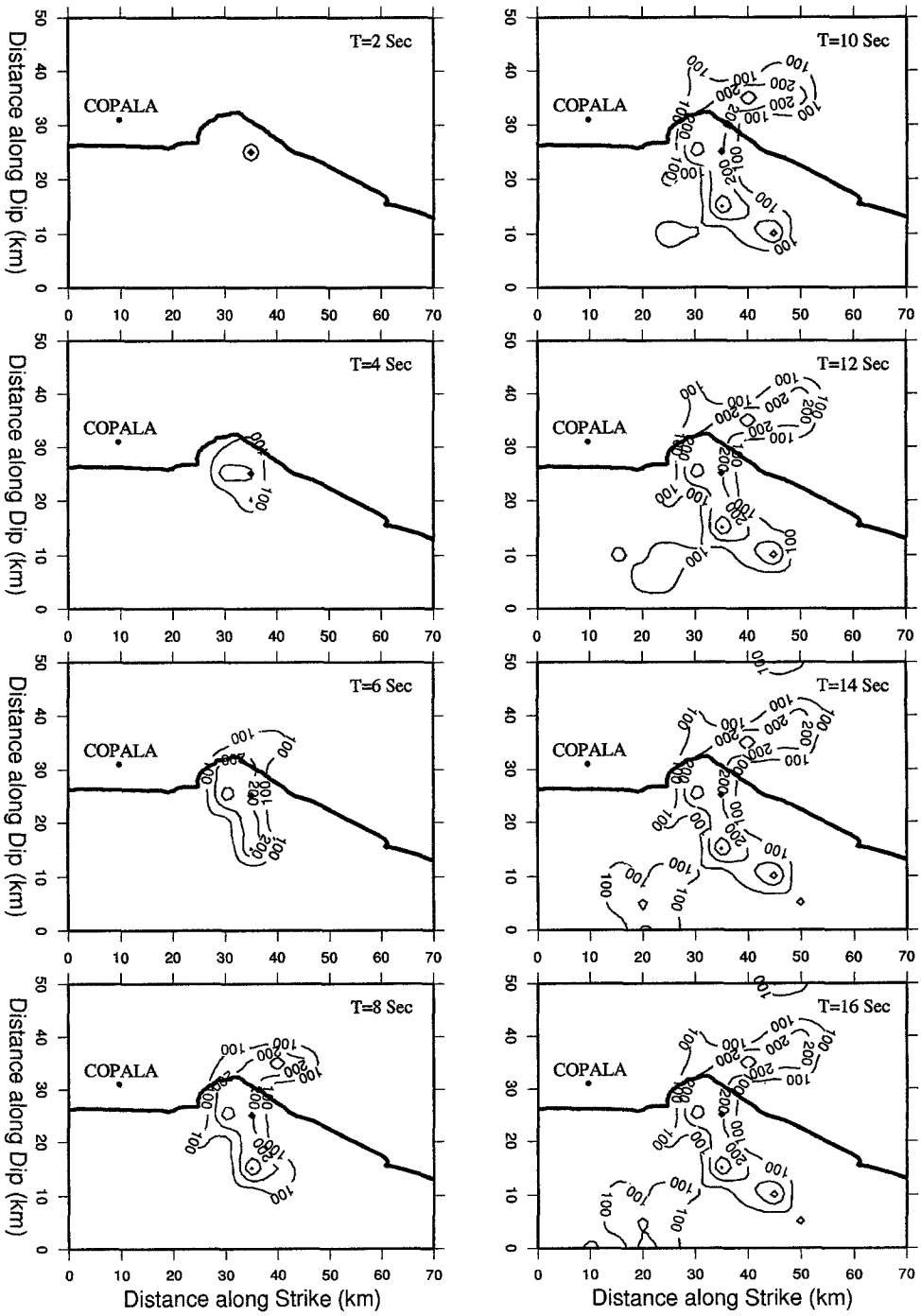


Figure 10. Snapshots of the slip distribution computed every 2 sec. Contour values are in centimeters. Bold line, coast; black diamond, mainshock epicenter.

the sum over time of the total moment release on the fault plane, which shows a total duration of about 14 sec. The normalized moment rate function is shown in Figure 7.

Discussion and Conclusions

We have used teleseismic, regional, and local seismograms and accelerograms to study the source characteristics of the 14 September 1995, Copala, Mexico, earthquake. In the analysis of the teleseismic and the regional data, the empirical Green's function technique was employed. The directivity and the source-time function (STF) inferred from these two data sets are consistent: the rupture initiated at a depth of about 16 km at the interface of the subducted Cocos plate and continental Mexico, and propagated updip, roughly, in the direction of 165° ± 10° N. The source duration was about 12 sec. Although we had only five regional BB seismograms, the surface-wave deconvolution of these data gave very stable results. The directivity effect is clearly visible in the apparent STFs, and two episodes of energy release can be identified in the apparent STFs at stations away from the direction of the rupture propagation. Clearly, the EGF deconvolution of regional mainshock data yields higher resolution of the STF. An additional advantage of using regional over teleseismic data in studying the directivity and STF comes from the fact that a smaller event can be taken as an EGF. Our experience from studying the Copala earthquake shows that for teleseismic analysis of Mexican earthquakes, we need EGFs with $M \geqq 5$. If in the analysis of future earthquakes we wish to use an aftershock as an EGF, then we may have to wait for some time since, generally, Mexican events generate anomalously low number of large aftershocks (Singh and Suárez, 1988). This, in some cases, may make the task of rapid estimation of STF, using teleseismic data, hopeless. In using the regional data, events with $M \geqq 4.5$ may have acceptable signal-to-noise ratio to qualify as EGFs. This and the fact that many of the stations of the Mexican broadband seismological network will soon transmit the data in near real time (at present, this is true for only 5 of the 15 stations) suggest that the goal of rapid estimation of STF may be better served by the use of regional data.

The inversion of displacement traces from two near-source stations shows that the rupture propagated in two directions; one of these directions coincides with that revealed from the analysis of teleseismic and regional data (~N165° E) and the other toward ~70° N, a direction in which damage occurred during the earthquake. The rupture area was roughly 35 × 45 km. This area is in agreement with the minimum length estimated from regional data but is much smaller than the aftershock area.

Acknowledgments

We thank C. J. Ammon and C. Mendoza for providing us with their codes and for many helpful discussions. Code AXITRA was provided by O. Coutant. The dedication of Jesus Pérez and Jorge Estrada in maintaining the Mexican broadband network is acknowledged. We thank IRIS Data Management Center and GEOSCOPE for access to their data. We are thankful to T. Mikumo for his constructive remarks. The research was partially funded by DGAPA, UNAM projects IN100795 and IN102494, and by European Union (Grant CI1-CT92-0036).

References

Ammon, C. J., A. A. Velasco, and T. Lay (1993). Rapid estimation of rupture directivity: application to the 1992 Landers (Ms = 7.4) and Cape Mendocino (Ms = 7.2) California earthquakes, *Geophys. Res. Lett.* **20,** 97–100.

Ammon, C. J., T. Lay, A. A. Velasco, and J. E. Vidale (1994). Routine estimation of earthquake source complexity: the 18 October 1992 Colombian earthquake, *Bull. Seism. Soc. Am.* **84,** 1266–1271.

Anderson, J. G., S. K. Singh, J. M. Espindola, and J. Yamamoto (1989). Seismic strain release in the Mexican subduction thrust, *Phys. Earth Planet. Interiors* **58,** 307–322.

Anderson, J. G., R. Quaas, S. K. Singh, J. M. Espinosa, A. Jimenez, J. Lermo, J. Cuenca, F. Sánchez-Sesma, R. Meli, M. Ordaz, S. Alcocer, B. López, L. Alcántara, E. Mena, and C. Javier (1995). The Copala, Guerrero, Mexico earthquake of September 14, 1995 (Mw = 7.4): a preliminary report, *Seism. Res. Lett.* **66,** 11–39.

Astiz, L. and H. Kanamori (1984). An earthquake doublet in Ometepec, Guerrero, Mexico, *Phys. Earth Planet. Interiors* **34,** 24–45.

Beroza, G., J. A. Rial, and K. C. McNally (1984). Source mechanisms of June 7, 1982 Ometepec, Mexico earthquakes, *Geophys. Res. Lett.* **11,** 689–692.

Bouchon, M. (1979). Discrete wave number representation of elastic wave field in three space dimensions, *J. Geophys. Res.* **84,** 3609–3614.

Bouchon, M. and K. Aki (1977). Discrete wave number representation of seismic source wave fields, *Bull. Seism. Soc. Am.* **67,** 259–277.

Campillo, M., S. K. Singh, N. Shapiro, J. Pacheco, and R. B. Herrmann (1996). Crustal structure south of the Mexican volcanic belt, based on group velocity dispersion, *Geofis. Intern.* **35,** 361–370.

Courboulex, F., J. Virieux, and D. Gibert (1996). On the use of cross-validation theory and simulated annealing for deconvolution, *Bull. Seism. Soc. Am.* **86,** 1187–1193.

Courboulex, F., S. K. Singh, J. F. Pacheco, and C. J. Ammon (1997). The 1995 Colima-Jalisco, México, earthquake (Mw 8): A study of the rupture process, *Geophys. Res. Lett.,* **24,** 1019–1022.

Gomberg, J. S., K. F. Priestley, T. G. Masters, and J. N. Brune (1988). The structure of the crust and upper mantle of northern Mexico, *Geophys. J.* **94,** 1–20.

Gonzalez-Ruiz, J. R. and K. C. McNally (1988). Stress accumulation and release since 1882 in Ometepec, Guerrero, Mexico: implication for failure mechanisms and risk assessments of a seismic gap, *J. Geophys. Res.* **93,** 6297–6317.

Hartzell, S. H. (1978). Earthquakes aftershocks as Green's functions, *Geophys. Res. Lett.* **5,** 1–4.

Helmberger, D. and R. A. Wiggins (1971). Upper mantle structure of the mid-western United States, *J. Geophys. Res.* **76,** 3229–3245.

Irikura, K. (1983). Semi-empirical estimation of strong ground motions during large earthquakes, *Bull. Disast. Prev. Res. Inst., Kyoto Univ.* **33,** 63–104.

Iwan, W. D., M. A. Moser, and C. Peng (1985). Some observations of strong-motion earthquake measurement using a digital accelerograph, *Bull. Seism. Soc. Am.* **75,** 1225–1246.

Lawson, C. L. and R. J. Hanson (1974). *Solving Least Squares Problems,* Prentice Hall Inc., Englewood Cliffs, New Jersey, 340 pp.

Mendoza, C. and S. H. Hartzell (1988). Inversion for slip distribution using teleseismic P waveforms: North Palm Springs, Borah peak, and Michoacan earthquakes, *Bull. Seism. Soc. Am.* **78,** 1092–1111.

Mori, J. and S. H. Hartzell (1990). Source Inversion of the 1988 Upland, California, Earthquake: determination of a fault plane for a small event, *Bull. Seism. Soc. Am.* **80,** 507–518.

Mueller, C. (1985). Source pulse enhancement by deconvolution of an empirical Green's function, *Geophys. Res. Lett.* **12,** 33–36.

Nishenko, S. P. and S. K. Singh (1987a). The Acapulco-Ometepec, Mexico earthquakes of 1907–1982: evidence for a variable recurrence history, *Bull. Seism. Soc. Am.* **77,** 1359–1367.

Nishenko, S. P. and S. K. Singh (1987b). Conditional probabilities for the recurrence of large and great interplate earthquakes along the Mexican subduction zone, *Bull. Seism. Soc. Am.* **77,** 2095–2114.

Randall, G. E., C. J. Ammon, and T. J. Owens (1995). Moment tensor estimation using regional seismograms from a Tibetan plateau portable network deployment, *Geophys. Res. Lett.* **22,** 1665–1668.

Santoyo, M. A. (1994). Estudio del proceso de ruptura del sismo del 25 de Abril de 1989 usando registros de movimientos fuertes y telesismicos. *Master's Thesis,* UNAM, Ciudad Universitaria, Coyoacan, Mexico D.F.

Shapiro, N. M., M. Campillo, A. Paul, S. K. Singh, D. Jongmans, and F. J. Sanchez-Sesma (1997). Surface-wave propagation across the Mexican volcanic Belt and the origin of the long-period seismic-wave amplification in the Valley of Mexico, *Geophys. J. Int.* **128,** 151–166.

Singh, S. K. and G. Suárez (1988). Regional variation in the number of aftershocks (mb $\geq$ 5) of large subduction zone earthquake (Mw $\geq$ 7), *Bull. Seism. Soc. Am.* **78,** 230–244.

Singh, S. K., L. Astiz, and J. Havskov (1981). Seismic gaps and recurrence periods of large earthquakes along the Mexican subduction zone: a reexamination, *Bull. Seism. Soc. Am.* **71,** 827–843.

Singh, S. K., J. M. Espindola, J. Yamamoto, and J. Havskov (1982). Seismic potential of the Acapulco-San Marcos region along the Mexican subduction zone (1982), *Geophys. Res. Lett.* **9,** 633–636.

Singh, S. K., M. Rodriguez, and L. Esteva (1983). Statistics of small earthquakes and frequency of occurrence of large earthquakes along the Mexican subduction zone, *Bull. Seism. Soc. Am.* **73,** 1779–1796.

Sipkin, S. A. and A. L. Lerner-Lam (1992). Pulse shape distortion introduced by broadband deconvolution, *Bull. Seism. Soc. Am.* **82,** 238–258.

Velasco, A. A., C. J. Ammon, T. Lay, and J. Zang (1994). Imaging a slow bilateral rupture with broadband seismic waves: the September 2, 1992 Nicaragua tsunami earthquake, *Geophys. Res. Lett.* **21,** 2629–2632.

Wennerberg, L. (1990). Stochastic summation of empirical Green's functions, *Bull. Seism. Soc. Am.* **80,** 1418–1432.

Zollo, A., P. Capuano, and S. K. Singh (1995). Use of a small earthquake record to determine source function of a larger earthquake: an alternative method and an application, *Bull. Seism. Soc. Am.* **85,** 1249–1256.

Zuñiga, F. R., C. Gutierrez, E. Nava, J. Lermo, M. Rodriguez, and R. Coyoli (1993). Aftershocks of the San Marcos earthquake of April 25, 1989 (Ms = 6.9) and some implications for the Acapulco-San Marcos, Mexico, seismic potential, *Pageoph* **140,** 287–300.

Instituto de Geofisica, UNAM
Ciudad Universitaria
Coyoacan, 04510 Mexico D.F.

Manuscript received 26 November 1996.

1.6 Etude du séisme d'Annecy (Mw 4.9)

Travailler sur des séismes de petite taille n'est pas facile. Dans les régions à faible sismicité ce travail est pourtant nécessaire, puisque les petits séismes font partie des faibles témoins que nous avons de l'activité tectonique des zones, mais aussi parce qu'ils constituent une menace pour nos sociétés. L'étude des ces séismes nécessite une bonne connaissance des signaux sismologiques et de leurs limites, et la recherche de solutions méthodologiques adaptées.

Alors que j'étais encore au Mexique, un séisme de magnitude Ml = 5.0 frappait la France. Au Mexique les séismes de magnitude 5 sont à peine répertoriés dans les journaux, mais en France cet événement a eu un retentissement énorme. Il faut dire que l'événement était situé à très faible profondeur sous la ville d'Annecy. De très nombreux dégâts matériels ont été répertoriés (Chutes de cheminées, effondrement des faux plafonds, fissures profondes …) qui ont été estimés à 50 millions d'Euros (Figure 1. 9). L'intensité VIII a été atteinte sur l'échelle MSK. Cet événement a été suivi par un nombre très élevé de répliques [*Thouvenot et al.*, 1998].



Figure 1. 9 : Aperçu des dégâts matériels occasionnés par le séisme d'Annecy (pas de victimes).

A mon retour en France, l'institut de recherche et de sureté nucléaire (IRSN) m'a proposé de travailler sur cet événement. Il s'agissait de tenter de d'utiliser toutes les données françaises disponibles de l'époque pour tenter de comprendre la source de cet événement.

J'ai alors entrepris un travail de récupération des données disponibles en France (espérons qu'avec le réseau RESIF quelques clics suffiront bientôt, mais à l'époque cela n'était pas le cas !), Suisse et Italie. Il me fallait les données du choc principal mais aussi celles d'un ou deux séismes de magnitude plus faible pour les utiliser comme fonction de Green empiriques. Beaucoup de stations étaient de courte période, situées à des distances régionales de l'épicentre, beaucoup avaient une faible dynamique, ce qui entrainait la saturation pour les stations les plus proches et un mauvais enregistrement des répliques pour les stations plus lointaines.

Apres avoir travaillé sur les magnifiques données des gros séismes mexicains, j'avoue que ce travail m'a paru fastidieux, même si le chalenge était intéressant. La rencontre avec Nicolas Deichmann (ETH Zurich) et la collaboration que nous avons menée sur l'étude de ce séisme en a finalement fait un sujet d'étude passionnant.
Assez vite, nous avons réalisé que ce petit séisme avait une source complexe avec deux épisodes distincts de libération d'énergie (2 sous événements). Cette fonction source apparente bimodale ne se

voyait que sur les stations situées vers le nord. Les stations du sud donnaient un pulse simple (Figure 1. 10). Une seule solution pour expliquer ce comportement : un effet de directivité.

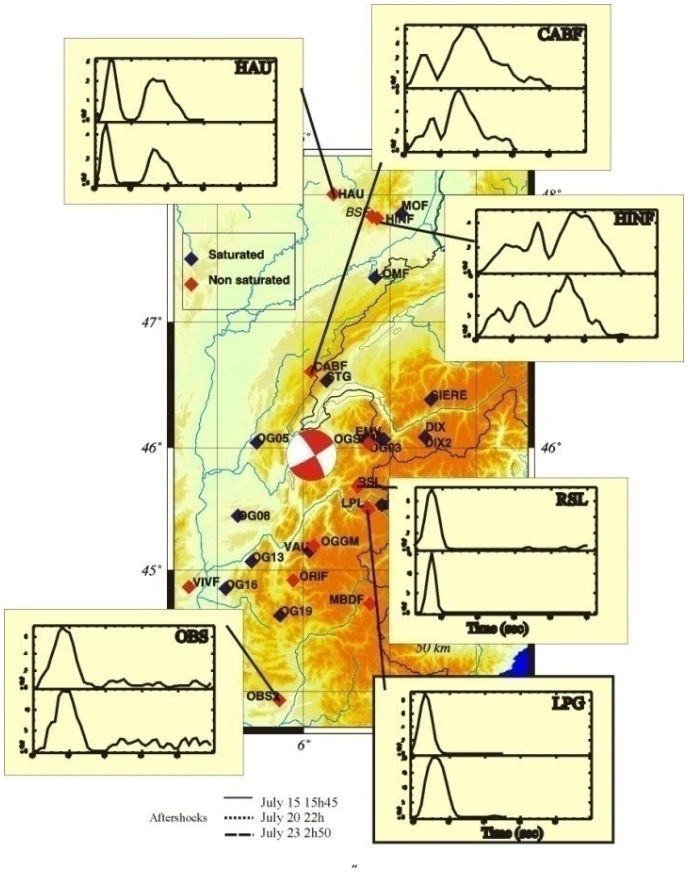


Figure 1. 10 : Fonctions source apparentes obtenues avec deux EGF distinctes à chaque fois sur quelques stations significatives du réseau

Nicolas Deichmann, a entrepris de regarder les signaux du choc principal (les signaux bruts, sans les déconvoluer) et de mesurer la largeur du premier pulse de l'onde P sur les données en vitesse. Il a d'ailleurs montré que l'observation directe du signal est dans certains cas plus fiable que la déconvolution par fonction de Green empiriques [*Deichmann*, 1999]. Ce travail a permis d'ajouter plusieurs stations dont le signal saturé ne permettait pas une analyse par EGF. Nos deux analyses ont convergé, ce qui nous a permis de localiser le deuxième pulse de la fonction source et de proposer un scenario de propagation de la source de ce séisme.

Nous obtenons grâce à notre analyse la taille maximale de la faille et la localisation du deuxième patch de libération d'énergie par rapport au premier. Nous proposons alors trois scenarios possibles pour la propagation de la rupture sur la faille. Une propagation sur le segment nord uniquement, une propagation sur le segment sud uniquement ou bien une rupture qui aurait sauté d'un segment à l'autre. Différents argument (que vous trouverez dans la partie « discussion » de l'article) nous amènent à préférer le deuxième scenario (Figure 1. 11).

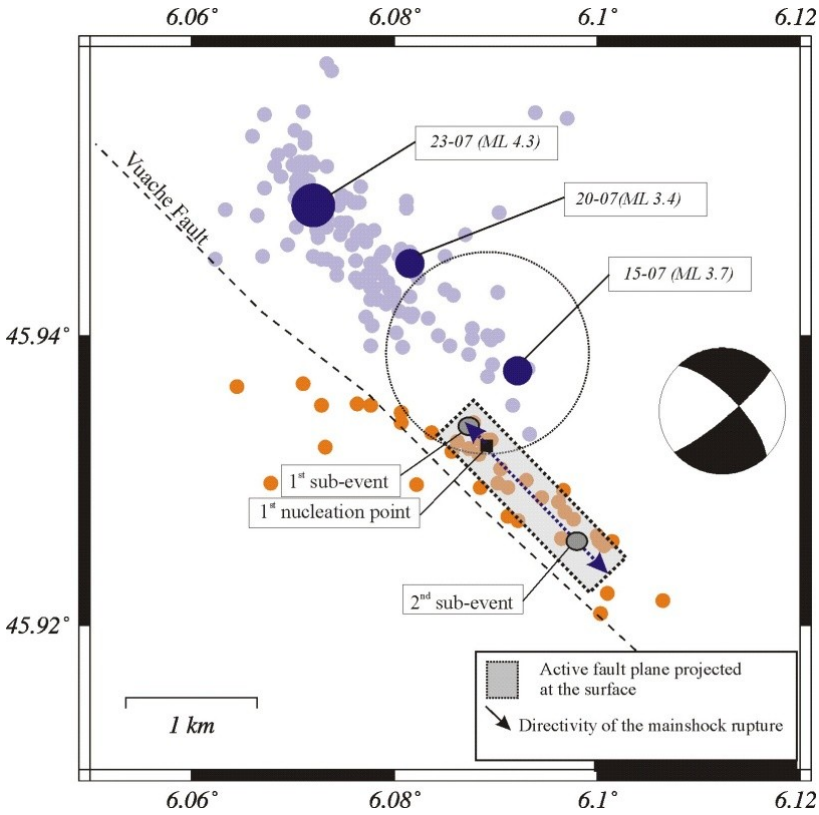


Figure 1. 11 : Deux segments de faille ont été activés durant le séisme d'Annecy. La rupture a certainement eu lieu sur le segment sud. Le cercle noir représente l'incertitude sur la localisation de l'épicentre.

Ce travail montre qu'un séisme de magnitude faible peut avoir une rupture complexe, et que la taille de la faille activée par les répliques est bien supérieure à la taille de la rupture du choc principal. Nous avons également montré qu'il était possible d'aller loin dans l'analyse de la rupture d'un petit séisme, et c'était la première fois en France.
Cette étude montre également que les modèles très simples utilisés pour les séismes de magnitude modérés ne sont pas toujours justifiés.

Geophys. J. Int. (1999) **139,** 152–160

Rupture complexity of a moderate intraplate earthquake in the Alps: the 1996 *M*5 Epagny–Annecy earthquake

Françoise Courboulex,[1] Nicholas Deichmann[2] and Jean-Christophe Gariel[3]

[1] *UMR Géosciences Azur, UNSA, CNRS,* 06560 *Valbonne, France. E-mail: courboul@faille.unice.fr*
[2] *Swiss Seismological Service, ETH-Hönggerberg,* 8093 *Zürich, Switzerland*
[3] *Institut de Protection et de Sureté nucléaire,* 92265 *Fontenay aux Roses, France*

Accepted 1999 May 21. Received 1999 May 17; in original form 1998 November 20

SUMMARY

The magnitude 5 Epagny–Annecy earthquake of 1996 July 15 is the largest seismic event to have occurred in the Alps since the introduction of modern digital instrumentation. This strike-slip event was located on the Vuache Fault, near the town of Annecy, in the northern French Alps.

The aim of our work was to retrieve the main parameters of the rupture process of this earthquake from seismograms recorded at local and regional distances (20–300 km). To eliminate path and site effects from the seismograms, we compared the main shock recordings at each station with those of the largest aftershocks nearby. We used a combination of techniques, including pulse-width measurements and cross-correlation of velocity traces, comparison of *P*-wave displacement pulses, and empirical Green's function deconvolution, to retrieve the apparent duration of the rupture process as seen at each station. Our results demonstrate that, in the absence of on-scale data, *P*-wave pulse-width measurements on clipped signals can be misleading if the rupture process is complex. In the case of the Annecy earthquake, comparisons of on-scale *P*-wave displacement seismograms and the empirical Green's function deconvolutions show that the rupture process consisted of at least two subevents separated by 0.2–0.3 s, and with a total duration of about 0.5 s. The systematic azimuthal dependence of both the shape and duration of the apparent source-time function is consistent with a nearly unilateral propagation of the main rupture phase in a southeast direction along the fault plane and parallel to the direction of slip. An isochron analysis reveals that the first subevent occurred slightly to the northwest of the nucleation point but that the second subevent was located further to the southeast, thus confirming the overall rupture directivity towards the southeast. An interpretation of our results in light of the previously documented aftershock distribution and of observations of ground cracks in the epicentral area suggests that the main shock occurred on the Vuache Fault, and that rupture in a northwest direction was inhibited by a right-lateral stepover in the fault. Accordingly, the vast majority of the subsequent aftershocks, which include several magnitude 3–4 events, occurred on a fault segment that is slightly offset from the inferred surface trace of the Vuache Fault and that was activated by the main shock.

Key words: Alps, earthquake-source mechanism, Green's function, intraplate, rupture.

INTRODUCTION

Most seismic source studies have been undertaken for earthquakes with magnitudes larger than 6. The reason for this is not only the social impact of such large events, but also the need for there to be enough records of the required quality. Recently, with the development of dense seismic networks, more and more seismologists have tried to study the rupture process of moderate and small earthquakes (Hough 1996; Beroza & Ellsworth 1996; Mori 1996; Courboulex *et al.* 1996; Haddon & Adams 1997; Courboulex *et al.* 1998; Fletcher & Spudich 1998). However, these studies are still rare because of the lack or the low quality of near-source data and because of difficulties in the interpretation of the results. In regions such as central Europe, where no large earthquakes have been recorded, it is especially important to study in detail the rupture processes of moderate-size events, since they are the only witness of rapid movement on active faults.

© 1999 RAS

In this paper we study the source process of the Epagny–Annecy earthquake of 1996. This event, which occurred on 1996 July 15 at 00:13 near the city of Annecy, in the northern part of the French Alps, reached an epicentral intensity of VII–VIII (MSK) and caused total damages to buildings estimated at 300 million French francs (about 50 million US dollars). Magnitude estimates range between 4.2 and 5.3 with a median value of 5.0 (Thouvenot *et al.* 1998). A comprehensive paper by Thouvenot *et al.* (1998) presents the main-shock and the aftershock locations and focal solutions, as well as details of the seismotectonic setting, site effects and other coseismic phenomena.

For our purpose, the Epagny–Annecy event is of particular interest for several reasons:

(1) it is the most significant earthquake to have occurred in the Alps since the beginning of digital instrumental observations (Vogt 1979; Nicolas *et al.* 1990; Lambert & Levret-Albaret 1996) and has been recorded by many stations at local and regional distances in France, Italy and Switzerland;

(2) it was followed by several hundreds of aftershocks which were also recorded by local and regional seismic networks;

(3) it is clearly related to a well-known strike-slip fault that reaches the surface (the NW–SE-trending Vuache fault), as demonstrated by the focal mechanism (Fig. 1), the aftershock locations (Fig. 9) and the shallow focal depth of 2–3 km (Thouvenot *et al.* 1998).

The aim of this study is to retrieve the source dimension, the duration of the rupture process, its directivity and its relation to the aftershock distribution. Using all the available recordings of the main shock and the largest aftershocks, we adopted an empirical Green's function approach to remove the contributions of path and instrument from the seismograms of the main shock.

AVAILABLE DATA

The Epagny–Annecy earthquake was recorded by many seismic networks in France (LDG[1], IPSN[2], Sismalp[3], Renass[4], TGRS[5], Rosalp[6], RAP[7]), in Italy (Dister[8]) and in Switzerland (SED[9]).

We made a selection among this large number of records: first, we kept only the stations that recorded both the main shock and at least one of the largest aftershocks that was suitable as an empirical Green's function; second, we selected the seismograms that were recorded at a sampling frequency higher than 60 Hz, in order to be able to work on small events (magnitude 3–4). This left us with 36 stations that provided either local seismograms with a *Pg* wave as first arrival or regional seismograms with a *Pn* wave as first arrival. From these stations, 16 records were clipped because of insufficient dynamic range and 20 were on-scale. We decided to analyse clipped and unclipped seismograms separately in order to check whether these two types of data give the same results. The final set of stations used is shown in Fig. 1, with different symbols depending on whether the main shock records were clipped or not.

[1] Laboratoire de Géophysique du Commisariat à l'énergie atomique.
[2] Institut de Protection et de Sureté Nucléaire.
[3] Dense short-period network operated by the Observatory of Grenoble.
[4] Réseau National de surveillance sismique.
[5] Broad-band network operated by the UMR Géosciences Azur.
[6] Broad-band network operated by Observatory of Grenoble.
[7] Réseau Accélérométrique permanent Français.
[8] Dipartimento di Scienze della Terra, Genova.
[9] Swiss Seismological Service.

DATA ANALYSIS

One difficulty in seismic source studies is the removal of path and site effects from the observed seismograms. In the case of the Annecy earthquake, this removal is not easy because the crustal structure in the Alps is complex and not well known and because the source was shallow (2–3 km), causing the ray paths to be strongly affected by the near-surface layers. At the relatively high frequencies of interest here, it is therefore impossible to compute theoretical Green's functions with sufficient accuracy. A common approach to circumventing this problem is to use the seismograms of a smaller event as an empirical Green's function (EGF) (Hartzell 1978; Mueller 1985). The conditions for this technique to work are that the source of the smaller event is located close enough to the hypocentre of the main shock and that it has a similar focal mechanism. Moreover, the small event must be sufficiently

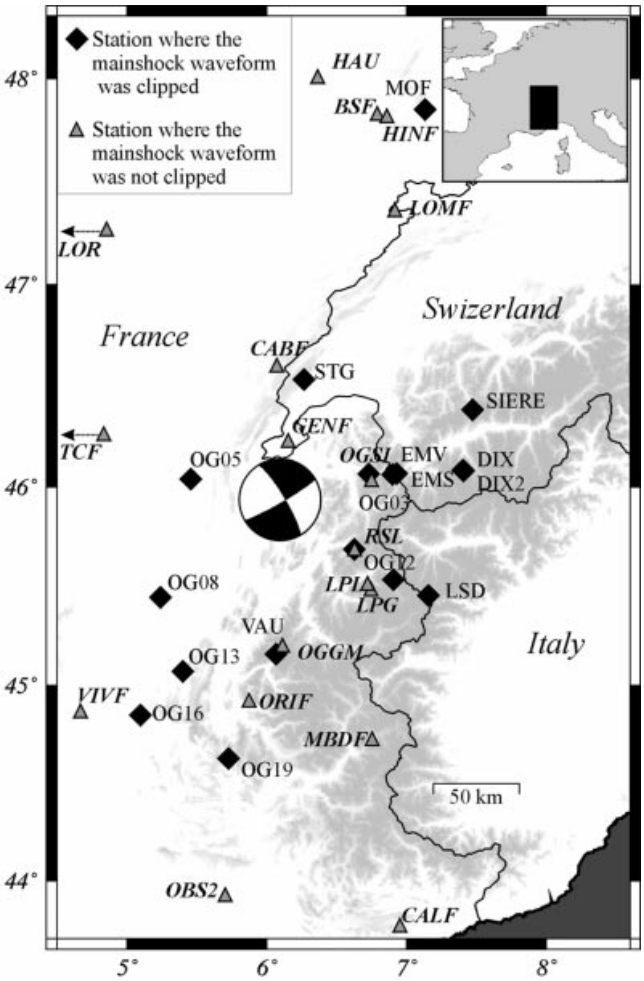


Figure 1. Focal mechanism of the 1996 July 15 Epagny–Annecy event from Thouvenot *et al.* (1998) and stations that were used in this study. Black diamonds represent those stations at which the records of the main shock are clipped, whereas grey triangles correspond to those stations from which unclipped records are available.

small that the duration of its source-time function (STF) is short enough to be negligible compared with that of the main shock while still being strong enough to provide records with good signal-to-noise ratios at a large number of stations. In our case, we chose as EGFs two aftershocks with magnitudes M_L (estimated by Renass) equal to 3.7 and 3.4. The first one occurred about 5 hr after the main shock and was located almost at the same point (Thouvenot *et al.* 1998). The second one, which occurred 5 days later (1996 July 20 22:04), was located 1.5 km to the northwest, at a slightly shallower depth than the main shock. Both events have a strike-slip focal mechanism very similar to the one of the main shock (difference in strike $<14°$, difference in dip $<10°$; F. Thouvenot, personal communication).

The deconvolution of the main shock by the EGF results in an apparent relative source-time function (ARSTF). This ARSTF represents the temporal history of the moment release at the source as seen from a given station. It is 'apparent' because the shape of the source-time function depends on the direction from which the rupture propagation is viewed, and it is 'relative' because it is scaled by the moment of the EGF and its duration is reduced by the source duration of the EGF. We performed the deconvolution in the time domain using a non-linear deconvolution method with positivity constraint (Courboulex *et al.* 1996) on the two EGFs separately. The use of more than a single event as EGF is very important in such an analysis to confirm the reliability of the results.

Waveform comparison and EGF deconvolution

Before performing the EGF deconvolutions, we systematically compared the waveforms of the main shock and the aftershocks at each station that provided unclipped records. It is important to note that we used only *P* waves, because the *S* waves were very complex and could not be identified clearly. This may be a result of the shallow depth of the hypocentres, which leads to the generation of strong surface waves that reach the station at almost the same time as the *S* waves.

At many stations, the main shock and the aftershock waveforms are similar, and the *P*-wave arrivals have a simple shape (e.g. station RSL in Fig. 2). At other stations, both the displacement and the velocity traces of the main shock feature a double-pulse *P*-wave onset, which is not seen in the seismograms of the aftershocks (e.g. station CABF in Fig. 2). Moreover, in all cases showing signs of a double-pulse *P*-wave onset, cross-correlations of the main shock velocity signals with those of the aftershocks result in a maximum of the correlation coefficient when the aftershock is shifted by almost 0.3 s relative to the observed first breaks ($\delta\tau$ in Fig. 2). Shifted in this way, the *P*-wave onset of the aftershock is aligned with the second pulse of the main shock. This is because the second pulse is in general larger and longer than the first one and thus dominates the later stages of the seismograms.

The results of the EGF deconvolutions confirm that the double pulse is a feature of the STF of the main shock, but that it is not seen at all azimuths (see Fig. 2). Indeed, the double-pulse ARSTFs with a relatively long overall duration are observed only at stations situated north of the epicentre, while at all other stations the ARSTFs are simpler and shorter (Fig. 3). The durations of the apparent source-time function measured directly on the displacement pulse, and on the result of EGF deconvolution are reported in Table 1.

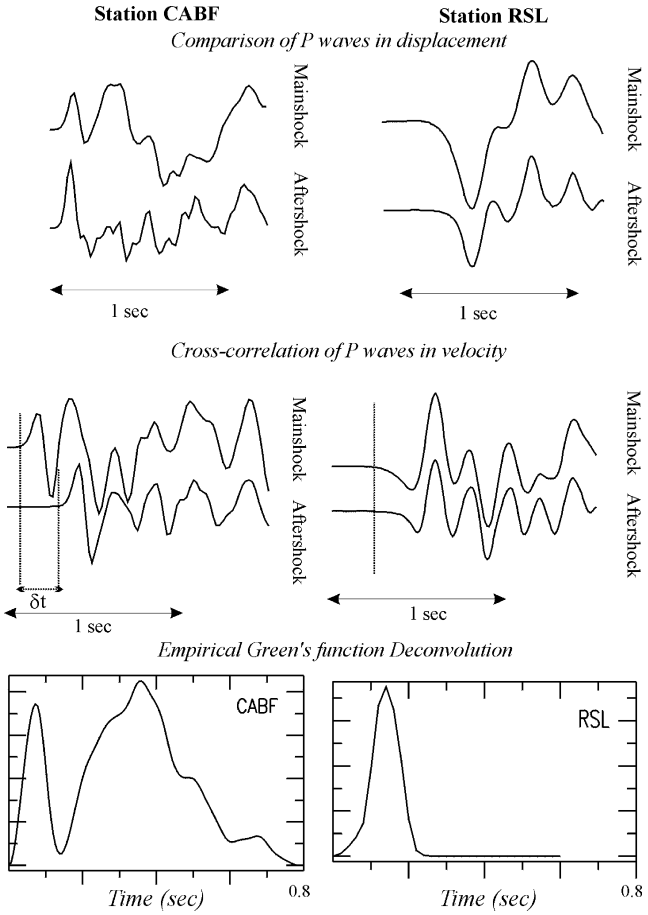


Figure 2. Examples of displacement and velocity waveforms of the main shock compared with those of the aftershock of 1996 July 15 05:46, and results of the EGF deconvolution at stations located north (CABF) and southeast (RSL) of the epicentre. The displacement traces at RSL were corrected for the response of the 1 Hz seismometer before integration.

It is clear that such behaviour is not compatible with a symmetric or bilateral rupture expansion. Based on the fact that the fault plane strikes in the direction of the Vuache Fault (Thouvenot *et al.* 1998), and that all the double-pulse long-duration STFs are observed at stations north of the epicentre, we expect that the rupture consisted of at least two subevents and propagated preferentially towards the southeast.

Pulse-width measurements

As first demonstrated by O'Neill & Healy (1973), an alternative method of obtaining information about the duration of the STF consists of measuring the width of the first half-cycle of the *P*-wave onset as recorded by a standard seismometer sensitive to ground velocity. This method is simple and has the advantage of being applicable also to severely clipped seismograms. The observed pulse width is a function of the rise time of the STF, modified by broadening due to the response of the recording instrument as well as to attenuation and scattering along the path. In a first approximation, the path and instrument contributions to the pulse widths at each station can be corrected by subtracting the pulse width of a smaller event (Frankel & Kanamori 1983). Provided that possible directivity effects of the

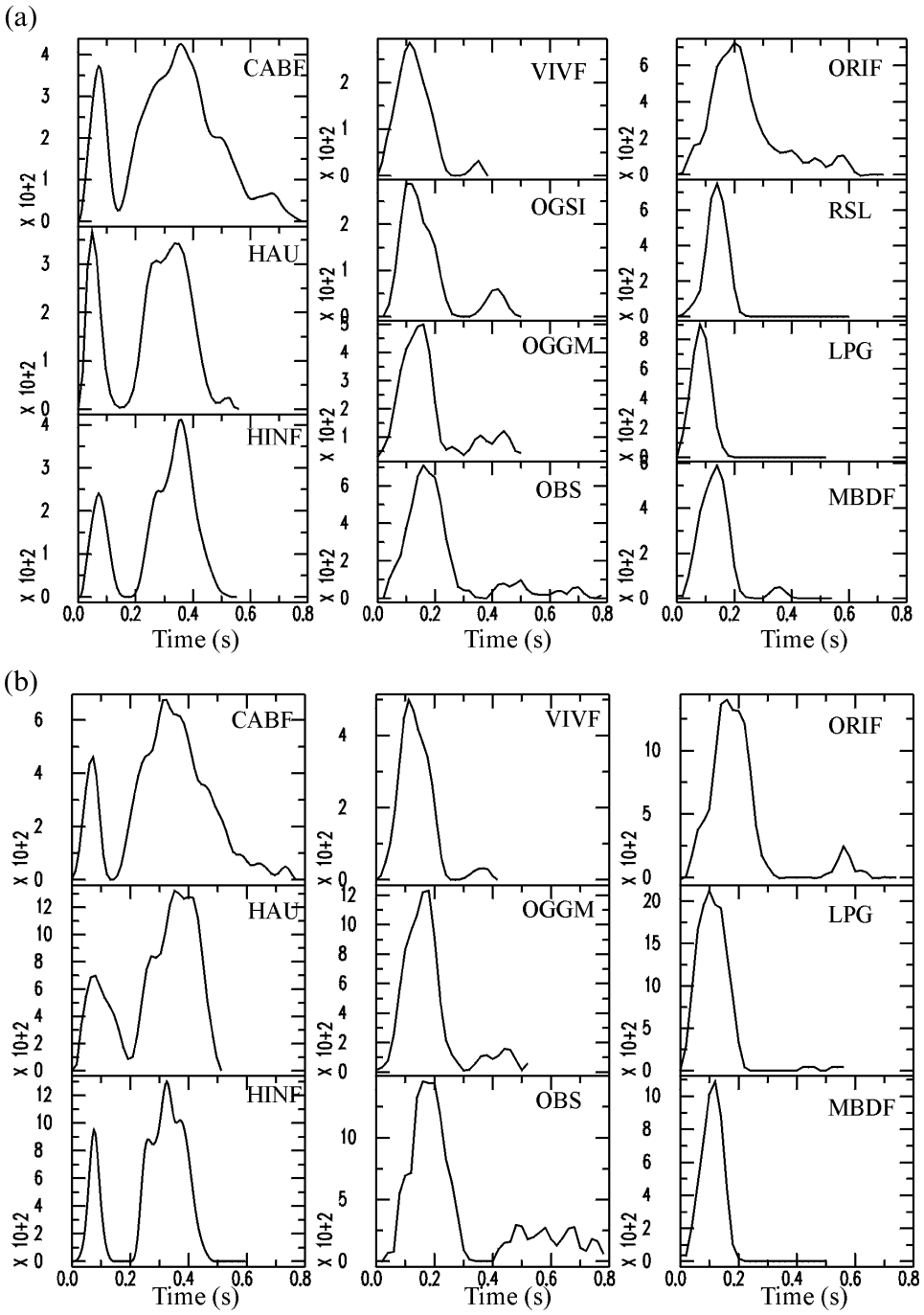


Figure 3. Deconvolution results with: (a) the $M_L = 3.7$ and (b) the $M_L = 3.4$ aftershock as EGF.

smaller event's rupture process are negligible, this technique will in general give a reliable measure of azimuthal variations in the apparent duration of the main shock STF.

As illustrated by the example shown in Fig. 4, the relative pulse widths measured from clipped seismograms at all stations situated north of the epicentre are consistently smaller than those observed at stations south of the epicentre. From pulse-width measurements on clipped records alone we would thus conclude that, contrary to the results of the EGF deconvolutions, the rupture propagated towards the northwest. Obviously, the reason for this discrepancy is that on the clipped records we cannot recognize the fact that towards the north the STF of the main shock appears as a double pulse and that at the northern stations we have therefore measured only the relative duration of the first pulse. This shows that, in the presence of undetected rupture complexities, a naive application of the pulse-width method can produce severely misleading results.

INTERPRETATION

Unilateral rupture model

To visualize the distribution of the double- and single-pulse source-time functions relative to the focal mechanism, we

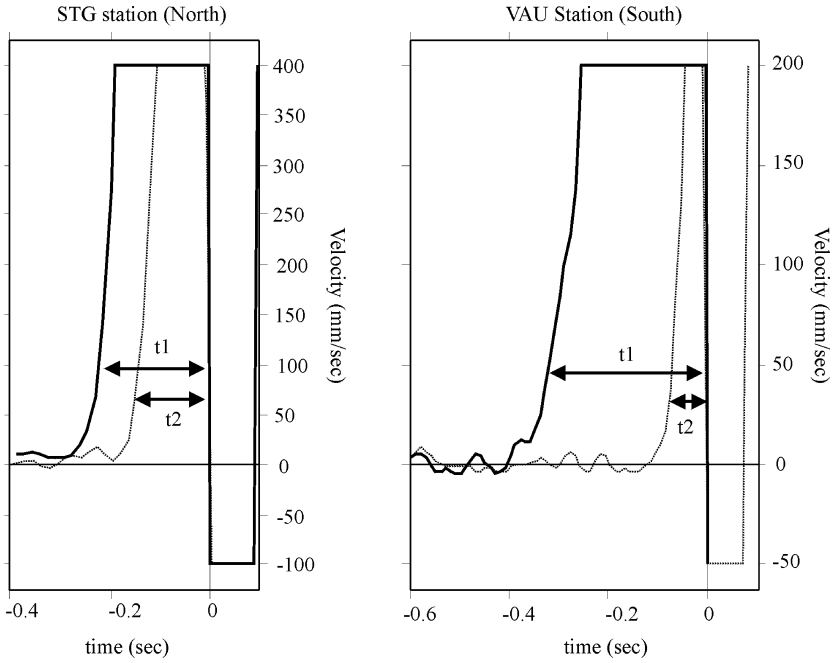


Figure 4. Examples of two pulse-width measurements on clipped seismograms.

Table 1. *P*-pulse duration and apparent relative STF duration for each station that recorded the main shock without saturation. 'u' indicates that the value was undefined.

station name	network	epicentral distance (km)	azimuth (°)	*P* pulse duration (s)	ARSTF duration (s)
OGSI	RAP	48	78	0.3	0.25
OGGM	Rosalp	82	174	0.27	0.3
CABF	LDG	75	2	0.55	0.6
HINF	LDG	219	18	0.5	0.5
BSF	LDG	217	15	0.45	u
HAU	LDG	230	5	0.45	0.5
LOR	LDG	226	310	0.6	u
VIVF	LDG	160	221	u	0.25
TCF	LDG	302	276	0.6	u
ORIF	LDG	114	185	u	0.3
LPL	LDG	69	133	0.2	0.2
LPG	LDG	71	134	0.2	0.2
MBDF	LDG	143	161	u	0.15–0.2
CALF	TGRS	350	124	0.2	u
OBS	IPSN	226	187	0.3	0.3
RSL	Sismalp	50	124	0.2	0.2
LOMF	Renass	167	20	0.45	0.45

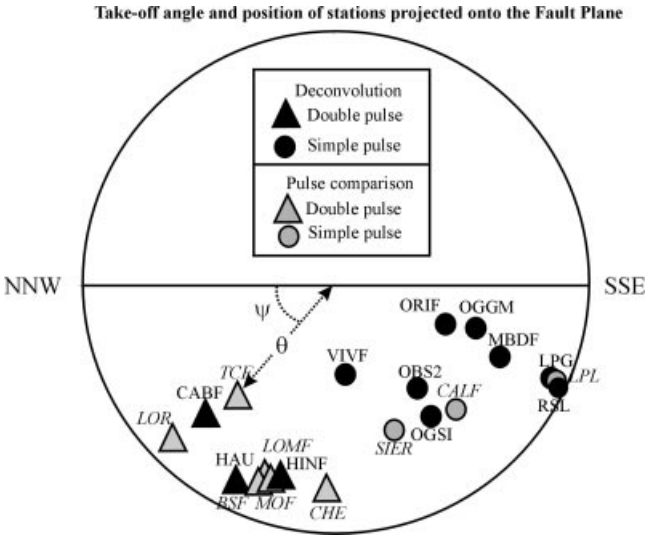


Figure 5. The observed *P* displacement pulses and apparent source-time functions in an equal-area stereographic projection onto the focal sphere viewed along the normal to the fault plane. θ_i is the angle between the ray and the fault normal. ψ_i, measured in the plane of the fault, is the angle between the ray and the strike of the fault.

projected each observation onto the fault plane (Fig. 5). The azimuth and take-off angles of the rays to each station were converted to the angles between the rays and the normal to the fault, θ_i, at the ith station, and between the rays and the strike of the fault, ψ_i, for a fault with strike, dip and rake of 316°, 70° and −10° derived by Thouvenot *et al.* (1998). The take-off angles were calculated for a focal depth of 2 km based on the velocity model used by Thouvenot *et al.* (1998). Since the source is located in the sedimentary layers close to the boundary to the crystalline basement and because of the strong velocity increase across this boundary, all first arrivals beyond an epicentral distance of about 20 km leave the source as down-going rays. Therefore, all our data points come to lie in the lower half of the fault plane. Fig. 5 shows that the projections of the double- and single-pulse source-time functions onto the fault plane separate into two distinct groups. For a unilaterally propagating rupture on a circular fault, the duration of the apparent moment-rate function at the ith station, τ_i, is given by

$$\tau_i = L[1/V_r - 1/c \sin\theta_i \cos(\psi_r - \psi_i)], \quad (1)$$

with L the source diameter, V_r the rupture velocity, c the phase velocity, θ_i the angle between the ray and the normal to the

fault, ψ_i the angle between the ray and the strike of the fault, and ψ_r the direction of rupture propagation (Boatwright 1980). Both ψ_i and ψ_r are measured in the plane of the fault. For given values of τ_i, θ_i and ψ_i and fixed values of c and V_r, we can solve eq. (1) for L as a function of ψ_r. In practice, this gives a different value of L for each observation τ_i.

Increasing ψ_i in steps of 5° over the range between 0° and 360°, we calculate an average value of L over all stations for each value of ψ_r, and search for that ψ_r which minimizes the sum of the squared differences between the observed and calculated τ_i. With reference to Fig. 5 and to the given orientation of the fault plane, $\psi_r = 0°$ or 180° corresponds to a purely horizontal rupture propagation towards the NW (0°) or SE (180°), whereas $\psi_r = 90°$ or 270° corresponds to a purely downward (90°) or upward (270°) rupture direction. Assuming a P-wave velocity of 5.35 km s^{-1} (Thouvenot *et al.* 1998) and an average rupture velocity of 2.7 km s^{-1}, we obtain $\psi_r = 180°$ and $L = 915$ m. The fit between observed and calculated τ_i is better for the single-pulse STFs at the stations with $\psi_i > 120°$, situated in the southeast quadrant relative to the epicentre, than for the double-pulse STFs observed at the stations to the north (Fig. 6). To judge whether the assumption of a unilateral rupture propagation is justified and assess to what extent the rupture direction can be constrained by the available data, we have calculated the mean of the misfit (the squared differences between the observed and calculated τ_i) for every 5° increment in ψ_r. From the resulting plot in Fig. 7, we see that this misfit function has a broad minimum over the range $130° < \psi_r < 250°$. Thus, due to the fact that all our observations correspond to downgoing rays, which span a range of ψ_i of only 120°, the vertical component of the rupture direction is poorly constrained.

It can be argued that, because of the contribution of the small event's STF to the EGF, the deconvolution procedure underestimates the true duration of the STF of the main shock. Considering the magnitude of the EGF events that we used, this deficit could amount to about 0.1 s. As shown by the corresponding misfit function in Fig. 7, adding 0.1 s to all our estimates of τ_i does not change the resulting rupture direction significantly. Similarly, using a different average rupture velocity raises the overall misfit by only a small amount and does not affect the location and breadth of its minimum in a significant way (Fig. 7).

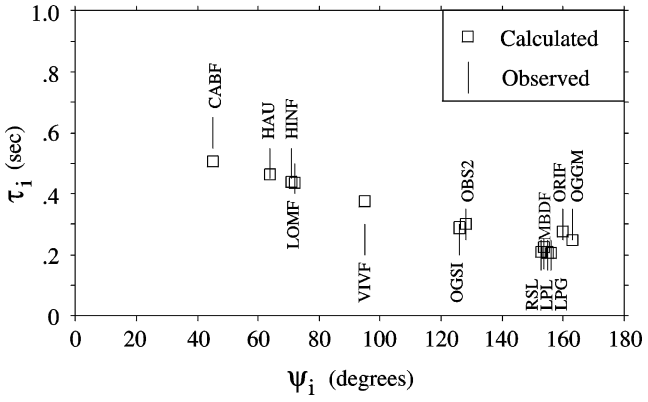


Figure 6. Observed (vertical bars equal to uncertainties) and calculated (squares) values of τ_i as a function of ψ_i.

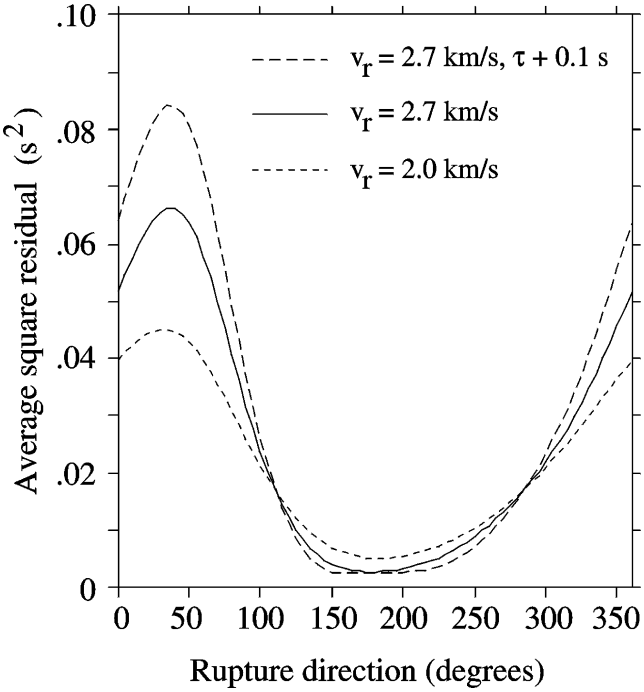


Figure 7. The rms of the differences between the observed and calculated τ_i as a function of ψ_i for various rupture velocities V_r and for τ_i increased by 0.1 s (see text for further explanations).

Subevent location

Based on the values of the ARSTF reported in Table 1, it is possible to estimate the maximum area that was activated during the main shock rupture by constructing the isochrons over the fault (Bernard & Madariaga 1984; Spudich & Frazer 1984; Zollo & Bernard 1991). Starting from the nucleation point (S0 in Fig. 8), the rupture propagates circularly with a constant rupture velocity, and slip is assumed to have a step-like shape in time. An isochron is defined as the locus of all points on the fault from which seismic radiation reaches a given station at a given time t,

$$t = T_R(r_0, r_1) + T_C(r_0, x), \tag{2}$$

where r_0 and r_1 are the nucleation point and the isochron point, and x denotes the receiver position. T_R represents the rupture time, while T_C is the wave propagation time (the P-wave velocity is set to 5.35 km s^{-1} in the medium around the source). We drew the isochrons that delimit the final extension of the rupture for each station. The intersection of the areas delimited by isochrons defines the region of the fault plane that must contain the rupture. This area depends on the rupture velocity. In order to estimate the maximum area of the fault we chose a velocity of 3 km s^{-1}, which can be considered as an upper bound in the sedimentary layer that contains the source.

Fig. 8 shows the isochrons that correspond to six stations distributed over a representative set of azimuths. The intersection of the areas delimited by isochrons gives an estimate of the dimensions of the active fault plane. The grey zone in Fig. 8 represents the rectangular fault that corresponds most closely to the intersection of the areas delimited by the isochrons. Since the rupture velocity that we used is high (3 km s^{-1}), this area, estimated at 2.5 km^2, gives an upper

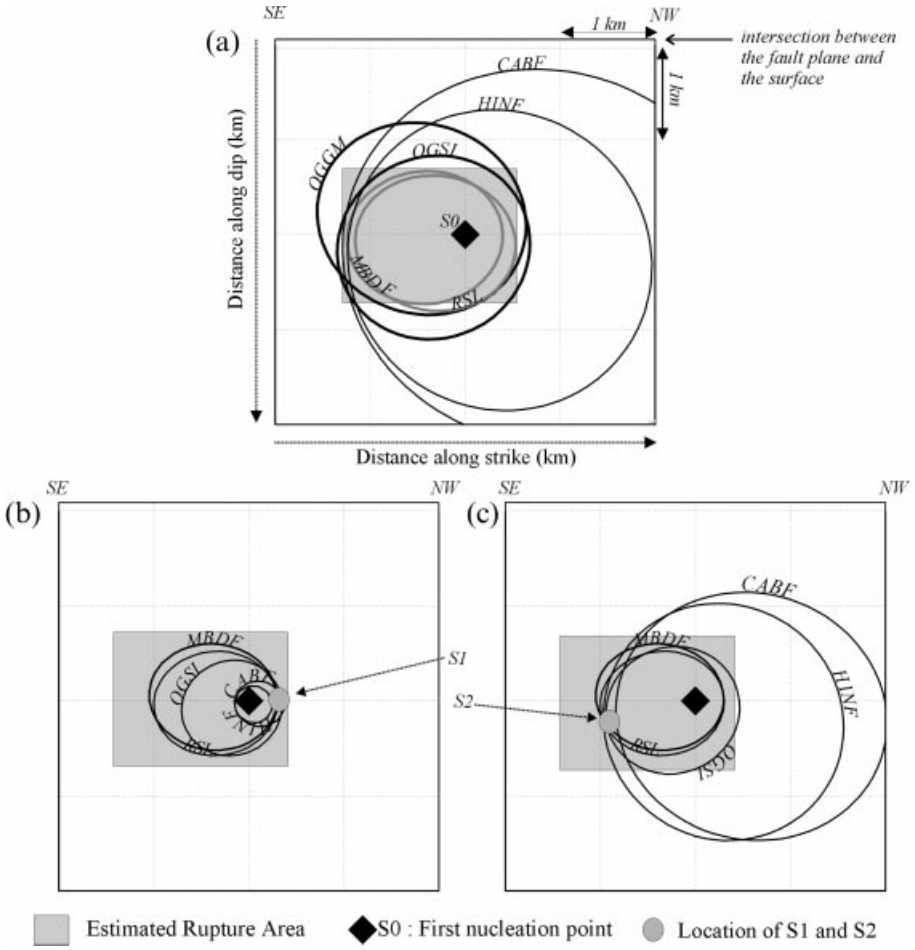


Figure 8. (a) Isochrons corresponding to the total duration of the apparent relative source-time functions represented on the fault plane (the origin of the depth scale along the fault corresponds to the surface). (b) Isochrons corresponding to the peak of the first subevent. (c) Isochrons corresponding to the peak of the second subevent.

bound to the rupture dimension. With the seismic moment equal to 1.9×10^{16} N m (computed from records of a Swiss accelerometer, located 30 km from the epicentre), we obtained an average displacement of 30 cm and a stress drop of 5.5 MPa.

Having obtained an estimate of the total rupture area, we can now locate the two subevents on the fault plane. For this purpose, on the ARSTFs of Fig. 3 we measure the time between the beginning of the rupture and the peak of each subevent. The first subevent, S1, can be seen at every station, whereas S2 is separated clearly from S1 only at the three stations CABF, HAU and HINF to the north and less clearly at station OGSI to the east. At the stations south and southeast of the epicentre, such as MBDF and RSL, the overall rupture directivity has caused the signals of the two subevents to merge into a single pulse. For these two stations we have taken the time from onset to the peak of the ARSTF (the rise time) as representative of both subevents. The isochrons corresponding to the delays of S1 and S2 determined in this manner are shown in the lower part of Fig. 8. The only region where the isochrons of S1 intersect is located about 250 m northwest of the nucleation point, whereas the second subevent, S2, is located about 900 m to the southeast.

It is important to remember that the absolute locations of the subevents depend strongly on the rupture velocity, which could not only be different from the one chosen for our model, but could also vary over the duration of faulting (e.g. Deichmann 1997). However, the general picture would remain the same, with a first subevent close to the hypocentre towards the northwest and a second subevent further away towards the southeast. The fact that the first subevent is located towards the northwest agrees with the interpretation of pulse-width measurements performed on the clipped data, which are based on the first pulse alone.

RELATION TO THE AFTERSHOCKS

The aftershock locations determined by Thouvenot *et al.* (1998), based on data from a temporary seismic network installed in the epicentral area two days after the main shock, delineate two fault segments separated by a right-lateral step-over of about 500 m. The larger segment, with the higher seismic activity in terms of both the number and the size of the events, is to the north and somewhat displaced from the surface trace of the Vuache Fault, while the other is more to the south and closer to the fault trace. Although Thouvenot *et al.* (1998) made an effort to constrain the main shock location with the results of the aftershock measurements and place its epicentre at the southeastern end of the northern fault segment, the remaining location uncertainty can not exclude it from having occurred on the southern segment instead.

Given this uncertainty, Fig. 9 illustrates two end-member scenarios of possible locations of the main shock rupture area relative to the aftershocks: in the first case, the rupture of the main shock nucleated close to the southeastern end of the northern segment and propagated mainly away from the more active part of the aftershock zone, while in the second case it nucleated and propagated along the southern segment. As noted above, the size of the main shock rupture area in Fig. 9 must be regarded as an upper bound.

DISCUSSION AND CONCLUSIONS

The aim of this study was to retrieve the main characteristics of the rupture process of the Epagny–Annecy earthquake using all the available data.

The analysis of the raw *P*-wave displacement seismograms and the EGF deconvolutions show that the rupture process consisted of at least two subevents. Moreover, the azimuthal dependence of the durations of the apparent source-time functions obtained from the EGF deconvolution as well as the fact that the double pulse is visible only on stations north of the epicentre provide evidence for a strong unilateral component of the rupture propagation towards the southeast along the strike of the fault and roughly parallel to the direction of slip. The isochron analysis indicates that a small amount of rupture propagation towards the northwest occurred during the early stages of the rupture process, corresponding to the first subevent, and that the second subevent corresponds to the main part of the rupture, which propagated towards the southeast.

In an attempt to interpret these results in terms of the fault geometry derived from the trend of the Vuache Fault, from the focal mechanism of the main shock and from the aftershock distribution documented by Thouvenot *et al.* (1998), we consider three scenarios: (1) the rupture area of the main shock is entirely part of the northern fault segment; (2) it is entirely part of the southern segment; or (3) the rupture nucleated on the northern segment, producing the first subevent, and then jumped to the southern segment, where it continued to propagate towards the southeast. Because of our lack of unclipped near-source seismograms for the main shock and the limited coverage of the focal sphere of the available data, our results on their own do not allow us to distinguish between these three possibilities. Nevertheless, we can examine the implications of these different scenarios in the light of other observations and arguments.

In the first case, the main shock did not occur on the Vuache Fault but on a fault segment parallel to it. For some not immediately apparent reason, the rupture stopped propagating towards the northwest, and then the main rupture phase propagated away from the area featuring the highest aftershock activity into a region with very few aftershocks. Fletcher & Spudich (1998) observed an apparent lack of correlation between rupture directivity and concentration of aftershock activity in their analysis of three moderate earthquakes on the San Andreas Fault. Therefore, this somewhat counterintuitive behaviour is not a sufficient reason to exclude this scenario. In the second case, the main shock actually nucleated on the Vuache Fault but was prevented from propagating further to the northwest by the apparent stepover in the fault and was thus forced to propagate mainly towards the southeast, as documented by the second subevent. In this scenario, the first subevent would correspond to a stopping phase originating from the northwestern edge of the rupture area, in agreement with the fact that it is observed as a separate phase only in a sector north of the epicentre. The third scenario, which invokes

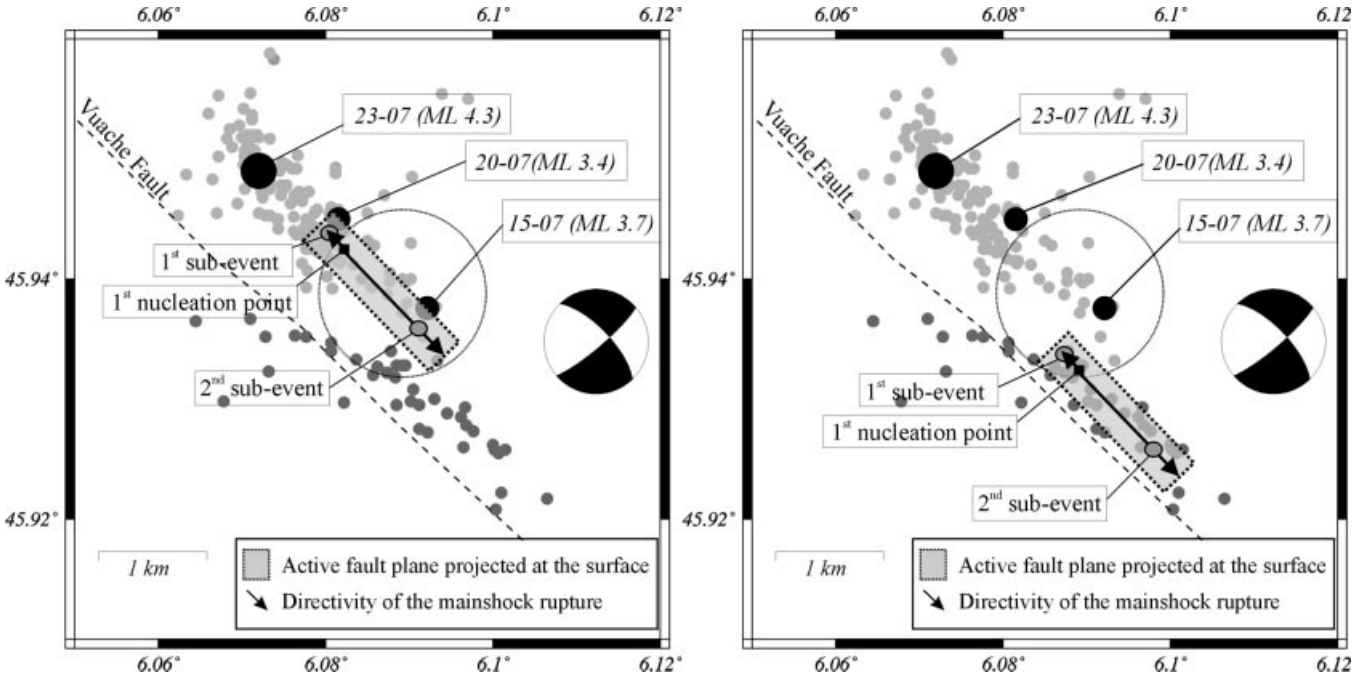


Figure 9. Aftershock locations and focal mechanism from Thouvenot *et al.* (1998). The largest aftershocks are labelled and the circle shows the estimated uncertainty of the main shock's epicentral location. A projection of the fault plane obtained from the isochron analysis is represented by a grey rectangle on which are shown the estimated locations of the first and second subevents as well as the rupture directivity. The two diagrams show the location of the main shock rupture assuming it is part of either the northern (left) or southern fault segment (right).

a rupture process occurring on two separate fault segments, is appealing, because it gives an intuitively plausible explanation for the observation of two subevents. A similar behaviour, with a rupture front that jumps across a stepover from one fault segment to the next, was observed in the 1992 Landers earthquake (Wald & Heaton 1994). However, as in the first scenario, we have to ask why the rupture did not continue further to the northwest, along a segment which, judging from the enhanced aftershock activity, was obviously ready to slip.

In addition to the arguments mentioned above, we favour the second scenario, in which the entire main shock rupture occurred on the southern fault segment and thus on the Vuache Fault, for the following reasons. The estimated total rupture area is compatible with the aftershock distribution on the southern segment. The fact that the number and magnitudes of the southern aftershocks are considerably smaller than those of the northern ones is evidence that most of the stress had already been released by the main shock. Conversely, the stepover in the fault, which prevented the rupture from propagating further to the northwest, then led to a stress increase on the northern segment. This stress increase was then released over the subsequent days and weeks with a large number of aftershocks, including several events of magnitude 3 and 4. Moreover, important evidence in favour of the main shock having occurred on the southern segment is the observation of cracks in the ground and in the runway of the Meythet–Annecy airport exactly where the extrapolated fault plane of the southern fault segment intersects the ground surface (Thouvenot *et al.* 1998). These cracks certainly did not occur as a consequence of the aftershocks alone.

Whatever interpretation one favours, our analysis of the rupture process of the Epagny–Annecy earthquake clearly shows that even moderate events of magnitude 5 can have complex rupture histories. It is also clear that, in addition to the known local site effects, the strong directivity effects due to an asymmetric rupture propagation can have significant consequences for the damage potential of such earthquakes.

ACKNOWLEDGMENTS

We thank the various groups that helped us retrieve the data necessary for this work and especially Marc Nicolas from LDG. We are grateful to François Thouvenot for providing us with the aftershock locations and focal mechanisms as well as for several helpful discussions. This work has been funded by the European project ENV4-CT96–0296 and the IPSN. (Publication no. 237 of UMR Géosciences AZUR and no. 1073 of the Institute of Geophysics, ETH-Zürich.)

REFERENCES

Bernard, P. & Madariaga, R., 1984. A new asymptotic method for the modelling of near-field accelerograms, *Bull. seism. Soc. Am.,* **74,** 539–557.

Beroza, G.C. & Ellsworth, W.L., 1996. Properties of the seismic nucleation phase, *Tectonophysics,* **261,** 209–227.

Boatwright, J., 1980. Spectral theory for circular seismic sources: simple estimates of source dimension, dynamic stress drop and radiated energy, *Bull. seism. Soc. Am.,* **70,** 1–28.

Courboulex, F., Virieux, J., Deschamps, A., Gibert, D. & Zollo, A., 1996. Source investigation of a small event using empirical Green's functions and simulated annealing, *Geophys. J. Int.,* **125,** 768–780.

Courboulex, F., Deschamps, A., Cattaneo, M., Costi, F., Deverchère, J., Virieux, J., Augliera, P., Lanza, V. & Spallarossa, D., 1998. Source study and tectonic implications of the April 21, 1995 Ventimiglia (border of Italy and France) earthquake ($M_L = 4.7$), *Tectonophysics,* **290,** 245–257.

Deichmann, N., 1997. Far field pulse shapes from circular sources with variable rupture velocities, *Bull. seism. Soc. Am.,* **87,** 1288–1296.

Fletcher, J. & Spudich, P., 1998. Rupture characteristics of the three M 4.7 (1992–94) Parkfield earthquakes, *J. geophys. Res.,* **103,** 835–854.

Frankel, A. & Kanamori, H., 1983. Determination of rupture duration and stress drop for earthquakes in southern California, *Bull. seism. Soc. Am.,* **73,** 1527–1551.

Haddon, R. & Adams, J., 1997. Anatomy of a small intraplate earthquake: a dissection of its rupture characteristics using regional data, *Geophys. J. Int.,* **129,** 235–251.

Hartzell, S., 1978. Earthquakes aftershocks as Green's functions, *Geophys. Res. Lett.,* **5,** 1–4.

Hough, S.E., 1996. Observational constraints on earthquake source scaling: Understanding the limits in resolution, *Tectonophysics,* **261,** 83–95.

Lambert, J. & Levret-Albaret, A., 1996. *Mille Ans de Séismes en France, Catalogue d'épicentres, Paramètres et Références,* Ouest Editions, Nantes.

Mori, J., 1996. Rupture directivity and slip distribution of the M 4.3 foreshock to the 1992 Joshua Tree earthquake, Southern California, *Bull. seism. Soc. Am.,* **86,** 805–810.

Mueller, C., 1985. Source pulse enhancement by deconvolution of an empirical Green's function, *Geophys. Res. Lett.,* **12,** 33–36.

Nicolas, M., Santoire, J.P. & Delpech, P.Y., 1990. Intraplate seismicity new seismotectonic data in western Europe, *Tectonophysics,* **179,** 27–53.

O'Neill, M.E. & Healy, J.H., 1973. Determination of source parameters from P-wave rise time, *Bull. seism. Soc. Am.,* **63,** 599–614.

Spudich, P. & Frazer, L.N., 1984. Use of ray theory to calculate high frequency radiation from earthquake sources having spatially variable rupture velocity and stress drop, *Bull. seism. Soc. Am.,* **74,** 2061–2082.

Thouvenot, F., Fréchet, J., Tapponnier, P., Thomas, J.C., Le Brun, B., Ménard, G., Lacassin, R., Jenatton, L., Grasso, J.R., Coutant, O., Paul, A. & Hatzfeld, D., 1998. The M_L 5.3 Epagny (French Alps) earthquake of 15 July 1996: a long-awaited event on the Vuache fault, *Geophys. J. Int,* **135,** 876–892.

Vogt, J., ed., 1979. Les tremblements de Terre en France, *Mém. Bur. Rech. géol. min.,* no. 96.

Wald, D.J. & Heaton, T.H., 1994. Spatial and temporal distribution of slip for the 1992 Landers, California, earthquake, *Bull. seism. Soc. Am.,* **84,** 668–691.

Zollo, A. & Bernard, P., 1991. How does an asperity break? New elements from the waveform inversion of accelerograms for the 2319 UT, October 15, 1979, Imperial Valley aftershock, *J. geophys. Res.,* **96,** 549–573.

1.7 Le séisme d'Athènes de 1999 (Mw 5.9)

Cette étude a été initiée par ma participation à un projet européen : PRESAP « Towards practical, real-time estimation of spatial aftershock probabilities: a feasibility study in earthquake hazard » . La question centrale posée dans ce projet était : « Est il possible de prévoir dans les minutes qui suivent un séisme où vont avoir lieu les plus fortes répliques ». Il s'agissait de travailler à la fois sur les modèles numériques de diffusion des contraintes et sur quelques séismes réels bien instrumentés. Le séisme d'Athènes de magnitude Mw 5.9 a été choisi comme un cas « test ».

Ce séisme a eu lieu sur une faille de la banlieue d'Athènes, c'est-à-dire dans une zone fortement peuplée. Il a causé des dégâts considérable aux bâtiments, dont l'effondrement a engendré la mort de 150 personnes et plus de 2000 blessés (Figure 1. 12).



Figure 1. 12 : Aperçu des dommages dus au séisme d'Athènes

Ce séisme a eu lieu sur une faille normale non répertoriée comme active. Aucun événement historique ou instrumental n'avait été reporté dans cette zone. Il a généré une rupture qui a vraisemblablement atteint la surface (Figure 1. 13).

Les données locales étaient peu nombreuses et souvent saturées. Nous avons donc travaillé principalement sur les données régionales.
Pour la première fois, je me retrouvais dans une position ou c'est moi qui encadrais un post-doc. Encadrer dans ce cas de figure est un mot un peu fort puisque David Baumont, qui rentrait à peine des Etats Unis m'a lui-même beaucoup appris, en particulier sur les ondes de surface.

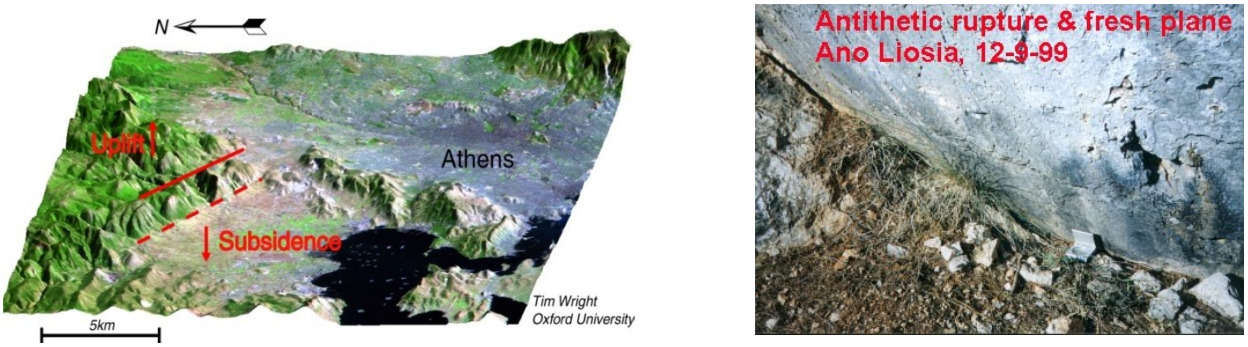


Figure 1. 13 : Fonctionnement de la faille normale responsable du séisme d'Athènes et rupture de surface associée (Tim Wright, Oxford University)

Le premier article présenté ici décrit l'inversion de la source que nous avons effectuée à partir des données régionales et des ondes de surface en utilisant deux fonctions de Green empiriques de magnitude plus faible. L'expérience de David Baumont dans le traitement des ondes de surface et les méthodes d'inversion linéarisées a été un apport considérable à ce travail. Le second article va un peu plus loin puisque nous avons utilisé également des données interférométriques (Figure 1. 14).

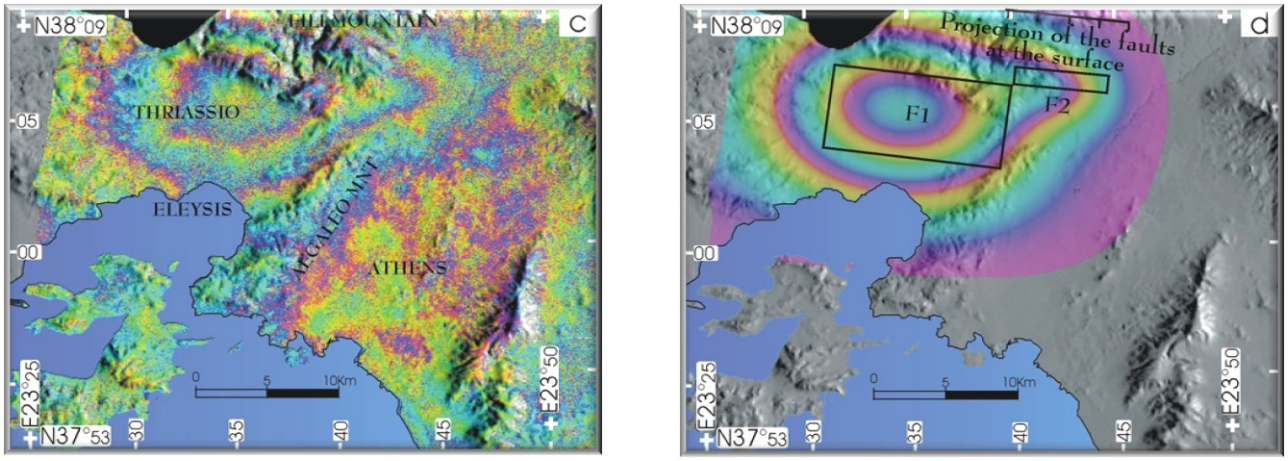


Figure 1. 14 : Interférogramme calculé et simulé (Kontoes et al, 1999)

Nous obtenons très vite des résultats différents selon que l'on inverse les données sismologiques seules ou les données géodésiques seules. Des tests seront effectués sur les jeux de données pour comprendre l'origine de ces différences. Nous proposons enfin une distribution du glissement haute fréquence ou cosismique différente de la distribution du glissement vue par l'interférométrie radar sur une période de temps beaucoup plus longue (Figure 1. 15). Cette mise en évidence d'un signal non-cosismique pour un séisme d'une magnitude aussi faible n'est pas couramment reporté dans la littérature.

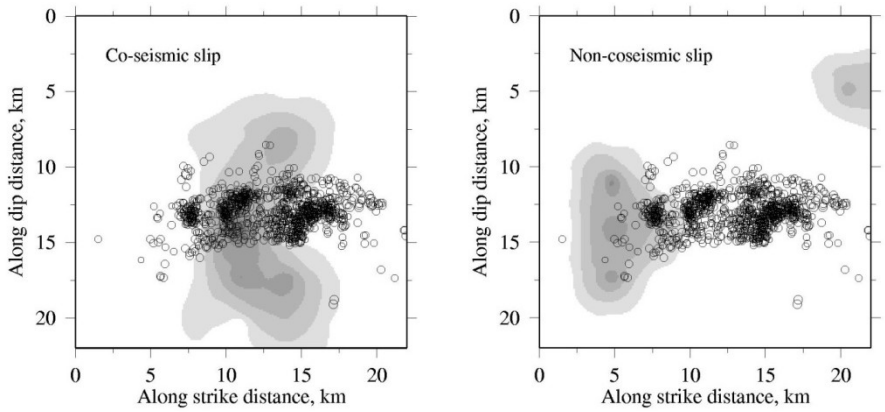


Figure 1. 15 : Glissement cosismique et non-cosismique obtenu pour le séisme d'Athènes grâce aux données sismologiques et géodésiques.

Geophys. J. Int. (2004) **158,** 1078–1087 doi: 10.1111/j.1365-246X.2004.02374.x

Complex kinematic rupture of the Mw 5.9, 1999 Athens earthquake as revealed by the joint inversion of regional seismological and SAR data

D. Baumont,[1] O. Scotti,[1] F. Courboulex[2] and N. Melis[3]

[1] *IRSN/DEI/SARG/BERSSIN,* 60-68 *Av. du Général Leclerc,* PO Box 17, *Fontenay aux Roses* 92262, *France. E-mail: david.baumont@irsn.fr*
[2] *Géosciences Azur,* 250 *Av. Albert Einstein, Valbonne* 06560, *France*
[3] *NOA-IG,* PO Box 20048, *Lofos Nymfon, Athens* GR-118 10, *Greece*

Accepted 2004 May 28. Received 2004 April 29; in original form 2003 August 7

SUMMARY

Slip distributions of the moderate magnitude (Mw 5.9), 1999 Athens earthquake, inverted from surface waves and interferometric Synthetic Aperture Radar (SAR) images, show very different characteristics. The robustness analysis proposed in this study, confirms the discrepancy between the well-constrained features of each individual solution. Irrespective of the hypotheses we made (data/modeling errors, slow deformation, post- or pre-seismic slip), the joint inversion of the two data sets led to a complex and heterogeneous rupture model. This model is characterized by a short rise time (<5 s) slip patch centred on the hypocentre, extending bilaterally up to 4 km depth and down to 17 km and releasing approximately 70 per cent of the total moment. Located further to the WNW and releasing the remaining 30 per cent of the total moment, a long rise time slip patch extends from 8 to 17 km depth. If the short rise time slip patch propagated above and below the brittle zone delineated by the aftershocks, the long rise time slip patch (slow deformation) appears to be mostly confined below the brittle zone. This unified model satisfies the analysis of the seismic and geodetic slip distributions as well as the location of the aftershock sequence and attests to the diversity of the crustal response even for moderate size faults.

Key words: complex slip distribution, joint inversion, moderate magnitude earthquake, slow deformation.

1 INTRODUCTION

On 1999 September 7, a moderate magnitude (Mw 5.9), crustal earthquake occurred less than 10 km to the west of the metropolitan area of Athens (Fig. 1). Despite its moderate size, this earthquake caused extensive damage in Athens and its surroundings, especially in the northern and western suburbs where the macroseismic intensities reached IX locally (Anastasiadis *et al.* 1999). Some 100 buildings collapsed (among which were reinforced concrete buildings) and more than 10 000 buildings were declared to be either heavily damaged or damaged beyond repair. One hundred and forty-three people died and approximately 100 000 people were homeless during the first days following the earthquake.

Moderate magnitude earthquakes occurring at close distances to a densely populated area or a strategic installation represent the typical seismic hazard in Europe and yet little is known about their rupture process and kinematic characteristics compared to large earthquakes. Indeed, moderate earthquakes have a rich frequency content, which is difficult to model, and are usually poorly recorded. In this respect, the Athens earthquake is exceptional: (i) the main shock and the largest aftershocks were recorded by a remarkably good azimuthal coverage of regional broad-band stations (Stavrakakis *et al.* 2002) and (ii) numerous SAR images were available. On the one hand, several rupture models were proposed for the Athens earthquake based on the analysis of regional broad-band data using an empirical Green function (EGF) approach. By forward modelling, Tselentis & Zahradnik (2000b) proposed a 10-km asperity rupture model. Baumont *et al.* (2002) and Roumelioti *et al.* (2003) inverted the apparent source time functions (ASTFs) for a more detailed rupture model (Fig. 2), showing a bilaterally upward and downward propagating rupture of roughly similar amplitude and extent. Only the details of the slip distributions are different as a result of differences in the calculated ASTFs and in the modelling parametrization. On the other hand, Kontoes *et al.* (2000) computed several SAR interferometric deformation field images, showing two asymmetric fringes. To satisfactorily model this asymmetry, the authors appealed to two distinct, non-coplanar, N116°, 54° south dipping faults with homogeneous slip. According to their model, the total moment released is of the order of 1.5×10^{18}N m, which is 30–50 per cent larger than the seismic moment estimates (Table 1). Compared to the seismic rupture models, this model is suggesting the existence of a larger amount of slip at depth.

In this paper, we test whether the discrepancy between seismic and geodetic models could be explained by data and modelling errors

© 2004 RAS

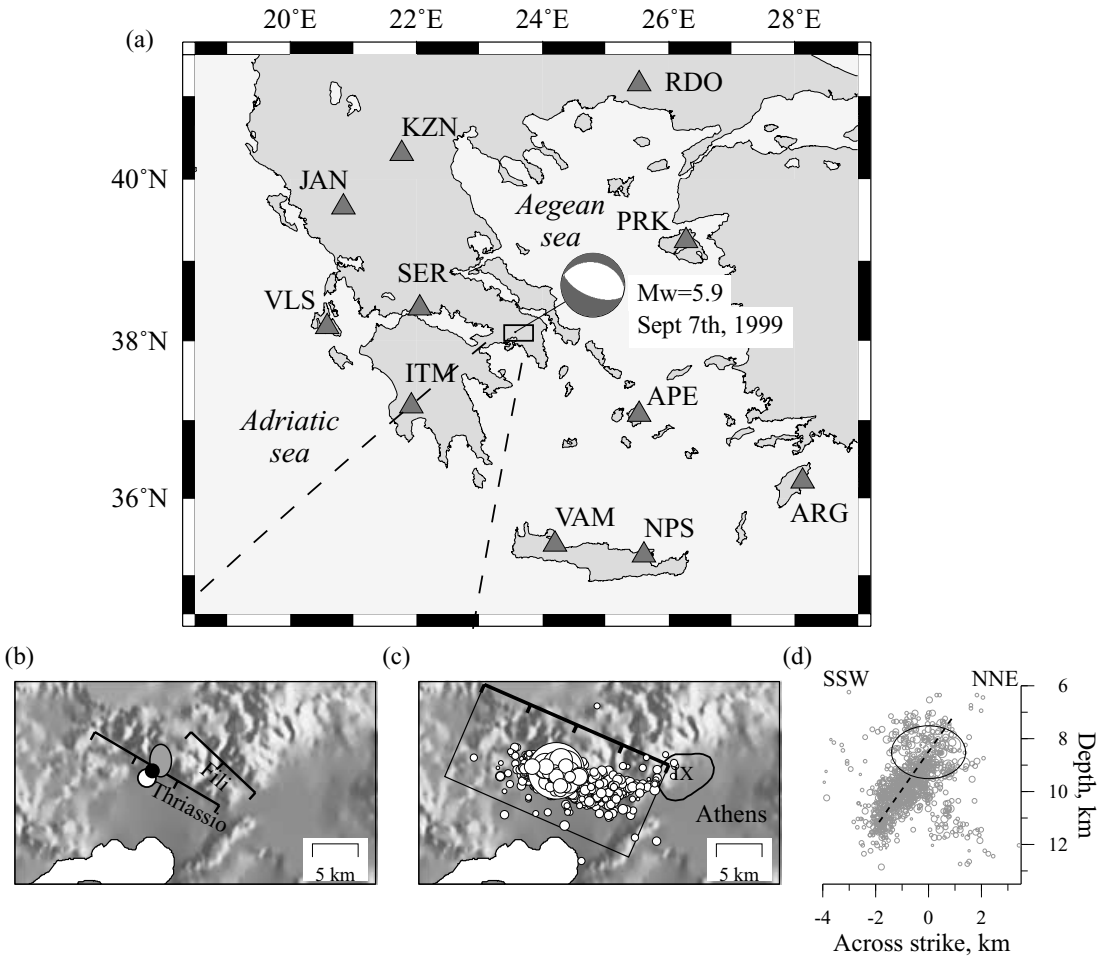


Figure 1. (a) Map of regional broad-band stations used in this study (triangles) showing their optimal distribution with respect to the epicentre of the Athens 1999 earthquake. The National Observatory of Athens operates these stations with the exception of Sergoula (SER), which is operated by Patras and Prague universities. The focal mechanism calculated by Zahradnik (2002) shows an almost east–west oriented normal fault. (b) Epicentre location proposed by Papadimitriou *et al.* (2000) (white ellipse) and by the International Seismological Centre (grey ellipse) relative to the Thriassio and Fili faults (black lines). The epicentral location of the initial model is also shown in black (Table 1). (c) Initial fault model used in this study relative to our best relocated aftershocks. These aftershocks, recorded by a temporary network (run by the NOA between 1999 September 13 and November 11), were relocated using a Joint Hypocentre Determination procedure (Pujol 1988). (d) Our best relocated events highlight a 55°, south dipping fault plane.

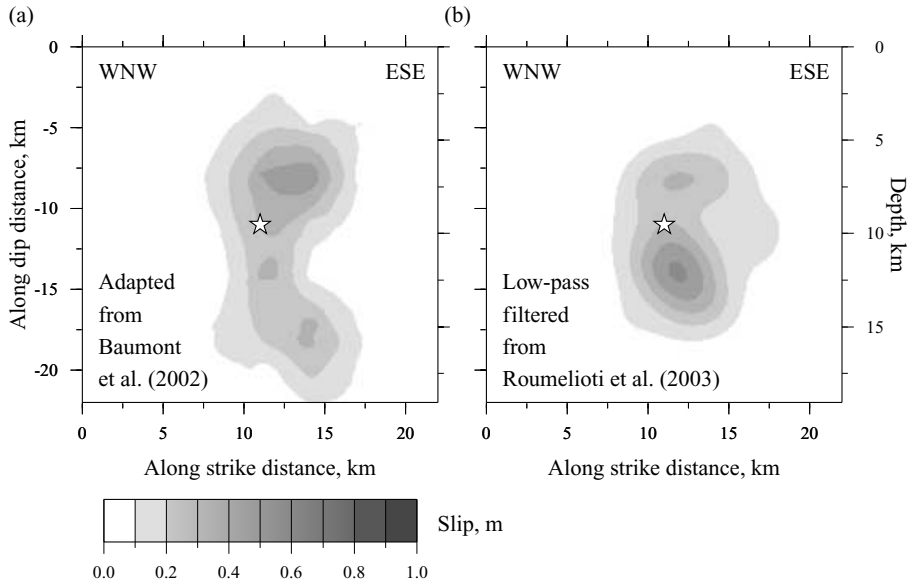


Figure 2. Comparison between the slip distributions obtained by (a) Baumont *et al.* (2002) and (b) Roumelioti *et al.* (2003).

Table 1. Locations, focal mechanisms and seismic moment of the 1999 Athens earthquake reported by different institutes or authors.

Longitude (°)	Latitude (°)	Depth (km)	Strike (°)	Dip (°)	Rake (°)	Mo (10^{18}N m)	Institute or authors
23.58	38.08	16.8	113	39	−90		Papadopoulos *et al.* (2000)
23.582	38.122	9.4					ISC bulletin
23.605	38.119	8.0	136	56	−82	0.9	USGS-NEIC
23.565	38.105	8	105	55	−80	1.0	Papadimitriou *et al.* (2000)
23.640	37.870	15.00	116	39	−81	1.1	HRVD-CMT
23.54	38.06	10	115	57	−80	0.9	Louvari & Kiratzi (2001)
		10	115	60	−80	0.6	Sargeant *et al.* (2002)
			112	61	−84		Zahradnik (2002)
			117	52			Tselentis & Zahradnik (2000a)

USGS-NEIC is U.S Geological Survey, National Earthquake Information Center.

Table 2. Parameter space explored in this study and optimal values inverted or fixed (shaded) corresponding to the results presented in Figs 2, 4 and 6.

		Parameter space	Fig. 2	Fig. 4	Fig. 6
Hypocentre	Longitude	23.572° ± 3 km	23.572°	23.584°	23.582°
	Latitude	38.112° ± 3 km	38.112°	38.124°	38.122°
	Depth (km)	8 to 16	9.5	9.6	9.5
Geometry	L ×W (km^2)	22 × 18, 22 × 22, 35 × 22	118	138	148
	Strike (°)/dip (°)	112/40, 50, 60		112/60	
	Rake (°)	−84; −110 to −70		−84	
Rupture model	Corr. length (km)	4 or 10	4	10	4
	Slip (m)	0 to 1	0.29	0.43	0.36
	Rise (s)	0 to 5	1.4	–	1.8
	Vr (km s^{-1})	2.5 to 3.2	2.9	–	2.9
	M_0 (10^{18} N m)	–	1.1	1.8	1.6
	Stress drop (MPa)	–	2	3	2
	rms_{ASTFs} (10^6 N m s^{-1})	–	1.6	–	2.2
	rms_{SAR} (mm)	–	–	6.1	8.2

and propose a robustness scheme to outline the well-constrained features of each individual solution. The different hypotheses tested through a joint inversion allow us to propose a new rupture model for the Athens earthquake that satisfactorily predicts both the geodetic and seismic data.

2 FAULT PARAMETRIZATION

Published earthquake parameters are listed in Table 1. Our fault model (Table 2) is composed of a single plane centred on the hypocentre. Among the various published solutions, we chose epicentral locations within the solutions of Papadimitriou *et al.* (2000) and the International Seismological Centre (ISC; Fig. 1b) and tested for a hypocentral depth between 8 and 17 km. The fault dimensions were chosen to include all the previous estimates of rupture area: 20 × 16 km^2 based on the aftershock distribution (Tselentis & Zahradnik 2000b), 10 × 11 km^2 by inverting SAR data (Kontoes *et al.* 2000), 18 × 10 km^2 by modelling far field body waves (Louvari & Kiratzi 2001), and 10 × 15 km^2 by inverting the ASTFs (Baumont *et al.* 2002; Roumelioti *et al.* 2003).

Two 110–130°N, south dipping normal faults are clearly expressed on the morphology of the epicentral area, the Fili and Thriassio faults, however, the field investigation did not allow a direct identification of the activated fault, since no extended surface rupture was observed (Pavlides *et al.* 2002). According to published aftershock distributions and focal mechanism solutions, the rupture occurred on a 110–140°N, 40–60° dipping normal fault. Following the focal mechanism solution proposed by Zahradnik (2002) and our aftershock distribution (Fig. 1d), the fault strike and dip angles were fixed at 112°and 60°, respectively. Alternative fault geometries were tested and did not affect the main characteristics of either the geodetic or the seismic rupture models. The rake was fixed to −84°. The fault model was subdivided using a regular grid mesh of 3 by 3 km^2. For each sub-fault, we define a physically reasonable range of values for the slip amplitude, the rupture and the rise time. Two correlation lengths were tested. The seismic moment used to normalize the ASTFs was fixed at 1.1 × 10^{18} N m.

3 IMPACT OF SURFACE-WAVE MODELLING ON THE SEISMIC RUPTURE MODEL

In our previous study (Baumont *et al.* 2002), we did not take into account the sensitivity of surface-waves to the assumed source depth, which may modify the slip distribution and may reduce the discrepancy between the geodetic and seismic slip models. In order to estimate a surface-wave depth correction, we assume that surface-wave records can be modelled by summing the first three modes. Using the regional velocity model proposed by Tselentis & Zahradnik (2000b), we model the seismograms up to 2 Hz through a mode summation approach (Herrmann 2002). We consider a source-station distance of 200 km, and perform several computations with a source located

at different depths between 2 and 20 km. The resulting relative amplitude change of the surface waves as a function of the source depth is used to model the ASTFs more correctly.

ASTFs were retrieved from the most energetic phases, i.e. the Rayleigh and Love waves, filtered (0.08–10 Hz) to insure a good signal-to-noise ratio. We applied a time-domain iterative deconvolution with positivity constraints. To get rid of the frequencies higher than the EGF corner frequency, a Gaussian filter (2 Hz) was applied. Three EGFs were considered to evaluate the ASTFs and their uncertainties. ASTFs were inverted for the kinematic rupture model using a damped-least square scheme with inequality constraints accounting for our surface-wave depth correction. The ASTF uncertainties were introduced through a covariance matrix on data reduced to its diagonal elements. We fixed the hypocentre at 9.5 km depth close to the ISC determination (Table 1). Fig. 3 shows one of our best inversion solutions using this new ASTF modelling. This rupture

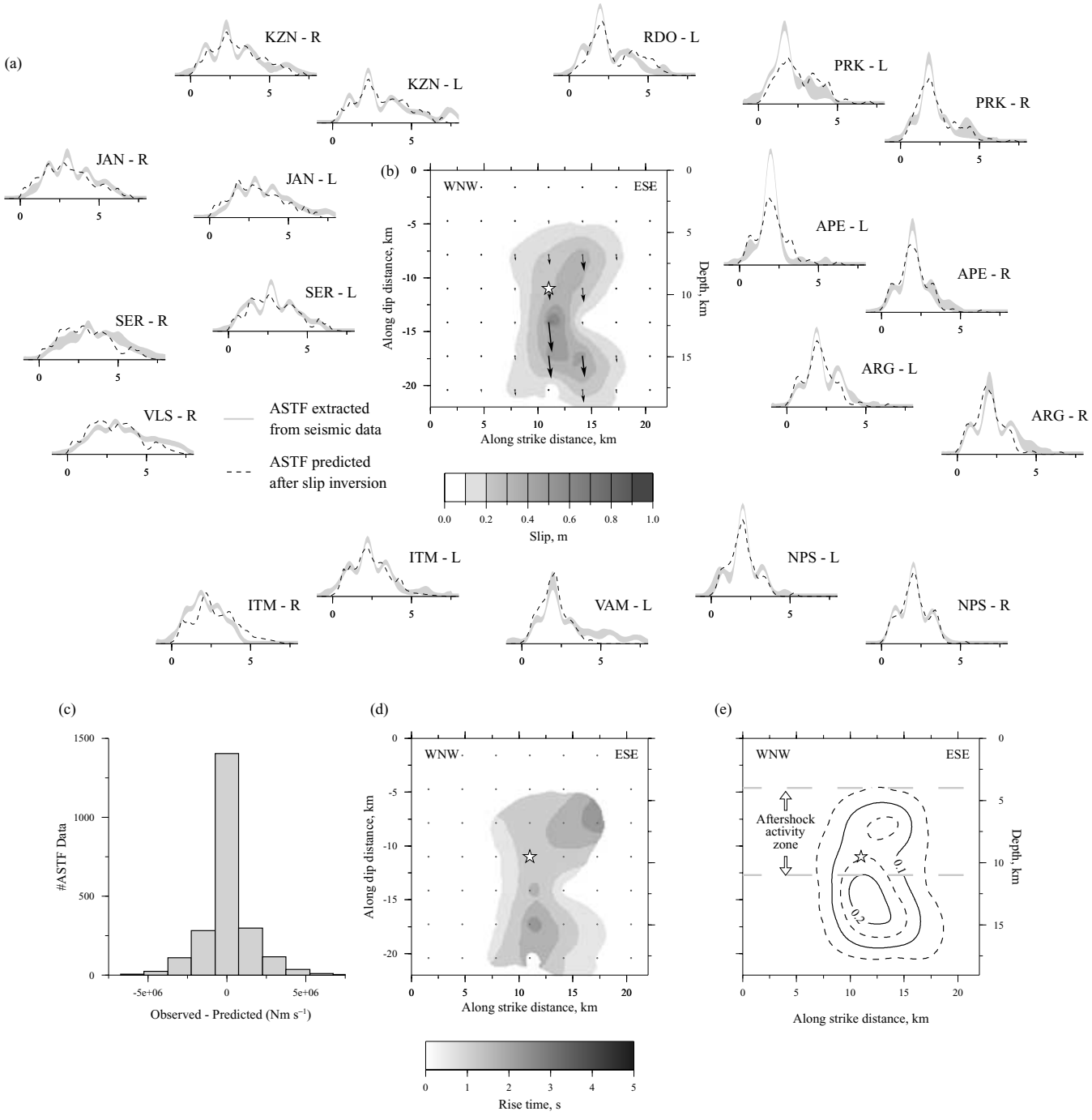


Figure 3. Best kinematic rupture model for the Athens earthquake inverted from Rayleigh (R) and Love (L) waves assuming a surface wave depth correction (see text). (a) Azimuthal variations of ASTFs (after Baumont *et al.* 2002) and associated uncertainties (shaded grey areas). The ASTFs were normalized using the seismic moment of the Harvard CMT Catalog (HRVD-CMT) solution (Table 1). (b) Slip and (d) rise time distributions inverted from the ASTFs data assuming the fault geometry shown in Fig. 1c (see Table 2). This rupture model predicts satisfactorily the ASTFs (dashed lines in a) with (c) an rms of 1.6×10^6 N m s^{-1}. Notice that rms was normalized by the shear modulus value (3×10^{10} N m^{-2}). (e) Robustness analysis highlighting the coherent features (see text). The aftershock activity zone (Voulgaris *et al.* 2000) suggests that the rupture propagated below the base of the brittle zone.

model satisfactorily predicts both the amplitudes and timing of the peaks observed in the ASTFs, with an rms of 1.6×10^6 N m s^{-1} (Figs 3a and c). The rupture is characterized by a bilateral upward and downward propagation covering 120 km^2 (Fig. 3b). Although the mean slip amplitude is equal to approximately 30 cm, the slip is heterogeneous, reaching 60 cm locally in the deeper part of the fault. The rupture velocities average around 2.9 km s^{-1}, but are poorly constrained. Rise time values (Fig. 3d) vary between 0.5 and 2.5 s. In this model the rupture lasts roughly 5 s.

Thus, accounting for the surface wave sensitivity to depth results in an overall transfer of slip (of the order of 20 per cent) from the shallowest part of the fault to the deeper part (*cf.* Figs 2a and 3b), but does not affect the geometry of our slipping patch.

4 IMPACT OF ASTF ERRORS ON THE SEISMIC RUPTURE MODEL

As previously mentioned, three EGFs were considered to estimate the ASTFs and their uncertainty. Nonetheless, these uncertainties do not cover the differences between our ASTFs and those obtained by Roumelioti *et al.* (2003). In order to further qualify the robustness of the main features of our seismic slip solution, we performed a stochastic exploration of the model space and retained all models with an rms value as large as 2×10^6 N m s^{-1}. Starting from our best solution, which has an rms of 1.6×10^6 N m s^{-1}, a set of models was generated by random perturbation. At each iteration, the random model is allowed to change up to 2 cm for the slip amplitude and up to 0.1 s for rupture time and rise time. The new model is retained if it satisfactorily reproduces the ASTFs. The parameter space is then re-explored (30 000 times) starting from the most updated model and only 600 are retained. Because strike and dip angles have only a minor effect on the solution, they were kept fixed. The hypocentral depth was also kept fixed considering the narrow range of the best determinations (8 to 10 km).

To highlight the coherent features of the slip distributions, the 600 models are low-pass filtered (10-km-cut-off wavelength) and the lowest slip value is reported at each grid point (Fig. 3e). As testified by this robustness analysis, the main characteristics of the slip distribution (the extension of the fault and the presence of two slipping patches vertically aligned on either side of the hypocentre) are well constrained.

It is interesting to compare the repartition of the slip with the aftershocks because they may help delimit the base of the brittle zone. Indeed, the aftershock sequence recorded by the NOA temporary network outlines a 15-km-long region between 6 and 12 km depth (Figs 1c and d). The complete data set published by Papadimitriou *et al.* (2002) and Voulgaris *et al.* (2000) shows more activity to the west but remains mostly confined above 11 km depth. The rupture may have thus propagated below the brittle zone (Fig. 3e).

5 SINGLE FAULT, GEODETIC RUPTURE MODELS

As previously explained, Kontoes *et al.* (2000) appealed to two distinct, non-coplanar, 116°N, 54° south dipping faults with homogeneous slip to model the asymmetry of the surface deformation field. Because the seismological data cannot confirm or exclude the activation of a second fault plane, we prefer to address the question of whether a single heterogeneous fault segment could equally well satisfy the asymmetric deformation field.

The observed deformation field (Fig. 4a) is regularly sampled (36 points). We can rule out any significant potential biases in the deformation data as a result of troposphere perturbations. Indeed, Kontoes *et al.* (2000) showed in their analysis that an additional SAR interferogram covering a different time period [1997 November 27 to 1999 September 23] led to a very similar image. Data errors were deduced from the comparison of these two interferograms and fixed to 4 mm for the inner fringes and to 8 mm for the ill-defined fringe of zero deformation. The uncertainties on the SAR data were introduced through a covariance matrix on data reduced to its diagonal elements. However, because the least-squares criteria can be sensitive to a very small number of data with large errors, low weights were applied to data with large deviations from the values predicted by the current model. The deformation field is modelled using the analytical solution of Okada (1992) in a homogeneous, elastic, half-space. Because slip models inverted from geodetic data are sensitive to the fault location, we invert for both the slip distribution and the hypocentre location (within the *a priori* uncertainty; Table 2) through an iterative weighted least-squares scheme with inequality constraints (Menke 1984). As a reminder the fault model is centred on the hypocentre.

Fig. 4(d) shows our best slip model as well as the predicted and observed SAR interferograms covering the period [1998 September 19 to 1999 October 9]. The synthetic interferogram (Fig. 4b) reproduces well the inner fringes, but not the poorly defined zero-deformation fringe. Our best geodetic slip model exhibits features that are significantly different from the seismological solutions (Figs 2 and 3): a main slip patch located in the WNW deep part of the fault (mean amplitude equal to 45 cm) and a minor one in its ESE shallow part (mean amplitude equal to 20 cm). This model is overall very similar to the one proposed by Kontoes *et al.* (2000) in the sense that the two slipping patches/dislocations inverted have comparable spatial dimensions and amplitudes. The moment released was estimated at approximately 1.8×10^{18} N m (Table 2), which is close to the estimation of Kontoes *et al.* (2000), but larger than the seismic moment estimations (Table 1). The fault location we inverted is within the error bars of the ISC determination, while its depth remained unchanged. These results are not affected by the initial hypocentral location tested between 8 and 17 km. The fault trace projection lies on the NW extension of the Fili fault.

Several other inversions were made:

(i) considering only the 28- and 56-mm fringes;

(ii) considering the other available interferogram (Kontoes *et al.* 2000);

(iii) allowing the rake to vary smoothly between $-110°$ and $-70°$ (which allowed a better modelling of the zero-deformation fringe).

Nevertheless, the main characteristics of the geodetic slip distribution remain. As for the seismological data, the robustness analysis of this solution confirms that the main features of the slip model are well constrained (Fig. 4e) and differ significantly from the ones inverted from seismological data (Fig. 3e).

6 SLIP MODELS FROM THE JOINT INVERSION OF GEODETIC AND SEISMIC DATA

As demonstrated in the previous sections, the seismic and geodetic data produce slip distributions with well-resolved but very different characteristics. Two hypotheses can be proposed to interpret the origin of this discrepancy: (i) data/modelling errors and/or (ii) differences in the bandpass of the two data sets.

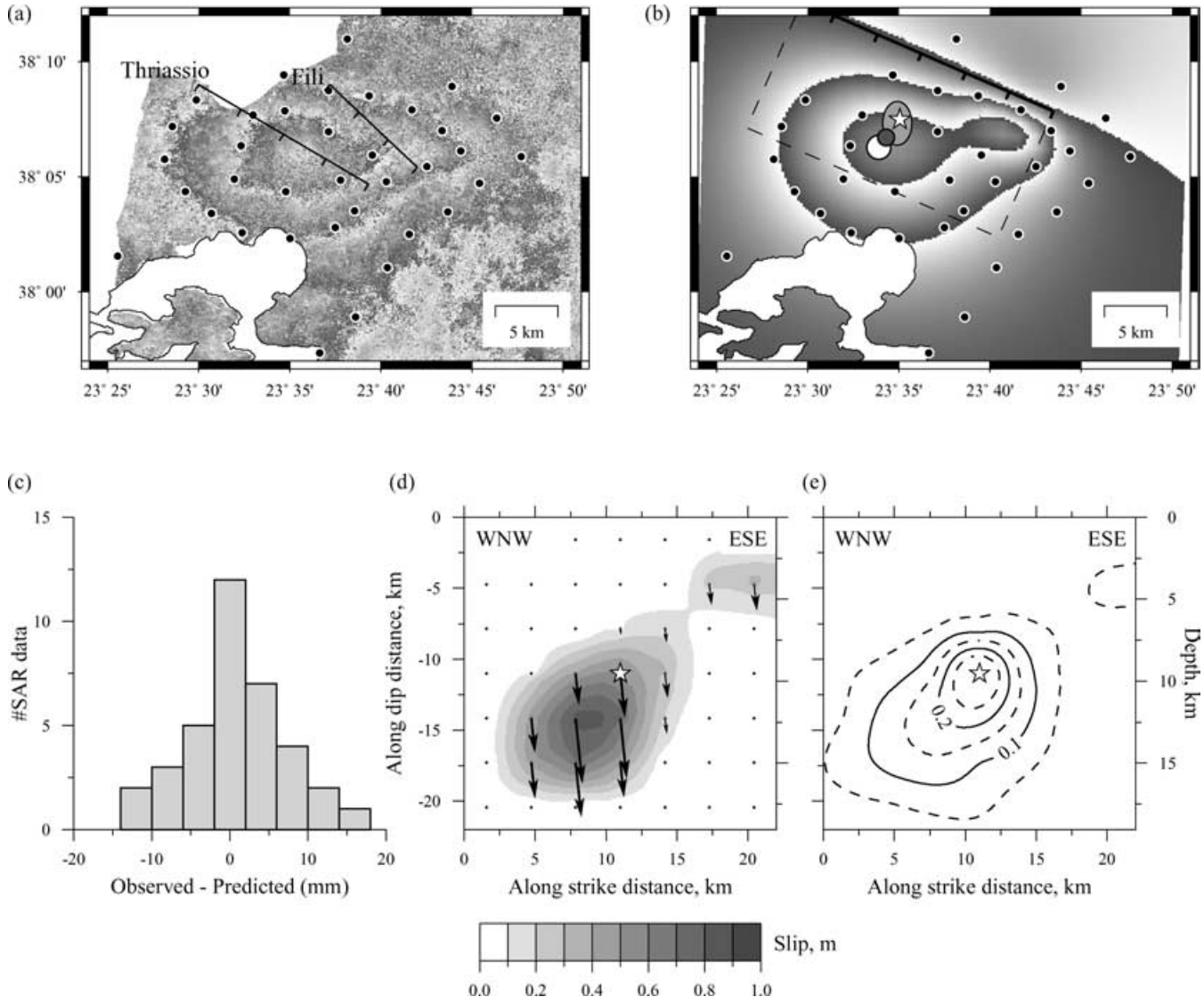


Figure 4. Best rupture model inverted for the Athens earthquake from geodetic data. (a) SAR interferogram spanning the period [1998 September 19 to 1999 October 9] computed by Kontoes *et al.* (2000). (b) The best fault location (star) is within the error bars of the ISC determination (see legend of Fig. 1). The synthetic interferogram reproduces well the inner fringes with (c) an rms around 6 mm. (d) Our best slip model is characterized by a main slip patch located in the WNW deep part of the fault and a minor one in the ESE shallow part. The corresponding moment, 1.8×10^{18} N m, is larger than the seismological estimates (Table 1). (e) Robustness analysis showing that the ESE patch is at the limit of the resolution, whereas the main WNW patch is well constrained.

6.1 Hypothesis 1: data/modelling errors

Assuming that the discrepancy is only the result of data/modelling errors, we perform a joint inversion in order to produce a model that predicts reasonably well both data sets. We adopt the approach proposed by Julià J. *et al.* (2000), in which each data set is equally weighted through an error function, defined as follows:

$$\mathrm{Err} = \left[\frac{(1-p)}{N} \sum_{i=1}^{N} \left(\frac{\delta \mathrm{ASTF}_i - G_{ij} \delta X_j}{\sigma_i} \right)^2 + \frac{p}{M} \sum_{i=1}^{M} \left(\frac{\delta \mathrm{SAR}_i - H_{ij} \delta X_j}{\sigma_i} \right)^2 \right]. \quad (1)$$

δASTF and δSAR describe the residual data, $G$and $H$the partial derivative matrices and δX the model correction. The partial derivative matrices were previously defined for the seismological and geodetic data. To equalize the data contribution of each data set and limit physical unit problems, the individual errors are divided by the number of data points (Nor M) and by the data variance (σ^2). To modify the relative influence of each data set, a p-weighting factor is introduced in the joint inversion scheme. Fig. 5 shows the degradation of each data set rms with respect to their best individual fit as a function of the p-weighting factor. For $p = 0$, the solution is constrained by the ASTFs, whereas for $p = 1$, the solution is controlled by the SAR data. The model space explored and the inversion scheme are similar to the ones considered in the previous sections. Several inversions were performed testing various hypocentral locations (ATHU, ISC), fault dips (50°to 60°), elastic parameters [$1 - (Vp/Vs)^2 = 0.6$ to 0.7], starting models (homogeneous, pulse, best seismological or geodetic models).

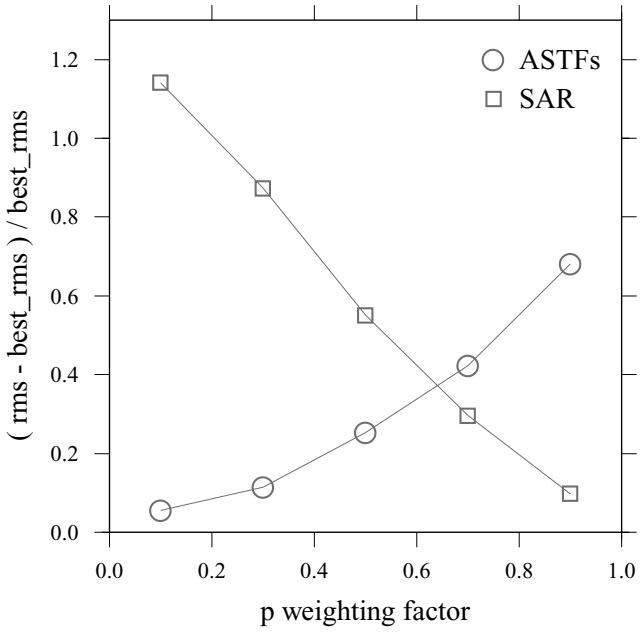


Figure 5. Degradation of each data set rms with respect to their best individual fit as a function of the *p*-weighting factor used in the joint inversion scheme. For $p = 0$, the solution is constrained by the ASTFs, whereas for $p = 1$, the solution is controlled by the SAR data. The choice of *p*is subjective, nonetheless, in this case (Fig. 6), $p = 0.65$ appears as a good compromise.

The best inverted models were found assuming our previous fault geometry (described in Table 2), a starting slip model given by the geodetic solution (Fig. 4) and a $p = 0.65$, which is a good compromise between the two data sets (Fig. 5). As shown in Fig. 6(a), the rupture model satisfactorily predicts the ASTFs, in particular the amplitudes and timing of the observed peaks at the stations located between 45°N and 225°N (PRK, APE, ARG, NPS, VAM and ITM). The predicted ASTFs are nonetheless (i) too long at PRK, APE, ARG and NPS and (ii) too impulsive at JAN, SER and VLS. Concerning the geodetic data, our slip model reproduces well the observed 28-mm fringe and to a lesser extent the 56-mm fringe (Fig. 6f). The resulting slip model (Fig. 6b) shows an overall rupture area (150 km^2) similar to the one delineated by the geodetic solution (Fig. 4). The details of the slip distribution in the central part of the fault are very similar to the seismic solution (Fig. 3). The mean and maximum slip values are equal to approximately 0.4 and 1 m and the estimated stress drop is on the order of 2 MPa. In this model, the average rupture velocity is approximately 2.9 km s^{-1}. The rise time distribution is however very heterogeneous. In the central part of the fault, the rise time is similar to the one previously inverted from seismic data (Fig. 2d), between 0.5 and 2.5 s, whereas in the WNW patch, a long rise time value (close to our 5-s upper limit value) is required.

Compared to the seismic models, the joint models we obtained are characterized by the presence of additional slip patches in the WNW deeper part of the fault and in its ESE shallower part, required to fit the geodetic data (irrespective of the SAR interferogram considered). These patches are not artefacts resulting from an underestimation of the seismic moment used to normalize the ASTFs. Indeed, changing the value of M0 would only result in a homothetic change of the slip distribution inverted from the ASTFs.

6.2 Hypothesis 2: differences in the bandpass of the two data sets

In this hypothesis, we investigate the possibility that the discrepancy between the seismic and geodetic slip models is the result of differences in either the time window over which the observations are made (a few seconds for the seismic data, a few weeks for the geodetic data), or the frequency content of the data (ASTFs are bandpass filtered).

Pre-shock and aftershock activity may have contributed to the deformation registered by the SAR data. However, the regional network recorded little activity before the main shock (Papadopoulos *et al.* 2000), excluding any significant seismic deformation, and the aftershocks were located at shallower depths (Voulgaris *et al.* 2000) than the WNW slip patch. Concerning the ESE additional patch, we cannot exclude an aftershock contribution to this additional slip.

The additional slip patches could also be associated with a slow deformation, too low frequency to be detected in the ASTFs analysis. Following Fig. 6(d), we relaxed the constraint on the rise time and allowed it to vary up to 100 s. The resulting joint solution produces a better fit to the data, equivalent to the individual solutions. We performed a similar robustness analysis on this last joint solution. For each solution retained, we separated the short rise time (<5 s) contributions from the longer ones. As shown in Fig. 7, the well-constrained features of the joint solutions are: (i) a short rise time contribution extending above and below the brittle zone and (ii) a long rise time contribution (slow deformation) corresponding to the additional slip required by the geodetic solution (Fig. 4e) in the WNW deeper part of the fault, located below the brittle zone.

7 DISCUSSION AND CONCLUSIONS

Slip distributions of the moderate magnitude (Mw 5.9), 1999 Athens earthquake inverted from broad-band seismic recordings and from interferometric SAR images have very different characteristics. Through a sensitivity study to the model parameters and a robustness analysis of the solutions, we showed that the main features inverted from each data set alone are well constrained.

Two hypotheses were tested through a joint inversion to explain the origin of this discrepancy: (i) data/modelling errors and (ii) differences in the bandpass of the two data sets. Irrespectively of the hypotheses, the new rupture model that emerges from this study is composed of two well-constrained slip patches with different rise times. The short rise time (approximately 1–2 s) patch is centred on the hypocentre and released approximately 70 per cent of the total moment. Interestingly, the rupture propagated bilaterally above and below the brittle zone as delimited by the aftershock activity. The remaining 30 per cent of the total moment was released further to the WNW, through a slow deformation process confined below the brittle zone.

Slow deformation processes have been reported at depth following large earthquakes along subduction zones (e.g. Bürgmann R. *et al.* 2001; Ruegg *et al.* 2001; Yagi *et al.* 2001) and along strike-slip plate boundaries (Ergintav *et al.* 2002; Bürgmann R. *et al.* 2003). Recent data have also documented the occurrence of seismically induced deformation in the upper few kilometers of the crust along secondary faults (Fialko *et al.* 2002). Although in the case of the Athens earthquake, it is not possible to conclude the timing of this slow deformation (pre-seismic, coseismic, or post-seismic), the analysis of the seismic and geodetic slip distributions combined with the

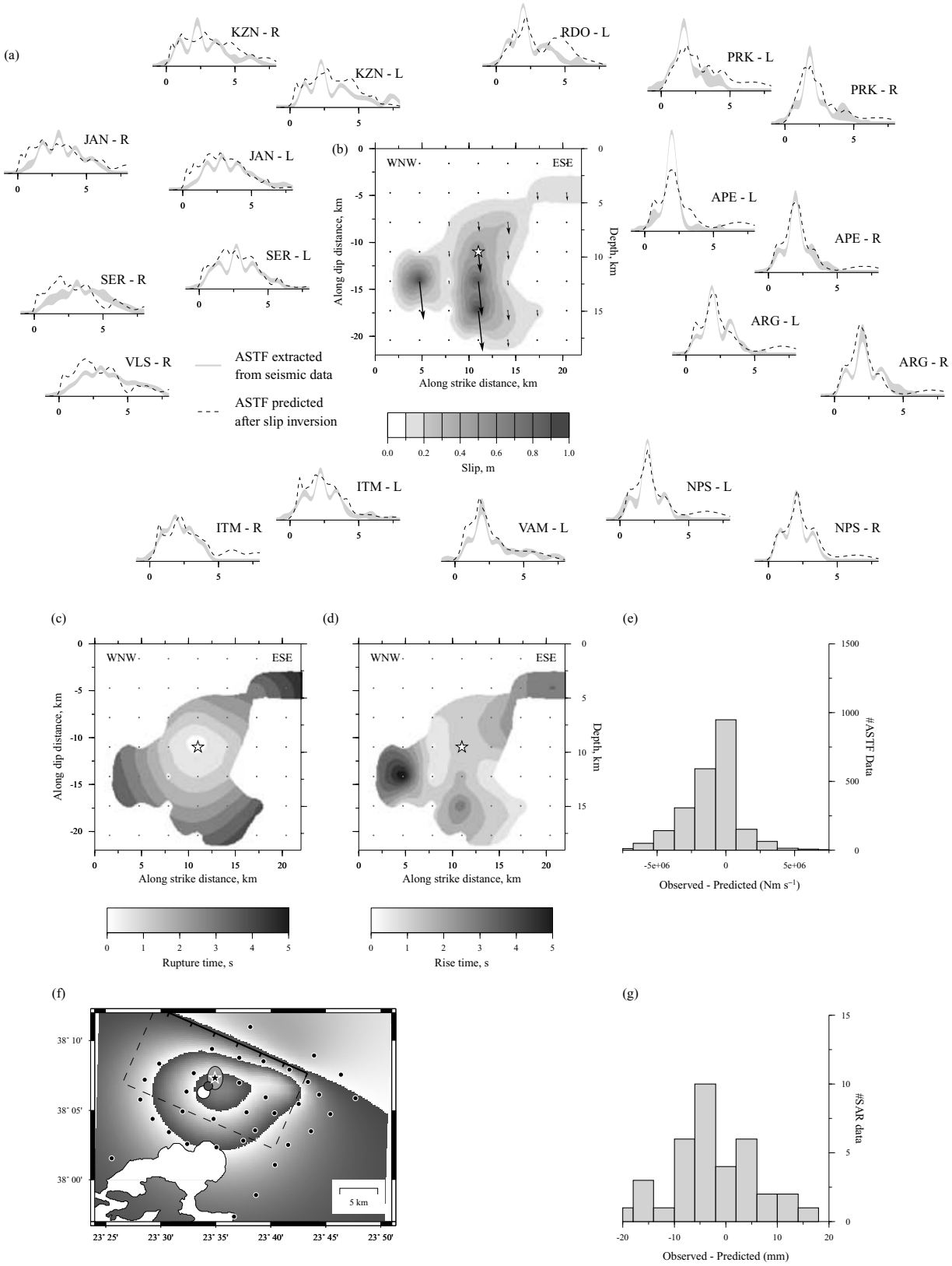


Figure 6. Best rupture model jointly inverted from seismic and geodetic data ($p = 0.65$) assuming only data/modeling errors (see text). We fixed the hypocentre after the ISC location (Table 2) and used the best geodetic solution as a starting model. (b) The slip distribution exhibits additional slip patches to the WNW and ESE compared with the seismic slip model (Fig. 3b). (c) The rupture is quasi-circular with an average rupture velocity of 2.9 km s^{-1}. (d) The rise time distribution is rather heterogeneous and covers the space model (Table 2). Notice the long rise time required by the WNW slip patch. (a) The predictions (dashed lines) of the ASTFs are slightly degraded for eastern and western stations compared to those obtained in Fig. 3, as well as (f) the predicted interferogram compared to Fig. 4, as shown by (e, g) skewed misfit distributions (ASTFs rms $= 2.2 \times 10^6$ N m s^{-1}, SAR rms $= 8.2$ mm).

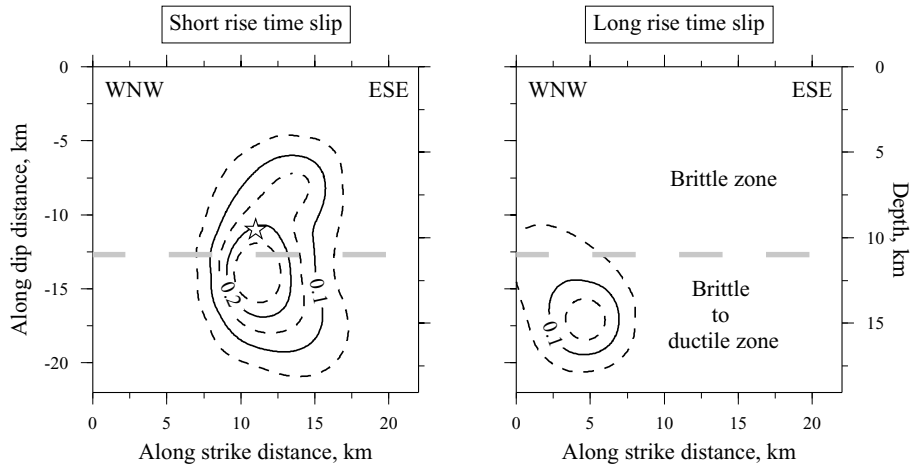


Figure 7. Well-constrained features of our best joint solution allowing for slow deformation (see text). This robustness analysis is based on a stochastic exploration retaining all models with $\mathrm{rms}_{\mathrm{SAR}} < 9$ mm and $\mathrm{rms}_{\mathrm{ASTFs}} < 2 \times 10^6$ N m s^{-1}. Whereas the short rise time (<5 s) slip patch propagated above and below the base of the brittle zone, as delineated by the depth of the aftershocks (see Fig. 3c), the long rise time slip patch appears to be mostly confined below.

aftershock locations provides further evidences for the diversity of the crustal response even for moderate size faults.

ACKNOWLEDGMENTS

The manuscript was greatly improved thanks to the comments of two anonymous reviewers and the editor R. Madariaga. The authors are very grateful to P. Briole and H. Kontoes for providing us with the SAR interferograms and for very fruitful discussions concerning the interpretation and the quantification of the errors. The authors thank the Patras University and the Prague Group for providing the data at SERGOULA station, Dr Stavrakakis, director of the Geodynamics Institute of NOA, for providing the aftershock data and R. Roumelioti for providing the data used in Fig. 2(b). The authors are grateful to the European Space Agency (ESA) for providing ERS2 SAR data. This work was partially funded by the European project PRESAP n° EVG1-CT-1999-00001 under the contract IPSN-30000826. Publication Geosciences AZUR n° 616.

REFERENCES

Anastasiadis, A.N. *et al.*, 1999. The Athens (Greece) Earthquake of September 7, 1999: Preliminary Report on Strong Motion Data and Structure Response, The Institute of Engineering Seismology and Earthquake Engineering (ITSAK), Thessaloniki, Greece (accessed 2003 July 9; http://www.itsak.gr/report.html).

Baumont, D., Courboulex, F., Scotti, O., Melis, N. & Stavrakakis, G., 2002. Slip distribution of the Mw 5.9, 1999 Athens earthquake inverted from regional seismological data, *Geophys. Res. Lett.,* **29**(15), doi:10.1029/2001GL014261.

Bürgmann, R., Kogan, M.G., Levin, V.E., Scholz, C.H., King, R.W. & G. Steblov, M., 2001. Rapid aseismic moment release following the 5 December, 1997 Kronotsky, Kamchatka, earthquake, *Geophys. Res. Lett.,* **28,** 1331–1334.

Bürgmann, R., Calais, E., Freed, A., Freymueller, J.T. & Hreinsdóttir, S., 2003. Mechanics of Postseismic Deformation Following the 2002, Mw = 7.9, Denali Fault Earthquake, *EOS, Trans. Am. geophys. Un.,* Fall Meet. Suppl., **84**(46), Abstract G21B-0270.

Ergintav, S., Bürgmann, R., McClusky, S., Cakmak, R., Reilinger, R.E., Lenk, O., Barka, A. & Özener, H., 2002. Postseismic deformation near the Izmit earthquake (17 August 1999, M 7.5) rupture zone, *Bull. seism. Soc. Am.,* **92,** 194–207.

Fialko, Y., Sandwell, D., Agnew, D., Simons, M., Shearer, P. & Minster, B., 2002. Deformation on nearby faults induced by the 1999 Hector mine earthquake, *Science,* **297,** 1858–1862.

Harvard CMT Catalog, On-line Catalog, available at http://www.seismology.harvard.edu/CMTsearch.html.

Herrmann, R.B., 2002. *Computer programs in seismology. Volume III: An overview of synthetic seismogram computation*, Saint Louis university, Missouri.

International Seismological Centre, 2001. *On-line Bulletin* International Seismological Centre, Thatcham, UK, available at http://www.isc.ac.uk/Bull.

Julià, J., Ammon, C.J., Herrmann, R.B. & Correig, A.M., 2000. Joint inversion of receiver function and surface wave dispersion observations., *Geophys. J. Int.,* **143,** 99–112.

Kontoes, C., Elias, P., Sykioti, O., Briole, P., Remy, D., Sachpazi, M., Veis, G. & Kotsis, I., 2000. Displacement field and fault model for the September 7, 1999 Athens earthquake inferred from ERS2 satellite radar interferometry, *Geophys. Res. Lett.,* **27**(24), 3989–3992.

Louvari, E. & Kiratzi, A., 2001. Source parameters of the 7 September 1999 Athens (Greece) earthquake based on teleseismic data, *J. Balkan Geophys. Soc.,* **4**(3), 51–60.

Menke, W., 1984. *Geophysical data analysis: Discrete inverse theory*, Academic Press, Inc., Orlando.

Okada, Y., 1992. Internal deformation due to shear and tensile faults in a half-space, *Bull. seism. Soc. Am.,* **82**(2), 1018–1040.

Papadimitriou, P, Kaviris, G., Voulgaris, N., Kassaras, I., Delibasis, N. & Makropoulos, K., 2000. The September 7, 1999 Athens earthquake sequence recorded by the Cornet Network: preliminary results of source parameters determination of the mainshock, *Annales Geologiques des Pays Helleniques, 1e Serie,* **T. XXXVIII, Fasc. B.,** 29–35.

Papadimitriou, P., Voulgaris, N., Kassaras, I., Kaviris, G., Delibasis, N. & Makropoulos, K., 2002. The Mw = 6.0, 7 September 1999 Athens earthquake, *Natural Hazards,* **27,** 15–33.

Papadopoulos, G.A., Drakatos, G., Papanastassiou, D., Kalogeras, I. & Stavrakakis, G., 2000. Preliminary results about the catastrophic earthquake of 7 September 1999 in Athens, Greece, *Seism. Res. Lett.,* **71**(3), 318–329.

Pavlides, S.B., Papadopoulos, G. & Ganas, A., 2002. The fault that caused the Athens September 1999 Ms = 5.9 earthquake: Field observations, *Natural Hazards,* **27,** 61–84.

Pujol, J., 1988. Comments on the joint determination of hypocenters and station corrections, *Bull. seism. Soc. Am.,* **78,** 1179–1189.

Roumelioti, Z., Dreger, D., Kiratzi, A. & Theodoulis, N., 2003. Slip distribution of the September 7, 1999 Athens earthquake inferred from an empirical Green's function study., *Bull. seism. Soc. Am.,* **93**(2), 775–782.

Ruegg, J.C., Olcay, M. & Lazo, D., 2001. Co-, post- and pre (?)-seismic displacements associated with the Mw 8.4 southern Peru earthquake of 23 June 2001 from continuous GPS measurements, *Seism. Res. Lett.,* **72**(6), 673–678.

Sargeant, S.L., Burton, P.W., Douglas, A. & Evans, J.R., 2002. The source mechanism of the Athens earthquake, September 7, 1999, estimated from P seismograms recorded at long range, *Natural Hazards,* **27,** 35–45.

Stavrakakis, G.N., Chouliaras, G. & Panopoulou, G., 2002. Seismic source parameters for the Ml = 5.4 Athens earthquake (7 September 1999) from a new telemetric broad band seismological Network in Greece, *Natural Hazards,* **27,** 47–60.

Tselentis, G.-A. & Zahradnik, J., 2000a. Aftershock monitoring of the Athens earthquake of 7 September 1999, *Seism. Res. Lett.,* **71**(3), 330–337.

Tselentis, G.-A. & Zahradnik, J., 2000b. the Athens earthquake of 7 September 1999, *Bull. seism. Soc. Am.,* **90**(5), 1143–1160.

U.S Geological Survey, National Earthquake Information Center (USGS-NEIC), On-line Catalog, available at http://neic.usgs.gov/neis/sopar.

Voulgaris, N., Kassaras, I., Papadimitriou, P. & Delibasis, N., 2000. Preliminary results of the Athens September 7, 1999 aftershock sequence, *Annales Geologiques des Pays Helleniques, 1e Serie,* **T. XXXVIII, Fasc. B.,** 51–62.

Yagi, Y., Kikuchi, M. & Sagiya, T., 2001. Co-seismic slip, post-seismic slip, and aftershocks associated with two large earthquakes in 1996 in Hyuganada, Japan, *Earth Planets Space,* **53,** 793–803.

Zahradnik, J., 2002. *Focal mechanism of the Athens 1999 earthquake by ASPO method*, Research report, Department of Geophysics, Charles University, Prague.

1.8 Conclusions

Revenir à l'origine du tremblement de terre, à sa source en profondeur à partir des données enregistrées en surface est un chalenge qui est loin d'être résolu. Des données de plus en plus nombreuses et d'origine différente sont maintenant utilisées pour tenter de remonter le temps, reconstituer le scenario de la rupture, et également comprendre les forces qui sont à l'origine du phénomène.

Les différents travaux que j'ai entrepris sur la source, souvent en collaboration avec d'autres chercheurs et quelques étudiants m'ont permis d'étudier des séismes de magnitude variée.

Ces études ont permis d'obtenir des résultats sur le comportement de la rupture :

- La directivité du séisme de Colima-Jalisco et sa vitesse de rupture moyenne (2.8 km/sec). Le caractère bimodal et complexe de cette source.
- La propagation de la rupture du séisme de Copala en fonction du temps et sur le plan de faille. La propagation vers le haut (updip) de la rupture.
- La détermination du plan de faille actif (pseudo-vertical) pour un séisme de subduction de profondeur intermédiaire.
- La mise en évidence d'une rupture bimodale pour le petit séisme d'Annecy et l'utilisation de cette fonction source complexe pour proposer deux scénarios de rupture. Ce travail a sans doute été celui qui a demandé le plus de détermination à cause de la qualité des données.
- Une inversion du séisme d'Athènes à des distances régionales et la mise en évidence d'un mouvement intersismique grâce aux données d'interférométrie radar.

J'ai également participé à l'étude et l'inversion d'autres événements en Italie, au Chili, au Mexique, dans la région de Nice, etc… A chaque fois, grâce aux méthodes de fonctions de Green empiriques, il a été possible de mettre en évidence la complexité de la rupture qui est réelle même pour des événements de magnitude réduite. La directivité affecte vraisemblablement toutes les tailles de séisme et la chute de contrainte d'un séisme modéré peut être aussi forte que celle d'un gros séisme. L'hypothèse de self-similarité semble conservée.

CHAPITRE 2

Etudes de la sismicité :
DES PETITS SEISMES POUR IMAGER LES FAILLES ACTIVES

2.1 Introduction

Les découvertes en Sciences de la Terre s'appuient sur la collecte de données nouvelles et sur des méthodes pour les faire parler. Dès ma prise de fonction au laboratoire Géoazur je me suis intéressée de près à l'enregistrement et à la valorisation des données réelles. J'ai assuré notamment le pilotage du réseau RAP Sud-Est pendant quatre ans en collaboration avec Anne Deschamps, Didier Brunel, Christophe Maron et Sylvain Vidal (CETE Méditerranée). J'ai également participé à plusieurs campagnes de terrain dans le but de collecter des données pour mieux comprendre la géodynamique d'une région (Grèce, Tibet, Mexique …).

Deux campagnes ont été particulièrement importantes pour moi : la première est la campagne d'enregistrement des répliques de la crise de Colfiorito en Italie en 1997. Pour la première fois, je me rendais dans une zone en Europe fortement touchée par un séisme et je touchais du doigt la détresse des gens déracinés de leur village. J'ai été lors de ce séjour en Italie fortement impressionnée par l'efficacité de la protection civile italienne (ceci a été a nouveau le cas lors du séisme de l'Aquila en 2009) et par le dynamisme des équipes de chercheurs italiens. Le traitement et l'analyse des données de cette crise m'ont occupée pendant deux années. Les principaux résultats obtenus sont présentés dans le paragraphe 2.3.

La deuxième campagne qui a marqué mon parcours professionnel est la campagne SALAM (Sismologie et ALéas dans les Alpes Maritimes) en 2000-2001. C'était la première campagne que je coordonnais, avec l'aide précieuse d'Anne Deschamps, de Christophe Larroque mais aussi de la plupart des chercheurs de l'équipe DRO (Déformation Rupture et Onde) alors dirigée par Eric Calais et de l'équipe risque sismique du CETE Méditerranée. Nous avons eu une chance inimaginable lors de cette campagne puisque nous avons pu enregistrer une crise sismique d'environ 400 événements dans une période de 2 mois au centre du réseau temporaire que nous avions installé (juste où il fallait et au bon moment !). Je ne suis pas sure qu'une telle chance se présentera de sitôt ! Vous trouverez les détails des résultats de cette campagne dans le paragraphe 2.4.

2.2 Méthodes de localisation et relocalisations relatives

Cette partie de mon travail ne m'a pas amenée à des développements méthodologiques particuliers. Je me suis plutôt attachée à rechercher dans chaque cas les méthodes adéquates et à les adapter aux données disponibles.

Lorsque l'on traite des données de campagne, une partie non négligeable du temps consiste à récupérer les données sur les disques, effectuer les corrections horaires et mettre au point une chaine de traitement qui permette une récupération facile du travail. Dans notre cas, nous souhaitions également nous partager le travail de pointé des ondes. Nous avons choisi pour cela le logiciel *SEISAN* [*Haskov and Ottemöller*, 1999] et mis au point une chaine de procédures pour traiter les données automatiquement et obtenir un passage facile entre *SEISAN* et les données en SAC [*Tapley and Tull*, 1992]. Cette chaine de traitement a été améliorée au cours des campagnes et est encore utilisée à présent.

Pour localiser les événements nous avons principalement utilisé les programmes *hypoinverse* [Klein, 1978] et *hypocenter* [Lienert et al., 1986]. Nous avons également dans certains cas mis en œuvre le programme de localisation *NONLINLOC* proposé par A. Lomax ([Lomax et al., 2000] ; voir l'excellent site d'Antony Lomax http://alomax.free.fr/nlloc/index.html pour la dernière version des codes et les articles de référence) qui utilise une méthode d'inversion non linéaire pour minimiser les résidus. Chaque programme fournit une localisation légèrement différente et surtout des incertitudes souvent incompatibles. Si l'on ajoute à cela la connaissance très imparfaite que nous avons du modèle de sous sol et son approximation en 1D, on se rend vite compte que l'estimation de l'erreur véritable sur la localisation d'un événement est mal contrainte et parfois complètement sous-évaluée dans la bibliographie.

Heureusement dans le cas où les stations sont très proches des événements, les résultats sont plus fiables et il est parfois même possible de chercher à réaliser une relocalisation relative des hypocentres. Cette approche permet de rendre la localisation indépendante du modèle de vitesse (dans une certaine limite) et d'obtenir une répartition très précise des épicentres les uns par rapport aux autres.
De nombreuses approches sont disponibles : elles travaillent soient sur la forme de l'onde elle-même soit simplement sur les temps d'arrivée [*Waldhauser and Ellsworth*, 2000]. Le but est de mesurer les décalages relatifs de temps d'arrivée d'une onde sur une même station pour un essaim de séismes. Ces décalages servent ensuite à relocaliser les événements par rapport à un événement pivot bien localisé (méthode du « Master event », [*Fréchet*, 1985]) ou bien les uns par rapport aux autres (méthode des « Multiplets »).

Nous avons mis en œuvre pour les données de la campagne SALAM une méthode de relocalisation relative par multiplets développée par J-L Got du LGIT initialement mise au point pour les séismes volcaniques [*Got et al.*, 1994]. Céline Gélis, à présent en poste à l'IRSN a beaucoup travaillé sur ces relocalisations relatives lors de son DEA.

La méthode de relocalisation relative [*Got et al.*, 1994] de séismes semblables utilisée repose sur l'observation suivante : deux séismes proches dans l'espace ont lieu dans des milieux physiques de nature et de structure très voisines, ils émettent par conséquent des rais qui parcourent des trajets quasiment identiques et sont soumis aux mêmes phénomènes physiques (atténuation, dispersion, rencontres d'hétérogénéités du milieu …) ; on considère donc que ces séismes possèdent des rais communs vers une même station. Si, de plus, les mécanismes au foyer sont de même nature, les formes d'onde émises par ces séismes se ressemblent fortement à chaque station où ils ont été enregistrés. De tels ensembles d'événements similaires sont nommés des familles ou multiplets. Comme ces séismes ne se sont pas produits exactement au même endroit, de petits décalages temporels entre les temps d'arrivée des ondes existent. On procède alors, comme pour une localisation absolue, à une linéarisation et une inversion du système. Dans ce cas, le système est construit à partir de l'ensemble des différents couples de séismes similaires au sein de chaque famille. Ces derniers sont alors localisés les uns relativement aux autres, de façon beaucoup plus précise qu'avec une simple localisation absolue. Cette méthode se déroule en deux étapes principales : la formation de familles d'événements similaires, puis la relocalisation relative de ces séismes au sein de chaque multiplet.

Il s'agit dans un premier temps de trouver des familles d'événements dont la forme d'onde présente de fortes similitudes. Cette étape se fait par cross corrélation des formes d'ondes spectrales. Si la corrélation est assez élevée alors on cherche à relocaliser les événements en transformant les délais en temps obtenus, en distances (Figure 2. 1). La localisation obtenue est ainsi d'une extrême précision (quelques dizaines de mètres).

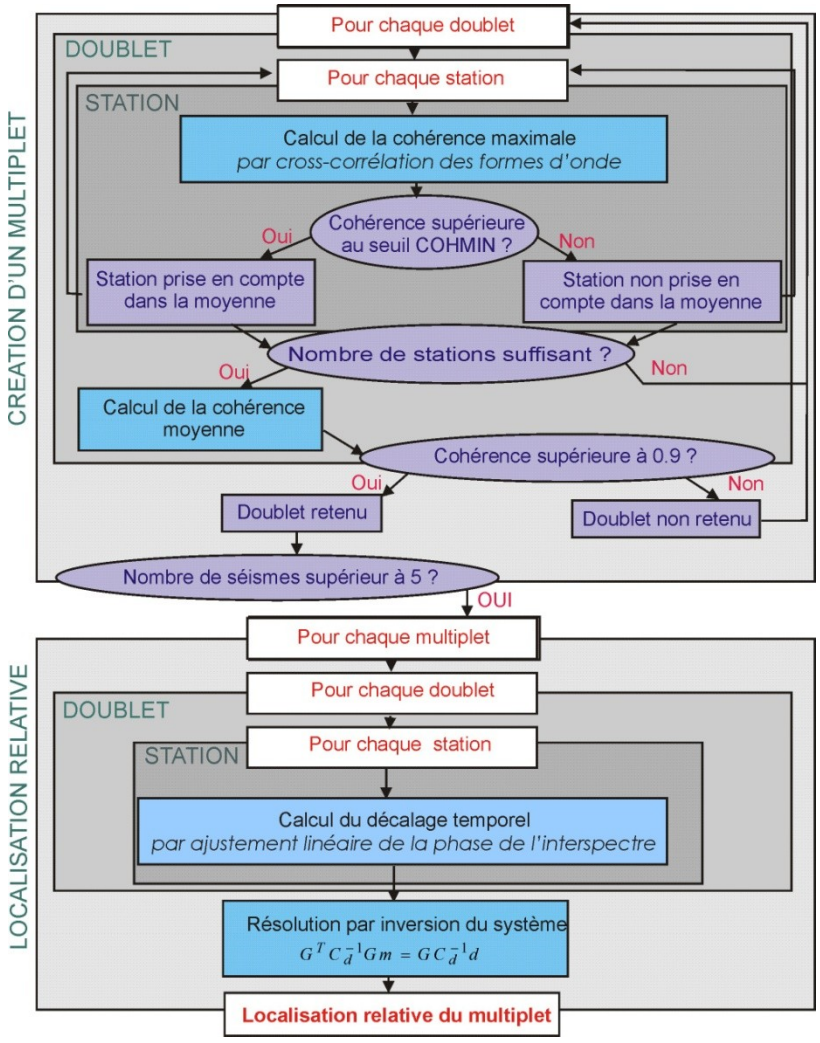


Figure 2. 1 : Principe de la relocalisation relative par multiplets [*Gélis*, 2002]

Ces méthodes de relocalisations relatives ont suscité un engouement considérable dans la communauté sismologique puisqu'elles ont permis de mettre en évidence des comportements tout à fait inattendus des failles [*Rubin et al.*, 1999; *Waldhauser and Ellsworth*, 2000]. Elles sont maintenant utilisées très fréquemment pour préciser des localisations absolues, et même tout récemment dans des procédures plus routinières [*Waldhauser*, 2009]. Il faut cependant les utiliser avec précaution car elles peuvent produire des alignements magnifiques mais totalement fictifs comme l'ont bien montré certaines études [*Michelini and Lomax*, 2004].

2.3 La crise sismique de Colfiorito

Les Apennins centraux sont régulièrement secoués par des séismes superficiels de magnitude modérée (magnitude ~ 6) particulièrement destructeurs (Figure 2. 2). Le récent séisme de L'Aquila de 2009 a eu lieu dans une zone de la chaine qui n'avait pas subi de séisme depuis longtemps. On s'attendait donc à un tel séisme. Pourtant, rien n'a été entrepris pour limiter les dégâts. Il existe pourtant des solutions pour conforter le bâti ancien et le rendre plus résistant aux séismes afin de préserver des vies humaines. Mais le choix des investisseurs ne va pas dans ce sens, et on attend la catastrophe pour reconstruire sur les ruines (on espère que les normes parasismiques seront respectées, mais ça n'est même pas sur).



Figure 2. 2 : Situation de la crise de Colfiorito par rapport aux événements sismiques d'avril 2009 dans les Apennins centraux et les Abruzzes (Document CEA).

Retour quelques années en arrière sur la crise sismique de Cofiorito. Le 26 septembre 1997, l'Italie centrale est frappée par une forte crise sismique qui cause des destructions considérables dans les villages des régions d'Ombrie et de Marche (Figure 2. 3). Des villages entiers sont inhabitables.



Figure 2. 3 : Dégâts occasionnés par les séismes de la crise de Colfiorito (Italie centrale).

Le premier séisme a eu lieu dans la nuit (26 septembre à 0h33). Il a réveillé tous les habitants de la région qui, pour la plupart ont jugé bon de passer le reste de la nuit dehors, s'attendant à d'autres secousses. C'est le lendemain, à 9h40 TU qu'a eu lieu la deuxième secousse, de magnitude plus forte (Mw 6). C'est elle qui a fait le plus de dégâts. On se souvient notamment des dommages occasionnés à la célèbre basilique d'Assise. Les destructions massives de plusieurs villages ont causé heureusement peu de victimes humaines (une dizaine), car la première secousse de la nuit a permis d'alerter les populations, et elles ont su réagir.

Ces deux chocs principaux ont été précédés par une augmentation de la microsismicité, et par un séisme de magnitude Mw 4 .5 qui, mais on ne l'a su qu'après, était un précurseur de la crise (le schéma a été a peu près le même pour le séisme de l'Aquila de 2009). La crise a duré très longtemps plongeant les populations dans une angoisse permanente. Durant trois semaines, la région a été secouée par des répliques incessantes. Six séismes de magnitude supérieure à 5 (entre 5 et 5 .4) ont eu encore lieu, puis, 18 jours après le choc principal, un séisme de magnitude 5.6 se déclenchait dans le sud de la zone (Figure 2. 4). Il ne s'agissait pas d'une séquence classique choc principal-réplique mais d'un comportement en essaim (ou crise) avec une forte migration de la sismicité.

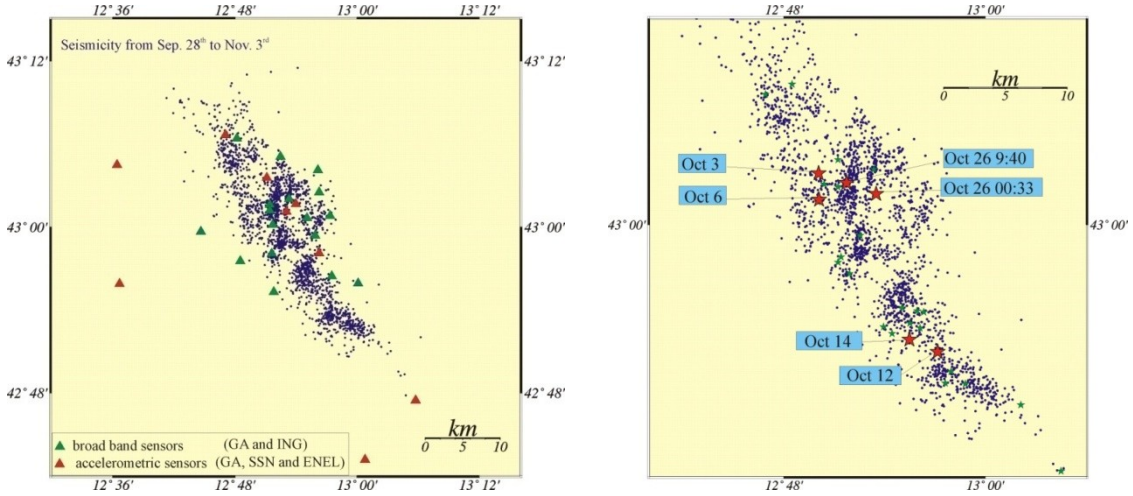


Figure 2. 4 : Epicentres des séismes de la crise de Colfiorito (3 semaines d'enregistrement). A gauche : Réseau de stations temporaires. A droite (zoom) : Les étoiles rouges représentent la localisation des séismes de magnitude > 5, les étoiles vertes les séismes 4 < M < 5.

Les secours sont très rapidement intervenus après le premier choc pour s'occuper des populations sinistrées et bâtir des logements de fortune (tentes, mobil home) pour les personnes qui ne pouvaient pas trouver refuge dans leur famille. Les scientifiques ont également régi sans tarder. Un réseau de stations temporaires a été installé rapidement par les équipes italiennes. C'est à cette occasion que les sismologues de Géoazur sont intervenus. Nous avons installé et maintenu une vingtaine de stations pendant toute la durée de la crise. Une partie de ces stations a été intégrée au réseau de détection.
Les excellentes données récoltées et le nombre très élevé de répliques (plus de 2000 en 1 mois) ont permis d'imager avec beaucoup de finesse les failles normales activées durant la crise ainsi que l'évolution spatio-temporelle de la crise

2.3.1 Imagerie des failles et distribution spatio-temporelle de la sismicité

Les travaux scientifiques menés sur les données de la séquence de Colfiorito sont nombreux. Les publications le sont également. J'ai choisi de faire figurer dans ce chapitre en entier les deux articles qui reflètent le mieux les travaux que j'ai réalisés sur le sujet. Le premier article [*Deschamps et al.*, 2000] a été publié dans un numéro spécial du *Journal of Seismology* consacré à la crise d'Ombrie-Marche. Il résume les résultats obtenus assez rapidement après traitement des données. Le second article [*Chiaraluce et al.*, 2004] présente une étude plus détaillée.

2.3.2 Etude des effets de site lithologiques et topographiques

Sous l'impulsion de Stéphane Gaffet, nous avons également mis en place une campagne destinée à mettre en évidence les effets de site lithologiques et topographiques en collaboration étroite avec les chercheurs italiens [*Gaffet et al.*, 2000].
L'idée était de profiter de l'extraordinaire activité sismique de la crise pour analyser les effets de site à partir de données réelles. Une zone s'est révélée particulièrement intéressante. Il s'agit de la vallée de Verchiano et des hameaux de Colle et Camino qui ont subi des dommages considérables alors qu'un autre village situé à 2 km de là, Curasci, n'a presque pas été endommagé (les constructions étaient à peu près identiques).
Afin d'étudier ce comportement particulier, nous avons installé un réseau de 11 stations 3 composantes sur une ligne coupant la vallée et allant jusqu'au sommet de la colline (Figure 2. 5) en passant par les villages de Colle (fortement détruit) et de Curasci (très peu détruit). Le réseau a enregistré 67 séismes en 4 jours. Une partie de ces événements venait d'un essaim situé à 10 km au nord et l'autre partie d'un autre essaim situé à 6 km au sud. Dans le même temps nous avons aidé à réaliser une campagne de sismique réflexion (dirigée par M. Dietrich du LGIT, Grenoble) afin de déterminer les principales caractéristiques des sédiments remplissant le bassin (Figure 2. 5).

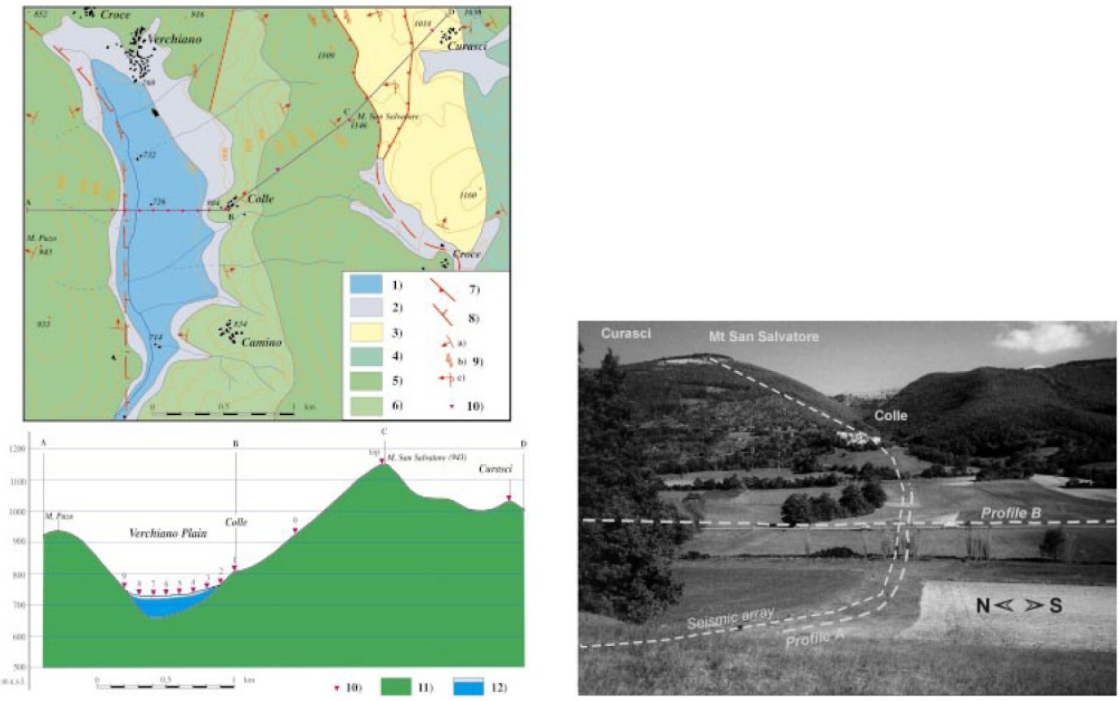


Figure 2. 5 : Gauche : Carte et profil de la campagne de mise en évidence des effets de site dirigée par S. Gaffet. Les stations sont indiquées par des triangles rouges. Droite : Photo indiquant la position des deux profils de sismique réfraction.

Plusieurs analyses ont été effectués sur les données récoltées : (1) une analyse temps-fréquence a permis de mettre en évidence rapidement les bandes de fréquence préférentiellement affectées par l'effet de site, (2) l'étude des rapports spectraux site/référence (pour les trois composantes) (3) l'étude des rapports spectraux Horizontal/Vertical (3) la comparaison des données avec une modélisation numérique (méthode des nombres d'onde discrets [*Bouchon*, 1973; *Gaffet*, 1995].

Les résultats concordent pour monter :

- un effet topographique au sommet du Mont Salvatore (amplification d'un facteur 6 à 8 dans une bande de fréquence allant de 2 à 10 Hz).
- un effet lithologique pouvant entrainer une amplification d'un facteur 10 au maximum dans une bande de fréquence allant de 1 à 10 Hz.
- une bonne adéquation entre les modélisations numériques et les résultats obtenus sur les données pour les effets de site lithologiques de la vallée.
- une sous estimation de l'effet topographique par les modélisations

mais surtout :

- des résultats similaires sur les données du village de Colle et de Curasci ! Il apparait donc clair que les forts dommages engendrés à Colle sont dus à la radiation de la source sismique ou bien à des fréquences excitées par les longueurs d'ondes d'un choc important mais non détectées par l'étude des répliques.

Ainsi, une étude préliminaire aurait pu prévoir de fortes amplifications dans la vallée, des amplifications importantes au sommet de la montagne mais il aurait été impossible de prévoir que l'un des villages allait être détruit et pas l'autre.

2.3.3 L'analyse des surfaces de rupture activées

Profitant de la bonne couverture du réseau temporaire et de l'occurrence d'un nombre important de répliques de magnitude élevée, j'ai entrepris un travail sur les liens entre la surface de rupture et la position des répliques. Ce travail était motivé par différents papiers que j'avais lus et qui tentaient de lier la directivité de la rupture avec la zone où les répliques avaient lieu préférentiellement. Mori [1993] propose par exemple que les répliques aient préférentiellement lieu dans la zone vers laquelle la rupture se propage. Or, mon expérience m'a plutôt montré le contraire.
J'ai donc cherché à analyser en détail cette base de données très fournie pour regarder les processus « à la loupe ».

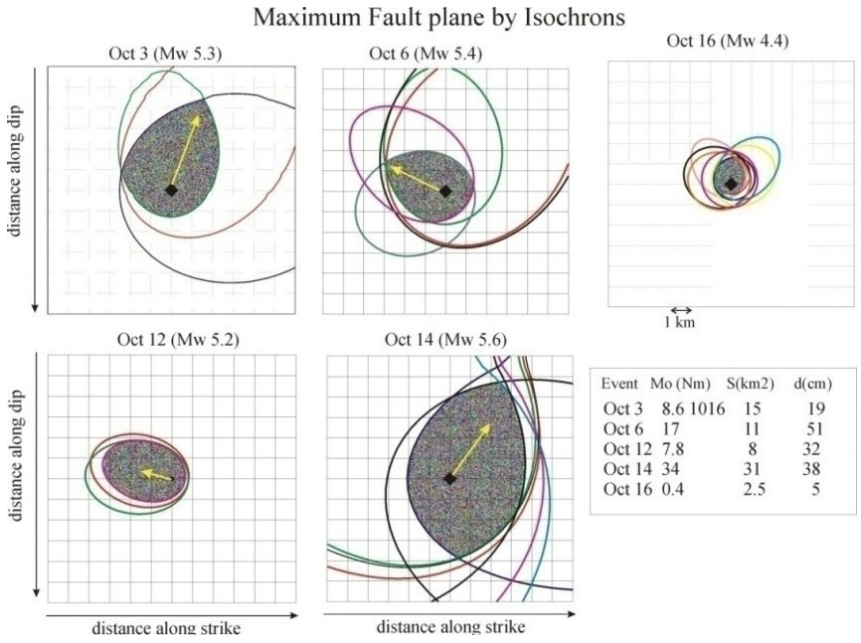


Figure 2. 6 : Surface maximale activée le long du plan de faille durant la rupture de 6 répliques principales de la crise de Colfiorito. La flèche jaune représente la directivité principale de la rupture. Les traits de couleurs sont les isochrones-limites.

J'ai finalement travaillé sur 5 séismes. Pour chacun de ces séismes j'ai cherché un ou plusieurs petits événements utilisables comme fonctions de Green empiriques. J'avais l'embarras du choix mais le processus a été quand même difficile à cause de la grande complexité dans la forme d'onde de ces événements, complexité certainement due à leur faible profondeur et à la complexité du milieu. Une fois ces déconvolutions effectuées, j'ai imagé les surfaces maximales de rupture grâce à la méthode du croissement d'isochrones présenté dans le chapitre 1 (Figure 2. 6).

J'ai ensuite analysé les liens entre ces surfaces de faille, la directivité principale et la position des répliques. Il apparait clairement à chaque fois, que les répliques ont lieu préférentiellement en dehors de la zone activée durant la rupture et dans une zone où peu de répliques avaient eu lieu au préalable (Figure 2. 7). Par contre, le lien entre la directivité de la rupture et l'activation des répliques n'est pas clair.

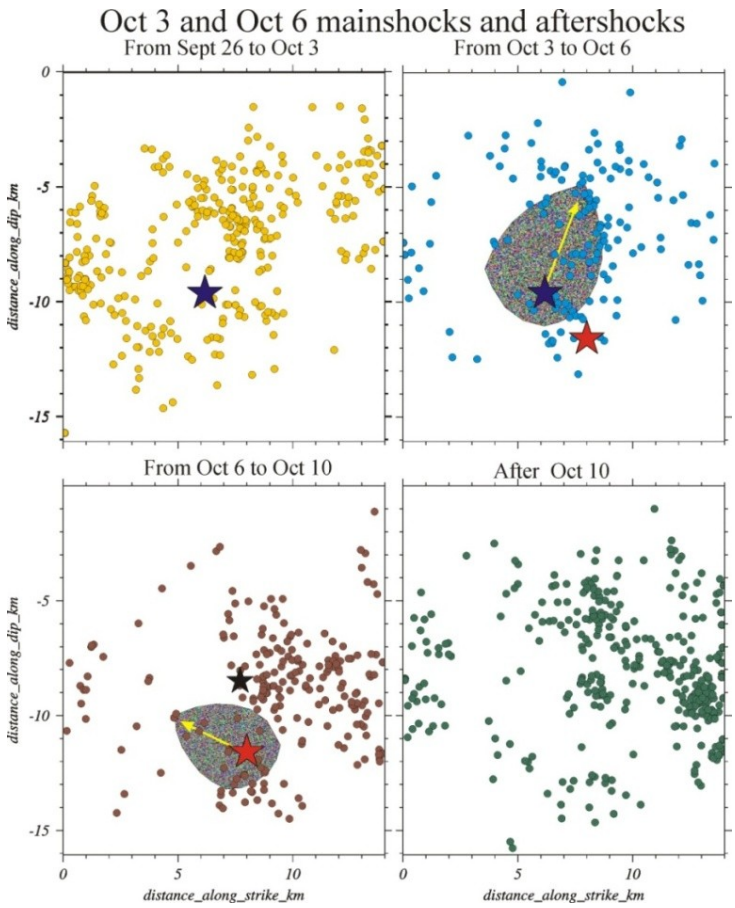


Figure 2. 7 : Sismicité projetée sur le plan de faille sur 4 périodes de temps. L'étoile noire représente d'hypocentre du séisme du 3 octobre, et l'étoile rouge celui du 6 oct. Les zones grisées représentent les surfaces de rupture maximales de ces deux séismes.

Les principaux résultats de cette étude sont résumés par ces question/réponses :

La position des répliques délimite-elle le plan de faille des séismes, comme souvent on en fait l'hypothèse ?
Dans le cas de séismes modérés comme ici : non ! Les répliques indiquent une taille de rupture beaucoup plus large que celle du séisme principal.
Les répliques ont-elle lieu sur le même plan de faille que le séisme ? Oui mais pas toutes.
La directivité de la rupture nous indique-t-elle la zone où l'on va avoir le plus de répliques : non !

Journal of Seismology **4:** 377–386, 2000.
© 2000 *Kluwer Academic Publishers. Printed in the Netherlands.*

Spatio-temporal distribution of seismic activity during the Umbria-Marche crisis, 1997

A. Deschamps[1], F. Courboulex[1], S. Gaffet[1], A. Lomax, J. Virieux[1], A. Amato[2], A. Azzara[2], B. Castello[2], C. Chiarabba[2], G.B. Cimini[2], M. Cocco[2], M. Di Bona[2], L. Margheriti[2], F. Mele[2], G. Selvaggi[2], L. Chiaraluce[3], D. Piccinini[3] & M. Ripepe[3]
[1]*UMR Géosciences Azur, CNRS/UNSA, 06560 Valbonne, France;* [2]*Istituto Nazionale di Geofisica, 00143 Rome, Italy;* [3]*University of Camerino, Camerino, Italy*

Received 13 April 1999; accepted in revised form 21 January 2000

Key words: Seismicity, Central Italy, Umbria-Marche, Aftershock sequence, seismic crisis

Abstract

We present the spatio-temporal distribution of more than 2000 earthquakes that occurred during the Umbria-Marche seismic crisis, between September 26 and November 3, 1997. This distribution was obtained from recordings of a temporary network that was installed after the occurrence of the first two largest shocks (Mw = 5.7, Mw = 6.0) of September 26. This network was composed of 27 digital 3-components stations densely distributed in the epicentral area. The aftershock distribution covers a region of about 40 km long and about 12 km wide along the NW-SE central Apennines chain. The activity is shallow, mostly located at less than 9 km depth. We distinguished three main zones of different seismic activity from NW to SE. The central zone, that contains the hypocenter of four earthquakes of magnitude larger than 5, was the more active and the more complex one. Sections at depth identify 40–50° dipping structures that agree well with the moment tensor focal mechanisms results. The clustering and the migration of seismicity from NW to SE and the general features are imaged by aftershock distribution both horizontally and at depth.

Introduction

The long seismic sequence that struck Umbria-Marche region during September–October 1997, was characterized by the occurrence of six earthquakes of magnitude larger than 5 in a period of 20 days. All these events had almost identical focal mechanisms (Ekström et al., 1998). Following the terminology proposed by Scholz (1990), this untypical aftershock sequence for a magnitude 6 event, if we refer to the largest event, characterizes a compound earthquake. The rupture process is unlikely to be explained only by an elastic fracture mechanism, but should also be related to temporal changes in stress in the highly faulted upper crust of the region.

A few hours after the first large shocks (Mw = 5.7, Mw = 6.0) of September 26, a dense seismological network was installed in the epicentral area by the Istituto Nazionale di Geofisica (ING), Camerino University (CU) and Géosciences Azur (GA) groups (Amato et al., 1998). Recordings of this network allowed us to analyze in detail the aftershock activity in relation to the location of the main large events. After a rapid view of the main regional features, we describe in this paper the temporary networks, the location procedure and present the aftershock distribution obtained, in space and time. This spatio-temporal distribution evidences the existence of several fault segments that have broken successively in time.

Main regional features

The seismic activity of the Central Apennines is well documented in the Italian historical earthquake catalogue (Boschi et al., 1995). Although many large events struck the central axis of the chain during the

Table 1. Temporary stations installed during the period September–October 1997; instrumental characteristics and recording periods

Code	Institution	Recorder	Sensor	Sample Rate	Mode	Operating dates
CAM	UC	MR 16bits	Vel3c 2 Hz	66	trigger	permanent
POP	UC	MR 16bits	Vel3c 2 Hz	66	trigger	07/09–31/10
CPQ	UC	MR 16bits	Vel3c 2 Hz	66	trigger	09/09–31/10
FND	UC	MR 16bits	Vel3c 2 Hz	66	trigger	28/09–31/10
CSC	UC	MR 16bits	Vel3c 2 Hz	66	trigger	29/09–31/10
FORC	ING	Reftek 24bit	CMG40 20 sec	100	continuous	26/09–29/09
COST	ING	Reftek 24bit	CMG40 20 sec	100	continuous	26/09–17/10
FREE	ING	Reftek 24bit	CMG40 20 sec	100	continuous	26/09–30/10
PALL	ING	Reftek 24bit	CMG40 20 sec	100	continuous	26/09–03/11
PENN	ING	Reftek 24bit	CMG40 20 sec	100	continuous	26/09–03/11
SCOP	ING	Reftek 24bit	CMG40 20 sec	100	continuous	26/09–03/11
SERR	ING	Reftek 24bit	CMG40 20 sec	100	continuous	28/09–03/11
RASE	ING	Reftek 24bit	CMG40 20 sec	100	continuous	28/09–03/11
CASB	ING	Reftek 24bit	CMG40 20 sec	100	continuous	29/09–03/11
PREC	ING	Reftek 24bit	CMG40 20 sec	100	continuous	17/10–03/11
CES9	ING	Len5800 12bit	Mark3d 1 Hz	125	continuous	27/09–03/11
FOR9	ING	Len5800 12bit	Mark3d 1 Hz	125	continuous	27/09–03/11
TAV9	ING	Len5800 12bit	Mark3d 1 Hz	125	continuous	27/09–03/11
CUP9	ING	Len5800 12bit	Mark3d 1 Hz	125	continuous	27/09–03/11
COL9	ING	Len5800 12bit	Mark3d 1 Hz	125	continuous	27/09–03/11
COLF	GA	Reftek 16bit	Mark3d 2 Hz	100	continuous	28/09–18/10
			CMG5 (acc)	200	trigger	28/09–18/10
ANNI	GA	Reftek 16bit	Mark3d 2 Hz	100	continuous	28/09–24/10
			CMG5 (acc)	200	trigger	28/09–24/10
SMAR	GA	Reftek 16bit	Mark3d 2 Hz	100	continuous	28/09–18/10
			CMG5 (acc)	200	trigger	28/09–18/10
LAZZ	GA	Reftek 16bit	Mark3d 2 Hz	100	continuous	18/09–24/10
			CMG5 (acc)	200	trigger	18/09–24/10
FEMA	GA	Titan 24bit	Mark3d 2 Hz	125	continuous	29/09–24/10
FRAN	GA	Titan 24bit	CMG40 60 sec	125	continuous	29/09–22/10
RASI	GA	Titan 24bit	CMG40 60 sec	125	continuous	29/09–03/10
SVIT	GA	Titan 24bit	CMG3T 125 sec	125	continuous	29/09–24/10
ROTE	GA	Titan 24bit	CMG3T 125 sec	125	continuous	29/09–01/10
						16/10–24/10

last centuries, none occurred close to Colfiorito. The largest historical earthquake that was reported nearby was the Norcia 1703 event, with an estimated magnitude of 6.7 (Boschi et al., 1995). This earthquake occurred to the south of the 1997 epicentral area and is described as a succession of 3 major events (January 14 and 16, February 2). Other long seismic sequences are documented in the past centuries, with some large events occurring within 10 to 20 days after the mainshock.

Concerning the more recent activity of the Central Apennines, the 1997 sequence occurred between the region near Norcia, struck in 1979 by a Mw = 5.7 event, (Deschamps et al., 1984) and a region near Gubbio, struck in 1984 by a Mw = 5.3 event (Haessler et al., 1988). The combined aftershock distribution of the 1979 and 1997 events is almost continuous and follows the trend of the high Apennines (Figure 1). Conversely, a gap and a slight lateral offset of seismicity is observed between the aftershock regions of the 1984 (Gubbio) and the 1997 events. The

Table 2. Temporary stations installed during the period September–October 1997: coordinates

Code	Latitude (deg. min)	Longitude (deg. min)	Elevation (meters)	(next)	Code	Latitude (deg. min)	Longitude (deg. min)	Elevation (meters)
CAM	43 08.39N	13 04.03E	570		CES9	43 00.66N	12 55.08E	1200
POP	42 59.34N	12 53.59E	850		FOR9	43 01.20N	12 51.42E	840
CPQ	43 00.98N	12 47.28E	430		TAV9	43 02.52N	12 56.28E	840
FND	43 02.35N	12 49.35E	940		CUP9	43 00.18N	12 51.72E	900
CSC	42 59.51N	12 57.29E	1120		COL9	43 02.04N	12 53.34E	990
FORC	43 01.62N	12 51.44E	920		COLF	43 01.13N	12 53.07E	904
COST	42 59.39N	12 55.89E	880		ANNI	43 03.57N	12 51.14E	1074
FREE	43 00.82N	12 57.36E	1060		SMAR	42 58.15N	12 56.27E	1061
PALL	42 55.31N	12 51.81E	660		LAZZ	42 51.61N	12 58.54E	485
PENN	43 05.09N	12 52.47E	1150		FEMA	42 55.94N	13 00.10E	1046
SCOP	42 57.55N	12 48.52E	570		FRAN	42 59.34N	12 49.88E	620
SERR	43 04.12N	12 56.15E	670		RASI	42 58.08N	12 51.63E	600
RASE	42 56.45N	12 57.52E	860		SVIT	42 59.68N	12 44.65E	278
CASB	43 06.41N	12 48.18E	570		ROTE	43 02.15N	12 58.56E	900
PREC	42 52.06N	13 01.22E	500					

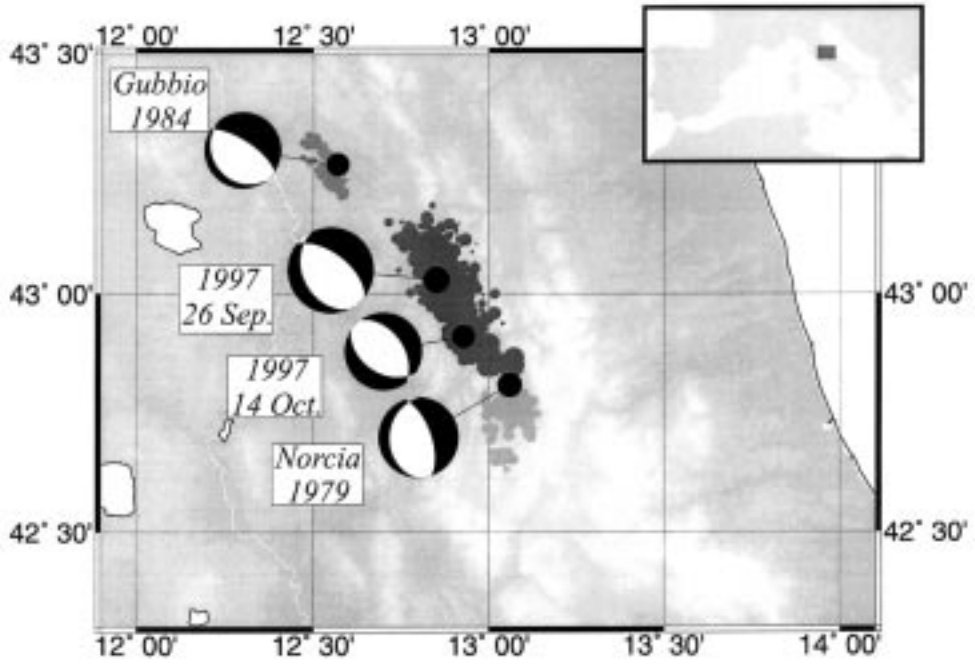


Figure 1. Mainshock CMT solution and aftershock sequences of: Norcia (1979), Gubbio (1984), and Colfiorito crisis (1997) on the topographic map of central Italy.

focal solutions of the largest shocks (Figure 1) show a NE-SW extension, consistent with other mechanisms observed along the Apenninic belt (Gasparini et al., 1985; Frepoli and Amato, 1997).

From the analysis of aftershocks recorded at local networks, Deschamps et al. (1984) and Haessler et al. (1988) proposed the activation of different fault segments for both the 1979 and the 1984 events. However, during the Norcia seismic sequence no large aftershocks occurred in the secondary (southern) earthquake cluster, whereas in the case of the Gubbio event the secondary fault was characterized by the occurrence of three aftershocks with magnitude larger than 4.

In the Colfiorito area, the active period began on September 3, 1997, with a Mw = 4.5 event followed by a relatively low level of seismic activity (Ripepe et al., 2000). The major part of the crisis developed after September 26 when a Mw = 5.7 event occurred at 00:33 and a Mw = 6.0 event at 9:40, both of them located by the Italian National Network in the Colfiorito region. Two more events (Mw = 5.2 and Mw = 5.4) occurred in the same region on October 3 and 6. The last two significant events (Mw = 5.2 and Mw = 5.6) occurred 15 km to the south-east, on October 12 and 14. Magnitudes are deduced from CMT seismic moment evaluation (Ekstrom et al., 1998). On April 3, 1998, a Mw = 5.1 event occurred in the northern sector of the seismic zone, which extended the active area to the north of about 10 km, partially filling the gap with the 1984 sequence.

The seismic moment release and the evolution with time of the cumulative number of events detected on the national network (complete for duration magnitudes larger than 2.4) is described on Figure 2. The seismic moment released during the September 26 events was only slightly more than 50% of the total moment released during the crisis. This does not correspond to the common observations of typical mainshock-aftershock sequences (Scholz, 1990), in which this percentage is significantly higher.

Seismic sequence location

Just after the occurrence of the Mw = 4.5 earthquake of September 3, CU installed in the Colfiorito area four 16-bit digital recorders with short period (2 Hz) sensors (Ripepe et al., 2000). The limited storage space available on these stations recording in trigger mode was full soon after the first September 26 event. Most of the records of aftershocks in the morning were lost.

On September 26, a few hours after the 00:33, Mw = 5.7 and the 09:40, Mw = 6.0 events, six Reftek equipped with broadband seismometers (CMG40) were installed by ING, and some other local stations were installed by CU. A day later, two more Reftek and a Lennartz network of five recording sites equipped with 3-components L4C sensors and radio link to a common recording site was installed. The continuous traces available in real time were useful to follow the seismicity and the migration of the activity. During the next three days, ING and GA collaborated to complete the network with digital continuously recording 3- and 6-components stations (3 Reftek and 5 Titan recorders); most of the sensors were broadband seismometers (CMG40 or CMG3); on the three 6 channel recorders, 2Hz seismometers were associated to high gain CMG5 accelerometers to allow the acquisition of unsaturated records of a large magnitude range. All velocity channels were recorded at 100 or 125 samples per sec, depending on the recording system, and the acceleration channels were recorded in trigger mode at 200 samples per sec. Time was controlled by GPS, that ensures errors in datation less than 0.002 sec even at isolated stations. The GA stations were removed on October 24, the ING stations on November 3. Two stations (COST and COLF) were moved towards the southern part of the seismic zone after the occurrence of the October 14 event, but the coverage in this part remained poor compared to the very dense coverage in the Colfiorito area (COLF station) (Figure 3). Instrumental characteristics and recording periods at each site are summarized in Table I. Stations coordinates are listed in Table II.

A list of about 2000 events, from September 26 to November 3, was selected from the Lennartz network records and distributed to all the participants as a basis for event extraction from the continuous records. This list was controlled later using the Italian National Network and is almost complete for aftershocks with duration magnitude larger than 3. Elaboration of the corresponding data and P and S phases picking were performed at ING, GA and CU with a common guideline for weights estimation. Readings from the nearest stations of the national permanent network were also used, in particular for the largest events. The locations presented hereafter were performed on the entire data set using HYPOINVERSE in a smoothed model based on the layered velocity model given in Table III (Deschamps et al., 1984). Due to the very

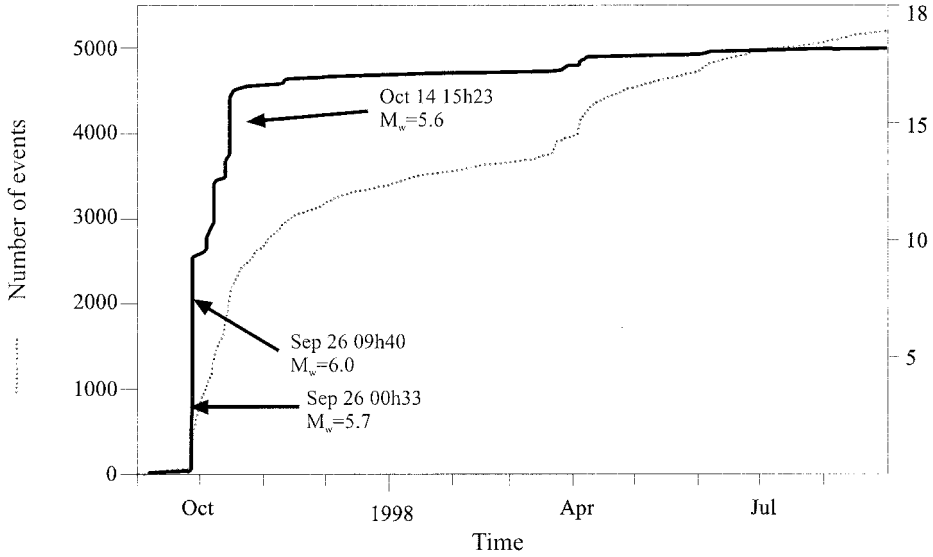


Figure 2. Cumulated number of event and seismic moment from September 1997 to September 1998 as determined by Italian National Network. For microseismicity, seismic moment is calculated from the local magnitude whereas the CMT seismic moment is used for the largest events. The space window is 80 km × 50 km around Colfiorito area. It does not include the northern crisis in March-April 1998.

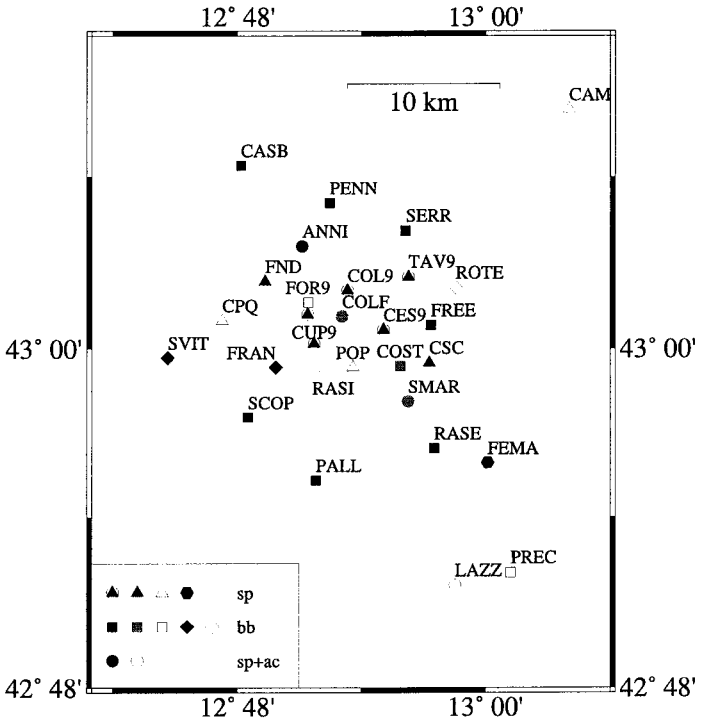


Figure 3. Temporary network used for location of the events discussed in this paper. Instrument characteristics reported in Table I are differentiated by different symbols: open symbols are used for stations installed some days after September 3, black symbols for stations that were running during the whole period, grey symbols for stations that were only partially running or moved during the period.

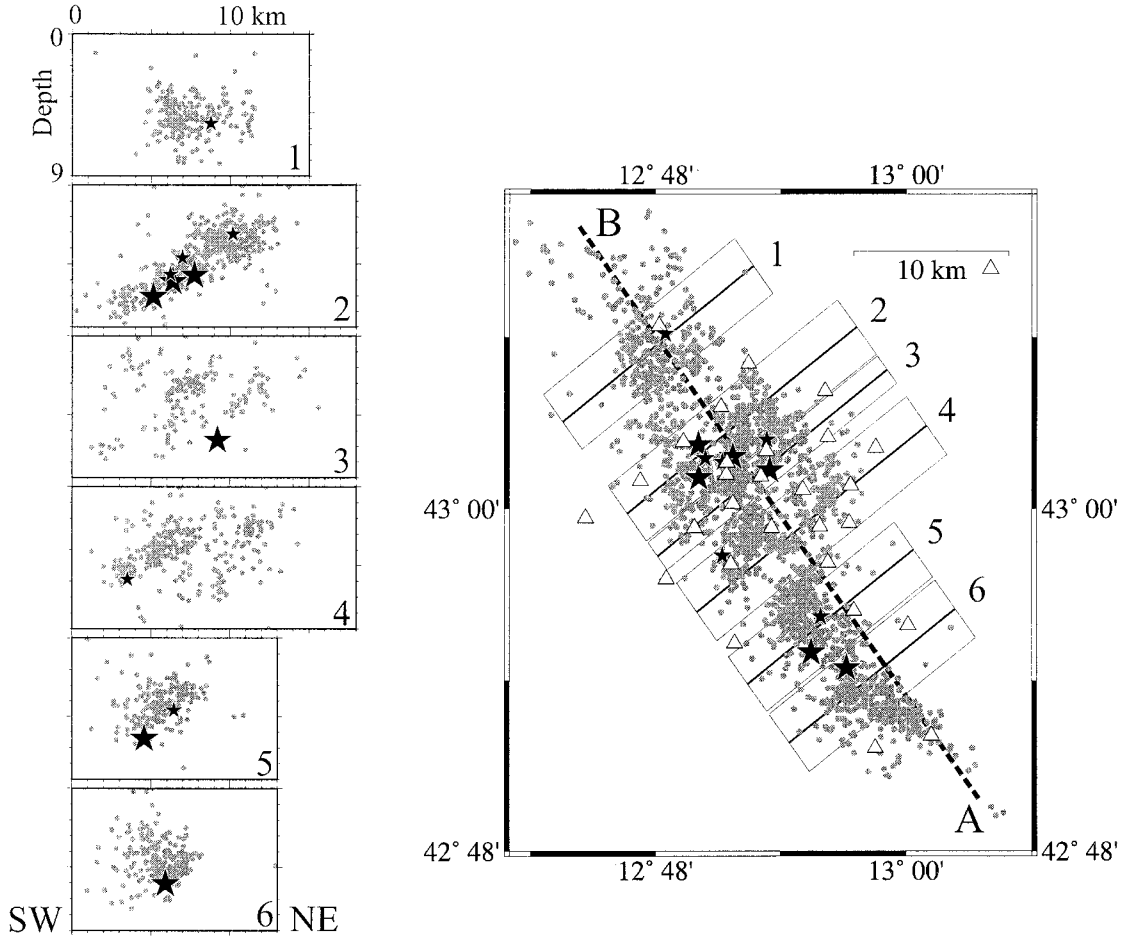


Figure 4. Aftershock distribution from September 26 to November 3, 1997 in space. Stars represent hypocenters of the largest events (large stars Mw > 5, small stars 4 < Mw < 5) localized by the temporary network and for which a seismic moment was evaluated from broad-band data (Morelli et al., 2000). Right: map where triangles represent the seismic stations that were used for this study. AB is the Y axis of Figure 5. Left: cross sections at six different locations given on the map.

dense 3-components station network and despite the fact that the seismicity is mostly shallower than 8 km, the locations are well constrained and the standard deviations are less than 0.7 km horizontally and 1.5 km vertically in the central zone. Uncertainties are larger in the northern and the southern zones and attemps to control these uncertainties will be described in an other work.

Earthquake distribution during the crisis

Figure 4 presents the global pattern of the seismicity and some selected vertical cross sections along the anti-apenninic direction. The activity was concentrated on a 40 km area elongated in the NW-SE direction, mainly shallower than 9 km. Hypocenters of the larger events (Mw > 4) localized with the temporary network and for which a moment magnitude is available from broad-band seismogram analysis (Morelli et al., 2000) are reported. Hypocenters of the September 26 events (00h33 and 09h40) are also added. These events occurred mainly in a narrow zone projected in Section 2 and 3. Three main zones can be identified:

– a northern zone in which no hypocenter of a large event (Mw > 5) was detected by the temporary network. This zone contains the fault plane of the largest event (Mw = 6.0) that occurred on September 26 at 09:40, as proposed by different authors using seismological data or SAR and GPS surface displacement modelling (Zollo et al., 1999; Stramondo et al.,

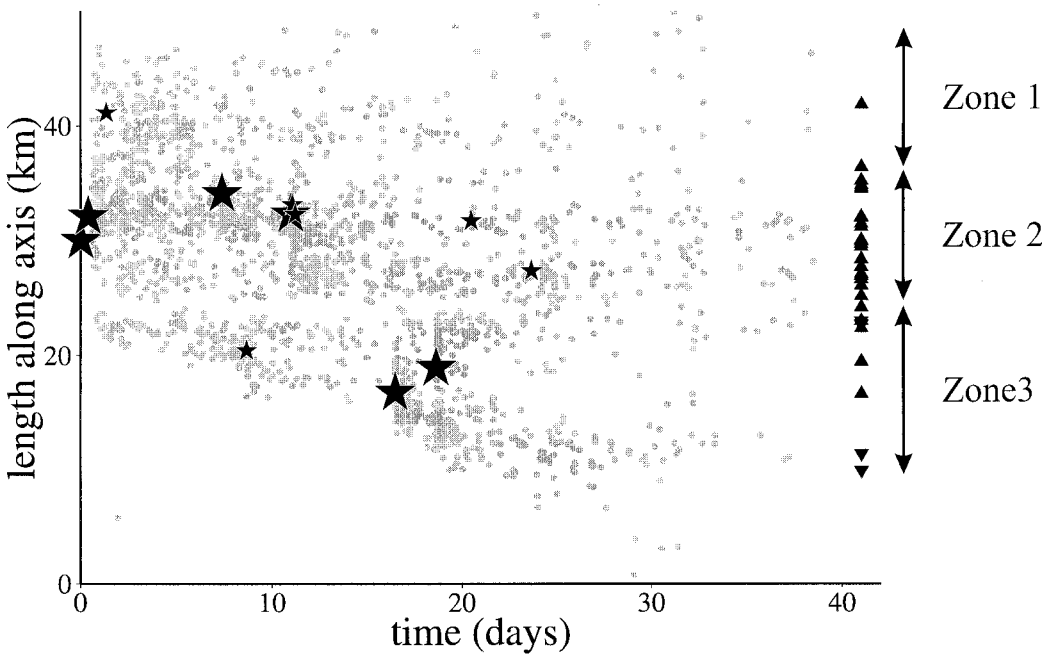


Figure 5. Aftershock distribution from September 26 to November 3, 1997 in time. On the X axis, the elapsed time from September 26 at 00h00 is reported while on the Y axis, the projection of the epicentral position along an horizontal axis oriented N35W is represented (axe AB in Figure 4). Stars as on Figure 4. The position of the seismological stations are represented by triangles on the right (reversed triangles for stations installed after the October 18).

1999; Hunstad et al., 1999). The bad azimuthal coverage of the temporary seismic network in this area makes the locations poorly constrained at depth. This can be seen on cross Section 1 (Figure 4) where no clear structure can be underlined.

– a central zone, 12 km long and almost as broad, where the distribution of epicenters is inhomogeneous, and clustered. The three sections across this zone (Figure 4, Sections 2, 3, 4) present clear evidence of low angle SW dipping structures compatible with one of the nodal planes of the CMT solutions. Whereas the seismicity on Section 2 evidences one only fault plane, on Sections 3 and 4 it suggests the presence of two parallel fault planes, separated by a distance of about 5 km and not connected at depth.

– a southern zone, as long as the previous one, but narrower, which is related to the activity of the October 14 event. This zone presents a very sharp north-eastern limit. Section 5, at a latitude where the station coverage insures good hypocenter determinations, shows a structure with a higher dip than in the previous sections. Because there is no change in the fault plane dip of the CMT solution (Ekström et al., 1998), this image could be produced by the effect of a section across a more complex fault structure.

Clustering and segmentation of the central area are also clearly observed in Figure 5 where epicenters are presented along a time axis starting from September 26 and a space axis oriented N35°W. Though the data set is not complete for the beginning of the sequence, the three zones described above can be very well identified: in zone 1 (from kilometer 37 to 48), we observe a typical aftershock distribution, with an activity that decreases in time and only one event of magnitude larger than 4; in zone 2 (from kilometer 24 to 37), the activity is intense and complex. Large events ($Mw > 4$) occurred during almost all the period. The activity following the two events of October 3 ($Mw = 5.2$) and October 6 ($Mw = 5.4$) can be interpreted as the activation of secondary fault segments. A lack of seismic activity at 24 km clearly separates this zone from the third one (from kilometer 5 to 23), where the seismicity migrates towards the south-east. A cluster occurred on October 4 and 5 with one event of magnitude $Mw = 4.7$, and three other events with Ml between 4 and 4.5 that can be considered as foreshocks of the October 12 and 14 main events. The extension of this active zone southwards continues even after the main events. Figure 6 presents the epicentral distribution of the activity in five-days periods. The

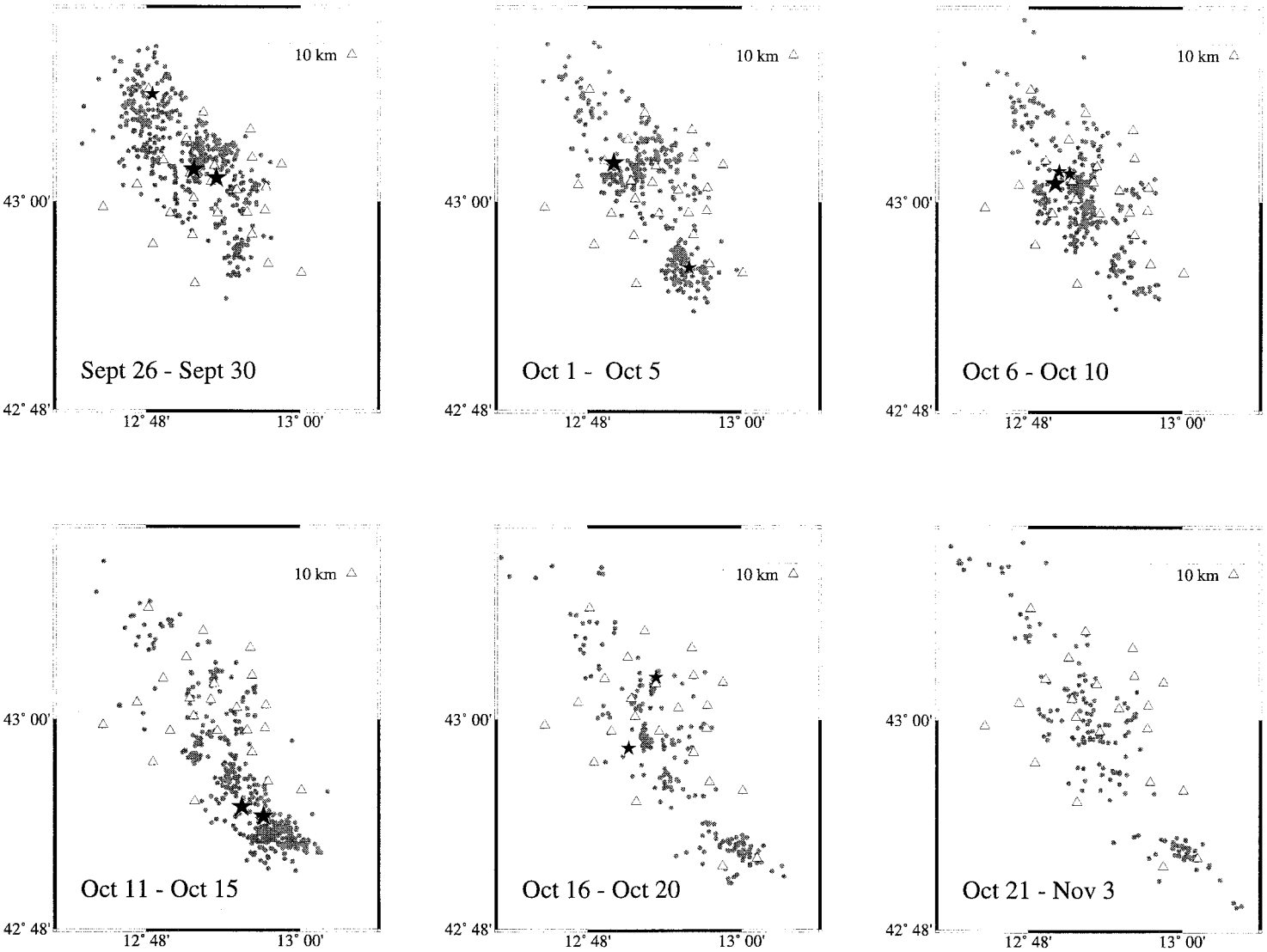


Figure 6. Migration of seismicity during six periods of five-days. Grey dots represent aftershock locations during a given period. Stars and triangles as on Figure 4. Only the stations that were running during the considered period are represented. On the first image, the locations of the two large events of September 26 are also reported.

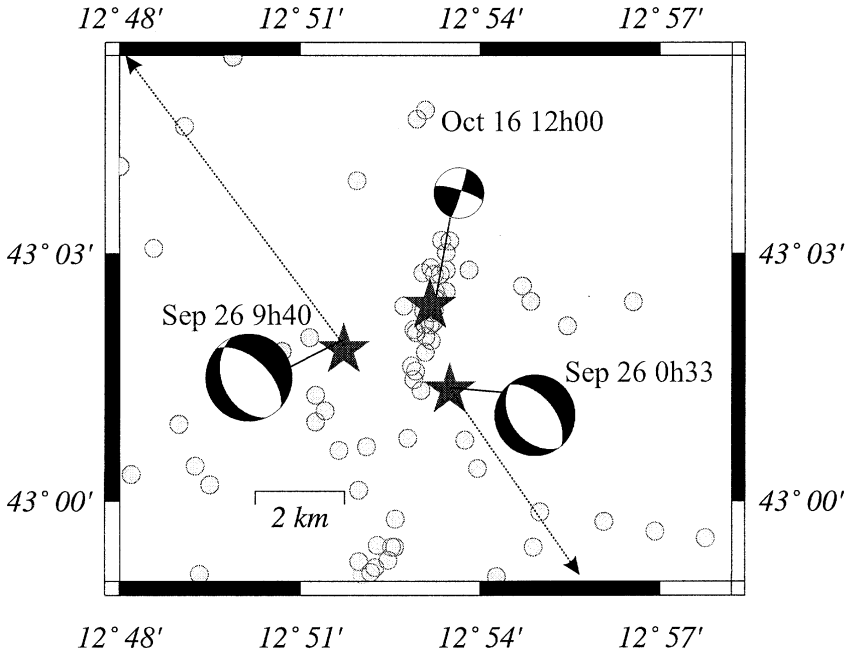


Figure 7. Zoom of the area where the October 16 (Mw = 4.3) strike-slip event occurred. The distribution of earthquakes from October 16 to October 20 clearly indicates that the north-south plane was the active one. The epicenter and focal mechanism of the two main events of September 26 are also represented.

epicenters of the events of magnitude larger than 4. are represented with small stars and the events larger than Mw = 4.5 with large stars. The time succession shows that a) most of the largest events could be related to their aftershock area; b) the seismic activity in the central area is very complex, showing gaps that are progressively filled (period from October 6 to 10 and from October 16 to 20). Such activity could be related to the observation on vertical sections 3 and 4 where parallel fault planes are suggested. The structure at depth of these clusters is not precise enough at the present stage of the study to understand the spatial relations between segments.

Looking more carefully at Figure 6, it is obvious that some north-south alignments of seismicity can also be evidenced. This is especially clear during the period from October 16 to October 20. If we make a zoom around the epicenter of the Mw 4.3 strike-slip event of October 16 (the largest strike-slip event of the crisis), we can clearly identify a N-S linear aftershock activity that is in good accordance with one of the fault plane of the CMT focal mechanism (Figure 7). This N-S feature, shallower than the normal fault structures, is very close to the epicenters of the two main events of September 26 and then, could have played the role of a left-lateral step-over between the two normal fault planes.

Conclusion

The seismic crisis that struck Umbria-Marche in September and October 1997 is characterized by (1) the occurrence of 6 events of magnitude between 5 and 6 during a period of 19 days; (2) more than 2000 smaller earthquakes localized by a dense portable seismic network clearly related to faults structure; (3) an important migration of the seismicity towards the south.

The epicenters cover a (10–12) × 40 km^2 area that follows the central Apennines NW-SE main direction. This direction is compatible with the focal mechanisms obtained from CMT for the largest events (Ekström et al., 1998), and with the fault position and extension of the mainshocks as deduced from seismic moment and surface displacement observed from SAR images (Hunstad et al., 1999). Depth of the activity is mostly confined to the upper 9 kilometers.

At the center of the seismic network, a good image of the complexity of the structures at depth was obtained. Cross-sections show that in Colfiorito

Table 3. Tabular velocity model used for locations (Figures 4, 5, 6). $v_P/v_S = 1.88$

Depth (km)	P-wave velocity (km s^{-1})
0.0	4.8
4.0	5.5
7.0	6.3
30.0	8.

region, parallel low angle dipping planes where activated during the crisis. It is also important to note that north-south very shallow structures where also activated during the crisis. The role of these structures have to be precised in a future work.

Acknowledgements

We thank all the persons who help us to install and maintain the network and process the records. We thank also the Italian National Network staff who provided preliminary origin times and magnitudes. This paper benefited from suggestions of two anonymous reviewers. This work was supported by CNRS program PNRN and EEC program ENV4-CT96-0296. It is contribution Géosciences Azur N^{o}285.

References

Amato, A., Azzara, R., Chiarabba, C., Cimini, G.B., Cocco, M., Di Bona, M., Margheriti, L., Mazza, S., Mele, F., Selvaggi, G., Basili, A., Boschi, E., Courboulex, F., Deschamps, A., Gaffet, S., Bittarelli, G., Chiaraluce, L., Piccinini, D. and Ripepe, M., 1998, The 1997 Umbria-Marche, Italy, earthquake sequence : a first look at the mainshocks and aftershocks, *Geophys. Res. Lett.* **25, 15**, 2861–2864.

Boschi, E., Ferrari, G., Gasperini, P., Guidoboni, E., Smiriglio, G. and Valensise, G., 1995, Catalogo dei forti terremoti in Italia dal 461 a.C. al 1980, Pubblicazione dell'Istituto Nazionale di Geofisica, 973 pp.

Deschamps, A., Iannaccone, G. and Scarpa, R., 1984, The Umbrian earthquake (Italy) of 19 September 1979, *Ann. Geophys.* **2, 1**, 29–36.

Ekström, G., Morelli, A., Dziewonski, A.M. and Boschi, E., 1998, Moment tensor analysis of the central Italy earthquake sequence of September-October 1997, *Geophys. Res. Lett.* **25, 11**, 1971–1974.

Frepoli, A. and Amato, A., 1997, Contemporaneous extension and compression in the Northern Apennines from earthquake fault plane solutions, *Geophys. J. Int.* **129**, 368–388.

Gasparini, C., Iannaccone, G. and Scarpa, R., 1985, Fault plane solutions and seismicity of the Italian Penninsula, *Tectonophysics* **117**, 59–79.

Haessler, H., Gaulon, R., Rivera, L., Console, R., Frogneux, M., Gasparini, C., Martel, L., Patau, G., Siciliano, M. and Cisternas, A., 1988, The Perugia (Italy) earthquake of 29 April 1984: a microearthquake survey, *Bull. Seismol. Soc. Am.* **78**, 6, 1948–1964.

Hunstad, I., Anzidei, M., Cocco, M., Baldi, P., Galvani, A. and Pesci, A., 1999, Modelling coseismic displacements during the 1997 Umbria-Marche earthquake (Central Italy), *Geophys. J. Int.* **139**, 283–295.

Morelli, A., Ekström, G. and Olivieri, M., 2000, Source properties of the 1997-98 Central Italy earthquake sequence from inversion of long-period and broad-band seismograms, this volume.

Ripepe, M., Piccinini, D. and Chiaraluce, L., 2000, Foreshock sequence of September 26, 1997 Umbria-Marche earthquakes, this volume.

Scholz, 1990, Mechanics of earthquakes, Cambridge University Press.

Stramondo, S., Tesauro, M., Briole, P., Sansosti, E., Salvi, S., Lanari, R., Anzidei, M., Baldi, P., Fornaro, G., Avallone, A., Buongiorno, M.F., Franceschetti, G. and Boschi, E., 1999, The September 26, 1997 Colfiorito, Italy, earthquakes : modeled coseismic surface displacement from SAR interferometry and GPS, *Geophys. Res. Lett.* **26**, 883–886.

Zollo, A., Marcucci, S., Milana, G. and Capuano, P., 1999, The 1997 Umbria-Marche (central Italy) earthquake sequence: insights on the mainshock ruptures from near source strong motion records, *Geophys. Res. Lett.* **26**, 3166–3168.

Bulletin of the Seismological Society of America, Vol. 94, No. 1, pp. 99–116, February 2004

Complex Normal Faulting in the Apennines Thrust-and-Fold Belt: The 1997 Seismic Sequence in Central Italy

by L. Chiaraluce, A. Amato, M. Cocco, C. Chiarabba, G. Selvaggi, M. Di Bona, D. Piccinini, A. Deschamps, L. Margheriti, F. Courboulex, and M. Ripepe

Abstract A long sequence of moderate-magnitude earthquakes ($5< M <6$) struck central Italy in September and October 1997. At the end of the sequence a year later, the seismogenic area extends for about 60 km along the Apennines. The analysis of historical seismicity suggests that this seismic sequence filled a >700-year gap in this portion of the chain. Other historical sequences in the same area are characterized by prolonged seismic release on adjacent fault segments, probably due to the involvement of shallow and complex structures inherited by the compressive tectonics. The distribution of seismicity and the fault-plane solutions show that the extension in this region is accomplished by normal faults dipping at relatively low angles (~40°) to the southwest. The focal mechanisms of the largest shocks reveal normal faulting with extension perpendicular to the Apenninic chain (northeast–southwest), consistently with the Quaternary tectonics of the internal sector of the northern Apennine belt and with previous earthquakes in adjacent regions. Three mainshocks occurred on distinct 5- to 10-km-long fault segments, adjacent and slightly offset between each other. High-quality aftershock locations show that seismicity is confined within the sedimentary Mesozoic cover in the upper 8 km of the crust and that most of the aftershocks are shallower than the largest shocks, which nucleated at ~6-km depth. Faults evidenced by aftershock locations have a planar geometry and show increased complexity toward the surface. Most of the aftershock focal mechanisms are dominated by normal faulting. Several strike-slip events occurred at shallow depths, reactivating portions of pre-existing thrust planes that segment the normal fault system. The spatiotemporal evolution of seismicity shows a peculiar migration of hypocenters along the strike of the main faults with multiple ruptures and the activation of fault segments before the occurrence of the main rupture episodes.

Introduction

A prolonged seismic sequence started on September 1997 in the Umbria–Marche Apennines, central Italy. The sequence included several shocks with M_W ranging between 5.0 and 6.0, which occurred during a 1-month period on a seismogenic volume expanding for nearly 60 km along the Apennines (Fig. 1) (Amato *et al.*, 1998; Deschamps *et al.*, 2000). This moderate-magnitude earthquake sequence caused a broad damage pattern and extensive concern among the population in the region. Due to the small hypocentral depths (<8 km) of these earthquakes, the ground shaking was notable. The presence of very ancient buildings in the area contributed to increasing the extent of the damage (Tertulliani, 2000). Despite the low magnitude of these shocks, 11 people died during the whole sequence. Luckily, none of the three largest shocks of the sequence, which took place on 26 September at 00:33 UTC (M_W 5.7, hereafter called "00:33") and 09:40 UTC (M_W 6.0, "09:40") and on 14 October at 15:23 UTC (M_W 5.6, "15:23"), occurred close to any large towns. The epicentral area of the 26 September shocks corresponds to the intramountain basin of Colfiorito. The highest intensities (VIII–IX degree in the Mercalli–Cancani–Seeberg [MCS] scale) were recorded in small villages located around the basin. Since people had already left their houses after the M_W 5.7 shock at night, the number of fatalities was strongly reduced when the M_W 6.0 earthquake occurred 9 hr later. A few hours after the occurrence of these two shocks, a dense seismic array was deployed in the epicentral area (Cattaneo *et al.*, 2000; Deschamps *et al.*, 2000). The analysis of seismic data recorded by the temporary network (Amato *et al.*, 1998) and centroid moment tensor (CMT) fault-plane solutions from regional and telesesimic waveforms (Ekström *et al.*, 1998) have shown that (1) the largest shocks ($5< M_W <6$) ruptured normal fault segments parallel to the trend of the Apenninic mountain belt (north-

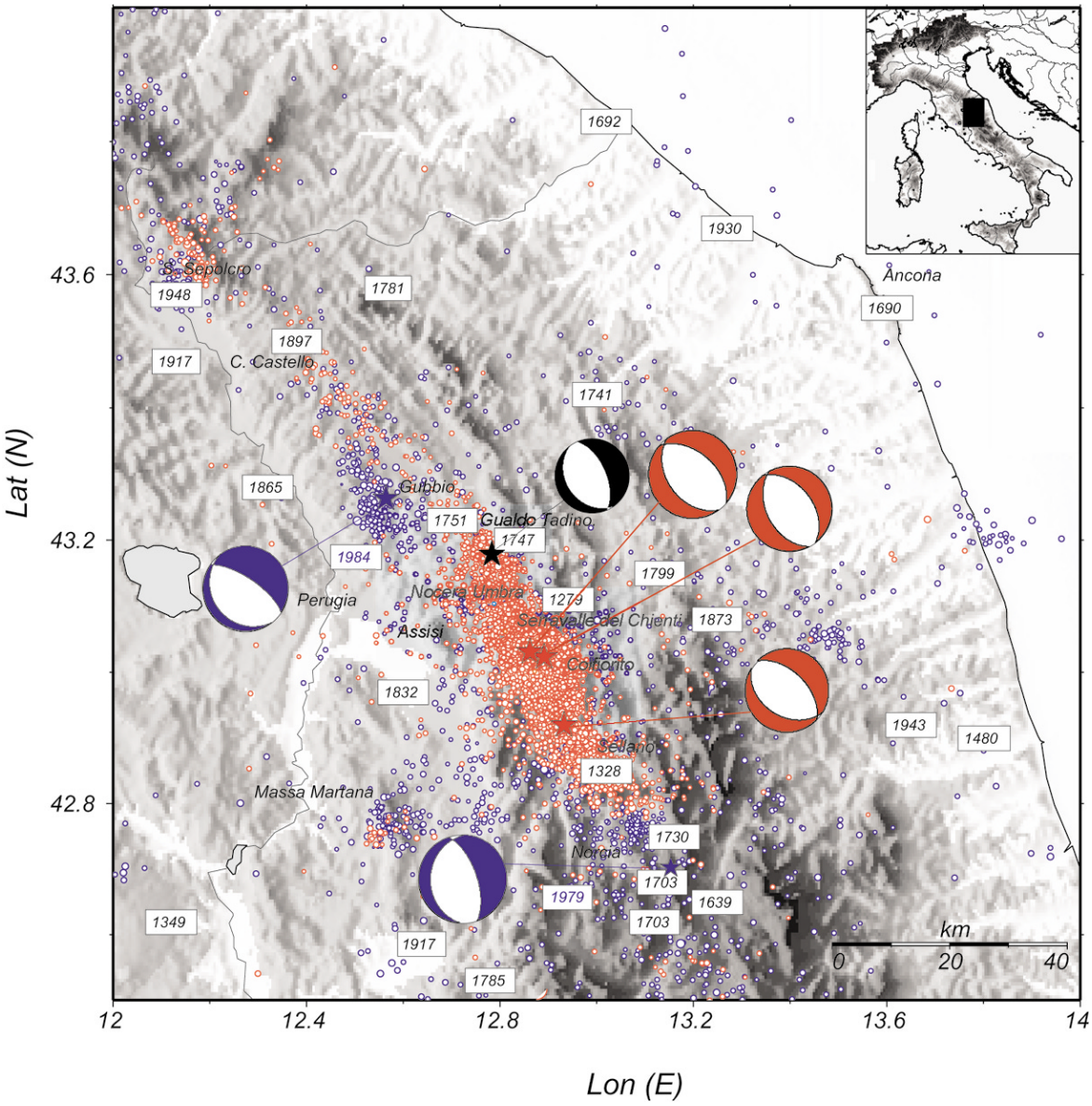


Figure 1. Map of seismicity of the Umbria–Marche sector of the Apennines. Blue and red symbols show the distribution of epicenters before and after 26 September 1997, respectively. The red focal mechanisms are those of the three largest shocks of the 1997 sequence (which occurred on 26 September at 00:33 and 09:40 GMT and on 14 October), whose epicenters are shown by the stars. Blue fault-plane solutions are those of the mainshocks of two recent seismic sequences that occurred in 1979 and 1984 in Valnerina and Gubbio, respectively (Deschamps *et al.,* 1984; Haessler *et al.,* 1988). The white rectangles show the distribution of historical seismicity (Boschi *et al.*, 1995) in the area. Plotted in black are the location (star) and the focal mechanism of the Gualto Tadino event that occurred on 3 April 1998, a few months after the beginning of the sequence.

west–southeast), (2) the faults are shallow (0–8 km) and dip to the southwest at relatively low angles (35°–45°), and (3) the largest shocks ruptured 5- to 10-km-long adjacent segments (Chiarabba and Amato, 2003; Chiaraluce *et al.*, 2003).

The analysis of strong motion and broadband seismic data (Zollo *et al.*, 1999; Capuano *et al.*, 2000; Pino and Mazza, 2000) revealed clear evidence of rupture directivity during the largest shocks of the sequence. Further details on fault geometry and slip distribution were derived from the modeling of Global Position System (GPS) and synthetic aperture radar (SAR) data (Hunstad *et al.*, 1999; Salvi *et al.*, 2000; Lundgren and Stramondo, 2002) and by the joint inversion of strong motion and geodetic data (Hernandez *et*

al., 1999). Evidence of surface breakage was observed after the mainshocks, and there have been diverse interpretations of these features either as a direct expression of fault rupture or as secondary induced effects (Galli and Galadini, 1999; Meghraoui *et al.*, 1999; Cello *et al.*, 2000; Cinti *et al.*, 2000). The repeated occurrence of shocks in a short time interval suggests interaction between adjacent fault segments that were modeled using the Coulomb stress transfer by Cocco *et al.* (2000). They showed that elastic interaction can promote the occurrence of only some of the shocks composing the sequence.

More recently, Chiarabba and Amato (2003) have inverted travel times picked on digital seismograms, recorded at the dense temporary network, to image a 3D velocity structure of the area and to relocate seismicity. We will use the earthquake locations resulting from this tomographic inversion to investigate the details of the seismic sequence and to compute aftershock fault-plane solutions using the 3D take-off angles for *P*-wave polarity data. Chiaraluce *et al.* (2003) located seismicity with a double-difference algorithm. Although this approach gives an accurate relative location of the aftershocks, it strongly reduces the available data set (up to 1/3 of the total). We investigate the tectonic setting of this portion of the Apennines and the kinematics of the normal faults that ruptured during the sequence. We first describe the occurrence and complexity of this sequence and its relation to the former seismicity of the region. In particular, we examine the historical seismicity to investigate if previous seismic sequences in the region were composed of multiple shocks with similar magnitudes. Therefore, we compare available CMT fault-plane solutions with polarity data from the local digital stations and determine the focal mechanisms for the whole aftershock sequence.

Tectonic Setting and Past Earthquakes in the Region

The northern Apennines consist of an arcuate collisional wedge, which developed in Neogene times as a consequence of the persistent eastward migration of compression front and back-arc extension. One of the more likely explanations for this is the retreat of a lithospheric slab over time (Malinverno and Ryan, 1986; Patacca and Scandone, 1989; Mariucci *et al.*, 1999). This process led to the buildup of a thrust-and-fold belt, where compressional earthquakes presently occur near the Adriatic coast and extension is accomplished by normal faulting earthquakes in the axial sector of the belt (Lavecchia *et al.*, 1994; Frepoli and Amato, 1997, 2000). The northern Apenninic arc is characterized by a seismotectonic setting different from that in the southern Apenninic arc, when considering the magnitude of the largest recorded events and the rate of seismic moment release (Anderson and Jackson, 1987; Westaway, 1992; Selvaggi, 1998). This different behavior has been attributed to differences in the deep structural setting and in the tectonic evolution of the two regions, on the basis of seismic tomography studies and subcrustal earthquake distribution analysis (Selvaggi and Amato, 1992; Amato *et al.*, 1993; Lucente *et al.*, 1999). The earthquakes of the 1997 sequence occurred at the Umbria–Marche boundary, just north of the separation between the two arcs.

Historical records show that large earthquakes, at least in the past 700 years, have not affected the Colfiorito area. The only earthquake documented in historical catalog to occur within the area is an event that struck Serravalle di Chienti and Nocera Umbra in A.D. 1279 (Fig. 1). Due to the limited number of available reports, its location is uncertain (Castelli *et al.*, 1997; Boschi *et al.*, 1998). However, it appears to have occurred close to the northernmost portion of the 1997 epicentral area (see figure 7 in Galli and Galadini [1999]). Thus, we can infer that the northernmost portion of the 1997 seismogenic structure has been locked at least over the past 700 years and the southern portion for an even longer period. On the other hand, the neighboring regions both to the north and to the south were struck by damaging earthquakes in the eighteenth century, as shown in Figure 1. To the south, a sequence that lasted for more than a year occurred in 1703, with a maximum intensity of XI (MCS) (Blumetti, 1995; Castelli *et al.*, 1997; Boschi *et al.*, 1998). Another important sequence occurred in 1730 with a maximum MCS intensity of X (Fig. 1). Similar to the 1997 sequence, both the 1703 and 1730 sequences did not have a single strong mainshock followed by smaller aftershocks but were characterized by a few strong shocks of similar size, which occurred within hours or days from each other. This prolonged seismic release, involving different fault segments, could be characteristic of this portion of the central Apennines, and there are some similarities between the 1703, the 1730, and the 1997 seismic sequences.

The 1703 seismic sequence had two mainshocks, which ruptured two adjacent zones of the belt on 14 January and on 2 February; this is similar to what happened in 1997 with the two shocks of 26 September at Colfiorito and 14 October near Sellano. The time elapsed between the two shocks is almost identical (19 and 18 days), and also the epicentral distance between them is comparable. The 1730 sequence had two shocks of similar magnitude on 12 May at 5:00 and 13:45 GMT, that is, with a time lag (8h45m) almost identical to that elapsed between the two mainshocks of the Colfiorito sequence on 26 September 1997 (9h07m). Six months after the two earthquakes in 1730, another seismic event struck in the area of Gubbio (nearly 60 km to the north) and was classified as VII–VIII on the MCS scale (Boschi *et al.*, 1995). It is interesting to note that the 1997 seismic sequence was also followed, nearly 6 months later, by an M_W 5.1 earthquake that struck Gualdo Tadino on 3 April 1998 (see Morelli *et al.*, 2000 and Fig. 1). The analysis of historical seismicity for the area of Gualdo Tadino shows that this zone was struck by a seismic sequence in 1751 and by a less intense sequence in 1747. In this case, there were also three strong shocks in a 6-hr time span. Therefore, prolonged seismic sequences with several earthquakes with similar magnitudes ($5 < M < 6$) seem to be a characteristic of this area.

It is worth observing that the analysis of recent seismicity does not reveal this peculiarity. In fact, the two most recent $M > 5$ earthquakes in this region (Fig. 1), namely the 1979 Norcia earthquake (M_S 5.8) (Deschamps *et al.*, 1984) and the 1984 Perugia–Gubbio shock (M_S 5.3) (Haessler *et al.*, 1988) had a single mainshock followed by their aftershocks. Moreover, the temporal evolution of instrumental seismicity in this area shows that earthquakes with magnitudes larger than 4.3 have their own sequence of aftershocks, such as those that occurred on 5 June 1993 near Perugia and on 12 May 1997 near Massa Martana (Fig. 1), just a few months before the beginning of the sequence near Colfiorito. Therefore, the analysis of instrumental seismicity of the past 20 years does not show any complex and prolonged seismic sequences with multiple shocks.

Seismic Data

In order to describe the pattern of seismicity in this area of the Apennines, we first analyze the Istituto Nazionale di Geofisica e Vulcanologia (INGV) catalog of locations obtained from the digital waveforms recorded by the permanent Italian seismic network since 1986. We have plotted with blue and red symbols in Figure 1 the epicenters of the earthquakes that occurred before and after 3 September 1997, when the Colfiorito foreshock occurred. Because of the rather sparse geometry of the permanent network, epicentral formal errors are generally about 2 km horizontally, while hypocentral depths have larger formal errors (Di Giovambattista and Barba, 1997). The analysis of instrumental seismicity confirms that the 1997 seismic sequence occurred in an area that was quiescent during the last decades (see also Console *et al.*, 2000). Figure 1 also shows that following the beginning of the Colfiorito sequence, there was an increase of seismicity to the northwest of the aftershock zone, between Gubbio, Città di Castello, and San Sepolcro.

The local temporary network that was installed a few hours after the largest shocks of 26 September was kept operational until 3 November 1997. It consisted of 33 stations (Fig. 2) equipped with three-component seismometers, most of which had broadband sensors, while a few stations were also equipped with strong motion sensors. The seismic stations operated in continuous recording mode and allowed us to collect more than 60 Gb of digital data. The processing of these data allowed us to associate more than 2500 seismic events with magnitudes larger than 2.5. Most recorders had a dynamic range of 24 bits, thus ensuring the recording of nonsaturated waveforms for most of the aftershocks. *P*- and *S*-wave arrival times were carefully handpicked on digital waveforms, and weights were assigned according to reading accuracy. The instrumental characteristics, the 1D hypocentral locations, and the general features of the temporal evolution of the 1997 sequence are reported in Deschamps *et al.* (2000). In describing the seismic sequence, we use the data recorded by the local digital network during its 40-day operational period.

The Seismic Sequence

We analyze the 3D earthquake locations of 2000 selected aftershocks with $M_D \geq 2.5$ computed by Chiarabba and Amato (2003) by inverting *P*- and *S*-wave arrival times with the SimulPS technique (Eberhart-Phillips and Reyners [1997] and references therein). The observed V_p and V_p/V_s heterogeneities (up to 15% in the uppermost crustal layers) produce hypocentral variations generally less than 1 or 2 km, with a tendency for the earthquakes to occur at the edge of high V_p anomalies (see Chiarabba and Amato [2003] for a comprehensive discussion). The 3D located earthquakes are strongly clustered. On average, vertical and horizontal formal errors are less than 0.5 km and are smaller (0.3 km) in the central area near the Colfiorito basin.

Mainshock Locations and Fault-Plane Solutions

The 1997–1998 seismic sequence was characterized by an unusual number of moderate-magnitude shocks ($M_W > 5$). Table 1 lists the locations of the earthquakes with $M > 4$ and includes the foreshock of 3 September 1997 (M_W 4.5) as well as an early aftershock ($M_L = 4.7$) of the 26 September events that occurred at 09:47 UTC (Cattaneo *et al.*, 2000). The foreshock sequence started with the event of 3 September and was followed by several hundreds of aftershocks (Ripepe *et al.*, 2000). Then, on 26 September, two mainshocks, at 00:33 (M_W 5.7) and 09:40 (M_W 6.0), occurred at 2- to 3-km distance from each other, rupturing two distinct fault segments (Fig. 2) in opposite directions (Amato *et al.*, 1998; Pino *et al.*, 1999; Zollo *et al.*, 1999): the first toward the southeast and the second toward the northwest (Pino and Mazza, 2000). Other $M > 5$ events occurred in the following days (Table 1), both in the area activated in September (3 October M_W 5.2 and 6 October M_W 5.4 shocks) and at its southern and northern edges (12 October M_W 5.2 and 14 October 1997 M_W 5.6 and 3 April 1998 M_W 5.1 shocks, respectively). Figure 2 shows the locations and fault-plane solutions of the foreshock and of the six $M_W > 5$ earthquakes together with the geometry and position of the three main faults inferred by modeling coseismic displacement resulting from SAR interferometry and GPS measurements (Salvi *et al.*, 2000).

The CMT fault-plane solutions of the largest shocks were determined by Ekström *et al.* (1998) and Morelli *et al.* (2000) using regional and teleseismic data. They showed that normal faulting with maximum extension oriented northeast–southwest was predominant during the sequence. This finding is in agreement with the analysis of other earthquakes that occurred in the region (Frepoli and Amato, 1997) and with the stress regime inferred for this area by Montone *et al.* (1999). Moreover, similar solutions were obtained with the CMT procedure for the two earthquakes that occurred in adjacent areas in 1979 and 1984 (Fig. 1).

The available *P*-wave polarity data for the largest shocks of the 1997 sequence are compared with the CMT

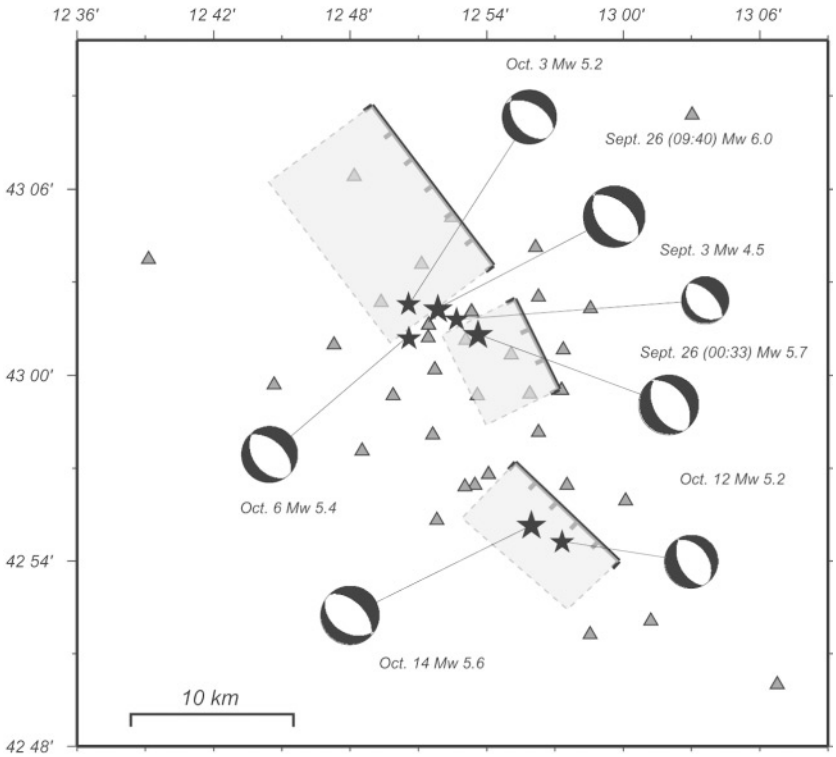


Figure 2. Distribution of temporary seismic stations, deployed on 26 September immediately after the first mainshock, which operated until 3 November 1997. The surface projections of the faults that ruptured during the three largest earthquakes of the sequence are drawn in the map. The fault-plane solution of the foreshock (M_W 4.5) and of the six shocks with magnitude larger than 5 is also shown.

fault-plane solutions in Figure 3. CMT solutions are quite consistent with *P*-wave polarity data, mostly for the earthquakes located in the northern part of the seismogenic volume: see for instance the 3, 6, and 16 October events in Figure 3. The focal mechanisms of the events located in the southern sector, where the network geometry is less dense (12 October and particularly 14 October), change significantly using 1D or 3D take-off angles, while for the others to the north the focal mechanisms are stable. This means that the fault-plane solutions of the southern events are velocity model dependent and consequently not completely reliable.

The distribution of *P*-wave polarities over the focal sphere for the 6 October earthquake (Fig. 3) suggests an oblique slip direction (rake $-50°$), which has been interpreted by Chiaraluce *et al.* (2003) in terms of reactivation of a pre-existing structure. This strike-slip component is not present in the CMT solution (rake $-80°$).

The occurrence of repeated shocks is explained by ruptures on adjacent fault segments, which contributed to activate an elongated 60-km seismogenic structure, that is, longer than the sum of individual fault lengths (Figs. 1 and 4). This is clearly shown by aftershock distribution; modeling of teleseismic (Ekström *et al.*, 1998), regional (Pino and Mazza, 2000), and strong motion (Zollo *et al.*, 1999) waveforms; as well as geodetic data (Hunstad *et al.*, 1999; Salvi *et al.*, 2000). The largest shocks nucleate at shallow depth (~6–7 km) at the base of the seismogenic volume (Table 1).

A further normal faulting earthquake (M_W 5.1) occurred on 3 April 1998 to the north of the seismogenic area near Gualdo Tadino (Fig. 1). This additional event and its aftershocks increased the overall extent of the seismogenic area along the Apenninic chain to more than 60 km. The Gualdo Tadino event was preceded on 26 March 1998 by a subcrustal M_W 5.3 earthquake, which is located at ~48 km depth and is likely to be related to the bending of the Adriatic lithosphere beneath the Apenninic belt (Selvaggi and Amato, 1992; Selvaggi, 2001). The similar epicentral location and the temporal proximity of these two earthquakes (Table 1) raises the intriguing question of whether deep and shallow earthquakes are linked and how. It is interesting to note that a small (M_L 2.3) subcrustal event also preceded the September 1997 mainshocks by 8 days (Cattaneo *et al.*, 2000).

Fault Geometries from Aftershock Distribution

In this section, we show and discuss the aftershock distribution using data from the temporary network. The high quality of the hypocentral locations allows us to define the geometry and faulting mechanisms of the activated faults. Figure 4 shows the epicenters of the 1982 aftershocks that occurred between 26 September and 3 November 1997. The epicentral distribution reveals the complexity of the seismogenic structure, which extends for about 60 km along the trend of the Apennines and 5–10 km perpendicularly. The width of the active area is larger in the northern sector than in the southern. The north–south alignment of hypocenters, already observed by Deschamps *et al.* (2000), is enhanced by the 3D locations (Fig. 4). Chiaraluce *et al.* (2003) interpreted this evidence as a strike-slip structure.

In Figure 5, we show a suite of 18, 2-km-wide vertical

Table 1
Hypocentral Parameters of the Largest Earthquakes in the Umbria–Marche Region (September 1997 through April 1998)

Date (yymmdd)	Time (hr)	Latiude	Longitude	d* (km)	M_L	M_W	Phases	EH	EZ
970903	22:07	43N00.71	12E52.72	4.4		4.5	9†	1.0′	2.5′
970926	0:33	43N01.20	12E53.30	6.7	5.7	5.7	14 (4)‡	1.0′	2.0′
970926	9:40	43N01.82	12E51.51	6.3	5.8	6.0	6 (1)‡	1.0′	2.5′
970926	9:47	43N06.41	12E48.19	2.6	4.7		9l	1.0′	2.5′
970926	13:30	43N01.25	12E56.68	3.9	4.3	4.5	9	1.0′	2.5′
970927	8:08	43N05.44	12E49.46	5.7	4.3	4.3	14	0.1	0.1
970927	17:13	43N01.21	12E50.37	5.6	4		29	0.1	0.1
970927	19:56	43N02.69	12E51.58	3.8	4		29	0.1	0.1
970928	11:24	42N58.82	12E51.79	1.4	3.7		24	0.1	0.1
971002	10:59	43N05.45	12E47.90	4.9	4.1		42	0.1	0.1
971003	8:55	43N02.11	12E50.59	4.4	5	5.2	38	0.1	0.1
971004	6:49	42N56.14	12E54.72	4.9	4.2		39	0.1	0.1
971004	15:07	42N56.36	12E56.01	4.7	4.2		40	0.1	0.1
971004	16:13	42N56.36	12E56.19	4.2	4.6	4.6	39	0.1	0.2
971004	18:47	42N56.36	12E56.28	4.3	4.1		38	0.1	0.1
971006	23:24	43N01.17	12E50.86	5.5	5.4	5.4	38	0.1	0.1
971007	1:24	43N01.80	12E51.01	4.7	4.2	4.2	42	0.1	0.1
971007	5:09	43N01.77	12E51.60	2.2	4.4	4.5	40	0.1	0.1
971012	11:08	42N55.17	12E56.98	4.6	5.2	5.2	43	0.1	0.1
971012	21:31	42N53.53	12E58.52	5.6	4		42	0.1	0.1
971013	11:01	42N54.04	12E58.14	5.2	4		40	0.1	0.1
971013	13:09	42N53.29	12E58.17	6.26	4.1		24	0.1	0.3
971014	15:23	42N55.59	12E55.53	5.18	5.6	5.6	38	0.1	0.2
971014	16:24	42N57.08	12E53.98	1.9	4		36	0.1	0.2
971014	23:23	42N58.10	12E52.22	4.74	4.2		32	0.1	0.1
971015	22:53	42N55.99	12E56.06	3.6	4.1		33	0.1	0.2
971016	4:52	42N57.10	12E55.04	3.44	4		40	0.1	0.1
971016	12:00	43N02.29	12E53.32	1.14	4.5	4.3	38	0.1	0.1
971016	17:31	42N52.73	13E01.58	4.5	4		47	0.1	0.1
971019	16:00	42N58.43	12E51.49	5.09	4.1	4.2	27	0.1	0.1
971020	1:27	42N59.94	12E52.77	1.63	3.3		39	0.1	0.1
971025	3:08	42N49.00	13E05.34	5.85	4.1		34	0.1	0.1
980326	16:26	43N08.01	12E48.15	47.7	5.4	5.3	19	1.0′	3.0′
980403	7:26	43N10.78	12E46.71	8.7	5.0	5.1	19	1.0′	3.0′

*Depths are relative to sea level, which is about 800 m below the average elevation of the region.
†Revised after Ripepe *et al.* (2000).
‡After Amato *et al.* (1998): number of stations within 100 (20) km.
lAfter Cattaneo *et al.* (2000).
"phases," is the number of *P*- and *S*-wave arrival times used for locations. M_L is after Casale and Mazza (2000); M_w is after Ekström *et al.* (1998) and Morelli *et al.* (2000). EH and EZ are horizontal and vertical formal errors from Hypoinverse (′) and SimulPS (see text for explanation).

sections, which cross the structure almost perpendicularly at different latitudes (see locations in Fig. 4). Sections 4, 5, and 6 of Figure 5 show that the fault corresponding to the 09:40 event dips to the southwest at an angle of about 35°–40°, consistent with one of the nodal planes of the CMT focal mechanism (Ekström *et al.*, 1998). Aftershocks are located between 1 and 8 km depth below sea level (b.s.l.), concentrating at depths above 6 km and shallower than the mainshock. The mainshock location was obtained using data from the national network and a few other permanent local stations belonging to regional networks only (Table 1), and it is affected by a large hypocentral uncertainty. The aftershocks clearly show that the 09:40 fault expands for at least 6 km from the hypocenter in the northwest direction (sections 4–6), which corresponds to the area of maximum slip according to geodetic and strong motion data (Hunstad *et al.*, 1999; Capuano *et al.*, 2000; Salvi *et al.*, 2000). To the north, the aftershock distribution is more scattered (sections 1–3) and may suggest the presence of a diffuse deformation zone, rather than that of a single fault. However, it must be noted that the station coverage is poorer in this region (Fig. 2) and the scattered pattern of seismicity could be affected by the network geometry.

Sections 7–9 in Figure 5 cross the fault that ruptured during the 00:33 event. In this central area, we note two subparallel faults: an eastern fault ruptured by the 00:33 event and a steeper western fault that ruptured with the M_W 5.4 shock of 6 October 1997 (23:24), described in the section Spatiotemporal Evolution of the Sequence. The 00:33 fault is less defined than the 09:40 fault for its smaller extent and because its early aftershocks, which occurred in the first 16 hr, were not recorded by the temporary network. Neverthe-

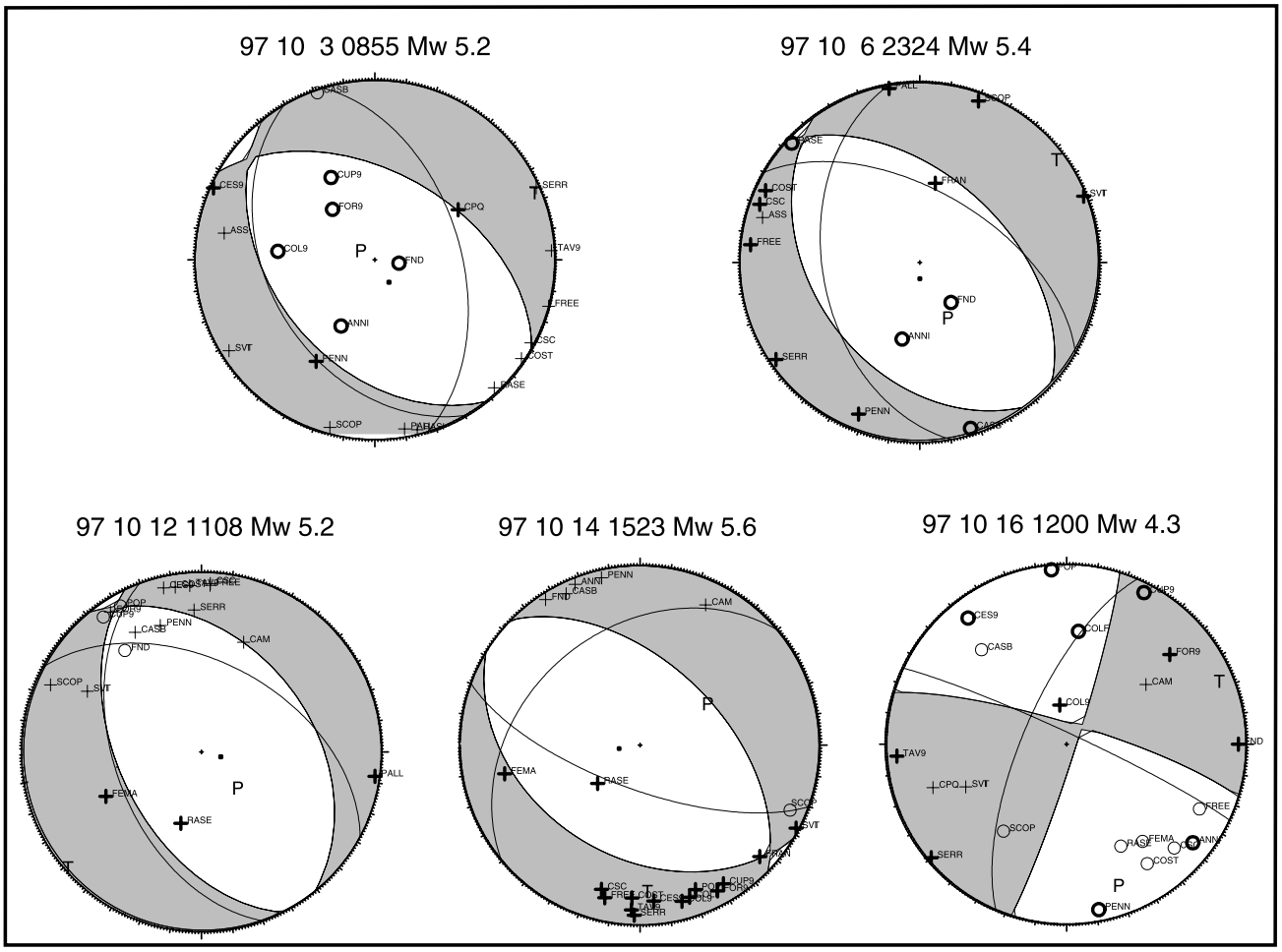


Figure 3. Comparison between *P*-wave polarity data (and resulting focal plane solutions, this study) and the CMT focal mechanisms (shaded).

less, the aftershocks delineate a fault plane with a dip to the southwest of about 40°, between ~6 and ~1 km depth (Fig. 5, sections 7, 8, 9). The aftershocks are mostly, but not exclusively, shallower than the mainshock, which is located at a depth of about 6 km. Section 10 crosses a region with sparse seismicity in the southern extent of the 00:33 fault. Sections 11–15 cut the region of the October 14 (15:23) mainshock (M_W 5.6). Since this event occurred during the operational period of the temporary network, its location is very well constrained (with horizontal and vertical formal errors less than 0.5 km). The hypocenter of the mainshock is located at the lower end of a southwest-dipping fault plane that is evident for about 6–8 km along the strike in a northwest–southeast direction and for about 5 km along the downdip direction from the mainshock nucleation toward the surface. The aftershock alignment delineating the fault plane is narrower and steeper than the fault plane delineated by the aftershocks to the north (compare section 13 with section 6). The southern sections (16–18) show a region of widespread seismicity, which may suggest that the deformation is released through smaller faults distributed over a broad volume. However, we can exclude this interpretation because Michelini *et al.* (2000), using data recorded by a different temporary network (unfortunately installed many days after the onset of the seismic sequence) and Chiaraluce *et al.* (2003), using a different location algorithm, both found clear evidence of a southwest-dipping fault as far south as section 16.

As seen in the vertical sections described earlier, the fault segments that ruptured during the 00:33 and 09:40 events have a rather simple planar shape with a dip of about 35°–40°. These two mainshocks nucleated in opposite directions and occurred within a few hours of each other. The 3 September M_W 4.5 foreshock nucleated at a depth of 4.4 km just in the middle of the two hypocenters of the 26 September mainshocks (see Figs. 4 and 6 and sections 7 and 8 of Fig. 5) and very close to the strike-slip event of 16 October (M_W 4.3). These closely spaced minor fault segments suggest the presence of a highly heterogeneous crustal volume at the boundary between the two main rupture planes.

In order to unravel the complexity of the fault geometry, we have drawn seven parallel, 1-km-thick east–west–trending

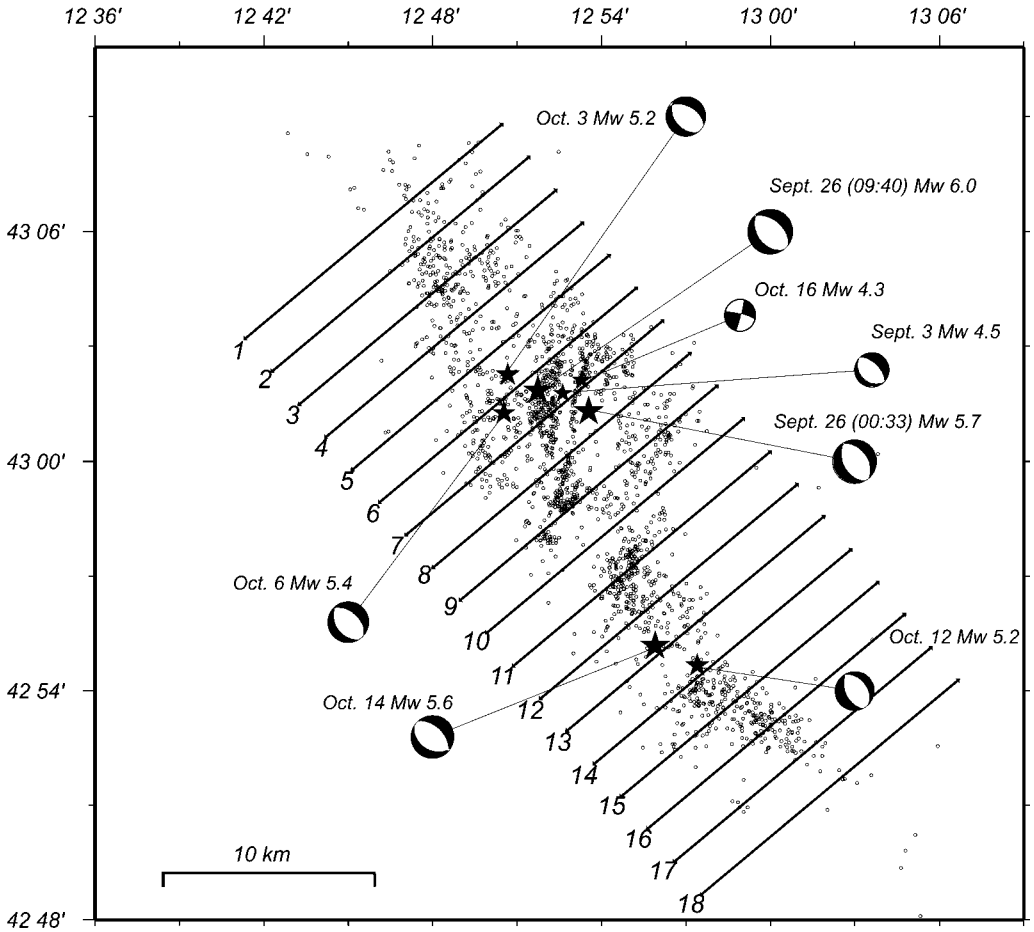


Figure 4. Map of epicenters of aftershocks relocated by Chiarabba and Amato (2003) with a 3D tomographic inversion. The solid lines show the position of 18 northeast–southwest vertical cross sections used in Figure 5.

sections across the two ~north–south linear clusters of aftershocks (Fig. 6a). Starting from the northernmost section, we see the 09:40 fault dipping to the west (section 1 of Fig. 6b). Moving to the south, sections 2 and 3 show the 09:40 fault splaying toward the surface in at least two minor nearly vertical faults. In sections 4 and 5, the 09:40 fault is still evident, from ~8 to ~4 km depth, whereas the shallower and steeper seismicity is related to the 6 October fault. This latter fault segment seems to be connected to the southernmost termination of the 09:40 fault. It must be observed that the north–south fault became active just after the 6 October event, culminating with an M_W 4.3 strike-slip shock on 16 October. Most of the aftershocks located along these shallow north–south structures show strike-slip focal mechanisms (see black solutions in Fig. 7), as we will discuss in the next paragraph.

The seismicity to the right (east) of the strike-slip fault, visible in sections 3–7 of Figure 6b, is related to the 00:33 fault. It is evident that the 00:33 and the 09:40 faults are almost parallel and are separated at depth by a distance that increases from north to south (compare section 3, where the two faults start to branch, and section 7, where the two faults are separated by 2–3 km), showing the presence of a left-lateral step between the two main faults.

Aftershock Fault-Plane Solutions

We computed fault-plane solutions using first motion polarity data for all those aftershocks for which more than 18 clear polarity observations were available and by using take-off angles and locations computed with the 3D velocity model proposed by Chiarabba and Amato (2003). Fault-plane solutions are computed by the FPFIT code (Reasenberg and Oppenheimer, 1985) and are shown in Figure 7. Despite the narrow azimuthal gap and the large number of available polarities, the distribution of seismic stations for those earthquakes located in the southern sector leads to poorly constrained solutions. This is probably due to the shallowness of these earthquakes, which causes the take-off angle of direct and refracted rays to lie close to the horizontal direction. For this reason, we select focal mechanisms of earthquakes that have an azimuthal gap less than 80° and contain at least two rays in the central part of the focal sphere

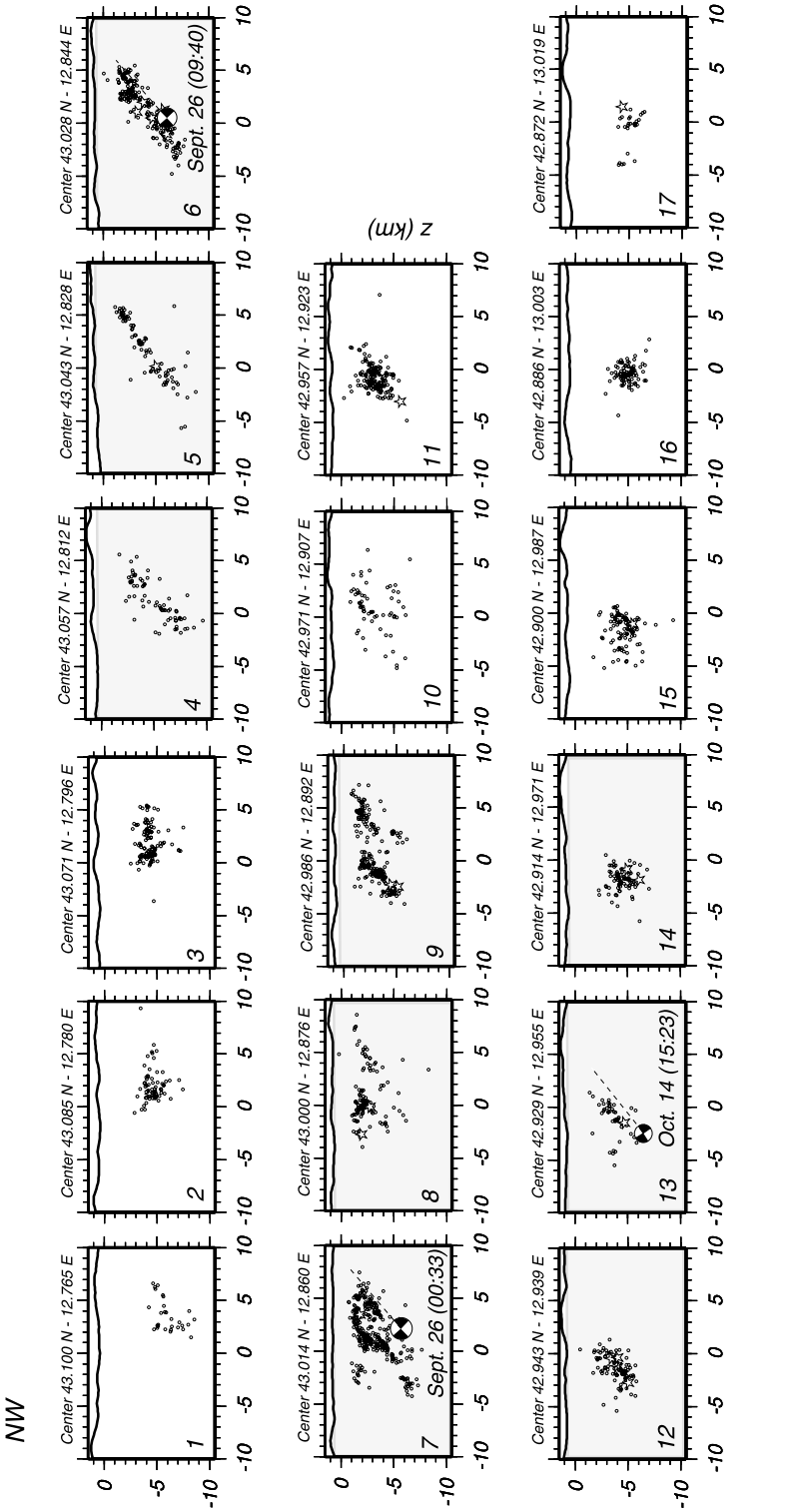


Figure 5. Eighteen vertical cross northeast–southwest sections 2 km wide mapping the seismogenic volume from the northwest to the southeast. The open stars show the position of the $M > 4$ events, while the focal mechanisms correspond to the three largest magnitude events.

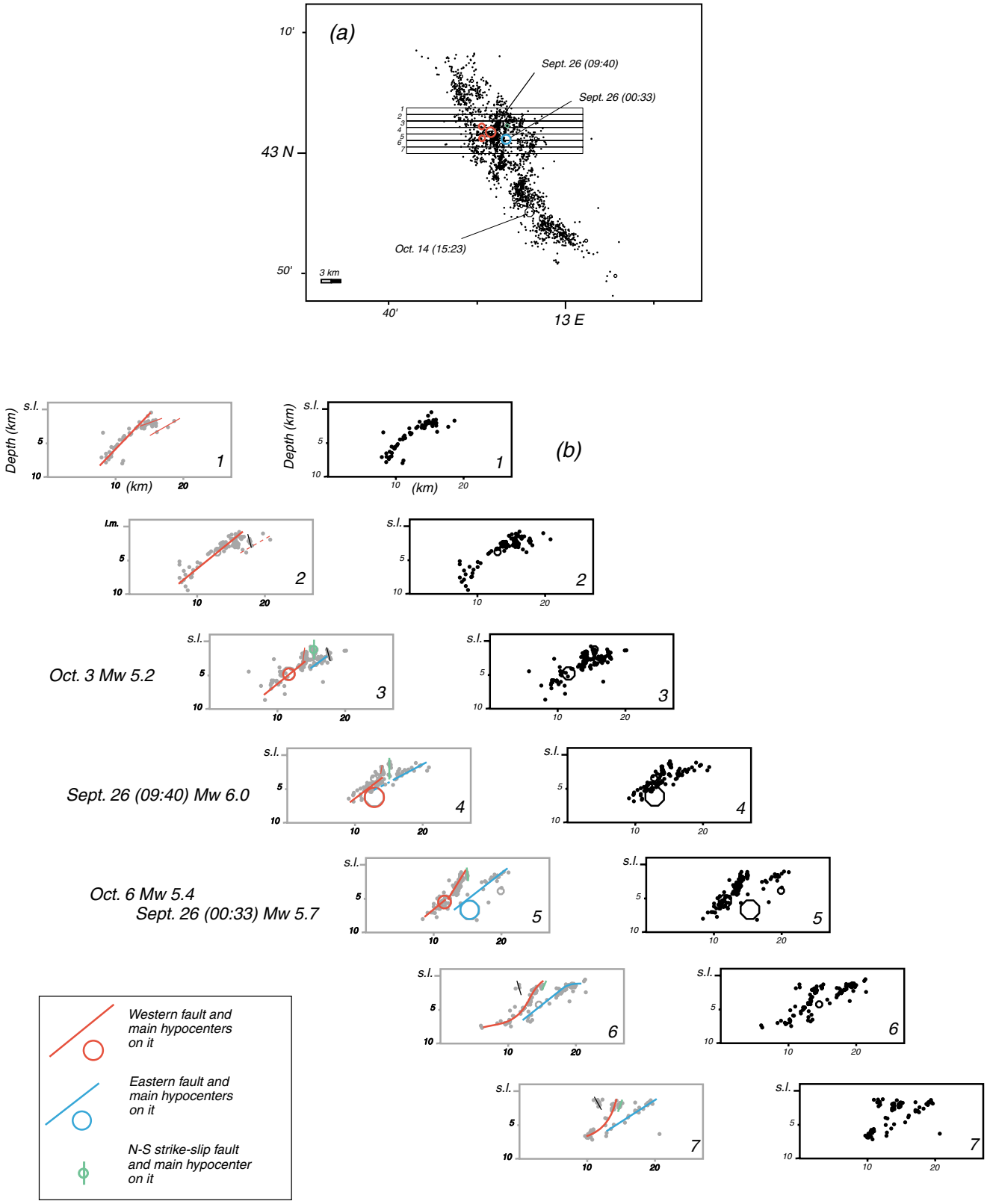


Figure 6. (a) Epicentral map showing the events in Figure 4. The events in the numbered blocks are shown in cross section in (b). The blocks are 1 km wide. (b) Cross sections for the events in (a). The segments drawn on the light gray sections allow imaging the apparent relative geometry.

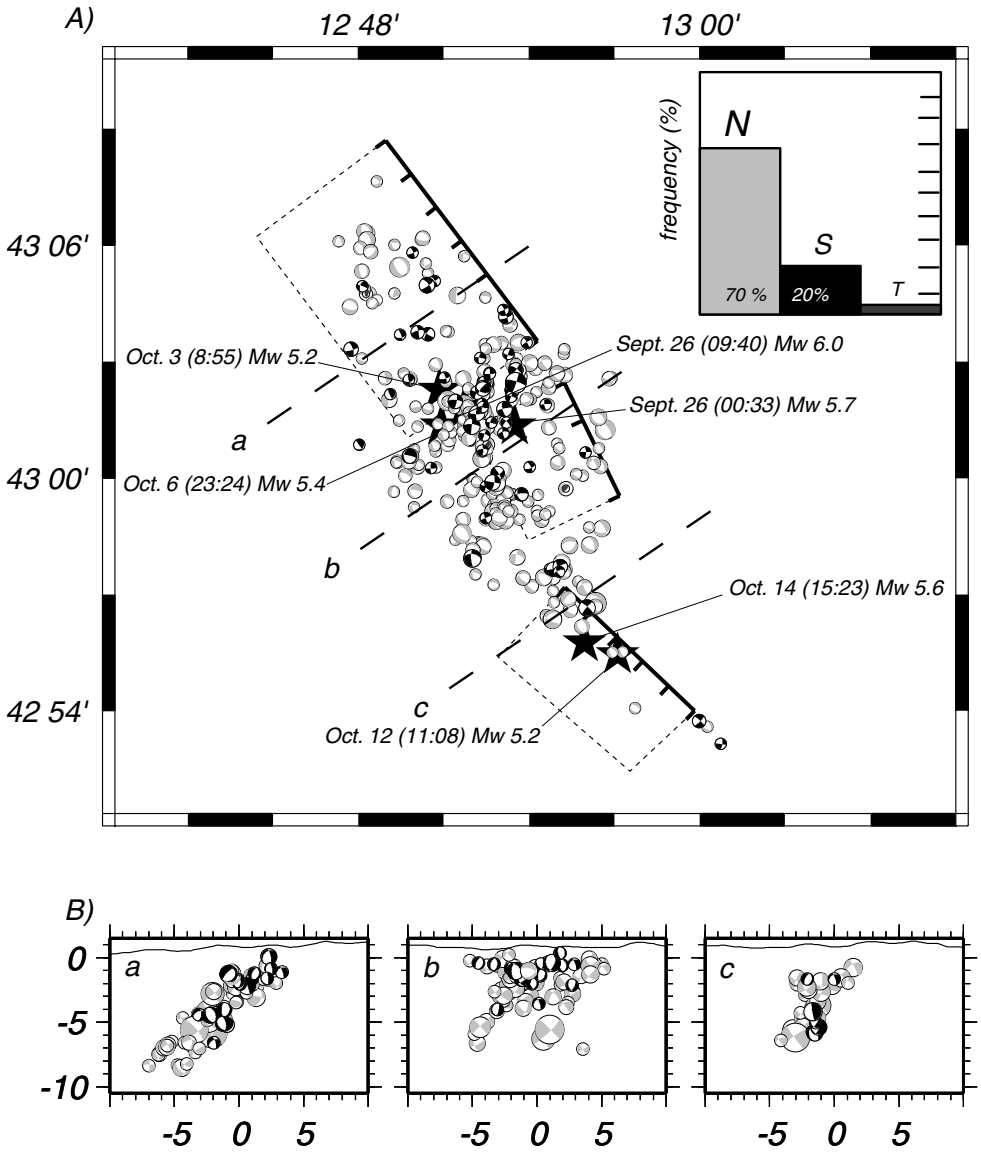


Figure 7. (a) Fault-plane solutions for a selected subset of 321 aftershocks. The focal mechanisms have been selected according to the criterion discussed in the text. The histogram plotted on the top right panel shows the distribution of faulting mechanisms: about 70% of events show normal faulting (gray, with rake equal to 270° ± 20°), 20% to strike-slip solutions (black), and only 5% to reverse faulting. (b) Three vertical cross sections mapping the solutions at depth.

(take-off close to the vertical). The resulting formal errors in strike, dip, and rake are about 10°, 15°, and 30°, respectively. This reduces the available fault-plane solutions from 780 to 321, which still samples homogeneously the area around the two main faults (Fig. 7).

The fault-plane solutions of the selected aftershocks are plotted in Figure 7 using a grayscale to identify the different mechanisms. The solutions are available, together with a related appendix, on the INGV Web page (www.ingv.it/roma/bssa). It is evident that most of the aftershocks have normal faulting mechanisms with an extension direction nearly northeast–southwest. Figure 7 also contains a histogram showing the distribution of fault-plane solutions: about 70% of the solutions show normal faulting (rake angles within the interval 270° ± 20°), ~20% exhibit strike-slip faulting, and fewer than 5% can be ascribed to pure thrust or oblique/reverse faulting (dark gray in Fig. 7). These results agree well with the uniformity of CMT fault-plane solutions for the largest earthquakes, pointed out by Morelli *et al.* (2000) and discussed before. The nodal planes of normal faulting aftershocks have a strike consistent with the fault planes that ruptured during the mainshocks and generally show a small either left-lateral or right-lateral strike-slip component. Normal faulting is associated to horizontal northeast–southwest

extension, and it is evident all over the region. Strike-slip earthquakes are mainly located along shallow (0–3 km) secondary north–south faults, well evident in map view, which extend for ~6 km (Figs. 4, 6 and 7). Thrust faulting earthquakes are not clustered and therefore do not highlight any clear structure.

Figure 8 shows the distribution of *T*- and *P*-axis trends for the selected events, while Figure 9 shows the distribution of these axes on map view. The extensional axis for most of the events is subhorizontal and has an average trend of 30° or 210°. In contrast, the azimuthal distribution of the compressive axis is not bimodal. *P*-axes have an average plunge of 60°, but their trends lie over a broad range of azimuths with a peak close to 135°, evidencing a rotation along the Apenninic direction (northwest–southeast). The *T* axes are mostly horizontal and oriented in the anti-Apenninic direction (northeast–southwest). This distribution of plunge and trends for *P* and *T* axes indicates that there is not any clear variation in the extension direction.

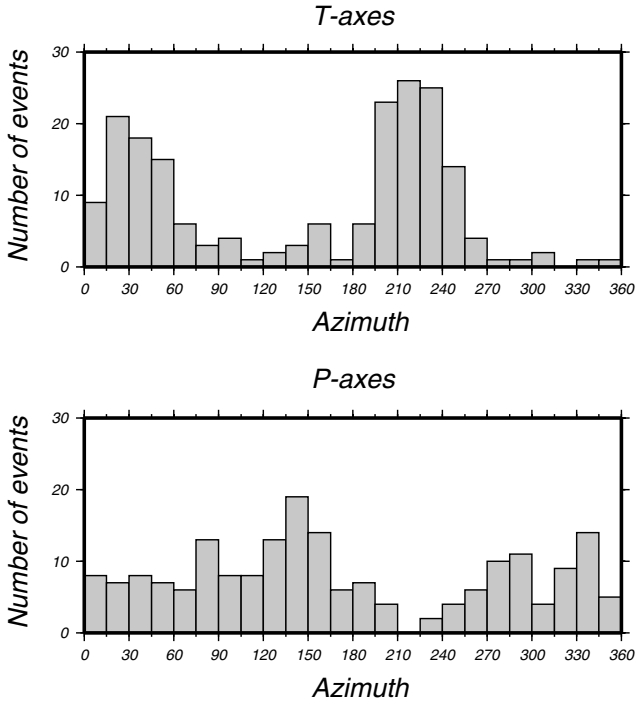


Figure 8. Histograms showing the distribution of azimuths of *T* and *P* axes for the selected fault-plane solutions. Most of the selected events have a nearly subhorizontal *T* axis oriented ~30° or ~210°. The trends of the *P* axes are distributed on a wide range of azimuth, and the average plunge is close to 60°.

Spatiotemporal Evolution of the Sequence

A clear migration of seismicity toward the boundary of the area was observed since the beginning of the sequence. In the months following the most active period of September 1997, seismic activity continued in the adjacent regions, culminating in an M_W 5.1 earthquake on 3 April 1998 near the town of Gualdo Tadino, about 20 km north of the mainshocks of 26 September (Fig. 1). The migration of seismicity along ~60 km of the Apennines is well evident in the space-time diagram shown in Figure 10. This figure emphasizes the migration of seismicity toward the southeast, culminating with the two earthquakes of 12 and 14 October, located near Sellano, which occurred 17 and 19 days later, respectively. This southeastward migration started at the beginning of October (Fig. 10). In contrast, aftershocks clustered at the northern edge of the seismic zone since the beginning of the sequence and the Gualdo Tadino event of 3 April 1998 occurred in an area previously struck by some aftershocks.

In April 1998, the extension of the activated region was about 60 km, which filled quite well the area left unbroken by earthquakes since the eighteenth century. Figure 10 also shows that the foreshock (September 3), and the seismicity immediately following it, is located in the zone separating the two rupture planes of the September 26 mainshocks. Figure 11 depicts the depth distribution of seismicity recorded during the 1997 seismic sequence: this figure shows that most of earthquakes are located at depths shallower than 7 km (90% of the events analyzed in this study; see the arrows in the figure) with a peak at depths ranging between 2 and 3 km b.s.l. This plot confirms that aftershocks of the 1997 seismic sequence are shallower than mainshocks, which nucleated at the base of the seismogenic volume (between 5 and 7 km). This figure also emphasizes that the complexity of the shallow crust (<3 km) played a dominant role in promoting shallow aftershocks on pre-existing fault planes, some of which have been inherited by the previous compressional tectonic phase.

The prolonged seismic activity and its recording by the dense temporary array gave us the unusual opportunity to see in detail how the microseismicity clustered on and around the fault planes before individual ruptures occurred. We describe the seismic activity before and after the four largest shocks of October (3, 6, 12, and 14). We have plotted in Figure 12a the seismicity distribution preceding and following the 3 October (M_W 5.2) event as well as the locations and the surface projection of the fault planes that ruptured during the two main events of 26 September (00:33 and 09:40). The three southwest–northeast cross sections of Figure 12a show the distribution of aftershocks that occurred in three time intervals: (1) 12 hr following the mainshock, (2) the previous 7 days, and (3) 12 hr after the mainshock through November 1997. Early aftershocks of 3 October occurred along the same plane delineated by the aftershocks of the 09:40 event dipping ~40° to the southwest, possibly filling an area of slip deficit during the main faulting episode on the 09:40 fault. However, the area that ruptured during the 3 October event is located well inside the maximum slip patch inferred for the 09:40 earthquake by modeling GPS and SAR data (Hunstad *et al.*, 1999; Salvi *et al.*, 2000). The subsequent seismicity is located either below or above the rupture zone of the 3 October event.

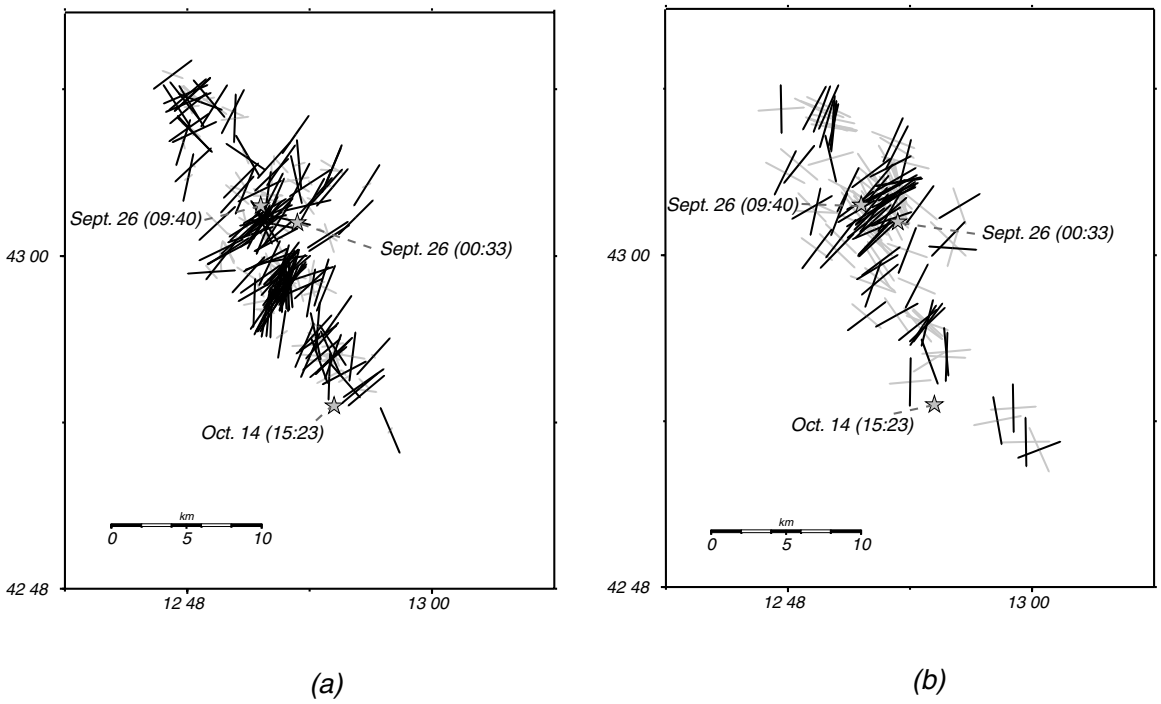


Figure 9. Maps showing the distribution of *T* (black segments) and *P* (gray segments) axes for (a) normal faulting and (b) strike-slip earthquakes. Stars show the positions of the three largest shocks of the sequence.

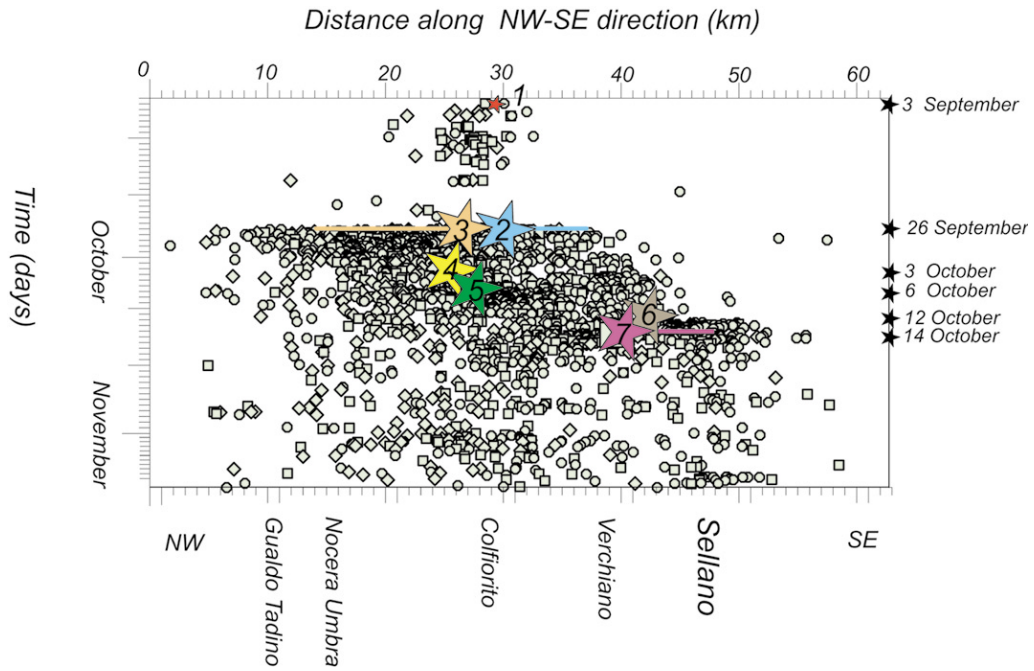


Figure 10. Space-time diagrams showing the seismicity pattern along a 62-km section oriented in the Apennine direction (northwest–southeast). Numbers identify the position of the 3 September foreshock (1) and the six $M > 5$ earthquakes (2–7) that occurred in the following months. The straight lines depict the expected fault length as derived from geodetic and ground-motion modeling (see text for references).

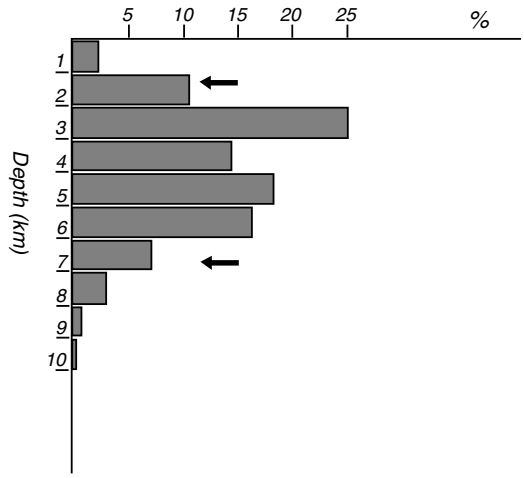


Figure 11. Depth distribution (b.s.l.) of aftershocks. Arrows define the depth interval containing the 90% of the seismicity.

The 6 October (M_W 5.4) event is located slightly to the southeast of the 09:40 fault segment (Fig. 12b), with many aftershocks delineating a steeper southwest-dipping fault. Early aftershocks of 6 October (see the two top panels in Fig. 12b) depict very clearly the fault plane, which dips ~70° to the southwest. A small area with a gap of seismicity on the fault plane is evident both before and after the 6 October event, indicating that the patch ruptured during this M_W 5.4 earthquake. The shallower portion of the 6 October fault is the first evidence of the activation of the north–south strike-slip structure, which develops in the subsequent period and culminates with the M_W 4.3 shock at 1.14 km depth.

Almost 2 weeks after 26 September, two other $M > 5$ events occurred, an M_W 5.2 on 12 October and an M_W 5.6 on 14 October, striking the Sellano area in the southern part of the seismogenic zone. To discuss the spatiotemporal evolution of seismicity in this area, we show the locations projected on the fault plane (Fig. 13a) and in cross section (Fig. 13b) of earthquakes that occurred before 12 October, between 12 and 14 October, and then after the 14 October shock. It appears that the fault was already active many days before the two shocks, mostly to the northwest and above the 14 October hypocenter. Then, the M_W 5.2 shock and related aftershocks ruptured the southern portion of the fault, leaving a ~4-km-wide area with still low seismicity, where the subsequent 14 October event nucleated. Aftershocks of the 14 October shock concentrate at both ends of the fault. In the few days after it, we also note that the same area is still without aftershocks, possibly suggesting that the area of maximum coseismic slip is located on both sides of the hypocenter, differently from what is observed for the two 26 September mainshocks that exhibit a clear directivity to the south and to the north, respectively. However, it must be noticed that the area to the northwest of the 14 October event was also active with $M > 4$ earthquakes throughout the whole sequence (white, gray, and black circles in Fig. 13a, distance from 0 to ~4 km). Figure 13b also shows the activation of the 14 October southwest-dipping fault (see open circles) before the occurrence of the main events.

Discussion and Conclusions

In this article we investigate the distribution of seismicity during the 1997 Umbria–Marche sequence and the complex normal fault system, which ruptured multiple segments with hourly and daily time lags. Seismicity shows a clear migration along the strike direction (northwest–southeast) of the main faults, corresponding to the Apennine orientation. The analysis of historical seismicity reveals that seismic sequences with multiple shocks with similar magnitude are common in this sector of the Apennines. Moreover, it suggests that the epicentral region was quiescent for at least the past 700 years. In fact, the spatiotemporal evolution of the 1997 sequence has several similarities with the sequences that occurred on the eighteenth century, both to the north and to the south of the Colfiorito area. All these seismic sequences (1703, 1730, and 1747–1751) are characterized by multiple ruptures in short time intervals. This complex behavior of faulting could be due to the high heterogeneity in the shallow crust of the central northern Apennines, characterized by fold-and-thrust structures inherited by the Neogene compressive tectonics.

Our results point out that the active northeast–southwest extension is accommodated by a thin northwest-trending fault zone composed by a few parallel normal fault segments, about 5–10 km long, with lateral steps of a few kilometers between each other. The seismic sequence affected almost 60 km of the Apenninic belt in a period lasting less than 7 months (September 1997–April 1998). All the rupture planes are shallow and southwest dipping at relatively low angles (~40°). The seismicity is confined to the upper 8 km of the crust, involving mostly the Mesozoic sedimentary cover (Collettini and Chiaraluce, 2000; Chiarabba and Amato, 2003). The rupture planes do not show any clear evidence of listric faults, as typically interpreted in this region based on seismic reflection data (Bally, 1986; Meghraoui *et al.*, 1999; Cello *et al.*, 2000). Aftershock focal mechanisms confirm a nearly horizontal northeast-trending extension, consistent with the mainshock faulting episodes. Strike-slip faults were activated during the 1997 sequence as secondary induced episodes that are restricted to the upper ~3 km of the crust. It is interesting to note that a major fault segment becomes active and visible with accurate hypocentral locations a few days before its activation with a large event.

The observed spatiotemporal behavior of the 1997 Umbria–Marche seismic sequence and the moderate magnitude of the largest shocks could be due to the combined effect of three apparently unlinked features: the presence of a puzzle of small-length pre-existing compressional structures upon which the relatively young normal faults are superimposed, the suggested presence of deep fluids (Chiodini

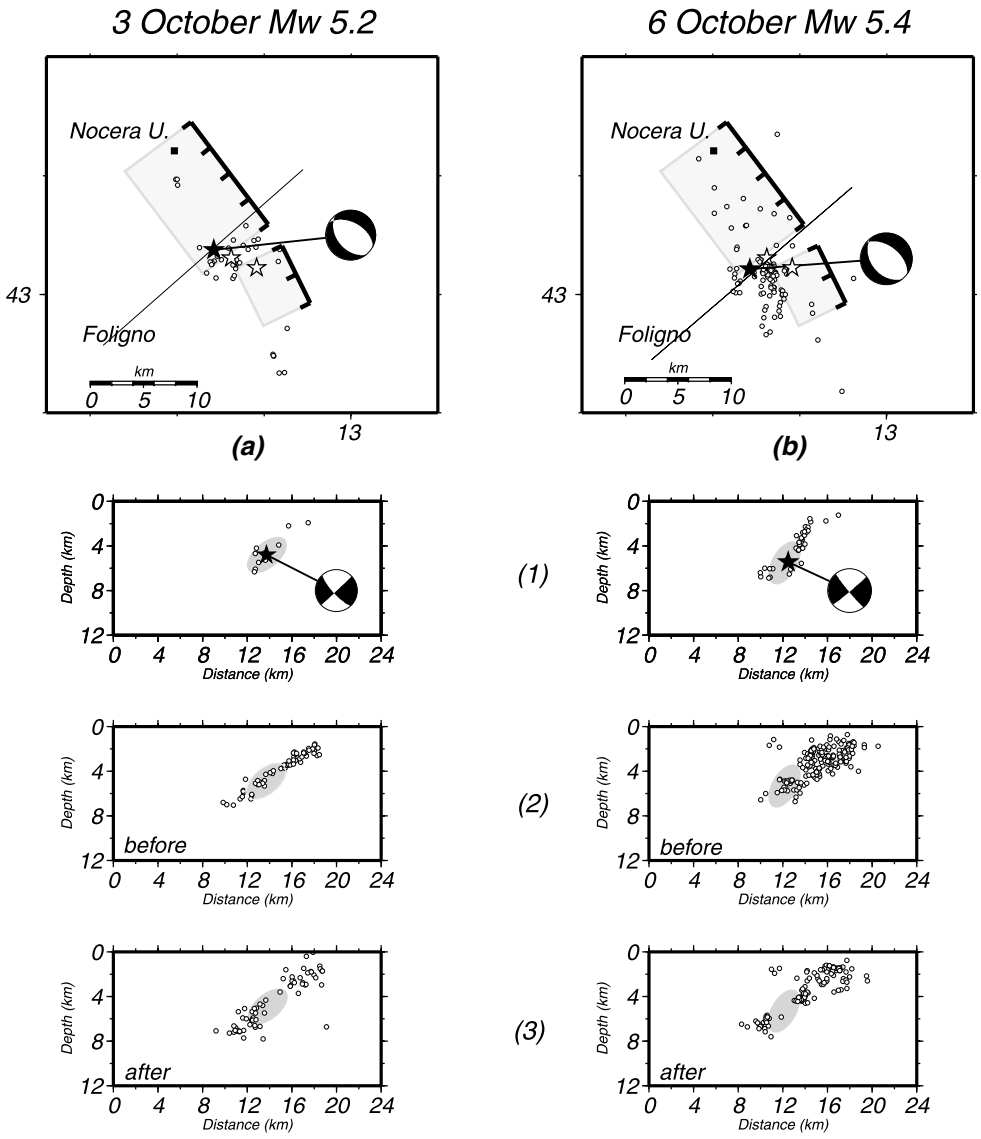


Figure 12. Distribution of seismicity associated with the (a) 3 October and (b) 6 October earthquakes. The maps show the mainshock epicenters (solid stars) and the fault-plane solutions for these two events (in a and b, respectively), the location of the two main events of 26 September (open stars), and their surface projection. The straight line in the map shows the position of the northeast–southwest vertical cross section used to image seismicity in the panels below. The cross sections show the seismicity that occurred in three time intervals: (1) 12 hr following the mainshock, (2) the previous 7 days, and (3) 12 hr after the mainshock through November 1997. The shaded areas depict the inferred portion of the fault planes ruptured during the (a) 3 October and (b) 6 October earthquakes.

and Cioni, 1989; Quattrocchi, 1999; Italiano, 2001; Collettini and Chiaraluce, 2000), and the low strain rate of the area (Selvaggi, 1998; Hunstad *et al.*, 2003). In such a complex structural setting, the activation of normal fault planes less steep than those suggested by mechanical models is not surprising. However, the lack of deformation estimates at the scale of the fault segments and the poor knowledge of the crust and fluid circulation in the area do not allow us to provide a more quantitative interpretation.

The very shallow cut-off of seismicity, which is also observed in other seismic sequences in the region (see Haessler *et al.* [1988] for the Gubbio 1984 sequence and Deschamps *et al.* [1984] for the 1979 Valnerina sequence), appears to be a regional feature that may be ascribed either to high temperature in the crust, promoting ductile deformation at relatively shallow depths, or more likely the presence of a shallow detachment. According to the interpretation of seismic reflection profiles, some authors (Barchi, 1998; Bon-

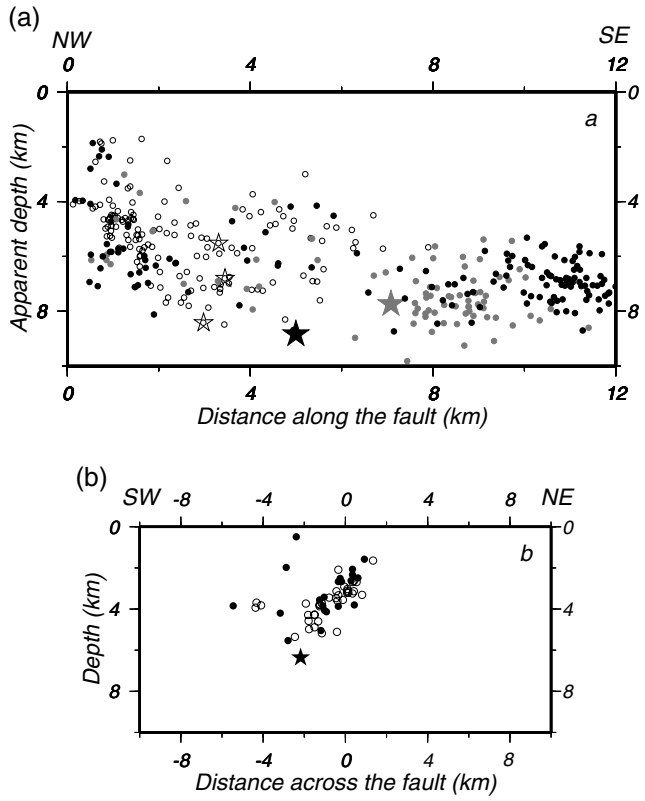


Figure 13. Distribution of seismicity on the fault plane (a) where the 12 and 14 October earthquakes nucleated and (b) on a northeast–southwest vertical cross section. White circles indicate the hypocenters of earthquakes that occurred before 12 October, gray circles depict those that occurred between 12 and 14 October, and black circles the seismicity following the 14 October Sellano mainshock (whose hypocenter is shown by a black star). The gray star indicates the hypocenter of the 12 October event, and white (open) stars indicate the locations of moderate events ($4 < M < 5$). The northeast–southwest cross section shown in (b) reveals that the fault was active before the two mainshocks, which ruptured distinct fault patches.

cio and Lavecchia, 2000) have suggested the presence of a regional normal fault dipping at low angle to the northeast, named the "Altotiberina fault," antithetic to the seismogenic fault system described in this study. The seismicity could be confined at depth by this regional fault. In this complex tectonic setting, with many pre-existing structures, we expect to have normal faulting at relatively low dip angles (40°) also in the presence of an extensional stress field with a nearly vertical σ_1.

The peculiar behavior of the 1997 and of some historical seismic sequences suggests that fault interaction due to stress transfer and/or fluid flow may play a dominant role in the spatiotemporal evolution of seismicity. The typical time delay between subsequent seismic events, which seems to characterize several sequences that occurred in the region, may be characteristic of the rheology and poroelastic behavior of the crust in this area (see King and Cocco [2001] and references therein). Our results show that two of the moderate-magnitude events, namely those of 3 and 12 October, seem to occur on the hanging wall or on the same fault planes of the 26 September and 14 October mainshocks, respectively. This could explain why they cannot be modeled in terms of elastic static stress transfer using Coulomb models, as found by Cocco *et al.* (2000).

The results presented in this study emphasize the importance of detailed microseismic data to constrain active tectonics, particularly in regions where the surface expression of seismic activity is barely visible.

Acknowledgments

We wish to thank the numerous people at the Istituto Nazionale di Geofisica & Vulcanologia who helped us during the field experiment and in processing and analyzing the data. We thank S. Gaffet, G. Bittarelli, G. B. Cimini, S. Mazza, and F. Mele for their efforts during the Colfiorito sequence and in interpreting the preliminary data. All the waveforms, arrival times, and locations of the 1997 Umbria–Marche aftershock sequence recorded by the temporary network are available under request at the Web site www.ingv.it/banchedati/banche.html. We are indebted to M. Cattaneo, C. Collettini, M. Barchi, A. Michelini, S. Stramondo, and E. Turco for helpful discussions and for their criticisms. We thank Jose Pujol and two anonymous referees for their comments that allowed us to improve the manuscript. Lauro Chiaraluce is supported by European Community project *PRESAP*. We thank the Italian Department for Civil Protection for supporting the INGV temporary network.

References

Amato, A., B. Alessandrini, G. B. Cimini, A. Frepoli, and G. Selvaggi (1993). Active and remnant subducted slabs beneath Italy: evidence from seismic tomography and seismicity, *Ann. Geofis.* **36,** 201–214.

Amato, A., R. Azzara, C. Chiarabba, G. B. Cimini, M. Cocco, M. Di Bona, L. Margheriti, S. Mazza, F. Mele, G. Selvaggi, A. Basili, E. Boschi, F. Courboulex, A. Deschamps, S. Gaffet, G. Bittarelli, L. Chiaraluce, D. Piccinini, and M. Ripepe (1998). The 1997 Umbria–Marche, Italy, earthquake sequence: a first look at the main shocks and aftershocks, *Geophys. Res. Lett.* **25,** no. 15, 2861–2864.

Anderson, H., and J. A. Jackson (1987). Active tectonics of the Adriatic region, *J. Geophys. Res. Astr. Soc.* **91,** 937–987.

Bally, A. W., L. Burbi, C. Cooper, and R. Ghelardoni (1986). Balanced sections and seismic reflection profiles across the central Apennines, *Mem. Soc. Geol. Ital.* **35,** 257–310.

Barchi, M., A. De Feyter, B. Magnani, G. Minelli, G. Pialli, and B. M. Sotera (1998). The structural style of the Umbria–Marche fold and thrust belt, *Mem. Soc. Geol. It.* **52,** 557–578.

Blumetti, A. M. (1995). Neotectonic investigations and evidence of paleoseismicity in the epicentral area of the January–February 1703, Central Italy, earthquakes, Assoc. of Eng. Geologists, special publication 6, 83–100.

Boncio, P., and G. Lavecchia (2000). A structural model for active extension in Central Italy, *J. Geodyn.* **29,** 233–244.

Boschi, E., G. Ferrari, P. Gasperini, E. Guidoboni, G. Smriglio, and G. Valensise (1995). *Catalogo dei forti terremoti in Italia dal 461 a.C. al 1980*, ING–SGA, Bologna.

Boschi, E., E. Guidoboni, G. Ferrari, and G. Valensise (1998). *I terremoti dell'Appennino Umbro–Marchigiano (area sud orientale dal 99 a.C. al 1984)*, ING-SGA, Bologna.

Capuano, P., A. Zollo, A. Emolo, S. Marcucci, and G. Milana (2000). Rupture mechanism and source parameters of Umbria–Marche main shocks from strong motion data, *J. Seism.* **4,** 463–478.

Castelli, V., G. Monachesi, and M. Stucchi (1997). La sismicità maggiore dell'Appennino Umbro–Marchigiano, rapporto tecnico inedito, Gruppo Nazionale per la Difesa dai Terremoti (GNDT-CNR).

Cattaneo, M., P. Augliera, G. De Luca, A. Gorini, A. Govoni, S. Marcucci, A. Michelini, G. Monachesi, D. Spallarossa, L. Trojani, and Xgumus (2000). The Umbria–Marche (Italy) earthquake sequence: analysis of the data recorded by the local and temporary networks, *J. Seism.* **4,** 401–414.

Cello, G., G. Deiana, L. Ferelli, L. Marchegiani, L. Maschio, S. Mazzoli, A. Michetti, L. Serva, E. Tondi, and T. Vittori (2000). Geological constraints for earthquake faulting studies in the Colfiorito area (central Italy), *J. Seism.* **4,** 357–364.

Chiarabba, C., and A. Amato (2003). V_p and V_p/V_s images in the M_w 6.0 Colfiorito fault region (central Italy): a contribution to understand seismotectonic and seismogenic processes, *J. Geophys. Res.* **108,** no. B5, doi 10.1028/2001JB001669.

Chiaraluce, L., W. L. Ellsworth, C. Chiarabba, and M. Cocco (2003). Imaging the complexity of an active normal fault system: the 1997 Colfiorito (central Italy) case study, *J. Geophys. Res.* (in press).

Chiodini, G., and R. Cioni (1989). Gas geobarometry for hydrothermal systems and its application to various Italian geothermal areas, *Appl. Geochem.* **4,** 564–572.

Cinti, F. R., L. Cucci, F. Marra, and P. Montone (2000). The 1997 Umbria–Marche earthquake (Italy) relation between the surface tectonic breaks and the area of deformation, *J. Seism.* **4,** 333–343.

Cocco, M., C. Nostro, and G. Ekström (2000). Static stress changes and fault interaction during the 1997 Umbria–Marche earthquake sequence, *J. Seism.* **4,** 501–516.

Collettini, C., and L. Chiaraluce (2000). A fluid dependent seismogenic model as possible explanation of the evolution of the 1997 Umbria–Marche (Italy) seismic sequence, 2000 AGU Fall Meeting, San Francisco, California, 15–18 December.

Console, R., C. Montuori, and M. Murru (2000). Statistical assessment of seismicity patterns in Italy: are they precursors or subsequential events? *J. Seism.* **4,** 435–449.

Deschamps, A., F. Courboulex, S. Gaffet, A. Lomax, J. Virieux, A. Amato, R. Azzara, B. Castello, C. Chiarabba, G. B. Cimini, M. Cocco, M. Di Bona, L. Margheriti, F. Mele, G. Selvaggi, G. Bittarelli, L. Chiaraluce, D. Piccinini, and M. Ripepe (2000). Spatio-temporal distribution of seismic activity during the Umbria–Marche crisis, 1997, *J. Seism.* **4,** 377–386.

Deschamps, A., D. Iannaccone, and R. Scarpa (1984). The Umbrian earthquake (Italy) of 19 September 1979, *Ann. Geophys.* **2,** no. 1, 29–36.

Di Giovanbattista, R., and S. Barba (1997). An estimate of hypocentre location accuracy in a large network: possible implications for tectonic studies in Italy, *Geophys. J. Int.* **129,** 124–132.

Eberhart-Phillips, D., and M. Reyners (1997). Continental subduction and three-dimensional crustal structure: the northern South Island, New Zealand, *J. Geophys. Res.* **102,** 11,843–11,861.

Ekström, G., A. Morelli, E. Boschi, and A. M. Dziewonski (1998). Moment tensor analysis of the central Italy earthquake sequence of September–October 1997, *Geophys. Res. Lett.* **25,** no. 11, 1971–1974.

Frepoli, A., and A. Amato (1997). Contemporaneous extension and compression in the Northern Apennines from earthquake fault-plane solutions, *Geophys. J. Int.* **129,** 368–388.

Frepoli, A., and A. Amato (2000). Fault-plane solutions of crustal earthquakes in southern Italy (1988–1995): seismotectonic implications, *Ann. Geofis.* **43,** no. 3, 437–467.

Galli, P., and F. Galadini (1999). Seismotectonic framework of the 1997–1998 Umbria–Marche (central Italy) earthquakes, *Seism. Res. Lett.* **70,** no. 4, 417–427.

Haessler, H., R. Gaulon, L. River, R. Console, M. Frogneaux, G. Gasparini, L. Martel, G. Patau, M. Siciliano, and A. Cisternas (1988). The Perugia (Italy) earthquake of 29 April 1984: a microearthquake survey, *Bull. Seism. Soc. Am.* **78,** no. 6, 1948–1964.

Hernandez, B., F. Cotton, M. Campillo, F. Courboulex, M. Cocco, and S. Stramondo (1999). Rupture history of the 1997 Umbria–Marche (central Italy) largest earthquakes from inversion of GPS, SAR, and near field seismological data, 1999 AGU Fall Meeting, San Francisco, California, 13–17 December.

Hunstad, I., M. Anzidei, M. Cocco, P. Baldi, A. Galvani, and A. Pesci (1999). Modelling coseismic displacement during the 1997 Umbria–Marche earthquakes (central Italy), *Geophys. J. Int.* **139,** 1–13.

Hunstad, I., G. Selvaggi, N. D'Agostino, P. England, P. Clarke, and M. Pierozzi (2003). Geodetic strain in peninsular Italy between 1875 and 2001, *Geophys. Res. Lett.* **30,** no. 4, 1811.

Italiano, F., G. Martinelli, and M. Nuccio (2001). Anomalies of mantle-derived helium during the 1997–1998 seismic swarm of Umbria–Marche, Italy, *Geophys. Res. Lett.* **28,** 838–842.

King, G. C., and M. Cocco (2001). Fault interaction by elastic stress changes: new clues from earthquakes sequences, *Adv. Geophys.* **44,** 1–38.

Lavecchia, G., F. Brozzetti, M. Barchi, J. Keller, and M. Menichetti (1994). Seismotectonic zoning in east-central Italy deduced from the analysis of the Neogene to present deformations and related stress fields, *Soc. Geol. Am. Bull.* **106,** 1107–1120.

Lucente, P., C. Chiarabba, G. B. Cimini, and D. Giardini (1999). Tomographic constraints on the geodynamic evolution of the Italian region, *J. Geophys. Res.* **104,** 20,307–20,327.

Lundgren, P., and S. Stramondo (2002). Slip distribution of the 1997 Umbria–Marche earthquake sequence: joint inversion of GPS and synthetic aperture radar interferometry data, *J. Geophys. Res.* **107,** no. B11, 2316, doi 10.1029/2000JB000103.

Malinverno, A., and W. B. F. Ryan (1986). Extension in the Tyrrhenian Sea and shortening in the Apennines as results of arc migration driven by sinking of the lithosphere, *Tectonics* **5,** 227–245.

Mariucci, M. T., A. Amato, and P. Montone (1999). Recent tectonic evolution and present day stress in the northern Apennines (Italy), *Tectonics* **18,** no. 1, 108–118.

Meghraoui, M., V. Bosi, and T. Camelbeeck (1999). Fault fragment control in the 1997 Umbria–Marche, central Italy, earthquake sequence, *Geophys. Res. Lett.* **26,** no. 8, 1069–1072.

Michelini, A., D. Spallarossa, M. Cattaneo, A. Govoni, and L. Montanari (2000). The 1997 Umbria–Marche (Italy) earthquake sequence: tomographic images obtained from data of the GNDT-SSN temporary network, *J. Seism.* **4,** 415–433.

Montone, P., A. Amato, and S. Pondrelli (1999). Active stress map of Italy, *J. Geophys. Res.* **104,** 25,595–25,610.

Morelli, A., G. Ekström, and M. Olivieri (2000). Source properties of the 1997–98 central Italy earthquake sequence from inversion of long-period and broad-band seismograms, *J. Seism.* **4,** 365–375.

Patacca, E., and P. Scandone (1989). Post-Tortonian mountain building in the Apennines: the role of the passive sinking of a relic lithospheric slab, in the lithosphere in Italy, in *Advances in Earth Science Reserch*, A. Boriani *et al.* (Editors), C.N.R., Acc. Nazionale dei Lincei, Roma, 157–176.

Pino, N. A., and S. Mazza (2000). The Umbria–Marche (central Italy) earthquakes: relation between rupture directivity and sequence evolution for the $M_w > 5$ shocks, *J. Seism.* **4,** 451–461.

Pino, N. A., S. Mazza, and E. Boschi (1999). Rupture directivity of the major shocks in the 1997 Umbria–Marche (central Italy) sequence from regional broadband waveforms, *Geophys. Res. Lett.* **26,** no. 14, 2101–2104.

Quattrocchi, F. (1999). In search of evidence of deep fluid discharges and pore pressure evolution in the crust to explain the seismicity style of the Umbria–Marche 1997–1998 seismic sequence (central Italy), *Ann. Geophys.* **42,** 608–636.

Reasenberg, P., and D. Oppenheimer (1985). FPFIT, FPPLOT, and FPPAGE: Fortran computer programs for calculating and displaying earthquake fault-plane solutions, *U.S. Geol. Sur. Open-File Rept. 85–739*.

Ripepe, M., D. Piccinini, and L. Chiaraluce (2000). Foreshock sequence of september 26th, 1997 Umbria–Marche earthquakes, *J. Seism.* **4,** no. 4, 387–399.

Salvi, S., S. Stramondo, M. Cocco, M. Tesauro, I. Hunstad, M. Anzidei, P. Briole, P. Baldi, E. Sansosti, G. Fornaro, R. Lanari, F. Doumaz, A. Pesci, and A. Galvani (2000). Modeling coseismic displacements resulting from SAR interferometry and GPS measurements during the Umbria–Marche seismic sequence, *J. Seism.* **4,** 479–499.

Selvaggi, G. (1998). Spatial distribution of horizontal seismic strain in the Apennines from historical earthquakes, *Ann. Geofisica* **41,** 241–251.

Selvaggi, G. (2001). Strain pattern of the southern Tyrrhenian slab from moment tensors of deep earthquakes: implications on the down-dip velocity, *Ann. Geofis.* **44,** 155–165.

Selvaggi, G., and A. Amato (1992). Subcustal earthquake in northern Apennines (Italy): evidence for a still active subduction? *Geophys. Res. Lett.* **19,** no. 21, 2127–2130.

Tertulliani, A. (2000). Qualitative effects of local geology on damage pattern, *Bull. Seism. Soc. Am.* **90,** 1543–1548.

Westaway, R. (1992). Seismic moment summation for historical earthquake in Italy: tectonic implications, *J. Geophys. Res.* **97,** no. 11, 15,437–15,464.

Zollo, A., S. Marcucci, G. Milana, and P. Capuano (1999). The Umbria–Marche 1997 (central Italy) earthquake sequence: insight on the mainshock rupture from near source strong motion records, *Geophys. Res. Lett.* **26,** 3165–3169.

Istituto Nazionale di Geofisica e Vulcanologia
Rome, Italy
(L.C., A.A., M.C., C.C., G.S., M.D.B., D.P., L.M.)

Geosciences Azur
University of Nice
Nice, France
(A.D., F.C.)

Università degli Studi di Camerino
(M.R.)

Manuscript received 26 February 2002.

2.4 La jonction Alpes-Bassin Ligure

Le laboratoire Géoazur est situé sur la côte d'Azur, une région très contrastée à bien des niveaux : Une bande littorale étroite accueille 80 % de la population dans une agglomération quasi continue entre Menton et Cannes en passant par la ville de Nice avec plus de 3 millions de personnes ; un arrière pays très rapidement montagneux avec une dizaine de sommets atteignant 3000 mètres à moins de 100 km de la mer ; un bassin Ligure limité au sud par la Corse qui atteint des profondeurs de 2200 m (pied de marge) à 30 km de la côte, et au maximum 2800 m.

L'UMR Géoazur accueille des chercheurs venant de partout et travaillant sur des régions du globe très variées. La plupart cependant s'intéressent à un moment ou à un autre de leur vie professionnelle à cette zone complexe mystérieuse et passionnante qui est en quelque sorte le chantier de proximité du laboratoire. On l'appelle d'ailleurs le « chantier régional ». En général, cet intérêt est réactivé à chaque secousse sismique perceptible. En ce qui me concerne, c'est à partir du séisme du 21 Avril 1995 (j'avais soutenu ma thèse le 14) que j'ai commencé à regarder de près cette région et à tenter de la comprendre. J'ai ensuite continué à travailler sur cette zone ; parfois de manière ponctuelle (localisation, calcul de mécanismes au foyer, encadrement d'étudiants) mais par moment de manière plus approfondie. La partie la plus intéressante de ce travail s'est effectuée en équipe, avec des sismologues bien sur, mais aussi avec des géologues et des géophysiciens marins. Christophe Larroque a été (et est toujours) un moteur formidable pour coordonner les études sur cette zone complexe. Les interactions avec Anne-Marie Duval du CETE m'ont également aidée à comprendre les enjeux du risque sismique dans cette zone [*Duval*, 2007]. Enfin mes travaux reposent bien entendus sur ceux de bien d'autres personnes avant moi (et en même temps), et en particulier Nicole Béthoux, Anne Deschamps, Jacques Deverchère et de nombreux étudiants.

2.4.1 Contexte et questionnement

Je ne vais pas me lancer dans une synthèse sismotectonique de la jonction Alpes Bassin Ligure car tout, ou presque vient d'être rassemblé dans la thèse d'HDR de Christophe Larroque [*Larroque*, 2009]. Je vous invite d'ailleurs à vous reporter à ce document très complet avant toute étude de la région. Je vais donc tenter de résumer les questions centrales qui ont animées mon travail sur la région. La brièveté de cette présentation va en choquer plus d'un, tant le sujet est dense complexe, et toujours le sujet de controverses, même au sein de notre laboratoire.

Où sont les failles actives ?

Durant les derniers cent millions d'années, l'évolution cinématique de l'ouest de l'Europe était dominée par la convergence entre les plaques Afrique et Eurasie qui a entraîné la subduction de l'Océan Téthys puis la collision des continents [*Dercourt et al.*, 1986]. L'évolution récente de cette zone aboutit à un puzzle de bassins (tels que le Bassin Ligure) et de chaînes (telles que l'arc de Nice et le Massif de l'Argentera) au sein de la zone de collision Afrique-Europe. La structure d'ensemble de la région présente donc un fort héritage structural et des contrastes importants à l'échelle de la croûte et de la lithosphère [*Blundell et al.*, 1992; *Thouvenot et al.*, 2007]. De nombreuses failles découpent la région, certaines s'enracinent à la base de la couverture sédimentaire, vers 1 ou 2 km de profondeur, comme les chevauchements frontaux des arcs de Nice et de Castellane [*Laurent et al.*, 2000], d'autres traversent la croûte cristalline sur plusieurs kilomètres d'épaisseur comme la faille Argentera-Bersezio. De nombreuses observations de terrain ont permis de montrer que les principales failles de la région ont été réactivées à plusieurs reprises durant cette longue histoire [*Corsini et al.*, 2004].

En tant que sismologue préoccupée par l'aléa sismique, la question centrale que je me pose est simple: où sont les failles actives et quels séismes peuvent elles générer ? La question est simple, mais malheureusement la réponse ne l'est pas. En effet dans cette région, les observations morphotectoniques, sismologiques et géodésiques ne fournissent que très rarement des certitudes dans ce domaine. Les causes sont les suivantes :

- le mouvement des plaques est extrêmement lent, comme le prouvent les récentes mesures de géodésie synthétisées par J.M. Nocquet [*Larroque et al.*, 2008] ;
- le taux d'érosion relativement élevé efface souvent les traces morphologiques des séismes ;
- les sédiments quaternaires sont rares ;
- la sismicité est diffuse … ou bien le parait.

Plusieurs projets ont été financés qui ont permis d'avancer à petit pas dans la connaissance de l'activité récente de la zone. En ce qui me concerne, j'ai travaillé sur cinq projets sur cette zone. Le plus récent, le projet QSHA (Quantitative Seismic Hazard Assesment, projet financé par l'Agence Nationale de la Recherche de 2005 à 2009), avait pour but de recenser les failles actives dans une petite zone 'Terre-Mer' autour de la frontière italienne (Figure 2. 8), de proposer des scénarios de séismes et de simuler les mouvements du sol en utilisant des méthodes diverses [*Virieux et al.*, 2009]. Une carte d'identité de quelques failles a été établie grâce au travail d'Oona Scotti (IRSN) et de Christophe Larroque (Figure 2. 9). Elle recense les divers indices d'activité relevés par différentes études sur un même objet dans une zone géographique restreinte [*Scotti et al.*, 2007].

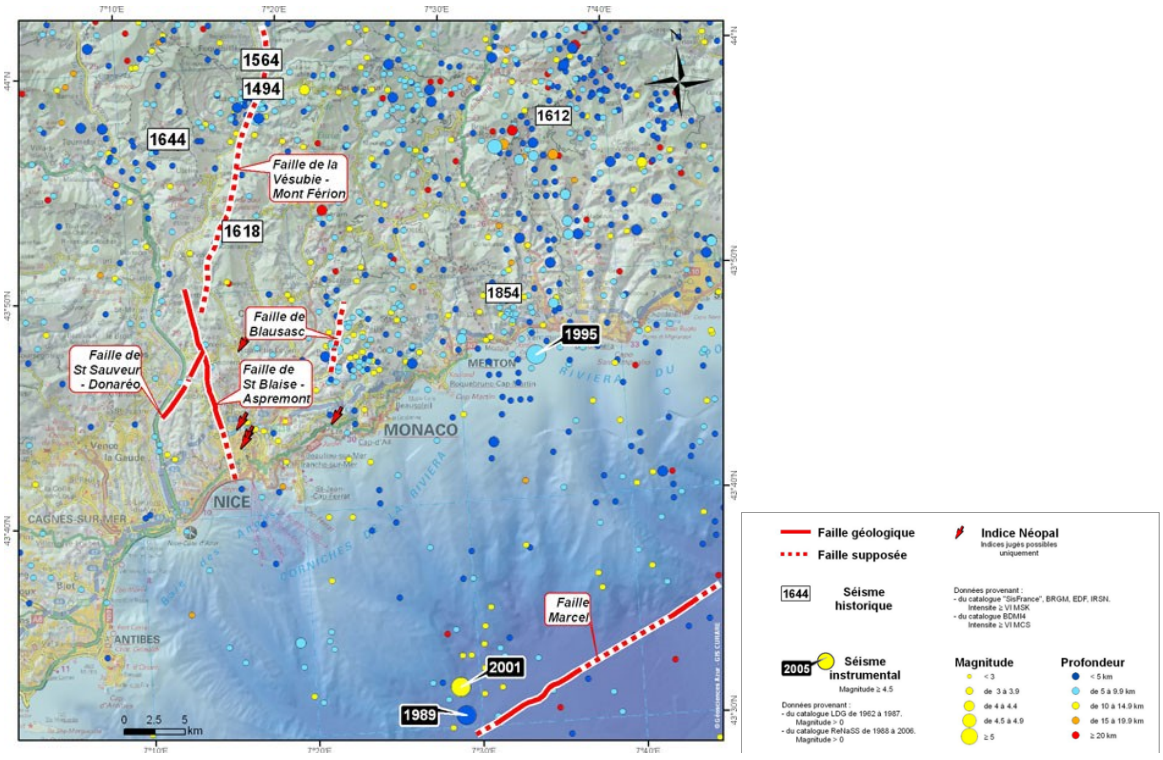
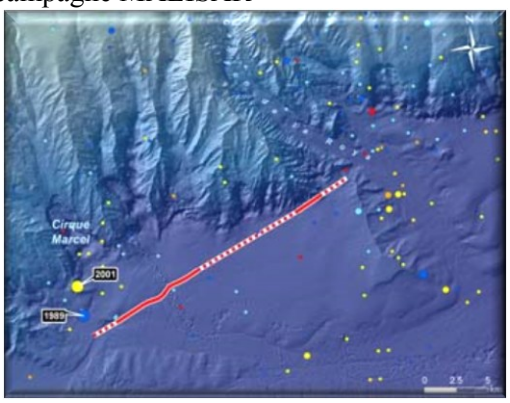


Figure 2. 8 : Carte des failles potentiellement actives répertoriées dans le projet QSHA [*Larroque et al.*, 2009]. Disponible sous http://qsha.unice.fr/WEB_WP2/index_Failles.php. Système d'information Géographique et cartographie : Jenny Trévisan.

Faille MARCEL :
Situation géographique sur la bathymétrie de la campagne MALISAR



Fiche descriptive

Contexte géologique	La faille Marcel se trouve au pied de la marge Ligure à environ 20 km au SE de Nice
Longueur	Environ 11 km
Direction moyenne	N 65E
Pendage	80° N
Cinématique	Décrochement sénestre

Segmentation			
	Non	Point ouest 43,505N 7,514E	Point est 43,567N 7,653E

Profondeur	Mini : 0 Maxi : 15 km
Indice pour la géométrie en profondeur	En surface les données de sismique et de sondeur à sédiment attestent d'une faille avec un pendage subvertical. En profondeur le mécanisme au foyer du séisme de 2001 montre un des plans nodaux avec un pendage de 40° vers le nord.
Profondeur sismogénique régionale	15 km
Magnitude possible	M=6,5
Sismicité actuelle	Séisme du 25/02/2001 (Ml=4,6) Séisme du 26/12/1989 (Ml=4,5)
Sismicité historique	Non répertoriée

Mécanisme au foyer	Date et magnitude	strike	dip	rake
	26/12/1989 Ml=4,5	231	36	-4
	20/12/2001 Ml=4,6	243	41	74

Indices de déformation récente	Un escarpement sous-marin de quelques dizaines de mètres de haut est attribué au fonctionnement de cette faille.
Bibliographie	Larroque C., Migeon S., Beslier M.O., Mercier de Lépinay B., Sage F., Cattaneo A., Corradi N., Cuppari A., Marsset B. et L. Brosolo (2006). Aléa sismique et aléa gravitaire sur la marge nord du bassin Ligure : Résultats préliminaires de la campagne MALISAR 1. Réunion des Sciences de la Terre, Dijon 04-08 décembre 2006, Volume des résumés p. 88.
Compilation	2007 – C. Larroque (UMR Géosciences Azur)

Figure 2. 9 : Faille MARCEL : Exemple de fiche d'identité (projet QSHA, [*Scotti et al.*, 2008]). Système d'information géographique et cartographie : Jenny Trévisan.

Récemment des datations isotopes cosmogéniques d'échantillons prélevés dans le nord du Mercantour suggèrent une activité tectonique intense durant l'Holocène ayant pu générer des séismes majeurs (M>7) [Sanchez et al., 2010a; Sanchez et al., 2010b].

Les séismes nous permettent-ils d'imager des failles dans cette zone ?

Les habitants de la région niçoise savent que le risque sismique n'est pas négligeable dans la région mais la plupart ont oublié que de forts séismes capables de détruire des bâtiments ont eu lieu dans le passé (Figure 2. 10). Les événements les plus notables sont le séisme de Roquebillière de 1564 et le séisme Ligure de 1887. Ce dernier a atteint l'intensité intensité IX dans certaines zones [*Laurenti*, 2006; *Scotti et al.*, 2004]. Il engendré des destructions massives dans les villages de la côte Ligure italienne et plus de 600 victimes (Figure 2. 11).

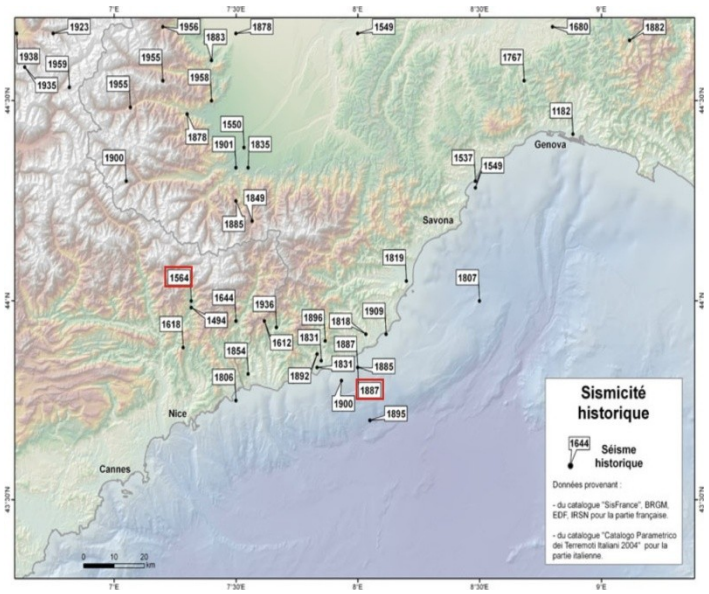


Figure 2. 10 : Carte de la sismicité historique pour les événements d'intensité supérieure à VI (d'après les données SISFRANCE et le Cataloguo Parametrico dei Terremoti Italiani 2004). Extrait de [Larroque, 2009].



Figure 2. 11 : Photos de destructions dues au séisme Ligure de 1887. A gauche un village de la côte Italienne Ligure, à droite des campements installés dans la ville de Nice. Photos extraites du livre d'André Laurenti [1998].

De nos jours, la côte d'Azur est régulièrement secouée par des séismes de magnitude modérée : 4 à 10 petites secousse par mois souvent imperceptibles, et un séisme plus fort (magnitude supérieure à 4.5) tous les 4 ou 5 ans. Le dernier séisme date de 2001, nous sommes donc en retard !

La qualité actuelle du réseau terrestre permet de détecter tous les séismes à terre de magnitude locale supérieure à 1.9. Dès que l'on s'éloigne des côtes, cette magnitude de complétude diminue. Deux catalogues de sismicité existent en France : celui du laboratoire de Géophysique (LDG) du Comissariat à l'Energie Atomique (CEA) et celui du Réseau National de Surveillance Sismique (RéNaSS). Chaque catalogue est bâti à partir d'un réseau de stations différent, de modèles de vitesse différents et d'algorithmes de localisation différents. Il est ainsi naturel que les cartes de sismicité obtenues ne soient pas identiques (Fig 2.12). Un troisième catalogue existe en France, celui du Bureau Central Sismologique Français (BCSF) qui combine des données du CEA et du ReNaSS et propose de nouvelles localisations et donc … une nouvelle carte. Si l'on affiche les trois cartes de la sismicité de la région, que l'on joue un peu sur les échelles et que l'on ne se soucie pas des incertitudes, on peut entrevoir de vagues alignements de la sismicité. Cependant, les travaux sérieux montrent que pour l'instant aucun alignement significatif n'a été obtenu avec les catalogues, en particulier dans la zone sud, à part sur la faille de Saorge-Taggia [*Turino et al.*, 2009].
Ce caractère diffus de la sismicité est-il représentatif du relâchement des contraintes dans notre région ou bien est-il dû simplement à la difficulté de localiser finement les événements ?

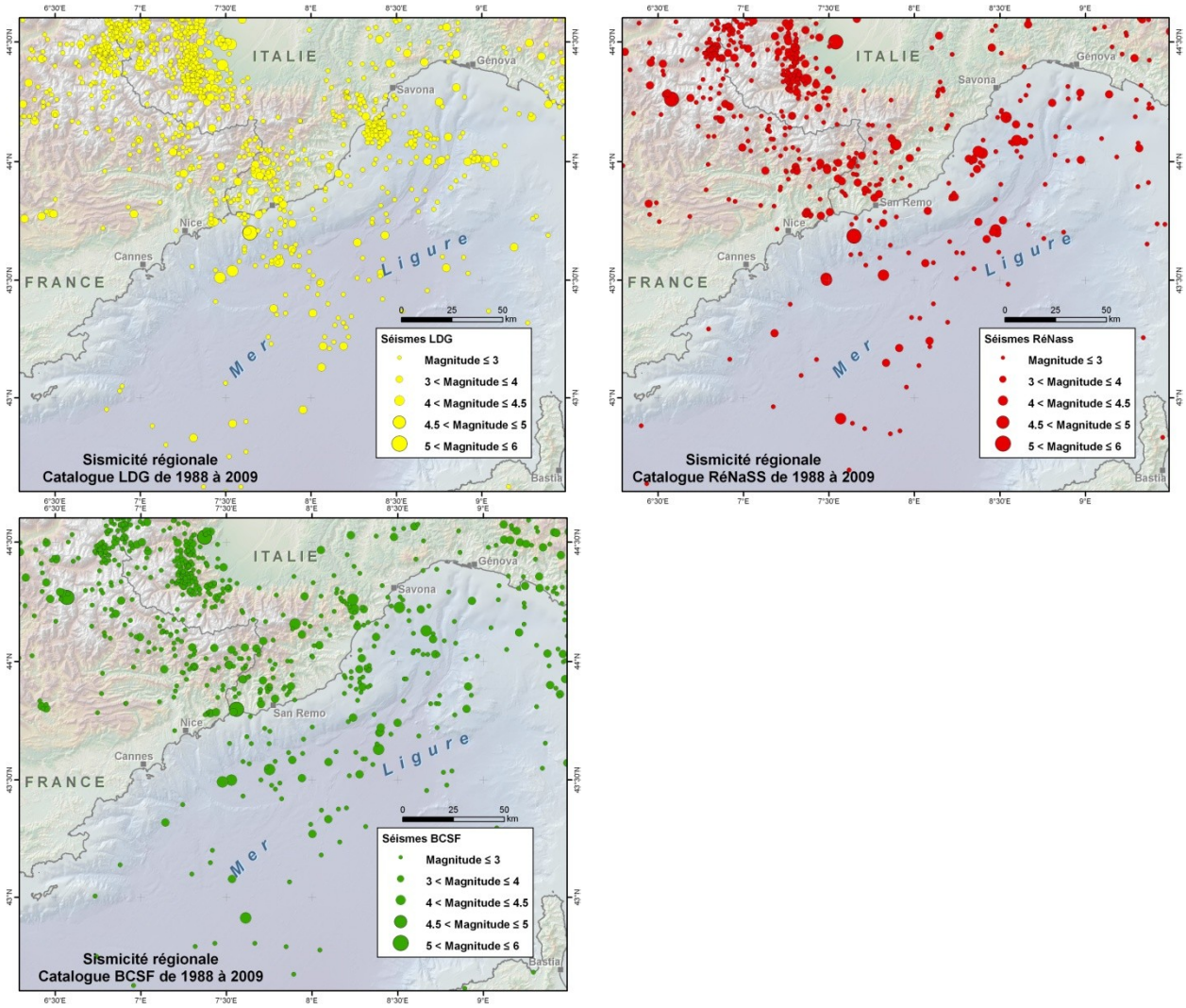


Figure 2. 12 : Epicentres des séismes de magnitude > 2.5 de 1988 à 2009 dessinés à partir des catalogues du LDG, du ReNaSS et du BCSF. Carte et système d'information géographique : Jenny Trévisan.

Je présente dans les chapitres qui suivent les principaux résultats des travaux que j'ai menés sur des séismes isolés ou des crises sismiques dans la région.

2.4.2 Etude de quelques petits séismes de la région

Le Séisme de Vintimille Mw 4.7

Ce séisme de magnitude relativement élevée pour la région a été très bien ressenti dans la ville de Nice. Il a causé quelques destructions dans la région épicentrale, notamment une chapelle déjà endommagée, mais aucun blessé.

Ce séisme a bien sur été enregistré par les stations des réseaux courte-période français (ReNaSS) et Italien (DISTER). Les signaux des stations de Nice représentés sur la Figure 2. 13 montrent tous une forte saturation. Cela était d'ailleurs le cas à chaque fois qu'un séisme de magnitude supérieure à 4 se produisait, le précédent datait de 1989 [*Béthoux et al.*, 1992].

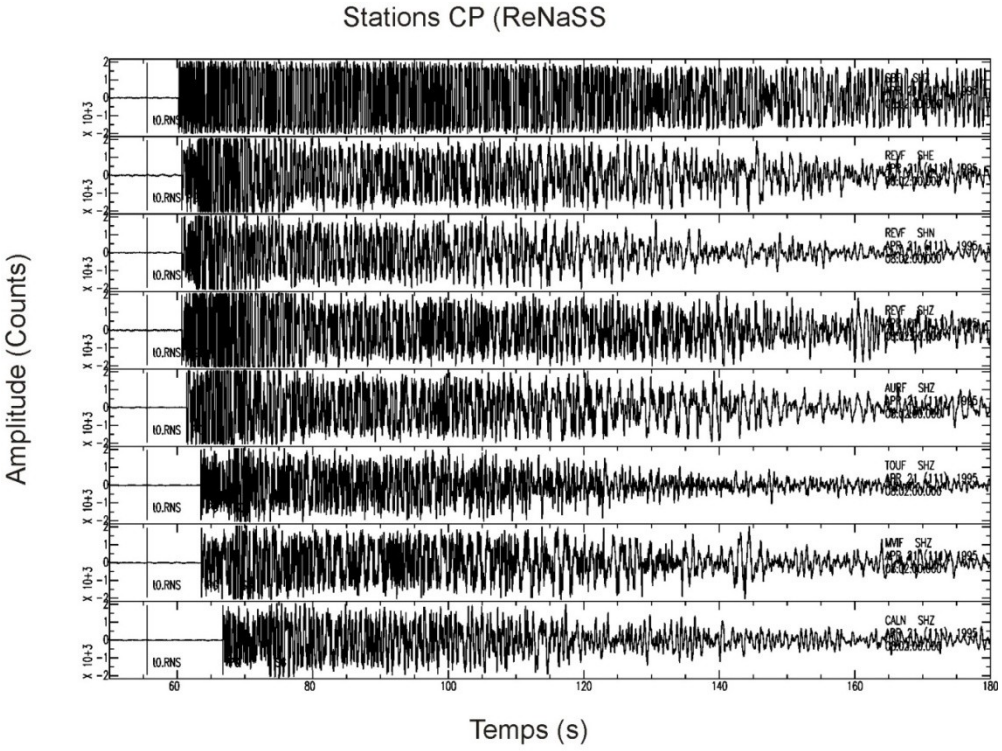


Figure 2. 13 : Enregistrements saturés du séisme du 21 Avril 1995 (Mw 4.7) sur les stations du ReNaSS de la région de Nice.

Néanmoins, cette fois ci il allait être possible pour la première fois de disposer d'enregistrements de qualité non saturés. En effet cette secousse a eu lieu alors que le réseau de stations « grande dynamique large bande » (TGRS) et le réseau accélérométrique permanent (RAP) se mettait en place dans la région sous la direction d'Anne Deschamps. L'enregistrement de la station large bande SAOF récemment installée est comparée à celle de la station courte période REVF sur la Figure 2. 14. Les distances épicentrales sont équivalentes pour les deux stations. Alors que les stations CP ne permettent qu'une étude du temps d'arrivée de l'onde P, les stations large-bande (et accélérométriques) permettent de retrouver tous les détails du mouvement du sol lors du passage de l'onde sismique.

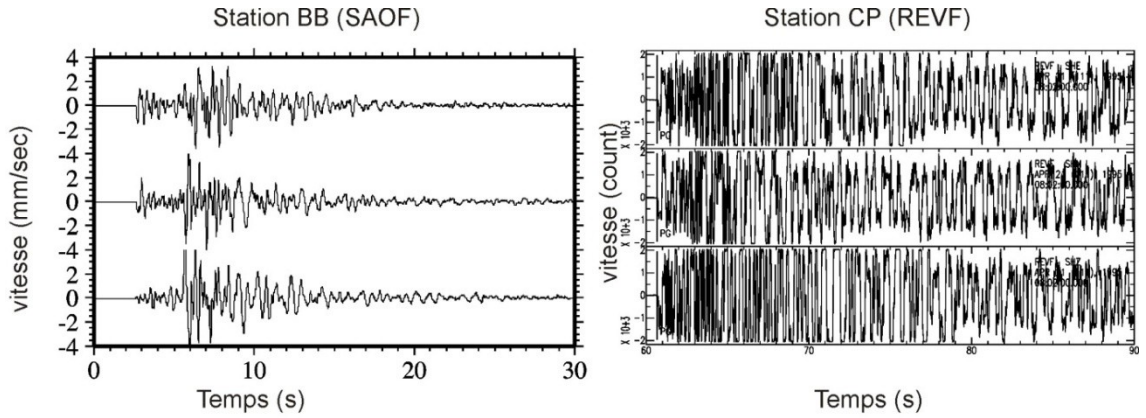


Figure 2. 14 : Enregistrement du séisme du 21 Avril sur une station large bande du réseau RAP-TGRS (gauche) et sur une station courte Période du ReNaSS (droite). La distance épicentrale est dans les deux cas d'environ 25 km.

Six heures après le choc principal, un réseau de 5 stations Reftek équipées de capteurs large-bande et accélérométriques était installé à terre. Un OBS était largué en mer 24 h plus tard. Ces stations ont permis de compléter le réseau de stations permanentes français et Italien et de raffiner les localisations des répliques.

J'ai pour la première fois réalisé l'étude complète d'un petit séisme en collaboration avec plusieurs collègues français et italiens : localisations, relocalisation relatives du choc principal par la méthode du master-event, calcul du moment sismique, mécanismes au foyer, inversion de la fonction source, tentative de détermination de la faille active.

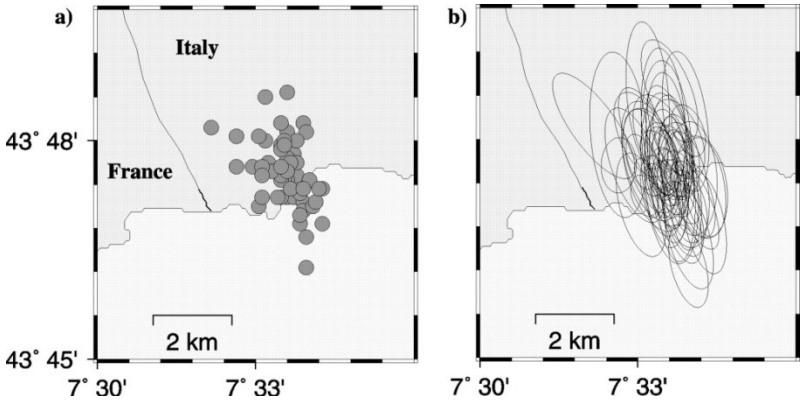


Figure 2. 15 : localisation et ellipses d'erreurs des répliques du séisme de Vintimille (Mw 4.7) avec la méthode hypoellipse [*Courboulex et al.*, 1998].

L'inversion de la fonction source constituait alors une première pour les séismes français. En effet la proximité de la station large bande SAOF (réseau RAP et TGRS) installée à Saorge a permis de réaliser des travaux fins et notamment de déconvoluer séparément les ondes P et S afin de tenter de détecter au mieux une éventuelle directivité de la rupture qui puisse nous permettre de discriminer le plan de faille actif.

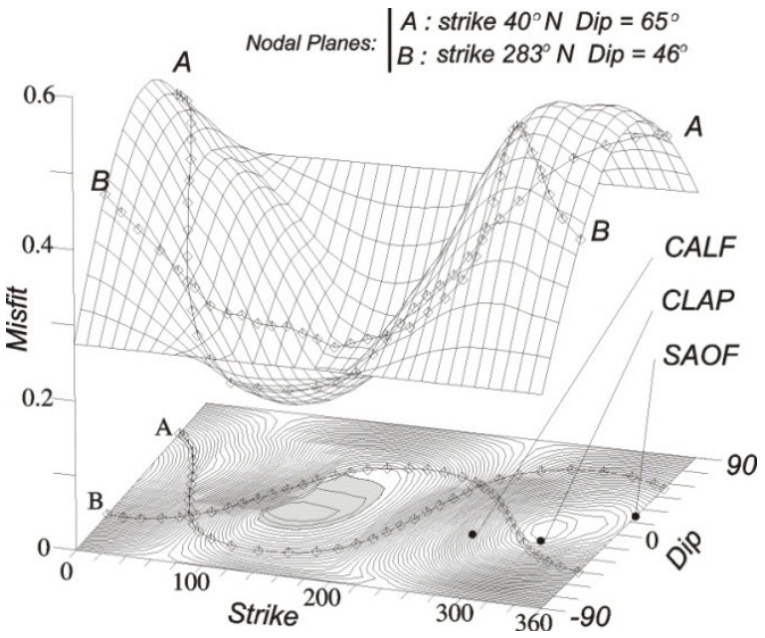


Figure 2. 16 : Recherche de la direction et du pendage du vecteur « directivité » qui minimise la fonction coût afin de déterminer le plan de faille le plus probablement actif durant la rupture [*Courboulex et al.*, 1998].

Cette première étude m'a permis de me rendre compte de la complexité de la zone et de la difficulté à faire le lien entre les structures géologiques visibles en surface et les failles activées lors des petits séismes en profondeur. Elle est publiée dans un article au Tectonophysics en 1998 (Courboulex et al, 1998).

Le séisme de Peille (Mw 3.4)

Quelques années plus tard, en novembre 1999, avait lieu un séisme qui allait être le début d'une aventure collective passionnante. C'était un petit séisme certes, sa magnitude atteignait péniblement Mw 3.4. Alors pourquoi ce petit séisme nous a-t-il tant intéressés. Il y a trois raisons à cela :

- Tout d'abord ce séisme a eu lieu à quelques kilomètres à peine de la ville de Nice, dans une zone de villages peuplés. Ce séisme étant extrêmement superficiel (~3 km), il a été bien ressenti par les habitants des villages environnants, mais également dans le centre ville de Nice. Il était donc particulièrement important de comprendre si ce séisme avait eu lieu sur une structure majeure, et si un séisme beaucoup plus gros pouvait se déclencher dans le futur au même endroit.

- La deuxième raison était qu'en 1999, nous avions enfin un bon réseau de stations sismologiques permanent qui allait nous permettre de travailler en détail sur l'événement, y compris à l'intérieur de la ville de Nice où 5 stations du réseau RAP avaient été installées pour enregistrer les effets de site.

- La troisième est que ce séisme avait lieu tout près d'une faille importante de la région, dont l'activité actuelle était supposée possible (Figure 2. 17). Or un lien clair entre séismes est faille n'a jamais été établi dans la région.



Figure 2. 17 : Un magnifique affleurement de la faille de Peille- Laghet. Cette faille peut-elle générer un séisme ?

Nous avons donc exploité au maximum les données récoltées et publié les résultats dans une note aux comptes rendus de l'académie des sciences [Courboulex et al., 2001]. Notons que pour ce petit séisme nous avons obtenu une mise en évidence claire des effets de site dans la ville de Nice, comme cela avait été préalablement observé par Anne-Marie Duval [*Duval*, 1994]. L'ellipse d'erreur présentée en pointillé sur la Figure 2. 18 nous montre que le réseau sismologique permanent n'était pas assez dense pour répondre à la question : le séisme a-t-il été généré par la faille de Peille-Laghet ? Nous répondrons à cette question un an plus tard …

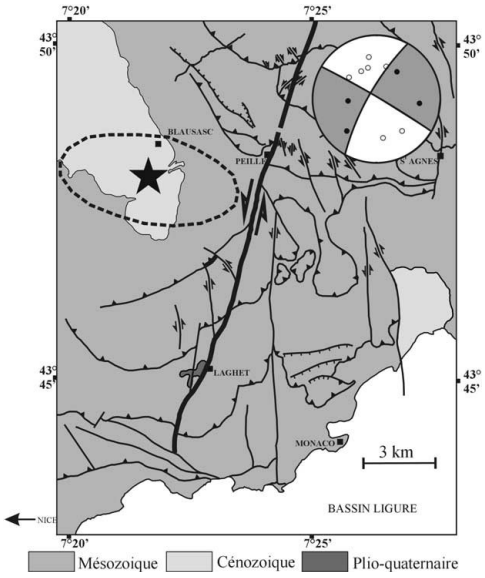


Figure 2. 18 : Localisation (étoile), ellipse d'erreur (pointillés) et mécanisme au foyer du séisme de Peille du 1er novembre 1999. Extrait de [*Courboulex et al.*, 2001].

Ce petit séisme est important car il a motivé la mise en place de la campagne SALAM un an plus tard …. juste au bon moment ! Il a été aussi le point de départ d'études pluridisciplinaires passionnantes.

2.4.3 La campagne SALAM (Sismologie et Aléas dans Les Alpes Maritimes)

Motivés par ce séisme (mais aussi par les autres), nous avons déposé un projet pour déployer un réseau dense de stations sismologiques et ainsi assurer une localisation des microséismes la meilleure possible. En effet, lors du séisme de Peille, nous avions pu obtenir de jolis résultats, mais pas assez de précision pour être sûr que la faille de Peille Laghet (FPL) était en cause ou bien qu'il s'agissait d'une autre faille. Les traces de mouvement sur la FPL qui pourraient correspondre au même type de champ de contrainte ne sont pas assez récentes pour attester de l'activité de cette faille.

Nous avons eu de vives critiques au début. Etait-il vraiment utile de poser un tel réseau et de mobiliser tant de personnes pour une région ou l'on avait si peu de chances d'avoir des événements ? Les critiques étaient fondées, mais nous avons quand même bien fait de ne pas les écouter.

La campagne baptisée SALAM (Sismologie et ALéas dans les Alpes Maritimes) est le volet sismologique d'un projet plus vaste qui a pour but de réévaluer le potentiel sismogène de la jonction Alpes-bassin Ligure. Ce projet a été financé par le programme PNRN2000 et l'équipe DRO (Déformations Ruptures et Ondes) de l'UMR Géoazur. Il bénéficie également du soutien logistique du CETE Méditerranée et de l'observatoire de Monaco.

Le réseau est composé de 20 stations sismologiques temporaires installées dans les Alpes Maritimes pendant une durée de 6 mois (15 Oct 2000- 15 Avril 2001). L'enregistrement est effectué en continu à 125 Hz ou 200 Hz selon les stations. Les 20 stations 3-composantes sont constituées de 8 stations du parc national Lithoscope, 4 stations de l'UMR Géoazur, 6 stations du CETE Méditerranée et 2 stations de l'observatoire de Monaco. Ces stations sont équipées d'1/3 de capteurs large bande CMG40, 1/3 de capteurs courte période « dits capteurs chinois » (2Hz) et 1/3 de capteurs à bande intermédiaires (Lennartz 0.2 Hz). En parallèle, il est prévu de larguer des OBS pour compléter le réseau en mer.

De très nombreuses personnes ont participé à l'installation des stations. Je pense notamment à Claude Vallet qui nous a accompagnés tout au long de la campagne avec courage et détermination (Il a creusé une grande partie des trous quand j'étais sur le terrain(, à Jean Virieux (et ses sacs de béton), à Anne Deschamps, à Sylvain Vidal (CETE) qui a installé et maintenu les stations du CETE, à Jean-Louis Perez (CETE) et Philippe Mondielli de Monaco qui nous ont aidés à la reconnaissance des sites, à Nicole qui s'est surtout occupée des OBS (voir la suite) ainsi que Yann Hello, Tony Monfret, Antony Lomax, Jacques Deverchère, Eric Calais (qui alors directeur d'équipe m'a incitée à coordonner la campagne et je l'en remercie) et tous les autres qui ont donné de leur énergie et de leur temps sans savoir où cela allait mener.

Nous avons fait le choix de fabriquer des sites réutilisables dans le futur en coulant une petite dalle de béton pour le capteur et en y fixant un tube en PVC (Figure 2. 19). Chaque site était soigneusement identifié par une fiche comprenant la carte 25 000ème pour s'y rendre ainsi que les contacts sur place. On peut maintenant, grâce à Jenny Trévisan, trouver ces informations sur le système d'information Géographique du laboratoire accessible via le site web.



Figure 2. 19 : Campagne SALAM (Sismologie et Aléas dans les Alpes Maritimes)

Le réseau était en place et opérationnel mi-octobre, alors que les premières pluies diluviennes s'abattaient sur la région. Les rotations toutes les trois semaines sur les stations se passaient bien. Un jour, au mois de Novembre, un journaliste nous a contacté (cela arrive assez souvent) car des habitants de la vallée du paillon avaient senti des secousses dans la nuit. Rien de spécial sur les stations du ReNaSS. Nous avons alors été récupérer quelques disques de stations pour les analyser et nous nous sommes rendus compte qu'il y a avait bel et bien une activité sismique très proche des villages concernés. Le catalogue du ReNaSS a enregistré ce mois ci une petite augmentation du nombre de séismes : 20 au lieu des 5-10 habituellement détectés. Notre réseau temporaire permettait le même mois de détecter 150 événements. C'est le mois suivant que la crise a été la plus intense avec un pic d'activité les 19 et 20 décembre. Plus de 220 séismes sont enregistrés ce mois là alors que le réseau ReNaSS n'en voit que 30 (voir la figure 5 de l'article qui suit).

Le paroxysme de la crise est atteint le 19 décembre ou 60 séismes sont enregistrés (Figure 2. 20). Le plus fort a une magnitude Mw 3.4. Il est situé exactement au même endroit que le séisme de Peille qui avait eu lieu 1 an avant ! Ce séisme a engendré des intensités macrosismiques atteignant V (échelle EMS98) dans la zone épicentrale (Figure 2. 21).

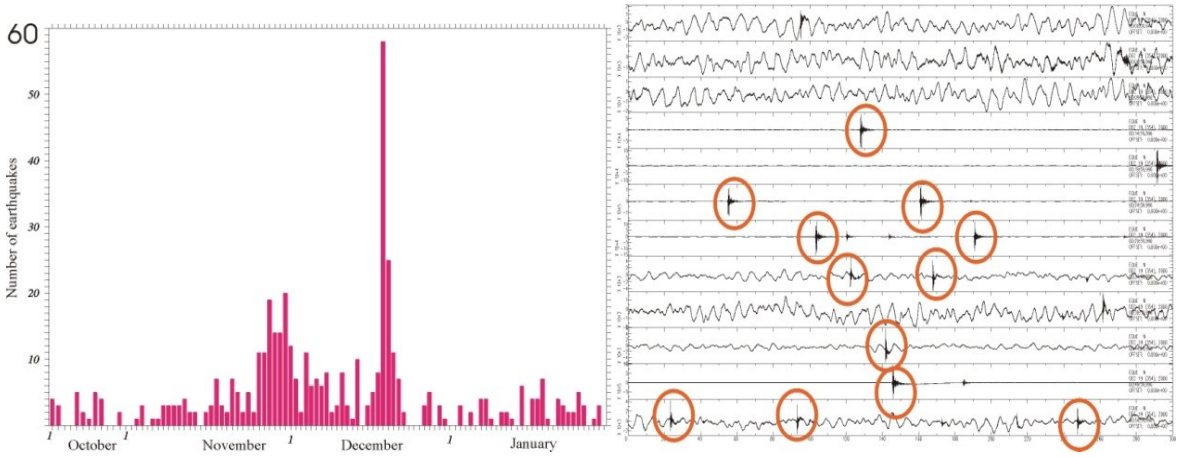


Figure 2. 20 : Gauche : nombre de séismes détectés par jour par le réseau SALAM. Droite : enregistrement continu du mouvement du sol pendant une heure le 19 Décembre 2000 sur la station EQUE, située près des épicentres.

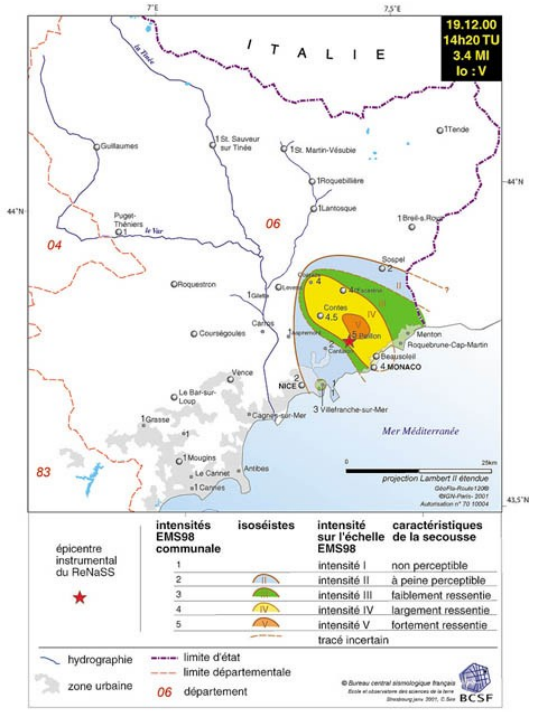


Figure 2. 21 : carte des isoséistes réalisée par le BCSF à partir des intensités communales reportées (échelle EMS98).

La crise sismique a donc eu lieu en plein milieu du réseau dense que nous venions d'installer. Les données récoltées allaient nous permettre des analyses fines de la position des événements et aussi des relations entre ceux-ci et la géologie.
Les résultats et hypothèses sont présentés dans deux articles ; L'un a été écrit assez rapidement pour la revue *Geophysical Research Letters* [*Courboulex et al.*, 2003] , le deuxième, plus complet, présente

l'étude détaillée que nous avons réalisée sur cette crise. Le très grand nombre d'auteurs de cet article reflète combien ce travail a mobilisé de monde. Pour certains, la contribution a concerné le travail de terrain ou le traitement préliminaire des données, pour d'autres il s'est agit d'un travail de longue haleine. C'est le cas d'Anne Deschamps qui est troisième auteur de cet article car on ne peut pas être trois premiers auteurs. C'est également le cas de Céline Gélis qui a beaucoup contribué à cet article par les résultats de la relocalisation de son travail de DEA. Carine Kohrs Sansorny s'est impliquée particulièrement dans la simulation des données d'un séisme futur. Cela faisait partie de son travail de thèse, qui sera développé dans le chapitre suivant. Enfin bien sur, cet article reflète une réelle collaboration avec des géologues, Christophe Laroque bien-sûr, mais aussi Julien Charreau qui a travaillé pendant son DEA avec Jean-François Stéphan et Jean-Louis Perez, sur l'étude du lien entre la faille de Peille-Laghet et la crise sismique de Blausasc.

2.4.4 Le séisme de Nice

Mais cela n'était pas fini ! A peine remis de nos émotions, et surtout en plein travail de traitement des données, le 25 février 2001, un séisme, plus gros cette fois ci survient au large de Nice. C'est un séisme de magnitude Ml 4.6 (ReNaSS) qui a lieu à 25 km des côtes. Il est ressenti (et entendu) dans tout le département. Le réseau téléphonique est saturé pendant ½ heure. Christophe Maron et Didier Brunel sont très vite au laboratoire (c'est un dimanche soir) Ils interrogent dès que cela est possible les stations (les données étaient transmises par voie téléphonique), en particulier pour éviter une éventuelle saturation des stations du RAP de la ville de Nice. Les données sont magnifiques.

Je me souviens encore du petit frisson que j'ai eu en sachant très vite que le séisme avait eu lieu en mer et que les OBS avaient du l'enregistrer. Enfin un beau séisme sur des OBS ! Je me suis malheureusement trompée car les OBS avaient été repêchés la veille, leur autonomie ne permettant pas de les laisser plus longtemps au fond. Réagissant très vite, l'équipe marine (N. Béthoux, Y. Hello, A. Anglade) a préparé et largué 8 OBS dans la zone épicentrale le 28 février. Ce délai de 3 jours correspond à la préparation nécessaire des OBS et à leur test. Finalement il a mieux valu que les OBS soient remontés avant le gros séisme car ils n'étaient pas bien placés … alors que le largage suivant était parfait. Peu de répliques mais la possibilité d'obtenir des localisations plus précises et en particulier d'avoir enfin une bonne confiance dans la profondeur des sources qui était de 12 à 13 km pour les répliques.

Les données de ce séisme ont permis diverses études : Mécanisme au foyer et moment sismique (B. Delouis et moi-même), études des tracés de rais (M. Régnier), relocalisation du choc principal grâce aux répliques (A. Deschamps, N. Béthoux). Malheureusement l'article prévu sur cet événement n'a jamais été écrit, c'est pour cette raison que figurent les caractéristiques principales de l'événement dans le papier présenté ici.

Geophys. J. Int. (2007) **170,** 387–400 doi: 10.1111/j.1365-246X.2007.03456.x

Seismic hazard on the French Riviera: observations, interpretations and simulations

F. Courboulex,[1] C. Larroque,[1] A. Deschamps,[1] C. Kohrs-Sansorny,[1] C. Gélis,[1] J. L. Got,[2] J. Charreau,[1] J. F. Stéphan,[1] N. Béthoux,[1] J. Virieux,[1] D. Brunel,[1] C. Maron,[1] A. M. Duval,[3] J-L. Perez[3] and P. Mondielli[4]

[1] *Géosciences Azur, Nice Sophia-Antipolis University, CNRS, Paris* 6 *University, IRD,* 250 *av Einstein,* 06560 *Valbonne, France. E-mail: courboulex@geoazur.unice.fr*
[2] *LGIT, Université de Savoie,* 73376 *Le Bourget du Lac, France*
[3] *CETE Méditerranée, ERA risque sismique,* 56 *bd Stalingrad,* 06300 *Nice, France*
[4] *Direction environnement urbanisme et construction, Principauté de Monaco*

Accepted 2007 March 28. Received 2006 December 22. in original form 2005 October 20

SUMMARY

We present here a detailed analysis of a seismic data set recorded by a dense seismological network installed over 6 months in the southeast of France. This experiment was set-up at the boundary between the Ligurian basin and the southern subalpine thrust belt (the Nice arc), which is a complex tectonic region that undergoes low to moderate seismicity. We recorded more than 500 microearthquakes, among which 348 occurred exactly in the centre of the network during a very active seismic sequence that lasted mainly over 2 months.

We performed an absolute location of all of the events and calculated the magnitudes. Then we applied a cross-correlation technique to gather similar events and to relocate relatively few of them. This method revealed a very clear alignment of 19 events in a direction N120° oblique to the N20° general trend of seismicity. Focal mechanisms were determined for the four largest events and composite solutions for 32 smaller ones. Both the alignments of the earthquakes and the focal solutions revealed that two oblique segments of the fault were activated during the crisis.

The main segment (8 km long) that was oriented NNE with a left-lateral strike slip movement is called the Blausasc fault. Taking into account the tectonic evolution and the relationships between surface structures and the distribution of earthquakes, and through a paleaoreconstruction of the tectonic evolution, we propose that the Blausasc fault is the hidden root of the Peille-Laghet fault, which has a mapped length of at least 15 km. The smaller segment (0.6 km long) that was activated during the crisis could be interpreted as an antithetic Riedel fracture.

The active Blausasc fault is located in a densely populated zone, at only 10 km from the crowded cities of Monaco and Nice. It is thus particularly interesting to analyse it for hazard assessment. In the last section, we present a simulation that is aimed at predicting what the ground motion in the city of Nice would be like if an earthquake of magnitude 5.7 occurs on this fault. For this, we used the recordings of the largest event of the seismic sequence ($Ml = 3.2$) and an empirical Green's function summation scheme to simulate the ground motion at two stations situated in urban environments. The values obtained show that especially on soft soil sites, the effects of such an earthquake would be considerable in the city of Nice.

Key words: earthquake location, earthquake-source mechanism, fault tectonics, microseismicity, seismotectonics, strong ground motion.

1 INTRODUCTION

The southeast of France (Fig. 1) is a region where the seismicity is low to moderate. It is an area where we can record daily microseismicity, and about every 5 yr there is an earthquake of magnitude 4.5–5 that is felt by the population without causing real damage. In this context, is it particularly important to study the seismogenic potential of this region? The answer is yes, because large

© 2007 The Authors
Journal compilation © 2007 RAS

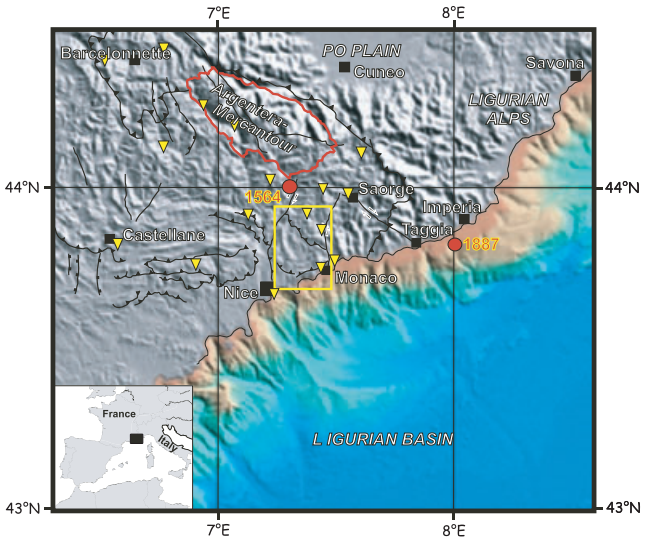


Figure 1. Topographic and bathymetric representation of the Alps–Ligurian basin junction. The northern Ligurian continental margin and the deep oceanic Ligurian basin (data from IFREMER) are in colour, and the onshore domain is in shaded grey (data from GT0P030). The Nice area is surrounded by the Castellane arc t o the west, the Nice arc and the Argentera-Mercantour massif (red line) to the North and the Ligurian oceanic basin to the south. The major faults are in black and the yellow rectangle is the location of Fig. 3. The green triangles represent the stations of the permanent seismic networks in 2001. The yellow dots are the macroseismic epicentres of the two major historical earthquakes. Inset: relative location of Fig. 1 in the western European surrounding.

destructive earthquakes have occurred in this region in the past. During the XVI century, one or two seismic events destroyed numerous villages just inland from Nice (Working Group CPTI 1999; Larroque *et al.* 2001). Their magnitudes and locations cannot be established precisely, but the damage they caused is mentioned in many documents. More recently, in 1887, an earthquake of an estimated magnitude of 6.5 (Ferrari 1991; Eva & Rabinovich 1997; Scotti & Levret 2000; Bakun & Scotti 2004) occurred offshore, within a few kilometres of the Italian Ligurian coast. This earthquake killed hundreds of people.

These destructive events demonstrate that the seismic hazard in this zone should not be neglected, and they justify a precise study for a better definition of its seismogenic potential. If we consider the high density of population on the French Riviera and its constant expansion, it appears that the seismic risk has to be seriously taken into account in this area.

Even if western European countries are considered as areas of low to moderate seismicity, the permanent and temporary seismic networks allow recording of significant organized seismic activity, even in France (Pauchet *et al.* 1999; Souriau *et al.* 2001; Thouvenot *et al.* 2003; Perrot *et al.* 2005). In our region of interest (Fig. 1), the permanent network is quite dense and allows the location of most of the earthquakes of magnitudes equal to or larger than 2. Nevertheless, seismicity maps that are obtained with these earthquake locations appear very diffuse, and have not enabled us to distinguish any alignments of events that can clearly highlight the activity of faults (Fig. 2a). Therefore, the location, geometry and seismogenic potential of active faults are poorly described in this region, which makes it difficult to estimate the seismic hazard.

To obtain better precision in microearthquake location and a better idea of the active segments of faults, we installed over a 6-month period a very dense seismic network in a small zone that was suspected

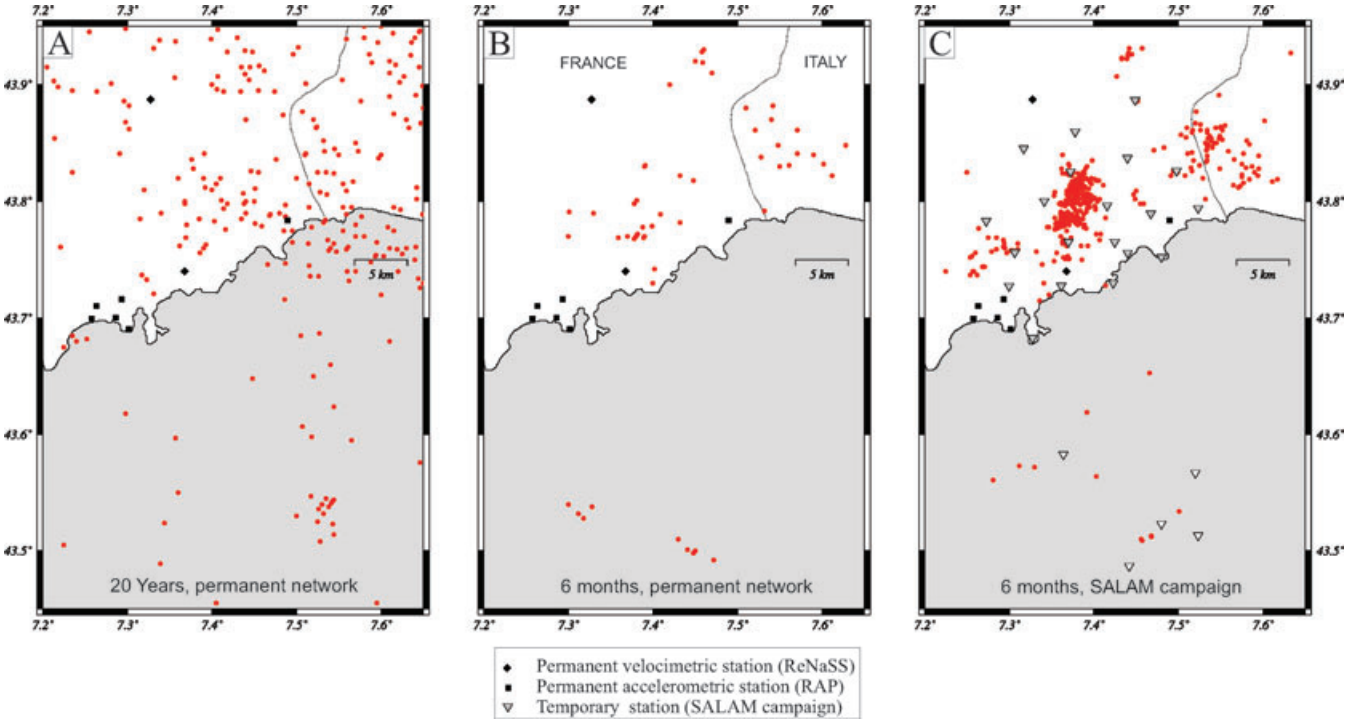


Figure 2. (a) The seismicity detected by the permanent seismic network (ReNaSS) over 20 yr (February 1980–October 2000), (b) over 6 months (October 2000–April 2001, the SALAM period) and (c) the seismicity detected by the temporary dense SALAM network (October 2000–April 2001). Trian gles are the onshore and OBS stations of the SALAM network, squares and diamonds are the stations of RAP (Réseau Accélérométrique Permanent) and ReNaSS (Réseau National de Surveillance Sismique) permanent networks, respectively.

© 2007 The Authors, *GJI*, **170,** 387–400
Journal compilation © 2007 RAS

of being active. This work was completed with a morphotectonic investigation in the field, from aerial photographs and satellite images.

During the SALAM period (October 2000–April 2001), three areas were particularly active (Fig. 2c): a small zone inland (15 km north of the city of Nice) in the centre of the seismological network experienced a seismic crisis that will hereafter be referred to as the Blausasc sequence; an offshore zone (25 km south of the city of Nice) where an earthquake of magnitude $Ml = 4.6$ occurred; and an eastern zone in Italy. Here, we focus on the first zone and present the new seismological and geological data that have been collected along with their analysis using different methods. We show that the inland seismicity during this period revealed clear alignments, and we try to establish their link with the traces of faults and the geological evolution of the area. We then take advantage of the new data collected during this period to simulate a hypothetical larger earthquake on the same fault and its recording in the city of Nice, using an empirical Green's function summation method.

2 TECTONIC AND SEISMOTECTONIC CONTEXT

2.1 Regional tectonic setting

The Nice area is a complex topographical and geological junction between an onshore domain, the southern French Alps, and an offshore domain, the Ligurian basin (Fig. 1). The southern French Alps are made of the high elevation massif of the Argentera and the southern subalpine massifs (the so-called 'arc de Nice' and 'arc de Castellane'). The Argentera massif is a remnant of the Variscan orogen situated along a margin of the old European platform (Ferrara & Malaroda 1969). It is now the southwestern-most external crystalline massif of the Alps, extending 50 km in a NW–SE direction at 80 km from the coast. The subalpine massifs correspond to the Meso-Cenozoic sedimentary cover that was deposited above the basement of the Argentera on the northern Tethyan margin (e.g. De Graciansky *et al.* 1989).

During the last hundred million years, the kinematic evolution of the western European margin has been dominated by the convergence between the Eurasia and Africa plates, which led to the subduction of the Tethyan ocean and then the collision between the continental blocks (Dercourt *et al.* 1986; Dewey *et al.* 1989). Crustal shortening started in the southwestern Alps from around 20 Ma up to the present day, uplifting part of the Variscan basement and leading to the Argentera massif emplacement (Tricard 1984). These deformations also involved the sedimentary cover, which was thrust into a more external position, where it now forms the southern subalpine massifs (Riccou & Siddans 1986). The Castellane and Nice arcs are composed of a series of south-verging fold and thrusts involving the raising of the Mesozoic to Palaeogene sediments above a basal décollement zone in the upper Triassic evaporites.

In the southern French Alps, before the major neogene compressional alpine phase, the basement and sedimentary cover underwent extensional phases of deformation from the early Jurassic up to the Cretaceous (Dardeau 1988). These synsedimentary extensional phases reactivated hercynian faults with NNE–SSW and NNW–SSE trends in the basement (Arthaud & Matte 1975). De Graciansky & Lemoine (1988) proposed that the early Cretaceous extensional faulting in this part of the European continent was related to the opening of the Atlantic Ocean.

East of the Nice arc, the Italian Liguria province corresponds to the internal alpine nappes (Malaroda *et al.* 1970; Bogdanoff *et al.* 2000). Thick helminthoides flysch series of Cretaceous age were thrust southwestward during the Cenozoic (Kerckhove 1969). Moderate seismicity has also been reported (Bossolasco *et al.* 1972; Maddedu *et al.* 1997; Eva & Solarino 1998) and, for instance, the Saorge-Taggia fault appears to be one of the major active structures (Hoang-Trong *et al.* 1987; Marini 1987; Larroque *et al.* 2001).

Offshore, the present-day western Mediterranean setting results from an incomplete collision between the Africa and Eurasia plates. The narrow Ligurian oceanic basin (Rollet *et al.* 2002) opened during the convergence between the two plates: the continental rifting started at 30 Ma and led to the anticlockwise rotation of the Corsica-Sardinia continental block and to the oceanic spreading in the centre of the basin. The extension ended at 16 Ma (Montigny *et al.* 1981; Edel *et al.* 2001).

Therefore, the southern Alps–Ligurian basin junction is a particularly complex geological domain with a strong tectonic inheritance, large cumulated deformations, and a major continent–ocean boundary. Several of these structures could be reactivated in the present-day state of stress.

2.2 Present-day kinematics and state of stress

The convergence between the Africa and Eurasia plates currently continues at a rate of 6.2 ± 0.5 mm yr^{-1} in a N343° ±9° direction at the longitude of the western Alps, according to the Nuvel-1A plate motion model (DeMets *et al.* 1994). From models based on geodetic data, numerous authors (e.g. Sella *et al.* 2002; Nocquet & Calais 2003) have proposed 30–60 per cent lower convergence velocities in a N300° to N350° direction. For this reason, the dynamics of active deformation in the western Alps is often thought to be as a consequence of the Africa–Eurasia collision (Mueller *et al.* 1992; Eva & Solarino 1998). Nevertheless, geodetic data attest that: (1) no significant movement occurs between the Corsica-Sardinia block and the western Alps (Vigny *et al.* 2002; Nocquet & Calais 2003) and (2) the major part of the Africa–Eurasia convergence is accommodated southwards along the Maghrebides boundary. Therefore, the current strain pattern in the western Alps could be mainly controlled by the counter-clockwise rotation of the Adriatic microplate around a pole located in the Po Plain (Calais *et al.* 2002).

From the inversion of microtectonic data, Ritz (1992) and Rebaï *et al.* (1992) proposed that in the southern subalpine massifs the regional stress field was homogenous, with a reverse faulting stress regime (σ_1 horizontal with a roughly N–S direction) during the Plio-Quaternary era. Many focal mechanisms have been determined in the last 30 yr (Madeddu *et al.* 1997; Eva & Solarino 1998; Baroux *et al.* 2001). The focal solutions of these earthquakes are homogeneous and allow us to propose that the *P*-axes of earthquakes (trend NW–SE to N–S) are near the maximum compressive stress direction (McKenzie 1969). In the southern subalpine massifs, the focal mechanisms of the earthquakes are consistent with a strike-slip faulting stress regime (σ_2 vertical and a N155° trending σ_1 axis). Offshore, in the Ligurian basin, Baroux *et al.* (2001) determined a reverse faulting stress regime with a N115° trending σ_1 axis.

2.3 Historical and instrumental seismicity

The importance of historical seismicity in the Alpes Maritimes is easy to detect in the many villages inland from Nice, where the occurrence of earthquakes is often mentioned. Over the last thousand years to 1920, the far southeast of France and northwestern Italy experienced 58 historical indexed earthquakes (Larroque *et al.* 2001). At least two of these earthquakes caused many casualties:

© 2007 The Authors, *GJI*, **170,** 387–400
Journal compilation © 2007 RAS

the Roquebillière earthquake (1564), and the Ligurian earthquake (1887) that reached an intensity of X MCS (Mercali, Cancani and Sieberg scale; Working Group CPTI 1999; Lambert & Levret 1996). The Ligurian earthquake also produced tsunamis that were seen to have run-up heights of around 1–2 m (Eva & Rabinovitch 1997). Whereas the 1887 Ligurian earthquake was located quite a way offshore, this was not the case for the 1564 event (Fig. 1). Indeed, this latter event was located to the village of Roquebillière (Vesubie Valley) because of the large damage that was seen there, although this damage could be due to site or induced effects, like landslides, phenomena that are still important today. A study by Gauberti (1973) shows that this event also caused important damage in the village of Peille, situated at only 15 km from the city of Nice, in the region of interest of this article. In general, locations of historical earthquakes are not accurate enough to associate them with faults.

The instrumental seismicity that has been gathered since 1960 was more accurately determined from 1976, when the permanent stations of the Réseau National de Surveillance Sismique Français (ReNaSS) network were installed. Now, there is a quite dense seismic network (Fig. 1): 11 short-period stations (six from ReNaSS, four from Sismalp and one from CEA: Commissariat à l'Energie Atomique); four broad-band stations (ReNaSS-TGRS network) and 10 accelerometers (RAP: Réseau Accélérométrique Permanent) are operating in the Alpes-Maritimes region. Due to this network, an earthquake of magnitude greater than 4.5 is recorded on average every 5 yr, along with daily microseismicity. The repartition of epicentres enables the highlighting of some major active structures, like the Saorge-Taggia fault (Fig. 1) that is mainly situated in Italy (Hoang Trong *et al.* 1987), and the Argentera-Bersezio fault in the north of the region (Grellet *et al.* 1993), although the majority of the seismicity appears diffuse and not easily related to geological structures. Both inland and offshore, evidence of epicentre alignments are not clear at all, and it is necessary to have a denser seismological network to be able to image precisely the activity of segments of faults. In 1999, an earthquake of magnitude *Ml* 3.2 occurred at 15 km from the city of Nice. The studies of this event have revealed that it could have been due to a left-lateral fault called the Peille-Laghet fault (Courboulex *et al.* 2001). This small earthquake has made us think that this fault could be active, and, because of its proximity to a densely populated area, very dangerous. This is the reason why we decided to further investigate this segment of the fault and installed a dense temporary network during a period referred to as SALAM.

2.4 Seismotectonic pattern of the SALAM campaign area

Following the 1999 November 1, Peille earthquake (Courboulex *et al.* 2001), the SALAM experiment was installed at the frontal part of the Nice arc (Figs 1 and 3). The Nice arc is a complex tectonic zone

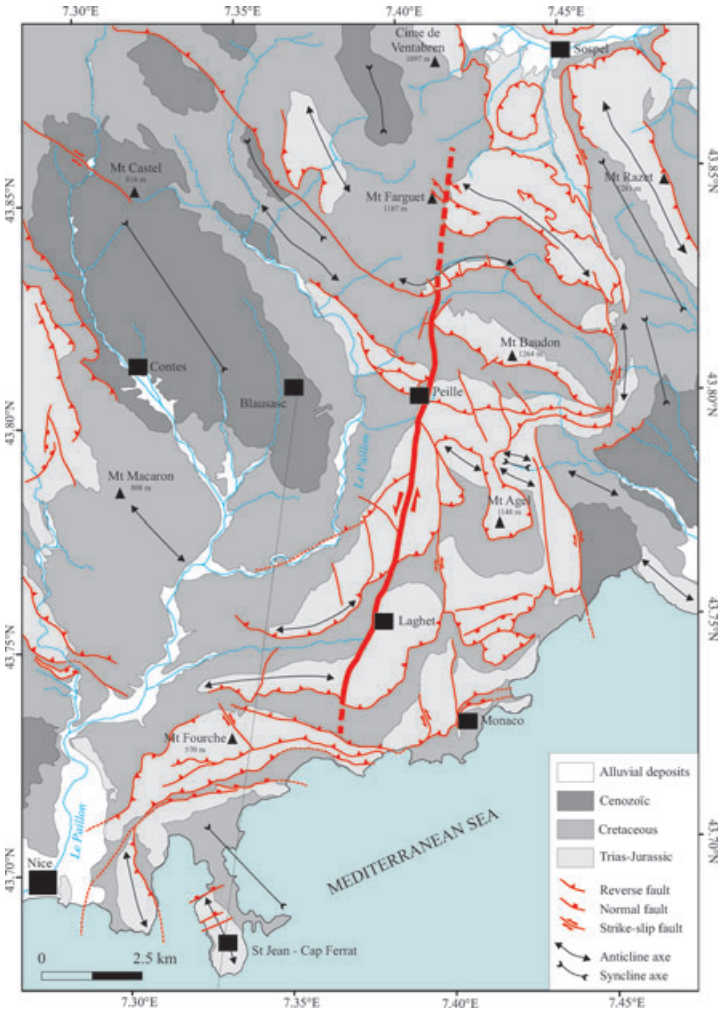


Figure 3. Tectonic map of the study area (frontal part of the Nice arc). The Peille-Laghet fault is in bold and the grey line from Blausasc to Saint Jean Cap-Ferrat corresponds to the geological cross-section of Fig. 4.

© 2007 The Authors, *GJI*, **170,** 387–400
Journal compilation © 2007 RAS

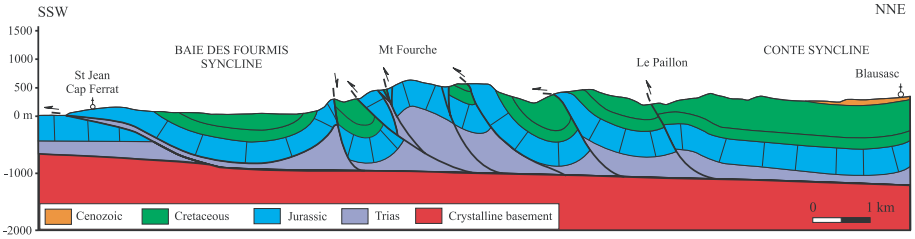


Figure 4. Geological cross-section from Blausasc to Cap-Ferrat (see Fig. 3 for location). The frontal part of the Nice arc corresponds to seven imbricate thrust-sheets made of sedimentary rocks from Triassic evaporites (décollement level) up to Cenozoic. At the frontal part of the belt, only the sedimentary cover appears to be thrust up, the crystalline basement is not involved by duplex structures.

with large folds trending NW–SE to E–W (Bulard *et al.* 1975; Perez 1975). These folds are crosscut by numerous south-verging thrust faults and strike-slip fault zones involving series of Mesozoic to Palaeogene sediments. The Nice arc is bounded by two large strike-slip fault zones to the west and east (Fig. 1). Inside these boundaries, the major structures are north-dipping thrusts trending roughly E–W and a NNE–SSW left-lateral strike-slip fault: the Peille-Laghet fault (Fig. 3).

The first compressional deformation started around 20 Ma and produced folding with NW-SE trends. The major alpine compressional phase took place around 8–5 Ma (Gèze 1960; Perez 1975; Riccou & Siddans 1986). The fold and thrust belt was moved southwards, above a décollement zone lying at the base of the sedimentary cover in Triassic evaporites. Below the sedimentary cover, the crystalline basement has undergone deformation since the Palaeozoic, with major hercynian basement structures striking E–W and NNE–SSW (Arthaud & Matte 1975; Debran-Passard *et al.* 1984).

In this area, seismic sections and boreholes do not exist. Therefore, the subsurface structure can only be based on geological knowledge. At the frontal part of the Nice arc, the thickness of the sedimentary rocks that are overlying the basement corresponds to the thickness of the layers from Trias up to Late Cretaceous. Taking into account that the thicknesses do not change significantly on the scale of the frontal belt, we measured the mean thickness of the different layers from the sections provided by river incisions and we propose a value of 1300 $\pm$ 300 m. From field data and cartography, we built a geological cross-section from Blausasc up to the coast (Fig. 4). As for the neighbouring Castellane arc (Laurent *et al.* 2000), the frontal part of the Nice arc is an imbricate stack of sedimentary thrust-sheets (Siddans 1979; Malavieille & Ritz 1989). The boundary between the sedimentary cover and the crystalline basement has a northward dip from -700 m under sea level below the Cap Ferrat to -1250 m below Blausasc. We propose that the basement-sedimentary cover interface is smooth because we have no evidence for deep-seated major basement structures and it is consistent with the thickness of the Mesozoic layers. From Blausasc to Cap Ferrat, the imbricate stack is made up of seven thrust sheets; it is bounded to the North and to the South by two major synclines: the Contes syncline and the Baie des Fourmis syncline, respectively.

From striation on fault planes, schistosity direction and fold direction, we determined a mean shortening in a N170° direction during the emplacement of the Nice arc. Unfortunately, it is not possible to build a cross-section according to the shortening direction because of local structural complexity and dense urbanization. Nevertheless, we tried to determine the displacement between Blausasc and the coast using the present-day base of the competent Jurassic limestones as a reference, to unfold the strata along the Blausasc-Cap Ferrat cross-section (Fig. 4). If we consider that the sedimentary cover south of the coastal domain is autochtonous, and taking into account the angle between the shortening direction and this cross-section, the unfolding of the stratas allows us to propose a range of shortening around 4–5 km along the N170° direction for the frontal part of the belt since 20 Ma. This value is consistent with the shortening calculated in the western part of the so-called Castellane arc (Laurent *et al.* 2000).

3 GENERAL RESULTS OF THE SEISMOLOGICAL SURVEY

3.1 Temporary network description

We installed a temporary seismic network that was composed of 20 stations, to complement the permanent network in a small zone (20 km $\times$ 20 km). The area covered by the temporary network concerns the eastern part of the French Riviera from the city of Nice to the Italian border (Fig. 2c), including Monaco (two stations). It was centred where the Peille earthquake occurred about a year before (Courboulex *et al.* 2001), close to the well-known Peille-Laghet fault.

All the stations installed were three-component digital recorders (16–24 bit) equipped with individual GPS receivers that ensured accurate time correction. About one third of the stations were equipped with CMG40 broad-band sensors, one third with 5 s Lennartz sensors, and the rest with 2 Hz sensors (L22). All of the stations worked in continuous mode with a sampling frequency of 125 or 200 Hz. The network was operating over a period of 6 months, from 2000 October 16 to 2001 April 24 and detected 582 events that were recorded by at least three stations in the region of interest, as illustrated in Fig. 2.

3.2 First location results

We picked the first arrival time of *P* and *S* waves on waveforms recorded by the temporary and permanent stations. For first locations of the whole data set, we used a simple layered model (Bertil *et al.* 1989). We identified 64 events as quarry blasts and ignored them. To do this, we first collected the carrier's information when possible. Then, we compared the seismicity map obtained during day and night-time periods and cancelled out two swarms of events that systematically occurred during the day around the same times. We believe that most of the artificial shots were removed through this analysis, but we are aware that a few shots may still be present in the catalogue.

Using the HYPOCENTRE code and SEISAN software (Haskov & Ottenmöller 1999), we finally located 518 earthquakes. This is seven times larger than the number of events located by the permanent network (Fig. 5). The usefulness of using a dense seismic network is seen clearly in Fig. 2, where the seismicity recorded by

© 2007 The Authors, *GJI*, **170,** 387–400
Journal compilation © 2007 RAS

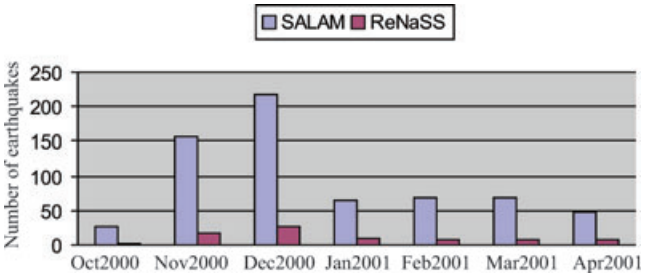


Figure 5. Number of earthquakes recorded per month by the permanent and the temporary networks during the SALAM campaign (2000 October 15 to 2001 April 15).

the permanent network over 20 yr (Fig. 2a) and the 6 months of the experiment network (Fig. 2b) are compared with the seismicity recorded by the SALAM network (Fig. 2c). It is obvious from these results that the scarcity of the seismicity maps obtained in this region by the permanent network does not reflect the real microseismic activity. Given the small magnitude of most of the events, the sensitivity of the permanent network does not enable the detection of structural alignments, if they exist.

A first look at the location results (Fig. 6) shows three main zones where the seismic activity was important during these 6 months of the temporary seismic network are as follows.

(1) A region in Italy that is very close to the France-Italy border.

(2) A zone situated offshore, where an earthquake of magnitude $Ml = 4.6$ occurred on 2001 February 25. A more complete study of this event will be the subject of another publication. We only report here, in Table 1, its location using the temporary and permanent networks and its focal mechanism determined from the polarities of direct and refracted *P* waves.

(3) A small zone inland in the centre of the network (around where the Peille event occurred in 1999) where 348 events were located. This crisis, called the Blausasc sequence, is detailed in the present study.

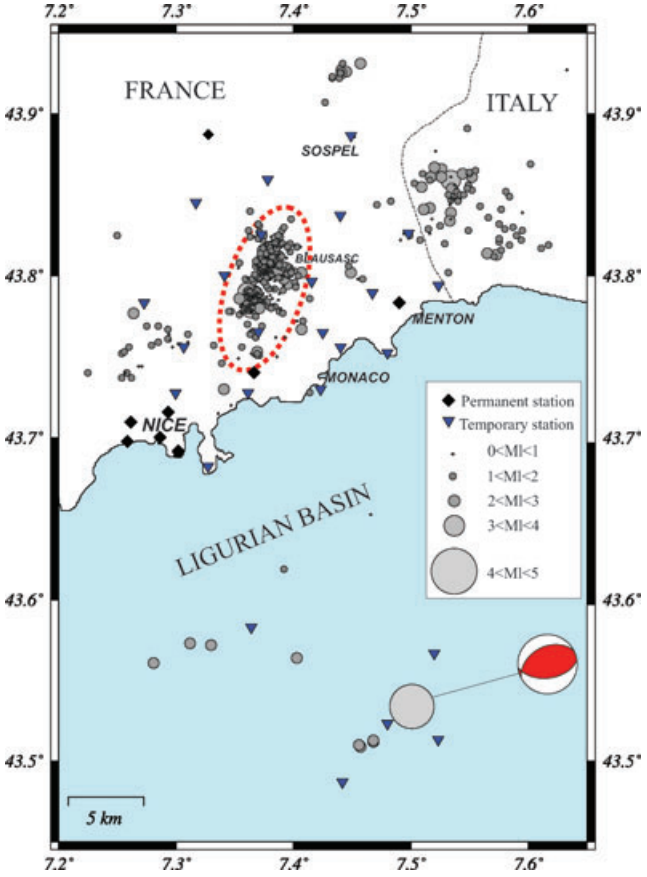


Figure 6. Localization and magnitude of the earthquakes recorded during the SALAM seismic experiment. The focal mechanism of the largest earthquake that occurred during the campaign (2001 February 25, *Ml* 4.6) has been computed using *P*-wave polarities on numerous stations. The red ellipse shows the location of the Blausasc sequence.

3.3 Magnitudes

We searched to determine a local magnitude for the 518 events located, calibrated on the magnitude *Ml* calculated by the ReNaSS. Using the 77 events for which magnitudes had been determined by the ReNaSS, we tried to fit the relation: $\mathrm{Log}(A) - Ml = e\log(D) + f$, where A is the maximum amplitude averaged on the three components, high pass filtered at 1 Hz for the broad-band sensors, *Ml* is the ReNaSS magnitude, and D is the hypocentral distance. Because some of our short period sensors did not have precise calibration, we could not properly retrieve the real amplitude at each station, in which case we used directly the rough values. We then obtained the different linear regressions for each station with an almost constant slope e and various values of f that account for the instrumental differences between the stations. We carried out different trials with a large number of the stations, and we finally obtained the most stable results using four of the best stations. The relation allows us to propose magnitude estimations for the whole data set, ranging from 0.1 to 4.6 (size of circles in Fig. 6).

3.4 Frequency–magnitude relations

The frequency–magnitude distribution (Gutenberg & Richter 1944) describes the power-law relation between frequency of occurrence and magnitude of earthquakes: $\mathrm{Log}\, N = a - b\, M$, where N is the cumulative number of earthquakes with magnitudes larger than M, and a and b are constants. We calculated the b value from the whole data set on the magnitude interval [1.2, 3.4] and obtained a value of 1.08 (Fig. 7a). The linear trend between magnitudes 1.2 and 3.4 indicates that the catalogue is complete for this range of magnitudes. The earthquake of magnitude 4.6 was not taken into account in the b-value calculation because it is not representative of such a short (6 months) period of seismicity. We show on Fig. 7(a) only the frequency–magnitude distributions obtained using the whole data set, although we also studied the data set that corresponds to the Blausasc sequence only, and the data set without the Blausasc sequence. The b value we obtained was in all cases very close to 1.

To have a more general view of the Gutenberg–Richter distribution in the southeast of France for a larger time of observation, we calculated the b value on 20 yr of seismicity recorded by the ReNaSS permanent network in a much larger area (Fig. 7b). The b value obtained is a little higher (from 1.1 to 1.2), calculated over the magnitude interval [2–4.3]. Magnitudes higher than 4.3 were not taken into account, the time period being certainly too short in comparison with the frequency of occurrence of earthquakes of these magnitudes. Assuming that the Gutenberg–Richter is time-independent and valid over the whole range of magnitude, linear extrapolation to higher magnitudes yields a recurrence time of

© 2007 The Authors, *GJI*, **170,** 387–400
Journal compilation © 2007 RAS

Table 1. Location and focal solutions of the main events that occurred during the SALAM campaign.

Date	Time	Latitude	Longitude	Depth	*Ml*	Strike	Dip	Rake	Reference on figures
2000/12/19	14:20:49	43.788	7.366	2.6	3.2	216	77	15	Event 1 on Fig. 8(a)
2000/12/20	5:45:14	43.790	7.361	2.6	3.0	216	79	10	Event 2 on Fig. 8(a)
2000/12/19	00:52:24	43.780	7.364	2.8	2.9	204	54	37	Event 3 on Fig. 8(a)
2000/12/21	6:35:54	43.790	7.362	2.7	2.4	224	71	23	Event 4 on Fig. 8(a)
1999/11/01[a]	17:22:33	43.789	7.367	3.0	3.4	209	75	−4	Event 5 on Fig. 8(a)
2001/02/25	18:34:43	43.53	7.48	11.	4.6	243	41	74	Fig. 6

[a]From Courboulex *et al.* (2001).

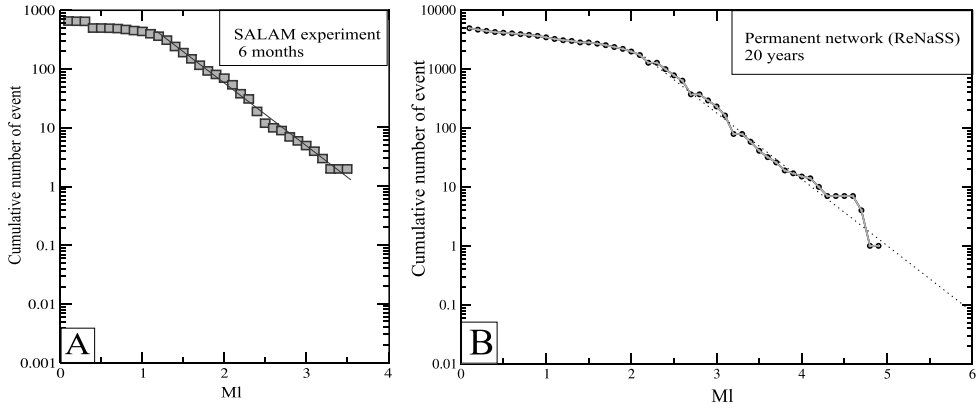


Figure 7. (a) Frequency–magnitude distribution of the events detected located during the 6 months of the SALAM experiment (latitude: 43.5°–44°, longitude: 7.2°–7.7°). (b) frequency–magnitude distribution of the events located over 20 yr by the ReNaSS permanent network (latitude: 43°–45°, longitude: 6.5°–8.5°).

200–300 yr for an $Ml \geq 6.0$ occurring anywhere in the geographical window considered.

It is important to note that to be able to infer anything about the return periods of larger earthquakes from a frequency–magnitude relation, the data set must fulfil the conditions of spatial and temporal stationarity, of completeness to a specified lower magnitude, and of statistical independence. We may consider that 20 yr of observations is a reasonable duration for the magnitudes we chose to study [2, 4.3]. However the conditions of spatial stationarity are subject to discussion in an area where different seismotectonic influences can be superimposed. For this reason, the return period value we obtained for an earthquake of magnitude 6 or more has to be taken cautiously, and only used to remind ourselves that the earthquake hazard of this region is not negligible.

4 THE BLAUSASC SEISMIC SEQUENCE

4.1 Description of the sequence

One month after the installation of the temporary seismic network, the inhabitants of several villages inland from Nice felt numerous vibrations, especially during the night. Most of the related seismic events were not detected at that time on the permanent network, but we quickly found that the temporary network was sufficiently sensitive to detect these microearthquakes. It was the beginning of a very active seismic sequence that occurred in the centre of our seismic network and so could be recorded with exceptional precision.

The Blausasc sequence mainly lasted from 2000 mid-November to the end of 2000 December, in a small 8 km × 4 km area, although it was still active until the end of the full period. We recorded 348 events in this small zone. The main shocks occurred on December 19 and 20, 2000, and were of magnitudes *Ml* 3.2 and 3.0, respectively. About 60 events occurred on 2000 December 19, which was the climax of the Blausasc seismic sequence.

These earthquakes were very well felt in the villages close to the epicentre (Blausasc, Peille and Contes) and generated some panic reactions. They were also well felt in the cities of Nice, Monaco and Menton. A macroseismic map published by the Bureau Central Sismologique Français (BCSF) indicated a macroseismic intensity (EMS98) of V in the epicentral zone (data are available on www.franceseisme.fr).

4.2 Absolute locations

The absolute locations of the Blausasc seismic sequence have been obtained for 348 events in a very small area (Fig. 8a). To obtain the best 1-D velocity model, we used the VELEST tomographic inversion method with 500 different input models. We found that with our data (many shallow small events in a small zone) this method did not enable us to obtain a better model than the simple initial model we used. Hence, we decided to keep a simple layered model in which velocity raises regularly with depth (Courboulex *et al.* 2003). We also looked for the best Vp/Vs ratio and found a value of 1.73. We obtained a low average rms of 0.09 s for the events of this zone with a very good azimuthal coverage and a distance to the closest station always smaller than 2.5 km (Fig. 6). The average vertical and horizontal errors raise 1.4 and 1.2 km, respectively.

The earthquakes were very shallow (0–3 km in depth) and were spatially separated into two groups of events by a 1-km-wide gap, with one in the north and the other in the south of the area (Fig. 8a). The epicentres appeared to be aligned on an 8-km-length structure oriented N20°. At depth, events in the north were 1–2.5 km deep and not so well aligned, contrary to the ones in the south, which were deeper and well aligned on a 70° dip plane (Fig. 8b). Therefore, we

© 2007 The Authors, *GJI*, **170,** 387–400
Journal compilation © 2007 RAS

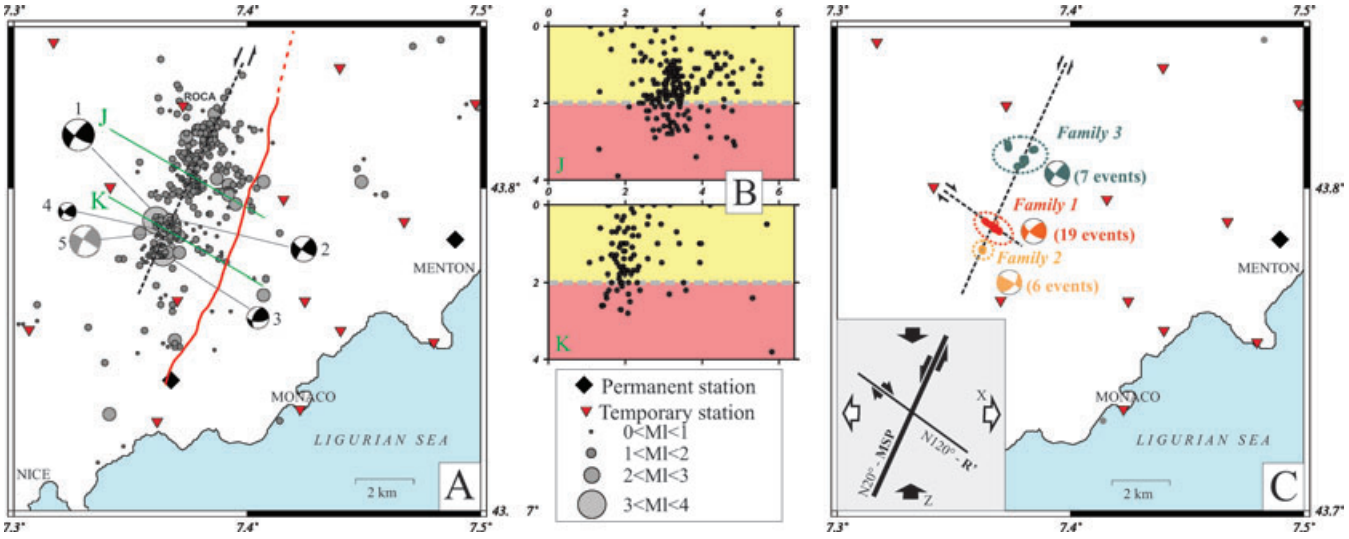


Figure 8. (a) Absolute location and magnitude of the earthquakes during the SALAM experiment in the small zone of the Blausasc sequence (grey circles) and individual focal mechanisms of the larger shocks (Numbers refers to Table 1). The red line is the surface trace of the Peille-Laghet fault. (b) Cross-sections (2 km width), the grey dotted line is the maximum depth for the sedimentary cover (yellow)–crystalline basement (red). (c) Relative relocation of the events of three families of multiplets and composite focal mechanism associated. Inset: interpretation of the N20° and N120° directions as the main shear plane (MSP) and a antithetic Riedel fracture (R') formed in a simple shear deformation regime; Z: shortening axis and X: lengthening axis.

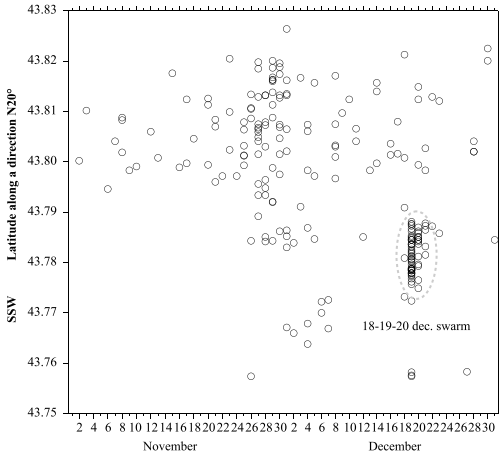


Figure 9. Migration of the seismicity from north to south during the Blausasc sequence. The epicentres are projected on a N20° axis (see Fig. 8).

highlighted the existence of an active fault plane, which we call here the Blausasc fault.

The spatiotemporal distribution of the epicentres showed the migration of the seismic activity from the north in 2000 November to the south in 2000 December (Fig. 9). The two main events took place in the southern part in 2000 December.

4.3 Relative relocations using multiplets analysis

To better locate the earthquakes, we performed their relative relocations using the multiplets analysis proposed by Got *et al.* (1994). Given the good distribution of stations around the hypocentres, this method should give reliable results.

First, we created families of similar events by using the cross-correlation of their waveforms. Then, we located events by pairs, transforming time delays into distances. This means that in a family, the events were located towards all other events belonging to the same family, and not towards one single master event (Fréchet 1985). As a consequence, the event locations were more precise and the shape, azimuth and dip of one family are less sensitive to the velocity model.

Due to this method, we defined three families of events located in three different parts of the fault (Fig. 8c): family 1 (19 events) was located in the centre of the fault segment that was activated during the crisis; family 2 (six events) in the southern part of the segment; and family 3 (seven events) in the northern part. Each of the families was determined with a high cross-correlation value (at least 0.9) on four stations. Only vertical components and *P* waves were used in this analysis. As an example, we show *P* waves of the 19 earthquakes that belong to family 1 that were recorded on the vertical component of station ROCA (Fig. 10). Even if the station is very close to the epicentres, the waveform is rather similar from one event to the other. Note that the total number of events that could be gathered into families was low (only 32). This is because the earthquakes occurred at shallow depths in a complex velocity medium and are recorded by nearby stations; therefore, the waveforms recorded are complex and not particularly similar to each other. This relocation study will give very precise information on the geometry of small parts of the fault that will complement the already good earthquake repartition we obtained with the absolute location method.

The results of relocation was surprising for family 1 (Fig. 11): a very clear alignment of the 19 events was obtained in a direction N120°, almost perpendicular to the main elongation of the seismicity along the Blausasc fault. At depth, the events belonging to this family were separated by 300 m at most. Location errors do not exceed 20 m horizontally and 50 m vertically. This result shows that a small fault (at least 600 m long), oblique with an angle of 70°–80° to the main N20° Blausasc fault, was activated during the crisis. If we observe in details the spatial and temporal distribution of small events, we can see that they do not follow a particular scheme (Fig. 12). Note that the two main shocks (magnitude 3.2 and 3.0) belong to this family. It is then very difficult to know on which of the two structures they occurred. We will see below that the focal solutions could not help us with this discrimination.

© 2007 The Authors, *GJI*, **170,** 387–400
Journal compilation © 2007 RAS

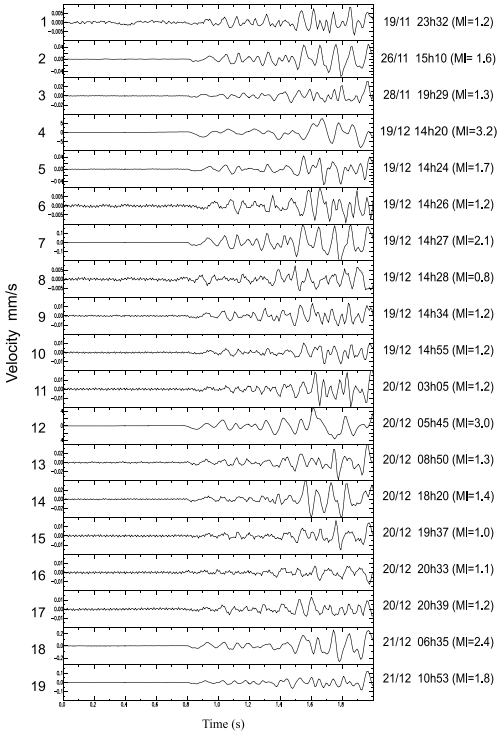


Figure 10. Vertical seismograms recorded on station ROCA for all the events of family 1. The location of station ROCA is shown in Fig. 8.

Family 2 contains earthquakes that occurred during a very short period of time (90 min) and very close together in the south of the area. Their relative relocation gives little improvement and groups them into a small zone of about 100 m radius. Family 3 regroups events that occurred in 2000 November in the northern part of the fault segment. They were too few to show any significant alignment and the relative relocation did not group them significantly.

Fig. 8(c) shows the relative relocations of the earthquakes that belong to these families. We used their relative relocation and kept the family barycentre.

4.4 Focal mechanisms

We calculated the focal mechanisms of the four largest events using the polarity of *P* waves on 14–19 stations well distributed in azimuth (Table 1, Figs 8a and 13). The strike slip solutions obtained are stable with depth. Note that the three focal mechanisms numbered 1, 2 and 4 in Table 1 correspond to three events of the same family and that, therefore, they should be almost identical.

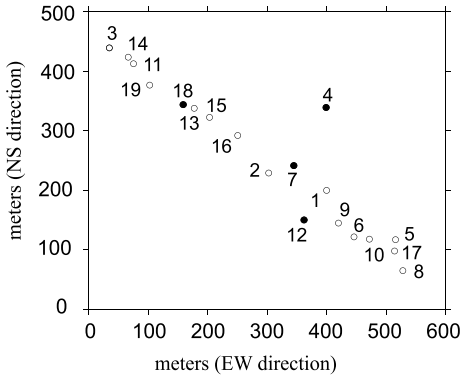


Figure 12. Details of the horizontal distribution of events of family 1 after relocation. The numbers refer to Fig. 10 and follow a chronological order.

For smaller events, we could not find stable focal solutions because they were recorded by too few stations. To nevertheless obtain better constrained solutions, we calculated composite focal mechanisms for the earthquakes of the three families determined before by cross-correlation methods. The similarities of the earthquake waveforms in each family ensure us that their focal mechanisms were highly similar. This approach enabled us to obtain three well-constrained solutions for the 32 events of the three families (Fig. 8c).

For almost all solutions (except for event 3) we retrieved an almost vertical plane oriented N20° to N40° that is in good agreement with the general trend of seismicity during the Blausasc sequence and a left lateral strike slip movement. The other nodal plane was mostly oriented N120°–N130°. This plane was in good agreement with the linear trend highlighted by the relative relocation of the events of family 1.

5 TECTONIC INTERPRETATION

During the Blausasc sequence, the major structure activated showed a trend of N20° and the faulting along the Blausasc fault extends from 3 km in depth up to 0.5 km in depth (Fig. 8a and b). In the morphology, the seismic alignment corresponds to the N20° direction of the Paillon valley (Fig. 3).

The present-day seismic sequence did not rupture the surface. Even if the seismicity was very shallow, field investigation in the Paillon valley did not reveal any recent traces of faulting, which is not surprising given the small magnitudes of the largest events of the Blausasc swarm.

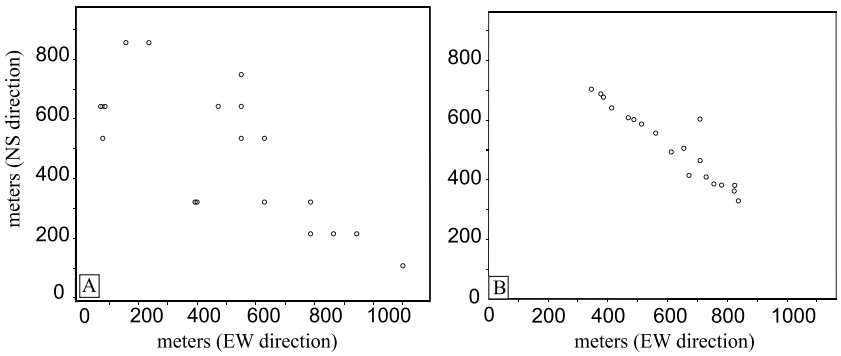


Figure 11. (a) Absolute location and (b) relative relocation of the earthquakes of family 1.

© 2007 The Authors, *GJI*, **170,** 387–400
Journal compilation © 2007 RAS

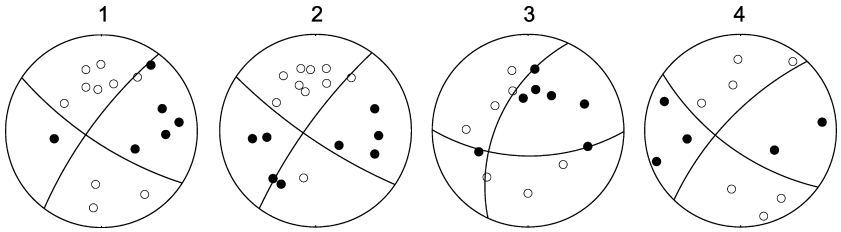


Figure 13. Focal solution of the largest events of the crisis. The numbers refer to Fig. 8(a) and Table 1.

The closest fault, the Peille-Laghet fault, is located about 2.5 km to the East of the Blausasc seismic swarm and showed a subparallel trend to the seismic alignment found there (Figs 3 and 8a). The Peille-Laghet fault is around 15 km long. It cross-cuts the sedimentary cover in a N20° strike and dips 70°W. Its geological evolution is complex: from normal faulting during the Cretaceous extensional phase (Dardeau 1988; De Graciansky & Lemoine 1988) to left-lateral strike-slip faulting during the Miocene compressional phases that involved the emplacement of the Nice arc (Malavieille & Ritz 1989; Ritz 1992). However, field and aerial photographic investigations showed no evidence of morphotectonic anomalies that would suggest Holocene activity of that fault.

Therefore, does a relationship exist between the seismicity and the faults mapped at the surface? The traces of the fault at the surface are part of the Nice arc that was decoupled from the crystalline basement during the major compressional phase (8–5 Ma) with the SSE thrusting of the sedimentary cover. If we take into account the 4–5 km displacement in a N170° direction, the palaeoposition of the Peille-Laghet fault is approximately on top of the Blausasc seismic alignment (Courboulex *et al.* 2003).

We have explored different solutions (e.g. strong bending of a single fault plane, two parallel faults, a flower structure) to explain the relationships between the present-day seismicity pattern and the regional tectonic evolution. Finally, we propose the following hypothesis (Fig. 14): (1) the Peille-Laghet normal fault developed during the Cretaceous times and (2) in late Miocene–Pliocene times, the compressional thin-skin tectonics led to the southward thrusting of the sedimentary cover. During this period, the inherited Peille-Laghet fault was reactivated: the upper part of the fault, which affects the sedimentary cover, was unrooted from its basement and reactivated as a lateral ramp by left-lateral faulting, whereas its basement part remained mainly inactive. In our interpretation, the Peille-Laghet fault has been inactive since the end of the Miocene–Pliocene thrusting. At present, faulting in the basement propagates in the sedimentary cover, delineating the Blausasc fault, under the Paillon valley but without reaching the surface.

6 SIMULATION OF A LARGER EVENT ON THE BLAUSASC FAULT

One objective of a seismic hazard analysis is to be able to predict the ground motions due to a future earthquake. This is especially important in regions were no large event has been recorded yet by seismological networks, like the south east of France. We propose in this paragraph to show how, in the region studied, the recordings of small events can be used to simulate a larger earthquake following an empirical Green's function approach (Hartzell 1978).

During the Blausasc sequence, a portion of the recently discovered active Blausasc fault was activated to a length of about 8 km. The larger earthquake that occurred during the Blausasc sequence on this structure had a magnitude $Ml = 3.2$, that is, a fault extension smaller than 1 km, although it is reasonable to think that the fault could generate a larger event (Kafka & Levin 2000). At least if the 8-km portion of the fault activated during the Blausasc sequence had broken in one go, we would expect a magnitude 5.7 earthquake (Wells & Coppersmith 1994).

We decided then to simulate the ground motions that would be generated by such an earthquake in the city of Nice. For this, we used the stochastic summation of empirical Green's functions developed by Kohrs-Sansorny *et al.* (2005). This method requires two input parameters: the moment and the stress drop ratios between the small event and the simulated one. It is well adapted for the simulation of moderate sized earthquakes in low seismicity areas. It has the great advantage of taking into account the path and site effects intrinsically and of reproducing a source model that is coherent with scaling laws. We used the recordings of the *Ml* 3.2 event of the Blausasc sequence as the empirical Green's function.

We present here the results obtained at two accelerometric stations belonging to the permanent RAP network inside the city of Nice: a station installed on the calcareous hills of the city (NBOR) and a station installed on alluvial deposits in the lower part of the city (NALS). Both time and frequency simulations (elastic response spectra with a damping of 5 per cent) are presented in Fig. 15. For each station, three accelerograms are shown above the 500 simulations realized. The differences between each other are only due to the stochastic method and not to parameters variability. We show, for the elastic response spectra, the results of 10 simulations and the average value over 500 simulations.

The peak ground acceleration (PGA) takes an average value of 1.5 m s^{-2} at station NALS, whereas it is smaller than 0.3 m s^{-2} for station NBOR. This large difference had been pointed out by previous studies on site effects in this area (Duval 1994; Duval *et al.* 1999; Semblat *et al.* 2000). Note that the duration of vibration is also much longer on NALS than NBOR. This method does not take into account the potential non-linear effects, but it is reasonable to think that they should not be dominant given the relatively small magnitude of the simulated event.

The PGA value of 1.5 m s^{-2} obtained in a central part of the city is rather important. If we refer to the paraseismic rules actually in application (EPS92), this value should theoretically be supported by recent buildings. Unfortunately, most of the constructions are old, and so, such an earthquake could generate important damage.

It is important to note that the simulation results strongly depend on the static stress drop value chosen for the simulated event (Kohrs-Sansorny *et al.* 2005). In this study, we present only the results obtained under the hypothesis that the static stress drop of the large event is the same than the one of the small event. If we had taken a larger value for the simulated event as it is suggested now by several authors (Beeler *et al.* 2003; Kanamori Rivera 2004), we would have obtained larger values for the accelerations in Nice. A more detailed study on this topic is in progress and will be the subject of another publication.

© 2007 The Authors, *GJI*, **170,** 387–400
Journal compilation © 2007 RAS

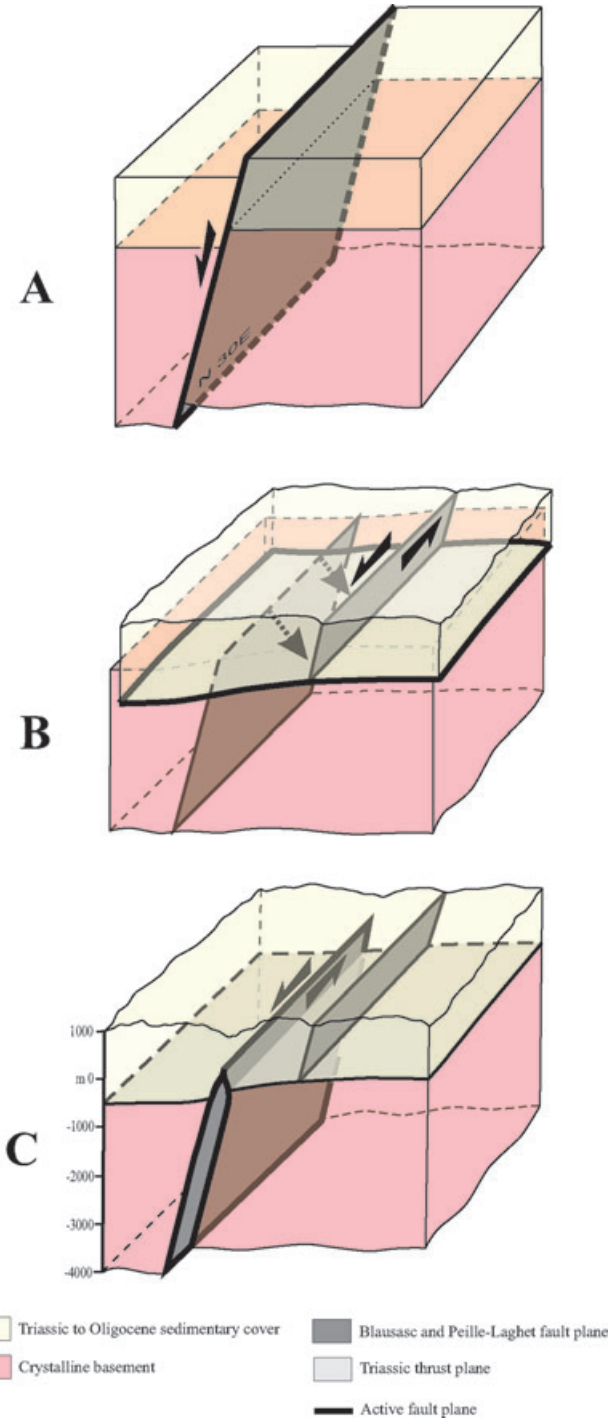


Figure 14. 3-D representations of the tectonic evolution of the Blausasc fault from the Cretaceous up to the present-day. (a) Cretaceous extensional faulting; (b) Miocene thin-skin deformations : coupling between N170° thrusting above the basal décollement and left-lateral faulting along the Peille-Laghet fault in the sedimentary cover and (c) Present-day reactivation of the deep part of the fault without propagation of the rupture at surface.

The example of simulation is presented here only to show how new data combined with an appropriated method allows us to obtain realistic simulations of the ground motion that would be generated in the city of Nice by a magnitude 5.7 earthquake occurring on the Blausasc fault.

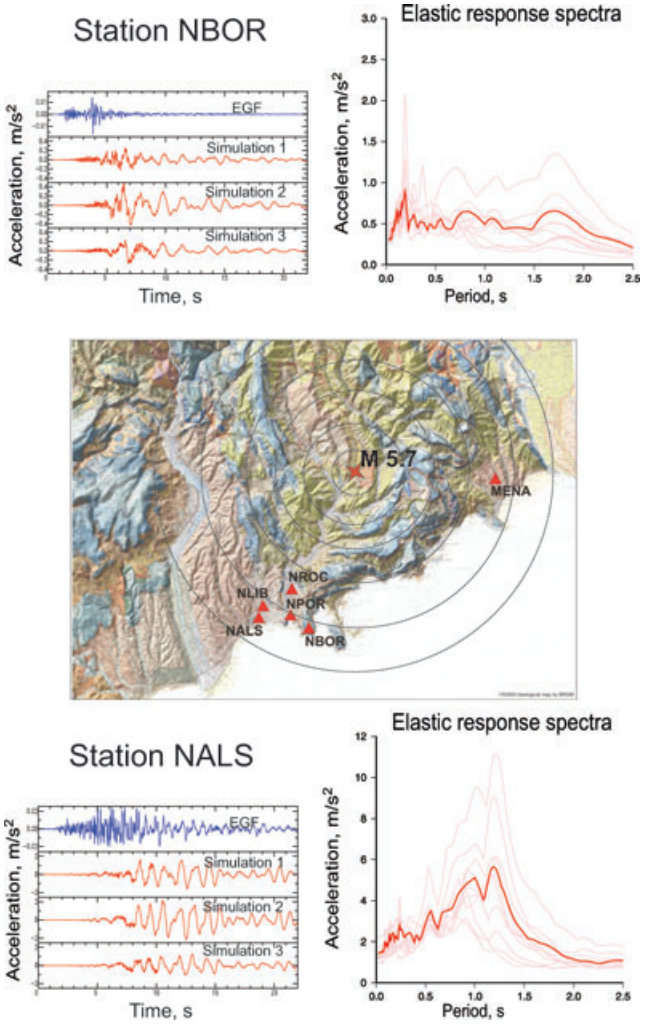


Figure 15. Ground motion simulations for a moderate size earthquake ($M = 5.7$) generated on the Blausasc fault, on two stations located in the city of Nice: NBOR is a rocksite station and NALS is situated on alluvial deposits. We present the North-South accelerograms that correspond to the small event taken as Empirical Green's Function (blue line), and three different simulations of the $M_w = 5.7$ earthquake (red line). The elastic response spectra are shown for 10 different simulations and for the average value over 500 simulations (bold red line). The stress-drop ratio between the small and the large event is taken equal to 1.

7 SYNTHESIS AND DISCUSSION

Due to the combination of absolute location and relative relocation, we have shown the existence of two until-now-unknown structures. The larger one (8 km long) trends N20° with a 70° dip to the west, and the smaller one (600 m long) trends N120°.

Referring to the long-term deformation of the region, left-lateral strike-slip faulting along N–NE fractures appears to be the dominant mechanism of deformation in this area. This is attested by the main alignment of epicentres of the 2000 December sequence, by the mechanism of the 1999 November event (Courboulex *et al.* 2001), and by the Peille-Laghet fault plane striations (Larroque *et al.* 2001). This tectonic regime is consistent with the strike-slip faulting stress field determined by Madeddu *et al.* (1997) and Baroux *et al.* (2001) SE of the Argentera Massif, with a NNW–SSE trending σ_1 axis. Nevertheless, although the N120° direction does not correspond to

© 2007 The Authors, *GJI*, **170,** 387–400
Journal compilation © 2007 RAS

major structures in the field, it is also very interesting because it fits the direction of the small alignment of earthquakes revealed by the relative relocation of the earthquakes of family 1 (Fig. 8c). These two families of earthquake alignments display a pattern of fractures formed by a simple shear deformation regime (e.g. Sylvester 1988, and inset on Fig. 8c): the main shear trends N20° and the antithetic Riedel fractures trends N120°. Consequently, we conclude that both planes have certainly been activated in the meantime or successively during the sequence.

Both faults were activated during the Blausasc sequence but we could not identify without doubt which of them generated the two main events. We tried here to detect an eventual directivity effect of the main shock rupture process that could help us to choose which fault was responsible for the main event. We tried first to invert the near field waveforms of the closest broad-band stations by a non-linear method (B. Delouis, personal communication, 2004), and then to apply an empirical Green's function deconvolution method (Courboulex *et al.* 1999). Unfortunately, neither of these methods gave us a reliable result.

One other interesting feature of this seismic sequence is the migration of seismicity that was observed. Indeed, events migrated from the North in 2000 November to the South in 2000 December. They went across a 1-km-wide gap that could be due to the presence of a barrier (Das & Aki 1977), transmitting stresses without slipping, or an asperity (Lay & Kanamori 1981), aseismically slipping. The smaller N120° fault was not active at the beginning of the Blausasc sequence and appears to have been activated by the conjugated N20° structure. Therefore, we are faced with the stress transfer problem between faults.

The energy repartition indicates that the Blausasc sequence is not a classical main shock-aftershock sequence. It could be a swarm (Scholtz 2002), and the influence of fluids could be important in this case. Indeed, the precipitation during the 2 months (2000 October, November) preceding the Blausasc sequence was four to five times greater than the monthly averages over the last 35 yr (Chamoux 1997). Nevertheless, the *b* value that was seen to be close to 1 (Fig. 7a) is not in good agreement with observations in many other studies that have shown unusually large *b* values when the presence of fluids is important (Scholtz 1968; Sykes 1970).

On a regional scale, the western part of the southern subalpine ranges, the Durance fault and the Trévaresse fault, display some very different features compared to the Blausasc fault, despite a similar state of stress (Baroux *et al.* 2001) and a similar geological setting (Sébrier *et al.* 1997; Chardon & Bellier 2003). For instance, the Moyenne Durance fault (located 150 km west of Nice) is probably the most active fault in the recent past. It is characterized by four historical earthquakes (MSK intensity $>$ VII) since 1509 (Levret *et al.* 1994), and by palaeoseismic events that produced more than one meter of reverse faulting displacement between 27 000 and 9000 BP (Sébrier *et al.* 1997). The instrumental seismicity is low in the area of Durance and Trévaresse, and the present-day deformation rate measured by geodesy is higher in the Nice arc (Ferhat *et al.* 1998; Calais *et al.* 2000). Therefore, the historical seismicity and palaeoseismic events are stronger and more numerous in the West than in the Blausasc area. Is this an indication that the next major earthquake in the southern alpine ranges could occur along the Blausasc fault or a neighbouring fault? This remark also refers to the seismic cycle, which remains a questionable theory in such a region of low deformation rate and strong structural heritage.

8 CONCLUSIONS

The new data collected during this experiment are important for seismic hazard estimation. First of all, this experiment points out that in such a region, a large part of the microseismicity cannot be detected and precisely located by permanent networks. Only a very dense seismic network allows us to underline the active structures.

Despite the difficulties in understanding the relationships between the tectonic evolution and the present-day seismic pattern in a complex geological area with low deformation rate, the results of the SALAM experiment allowed us to identify a new active fault, called the Blausasc fault. We propose that this active fault, set in the crystalline basement, is now hidden by the décollement of the sedimentary cover that occurred 8–5 Ma during the emplacement of the Nice arc. It attests that in the setting of fold and thrust belts there is not necessarily a direct relationship between the faults mapped at the surface and the potential seismic sources. It also highlights the importance of inherited structures in a complex intraplate surrounding.

The Blausasc fault is located at only 10 km from densely populated cities like Nice and Monaco and must be taken into account for seismic hazard assessment. These data enabled us to estimate what the ground acceleration could be in two points of the city of Nice if an earthquake of magnitude 5.7 occurs on this fault. The acceleration values obtained using the stochastic empirical Green's function summation method leads us to believe that such a moderate event would have important consequences on the French Riviera. It is important to remind oneself that the strong motion simulation presented in this study corresponds to a case where only the part of the fault that is known is activated, and that there is the possibility of having a much larger event in this zone. The consequences of such an earthquake would be dramatic, especially if cities are not prepared for such a catastrophe.

ACKNOWLEDGMENTS

We first thank S. Vidal for his role in the data acquisition. We thank Y. Hello and A. Anglade for their involvement in the marine part of the study. We also thank D. Baumont, S. Gaffet, B. Hustedt, A. Lomax, B. Marcaillou, T. Monfret, J-M Noquet, C. Pambrun, R. Pillet, C. Vallet and M. Vergnolle for their help during the field experiment, and E. Calais, B. Delouis and C. Beauval for fruitful discussions. This paper has been enhanced thanks to the remarks of Emmanuel Baroux and an anonymous reviewer. This work was funded by PNRN, ACI Catnat and MEDD thought RDT program. Publication no. 865 of Géosciences Azur.

REFERENCES

Arthaud, F. & Matte, P., 1975. Les décrochements tardi-hercynien du Sud-Ouest de l'Europe. Géométrie et essai de reconstitution des conditions de la déformation, *Tectonophysics,* **25,** 139–171.

Bakun, W. & Scotti, O., 2004. Regional intensity attenuation models for France and the estimation of magnitude and location of historical earthquakes. SCF-4, XXIX General Assembly of the European Seismological Commission, P6271, GFZ Postdam.

Baroux, E., Béthoux, N. & Bellier, O., 2001. Analyses of the stress field in southeastern France from earthquake focal mechanisms, *Geophys. J. Int.,* **145**, 336–348.

© 2007 The Authors, *GJI*, **170,** 387–400
Journal compilation © 2007 RAS

Beeler, N.M., Wong, T.F. & Hickman, S.H., 2003. On the expected relationships between apparent stress, static stress drop, effective shear fracture energy and seismic efficiency, *Bull. Seism. Soc. Am.,* **93**, 1381–1389.

Bertil, D., Béthoux, N., Campillo, M. & Massinon, B., 1989. Modeling crustal phases in southeast France from focal depth determination, *Earth Planet. Sci. Lett.,* **95**, 341–358.

Bogdanoff, S., Michard, A., Poupeau, G. & Mansour, M., 2000. Apatite fission track analysis in the Argentera massif: evidence of contrasting denudation rates in the external crystalline massifs of the western alps, *Terra Nova,* **12**, 117–125.

Bossolasco, M., Cicconi, G., Eva, C. & Pascale, V., 1972. La rete sismica dell'Istituto Geofisico di Genova e primi risultati sulla sismotettonica delle Alpi Maritime Occidentale e del Mar Ligure, *Riv. Ital. Geofis.,* **21**(5–6), 229–247.

Bulard, P.F. *et al.,* 1975. Sur la genèse des structures de l'Arc de Nice, *Bull. Soc. Géol. de France,* **XVII**(7), 6,939–944.

Calais, E. *et al.,* 2000. Crustal strain in the southern Alps, France, 1948–1998, *Tectonophysics,* **319**, 1–17.

Calais, E., Nocquet, J.M., Jouanne, F. & Tardy, M., 2002. Current extension in the central part of the western Alps from continuous GPS measurements, 1996–2001, *Geology,* **30**(7), 651–654.

Chamoux, C., 1997. *Structure spatiale des précipitations sur les Alpes Maritimes aux échelles mensuelle et annuelle. Mémoire de Maîtrise de Géographie Physique*, Université de Nice-Sophia Antipolis, 100 pp.

Chardon, D. & Bellier, O., 2003. Geological boundary conditions of the 1909 Lambesc (Provence, France) earthquake: structure and evolution of the Trévaresse ridge anticline, *Bull. Soc. Géol. Fr.,* **174**(5), 497–510.

Courboulex, F., Deichmann, N. & Gariel, J.C., 1999. Rupture Complexity of a moderate intraplate earthquake in the Alps: the 1996 M5 Epagny-Annecy Earthquake, *Geophys. J. Int.,* **139**, 152–160.

Courboulex, F, Duval, A.M., Deschamps, A., Lomax, A. & Larroque, C., 2001. All the small Peille (Alpes Maritimes, France) earthquake can teach us, *C. R. Acad. Sc. Paris,* **333**, 105–112.

Courboulex, F., Larroque, C., Deschamps, A., Gélis, C., Charreau, J. & Stéphan, J.F., 2003. An unknown active fault revealed by microseismicity in the south-east of France, *Geophys. Res. Lett.,* **30**(15), 1782, doi:10.1029/2003GL017171.

Dardeau, G., 1988. Tethyan evolution and alpine reactivation of Jurassic extensional structures in the French "Alpes Maritimes", *Bull. Soc. Géol. de France,* **4**(8), 651–657.

Das, S. & Aki, K., 1977. Fault planes with barriers : a versatile earthquake model, *J. Geophys. Res.,* **82**, 5658–5670.

Debran-Passard, S., Courbouleix, S. & Lienhardt, M.J., 1984. Synthèse géologique du Sud-Est de la France. Mémoire BRGM Fr. n°125, 615 pp.

De Graciansky, P.C. & Lemoine, M., 1988. Early Cretaceous extensional tectonics in the southwestern French Alps : a consequence of North Atlantic rifting during Tethyan spreading, *Bull. Soc. Géol. de France (8),* **IV**(5), 733–737.

De Graciansky, P.C., Dardeau, G., Lemoine, M. & Tricart, P., 1989. The inverted margin of the French Alps and foreland basin inversion, Inversion Tectonics, *Geol. Soc. Spec. Publ.,* **44**, 87–104.

DeMets, C., Gordon, R., Argus, D. & Stein, S., 1994. Effect of recent revisions to the geomagnetic reversal time scale on estimates of current plate motions, *Geophys. Res. Lett.,* **21**, 2191–2194.

Dercourt, J. *et al.,* 1986. Geological evolution of the Tethys belt from Atlantic to Pamirs since the Lias, *Tectonophysics,* **123**, 241–315.

Dewey, J., Helman, M., Turco, E., Hutton, D. & Knott, S., 1989. Kinematics of the western Mediterranean, in *Alpine Tectonics*, Vol. **45**, pp. 265–283, eds M. Coward, D. Dietrich & G. Parks, Geol. Soc. Spec. Publ.

Duval, A.-M., 1994. Détermination de la réponse d'un site aux séismes à l'aide du bruit de fond, *PhD thesis*, Université Pierre et Marie Curie, Paris, France.

Duval, A.-M., Méneroud, J.-P. & Vidal, S., 1999. La méthode "H/V bruit de fond" et ses applications aux études d'effet de site, Monographies d'Etudes et Recherches du réseau des LPC 96–97, pp 22–25 (document n°502 897), LCPC Publisher, Paris, France.

Edel, J.B., Dubois, D., Marchant, R., Hernandez, J. & Cosca, M., 2001. La rotation miocène inférieure du bloc corso-sarde; nouvelles contraintes paléomagnétiques sur la fin du mouvement, *Bull. Soc. Géol. Fr.,* **172**(3), 275–283.

Eva, E. & Solarino, S., 1998. Variations of stress directions in the western Alpine arc, *Geophys. J. Int.,* **135**, 438–448.

Eva, C. & Rabinovich, A.B., 1997. The Febuary 23, 1887 tsunami recorded on the Ligurian coast, western Mediterranean, *Geophys. Res. Lett.,* **24**, 2211–2214.

Ferhat, G., Feigl, K., Ritz, J.F. & Souriau, A., 1998. Geodetic measurement of tectonic deformation in the southern Alps and Provence, France, 1887–1994, *Earth Planet. Sci. Lett.,* **159**, 35–46.

Ferrara, G. & Malaroda, M., 1969. Radiometric age of granitic rocks from the Argentera massif (Maritime Alps), *Boll. Soc. Geol. It.,* **88**, 311–320.

Ferrari, G., 1991. The 1887 Ligurian earthquake: A detailed study from contemporary scientific observations, *Tectonophysics,* **193**, 131–139.

Fréchet, J., 1985. Sismogénèse et doublets sismiques. Thèse d'Etat, Univ. Sci. Technol. Médic. Grenoble, 207 pp., *PhD thesis*.

Gauberti, P., 1973. Peille, son histoire (3 tomes), unpublished book.

Gèze, B., 1960. La genèse néogène de l'arc de Nice. C.R. somm. Soc. Géol. de France, 33–34.

Grellet, B., Combes, P., Granier, T. & Philip, H., 1993. *Sismotectonique de la France métropolitaine*, Mémoire H.S. Soc. Géol. de France, 164, 1, 76 pp.

Got, J.L., Fréchet, J. & Klein, F.W., 1994. Deep fault plane geometry inferred from multiplet relative relocation beneath the south flank of Kilauea, *J. Geophys. Res.,* **99**(B8), 15 375–15 386.

Gutenberg, R. & Richter, C.F., 1944, Frequency of earthquakes in California, *Bull. Seismol. Soc. Am.,* **9034**, 185–188.

Hartzell, S., 1978. Earthquakes aftershocks as Green's functions, *Geophys. Res. Lett.,* **5**, 1–4.

Haskov, J. & Ottenmöller, L., 1999. SEISAN earthquake analysis software, *Seismol. Res. Lett.,* **70**, 532–534.

Kanamori, H., & Rivera, L., 2004. Static and dynamic scaling relations for earthquakes and their implications for rupture speed and stress drop, *Bull. Seismol. Soc. Am.,* **94**, 314–319.

Hoang Trong, P., Haessler, H., Holl, J.M. & Legros, Y., 1987. L'essaim sismique (Oct. 83–Jan. 84) de la moyenne vallée de la Roya (Alpes Maritimes): Activité récente d'un ancien système de failles conjuguées?, *C.R. Acad. Sci. Paris,* **304**, 419–424.

Kafka, A.L. & Levin, S.Z., 2000. Does the spatial distribution of smaller earthquakes delineate areas where larger earthquakes are likely to occur?, *Bull. Seismol. Soc. Am.,* **90(3)**, 724–738.

Kerckhove, C., 1969. La "zone du Flysch" dans les nappes de l'Embrunais-Ubaye (Alpes Occidentales), *Géol. Alpine,* **45**, 1–202.

Kohrs-Sansorny, C., Courboulex, F., Bour, M. & Deschamps, A., 2005. A two-stage method for ground-motion simulation using stochastic summation of small earthquakes, *Seismol. Soc. Am.,* **95**, 1387–1400.

Lambert, J. & Levret, A., 1996. *Mille ans de séismes en France*, Ouest Editions Presses Académiques, Nantes, 120 pp.

Larroque, C. *et al.,* 2001. Active deformation at the junction between southern French Alps and Ligurian basin, *Netherlands J. Geosci.,* **80**, 255–272.

Laurent O, Stéphan, J.F. & Popoff, M., 2000. Modalités de la structuration miocène de la branche sud de l'arc de Castellane (chaînes subalpines méridionales), *Géologie de la France,* **3**, 33–65.

Lay, T. & Kanamori, H., 1981. An asperity model of great earthquake sequences. in *Earthquake Prediction, an International Review; M. Ewing Ser. 4*, pp. 579–592, eds D. Simpson & P. Richards, American Geophysical Union, Washington, DC

Levret, A., Backe, J.C. & Cushing, M., 1994. Atlas of macroseismic maps for French earthquakes with their principal characteristics, *Nat. Haz.,* **10**, 19–46.

Maddedu, B., Béthoux, N. & Stéphan, J.F., 1997. Champ de contrainte postpliocène et déformations récentes dans les Alpes sud-occidentales, *Bull. Soc. Géol. de France,* **167**(6), 797–810.

Malaroda, R., Carraro, F., Dal Piaz, G., Franceschetti, B., Sturani, C., & Zanella, E., 1970. Carta geologica del Massiccio dell'Argentera alla scala 1/50 000, *Note illustrative Mem. Soc. Geol. It.,* **9**, 557–663.

Malavieille, J. & Ritz, J.F., 1989. Mylonitic deformation of evaporites in décollements: examples from Southern Alps, *France. J. Struc. Geol.,* **11**, 583–590.

Marini, M., 1987. Le deformazioni fragili del Pliocene Ligure; implicazioni nella geodynamica Alpina, *Mem. Soc. Geol. Ital.,* **29**, 157–169.

McKenzie, D., 1969. The relation between fault plane solutions for earthquakes and the directions of the principal stresses, *Bull. Seism. Soc. Am.,* **59**, 591–601.

Montigny, R., Edel, J.B. & Thuziat, R., 1981. Oligo-Miocene rotation of Sardinia : K-Ar and paleomagnetic data of tertiary volcanics, *Earth Planet. Sci. Lett.,* **54**, 261–271.

Mueller, B., Zoback, M.L., Fucks, K., Mastin, L., Gregersen, S., Pavoni, N., Stephansson, O. & Ljunggreen, C., 1992. Regional patterns of tectonic stress in Europe, *J. Geophys. Res.,* **97**, 11 783–11 803.

Nocquet, J.M. & Calais, E., 2003. Crustal velocity field of Western Europe from permanent GPS array solutions, 1996–2001, *Geophys. J. Int.,* **154**, 72–88.

Pauchet, H., Rigo, A., Rivera, L. & Souriau, A., 1999. A detailed analysis of the February 1996 aftershock sequence in the eastern Pyrenées, France, *Geophys. J. Int.,* **137**, 107–127.

Perez, J.L., 1975. La zone limite entre l'arc de Nice et l'arc de la Roya (Alpes Maritimes). Observations structurales. *Bull. Soc. Géol. de France,* **XVII**(7), 930–938.

Perrot, J. *et al.,* 2005. Analysis of the *M*w 4.3 Lorient earthquake sequence: a multidisciplinary approach to the geodynamics of the Armorican Massif, westernmost France, *Geophys. J. Int.,* **162**, 935–950.

Rebaï S., Philip H & Taboada, A., 1992. Modern tectonic stress field in the Mediterranean region : evidence for variation in stress direction at different scales, *Geophys. J. Int.,* **110**, 106–140.

Riccou, L.E. & Siddans, A., 1986. Collision tectonics in the western Alps, in *Collision Tectonics*, pp. 229–244, eds. M. Coward & A.C. Ries, Geol. Soc. Spec. Publ., 19.

Ritz, J.F., 1992. Tectonique récente et sismotectonique des Alpes du Sud, analyse en terme de contraintes, *Quaternaire,* **3**, 111–124.

Rollet, N., Déverchère, J., Beslier, M.O., Guennoc, P., Réhault, J.P., Sosson, M. & Truffert, C., 2002. Back arc extension, tectonic inheritance and volcanism in the Ligurian Sea, western Mediterranean, *Tectonics,* **21**(3), doi:10.1029/2001TC900027.

Scholtz, C.H., 1968. The frequency-magnitude relation of microfracturing in rock and its relation to earthquakes, *Bull. Seismol. Soc. Am.,* **58**, 399–415.

Scholtz, C.H., 2002. *The Mechanics of Earthquakes and Faulting*, 2nd edn, 471 pp, Cambridge University Press, Cambridge, United Kingdom.

Scotti, O. & Levret, A., 2000. How to calculate seismic parameters for large offshore historical earthquakes, Abstracts, ESC XXVII general assembly, Lisbon, Portugal, 10–15 September 2000 40.

Sébrier, M., Ghafiri, A. & Blès, J.L., 1997. Paleoseismicity in France: fault trench studies in a region of moderate seismicity, *J. Geodyn.,* **24**, 207–217.

Sella, G.F., Dixon, T.H. & Mao, A., 2002. REVEL: A model for recent plate velocities from space geodesy, *J. Geophys. Res.,* **107**(B4), doi: 10.1029/2000JB000033.

Semblat, J-F., Duval, A.-M. & Dangla, P., 2000. Numerical analysis of seismic wave amplification in Nice (France) and comparisons with experiments, *Soil Dyn. Earthquake Eng.,* **19**, 347–362.

Siddans, A., 1979. Arcuate fold patterns in the subalpine chains of Southeast France, *J. Struc. Geol.,* **1**, 117–126.

Sisfrance Historical Data Base, http://www.sisfrance.net/.

Souriau, A., Sylvander M, Rigo, A., Fels, J.F., Douchain, J.M. et Ponsolles, C. (2001). Sismotectonique des Pyrénées: principales contraintes sismologiques, *Bull. Soc. Géol. France,* **172**(1), 25–39.

Sykes, L.R., 1970. Earthquake swarms and sea-floor spreading, *J. Geophysic. Res.,* **75**, 6598–6611.

Sylvester, A., 1988. Strike-slip faults, *Geol. Soc Am. Bull.,* **100**, 1666–1703.

Thouvenot, F., Frechet, J., Jenatton, L. & Garmond, J.F., 2003. The Belledone border Fault: Identification of an active seismic strike-slip fault in the western Alps, *Geophys. J. Int.,* **155**, 174–192.

Tricard, P., 1984. From passive margin to continental collision: a tectonic scenario for the western Alps, *Am. J. Sci.,* **284**, 97–120.

Vigny, C. *et al.,* 2002. GPS network monitors the western Alps: deformation over a five-year period: 1993–1998, *J. Geodesy,* **76**, 63–76.

Wells, D.L. & Coppersmith, K.J., 1994. New empirical relationships among magnitude, rupture length, rupture width, rupture area, and surface displacement, *Bull. Seismol. Soc. Am.,* **84**, 974–1002.

Working Group CPTI, 1999. Catalogo Parametrico dei Terremoti Italiani, ING, GNDT, SGA, SSN, Compositori Eds, Bologna, 1999, ISBN 88-7794-201-0, 92 pp.

© 2007 The Authors, *GJI*, **170,** 387–400
Journal compilation © 2007 RAS

2.5 Conclusions

Des informations très importantes peuvent être obtenues sur les failles actives à partir de la position des épicentres des séismes. Les points principaux mis en évidence dans les études présentées dans ce chapitre sont :

- La complexité des réseaux de faille mis en jeu. Dans les deux cas (Colfiorito et Blausasc) il ne s'agit pas d'une seule faille mais d'un réseau de failles qui a joué. Ceci est particulièrement intéressant pour le séisme de Blausasc où l'on observe un alignement de la sismicité presque perpendiculaire à l'alignement principal. Ce comportement a été observé lors de quelques séismes récents comme le séisme de Totori au Japon [*Fukuyama et al.*, 2003] ou le séisme d'Al Hoceima au Maroc [*Tahayt et al.*, 2009].

- La migration de la sismicité tout au long de la crise. Celle ci est extrêmement nette sur Cofiorito, elle est également très claire sur la crise de Blausasc. Il est probable que les fluides jouent un rôle majeur dans cette migration.

- La déconnection possible entre ce que l'on voit en surface (affleurement de la faille) et ce qui se passe en profondeur. Dans les régions où la couverture sédimentaire a glissé sur le socle (principalement au miocène dans la région qui nous intéresse), il peut y avoir un décalage de quelques kilomètres (ici 2 km) entre la faille visible en surface qui est alors uniquement la partie décapitée inactive et la structure de profondeur. Cette hypothèse défendue dans notre article publié dans le *Geophysical Journal International* et dans le *Geophysical Research Letters* est réellement le fruit d'une approche pluridisciplinaire. Elle montre la force du travail en équipe mais également les limitations de l'analyse des structures de surface dans la quantification de l'aléa sismique.

- L'apport certain des réseaux sismologiques denses pour visualiser finement le déroulement d'une crise sismique.

- L'utilité du travail pluridisciplinaire.

CHAPITRE 3

Simulation des mouvements du sol : DES PETITS SEISMES POUR PREVOIR LES GROS

3.1 Introduction

L'inversion de la source sismique est un domaine passionnant, l'étude de la micro sismicité et de la géodynamique d'une zone l'est tout autant ; oui mais comment replacer ce travail pointu et fondamental dans le réel ? Comment relier ces processus naturels aux destructions et aux milliers de victimes causées chaque année par les tremblements de Terre ? Comment ce métier pouvait il aussi me relier à la réalité et aux humains ?

C'est en discutant avec Anne-Marie Duval du CETE Méditerranée, Myriam Bour du BRGM et l'équipe du BERSIN de l'IRSN (Oona Scotti, Catherine Berge, David Baumont) que j'ai peu à peu compris où se plaçait notre travail de sismologue par rapport aux prises de décisions réelles (zonage règlementaire, plan de prévention des risques, normes parasismiques) : la distance est énorme ! En participant à quelques réunions du groupe « mouvement du sol » de l'AFPS (association française du génie parasismique) alors animé par Catherine Berge j'ai compris qu'il y avait un domaine dans lequel je pouvais apporter une contribution : celui de la simulation des mouvements du sol. En effet, lorsqu'il s'agit de tester en dynamique la résistance d'un pont par exemple, les ingénieurs des structures ont besoin de signaux réalistes. Ils puisent en général alors dans des bases de données de mouvements forts, cherchant la trace d'un séisme de magnitude donnée enregistré à la même distance. Cependant ce tracé ne tient pas compte des conditions de propagation des ondes dans la zone, ni des effets de site.

L'idée de se servir des enregistrements des petits séismes pour simuler les signaux des séismes plus importants vient tout d'abord d'Hartzell [1978], puis a été développée par de nombreux auteurs et en particulier Irikura et son groupe au Japon [*Irikura*, 1983; 1986]. En France, Myriam Bour avait notamment effectué sa thèse sous la direction de Michel Cara à l'université de Strasbourg sur ce sujet, avant de travailler au BRGM [*Bour*, 1993; *Bour and Cara*, 1997]. Après discussion avec elle, nous avons convenu de proposer un sujet de thèse. L'idée était de profiter de nos deux expériences de fonctions de Green empiriques (elle pour les mouvements forts et moi pour la source) pour tenter de proposer une méthode, pourquoi pas, opérationnelle. Nous avons trouvé un financement de la région PACA et de la société ANTEA pour cette thèse. C'est Carine Kohrs-Sansorny qui a travaillé sur le sujet. A l'occasion de cet encadrement de thèse, j'ai été amenée à me familiariser avec des représentations peu utilisées en sismologie comme le spectre de réponse élastique, le PGA, le PGV, l'intensité d'Arias et bien d'autres. Plus récemment, une autre rencontre, celle de Céline Beauval, m'a aidée à me plonger dans un domaine qui m'était inconnu : celui de l'aléa sismique probabiliste. Nous avons entrepris un travail en commun pour tenter de combiner la méthode de simulation des mouvements du sol par EGF que nous avions développée et le calcul de l'aléa probabiliste. Les résultats obtenus sont prometteurs mais encore préliminaires. Ce travail s'est effectué avec Laetitia Honoré lors de son stage de master 2. Laetitia est actuellement en thèse sous ma direction.

Ce chapitre présente :

- Une brève introduction aux méthodes de simulation des mouvements du sol.
- La méthode de simulation des mouvements du sol SIMULSTOC
- Les tests de validation que nous avons effectués sur différentes bases de données réelles et en particulier les données du réseau RAP de Guadeloupe lors de la crise des Saintes de 2004.
- La méthode hybride EGF-probabiliste et un exemple d'application à la crise des Saintes.
- La simulation d'un séisme majeur en aveugle

3.2 Simulation des mouvements du sol

Il existe plusieurs pistes de travail lorsque l'on souhaite simuler les mouvements du sol dus à un séisme futur dans une zone.

La première consiste à utiliser des relations empiriques construites à partir des bases de données réelles (voir l'article de revue de Douglas [2003], Figure 3. 1 à droite). Le nombre et la qualité des stations sismologiques ayant considérablement augmenté dans le monde ces dernières années, ces bases de données sont de plus en plus étoffées. Les bases de données les plus riches étant certainement celles du Japon (Kiknet et Calnet), de Californie et de Taiwan. De nombreux articles sont régulièrement publiés pour proposer des nouvelles relations d'atténuation (appelées plus justement Empirical Ground Motion Prediction Models) qui prennent en compte des paramètres de plus en plus précis : type de mouvement sur la faille (normal, inverse, décrochant), Vs30 (vitesse des ondes S à 30 mètres), effet de directivité possible, et qui couvrent des zones nouvelles (voir le numéro spécial numéro 24 de la revue Earthquake Spectra de Février 2008). Dans les zones où la sismicité est faible ou modérée, il est toujours difficile d'établir ces lois. Certains proposent de travailler sur les mouvements faibles [*Drouet et al.*, 2005]. Cette piste est intéressante mais l'extrapolation des mouvements faibles aux mouvements forts n'est pas facile [*Cotton et al.*, 2008]. L'affinement des relations d'atténuation est une contribution indispensable à la définition de l'aléa sismique d'une zone. C'est en particulier un ingrédient essentiel dans la mise en œuvre d'un calcul probabiliste (nous le verrons plus loin). Cependant cette approche ne permet pas de produire des sismogrammes (ou accélérogrammes), elle ne permet pas de prendre efficacement en compte les effets de site, surtout lorsqu'ils sont complexes (effet topo, effet 3D, effets non linéaires).

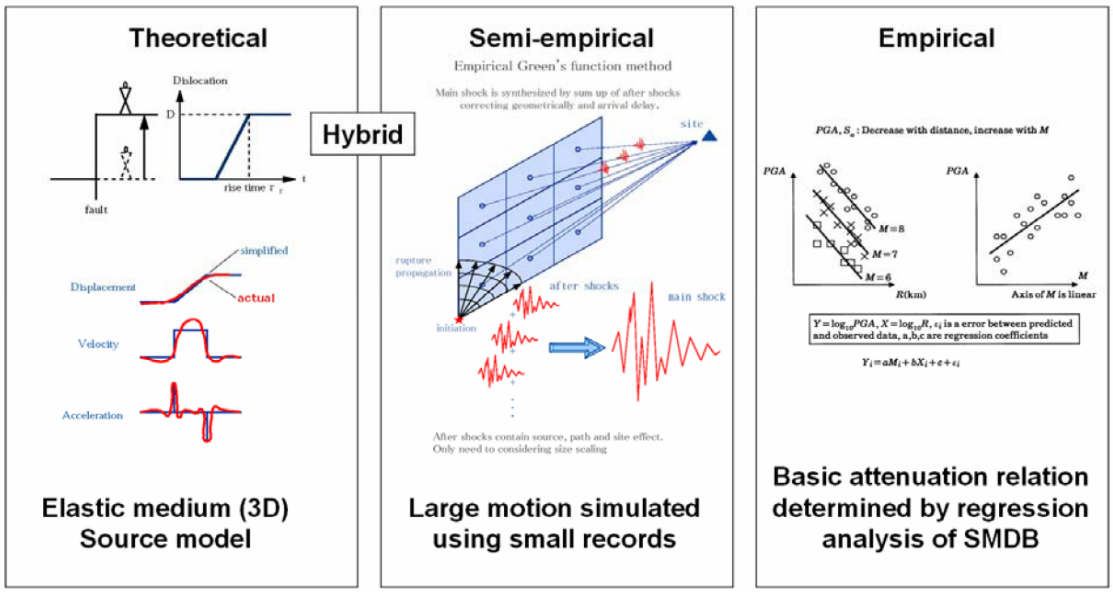


Figure 3. 1 : Trois types d'approches pour simuler le mouvement du sol engendré par un séisme (d'après une figure de Bruno Hernandez).

Une autre approche consiste à simuler des signaux de façon purement numérique (Figure 3. 1, à gauche). Les différentes méthodes qui existent (différences finies, éléments finis, éléments spectraux …), combinées avec des moyens de calcul toujours plus performants permettent dans certains cas d'obtenir des simulations à des fréquences relativement élevées : 1 à 2 Hz. L'avantage de cette approche est qu'elle permet de maitriser toutes les étapes du calcul, et ainsi de bien comprendre les

limitations imposées. Le projet QSHA (Quantitative Seismic Hazard Assesment) avait pour but de comparer les différentes méthodes de simulations sur des cas canoniques d'abord, puis sur des cas réels. Y ont participé le BRGM, le CEA, le CETE, le LGIT de Grenoble et Géoazur [*Virieux et al.*, 2009]. Les comparaisons des différentes simulations devraient être publiées bientôt. La principale limitation de cette approche réside dans la connaissance du milieu de propagation 3D. Ceci est d'autant plus important que l'on cherche à modéliser les hautes fréquences du signal sismique.

Une approche alternative consiste à combiner des données empiriques et la modélisation. Il s'agit vous le devinez d'utiliser des petits séismes comme fonctions de Green empiriques (Figure 3. 1, au centre). A l'inverse du travail présenté dans le chapitre 1, la fonction de Green empirique servira cette fois ci à représenter le mouvement du sol, au lieu de l'éliminer.

3.3 La méthode stochastique SIMULSTOC

Il était prévu lors de la thèse de Carine Kohrs-Sansorny de développer un code de simulation de fonctions de Green empiriques qui prenne en compte la cinématique de la source, dans la ligne du code développé préalablement par Myriam Bour dans sa thèse. C'est donc la première piste qui a été explorée et abondamment testée dans la thèse de Carine Kohrs-Sansorny [*Kohrs-Sansorny*, 2005].
Cependant, cette approche ne permettait pas d'obtenir une bonne reproduction à la fois des basses fréquences, des fréquences intermédiaires et des hautes fréquences. Carine Kohrs-Sansorny s'est alors tournée vers d'autres types de méthodes liant une approche stochastique avec des fonctions de Green empiriques. L'approche en deux étapes que nous avons retenue est inspirée par un article d'Ordaz [1995] lui-même inspiré des travaux de [*Joyner and Boore*, 1986] et de [*Wennerberg*, 1990]. L'idée n'est plus de chercher à simuler la source d'un séisme en particulier mais plutôt de simuler tous les accélérogrammes qui auraient pu être générés par un séisme de magnitude fixée sur une faille identifiée, à un endroit donné (en incluant des processus de rupture divers). C'est un point de vue totalement différent. Nous n'allons pas chercher à reproduire la forme d'onde dans ses détails en précisant un modèle de rupture unique mais une multitude de solutions possibles.

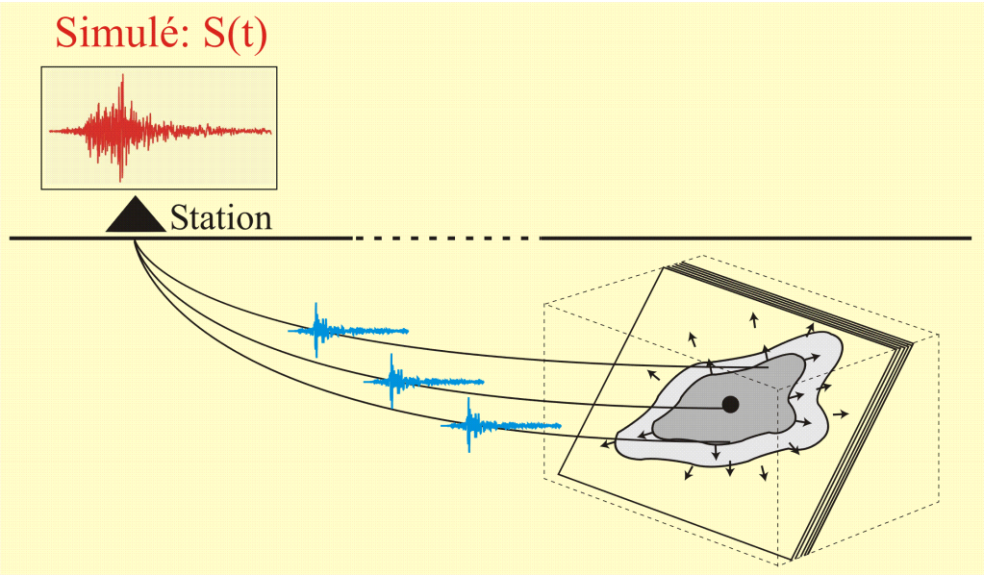


Figure 3. 2 : Principe de la simulation de mouvements forts par la méthode des fonctions de Green empiriques : l'enregistrement d'un petit séisme est combiné sur un plan de faille pour générer, à une station donnée, le signal d'un séisme plus fort.

Le code SIMULTOC génère 500 fonctions source équivalentes (ESTF) à l'aide d'un tirage aléatoire de points suivant une densité de probabilité dont la forme a été proposée par Ordaz [1995] pour permettre une bonne adéquation avec le modèle de Brune en oméga ω^{-2}. La largeur de la fonction densité de probabilité sera fonction du paramètre C, rapport des chutes de contraintes entre le gros et le petit séisme. Le tirage de N^4 points s'effectue en deux étapes (N^2_N^2 ou bien N^3_N ou bien N_N^3), N étant le rapport des moments sismiques entre le petit et le gros séisme. Cette sommation en deux étapes minimise le risque d'avoir des simulations trop semblables (surtout quand la différence de magnitude est importante entre le gros et le petit séisme, et donc le N est grand). Les détails de la méthode ainsi que le mode opératoire sont expliqués en détail dans l'article qui suit.

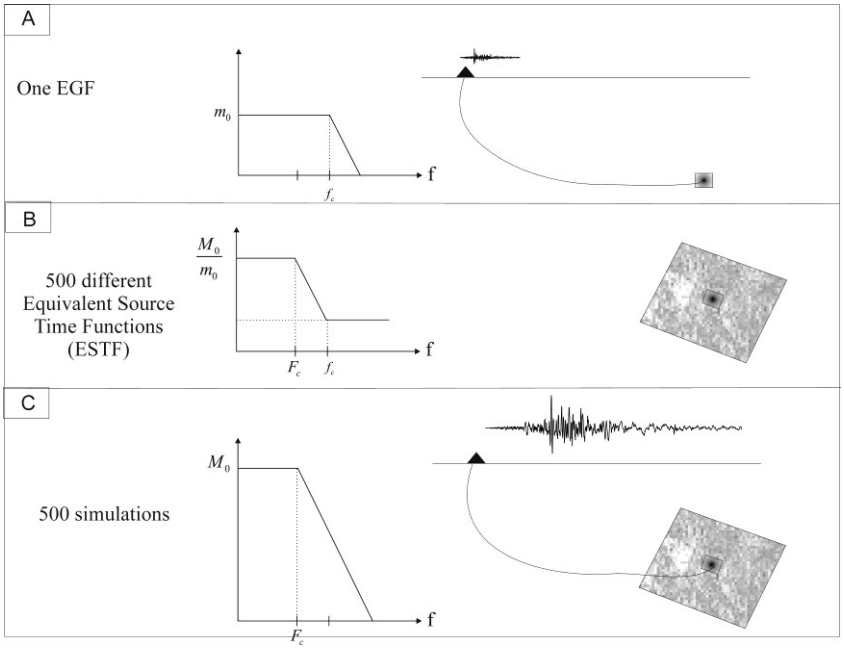


Figure 3. 3 : Principe de la méthode (code SIMULSTOC). A. L'enregistrement d'un petit séisme est considéré comme une fonction de Green empirique (spectre de Brune). B. On construit 500 fonctions sources équivalentes à un séisme de magnitude plus élevée. C. Ces ESTF sont convoluées avec l'EGF pour fournir 500 simulations du mouvement du sol.

Un des avantages de cette méthode est qu'elle nécessite très peu de paramètres d'entrée, contrairement aux autres méthodes habituellement utilisée pour la sommation des EGF [*Pavic et al.*, 2000]. Les premiers paramètres sont faciles à déterminer : il s'agit de la magnitude du séisme à simuler Mw, la magnitude du séisme utilisé comme EGF, mw, et la fréquence de coupure de ce séisme (obtenus sur les données). Le dernier paramètre est le plus délicat : il s'agit du rapport des chutes de contrainte entre le petit séisme et celui que l'on veut simuler. Au premier abord, on pourrait penser que ce rapport devrait être égal à 1. En effet on se trouve sur la même faille, dans un contexte sismotectonique identique, il n'y a, a priori pas de raison pour qu'il y ait des variations. Malheureusement les données nous montrent que ceci est souvent faux (mais pas toujours). Nous discuterons de la détermination de ce paramètre C dans chacun des articles présentés et dans la conclusion.

Bulletin of the Seismological Society of America, Vol. 95, No. 4, pp. 1387–1400, August 2005, doi: 10.1785/0120040211

A Two-Stage Method for Ground-Motion Simulation Using Stochastic Summation of Small Earthquakes

by Carine Kohrs-Sansorny, Françoise Courboulex, Myriam Bour, and Anne Deschamps

Abstract We present a two-stage method to simulate the ground motions produced by an earthquake by using stochastic summation of small earthquakes. In this method, identical small earthquakes are multiplied by a scaling factor and summed together with time delays randomly distributed, during the two stages, over the source duration. The summation scheme is characterized by four fundamental parameters: the number of summed small earthquakes, the scaling factor, and both probability densities of time delays used in the first and second stages. By a proper choice of these parameters, this method generates a large number of synthetic time histories that, on average, agree exactly with the ω^{-2} model in the whole frequency band. The produced time histories are sufficiently realistic and different from each other to be associated with a multitude of rupture processes that could happen during an earthquake. However, because the extended target fault is approximated by a point source, this method does not take into account possible directivity effects and is not appropriate to simulate ground motions for near-source sites. We test this method on the Oaxaca earthquake (1999, M_w 7.5, Mexico) at regional distances and on the two mainshocks of the Umbria Marche crisis (1997, M_w 5.7 and M_w 6.0, Italy) at local distances. We found that the simulated ground motions fit the observed data well, both in time and in frequency domains. Within simulation context, only specification of seismic moment and stress drop is required for the target event. Because the magnitude and then the seismic moment are necessarily specified, the stress drop plays a major role in ground-motion simulation.

Introduction

Estimation of ground motions from a future earthquake is a fundamental step to anticipate the possible damages and then to try to mitigate them. However, in many regions, the subsoil medium is not sufficiently known to simulate the wave's propagation in a relevant frequency band for earthquake-engineering purposes (between 0.1 and 20 Hz). An attractive approach to overcome this problem is to sum the recordings of small earthquakes delayed between each other so as to reproduce the rupture propagation effect. Each of the small-earthquake recordings represents all the propagation effects between the source and the receiver and then is regarded as an empirical Green's function (Hartzell, 1978). This method not only has the advantage of incorporating wave-propagation effects but also site effects. However, it is important to note that this method does not account for eventual nonlinear soil effects.

To simulate realistic source time histories in agreement with the present state of knowledge on source-scaling relations (source parameters and source spectra scaling relations with the ω^{-2} model [Brune, 1970]), the method requires an appropriate summation scheme. Many approaches have been proposed for summing small earthquakes. Some of these approaches, based on a deterministic extended-fault representation (Hutchings, 1994; Irikura and Kamae, 1994; Bour and Cara, 1997) are particularly suitable to simulate a specific rupture process, but consequently they also require a detailed description of the rupture process and then the specification of many poorly constrained source parameters (fault length and width, rupture velocity, position of the nucleation point, etc.) (Pavic *et al.*, 2000). Within the context of future earthquake simulation, in which uncertainty over the parameters is maximal, the stochastic approach is particularly interesting (Joyner and Boore, 1986; Wennerberg, 1990; Ordaz *et al.*, 1995). This approach, based on a point-source representation of the fault requires the specification of only two parameters for the target event: the seismic moment and the stress drop. Of course, many other approaches to simulate the ground motions produced by an earthquake exist. Some of them are particularly relevant because they lead over the ω^{-2} model (e.g., the stochastic method of Boore [1983, 2003] and the k^2 model of Herrero and Bernard [1994]). However, only few of these approaches have been modified

to be combined with empirical Green's functions. In this study, we focus on ground-motion simulation by using stochastic summation of small earthquakes (Joyner and Boore, 1986; Wennerberg, 1990; Ordaz *et al.*, 1995). This approach requires appropriate summation schemes to simulate the rupture process of the target earthquake. Within this framework, different summation schemes have been proposed. First, Joyner and Boore (1986) proposed a single-stage summation scheme. In this scheme, the delays between each small event summed were uniformly generated over the rupture duration of the target event. This study established some fundamental constraints over the summation scheme and, in particular, showed that a scaling factor was required to conform at low and high frequencies to the scaling laws. However, the uniform probability density produced holes at frequencies proportional to the corner frequency and unrealistic time histories. Then, Wennerberg (1990) showed that whatever probability density was used, a single-stage summation scheme was not able to produce a credibly complex source. Therefore, he proposed a summation scheme in two stages, based on a probability density for the time delays characterized by an amplitude spectrum determined by the ratio of ω^{-2} spectra. The time histories produced were more realistic, but included too many high frequencies compared with the expected ω^{-2} model. Finally, Ordaz *et al.* (1995) deduced a probability density, which exactly conforms to the ω^{-2} model, from the single-stage approach and the scaling laws. However, as pointed out by Wennerberg (1990) and Ordaz *et al.* (1995), the limit of this method is the simplicity of the source because of the single-stage approach.

In this article, we propose to deduce from the two-stages approach and the scaling laws, a summation scheme that produces time histories that are not only more realistic than those produced by a classical single-stage approach, but also are exactly in agreement with the ω^{-2} model in the whole frequency band. This summation scheme, inspired by the studies described previously (Joyner and Boore, 1986; Wennerberg, 1990; Ordaz *et al.*, 1995) is characterized by the following summation parameters: the number of summed small events, the scaling factor, and the probability densities of time delays used in the first and second stages. We assume that a single small-event record represents the Green's function for all points of the rupture area of the large earthquake. Then this method is only efficient in a context where the shortest distance between source and receiver is sufficiently large compared with the source dimensions and with the maximal wavelength we consider (far-field condition). After presenting our new method, we show some tests on both numerical and observed data.

Method

Presentation of the Summation Scheme in Two Stages

Using a small event (with associated seismic moment m_0 and corner frequency f_c) as empirical Green's function, our goal is to generate a multitude of possible time histories representative of a target event (seismic moment M_0, corner frequency F_c) and in agreement with the ω^{-2} model. We propose a random summation scheme in two independent stages inspired by the works of Joyner and Boore (1986), Wennerberg (1990), and Ordaz *et al.* (1995). In the first stage, a small number η_c of delays t_c are randomly generated with a probability density $\rho_c(t)$ over the whole source duration T_c. The source duration T_c is deduced from the corner frequency F_c of the main event: $T_c = 1/F_c$. Indications on the way we estimate the corner frequency will be given later in the application section. In the second stage, η_d delays t_d are once again generated with a second probability density $\rho_d(t)$ over a window duration $T_d \leq T_c$ centered on each delay generated in the first stage. In total $\eta = \eta_c \cdot \eta_d$ small events are summed together and scaled by a factor κ. We assume that a single small-event record represents the Green's function for all points of the large rupture area. In these conditions, for each realization k, the simulated large event $S_k(t)$ is given by the convolution between the numerical source time function $R_k(t)$ and the small-event record $s(t)$ selected as empirical Green's function (EGF):

$$S_k(t) = R_k(t) * s(t) \quad \text{with}$$
$$R_k(t) = \kappa \sum_{d=0}^{\eta_d - 1} \left[\sum_{c=0}^{\eta_c - 1} \delta(t - t_c(k) - t_d(k)) \right] \quad (1)$$

Using equation (1) and the derivations proposed by Joyner and Boore (1986) in their Appendix, it can be proved that if t_c and t_d are independent random delays, then the numerical source frequency content averaged over a large set of realizations tends to be:

$$R(f) = \eta\kappa. \left[\frac{1 + (\eta_c - 1) \cdot |\rho_c(f)|^2}{\eta_c} \right]^{1/2} \cdot \left[\frac{1 + (\eta_d - 1) \cdot |\rho_d(f)|^2}{\eta_d} \right]^{1/2} \quad (2)$$

where $|\rho_c(f)|$ and $|\rho_d(f)|$ are, respectively, the amplitude spectra of the density probabilities $\rho_c(t)$ and $\rho_d(t)$.

Determination of Summation Constraints

To constrain the summation scheme and to determine the fundamental parameters η, κ, $\rho_c(t)$, and $\rho_d(t)$, we consider the following two relationships between large and small earthquakes.

The first relationship is the well-known scaling relation of source parameters (Brune, 1970; Kanamori and Anderson, 1975), based on a constant stress drop condition. Today, many studies suggest that this condition is not appropriate for a wide range of magnitudes (Beeler *et al.*, 2003; Kanamori and Rivera, 2004). Then, assuming different stress drops $\Delta\Sigma$ and $\Delta\sigma$ for the large and small event, the common scaling relation $M_0 \alpha F_c^{-3}$ becomes $M_0 \alpha \Delta\Sigma . F_c^{-3}$. In these

conditions, the spectral relationship between large and small events is given by:

$$\frac{M_0}{m_0} = C.N^3 \quad \text{where} \quad C = \frac{\Delta\Sigma}{\Delta\sigma} \quad \text{and} \quad N = \frac{f_c}{F_c} \tag{3}$$

The second relationship is the scaling relation of source spectra, the well-known ω^{-2} model (Brune, 1970). The small earthquake, selected as empirical Green's function, is assumed to follow this model. To generate ground motions that statistically also reproduce this model (Fig. 1a), the source frequency content averaged over a large set of realizations (equation 2) must agree with the theoretical ratio $R_t(f)$ between the spectra of the large and small events (equation 4) (Fig. 1b):

$$R_t(f) = \frac{M_0}{m_0} \cdot \frac{1 + \left(\frac{f}{f_c}\right)^2}{1 + \left(\frac{f}{F_c}\right)^2}. \tag{4}$$

By definition of a probability density, $\rho_c(f)$ and $\rho_d(f) \rightarrow 1$ as $f \rightarrow 0$. If we require that they vanish as $f \rightarrow +\infty$, then to reproduce the low and high spectral content required by the ω^{-2} model (equation 4), taking into account the scaling relation of source parameters (equation 3), the parameters η and κ of equation 2 are determined by:

$$\eta = N^4 \quad \text{where} \quad \eta = \eta_c \cdot \eta_d \tag{5}$$

$$\kappa = \frac{C}{N} \tag{6}$$

Moreover, to also reproduce the intermediate frequency content and consequently be exactly in agreement with the ω^{-2} model in the whole frequency band, one solution (here presented for $\rho_c(f)$ and $\rho_d(f)$ real) is to generate delays according to the probability density functions $\rho_c(t)$ and $\rho_d(t)$ as follows:

$$\rho_c(t) = \int_{-\infty}^{+\infty} \frac{\sqrt{1 + \alpha_c\left(\frac{f}{F_d}\right)^2}}{1 + \left(\frac{f}{F_c}\right)^2} e^{2i\pi ft} df \quad \text{with}$$

$$\alpha_c = \frac{2}{1 + \left(\frac{F_c}{F_d}\right)^2} \tag{7}$$

$$\rho_d(t) = \int_{-\infty}^{+\infty} \frac{\sqrt{1 + \alpha_d\left(\frac{f}{f_c}\right)^2}}{1 + \left(\frac{f}{F_d}\right)^2} e^{2i\pi ft} df \quad \text{with}$$

$$\alpha_d = \frac{2}{1 + \left(\frac{F_d}{f_c}\right)^2} \tag{8}$$

$$\text{where} \quad F_d = \frac{1}{T_d} = \eta_c^{1/4} \cdot F_c \tag{9}$$

Note that the ability of this method to reproduce the ω^{-2} model not only depends on the constraints over the fundamental parameters η, κ, $\rho_c(t)$, and $\rho_d(t)$ (equation 5, 6, 7, and 8) but also depends on the constraint over the characteristic frequency F_d (equation 9). Appendix A describes the calculation details to retrieve the expressions $\rho_c(t)$ and $\rho_d(t)$. Ninety-five percent of the energy is concentrated inside the characteristic times (T_c and T_d, respectively, for the first and second stage) (Fig. 2). Of course, as for Ordaz *et al.* (1995),

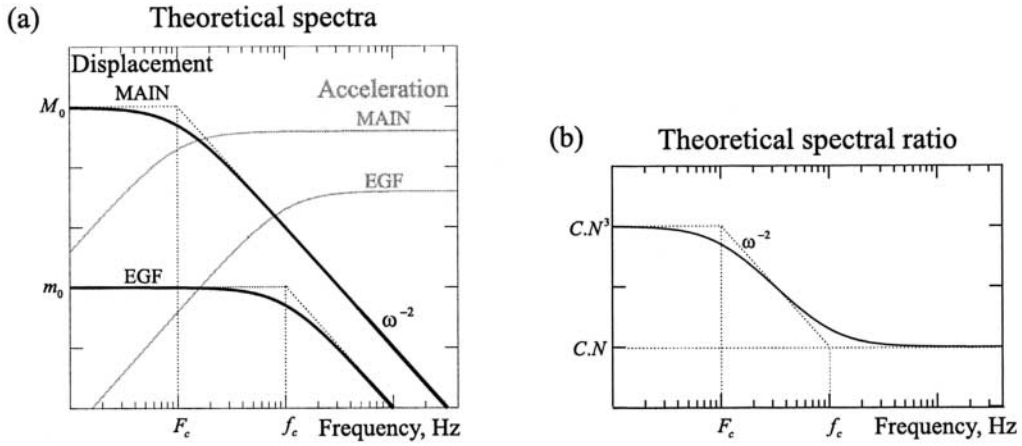


Figure 1. The ω^{-2} model. (a) Theoretical spectra of large and small events in displacement (in black) and acceleration (in gray). (b) Theoretical ratio between the spectra of large and small events.

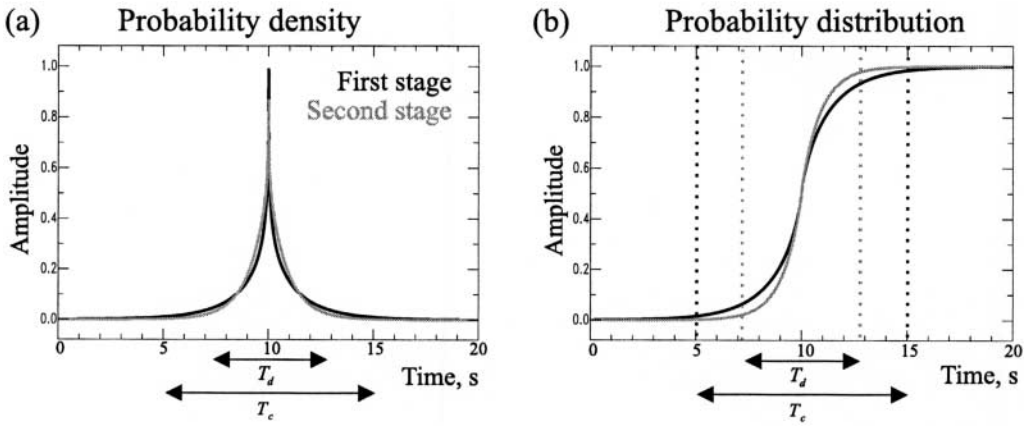


Figure 2. Probability density function (a) and probability distribution function (b) for the first stage (in black) and the second stage (in gray).

there is a nonzero probability that some delays are generated outside the time window T_c and then that few small events are summed outside the expected source duration. However, taking into account the small probability of such a configuration (5%), the consequences over the simulated seismograms are negligible. We propose to generate random delays with $\rho_c(t)$ and $\rho_d(t)$ by a method easy to implement: the rejection-acceptance method (see Appendix B).

Numerical Tests

For numerical tests, the seismic moment of the large event is assumed 1000 times larger than those of the small event (difference of magnitude units: $M_w - m_w = 2$). The stress drops are assumed equal. In total $\eta = 10^4$ small events represented by a Dirac delta function are summed together. The small-event parameters are normalized such that $f_c = 1$, $m_0 = 1$, and then $F_c = 0.1$ and $M_0 = 1000$. The numerical tests are computed for four kinds of summation scheme (Fig. 3): (1) Wennerberg [1990] in a single stage, (2) Wennerberg [1990] in two stages, (3) Ordaz *et al.* (1995) in a single stage, and (4) this study in two stages. For the two-stage methods, the number of delays generated in the first stage is fixed at $\eta_c = N$, and, consequently, the number of delays generated in the second stage take the value $\eta_d = N^3$ (equation 5).

In the frequency domain, only the single-stage summation proposed by Ordaz *et al.* (1995) and the two-stage summation proposed in this study produce synthetic time histories which, on average, exactly reproduce the reference model in the whole frequency band (Fig. 3e and f).

In the time domain, three synthetic time histories are represented for each summation scheme (Fig. 3a–d). The difference between each one is only the effect of different seeds for the generation of random delays and not the effect of parameters variability. Whereas the single-stage summation schemes (Fig. 3a and c) produce similar synthetic time histories, with an excessive concentration of energy around the half-duration of the rupture, the two-stage summation schemes (Fig. 3b and d) distribute energy during the whole rupture duration and produce different synthetic time histories that can be associated with a multitude of rupture processes.

Only the two-stage summation proposed in this study generates a large number of possible time histories while reproducing well the whole frequency band level. The variability introduced by the two-stage summation scheme proposed here is an important point for two reasons: first, this variability produces more realistic time histories, and second, within the framework of simulation, it is fundamental to generate a multitude of possible rupture processes. However, it is important to keep in mind that the ability of this method to reproduce the reference model depends on constraints previously established on the fundamental parameters: η, κ, $\rho_c(t)$, $\rho_d(t)$, and F_d (equations 5, 6, 7, 8, and 9). Using others values would produce results far away from the reference model (Fig. 4). Moreover, note also that the variability introduced is not only the result of the two-stage summation proposed here but also of the small number of delays η_c generated in the first stage (here, $\eta_c = N$). Indeed, increasing the number η_c of generated delays in the first stage would result in more similar time histories. In the extreme case where $\eta_c = N^4$, the two-stage summation scheme proposed here would become equivalent to the single-stage summation scheme proposed by Ordaz *et al.* (1995).

Application on Observed Data

Oaxaca Earthquake (1999, M_w 7.5, Mexico)

We apply our method to simulate the ground motions produced by the Oaxaca earthquake that occurred in the south of Mexico on 30 September 1999 (M_w 7.5). We selected as a suitable empirical Green's function the 1 October 1999 aftershock (M_w 4.65). Both earthquakes have been recorded by the permanent Mexican network on many stations (Singh *et al.*, 2000). The application of the EGF technique

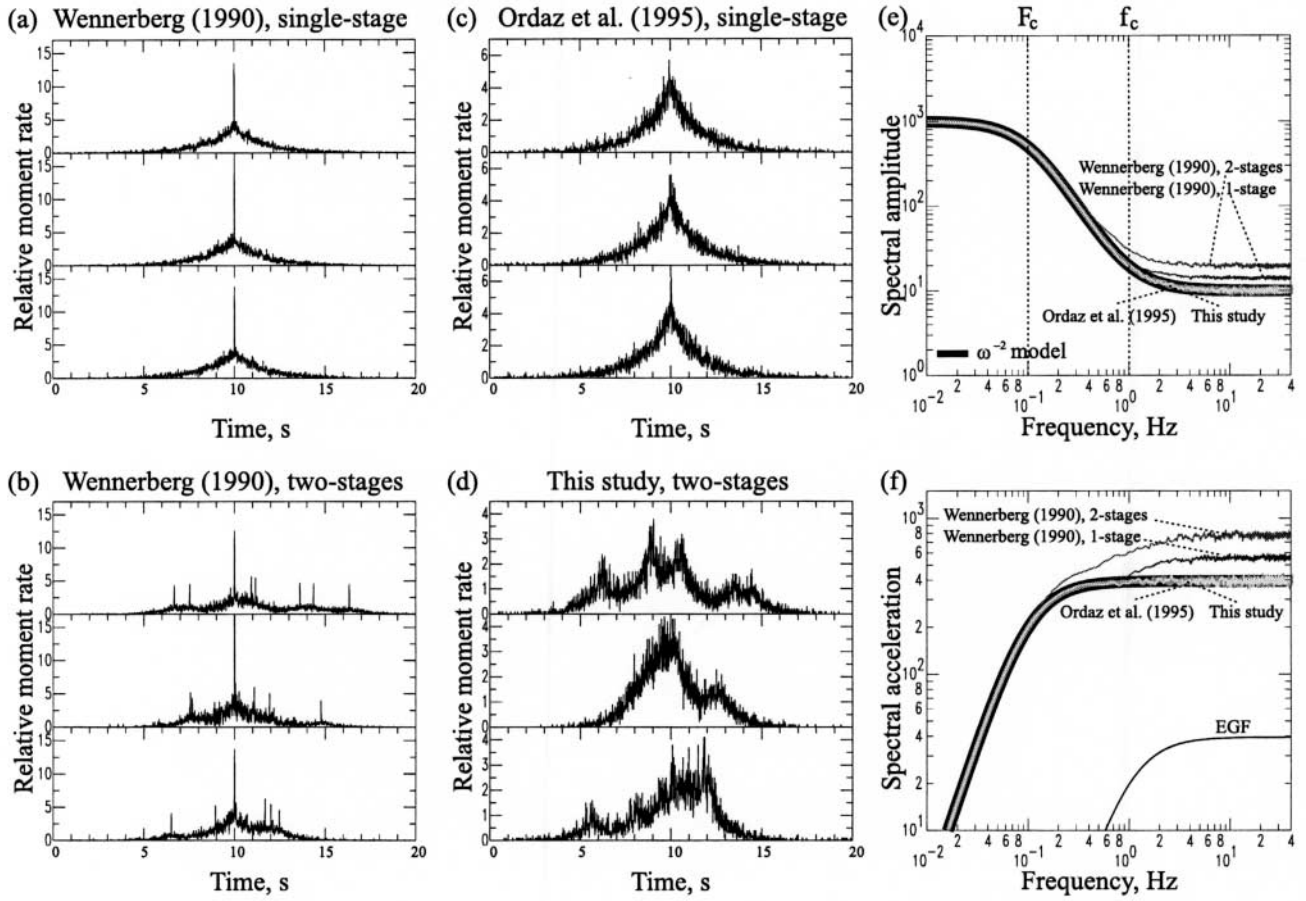


Figure 3. Numerical simulations using four different summation schemes. (a)–(d) For each summation scheme, three source time histories are represented over the 500 generated. The differences between each one are only due to the stochastic method and not to parameters variability. (e) Source frequency content averaged over 500 realizations for each summation scheme (gray scale) compared with the reference model (in black). (f) Spectral acceleration (averaged) obtained by the multiplication in the frequency domain between the source frequency content (averaged) and the theoretical spectrum of the small event (EGF). Note that this study, and the study of Ordaz *et al.* (1995) are both exactly in agreement with the reference model in the frequency domain. Parameters: $M_0 = 1000$, $m_0 = 1$, $f_c = 1$, $C = \Delta\Sigma/\Delta\sigma = 1$, $N = 10$, for the two-stage method $\eta_c = N$.

requires a distance between source and receiver larger than the length of the fault ($d \geq 90$ km for the Oaxaca earthquake [Hernandez *et al.*, 2001]). Then, three stations located at 400 km from the epicenter are used to compute this simulation. The source parameters used in the simulation are listed in Table 1. The parameters M_0, m_0, F_c, and $\Delta\Sigma$ come from the study of Singh *et al.* (2000). The corner frequency of the small event f_c is determined by comparison between the displacement source spectrum observed and the theoretical ω^{-2} model for all stations. The small event stress drop $\Delta\sigma$ is deduced by comparison between the spectral ratio of the mainshock to the aftershock and the ratio predicted by the ω^{-2} model.

The simulations of the Oaxaca earthquake produced by our method reproduce well the observed data. This is particularly evident when we compare the simulated response spectrum averaged over all realizations with the observed response spectrum for each station and each component (Fig. 5). Note that the averaged simulated response spectra presented here can be obtained by calculating the response spectra for signals, with modules equal to acceleration spectra averaged over all realizations and phases equal to the ones of each realization. We observe also a good fit between simulated and observed data for the acceleration, velocity, displacement time histories, and the Fourier displacement spectra (Fig. 6). Compared with other summation schemes (Fig. 7), the simulations generated with the single-stage methods are very similar to one another and reflect the occurrence of an unique rupture process, which differs only at high frequencies. For the two-stage methods, the simulations generated are different from one another and reflect the possible occurrence of a multitude of rupture processes. Ac-

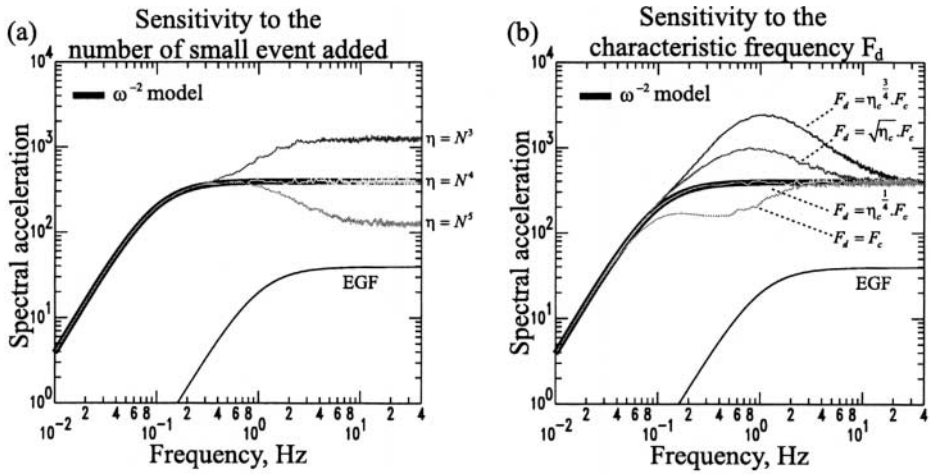


Figure 4. Numerical tests. Sensitivity of the simulated spectral acceleration averaged (in gray) to the number of summed small events (a) and the characteristic frequency F_d (b), in comparison with the ω^{-2} model (in black). Parameters: $M_0 = 1000$, $m_0 = 1, f_c = 1, C = \Delta\Sigma/\Delta\sigma = 1, \eta_c = N = 10$.

cording to the numerical tests, Wennerberg (1990) in two stages induces an important overestimation of the high-frequency content (factor 2). Only our method generates a large number of possible time histories while reproducing well the whole frequency band level and on particular, the high-frequency level.

Note that a stress drop 15 times bigger than the one of its aftershock was needed to reproduce the high-frequency level observed. This stress drop is totally in agreement with the important stress drop referred for this earthquake (Singh *et al.*, 2000). However, this large stress drop is an important point, because within the context of future earthquake simulation where the stress drop is unknown, this parameter will play a major role. Figure 8 shows, with numerical tests, the influence of the stress drop ratio chosen. The constant stress drop condition compared with the Oaxaca condition ($\Delta\Sigma \sim 15.\Delta\sigma$) would produce a large underestimation of the high-frequency content of the simulated spectrum (factor 6). This factor is very large and the stress drop variation expected is probably not so large in all regions. However, it points out the importance of estimating the simulation variability, taking into account the uncertainty concerning the stress drop ratio between large and small events.

Mainshocks of the Colfiorito, 1997 Crisis (M_w 5.7 and M_w 6.0, Italy)

We simulate the ground motions produced by the two mainshocks that occurred on 26 September 1997 in the Umbria-Marche region of central Italy (M_w 5.7, 00h33 and M_w 6.0, 09h40) (Amato *et al.*, 1998; Deschamps *et al.*, 2000). Despite the moderate magnitude of these events, they caused considerable damage in the epicentral area where 11 people were killed (Castro *et al.*, 2001) and several houses were destroyed. Source dimensions of these earthquakes have been estimated to 6 × 6 km and 12 × 7.5 km for the mainshocks of 00h33 and 09h40, respectively (Zollo *et al.*, 1999). We selected as empirical Green's function the 3 September 1997 foreshock (M_w 4.5) that gave rise to good recordings on station Assisi (ASS), located at 22 km from the epicenter. The source parameters used in the simulation are listed in Table 2. The parameters M_0, m_0, and $\Delta\Sigma$ come from the study of Zollo *et al.* (1999). The corner frequencies of the foreshock and the mainshocks are determined by comparison between the displacement source spectra observed and the theoretical ω^{-2} model on Assisi station. They are in agreement with the study of Capuano *et al.* (2000). The foreshock stress drop $\Delta\sigma$ is deduced as previously by comparison between the spectral ratio of the mainshock to the foreshock and the one predicted by the ω^{-2} model. The ground motions simulated reproduce well the observed ones. This is true for both mainshocks, over all the components (Fig. 9).

Table 1
Source Parameters of the Oaxaca Earthquake and the Aftershock Used as Empirical Green's Function

	Seismic Moment	Corner Frequency	Stress Drop
Mainshock	$M_0 = 10^{20}$ N m	$F_c = 0.11$ Hz	$\Delta\Sigma \sim 108$ bars
Aftershock	$m_0 = 9.4 \times 10^{15}$ N m	$f_c = 0.99$ Hz	$\Delta\sigma \sim 7.5$ bars

M_0, m_0, F_c, and $\Delta\Sigma$ come from the study of Singh *et al.* (2000).

Discussion and Conclusions

We presented a two-stage method to simulate the ground motions produced by an earthquake by using stochastic summation of small earthquakes. Our method, inspired by the works of Joyner and Boore (1986), Wennerberg (1990), and Ordaz *et al.* (1995), presents two main advantages. First, this method produces time histories that,

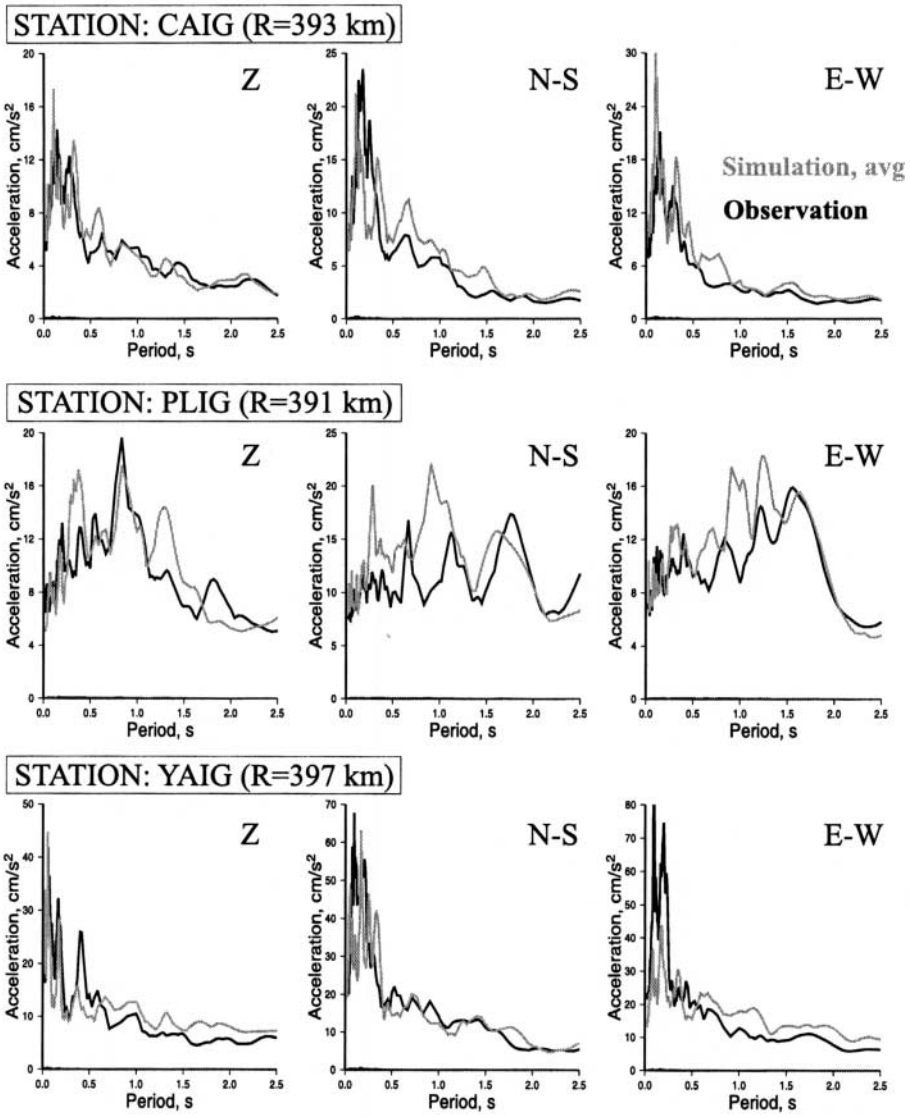


Figure 5. Simulation of the Oaxaca earthquake for the three components of three stations of the Mexican broadband network. The observed response spectrum (in black) (pseudo acceleration, damping = 5%) and the simulated response spectrum averaged over 500 realizations (in gray) are represented for each station and each component. Simulation parameters: $f_c = 0.99$ Hz; $C = 14.4$; $\eta_c = N = 9$.

on average, are in exact agreement with actual knowledge on scaling relations: the scaling source relations and the ω^{-2} model in the frequency domain (equation 3 and 4). Then, compared with a classical single-stage approach, the time histories produced are more realistic and sufficiently different from each other to be associated with a multitude of possible rupture processes. Consequently, for the same receiver, many simulations are available and can be used to characterize, from a statistical point of view, any ground-motion parameter in terms of mean value, standard deviation, *et al.* These results are obtained because of a well constrained two-stage summation scheme depending on four fundamental parameters: the number of summed small events (equation 5), the scaling factor (equation 6), and the probability densities used in the first and second stage (equations 7 and 8).

This two-stage model appears also to have a more physical meaning. Whereas in a single-stage approach, the seismic source is only composed of η punctual sources (Fig. 10a), in the two-stage approach, the seismic source is composed of $\eta_c \leq \eta$ patches (Fig. 10b). These patches could be characterized by their positions over the fault and the energy released by each of them. Assuming a uniform rupture velocity, their positions over the fault are only the result of the generation of random delays during the first stage, whereas the energy released by each of them is the result of the η_d

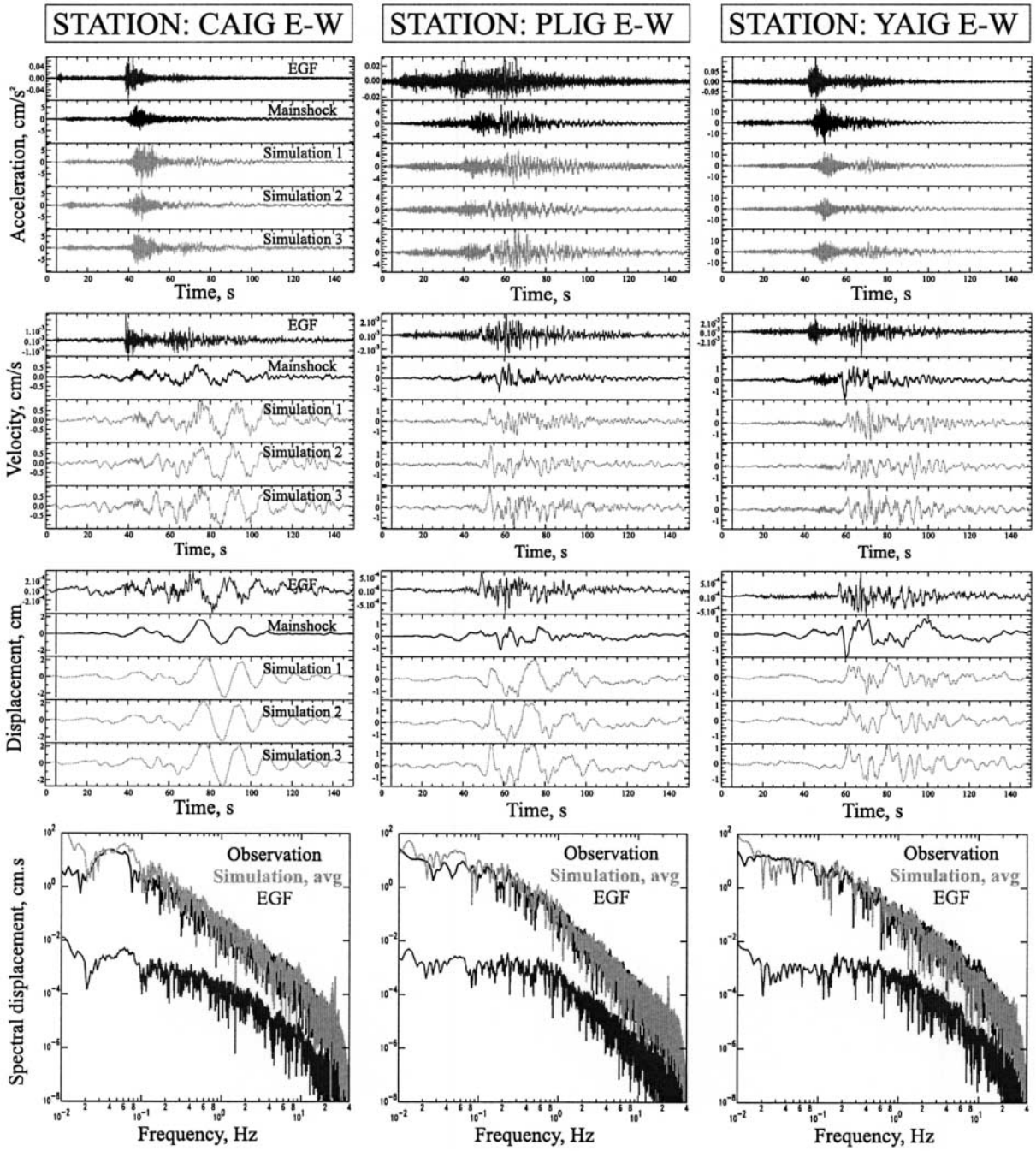


Figure 6. Simulation of the Oaxaca earthquake at three stations on the east–west component. Acceleration, velocity, displacement time histories, and displacement spectra for the small event (EGF in dark gray), the large event observed (in black), and the simulated (in light gray) are represented for each station. In the time domain, only three realizations are represented over the 500 generated. The simulated displacement spectrum (averaged) is obtained by computing the quadratic mean over 500 realizations.

small events summed during the second stage. Then, the first stage could be associated with the rupture propagation over the fault during the source duration T_c and the second stage could be interpreted as a break sequence of secondary sources during the duration T_d (time required to break each of the η_c patches present over the fault). With the introduction of this second level of rupture, our method is more in agreement with currently developed kinematic and dynamic models (Irikura and Kamae, 1994; Bour and Cara, 1997; Madariaga, 1976; Mikumo, 1994).

However, it is important to keep in mind that this method is unable to take into account possible directivity

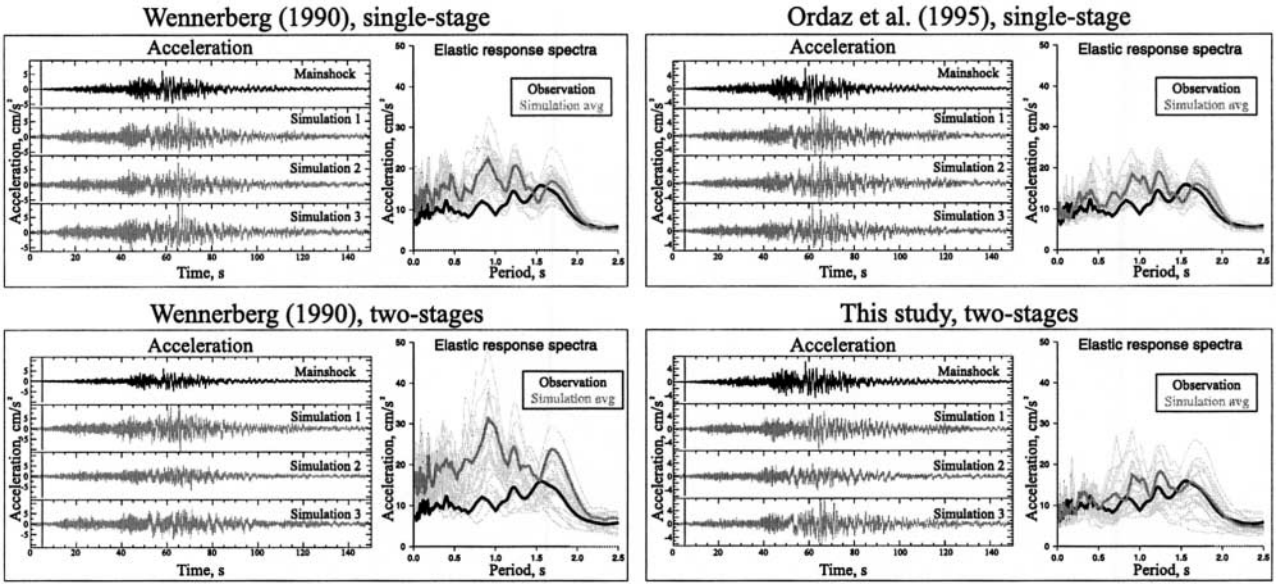


Figure 7. Simulation of the Oaxaca earthquake for the east–west component at PLIG station and for four different summation schemes. For each summation scheme, the acceleration and the elastic response spectra (pseudo acceleration, damping = 5%) for the large event observed (in black) and the simulated (in gray) are represented. In the time domain, three simulations are represented. In the frequency domain, the response spectrum averaged over 500 realizations (in thick gray) is superposed to those of 20 realizations (in thin gray) and to the observed one (in black).

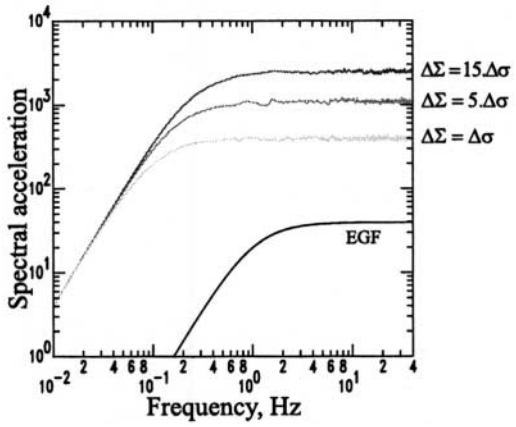


Figure 8. Numerical tests. Sensitivity of the simulated spectral acceleration (averaged) to the target event stress drop. Parameters: $M_0 = 1000$; $m_0 = 1$; $f_c = 1$; $C = 1$, 5, and 15; $\eta_c = N$.

effects because of the point-source approximation. This last point, in addition to the fact that only one empirical Green's function is used for all the faults, makes this method inappropriate to simulate ground motions for near-source sites. Therefore, this method is particularly adapted to simulate moderate events. It also has the great advantage of being easy to apply because only the seismic moment and the stress drop have to be specified for the target earthquake.

Application of this method to the Oaxaca earthquake (M_w 7.5, Mexico) and to the two mainshocks of the Umbria Marche crisis (M_w 5.7 and M_w 6.0, Central Italy) gives good results both in time and in the frequency domains. These good results are due to, of course, the two-stage summation scheme proposed here, but also to the set of parameters involved, which are: the corner frequency f_c of the small event, the seismic moment ratio between the large and small event M_0/m_0, and the stress drop ratio $\Delta\Sigma/\Delta\sigma$. Within the context of the applications presented in this article, these parameters

Table 2
Source Parameters of Colfiorito Mainshocks and the Foreshock Used as Empirical Green's Function

	Seismic Moment	Corner Frequency	Stress Drop
M_w 5.7 mainshock	$M_0 = 0.4 \times 10^{18}$ N m	$F_c = 0.5$ Hz	$\Delta\Sigma \sim 19$ bars
M_w 6.0 mainshock	$M_0 = 1.0 \times 10^{18}$ N m	$F_c = 0.3$ Hz	$\Delta\Sigma \sim 15$ bars
Foreshock	$m_0 = 5.6 \times 10^{15}$ N m	$f_c = 1.5$ Hz	$\Delta\sigma \sim 8.2$ bars

M_0, m_0, and $\Delta\Sigma$ come from the study of Zollo *et al.* [1999].

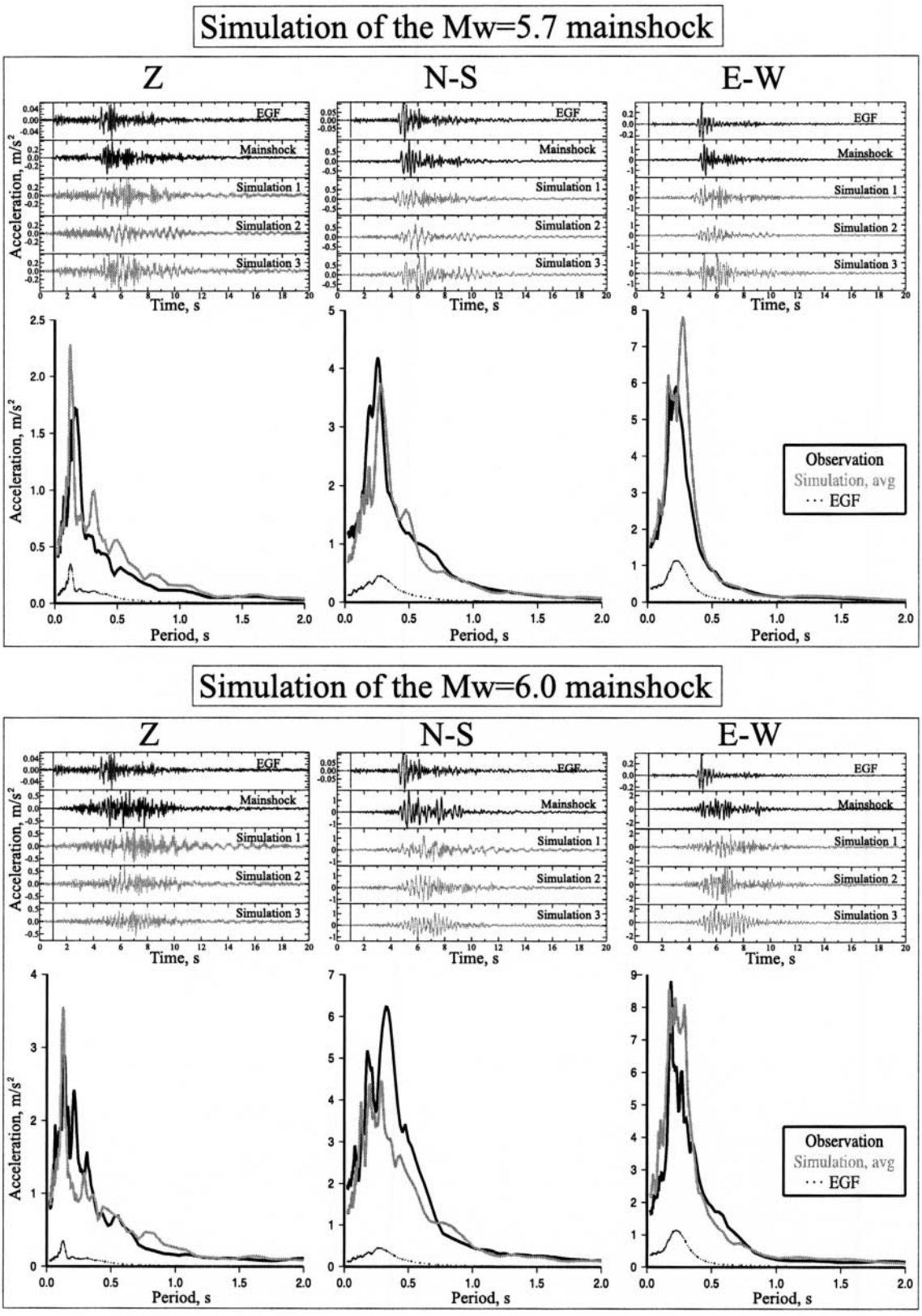


Figure 9. Simulation on Assisi station of Colfiorito crisis mainshocks (M_w 5.7 and M_w 6.0) for the three components. The acceleration and elastic response spectra (pseudo acceleration, damping = 5%) for the small event (EGF in dark gray), the large event observed (in black), and the simulated (in light gray) are represented for each mainshock and each component. In the time domain, only three realizations are represented over the 500 generated. In the frequency domain, the simulated response spectrum is a mean over 500 realizations. Simulation parameters: for the M_w 5.7 mainshock, $f_c = 1.5$ Hz; $C = 2.3$; $\eta_c = N = 3$; for the M_w 6.0 mainshock, $f_c = 1.5$ Hz; $C = 1.8$; $\eta_c = N = 5$.

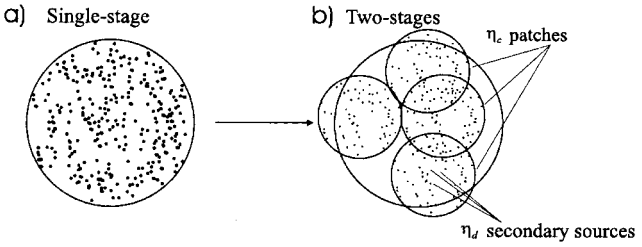


Figure 10. Kinematic spatial interpretation for the single-stage approach (a) and the two-stage approach (b) with a uniform rupture velocity.

have been chosen so as to be in agreement with the observations. Within the context of a future earthquake simulation (seismic moment specified) using a small event as empirical Green's function (seismic moment and corner frequency assumed known), the stress drop ratio between the large and small event becomes a crucial parameter to determine. Therefore, it is important to estimate the ground-motion variability, not only based on the variability of the time histories but also on the uncertainty concerning the stress drop ratio between the large and the small event.

Acknowledgments

We are grateful to I. Beresnev, L. Hutchings, and an anonymous reviewer for the interesting suggestions and constructive comments proposed to improve the manuscript. We thank J. Pacheco and S. K. Singh of the Instituto di Geofisica of Mexico (UNAM) for providing the seismogram datasets of the Oaxaca earthquakes. The ground-motion records of Umbria Marche are extracted from the CD-ROM, 2002 provided by the S.S.N.-Monitoring System Group. This research has been funded by the BRGM group and Provence-Alpes Côte d'Azur region. Publication No. 699 of Géosciences Azur.

References

Amato, A., R. Azzara, C. Chiarabba, G. B. Cimini, M. Cocco, M. Di Bona, L. Margheriti, S. Mazza, F. Mele, G. Selvaggi, A. Basili, E. Boschi, F. Courboulex, A. Deschamps, S. Gaffet, G. Bittarelli, L. Chiaraluce, D. Piccinini, and M. Ripepe (1998). The 1997 Umbria-Marche, Italy, earthquake sequence: a first look at the mainshocks and aftershocks, *Geophys. Res. Lett.* **25,** 2861–2864.

Beeler, N. M., T. F. Wong, and S. H. Hickman (2003). On the expected relationships between apparent stress, static stress drop, effective shear fracture energy and seismic efficiency, *Bull. Seism. Soc. Am.* **93,** 1381–1389.

Boore, D. M. (1983). Stochastic simulation of high-frequency ground motions based on seismological models of the radiated spectra, *Bull. Seism. Soc. Am.* **73,** 1865–1894.

Boore, D. M. (2003). Simulation of ground motion using the stochastic method, *Pure Appl. Geophys.* **160,** 635–676.

Bour, M., and M. Cara (1997). Test of a simple empirical Green's function method on moderatesized earthquake, *Bull. Seism. Soc. Am.* **87,** 668–683.

Brune, J. N. (1970). Tectonic stress and the spectra of seismic shear waves from earthquakes, *J. Geophys. Res.* **75,** 4997–5009.

Capuano, P., A. Zollo, E. Emolo, S. Marcucci, and G. Milana (2000). Rupture mechanism and source parameters of Umbria-Marche mainshocks from strong ground motion data, *J. Seism.* **4,** 463–478.

Castro, R. R., A. Rovelli, M. Cocco, M. Di Bona, and F. Pacor (2001). Stochastic simulation of strong-motion records from the 26 September 1997 (Mw 6), Umbria-Marche (Central Italy) earthquake, *Bull. Seism. Soc. Am.* **91,** 27–39.

Deschamps, A., F. Courboulex, S. Gaffet, A. Lomax, J. Virieux, A. Amato, A. Azzara, B. Castello, C. Chiarabba, G. Cimini, M. Cocco, M. Di Bona, L. Margheriti, F. Mele, G. Selvaggi, L. Chiaraluce, D. Piccinini, and M. Ripepe (2000). Spatio-temporal distribution of seismic activity during the Umbria-Marche crisis, 1997, *J. Seism.* **4,** 377–386.

Hartzell, S. H. (1978). Earthquake aftershocks as Green's functions, *Geophys. Res. Lett.* **5,** 1–4.

Hernandez, B., N. M. Shapiro, S. K. Singh, J. F. Pacheco, F. Cotton, M. Campillo, A. Iglesias, V. Cruz, J. M. Gómez, and L. Alcántara (2001). Rupture history of September 30, 1999 intraplate earthquake of Oaxaca, Mexico (Mw = 7.5) from inversion of strong-motion data, *Geophys. Res. Lett.* **28,** 363–366.

Herrero, A., and P. Bernard (1994). A kinematic self-similar rupture process for earthquakes, *Bull. Seism. Soc. Am.* **84,** 1216–1228.

Hutchings, L. (1994). Kinematic earthquake models and synthesized ground motion using empirical Green's functions, *Bull. Seism. Soc. Am.* **84,** 1028–1050.

Irikura, K., and K. Kamae (1994). Estimation of strong ground motion in broad-frequency band based on a seismic source scaling model and an empirical Green's function technique, *Ann. Geofis.* **37,** 1721–1743.

Joyner, W. B., and D. M. Boore (1986). On simulating large earthquakes by Green's function addition of smaller earthquakes, in *Earthquake Source Mechanics*, Vol. **37,** *Maurice Ewing Series 6*, S. Das, J. Boatwright, and C. H. Scholtz (Editors), American Geophysical Union, Washington, D.C., 269–274.

Kanamori, H., and D. L. Anderson (1975). Theoretical basis of some empirical relations in seismology, *Bull. Seism. Soc. Am.* **65,** 1073–1095.

Kanamori, H., and L. Rivera (2004). Static and dynamic scaling relations for earthquakes and their implications for rupture speed and stress drop, *Bull. Seism. Soc. Am.* **94,** 314–319.

Madariaga, R. (1976). Dynamic of an expanding circular fault, *Bull. Seism. Soc. Am.* **66,** 639–666.

Mikumo, T. (1994). Dynamic fault rupture processes of moderate-size earthquakes inferred from the results of kinematic waveform inversion, *Ann. Geofis.* **37,** 1377–1389.

Ordaz, M., J. Arboleda, and S. K. Singh (1995). A scheme of random summation of an empirical Green's function to estimate ground motions from future large earthquakes, *Bull. Seism. Soc. Am.* **85,** 1635–1647.

Pavic, R., M. G. Koller, P. Y. Bard, and C. Lacave-Lachet (2000). Ground motion prediction with the empirical Green's function technique: an assesment of uncertainties and confidence level, *J. Seism.* **4,** 59–77.

Singh, S. K., M. Ordaz, L. Alcántara, N. Shapiro, V. Kostoglodov, J. F. Pacheco, S. Alcocer, C. Gutiérrez, R. Quass, T. Mikumo, and E. Ovando (2000). The Oaxaca earthquake of 30 September 1999 (Mw = 7.5): a normal-faulting event in the subducted Cocos plate, *Seism. Res. Lett.* **71,** 67–78.

Wennerberg, L. (1990). Stochastic summation of empirical Green's functions, *Bull. Seism. Soc. Am.* **80,** 1418–1432.

Zollo, A., S. Marcucci, G. Milana, and P. Capuano (1999). The 1997 Umbria-Marche (central Italy) earthquake sequence: insights on the mainshocks ruptures from near source strong motion records, *Geophys. Res. Lett.* **26,** 3165–3168.

Appendix A: Determination of the Probability Density Solutions

For the source spectra averaged over all simulations (equation 2) to reproduce the ω^{-2} model (equation 4), it is necessary that $|\rho_c(f)|$ and $|\rho_d(f)|$ verify the equation as follows:

$$\left[\frac{1 + (\eta_c - 1) \cdot |\rho_c(f)|^2}{\eta_c}\right]^{1/2} \cdot \left[\frac{1 + (\eta_d - 1) \cdot |\rho_d(f)|^2}{\eta_d}\right]^{1/2} = \frac{1 + \left(\frac{f}{f_c}\right)^2}{1 + \left(\frac{f}{F_c}\right)^2} \quad \text{(A1)}$$

By replacing the expression $\left[1 + \left(\frac{f}{f_c}\right)^2\right] / \left[1 + \left(\frac{f}{F_c}\right)^2\right]$ with its equivalent expression

$$\frac{1 + \left(\frac{f}{F_d}\right)^2}{1 + \left(\frac{f}{F_c}\right)^2} \cdot \frac{1 + \left(\frac{f}{f_c}\right)^2}{1 + \left(\frac{f}{F_d}\right)^2},$$

one solution is to identify, respectively, the right and left member of equation A1, which gives the two equations as follows:

$$\left[\frac{1 + (\eta_c - 1) \cdot |\rho_c(f)|^2}{\eta_c}\right]^{1/2} = \frac{1 + \left(\frac{f}{F_d}\right)^2}{1 + \left(\frac{f}{F_c}\right)^2} \quad \text{(A2)}$$

$$\left[\frac{1 + (\eta_d - 1) \cdot |\rho_d(f)|^2}{\eta_d}\right]^{1/2} = \frac{1 + \left(\frac{f}{f_c}\right)^2}{1 + \left(\frac{f}{F_d}\right)^2}. \quad \text{(A3)}$$

The solutions of these two equations are:

$$|\rho_c(f)| = \frac{\sqrt{\left[1 + \lambda_c\left(\frac{f}{F_d}\right)^2\right] \cdot \left[1 + \alpha_c\left(\frac{f}{F_d}\right)^2\right]}}{1 + \left(\frac{f}{F_c}\right)^2} \quad \text{(A4)}$$

$$\text{with } \lambda_c = \frac{1 - \frac{1}{\sqrt{\eta_c}}\left(\frac{F_d}{F_c}\right)^2}{1 - \frac{1}{\sqrt{\eta_c}}} \text{ and } \alpha_c = \frac{1 + \frac{1}{\sqrt{\eta_c}}\left(\frac{F_d}{F_c}\right)^2}{1 + \frac{1}{\sqrt{\eta_c}}} \quad \text{(A5)}$$

and

$$|\rho_d(f)| = \frac{\sqrt{\left[1 + \lambda_d\left(\frac{f}{f_c}\right)^2\right] \cdot \left[1 + \alpha_d\left(\frac{f}{f_c}\right)^2\right]}}{1 + \left(\frac{f}{F_d}\right)^2} \quad \text{(A6)}$$

$$\text{with } \lambda_d = \frac{1 - \frac{1}{\sqrt{\eta_d}}\left(\frac{f_c}{F_d}\right)^2}{1 - \frac{1}{\sqrt{\eta_d}}} \text{ and } \alpha_d = \frac{1 + \frac{1}{\sqrt{\eta_d}}\left(\frac{f_c}{F_d}\right)^2}{1 + \frac{1}{\sqrt{\eta_d}}}. \quad \text{(A7)}$$

So that the expression under the square root always be positive, it is necessary that $\lambda_c \geq 0$ and $\lambda_d \geq 0$. These two inequalities imply the following framing of F_d:

$$\eta_d^{-1/4} \cdot f_c \leq F_d \leq \eta_c^{1/4} \cdot F_c \quad \text{(A8)}$$

By replacing equations 3 ($N = f_c/F_c$) and 5 in equation A8, we deduce an important constraint on F_d (equation A11), which implies that $\lambda_c = \lambda_d = 0$. We finally find the following constraints not only on F_d but also on the probability densities $\rho_c(t)$ and $\rho_d(t)$:

$$|\rho_c(f)| = \frac{\sqrt{1 + \alpha_c\left(\frac{f}{F_d}\right)^2}}{1 + \left(\frac{f}{F_c}\right)^2} \quad \text{with} \quad \alpha_c = \frac{2}{1 + \left(\frac{F_c}{F_d}\right)^2} \quad \text{(A9)}$$

$$|\rho_d(f)| = \frac{\sqrt{1 + \alpha_d\left(\frac{f}{f_c}\right)^2}}{1 + \left(\frac{f}{F_d}\right)^2} \quad \text{with} \quad \alpha_d = \frac{2}{1 + \left(\frac{F_d}{f_c}\right)^2} \quad \text{(A10)}$$

$$\text{where} \qquad F_d = \eta_c^{1/4} \cdot F_c \quad \text{(A11)}$$

Appendix B: Generation of Random Delays with the Probability Density Solutions

Because the probability density functions $\rho_c(t)$ and $\rho_d(t)$ (equations 7 and 8) are very similar, generation of random delays is only presented for the first-stage density function $\rho_c(t)$ associated with the characteristic frequencies (F_c, F_d). The extension to the second-stage density function $\rho_d(t)$ can be easily made by replacing the couple (F_c, F_d) with (F_d, f_c).

When the inverse probability distribution is not analytically known, the common inverse method requires some great computational complexity encountered by Ordaz *et al.* (1995). Then, one practical solution to generate random delays is the rejection-acceptance method. This method consists of two steps: first, generate random delays with a probability density near to the one required; then, reject some delays so as to bring back with delays following the expected probability density. To find probability densities near to the one required, we propose to frame the amplitude spectrum of the probability density $\rho_c(t)$ by the ones of two probability densities:

$$\frac{1}{1 + \left(\frac{f}{F_c}\right)^2} \leq |\rho_c(f)| \leq \frac{1 + \left(\frac{f}{F_d}\right)^2}{1 + \left(\frac{f}{F_c}\right)^2} \qquad \text{(B1)}$$

The Probability Density Double-Exponential (DBEXP)

At the left of the inequality, the amplitude spectrum $1/[1 + (f/F_c)^2]$ is always inferior compared with those of probability density $\rho_c(t)$. The resulting probability density function is composed by a double-exponential (DBEXP) given by:

$$\rho_{c_{\text{dbexp}}}(t) = \pi \cdot F_c \, e^{-2\pi F_c |t|} \qquad \text{(B2)}$$

Generation of random delays with the DBEXP density probability can be easily implemented using the common inverse method, based on the inversion of the probability distribution given by:

$$F_{c_{\text{dbexp}}}(t) = \int_{-\infty}^{t} \rho_{c_{\text{dbexp}}}(t)dt = \frac{1}{2} e^{2\pi F_c t} \quad \text{if} \quad t \leq 0 \qquad \text{(B3)}$$

Inverting the expression B3 for $t \leq 0$ and using the symmetry of $F_{c_{\text{dbexp}}}(t)$, the following procedure allows the generation of random delays according to the probability density DBEXP:

1. Generate a random number x with uniform probability density between [0, 1]
2. Apply the following transformation:

$$\begin{aligned} t &= \frac{1}{2\pi F_c} \ln(2x) && \text{if} \quad 0 \leq x \leq \frac{1}{2} \\ t &= -\frac{1}{2\pi F_c} \ln[2(1 - x)] && \text{if} \quad \frac{1}{2} \leq x \leq 1 \end{aligned} \qquad \text{(B4)}$$

The Probability Density Zero Phase Distribution (ZPD)

At the right of the inequality (equation B1), the amplitude spectrum $\left[1 + \left(\frac{f}{F_d}\right)^2\right] / \left[1 + \left(\frac{f}{F_c}\right)^2\right]$ is always superior to those of probability density $\rho_c(t)$. These expressions have been proposed with the characteristic frequencies (F_c, f_c) by Wennerberg (1990) under the name of ZPD for zero phase distribution. As previously, generation of random delays with the ZPD density probability can be implemented by using the common inverse method. The procedure is described in the Wennerberg (1990) appendix with the characteristic frequencies (F_c, f_c). The extension to the first-stage probability density is obtained by replacing the couple (F_c, f_c) by (F_c, F_d).

In Practice

To generate random delays following exactly the probability density $\rho_c(t)$, the rejection-acceptance method can be supported either by the probability density DBEXP or ZPD. Assuming that we use the probability density DBEXP, it is necessary to find a constant c, such as $c.\rho_{c_{\text{dbexp}}}(t)$, that will always be superior to $\rho_c(t)$ (Fig. 11a) and then apply it to the following procedure:

1. Generate a random number x with uniform probability density between [0, 1].
2. Apply the transformation B4 to generate random delays t with the probability density DBEXP.
3. Generate a random number y with uniform probability density between [0, 1].
4. Apply the condition of rejection-acceptation: if $c.\rho_{c_{\text{dbexp}}}(t) \cdot y \leq \rho_c(t)$, then t is accepted, else t is rejected (Fig. 11b) and it is necessary to start again at point 1.

UMR Géosciences Azur
CNRS UNSA
250 Av Albert Einstein
06560 Valbonne, France
(C.K-S., F.C., A.D.)

BRGM-ARN/MAS
Aménagement et Risques Naturels
117 Av de Luminy
BP 167
13009 Marseille, France
(C.K-S., M.B.)

Manuscript received 15 November 2004.

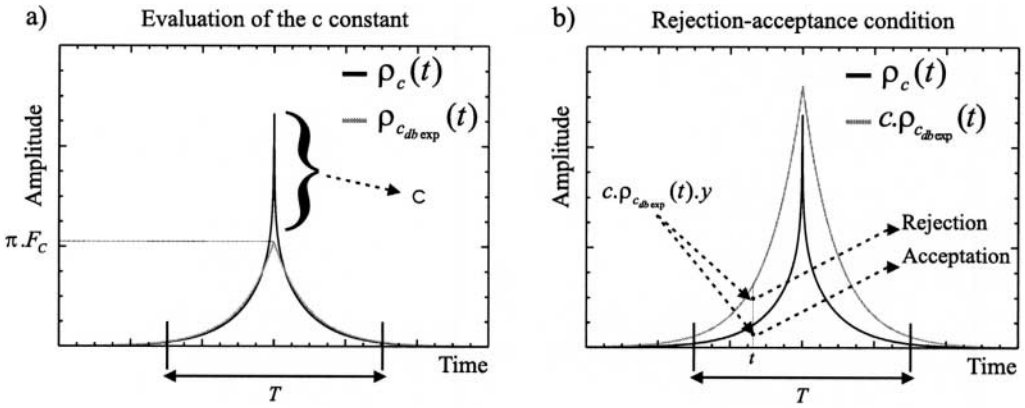


Figure 11. The rejection-acceptance method. (a) Evaluation of the constant c: the constant c is chosen so as to $c.\rho_{c_{\mathrm{dbexp}}}(t)$ be always superior to $\rho_c(t)$, but also the nearest as possible to maximize the efficiency of the method. (b) Rejection-acceptance condition: the delays t such as $c.\rho_{c_{\mathrm{dbexp}}}(t).y \geq \rho_c(t)$ are rejected. This reject corrects the wrong approximation of $\rho_c(t)$ by $c.\rho_{c_{\mathrm{dbexp}}}(t)$.

3.4 Validation sur des données réelles

3.4.1 Objectifs

Afin de valider notre méthode, nous l'avons testée sur des données réelles où un gros séisme a été effectivement enregistré. Les premiers tests ont été effectués sur des données du Mexique. Ils ont donné des résultats excellents mais les stations étaient disposées trop loin de l'épicentre pour avoir un intérêt en terme d'aléa sismique Nous avons ensuite travaillé sur la réplique principale du séisme de Colfiorito (crise d'Ombrie Marche, 1997). Les résultats étaient là aussi très bons mais malheureusement peu de stations se sont révélées utilisables.

Le test de la méthode le plus intéressant à été effectué sur la base de données constituée par le séisme des Saintes et ses principales répliques enregistrés sur les stations du Réseau Accélérométrique Permanent (le réseau RAP) des Antilles.

Nous avons pu ainsi travailler sur 10 petits séismes qui ont été successivement utilisés comme fonction de Green empiriques, ceci afin de :

- Tester l'influence du choix de la fonction de Green empirique sur la solution ;
- Evaluer l'influence de la variation de chute de contrainte sur les résultats ;
- Mesurer l'écart entre simulation et données avec des critères quantitatifs représentatifs ;
- Comparer les résultats avec ceux d'un modèle empirique de prédiction de mouvement du sol ;
- Tester la possibilité de calibrer le choix du paramètre C.

Notons que étude est intéressante également dans le contexte de la France métropolitaine, puisque le séisme des Saintes a des caractéristiques très proches d'un séisme de scénario probable dans les Alpes Maritimes (séisme superficiel de magnitude 6.3 à 24 km au large des côtes). La validation de la méthode sur le séisme des Saintes permet ainsi de proposer avec une plus grande confiance des simulations de mouvements du sol dans d'autres contextes.

3.4.2 La crise des Saintes de 2004

Le séisme de magnitude Mw 6.4 qui a frappé la Guadeloupe et la Dominique le 21 Novembre 2004 a fait de nombreux dégâts matériels et humains et a engendré des réactions de panique en particulier dans les iles des Saintes situées à une vingtaine de kilomètres à peine de l'épicentre. Le choc principal a été suivi de très nombreuses répliques détectées par les réseaux permanents de l'Observatoire volcanologique et sismologique de la Guadeloupe (IPGP). La plupart des séismes de magnitude supérieure à 4 ont été également bien enregistrés par les réseaux accélérométriques du RAP-IPGP et du BRGM (figure 3 de l'article qui suit) et ont pu être relocalisés par le Centre de données sismologiques des Antilles (CDSA) [*Bengoubou-Valerius et al.*, 2008]. La base de données constituée par ces événements est extrêmement intéressante pour tester la méthode de simulation par sommation de petits séismes SIMULSTOC ainsi que l'influence et la calibration possible du paramètre C.

Le travail présenté ici a été effectué en collaboration avec Julien Converset durant son stage de Master 2. Nous avons cherché à simuler le choc principal de la crise des Saintes en utilisant successivement plusieurs petits séismes assez différents pris comme fonction de Green empirique, afin de chercher à comprendre si ce choix est vraiment déterminant sur la qualité des simulations. Ce point est en effet très important lorsque l'on doit réaliser une simulation dans une zone à faible sismicité où il n'existe qu'un ou deux enregistrements de petits séismes et où, la question de la validité de l'approche se pose souvent.

Pour chaque petit séisme, nous déterminons d'abord une fréquence de coupure préliminaire en comparant les spectres de Fourier des signaux avec un modèle en ω^{-2} (Figure 3. 4). Nous déterminons

ensuite les valeurs de C et N les plus adéquates en analysant les niveaux haute et basse fréquence des rapports des spectres du séisme principal sur le petit séisme (Figure 3. 5).

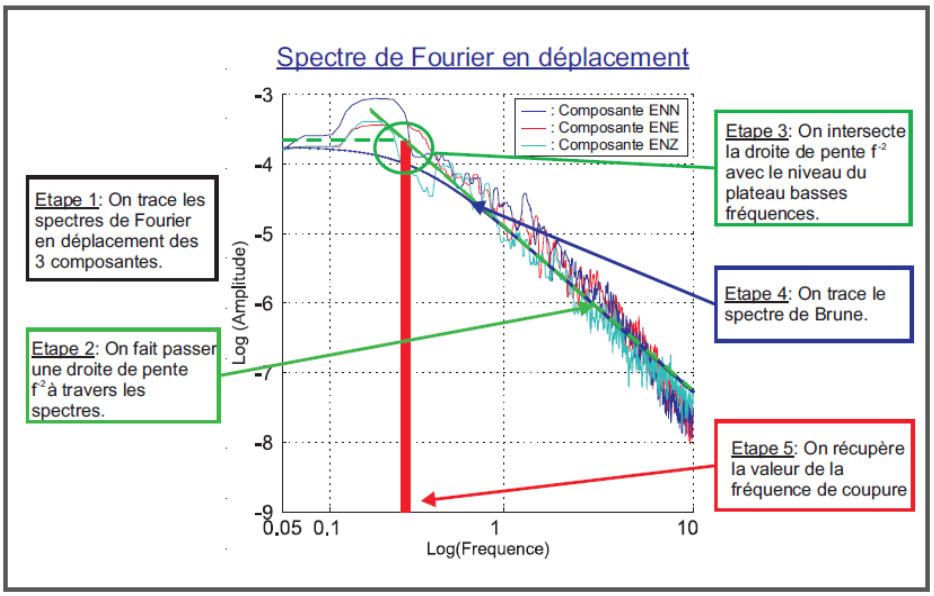


Figure 3. 4 : Détermination de la fréquence de coupure fc d'un séisme sur le spectre de Fourier en déplacement. Procédure interactive développée par Converset [2007].

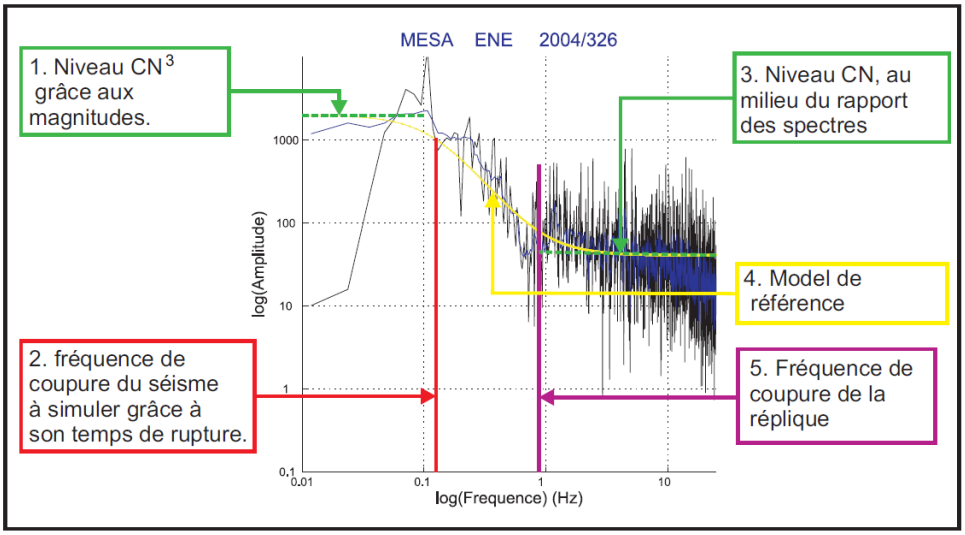


Figure 3. 5 : Détermination des paramètres d'entrée optimaux en utilisant le rapport des spectres de Fourier [*Converset*, 2007].

Nous obtenons un rapport C des chutes de contrainte statique entre le choc principal et ses répliques situé entre 3 et 7 pour la plupart des événements, mais C peut atteindre la valeur 15 pour l'un d'entre eux. Notons qu'il n'est jamais inférieur à 1, ce qui signifie que la chute de contrainte des répliques étudiées ici est toujours inférieure à celle du choc principal.

L'article qui suit présente les résultats principaux du travail effectué sur cette base de données. Notons que le même travail a été effectué sur la réplique principale du séisme qui a eu lieu quelques mois plus tard. Ce travail n'a pas été publié car les résultats obtenus allaient dans le même sens que ceux obtenus pour le choc principal, et donc n'apportaient pas d'élément nouveau à l'analyse.

Bulletin of the Seismological Society of America, Vol. 100, No. 1, pp. 116–130, February 2010, doi: 10.1785/0120080372

Ground-Motion Simulations of the 2004 M_w 6.4 Les Saintes, Guadeloupe, Earthquake Using Ten Smaller Events

by Françoise Courboulex, Julien Converset,* Julien Balestra, and Bertrand Delouis

Abstract The validity and the stability of a ground-motion simulation method based on the recordings of a single small event as an empirical Green's function (EGF) is tested on a seismic crisis that occurred 25 km offshore of the Guadeloupe Islands (Caribbean arc). We aim to determine if (1) the method enables us to reproduce the observed ground motion, (2) the choice of the small event taken as an EGF is crucial for the simulations, and (3) the method provides valuable results compared with ground-motion prediction equations (GMPEs). We have successively used the recordings of 10 small earthquakes (M_w 4.2–5.1) to simulate the ground motions generated by the mainshock (M_w 6.4), at 12 accelerometric stations. We first determined the moment and focal mechanisms of the 10 events chosen as an EGF, as well as the stress-drop ratio C between each of these events and the mainshock. Then, we simulated 500 accelerograms for each EGF and each station. A good reproduction of the mainshock response spectra, the peak ground acceleration, and the duration of the signal was obtained using 9 out of 10 EGFs. For stations with site effects, the results obtained are much closer to the real data than values given by the GMPEs on sediment sites. In the case of blind predictive simulation, we propose to calibrate the stress-drop ratio C through a comparison between the simulated response spectra on rock site stations and the values predicted by GMPEs.

Introduction

The Guadeloupe Islands (situated in the Caribbean arc) were struck by a magnitude M_w 6.4 earthquake on 21 November 2004. This crustal event occurred offshore at a shallow depth and was followed by numerous aftershocks from M_w 1.0 to 5.1. Three months later, a large aftershock occurred with M_w 5.9. Most of the events with magnitudes larger than 4.0 were very well recorded by the French accelerometric network, Réseau Accélérométrique Permanent (RAP), the data of which are freely accessible (Péquegnat *et al.*, 2008; see Data and Resources). We took advantage of this interesting dataset to test the validity of a simulation method based on empirical Green's functions (EGFs).

Simulating the ground motions that might be generated by a future earthquake is an important aspect of seismic hazard assessment. For this, we can distinguish three types of approach. The first (an empirical approach) consists of finding empirical equations fitting some parameters, typically pseudospectral acceleration. This approach is based on actual data and is essential for seismic hazard assessment (see Douglas, 2003, for a review), although it does not provide accelerograms in the time domain, and it does not take into account specific site effects.

The other family of approaches (the deterministic approaches) is based on the physical modeling of the whole process. The kinematic or dynamic source is modeled along with the wave propagation in heterogeneous media. This approach has the great advantage of helping us to understand the entire phenomena and to test many different configurations. Limitations arise as the underground medium is generally poorly known, and then the simulations are limited to low frequencies. When the velocity medium is well known, the computing time necessary to obtain a high-frequency 3D solution is still very high.

A hybrid approach was first proposed by Hartzell (1978), who took advantage of small-event recordings to accurately reproduce the source-receiver path. The small events, known as EGFs, are then combined to reproduce the waveform of a larger shock that is colocated and has the same focal mechanism. Based on this approach, many methods then have been proposed. A number of these assume an extended source with a kinematic description of the rupture process (rupture velocity, patches of asperities, rupture directivity). These methods usually allow very good reproduction of a given large event to be obtained (Hartzell, 1989; Hutchings, 1994; Irikura and Kamae, 1994; Bour and Cara, 1997; Burjanek and Zahradnik, 2007; Ruiz *et al.*, 2007). As in deterministic models,

*Now at Geoservices, Roissy, France.

there are difficulties arising from the need to define values for many of the input parameters, causing the variability of the results to be very high (Pavic *et al.*, 2000). Other methods propose that the summing up of the recordings of small earthquakes is statistically in agreement with the relevant earthquake scaling laws (Joyner and Boore, 1986, Wennerberg, 1990, Somerville, 1993; Tukmarkin and Archuletta, 1994; Zeng *et al.*, 1994; Ordaz *et al.*, 1995; Kohrs-Sansorny *et al.*, 2005; Di Alessandro and Boatwright, 2006).

We used the two-step method described by Kohrs-Sansorny *et al.* (2005), for which very few input parameters have to be specified. Given that the moment of the small event and the target earthquake is defined and that the corner frequency of the small event can be determined from the spectra, the only parameter that is crucial to determine is the stress-drop ratio, C, between the small and the target events.

Our objectives are to utilize the Les Saintes crisis dataset to test (1) the validity of the method to reproduce ground-motion values, (2) the influence of the choice of the small earthquake taken as an EGF, and (3) the interest of the EGF's method compared with ground-motion prediction equations. After a short description of the simulation method, we focus on data from the Saintes crisis. We determine the seismic moment and focal mechanisms of the 10 aftershocks used as empirical Green's functions, as well as the best stress-drop ratio value of each of them relative to the mainshock. We then present simulations results and compare them with real data and with a ground-motion prediction model using misfit criteria.

Simulation Method

Our aim is to generate a set of accelerograms that could realistically be generated by an earthquake of a given magnitude at some specific stations. We used a simulation method based on the empirical Green's functions approach (Hartzell, 1978). A small event is chosen close to the mainshock and with a similar focal mechanism. Its recordings, called empirical Green's functions, account for path and site effects at different stations (Fig. 1). We assume that the recordings of a single small event represent the Green's functions for all points of the fault plane activated during the large simulated event.

We used the two-step summation scheme proposed by Kohrs-Sansorny *et al.* (2005), which arose through the work of Joyner and Boore (1986), Wennerberg (1990), and Ordaz *et al.* (1995). A large number k of time histories called equivalent source time function (ESTF) is generated. The ESTFs are then convolved with the small-event recordings $s(t)$ to provide the synthetic signals $S_k(t)$,

$$S_k(t) = \mathrm{ESTF}_k(t) * s(t). \tag{1}$$

The ESTFs are generated in two steps. In the first stage, a number η_c of delays t_c are randomly generated with a probability density $\rho_c(t)$ over the whole source duration T_c. In the second stage, a number η_d of delays t_d are again generated with a second probability density $\rho_d(t)$ over a window duration $T_d \leq T_c$ centered on each delay generated in the first stage. Finally, $\eta = \eta_c \cdot \eta_d$ small events are summed together and scaled by a factor κ,

$$\mathrm{ESTF}_k(t) = \kappa \sum_{d=0}^{\eta_d - 1} \left[\sum_{c=0}^{\eta_c - 1} \delta(t - t_c - t_d) \right]. \tag{2}$$

The expressions of the probability density functions, as well as a detailed description of the method, can be found in Kohrs-Sansorny *et al.* (2005).

By an appropriate choice of the parameters η and κ,

$$\eta = \eta_c \cdot \eta_d = N^4 \quad \text{and} \quad \kappa = \frac{C}{N}, \tag{3}$$

where

$$N = \frac{f_c}{F_c}, \qquad C = \frac{\Delta\Sigma}{\Delta\sigma}, \quad \text{and} \quad T_c = \frac{1}{F_c},$$

the method produces time histories that, on average, are in agreement with the ω^{-2} model (Fig. 2; Aki, 1967; Brune, 1970) and respect a nonconstant stress-drop condition (Beeler *et al.*, 2003; Kanamori and Rivera, 2004).

Compared with the single-stage summation proposed by Ordaz *et al.* (1995), the time histories we produced using the two-step method have larger variability (Kohrs-Sansorny *et al.*, 2005; Honoré, 2008). This is particularly important when N is high; for example, when the magnitude of the target event is large compared to the magnitude of the small event taken as an EGF.

In the two-step process, we have the choice to distribute the energy in different ways: N and N^3, N^2 and N^2, or N^3 and N. We have tested the influence of each of these choices (Honoré, 2008). While the median value is quasi invariable, the value of sigma (standard deviation) changes a little. This

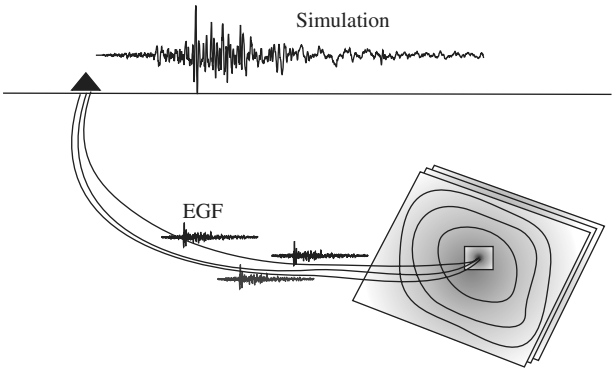


Figure 1. Principle of the EGF summation method. The recordings of a single small earthquake are combined several times to produce simulated recordings for a larger event at a given station.

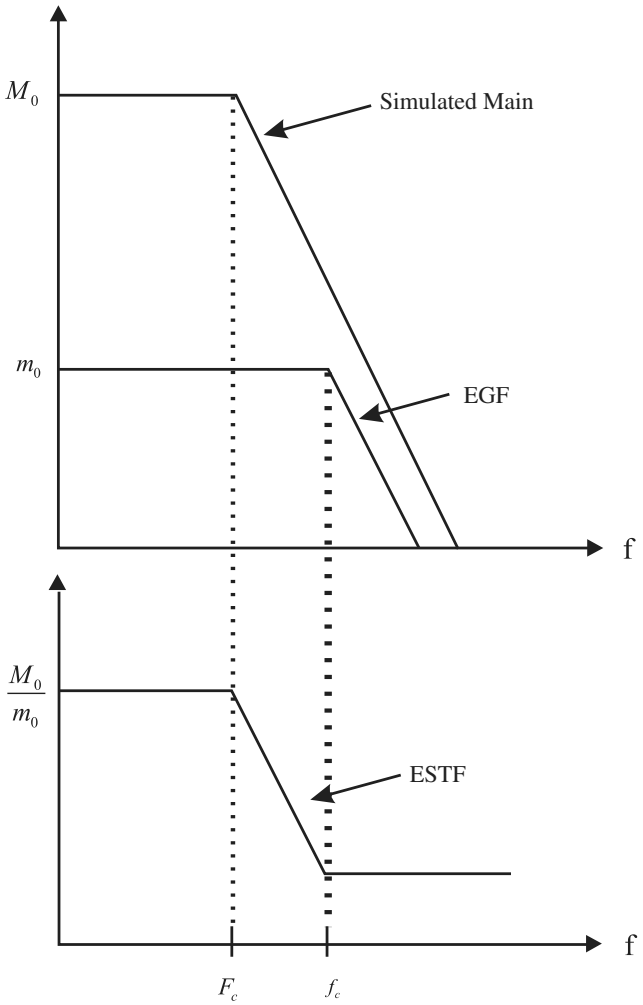


Figure 2. Top, theoretical ω^{-2} spectral model for the mainshock and the small event used as an EGF. Bottom, theoretical shape of the average equivalent source time function (ESTF) Fourier spectra. F_c, M_0, f_c, and m_0 are, respectively, the corner frequencies and seismic moments of the target earthquake and the small event used as an EGF.

can have an influence on probabilistic seismic hazard assessment (Beauval *et al.*, 2009) but is negligible in this study. In this article we took $\eta_c = \eta_d = N^2$.

In practice, we first generated 500 different time histories following the two-step summation scheme. These time functions can be assimilated with the source time function of the target event. The only difference is that their frequency content takes into account that the source of the small event taken as the EGF is already included in the EGF. For this reason, we call them equivalent source time functions (ESTFs). We then convolved each ESTF with the EGF for each of the stations and for each component, obtaining 1500 simulations for each station (i.e., 18,000 simulations for the 12 stations.)

In the present study, we have used this procedure for 10 different small events that were considered successively as the EGF. This means that we produced about 180,000 accelerograms (slightly less, as all the earthquakes were not recorded at all of the 12 stations).

The main interest of this method is that the number of input parameters is reduced. Indeed, the only parameters that have to be specified are:

- The seismic moment (m_0) and corner frequency (f_c) of the small event taken as an EGF; these can be determined from the data.
- The seismic moment (M_0) of the earthquake to be simulated (called the target event).
- The ratio C between the static stress drop of the target event ($\Delta\Sigma$) and that of the small event ($\Delta\sigma$).

This last parameter is the only one that is particularly difficult to determine when the target event is unknown. We will discuss its choice in the last section.

These parameters are linked by the relationship shown in equation (4):

$$CN^3 = \frac{M_0}{m_0}. \tag{4}$$

In this method, the definition of the source is purely temporal, and so we cannot take into account the specific directivity effects of the rupture process. It is important to understand that our aim was not to describe a specific rupture process but to generate a set of accelerograms that can represent most of the possible ground motions at a given site. The equivalent source time functions generated by the random process are different from each other, and they can indirectly account for different types of ruptures and produce large variabilities in the ground motion.

Of note, like most of the EGF methods, this method is not appropriate for the simulation of ground motion for near-source sites, and it cannot account for nonlinear effects. If we consider that nonlinear effects appear for peak ground acceleration (PGA) values higher than $0.25g$, this will not be a great limitation for our study.

Data from the Saintes Crisis

The main Les Saintes earthquake occurred on 21 November 2004 at 11:41 hr (coordinated universal time, UTC), about 25 km offshore to the south of Guadeloupe Island (French Antilles), which is situated in the Caribbean region. The shaking caused the death of one person, destroyed or damaged several houses, and generated many panic reactions in the population, especially on the Saintes Islands that are situated very close to the epicenter (Duval *et al.*, 2006). A maximum intensity of VIII on the European Macroseismic Scale (EMS98) was reported by the Bureau Central Sismologique Français on the Les Saintes Islands. The seismic moment of this event, given by the Global Centroid Moment Tensor (Global CMT) catalog (see Data and Resources), was M_0 3.44×10^{25} N m, which is equivalent to a magnitude of M_w 6.36. In the present study, we considered a magnitude of M_w 6.4. This shallow earthquake (14 km in depth, data from Centre de Données Sismologiques des Antilles [CDSA; see Data and Resources]), with a pure

normal focal mechanism (Global CMT), occurred on a normal fault that was previously described in the seismotectonic study of Feuillet *et al.* (2002). (See the Data and Resources section.)

The source processes of the mainshock were studied by Delouis *et al.* (2007). They demonstrated a total rupture duration of 8 sec, with a repartition of energy in two separate patches over the fault plane. The mainshock was followed by a huge number of aftershocks that were detected and located by the permanent seismic network of the Observatoire Volcanologique et Sismologique de Guadeloupe (Beauducel *et al.*, 2004; Institut de Physique du Globe de Paris, 2004). Fifty-one aftershocks had magnitudes greater than M_w 4.0 (Bertil *et al.*, 2005); and, three months later (on 14 February 2005), there was a large aftershock of M_w 5.8 (Global CMT).

In addition to the short-period seismic network, two permanent accelerometric networks were operating and allowed the recording of the mainshock without saturation and of most of the larger aftershocks (Fig. 3). Both of these networks are part of RAP, which is currently composed of about 120 stations (Péquegnat *et al.*, 2008). (See the Data and Resources section.)

One accelerometric network is managed by the Observatoire Volcanologique et Sismologique de Guadeloupe (OVSG-IPGP), and in 2004 it comprised 12 stations with Kinemetrics episensors (Fig. 3). (See the Data and Resources section.) Ten of them recorded the mainshock. In addition, two new stations (TDBA and TDHA) were installed on the Saintes Islands a few days after the mainshock.

The second network is managed by the Bureau de Recherches Géologiques et Minières (BRGM; see Data and Resources). It was composed of seven stations with SMACH sensors. Five of these were located in the city of Pointe à Pitre, at 50 km from the epicenter (Fig. 3). Their trigger levels were often high, and only few aftershocks could be recorded.

The precise localization of the mainshock and of the 51 largest aftershocks was performed by the CDSA (Bengoubou-Valerius *et al.*, 2008), using both velocimetric and accelerometric stations (Bertil *et al.*, 2004; Bertil *et al.*, 2005).

In the present study, we proposed to use the method described in the previous sections to simulate the ground motions generated by the mainshock using successively smaller events as an EGF. We selected the ten aftershocks that were best recorded by a large number of stations (Fig. 3, bottom).

Moment and Focal Mechanism of the Ten Small Earthquakes Used as an EGF

In order to determine the focal mechanism of aftershocks, we used the waveform modeling approach of Delouis and Legrand (1999) adapted to simple point sources. Data processing involves double integration to obtain displacement seismograms and bandpass filtering to reduce both the low-frequency noise produced by the integration process and the high-frequency content related to the complexity of the real earth structure. The low-cut frequency is adjusted for each station, depending of the level of low-frequency noise enhanced by the double integration. The lowest low-cut frequency used is 0.04 Hz. The high-cut frequency is fixed to 0.25 Hz for all stations.

Aftershocks are modeled here by point sources, with a source time function represented by a single isosceles triangle. The *a priori* information required on the source is the hypocenter and a first estimate of the magnitude. The rupture area (S), as well as the duration of the source time function, is scaled with the *a priori* magnitude and kept fixed in the inversion. This duration, contributing to the width of the waveforms, may be adjusted after inspection of the waveform modeling results. Four parameters are to be inverted: the strike, dip, and rake angles of the focal mechanism and the slip (Δu, dislocation value). The inversion is carried out with a two-step grid search in the 3D space of the focal mechanism parameters. The criterion of selection is the minimization of the normalized root mean square (rms) misfit error between the observed and computed waveforms. In the first step, the three angles (strike, dip, and rake) are evenly and uniformly sampled. The second step is a fine grid search around the minima of the rms function resulting from the coarse search. Those minima correspond to the best solutions obtained for each discrete value of the strike, dip, and rake parameters tested in the first step. They sample a large part of the focal mechanism solution space and are not restricted to the vicinity of the very best solution. In both steps of the inversion procedure, synthetic seismograms are computed for unit slip. The amplitude of synthetics and slip being linearly related, a loop on slip values is implemented within the rms computation algorithm. Synthetic seismograms are simply multiplied by the slip value before the rms calculation, and we finally retain the slip amplitude producing the lowest rms misfit. By combining the source area with the slip value found for the best solution, we compute the seismic moment and the moment magnitude M_w. Synthetic seismograms are computed using the discrete wave number method of Bouchon (1981), designed for 1D velocity models.

A specific layered velocity model is used for each station. Velocity models were determined using one of the aftershocks (14/12/2004 at 21:29 hr [UTC], 15.77° N, 61.49° W, depth 11 km, M_b 4.6; Bertil *et al.*, 2005). For that event, an initial inversion of the focal mechanism was performed with a starting moment magnitude equal to the body-wave magnitude M_b and a starting velocity model issued from the CRUST2.0 global crustal model at 2×2 degrees (Mooney *et al.*, 1998). Using the best focal mechanism found by this initial inversion, we tested several thousand combinations of layer thicknesses, velocities, and V_P/V_S ratios in order to improve the waveform modeling at each station. For a given station, the layered model providing the best waveform match was retained. The set of optimized velocity models was then used in the source inversions of the aftershocks listed in Table 1.

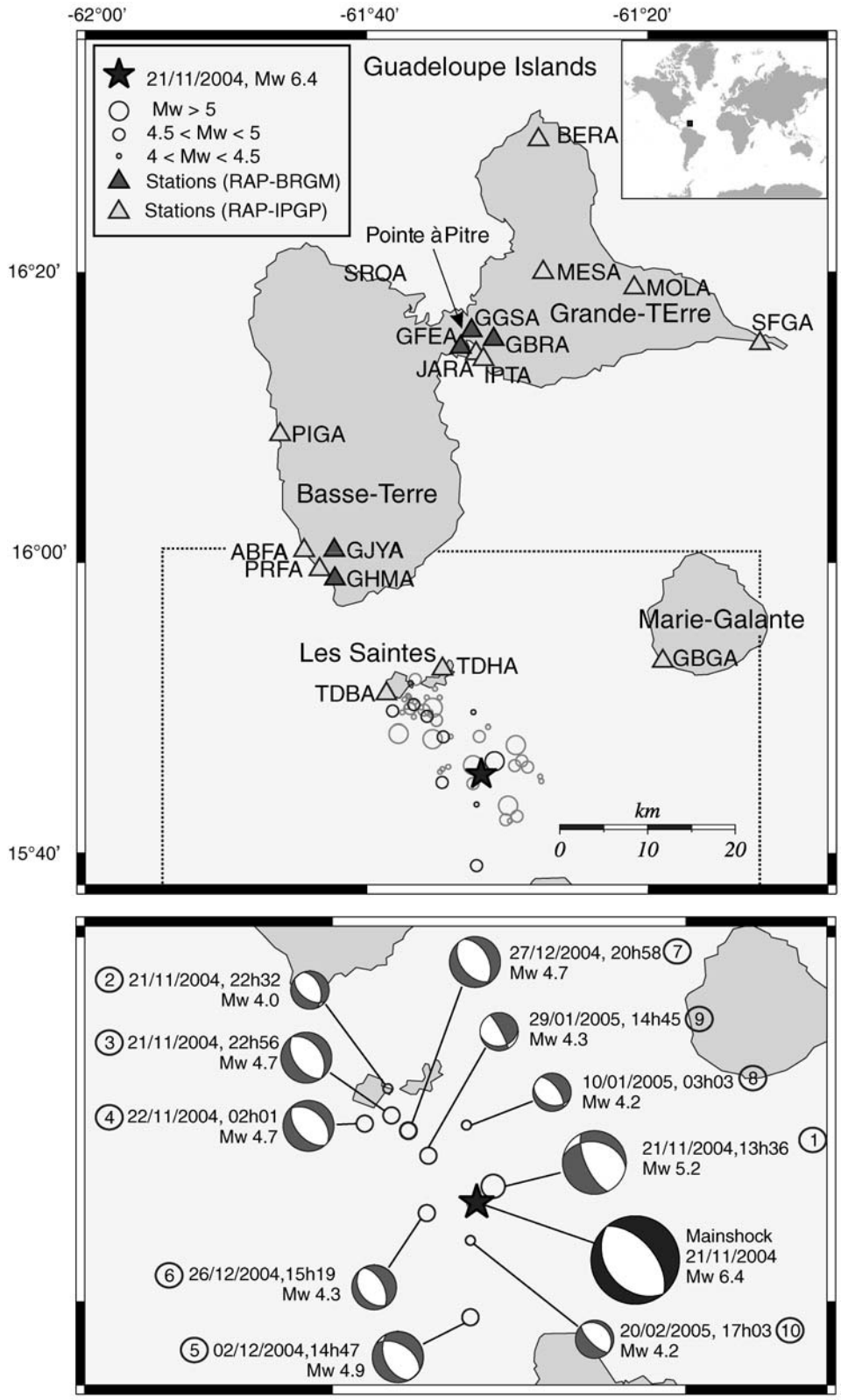


Figure 3. Top: black star, mainshock; gray circles (CDSA), largest aftershock epicenters. French permanent accelerometric network (RAP): light triangles, stations are maintained by the Observatoire Volcanologique et Sismologique de Guadeloupe—Institut de Physique du Globe de Paris (OVSG-IPGP); dark triangles, stations maintained by BRGM. Stations TDBA and TDHA were installed soon after the mainshock. Bottom: Zoom on the epicentral region and details of the 10 aftershocks used as an EGF, with their respective focal mechanisms determined in this study. The focal mechanism of the mainshock is the Global CMT solution. Times are shown in UTC.

Table 1

Characteristics of the 10 Events Chosen as an EGF in the Present Study

Event Number	Date (dd/mm/yyyy)	Origin Time (hr:min:sec. UTC)*	Focal Mechanism (strike/dip/rake)†	Magnitude (M_w)	Mainshock Simulation		
					Distance* EGF/M (km)	C‡	N‡
	21/11/2004	11:41:08	320/55/ − 90§	6.4			
1	21/11/2004	13:36:59	161/75/53	5.2	2.9	5.3	2.9
2	21/11/2004	22:32:08	340/45/ − 65	4.0	11	3.5	10.4
3	21/11/2004	22:56:32	145/50/ − 90	4.7	12.9	3.1	4.9
4	22/11/2004	02:01:19	140/50/ − 85	4.7	14.2	9.1	3.4
5	02/12/2004	14:47:53	155/47/ − 66	4.9	11.6	2.8	4.0
6	26/12/2004	15:19:15	135/35/ − 95	4.5	6.4	11	4
7	27/12/2004	20:58:14	138/54/ − 97	4.7	11.3	3.0	4.9
8	10/01/2005	03:03:26	109/33/ − 120	4.2	7.8	31.2	4.0
9	29/01/2005	14:45:34	76/33/ − 164	4.3	6.8	3.6	6.4
10	20/02/2005	17:03:53	317/20/ − 88	4.2	4	20.2	4.8

*Origin time and distances between mainshock and aftershock hypocenters are as deduced from the table given by the CDSA in Bertil *et al.* (2005).

†Focal mechanisms as computed in our study.

‡Parameters N and C are estimated by a spectral-ratio analysis.

§The focal mechanism of the mainshock is the Global CMT solution.

Depending on the availability of strong-motion records, and avoiding redundancy in the azimuth distribution of the stations, the source parameters were inverted using two to seven stations. The group of stations used for source inversion comprises the permanent stations GBGA, IPTA, PIGA, SFGA, and PRFA and the temporary stations TDBA and TDHA. We verified that, even with a small number of records (minimum 2), the strike, dip, and rake parameters were correctly constrained. The degree of constraint could be appreciated because the parameter space was extensively explored by the grid search.

An example of a source inversion result is shown in Figure 4 for the 27 December 2004 aftershock. Values obtained for the 10 aftershocks can be found in Table 1 and Figure 3.

Input Parameters: Stress-Drop Ratio

As mentioned previously, only a few input parameters are necessary for applying this two-step method described by Kohrs-Sansorny *et al.* (2005). For the mainshock, we took $M_w = 6.4$ and approximated $F_c = 1/8$ Hz from the rupture duration found by Delouis *et al.* (2007). All of the focal solutions were pure normal faults except two that had very small strike-slip components (Table 1). We considered that all these events could be tested as an EGF.

The other necessary input parameters for the simulations were N and C. N^4 is the number of summations of small earthquakes that were necessary to simulate the large earthquake. N is equal to the ratio between the corner frequency of the small earthquake and the corner frequency of the target earthquake. C is the ratio between the static stress drop of the target event and that of the small earthquake used as the EGF; it is linked to the moment ratio by equation (4).

When both the mainshock and the EGF recordings are available, the value of C can be obtained using a spectral ratio between the large and the small events (Hough and Kanamori, 2002):

$$\frac{\dot{M}(f)}{\dot{m}(f)} = \frac{M_0}{1 + (f/F_c)^2} \Big/ \frac{m_0}{1 + (f/f_c)^2}. \tag{5}$$

This method has the advantage of theoretically eliminating site and attenuation effects that could affect the determination of the parameters.

Practically, the low-frequency level is fixed using the M_0/m_0 value (sometimes it was reevaluated), and the corner frequency of the large event, F_c, is imposed. On the spectral ratio, we determined the values of CN that provided the best fit with the theoretical spectral ratio and deduced the values of f_c, N, and C. Note that N has to be an integer in the code, and so values of N' and C' have to be chosen to satisfy this constraint.

In the present study, we determined the input parameters that give us the best opportunity to fit the actual records. Of course, in the case of a blind simulation, the mainshock recordings would not be available, and then all of the parameters could not be determined in the same way. We will discuss this point and propose some solutions in the last section.

Simulation of the Mainshock

Simulation Results for Aftershock Number 6 as an EGF

We first present the simulations we obtained using a given small event taken as an EGF. For each simulation, the input parameters are presented in Table 1.

We started by selecting the aftershock that occurred on 26 December at 15:19 hr. This aftershock had an M_w 4.5, was located very close to the mainshock nucleation, and had a focal mechanism that was almost similar to the mainshock

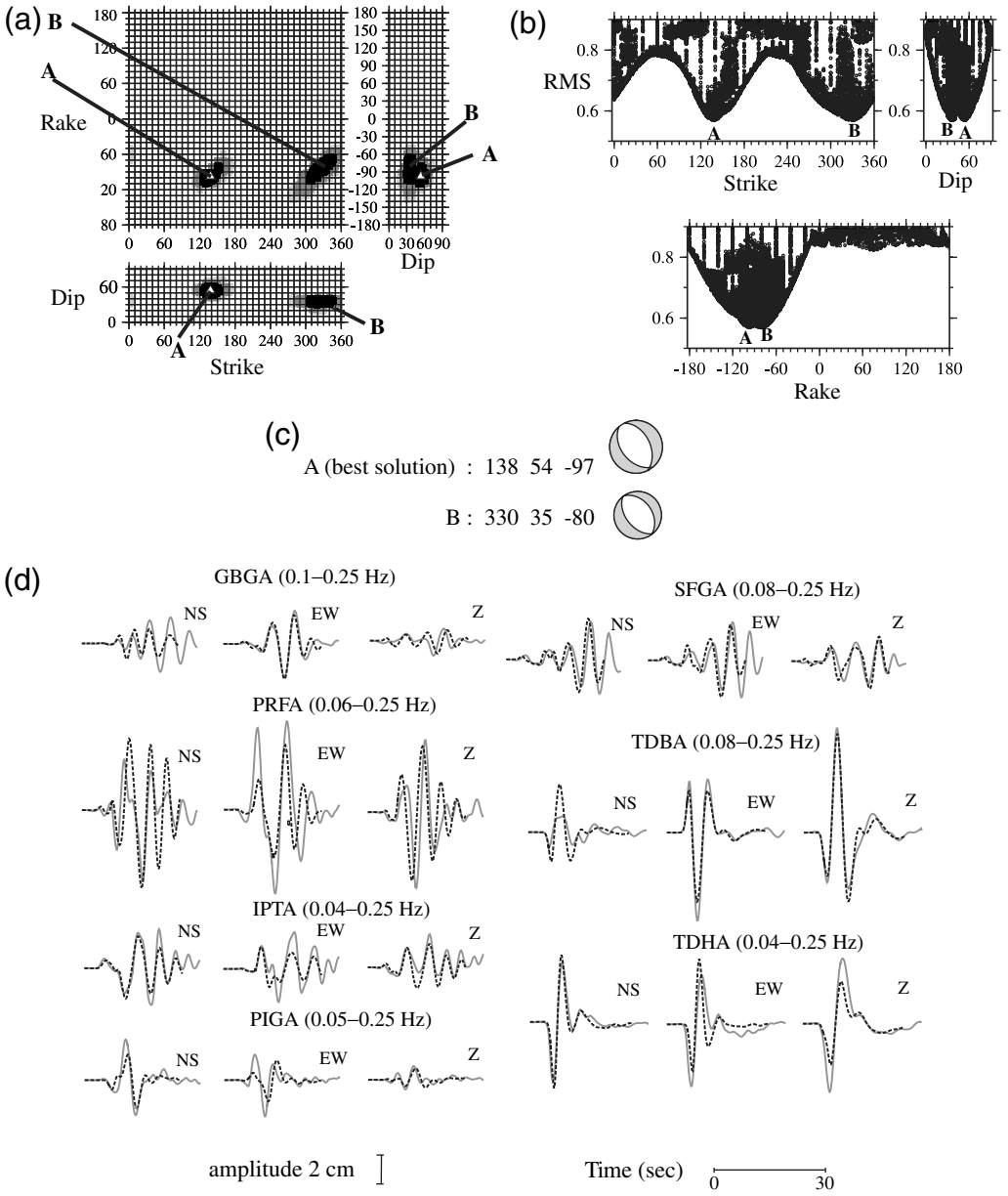


Figure 4. Result of the source inversion for the 27 December 2004 aftershock. (a) Solutions are projected and visualized on the strike–dip, strike–rake, and dip–rake planes. White triangle, the best solution found (rms = 0.57, labeled A); black, medium gray, and light gray, solutions for which the rms error increases by less than 5%, 15%, and 25% with respect to the lowest rms, respectively. A second minimum, labeled B, is found with similar rms values as solution A. Solutions A and B correspond approximately to the two nodal planes of the same focal mechanism, as shown in (c). (b) The rms misfit error is plotted as a function of each individual parameter: strike, dip, and rake. The best solutions A and B are indicated. (c) Gray shaded areas in compression, focal mechanisms of the best solutions A and B. (d) Comparison between observed (gray line) and computed (black dashed line) displacement seismograms for the best solution. The moment magnitude found for this event is 4.7. NS, north–south; EW, east–west; Z, depth = 11.4 km.

(aftershock number 6 in Fig. 3 and in Table 1). The recordings of this event were summed up on each component of all of the available stations to simulate an earthquake of magnitude M_w 6.4, using the parameters described in Table 1. For each simulation, we generated 500 synthetics with 500 different ESTFs, which can be interpreted as 500 different histories of the rupture processes. Each ESTF was convolved by the recordings of the small event on each component and at each available station.

In the present study, we worked on the horizontal components separately. The results are very similar for the east–west and north–south components, and so we chose to show the results only for the east–west component.

Figure 5 shows, as an example, the simulations for station GBGA. Three synthetic accelerograms (gray lines) are presented in acceleration, velocity, and displacement for the horizontal (east–west) component of station GBGA, as well as the actual signals of the EGF aftershock number 6 and

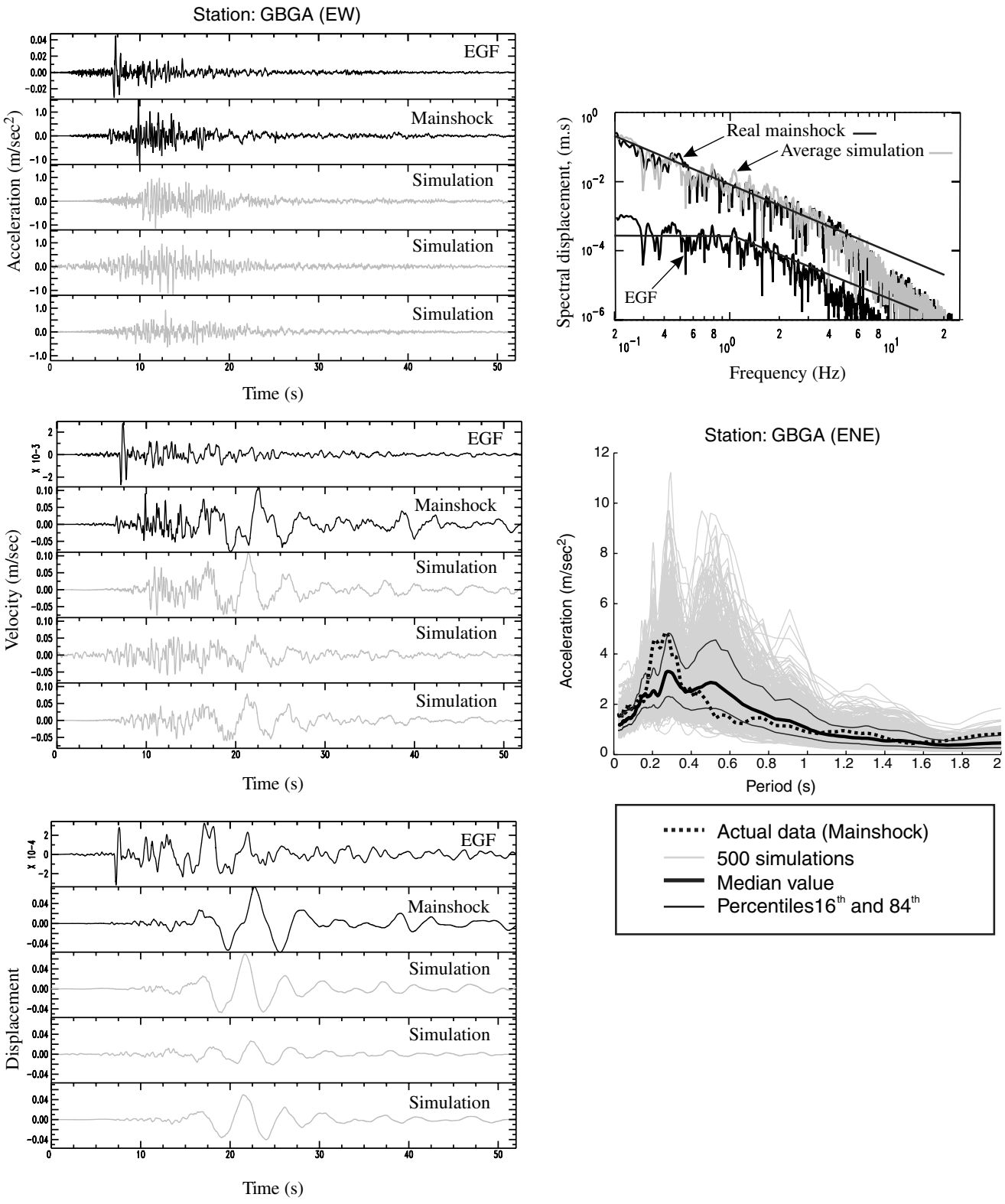


Figure 5. Left: Recordings of the mainshock, the aftershock that occurred on 26 December 2005 at 15:19 hr (EGF aftershock number 6 in Table 1 and Fig. 3) taken as an EGF, and three of the 500 simulations (gray) plotted in the time domain for acceleration, velocity, and displacement. East–west component only is presented. Right top: Fourier spectrum is presented for the mainshock; black line, Fourier spectrum of the small event taken as an EGF; gray line, average Fourier simulation. Right bottom: bold dotted lines, response spectra of the actual mainshock; gray lines, response spectra of the 500 simulations; bold black line, median; thin black lines, sixteenth and eighty-fourth percentiles.

the mainshock. It is interesting to note that on the velocity traces and, even more so, on the displacement traces, high amplitude and low frequency (about 10 sec) dominate the signal. This low frequency is well reproduced in the simulations, which means that it is also present in the recording of the small event used as an EGF. This low frequency observed in the earthquakes during the Les Saintes sequence has been interpreted by Jousset and Douglas (2007) as the possible presence of fluids in the source area. The empirical Green's functions approach enables us to reproduce this particular low frequency. This is really interesting for seismic hazard assessment, while the spectral displacement is used for the design of structures, such as long bridges and tall buildings (Jousset and Douglas, 2007).

The top right side of Figure 5 shows the amplitude of the Fourier spectra in displacement of the observed mainshock, the aftershock taken as an EGF, and the mean spectra (quadratic average) calculated on 500 simulations. The ω^{-2} spectral decay is rather well reproduced by the actual data and by simulations up to a frequency of about 20 Hz. After this value, the attenuation due to superficial layers imposes a slope that is more important for the decay (for the actual data and the simulations). At the bottom right side of Figure 5 are represented the elastic acceleration spectra (SA) with a damping of 5% for the mainshock and for the 500 different simulations, as well as the median value and sixteenth and eighty-fourth percentiles (68% of the simulations are comprised between these limits). An analysis focused on the simulation variability can be found in Beauval *et al.* (2009) using the same method and the same dataset.

Elastic response spectra are presented in Figure 6 for all the available stations. The fit between the simulations and the mainshock is very good for all of the frequencies for stations MOLA, IPTA, and GBGA. For stations GGSA, SROA, and PRFA, the shape of the response spectra is well reproduced, but the level is slightly over- or underestimated by the simulations. This difference is important only on GJYA, where the actual mainshock is larger than the highest simulations we generated. For stations PIGA, GFEA, and GHMA, the level is correctly reproduced, but a part of the spectra for frequencies 0.6–0.8 is not well reproduced in the simulations.

Some of the differences can be explained by the fact that the EGF approach is able to take into account site effects only when they identically affect the small and the large event waveforms (linearity). In some cases, the frequency content of the mainshock is certainly prone to resonant phenomenon, which is not the case for the small event.

Comparison with Ground-Motion Prediction Equations

The next step consists of comparing our results with ground-motion prediction equations (GMPEs). Douglas *et al.* (2006) examined the suitability of different GMPEs for the estimation of shaking in the French Antilles using the methodology proposed by Scherbaum *et al.* (2004). They found that none of the models considered were well adapted to the prediction of ground motion from shallow crustal earthquakes; however, the model of Ambraseys *et al.* (2005) generally provides the best fit to the observed shakings. Hence, it is this model that we used for our comparisons. The equation of Ambraseys *et al.* (2005) used moment magnitudes (M_w), and therefore no magnitude conversions were needed. It requires the specification of the type of faulting, where we used the coefficients given for normal faults. It predicted the values for the larger horizontal component, which is why we compared the east–west and north–south horizontal components separately.

We show a comparison of these GMPEs with the actual mainshock and the median value of our simulations in Figure 7, where the median value of the GMPEs is plotted as the black dotted line, and the sixteenth and eighty-fourth percentiles, which correspond to ±sigma for a logarithmic representation, are in gray. We present the results for three stations that are on rock sites, and for three stations that are on soil, following the information given by the CDSA Web site (see the Data and Resources section).

For the stations on rock (MOLA and PIGA), the recorded mainshock, the simulations, and the GMPEs are generally in good agreement. For station GHMA, it appears that the EGF simulation better reproduced the signal that was recorded. This latter station certainly has a topographic site effect (as described in the CDSA Web site), and this effect could not be reproduced by the GMPEs. For the three stations situated on soils, it is very clear that the EGF method greatly enhanced the soil ground-motion prediction compared with the GMPEs.

Simulation Results Using Successively the 10 Small Events as an EGF

The results that we have shown up to now were computed using the aftershock that occurred on 26 December at 15:19 hr as the only EGF (EGF aftershock number 6). The same simulations were calculated successively using the other nine small events chosen successively as the EGF (see Fig. 3 and Table 1 for the input parameters). For each EGF, we generated 500 synthetic signals on the available stations and the three components. The median values of the simulations obtained at the same six stations as in Figure 7 are represented in Figure 8 and are compared with the same GMPEs. We see immediately that the variability of the simulations is rather important. Nevertheless, at the stations situated on rock sites (without topographic effect), the simulations obtained with the various EGFs are included in the sixteenth and eighty-fourth percentiles of the GMPEs. For the other stations (soil or topographic site effect), the ground motions are better predicted by the EGF method, whatever the tested EGF.

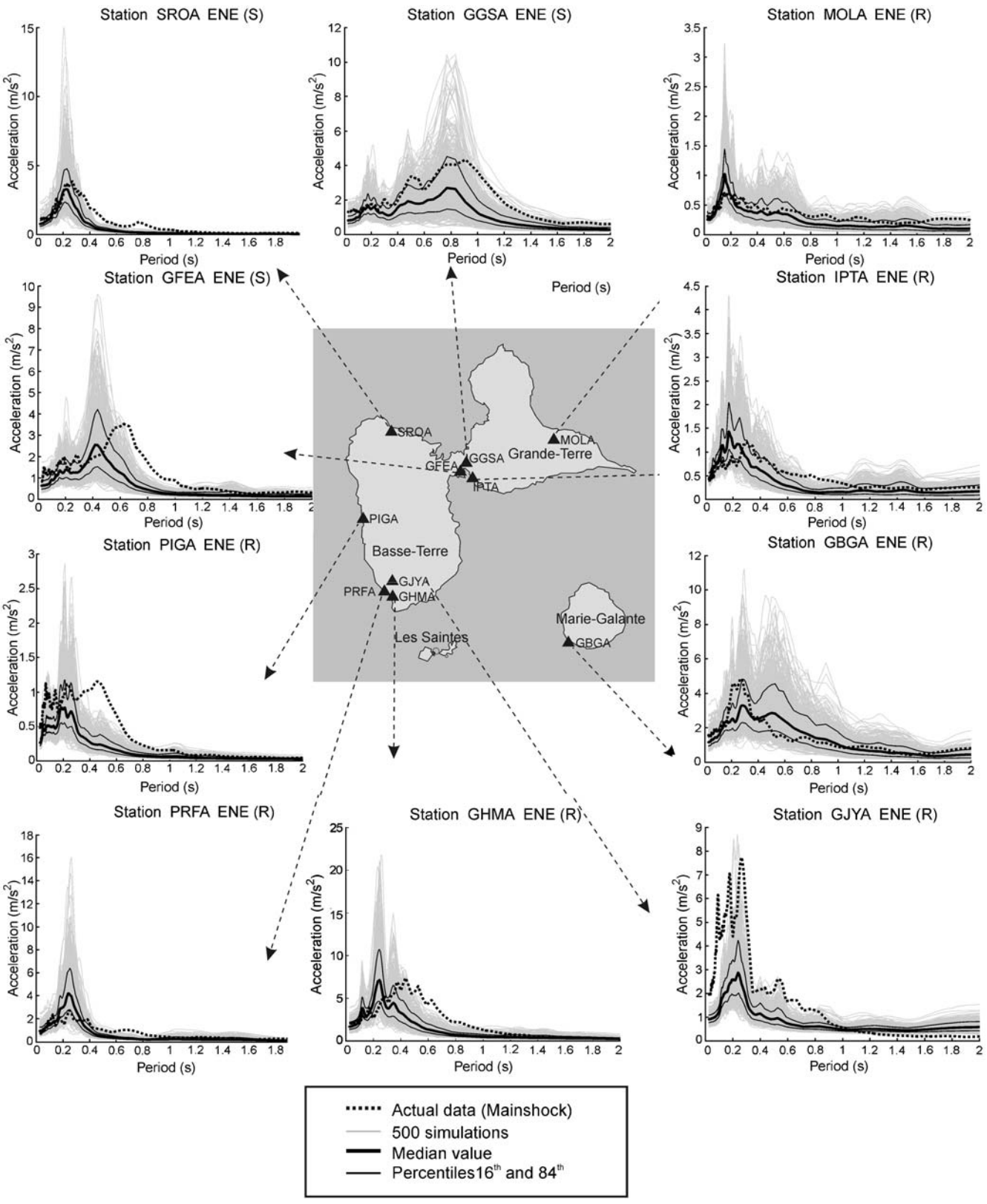


Figure 6. Simulation of the east–west component of the mainshock using aftershock number 6 as an EGF. Dotted black line, elastic response spectra (damping, 5%) for the actual mainshock; gray lines, 500 different simulations; bold line, the median value; black lines, sixteenth and eighty-fourth percentiles. As identified in the CDSA web site: (R), stations that are installed on rock sites; (S), stations that are installed on soils.

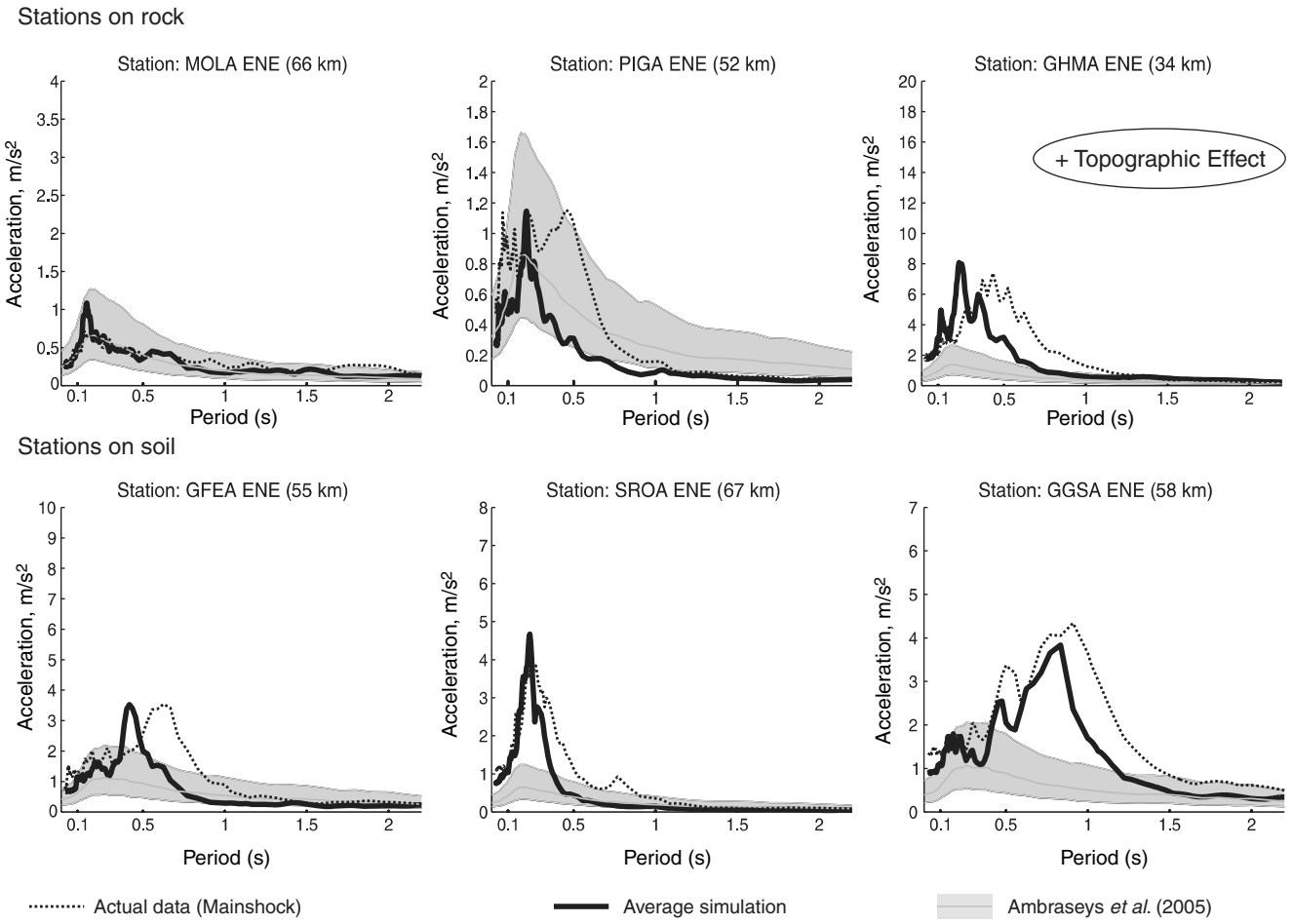


Figure 7. Comparison of the results obtained by EGF simulations with the values predicted by the GMPEs of Ambraseys *et al.* (2005) and the actual mainshock for six stations. Top: stations on rock sites. Bottom: stations on soil sites. Note that station GHMA has certainly a topographic site effect.

Criteria to Measure the Quality of Fit between Observed and Simulated Signals

To obtain a quantitative estimation of the quality of the fit between the simulations obtained using the different EGFs and the actual data, we compared the values obtained for the PGA, the peak ground velocity (PGV), and the relative significant duration of the signal (RSD) and compared point-to-point response spectral acceleration for 5% damping. The RSD corresponds to the duration for which the Arias intensity of the signal is between 5% and 95% (Arias, 1970; Trifunac and Brady, 1975). These parameters are of greatest interest to engineering seismologists.

Following the method proposed by Anderson (2004), the results are given as S scores between 0 and 10, computed as

$$S(p1, p2) = 10 \exp(-[(p1 - p2)/\min(p1, p2)]^2, \quad (6)$$

where $p1$ corresponds to a given measure (PGA, PGV, RSD, SA) for the observed data and $p2$ for the corresponding measures in the simulations.

A score between 0 and 4 represents a bad fit, a score between 4 and 6 is a middle score, a score between 6 and 8 is a good score, and a score greater than 8 represents an excellent fit (Anderson, 2004). Figure 9 shows the scores obtained for each EGF and all the available stations. In practice, we computed the scores on 25 simulations taken at random for the 10 small events used as EGFs and for all of the available stations. We first checked that the average values of these 25 simulations were meaningful compared with the 500 simulations.

For the PGA and PGV, we generally obtain values between 6 and 8 (i.e., good scores; Fig. 9). The fit for the duration (RSD) is a little better (between 7 and 9), and this factor is particularly interesting for the seismic hazard. The fits for all of the periods of the elastic response spectra give scores between 6 and 8, except for aftershock number 8, for which this is smaller. With the focal mechanism, distance, and depth of this event being almost the same as the mainshock, this bad value could be due to a directivity effect of the small event that disturbed the data at some of the stations. This could also indicate that the high value of C ($C = 31$ for this

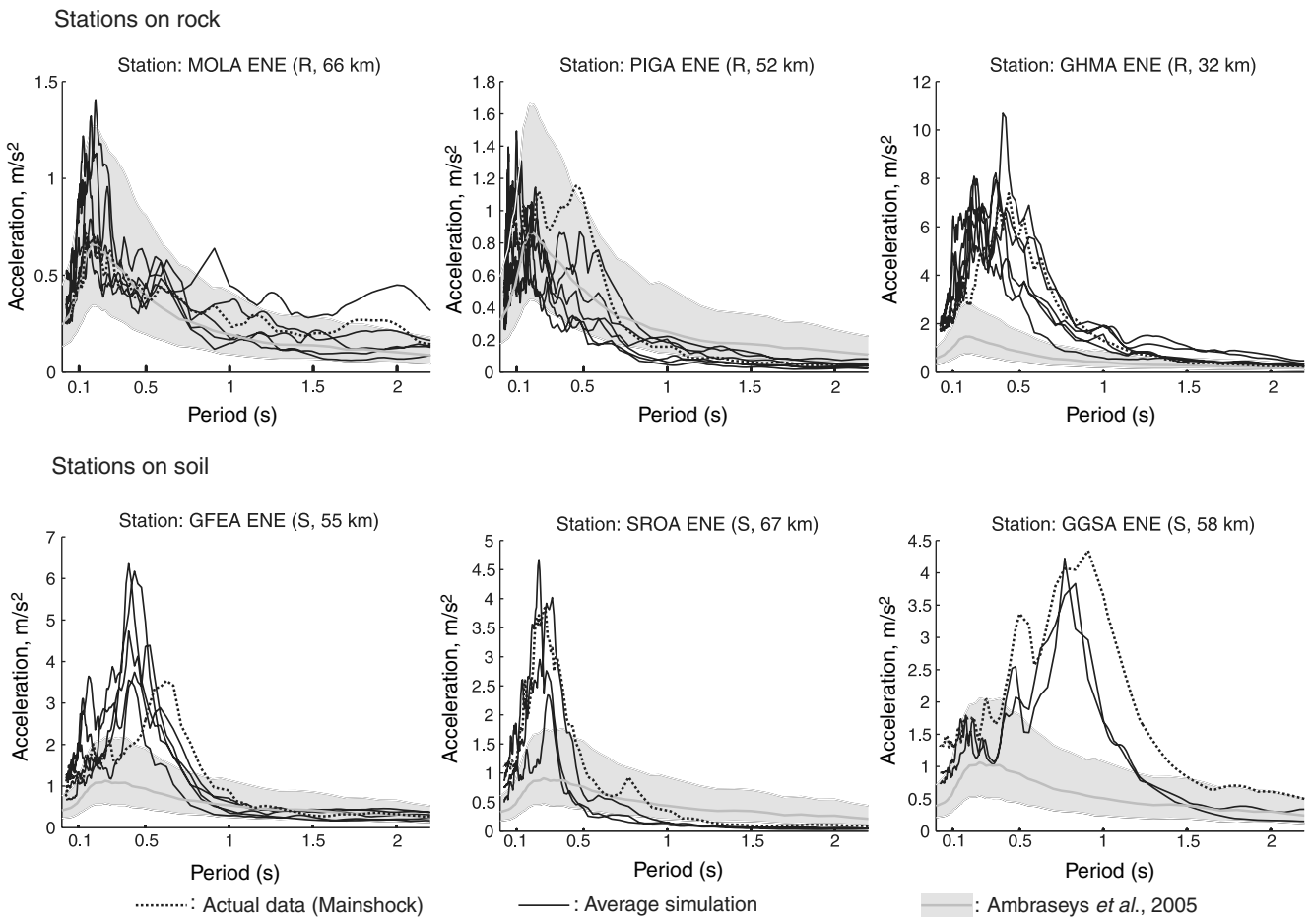


Figure 8. The average simulations are plotted for all of the available EGFs at each of the stations and are compared with the GMPEs of Ambraseys *et al.* (2005) ±sigmaand to the actual mainshock. Top: stations on rock sites. Bottom: stations on soil sites.

event, which is the largest value of the 10 EGFs) is not of significance.

We also made all of these comparisons station by station and for the different frequency bands, as suggested by Anderson (2004), but we could not find any clear tendencies that are worth discussing further here.

How to Calibrate the Stress-Drop Ratio *C* in Blind Simulations

The results presented here are based on preliminary determinations of the input parameters based on the analysis of the aftershock and the mainshock recordings. In an actual simulation context (i.e., when the mainshock has not yet occurred), the mainshock recordings are, of course, not available. In this context, the value of C (the stress-drop ratio) cannot be measured. So how can the value of C be estimated? Should we take $C = 1$ and then estimate that the stress drop of the target large event is the same as the stress drop of the small events chosen as an EGF? Should we test values of C between 1 and 100? Should we test values smaller than 1?

We propose a solution to obtain an estimation of the C value based on the GMPEs that are available for a region. A similar approach was described by Causse *et al.* (2008), in an attempt to calibrate several input parameters that were necessary for an EGF simulation method based on a kinematic description of the rupture process. In our case, the value of C is all that has to be calibrated. Figure 10 illustrates the concept here. On station MOLA, which is a good regular rock site station, we have plotted in gray the Ambraseys *et al.* (2005) GMPE median value and sixteenth and eighty-fourth percentiles. Then we have plotted the simulations obtained with one EGF (this example is computed using EGF aftershock number 6) with different values of C. Note that the discrete values arise because the parameter N must be an integer. The lowest simulation is computed with $C = 1.4$ and the highest with $C = 26$. If we consider that the GMPEs are well adapted to the region and could then reproduce the SA well enough on rock sites (which appears to be the case here), the representation used in Figure 10 provides an estimation of C. The value $C = 26$ supplies simulations that are clearly too high compared with the GMPEs. Simulations computed with $C = 1$ and $C = 3.2$ appear too small. The values $C = 5.5$ and $C = 11$ appear to fit the GMPEs rather well (the best value selected on the data was $C = 11$; see

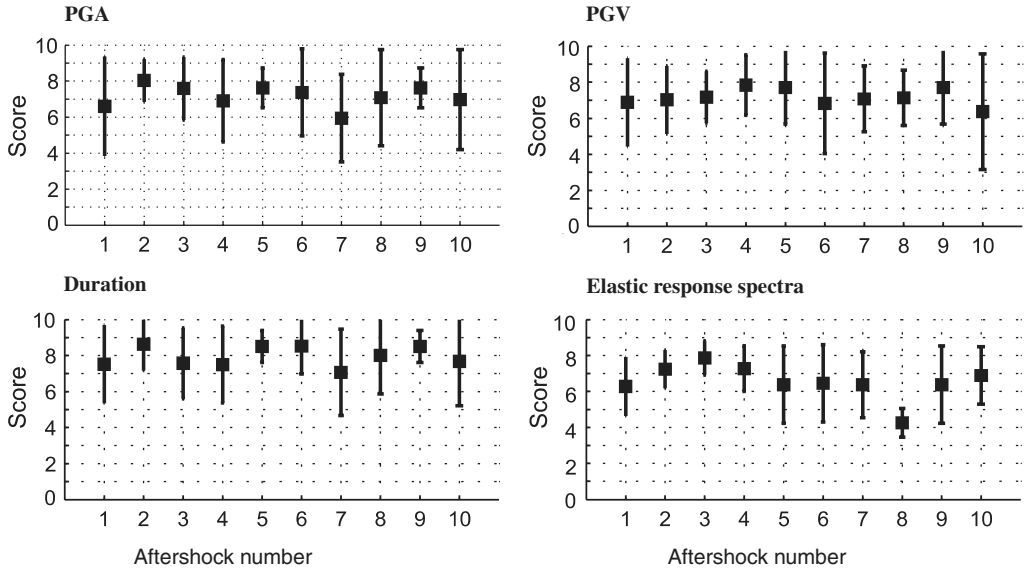


Figure 9. Scores obtained for the four different indicators computed according to Anderson (2004) for the 10 small events used as an EGF. Black squares, mean value obtained for each EGF; black bars, mean ±sigma.

Table 1). This approach could thus be developed to help in the choice of parameter C for blind simulations.

Discussion

The values of C that we have measured for our simulations vary between 3 and 31 from one aftershock to another one (Table 1). These values neither correlate with depth nor with magnitude, although it is true that the ranges of depth and magnitude of these 10 events might not be large enough to uncover any significant correlations. As the value of C is always larger than 1, this indicates that the static stress drop of the aftershocks used in the present study are always smaller than the stress drop of the mainshock. The stress drop, and more generally the scaling laws, for earthquakes have been investigated in a number of studies using recent high-quality waveform data (Ide and Beroza, 2001; Venkataraman *et al.*, 2002). It has been proposed that the stress drop is related to the size of an earthquake (Kanamori and Rivera, 2004), the maturity of the faults (Manighetti *et al.*, 2007), the position of the aftershocks relative to the main fault zone (off-fault or in-fault aftershocks), or, more generally, the seismotectonic context (Tajima and Tajima, 2007).

For a practical use of the SIMULSTOC code, a reasonable value of C needs to be chosen. We propose to calibrate this parameter using a ground-motion prediction model that has

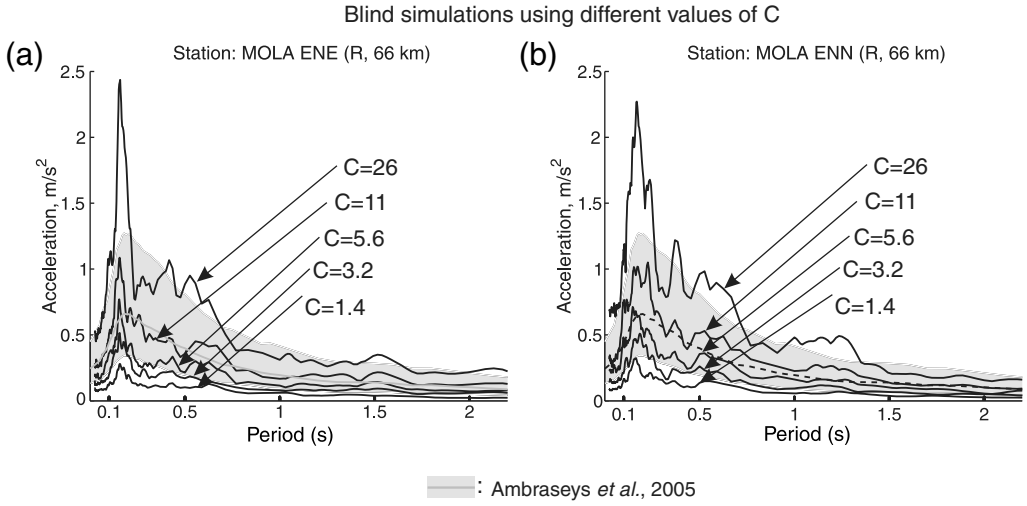


Figure 10. Simulations using EGF aftershock number 6 and the different values of C (stress-drop ratio between the large and the small events at station MOLA, a rock site station) and comparisons with the GMPEs of Ambraseys *et al.* (2005) for (a) east–west and (b) north–south components.

proven its efficiency for rock sites in a given region. This calibration should allow particularly good estimations of the ground motions that can be generated in future earthquakes, also in regions of low seismicity.

As the choice of the small event taken as an EGF does not appear to be crucial, this is also good news, especially for the region where few events can be used as the possible EGF. Nevertheless, with the directivity effect of the rupture process also being important for small events (Courboulex *et al.*, 1999; Boatwright, 2007), this remains an open problem for simulations.

Conclusion

The present study was carried out as a validation test. It has allowed us to demonstrate that the simple EGF summation procedures we have used (Ordaz *et al.*, 1995, Kohrs-Sansorny *et al.*, 2005) can reproduce well the mainshock recordings at about 10 accelerometric stations and that this is the case for 9 of the 10 small events selected as EGFs. This result is important because, in regions of moderate to low seismicity, there is often only one well recorded aftershock from which the recordings can be used as an EGF for simulating a larger event, whereby the validity of such a single event is very often questioned.

The good reproduction of ground-motion values that we have obtained here is especially interesting for site-effect stations because these levels can certainly not be predicted by any ground-motion prediction models.

This method is very simple to use, it reveals its efficiency through this dataset, and it is promising for seismic hazard assessment. The main problem that remains is the evaluation of the input parameter C, which represents the stress-drop ratio between the small-event taken as an EGF and the larger event under simulation. We propose a calibration method that can provide values of C that are reasonable, based on a comparison of the simulation on rock sites with an adapted ground-motion prediction model.

Data and Resources

Accelerograms used in this study were recorded by the French accelerometric network RAP. (In Guadeloupe, a part of this network is managed by BRGM and the other one by OVSG-IPGP). The Global Centroid Moment Tensor Project (formerly the Harvard Centroid Moment Tensor Project) can be found at www.globalcmt.org/CMTsearch.html (last accessed 11 October 2008). Waveforms are freely accessible on the RAP web site (http://www-rap.obs.ujf-grenoble.fr/) and constitute an interesting database for many studies. Information on the stations can be found on the CDSA Web site available at http://www.seismes-antilles.fr/. The CRUST2.0 global crustal model is available at http://igppweb.ucsd.edu/~gabi/crust2.html.

Acknowledgments

We thank the teams who are in charge of the accelerometric stations in the field (Observatoire Volcanologique et Sismologique de Guadeloupe—Institut de Physique du Globe de Paris [OVSG-IPGP] and Bureau de Recherches Géologiques et Minières [BRGM]) and those who have worked on the database in Guadeloupe and in the data management center of the Réseau Accélérométrique Permanent (RAP) network in Grenoble. We thank Dr. Danilo Galluzzo and an anonymous reviewer who helped to enhance this article. This research has been partially supported by the French Agency of Research through the contract ANR-05-CATT-011-03 (Quantitative Seismic Hazard Assessment project) and by the working group of Groupement d'intérêt scientifique (GIS) RAP.

References

Aki, K. (1967). Scaling laws of seismic spectrum, *J. Geophys. Res.* **72,** 1217–1231.

Ambraseys, N. N., J. Douglas, S. K. Sarma, and P. M. Smit (2005). Equation for the estimation of strong ground motions from shallow crustal earthquakes using data from Europe and the middle East: Horizontal peak ground acceleration and spectral acceleration, *Bull. Earthq. Eng.* **3,** 1–53.

Anderson, J. G. (2004). Quantitative measure of the goodness-of-fit of synthetic seismograms, paper no. 243, in *Proc. of Thirteenth World Conference on Earthquake Engineering*. Vancouver, Canada, 8 August 2004, 14 pp.

Arias, A. (1970). A measure of earthquake intensity, in *Seismic Design for Nuclear Power Plants*, Hansen, R. J. (Editor), The M.I.T. Press, Cambridge, Massachusetts, 438–483.

Beauducel, F., S. Bazin, and M. Bengoubou-Valérius (2004). Loi d'atténuation B-Cube pour l'évaluation rapide des intensités sismiques probables dans l'Archipel de Guadeloupe, Rapport Interne, OVSG-IPGP-UAG, 12 pp.

Beauval, C., L. Honoré, and F. Courboulex. (2009)Ground-motion variability and implementation of a probabilistic-deterministic hazard method, *Bull. Seismol. Soc. Am.* **99,** 2992–3002.

Beeler, N. M., T. F. Wong, and S. H. Hickman (2003). On the expected relationships between apparent stress, static stress drop, effective shear fracture energy and seismic efficiency, *Bul. Seismol. Soc. Am.* **93,** 1381–1389.

Bengoubou-Valerius, M., S. Bazin, D. Bertil, F. Beauducel, and A. Bosson (2008). CDSA: a new seismological data center for the French Lesser Antilles, *Seismol. Res. Lett.* **79,** no. 1, 90–115.

Bertil, D., S. Bazin, D. Mallarino, and F. Beauducel (2004). Séisme des Saintes 21 Novembre 2004, Rapport de Synthèse de Données Sismologiques des Antilles (CDSA), 8 Décembre 2004.

Bertil, D., S. Bazin, D. Mallarino, and F. Beauducel (2005). Localisation des principales répliques su séisme des Saintes du 21 Novembre 2004, Rapport du Centre de Données Sismologiques des Antilles (CDSA), 15 Avril 2005.

Boatwright, J. (2007). The persistence of directivity in small earthquakes, *Bul. Seismol. Soc. Am.* **97,** 1850–1861.

Bouchon, M. (1981). A simple method to calculate Green's functions for elastic layered media, *Bul. Seismol. Soc. Am.* **71,** 959–971.

Bour, M., and M. Cara (1997). Test of a simple empirical Green's function method on moderate sized earthquake, *Bull. Seismol. Soc. Am.* **87,** 668–683.

Brune, J. N. (1970). Tectonic stress and the spectra of seismic shear waves from earthquakes, *J. Geophys. Res.* **75,** 4997–5009.

Burjánek, J., and J. Zahradník (2007). Dynamic stress field of a kinematic earthquake source model with k-squared slip distribution, *Geophys. J. Int.* **171,** 1082–1097, doi 10.1111/j.1365-246X.2007.03548.x.

Causse, M., F. Cotton, C. Cornou, and P.-Y. Bard (2008). Calibrating median and uncertainty estimates for a practical use of empirical Green's functions technique, *Bull. Seismol. Soc. Am.* **98,** no. 1, 344–353.

Courboulex, F., N. Deichmann, and J. C. Gariel (1999). Rupture complexity of a moderate intraplate earthquake in the Alps: The 1996 *M* 5 Epagny-Annecy Earthquake, *Geophys. J. Int.* **139,** 152–160.

Delouis, B., and D. Legrand (1999). Focal mechanism determination and identification of the fault plane of earthquakes using only one or two near-source seismic recordings, *Bull. Seismol. Soc. Am.* **89,** 1558–1574.

Delouis, B., M. Vallée, and V. Cruz-Atienza (2007). The $M_w = 6.3$ Saintes earthquake (West Indies): Source kinematics determination and uncertainties in a poorly known crustal structure, *Geophys. Res. Abstr.*, **9,** 10,050.

Di Allessandro, C., and J. Boatwright (2006). A stochastic estimate of ground motion at Oceano, California, for the *M* 6.5 22 December 2003 San Simeon earthquake, derived from aftershocks recordings, *Bull. Seismol. Soc. Am.* **96,** 1437–1447.

Douglas, J. (2003). Earthquake ground motion estimation using strong-motion records: A review of equations for the estimation of peak ground acceleration and response spectral ordinates, *Earth. Sci. Rev.* **61,** 43–104.

Douglas, J., D. Bertil, A. Roullé, P. Dominique, and P. Jousset (2006). A preliminary investigation of strong ground motion data from the French Antilles, *J. Seismol.* **10,** 271–299.

Duval, A. M., E. Bertrand, S. Vidal, G. Verrhiest, G. Jacquet, and H. Nahornyj (2006). Combined survey of site effects and damage in Les Saintes Guadeloupe, after the 2004 earthquake, *Third International Symposium on "The Effects of Surface Geology on Seismic Motion" (ESG 2006)*, Grenoble, France, 30 August–3 Sept 2006.

Feuillet, N, I. Manighetti, P. Tapponnier, and E. Jacques (2002). Arc parallel extension and localization of volcanic complexes in Guadeloupe, Lesser Antilles, *J. Geophys. Res.* **107,** no. B12, 2331.

Hartzell, S. (1978). Earthquake aftershocks as Green's functions, *Geophys. Res. Lett.* **5,** 1–4.

Hartzell, S. (1989). Comparison of waveform inversion results for the rupture history of a finite fault: Application to the 1986 North Palm Springs, California, earthquake, *J. Geophys. Res.* **94,** 7515–7534.

Honoré, L. (2008). Mise au point d'une méthode hybride d'évaluation de l'aléa sismique, *Master's Thesis*, University Nice Sophia-Antipolis, France.

Hough, S. E., and H. Kanamori (2002). Source properties of earthquakes near the Salton Sea triggered by the 16 October 1999 *M* 7.1 Hector Mine, California, earthquake, *Bull. Seismol. Soc. Am.* **92,** 1281–1289.

Hutchings, L. (1994). Kinematic earthquake models and synthesized ground motion using empirical Green's functions, *Bull. Seismol. Soc. Am.* **84,** 1028–1050.

Ide, S., and G. C. Beroza (2001). Does apparent stress vary with earthquake size?, *Geophys. Res. Lett.* **28,** 3349–3352.

Institut de Physique du Globe de Paris (IPGP) (2004). Bilan mensuel de l'activité volcanique de la Soufrière de Guadeloupe et de la sismicité régionale, Public reports of OVSG-IPGP, Institut de Physique du Globe de Paris, http://www.ipgp.jussieu.fr, ISSN 1622-4523.

Irikura, K., and K. Kamae (1994). Estimation of strong ground motion in broad-frequency band based on a seismic source scaling model and an empirical Green's function technique, *Ann. Geophys.* **37,** 1721–1743.

Jousset, P., and J. Douglas (2007). Long-period earthquake ground displacements recorded on Guadeloupe (French Antilles), *Earthq. Eng. Struct. Dynam.* **36,** 949–963.

Joyner, W. B., and D. M. Boore (1986). On simulating large earthquakes by Green's functions addition of smaller earthquakes, in *Earthquake Source Mechanics*, Maurice Ewing Series 6, S. Das, J. Boatwright, and C. H. Scholtz (Editors), **37**, American Geophysical Union Washington, D.C., 269–274.

Kanamori, H., and L. Rivera (2004). Static and dynamic scaling relations for earthquakes and their implications for rupture speed and stress drop, *Bull. Seismol. Soc. Am.* **94,** 314–319.

Kohrs-Sansorny, C., F. Courboulex, M. Bour, and A. Deschamps (2005). Strong ground motion simulation using stochastic summation of small earthquakes: A two-stage method for ground-motion simulation using stochastic summation of small earthquakes, *Bull. Seismol. Soc. Am.* **95,** 1387–1400.

Manighetti, I., M. Campillo, S. Bouley, and F. Cotton (2007). Earthquake scaling, fault segmentation, and structural maturity, *Earth Planet. Sci. Lett.* **253,** 429–438.

Mooney, W. D., G. Laske, and G. Masters (1998). Crust 5.1: A global crustal model at 5×5 degrees, *J. Geophys. Res*. **103,** 727–747

Ordaz, M., J. Arboleda, and S. K. Singh (1995). A scheme of random summation of an empirical Green's function to estimate ground motions from future large earthquakes, *Bull. Seismol. Soc. Am.* **85,** 1635–1647.

Pavic, R., M. G. Koller, P. Y. Bard., and C. Lacave-Lachet (2000). Ground motion prediction with the empirical Green's function technique: An assessment of uncertainties and confidence level, *J. Seismol.* **4,** 59–77.

Péquegnat, C., P. Guéguen, D. Hatzfeld, and M. Langlais (2008). The French accelerometric network (RAP) and National Data Centre (RAP-NDC), *Seismol. Res. Lett.* **19,** no. 1, 81–89.

Ruiz, J., D. Baumont, P. Bernard, and C. Berge-Thierry (2007). New approach in the kinematic k^{-2} source model for generating physical slip velocity functions, *Geophys. J. Int.* **171,** no. 2, 739–754.

Scherbaum, F., F. Cotton, and D. Smit (2004). On the use of response spectral-reference data for the selection and ranking of ground-motion models for seismic-hazard analysis in regions of moderate seismicity: The case of rock motion, *Bull. Seismol. Soc. Am.* **94,** no. 6, 2164–2185.

Somerville, P. (1993). Engineering applications of strong ground motion simulation, *Tectonophysics* **218,** 195–129.

Tajima, R., and F. Tajima (2007). Seismic scaling relations and aftershock activity from the sequences of the 2004 mid Nigata and the 2005 west off Fukuoka earthquakes (M_w 6.6) in Japan, *J. Geophys. Res.* **112,** no. B10302, doi 10.1029/2007JB004941.

Trifunac, M. D., and A. G. Brady (1975). A study on the duration of strong earthquake ground motion, *Bull. Seismol. Soc. Am.* **65,** 581–626.

Tumarkin, A. G., and R. J. Archuleta (1994). Empirical ground motion prediction, *Ann. Geophys.* **37,** 1691–1720.

Venkataraman, A., L. Rivera, and H. Kanamori (2002). Radiated energy from the October 16, 1999 Hector Mine earthquake: Regional and teleseismic estimates, *Bull. Seismol. Soc. Am.* **92,** 1256–1265.

Wennerberg, L. (1990). Stochastic summation of empirical Green's functions, *Bull. Seismol. Soc. Am.* **80,** 1418–1432.

Zeng, Y. H., J. G. Anderson, and G. A. Yu (1994). Composite source model for computing realistic synthetic strong ground motions, *Geophys. Res. Lett.* **21,** 725–728.

Géoazur
University of Nice Sophia Antipolis
CNRS, Observatoire de la Cote d'Azur
250 av Einstein 06560 Valbonne, France
courboulex@geoazur.unice.fr

Manuscript received 19 December 2008

3.5 Simulation d'un séisme futur

Forts de notre expérience sur la crise des Saintes, nous nous sommes lancés dans des simulations de séismes réels.
En fait la chronologie n'a pas été exactement celle là puisque nous avions commencé à travailler sur les simulations depuis longtemps mais certains éléments nous manquaient pour proposer une publication satisfaisante.
Notre terrain d'expérimentation a été la côte d'Azur. La thèse de Carine Kohrs-Sansorny, financée par la région PACA (Provence Alpes Côte d'Azur) avait pour but de proposer des simulations réalistes de mouvements du sol pour un séisme important dans la région. Les premiers résultats de simulation sur la côte d'Azur ont donc été obtenus par Carine Kohrs-Sansorny à la fin de sa thèse puis lors du post-doctorat qu'elle a réalisé au laboratoire. Etienne Bertrand du CETE Méditerranée a également contribué à ce travail. C'est ensuite Jérôme Salichon dans le cadre du projet QSHA (Quantitative Seismic Hazard Assessment) qui a pris la suite de ce travail qui a abouti à la toute récente publication présentée ici.

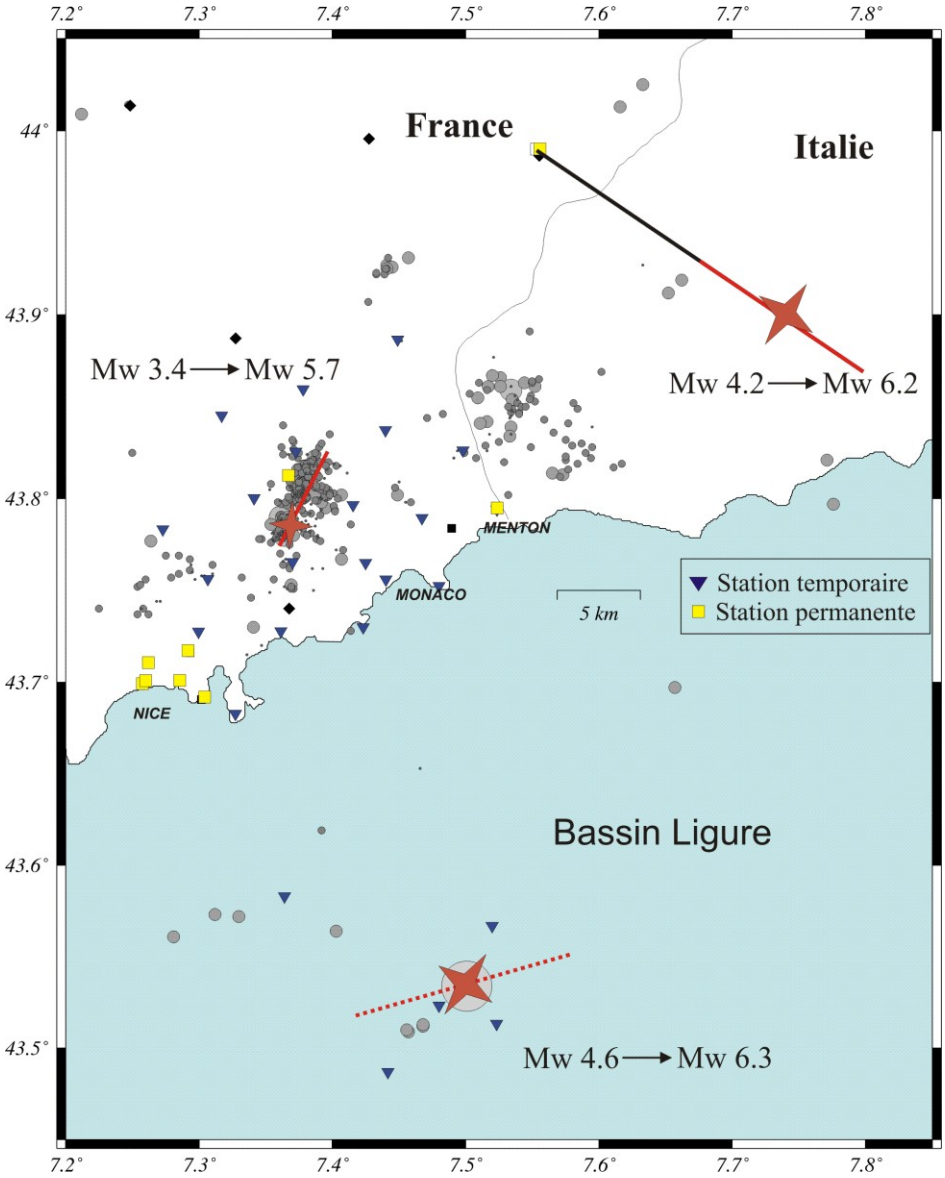


Figure 3. 6 : Localisation des trois séismes de référence. Les points gris correspondent à la sismicité enregistrée durant les six mois de la campagne SALAM. Les traits rouges correspondent à la longueur de faille activée dans nos simulations.

Nous avons dans les Alpes Maritimes tenté de tirer parti des trois séismes les mieux enregistrés pour réaliser des simulations de séismes plus gros. Trois zones source ont été testées (Figure 3. 6):

- **La faille de Blausasc** : nous avons tiré parti du séisme de magnitude Mw 3.4 qui a eu lieu durant la crise de Blausasc pour simuler un séisme plus fort sur la même faille. La taille du séisme que nous avons simulé a été choisie en prenant la longueur du segment de faille activé par les répliques durant la crise de Blausasc. Nous avons ainsi quantifié les mouvements du sol qui pourraient être engendrés par un séisme de magnitude 5.7 dans la ville de Nice et aux alentours (Figure 3. 7). Ce travail a été partiellement publié dans l'article du *Geophysical Journal International* présenté dans ce manuscrit (Chapitre 2, paragraphe 2.4).

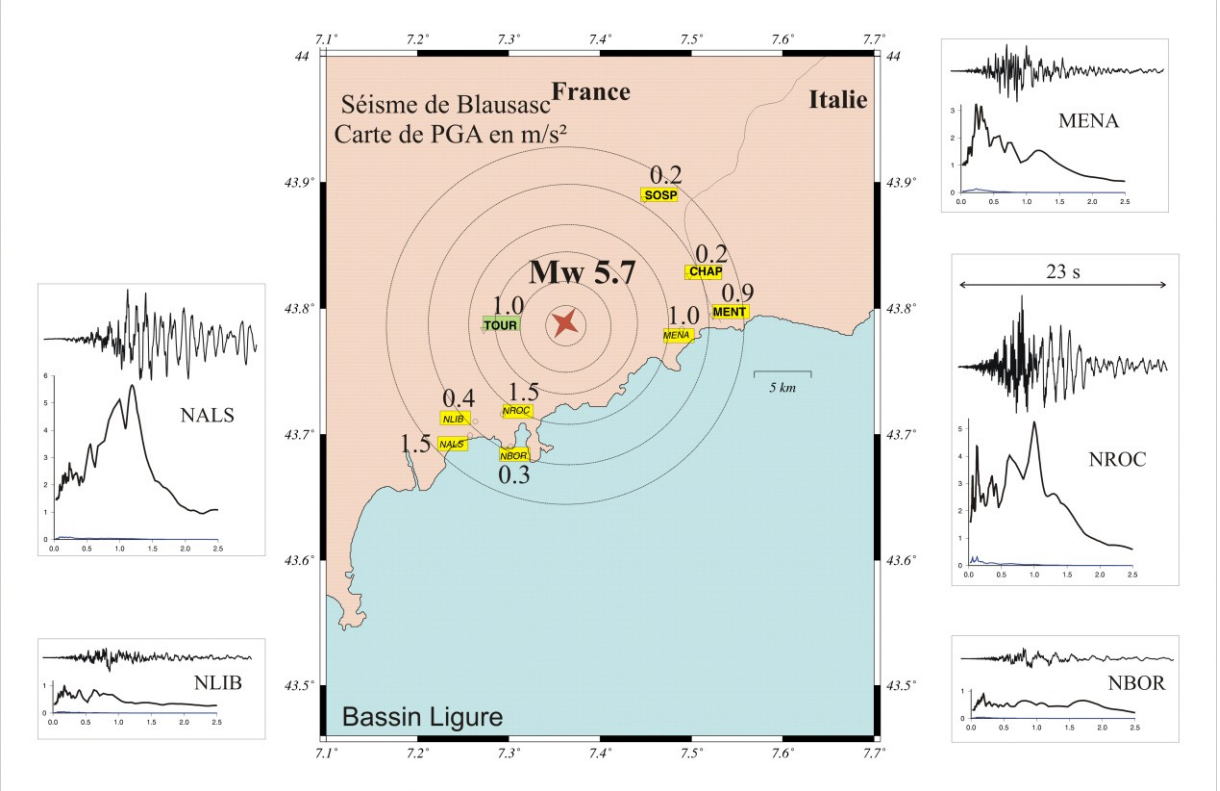


Figure 3. 7 : Simulation des mouvements forts du sol produits par un séisme de magnitude 5.7 sur la faille de Blausasc sous l'hypothèse d'une chute de contrainte identique pour le séisme de référence et son EGF. Pour chaque station du réseau RAP à Nice et à Menton (en jaune) sont représentés un accélérogramme correspondant à une réalisation « moyenne » et le spectre de réponse accélération-période moyen. Les valeurs numériques indiquées sur les stations correspondent au PGA moyen pour cette simulation.

- **La faille de Saorge Tagia**. Cette faille est la plus active de la zone. Une microsismicité régulière y est recensée ainsi que des petites crises sismiques plus ou moins alignées sur la faille [*Turino et al.*, 2009]. En Septembre 2006, un séisme de magnitude 4.2 (appelé le séisme de San Remo) a eu lieu sur l'une des portions de cette faille (il vaut mieux d'ailleurs parler de réseau de failles dans cette zone). Ce séisme a été très bien enregistré par les réseaux permanents en place (réseau large bande, courte période et accélérométrique). Nous avons réalisé des simulations d'un séisme de magnitude 6.3 sur toutes les stations disponibles du réseau (Figure 3. 8). Pourquoi avoir choisi cette magnitude ? Parce qu'elle correspond aux magnitudes estimées pour les séismes historiques

majeurs dans cette zone. Les résultats de ce travail n'ont pour le moment pas été publiés. Une étude plus approfondie de la variabilité des simulations doit au préalable être mise en œuvre.

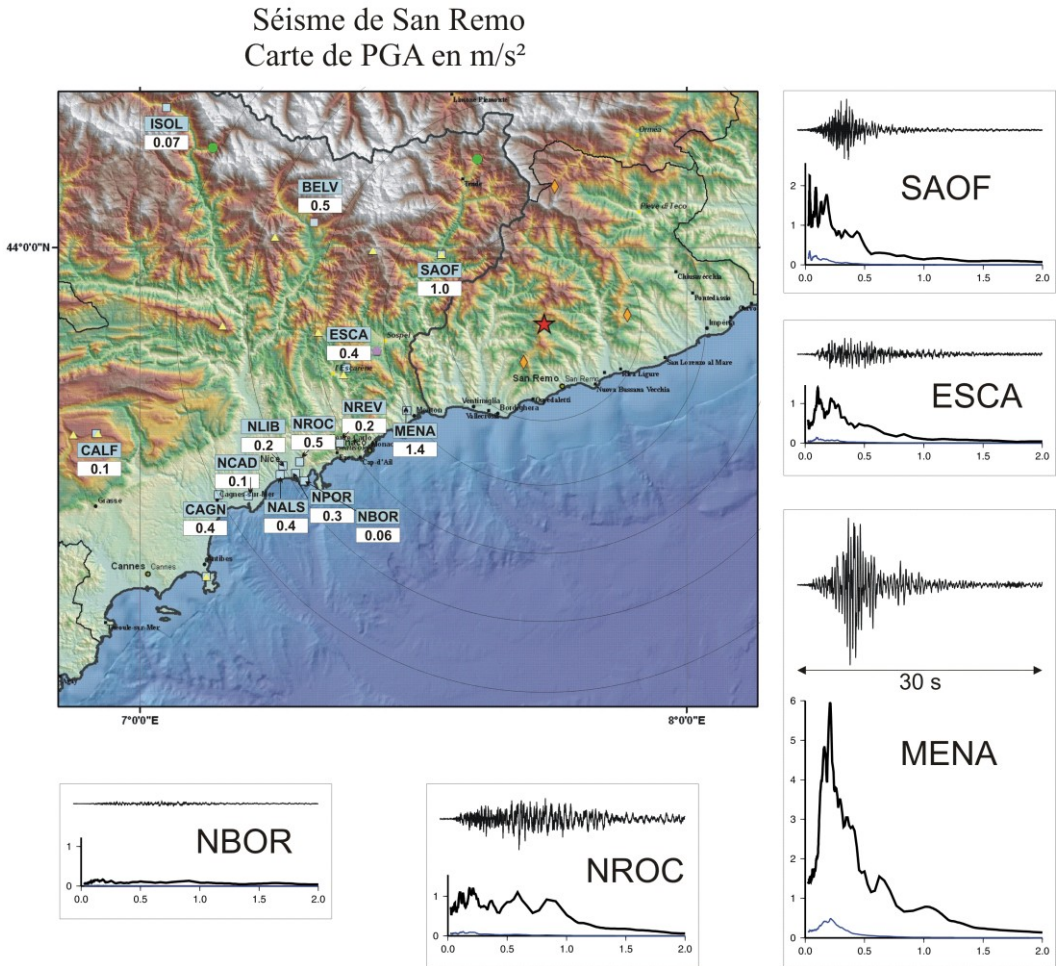


Figure 3. 8 : Simulation des mouvements forts du sol produits par le séisme de San Remo sous l'hypothèse d'une chute de contrainte identique pour le séisme de référence et son EGF. Pour chaque station du réseau RAP à Nice et à Menton sont représentés un accélérogramme correspondant à une réalisation « moyenne » et le spectre de réponse accélération-période moyen. Les spectres de réponse du petit séisme utilisé comme EGF sont représentés en bleu.

- La faille Marcel qui se trouve à une vingtaine de kilomètres des côtes et dont la trace a probablement été identifiée dans la bathymétrie (Figures 2.8 et 2.9). Cette zone a été le siège de deux séismes récents : celui de décembre 1989 [*Béthoux et al.*, 1992], et celui de février 2004 dont nous avons déjà parlé dans le chapitre précédant. Ces deux séismes sont de magnitude et de mécanismes au foyer similaires. Nous avons utilisé les enregistrements du séisme de 2001 pour simuler un séisme de magnitude 6.3 (scénario du projet QSHA). Les résultats de ses simulations sur la zone urbaine de Nice sont présentés dans l'article qui suit.

Si l'on compare les résultats de ces trois séismes, on se rend compte que c'est le séisme à terre de magnitude inférieure qui est susceptible de générer les accélérations les plus importantes dans la ville de Nice.

J Seismol (2010) 14:523–541
DOI 10.1007/s10950-009-9180-0

ORIGINAL ARTICLE

A Mw 6.3 earthquake scenario in the city of Nice (southeast France): ground motion simulations

Jérome Salichon · Carine Kohrs-Sansorny · Etienne Bertrand · Françoise Courboulex

Received: 15 February 2009 / Accepted: 2 November 2009 / Published online: 26 November 2009
© Springer Science + Business Media B.V. 2009

Abstract The southern Alps–Ligurian basin junction is one of the most seismically active zone of the western Europe. A constant microseismicity and moderate size events ($3.5 < M < 5$) are regularly recorded. The last reported historical event took place in February 1887 and reached an estimated magnitude between 6 and 6.5, causing human losses and extensive damages (intensity X, Medvedev–Sponheuer–Karnik). Such an event, occurring nowadays, could have critical consequences given the high density of population living on the French and Italian Riviera. We study the case of an offshore Mw 6.3 earthquake located at the place where two moderate size events (Mw 4.5) occurred recently and where a morphotectonic feature has been detected by a bathymetric survey. We used a stochastic empirical Green's functions (EGFs) summation method to produce a population of realistic accelerograms on rock and soil sites in the city of Nice. The ground motion simulations are calibrated on a rock site with a set of ground motion prediction equations (GMPEs) in order to estimate a reasonable stress-drop ratio between the February 25th, 2001, Mw 4.5, event taken as an EGF and the target earthquake. Our results show that the combination of the GMPEs and EGF techniques is an interesting tool for site-specific strong ground motion estimation.

Keywords Strong ground motion · Seismic hazard · Ground motion simulations · Empirical green's functions · Ligurian basin · Alps · Mediterranean Sea

J. Salichon · C. Kohrs-Sansorny · F. Courboulex
Observatoire de la Côte d'Azur,
Géoazur Nice-Sophia Antipolis University,
CNRS, Nice, France

E. Bertrand
LCPC-CETE Méditerranée, Nice, France

J. Salichon (✉) · E. Bertrand (✉) · F. Courboulex (✉)
Géoazur, 250 rue Albert Einstein, Sophia Antipolis,
06560 Valbonne, France
e-mail: salichon@geoazur.unice.fr
e-mail: etienne.bertrand@developpement-durable.gouv.fr
e-mail: courboulex@geoazur.unice.fr

1 Introduction

The region of interest is situated in the southeast of France at the junction between the Alps and the Ligurian basin. In this zone, a regular microseismicity is recorded, and every 4 to 5 years, an earthquake with a magnitude larger than 4.5 occurs (Fig. 1). These moderate size events are usually felt by the population but have never caused noticeable damage. However, some destructive earthquakes have struck the region in the past. In 1564, an inland earthquake completely

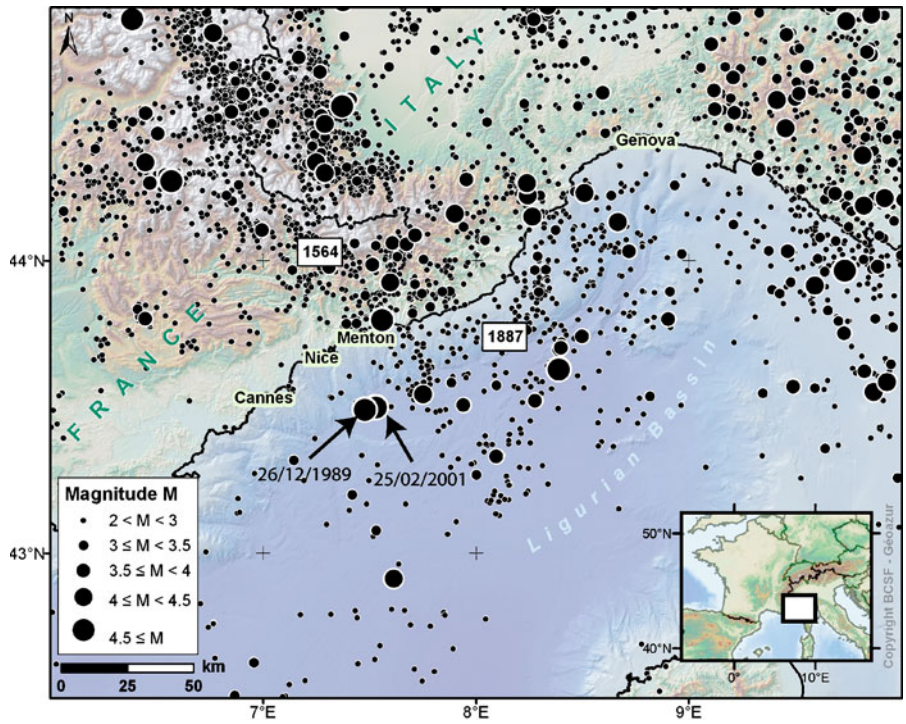


Fig. 1 Overview of the Ligurian (Southern Alps) region and the Nice city area. *Black filled circles* indicate the instrumented seismicity for the period 1988 to 2001 from the Bureau Central Sismologique Français database (http://www.seisme.prd.fr). Topography and bathymetry is a synthesis of the 50-m database of the Institut Géographique National (www.ign.fr), SRTM 90-m database, IBCM 100-m database, and the IFREMER multifaisceau 2003 database

destroyed a village located 50 km north of Nice and caused several victims (Lambert et al. 1994). More recently, a major earthquake occurred offshore, in the Ligurian Sea, close to the Italian coast. This event on February 1887 reached an intensity of X (Medvedev–Sponheuer–Karnik), caused the death of 600 persons on the Italian coast, and a few casualties on the French coast between Menton and Nice. Its magnitude was estimated to be at least $M = 6.3$ (Ferrari 1991; Bakun and Scotti 2006). If such an earthquake were to occur today, it would be more likely to produce more destruction because of the higher population density in the French and Ligurian Riviera (about two million inhabitants). Thus, it is of utmost importance to assess the seismic risk in this region.

Ground motion simulation is a key step in the evaluation of the possible impact of a seismic event in an urban area. Because of this, it is essential in the preparedness for crisis. Local site effects have long been recognized as an important factor contributing to variations in strong ground motion. Therefore, these effects also contribute directly to the distribution of the consequences of a given earthquake over a city.

The strength of shaking at a particular location from an earthquake scenario can be estimated by ground motion prediction equations (GMPEs) fitted to strong-motion data from past earthquakes (see Douglas 2003 for a review). These equations typically include only the most obvious explanatory parameters: magnitude, distance, local site conditions, and sometimes a few others (focal mechanism for example). Nevertheless, the site conditions are often only roughly taken into account. Various approaches have been used, from simple binary rock/soil classifications (e.g., Berge-Thierry et al. 2003) to the explicit use of shear-wave velocity (e.g., Next Generation Attenuation project, Power et al. 2008). However, the simplified evaluation of local seismic responses on soft soil deposits obtained through these approaches may not be accurate. Indeed, they take into account an average soil response that can hardly be representative of particular soil such as very soft soil, very thick soil, or artificial fills. Moreover, topographic effects and, more generally, all the 3D effects cannot be taken into account.

GMPEs have already been applied to Nice to evaluate the ground motion at rock sites for

reference earthquakes (e.g., Mouroux et al. 2004). To take into account the local site effect that has been detected in the major part of the city (Duval 1996; Duval et al. 2001), these studies modify the ground motion assessed at the rock site by the use of a numerical 1D soil response simulation (Bard et al. 2005) or simply by the use of the seismic French code soil classification (Stieltjes et al. 1996). These microzonation studies are based on a geotechnical model of the quaternary deposits under the city (Bertrand et al. 2007) and lead in shaking maps over the whole city of Nice. However, the site effects in Nice are known to be influenced by the geometry of the basin (Semblat et al. 2000), and the 1D simulations do not match the experimental measurements at least in some parts of the city (Régnier et al. 2008; Gélis et al. 2008).

Our work is part of the Quantitative Seismic Hazard Assessment project. This project aims at comparing different 3D wave propagation simulation methods for ground motion evaluation in the Nice, Grenoble, Algiers, and Naples areas with the same input parameters. Most of the methods included the source complexity and the travel path from the source to the surface. Unfortunately, these deterministic methods are insufficient in predicting the seismic motion above a few hertz. The resulting ground motion also depends drastically on the accuracy of the velocity models. Thus, most of them do not consider any amplification, due to the quaternary deposits.

To predict broadband ground motion, we used a simulation approach based on the combination of the site-specific empirical Green's function technique (EGF) and the GMPEs. We first simulated broadband seismic motion in a frequency domain of engineering interest. For that purpose, we use the empirical–stochastic EGF summation method set up by Kohrs-Sansorny et al. (2005) to generate large sets of ground motion corresponding to the target earthquake. The EGF method has the great advantage to account for the wave path in a complex medium: The simulations include the azimuth-dependent propagation effects at regional scale and account for the local 3D site effects under the assumption of linearity. The Mw 4.5 earthquake of February 25, 2001 is taken as an EGF to compute seismic motion that could

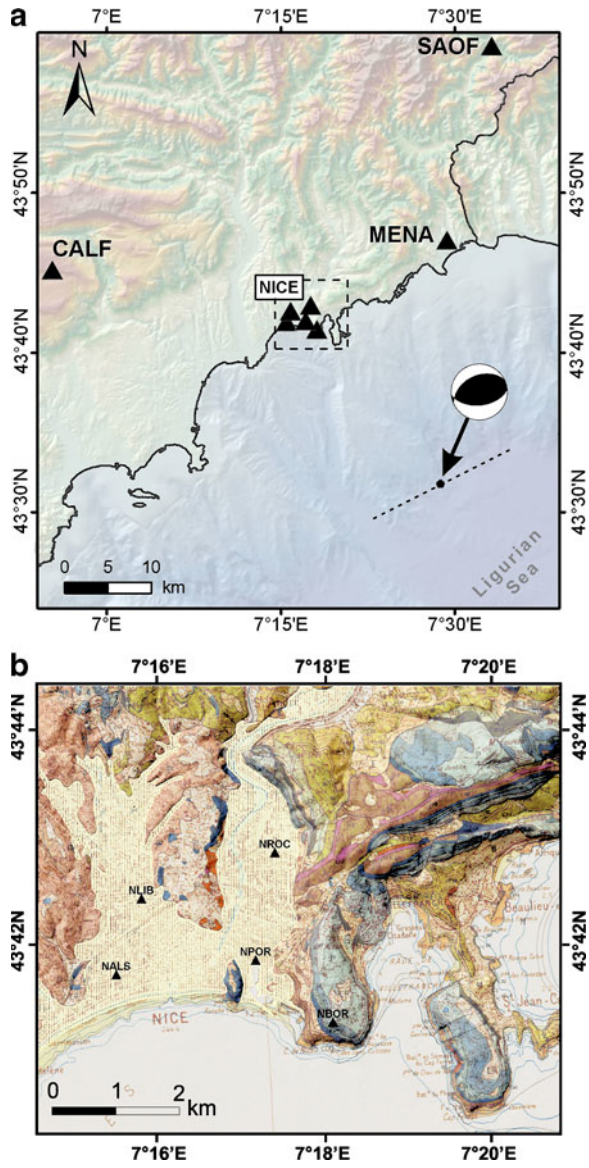


Fig. 2 **a** Situation map with location of the February 25th, 2001 Mw 4.5 earthquake indicated by a *black dot* and its focal mechanism. *Dotted line* indicates a hypothetical fault length of about 18 km long corresponding to the Mw 6.3 target event (as defined in the QSHA project). *Black triangles* correspond to seismic stations where the simulations are performed. *Dotted box* corresponds to the area shown in **b** (see legend of Fig. 1 for topography and bathymetry references). **b** Geological setting of the city of Nice. The quaternary alluvial deposits area where the stations NALS, NLIB, NROC, and NPOR are located are indicated by the *whitened area* superimposed on the geological map (BRGM map, 1:50,000). The station NBOR is located on Jurassic limestone bedrock (*bluish area*)

be generated in the Nice area by an earthquake with a magnitude equivalent to the 1887 event (Mw 6.3) occurring about 25 km offshore, south of the city (Fig. 2). We then propose a combined use of this method with different GMPEs to calibrate our simulations. Our results are compared with the new French seismic regulation derived from the Eurocodes 8 paraseismic rules (EC8).

2 The studied area

2.1 Seismotectonic context

The junction between the southern French–Italian Alps and the Ligurian basin is one of the most seismically active areas among the western European countries. It is defined by a daily microseismicity, moderate events ($M > 4.5$) occurring about every 5 years, and a few large, destructive historical earthquakes ($M > 6$). The origin of this activity is complex and still the subject of debate. The region presents a strong topographic gradient with heights ranging from 3,000 m on the Argentera Alpine massif to 2,500 m under the sea level in the Ligurian basin within a short distance (about 100 km). A strong structural inheritage results from a 50-My geological evolution combining different geodynamical processes such as continental collision and ocean basin opening. The convergence of the Africa plate toward Eurasia now occurs at a rate of 4–5 mm/year in a N $309 \pm 5°$ direction at the longitude of the western Alps (Nocquet and Calais 2003; McClusky et al. 2003). This shortening is mainly accommodated along the Maghrebides (Nocquet and Calais 2004; Serpelloni et al. 2007); nevertheless, recent global positioning system (GPS) measurement shows that near 10% of this deformation is accommodated further to the north between Corsica and the Alps (Larroque et al. 2008). This shortening and the rotation of the Adriatic microplate (Calais et al. 2002) could be the main cause of seismic activity in the region, but other factors could also be important, such as the gravitational effects (body forces) caused by the presence of the Alpine massif and/or the thermomechanical effects at the continent/Ligurian ocean boundary (Béthoux et al. 2008; Larroque et al. 2008).

One of the most seismically active zones in this region is situated in the northern part of the Ligurian basin (the southern part being almost aseismic). The magnitude of the earthquakes ranging from 3.0 to 6.0 reveals inverse or strike slip solutions compatible with a compressional state of stress (Béthoux et al. 1988; Ritz 1992; Madeddu et al. 1996; Baroux et al. 2001).

2.2 The Mw 4.5 Nice earthquake (2001)

Two moderate size events ($M > 4$) occurred offshore at about 25 km toward the southwest of Nice on December 26th, 1989 (Ml 4.5) and on February 25th, 2001 (Ml 4.6). Both have been generated by the movement of a reverse fault roughly parallel to the French Riviera coastline (Béthoux et al. 1992; Courboulex et al. 2007). These events were strongly felt by the population in a large area—from the Italian border to the city of Cannes without causing damage to construction (BCSF report 1992, 2006). They occurred offshore at the base of the continental slope. A recent bathymetric and seismic survey reveals morphotectonic features at the place of both epicenters, which could be related to an active fault (Larroque et al. 2006; Scotti et al. 2008). In Italy, tens of kilometers to the east, another structure has been detected in the area of the Ligurian earthquake (February 23, 1887).

We focus on the February 25th, 2001 event (Table 1) because it was very well recorded by seismic networks: the short period network belonging to the French seismic monitoring office (ReNaSS) that proposed a magnitude Ml = 4.6, the broadband network (Tres Grande Resolution Sismologique), the permanent accelerometric network (RAP; Péquegnat et al. 2008), and a temporary network that was running during this period (Courboulex et al. 2007). From broadband data, Delouis (personal communication) derived a

Table 1 January 25th, 2001 event hypocenter location and focal mechanism (after Courboulex et al. 2007)

Latitude (deg)	Longitude (deg)	Depth (km)	Strike (deg)	Dip (deg)	Rake (deg)	Ml
45.53	7.48	11	243	41	74	4.6

moment magnitude of Mw = 4.5 using a waveform inversion method (Delouis and Legrand 1999). The maximum macroseismic intensity was reported in the coastal area to be V on the EMS98 scale. This event is the best recorded event that occurred in this area. It will be used hereafter as empirical Green functions for the simulation of a larger event.

3 Geological setting, network, and station sites

The city of Nice is almost entirely built on three main types of geological formation (Fig. 2). Most of the city—the city center, the old town, the Baie des Anges coast, and the western part of the city—lie on old and recent fluviatile alluvium of the Var and Paillon valleys. The alluvial plain of the Paillon consists of pebbly and silty alluvium, including some sandy layers or lenses of which location is barely known. In the southern part of the valley, these deposits can be more than 60 m thick (Bertrand et al. 2007).

Experimental measurements of site effects (Duval 1996) using microtremor and earthquake recordings clearly indicate that site amplifications occur in the basins of Nice. The amplification of seismic motion occurs between 1 and 2 Hz at the center of the alluvial filling (Semblat et al. 2000; Bard et al. 2005). Above the thickest part of the alluvial basin, the amplification factor determined by the site/reference spectral ratio computation reaches a maximum value of about 20 around a frequency of 1 Hz on the horizontal component. However, this resonance frequency shows a strong dependency on the thickness of the alluvial surface layers (Duval 1996; Bertrand et al. 2007), which corresponds to current theory of wave trapping in sedimentary layers.

The characteristics of this area made particularly interesting the installation of a local permanent seismological network. As part of the French RAP, five accelerometric stations have been installed in the city of Nice since 1995 (Pequegnat et al. 2008). Each accelerometric station is constituted of a strong-motion sensor (Güralp-CMG5 or Kinemetrics-Episensor), and a 24-bit three-component digitizer (Agecodagis-Titan), all sampling at 125 Hz. The time is calibrated with a GPS receiver. Both the Géoazur Laboratory and the CETE Méditerranée laboratory maintain the network in southeastern France. All the data are collected and distributed by the online database (http://www-rap.obs.ujf-grenoble.fr) managed by the RAP central site in Grenoble. Thanks to the homogeneity and the quality of the data stored in the database, it gives reliable value of the peak ground acceleration recorded in case of strong events. The great sensitivity of the stations allows the detection of low-to-moderate earthquakes ($M < 3$), and simultaneously, their dynamical properties allows the recording of the ground motion produced by events of stronger magnitudes ($M > 5$) without any overflow. The main scientific objectives are increased knowledge of source effects and seismic motion, the propagation and attenuation phenomena, the analysis of site effects, and the experimental assessment of structures' vulnerability. The network in Nice is designed particularly to study site effects, as some stations are located in the alluvial basins and others on rocky sites. The number of accelerometric stations in the region of Nice is continually increasing, and in 2001, eight stations were available in Nice and its vicinity (Table 2). Stations NPOR, NROC, NLIB, and NALS are located on the quaternary filling in the city of Nice while MENA, CALF, SAOF, and NBOR are located on rock sites (Fig. 2).

Bertrand et al. (2007) proposed a 3D model of the quaternary fillings in Nice from the synthesis of all the available geological, geotechnical, and geophysical data over the city. This model is also inferred from ambient vibration recordings analysis (Bard et al. 2005; Bertrand et al. 2007). According to this model, the quaternary alluvium thickness reaches 70 m under NALS, 52 m under NROC, 45 m under NPOR, and 34 m under NLIB. The mean S-wave propagation velocity (Vs30) given under these stations by the model is equal to 235, 260, 250, and 240 m s^{-1}, respectively.

NBOR is the station that is closest to the alluvial basins of Nice. Furthermore, the site where this station is installed is characterized by a flat seismic response (Drouet 2006). Therefore, this station is often considered as a reference station for site effect studies in Nice (Duval 1996; Semblat et al. 2000).

Table 2 Distances to the EGF hypocenter, soil types, quaternary alluvial deposit thickness, and mean S-waves propagation velocity (Vs30) of the accelerometric stations used in this study

Stations	Distance (km)	Soil type	Alluvial deposit thickness (m)	Vs30 (m s^{-1})
NBOR	25.7	Rock	–	1,400
NPOR	27.6	Sediment	45	250
MENA	28.3	Rock	–	–
NROC	28.4	Sediment	52	260
NALS	29.7	Sediment	70	235
NLIB	30.1	Sediment	34	240
CALF	63.5	Rock	–	–
SAOF	51.3	Rock	–	–

All the RAP stations in Nice recorded the Mw 4.5 February 25th, 2001 earthquake with a very good signal-to-noise ratio. In this study, we selected 70 s of recordings (10 s before P arrival) at each station as EGFs for our simulations.

4 Method

We aim to simulate a set of accelerograms that could be generated by an offshore Mw 6.3 earthquake at given sites of the city of Nice. In order to obtain realistic signals in a large frequency band that properly take into account path and site effects, we use an EGF approach (Hartzell 1978). The principle is to simulate the recordings of a hypothetic future earthquake using the actual recordings of a smaller one (Fig. 3). The small event recordings, indeed, contain rich information on path and site effects that could not be reproduced by a numerical modeling at high frequencies.

We chose in this work the two-step summation scheme proposed by Kohrs-Sansorny et al. (2005) and implemented in SIMULSTOC code that has the advantage in necessitating few input parameters and then allows generating in a quick computation time a large number of possible accelerograms. This method is based on the work of

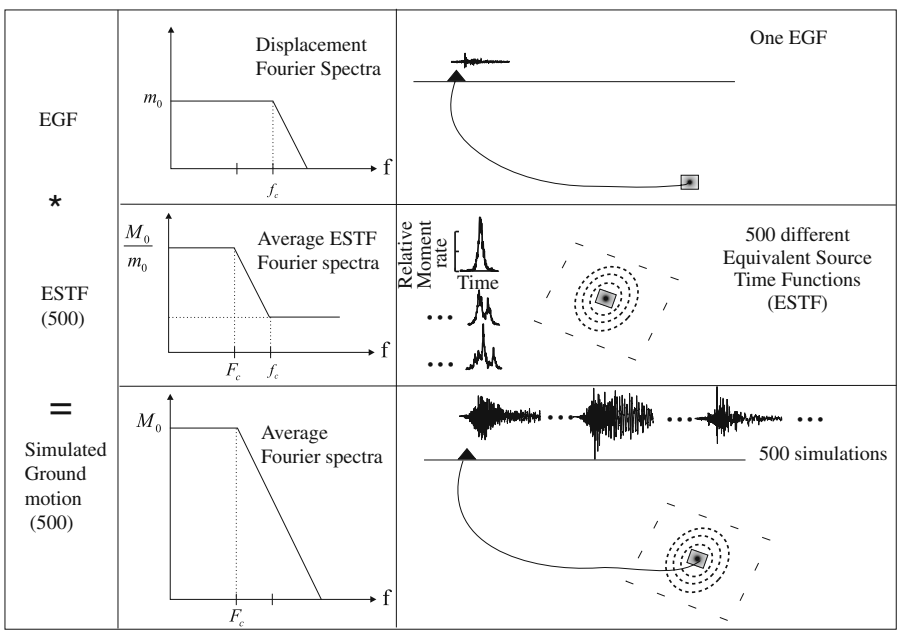


Fig. 3 Schematic view of the EGF summation method. **a** The EGF is the waveform recorded by a small event. The source is modeled by an ω^{-2} Brune spectra. **b** We construct 500 different ESTFs that accounts for different rupture process for a larger event. *Bottom* Each ESTF is convolved by the EGF to give the 500 simulated accelerograms

Joyner and Boore (1986), Wennerberg (1990), and Ordaz et al. (1995).

We first generate a large number (500) of equivalent source time functions (ESTFs). These ESTFs represent the time histories of the liberation of energy over the fault at frequencies lower than the corner frequency of the small event taken as EGF (Fig. 3). They are generated by a random process in two steps following two probability densities functions which shape has been proposed by Ordaz et al. (1995). The differences in the ESTF can indirectly account for different types of ruptures and produce a large variability in ground motions. This variability was recently studied by Beauval et al. (2009). We then convolve each ESTF with the EGF at each station and each component. The higher frequency part of the spectrum ($> f_c$) is then directly modeled by the spectrum of the small event and enables to obtain simulations at high frequency (Fig. 3).

The method produces synthetic time histories that, on average, are in agreement with the ω^{-2} model (Aki 1967; Brune 1970) and respect a non-constant stress-drop condition (Beeler et al. 2003; Kanamori and Rivera 2004). The interest of the method is that it requires few parameters to be applied: (1) the seismic moment (m_o) and corner frequency (f_c) of the small event taken as EGF, (2) the seismic moment (M_o) of the target earthquake, and (3) the ratio C between the static-stress drop of the target event ($\Delta\Sigma$) and that of the small event ($\Delta\sigma$).

The parameters are linked by the relationships:

$$M_o/m_o = CN^3, \text{ where}$$
$$N = f_c/F_c \text{ and } C = \Delta\Sigma/\Delta\sigma \quad (1)$$

Note that in the SIMULSTOC code, N is a scaling parameter that must be an integer. For this reason, only discrete values of F_c and C can be selected. All the details of the method can be found in Kohrs-Sansorny et al. (2005).

Among the necessary input parameters, C is the only one that is really difficult to define. For a practical use in the simulation, we propose further to adjust it, using the GMPEs. Note that the same ground motion simulation method has also been used recently in the objective to be included in a probabilistic seismic hazard analysis (Arroyo and Ordaz 2007; Beauval et al. 2009).

5 Simulation of a Mw 6.3 earthquake

5.1 Source modeling parameters

The February 25th event of 2001 (Mw 4.5) is taken as an empirical Green's function to simulate the target event with an inferred moment magnitude of 6.3. The inspection of the EGF data from the eight accelerometer stations gives an average corner frequency of about 1 Hz, assuming a Brune's ω^{-2} theoretical model (Fig. 4). Determination of a relevant value of C (ratio between the stress drop of the target event and the one of the small event) is a crucial point. We first present the results with $C = 1$ and then propose a way to calibrate the C value.

5.2 Constant stress-drop ratio

First, we examine the simulation under the well-used assumption of a common static stress drop for the small event and the target one ($C = 1$). Figure 5a presents the EGFs and a sample of five realizations out of the 500 generated at two stations, NALS and NBOR (N–S component). These nearby stations present different soil conditions. The strong site effect at station NALS is clearly observed on the accelerograms in terms of amplitude and duration when compared to station NBOR. The maximum amplification of the ground motion at station NALS reaches values about 10 with respect to NBOR. The aleatory shapes of the accelerograms are given by the convolution of the EGFs and the various random rupture processes (ESTFs). The simulations are also analyzed in terms of acceleration elastic response spectra (5% damping) as it is used extensively in earthquake engineering practices (Fig. 5b). It describes the maximum response of a single degree of freedom system to particular input motion as a function of natural period and damping ratio of the system. As for the time series, we obtain various possible acceleration spectra with a large range of values. Beauval et al. (2009) checked

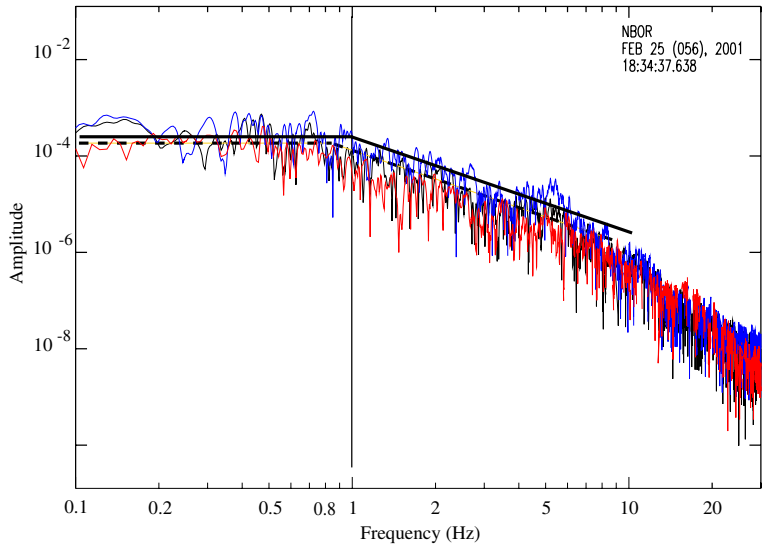


Fig. 4 Fourier displacement spectra at rock-site station NBOR (three components). *Dotted lines* show the ω^{-2} model and the corner frequency (0.83 Hz) inferred for this station. *Black lines* indicate the average ω^{-2} model and corner frequency (1 Hz) deduced from the displacement spectra of the eight stations used in this study

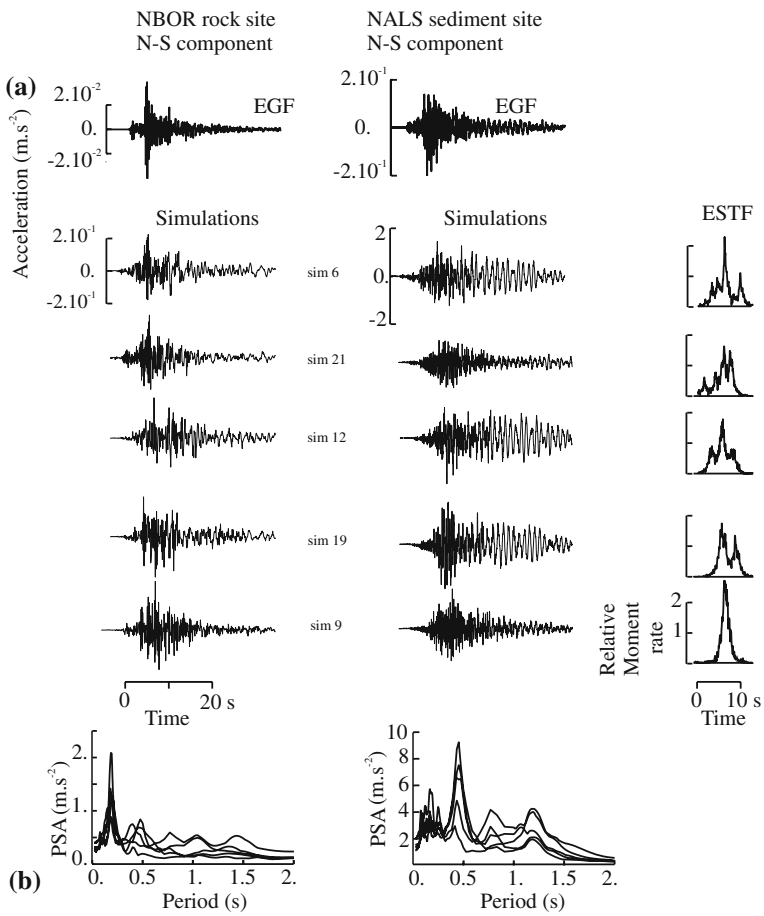


Fig. 5 **a** N–S accelerograms at station NBOR (*left*) and NALS (*right*). The recorded waveforms of the EGF are shown at the *top*. We present a set of five realizations at $C = 1$ and their corresponding equivalent source time function (*ESTF*). **b** The acceleration elastic response spectra (5% damping) of the five simulated accelerograms at stations NBOR (*left*) and NALS (*right*)

that these spectral accelerations were following a log-normal distribution. To describe our results, we simply use the mean values in log unit or the corresponding median values in the considered unit. In the same manner, we use the standard deviation (sigma) in log unit or the 16th and 84th percentiles of the realizations in the considered unit to represent the ground motion variability.

The largest spectral accelerations are found for the N–S component, and we will refer to it in the following analysis. Figure 6 displays the response spectra of the whole accelerogram population at each station. It represents the large aleatory variability of the response spectra (light gray lines) summarized by the median (black lines) and the 16th and 84th percentiles (dotted lines). As previously observed (L. Honoré, personal communication), the percentiles show that the scattering of the response spectra is larger at sediment sites (NALS, NPOR, NROC, NLIB) than at rock sites (NBOR, CALF, MENA, SAOF). This difference is related to the larger amplitudes at high frequency in the EGFs at sediment sites combined with various source processes. The response spectra medians obtained at sediment sites clearly exhibit the local site effects. The NALS response median spectrum shows large amplitudes in the range of natural periods between 0 and 1.5 s, whereas at NPOR and NROC, large amplitudes are seen over a range between the periods at 0 and 1 s. NLIB exhibits lower amplitudes in the range of 0 to 0.5 s. These results are in

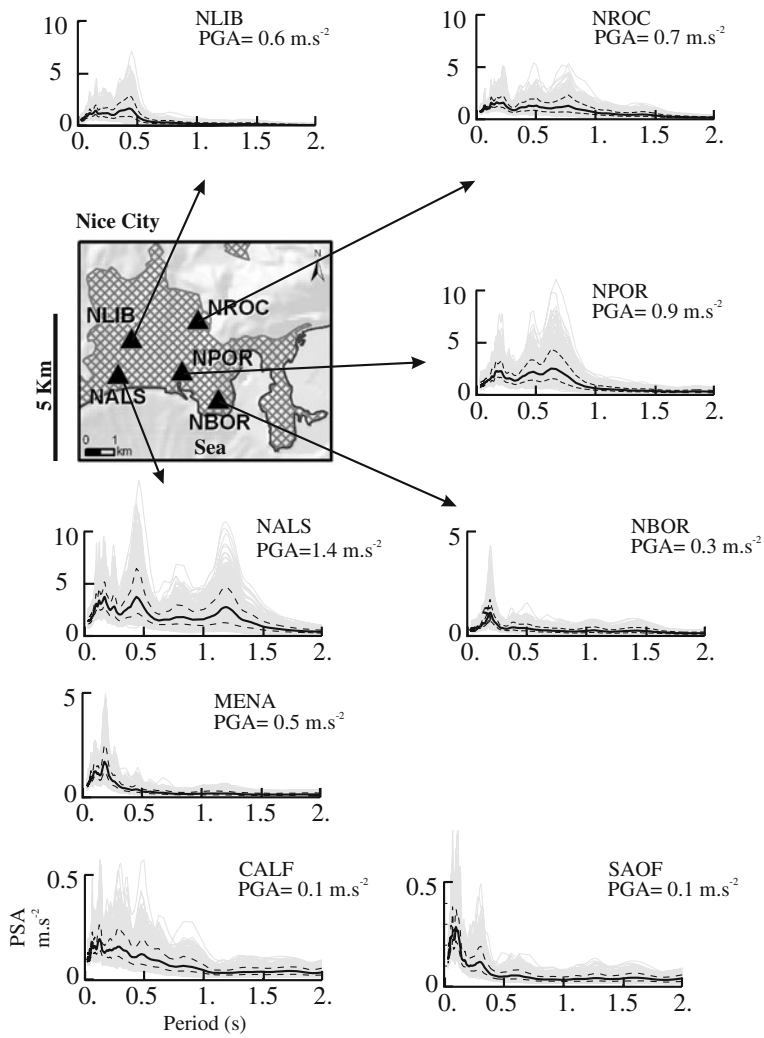


Fig. 6 Acceleration response spectra curves (N–S component) for a simulation at a constant stress drop ($C = 1$). A map indicates the stations located within the Nice city. The *gray lines* correspond to the 500 realizations output. The *black line* is the median value of the realizations. The *upper dotted line* is the 84th percentile indicator; the *lower dotted line* is the 16th percentile (e.g., 68% of the simulations are comprised between these limits)

agreement with the previous site effect studies of Bard et al. (2005), Duval (1996), and Duval et al. (2001). The strongest simulated peak ground acceleration (PGA) is found at sediment site station NALS (PGA = 1.4 m s^{-2}). Other stations located at sediment sites NPOR (PGA = 0.9 m s^{-2}), NLIB (PGA = 0.6 m s^{-2}), and NROC (PGA = 0.7 m s^{-2}) exhibit lower but still noticeable PGA. The stations CALF and SAOF show lower amplitudes due to their location on rock and their larger distance to the source.

The MENA spectral acceleration is found slightly larger than the spectral acceleration at NBOR, despite its further location to the source. Such amplification was observed by Drouet (2006) and could be due to the site topography or to its geological settings since this station is the only one located on Pliocene conglomerates. Another reason could be signal deamplification of the station NBOR (A.M. Duval, personal communication).

The simulation at constant stress drop is a very useful way to provide information to compare ground motion from station to station. We further complete this study focusing on the ground motion variability with stress-drop ratio changes. Indeed, in a previous study, Kohrs-Sansorny et al. (2005) showed that the adjustment of the input parameters, particularly the stress-drop ratio C, is essential to provide synthetic data whose frequency contents and amplitudes are compatible with observed data.

5.3 Stress-drop ratio variation effect

The stress-drop ratio parameter, C, is not a fixed parameter because we have no a priori constraints on the static stress drop of the target event. We run therefore different simulations for which the stress-drop ratio C is set at different values assuming a constant seismic moment ratio CN^3 (Eq. 1), N being an integer.

Table 3 presents the values we have tested between $C = 1$ and $C = 18.6$, which corresponds to values of the corner frequency of the target event between $F_c = 0.125$ Hz and $F_c = 0.333$ Hz. If we assume that the total rupture duration Tr $\sim 1/F_c$ (Hanks and McGuire 1981), this implies that we tested rupture duration from 3 to 8 s for the target event. This can be interpreted as earthquakes with increasing rupture length, or decreasing average rupture velocity, or unilateral versus bilateral rupture process.

Table 3 Target event corner frequencies and stress-drop values inferred from Eq. 1

Fc (Hz)	0.125	0.166	0.2	0.25	0.333
Stress-drop ratio C	1	2.3	4	7.8	18.6

We studied the effects of these various stress-drop ratios on the ground motion simulations. Figure 7a shows the mean ESTF Fourier spectra for different increasing values of C and then decreasing values of F_c. At low frequencies ($f < F_c$), the spectra remain constant whatever the stress-drop parameter C and stay equal to the seismic moment ratio between the small event and the target one.

At high frequencies ($f > f_c$), the ESTF Fourier spectra present a plateau whose level is dependent on C and the scaling parameter N. When the ESTF is convolved with the EGF, the EGF Fourier spectra amplitudes at high frequencies above f_c are modified in a constant manner depending on C and N (Table 4). The resulting synthetic waveforms will then present a significant change in their high frequencies amplitudes.

The elastic response spectra (Fig. 7b) are similarly affected at low periods ($<1/f_c$). We also observe that the standard deviations of the spectral acceleration distributions remain fairly constant from one stress-drop ratio to another. These sigmas seem to be frequency and site dependent as noticed by L. Honoré (personal communication). The different simulations provided here show the large high frequency range of possible ground motion obtained for a given magnitude when source properties, represented here by the static stress-drop ratio, are not constrained.

We also estimate the seismogram duration, e.g., the time interval across which 90% of the total energy is recorded (Trifunac and Brady 1975), by taking the median over the whole seismograms population. C influences the seismogram duration with a decreasing signal length as C increases. This decreasing duration estimation is related to the shorter duration of the ESTFs as C increases (Table 4).

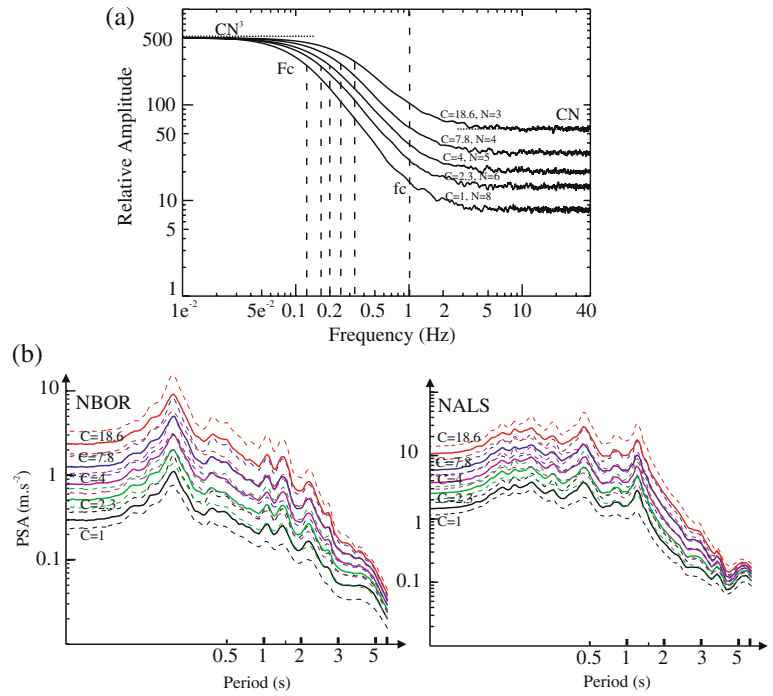


Fig. 7 Influence of stress-drop ratio parameter on the simulation outputs. **a** The means of the simulated Mw 6.3 ESTF Fourier spectra are shown for different C values. The corner frequencies are indicated by the *dotted lines*. The change in the target event frequency corner F_c is indicated. At low frequency ($<F_c$), the frequency amplitudes remain constant and equal to the seismic moment ratio (CN^3). At high frequencies ($>f_c$), the frequency amplitudes remain constant and equal to CN (Kohrs-Sansorny et al. 2005). **b** The median response spectra acceleration curves in the periods 0–2 s are shown for the N–S component of stations NBOR (*left*) and NALS (*right*). The standard deviations (sigmas) are indicated by the *dotted lines*. *Curves* are labeled with their corresponding C

6 A combined EGF and EGMPEs approach

6.1 Calibration of the stress-drop ratio

The simulation process applied in this paper relies on the use of the entire information content of the EGF signal scaled to a Mw 6.3 event. As already mentioned, path, topographic, and 3D local site effects are included in the final results. The simulation provided in our process is thus well suited for site-specific ground motion assessment whatever the propagating medium. Nevertheless,

Table 4 Median PGA values and median seismograms duration estimated from the simulation for several C values at N–S components

	PGA (m s^{-2}) NBOR	PGA (m s^{-2}) NALS	Duration NBOR (s)	Duration NALS (s)	$f > f_c$ amplification
$C = 1$	0.3	1.4	21.1	27.1	1
$C = 2.3$	0.5	2.5	19.5	25.9	1.7
$C = 4$	0.8	3.7	18.8	25.5	2.5
$C = 7.8$	1.3	5.8	17.3	24.8	4
$C = 18.6$	2.3	10.5	16.7	24.2	7

The mean amplification factor for the high frequency domain is also displayed with regards to accelerograms at $C = 1$. The amplification factor is obtained through the ratio $C_i N_i / C_1 N_1$ where $C_1 N_1$ corresponds to the simulation at $C = 1$ (see Eq. 1 and Table 3)

we are limited by the unconstrained parameter C.

In order to adjust C, we compare the acceleration response spectra obtained with the ones described by several GMPEs taken from the literature. The GMPEs are based on ground motion recorded during past earthquakes and usually include a suite of different source mechanisms and site conditions. The GMPEs provide average ground motion parameters as a function of distance and magnitude. They are given for a defined tectonic region and a given soil class. But accounting for the precise local site specificities in the GMPEs is difficult. However, GMPEs have shown a certain accuracy to predict strong ground motion on rock site when some precautions are taken

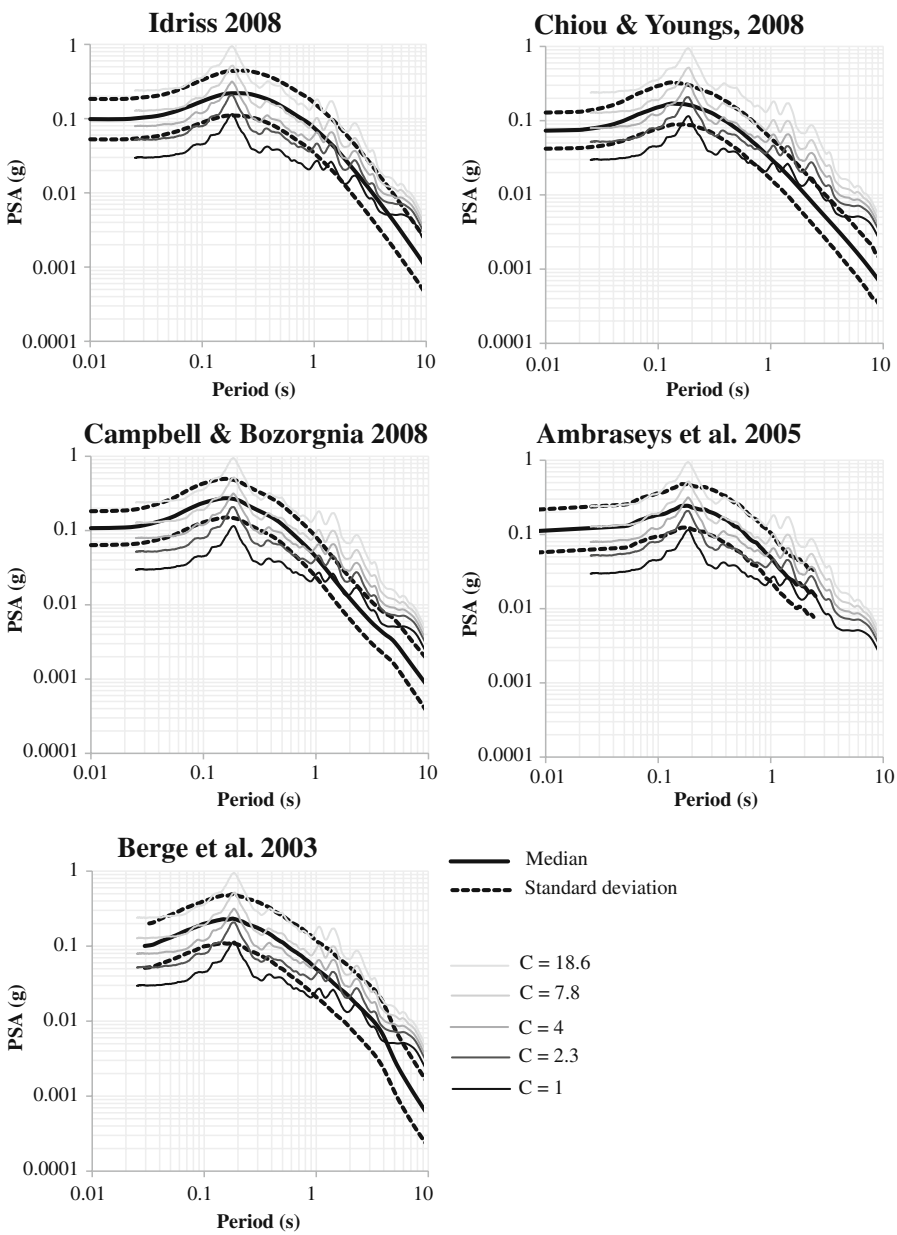


Fig. 8 Comparison of the acceleration response spectra and GMPEs at station NBOR. Acceleration response spectra for different C are shown with *thin lines* (*light to dark gray*). GMPEs are shown with *black thick lines*, and the *dotted lines* correspond to the standard deviation (sigmas)

into account (Cotton et al. 2006). We therefore calibrate the parameter C at the reference rock station NBOR.

In our study, we must consider GMPEs using data sets coming from other areas because the low seismic activity in France does not allow to obtain a specific empirical ground motion model. Five GMPEs are considered in order to capture the epistemic uncertainty in ground motion prediction, following Cotton et al. (2006). Three equations were built in the frame of the Next Generation Attenuation Project (Power et al. 2008; Idriss 2008; Chiou and Youngs 2008; Campbell and Bozorgnia 2008). They are derived from the same worldwide database but use a different formulation. The two others equations are mainly derived from European data (Berge-Thierry et al. 2003; Ambraseys et al. 2005). These five GMPEs meet the best criteria of relevance considered in the study of Cotton et al. (2006) such as the tectonic regime, the database used, and the date of publication. The parameters considered as input of the GMPEs are consistent with the Mw = 6.3 scenario earthquake recorded at NBOR (i.e., thrust fault, epicentral distance $Re = 30$ km, Joyner–Boore distance Rjb = 26 km, hypocentral depth $h = 11$ km, rock site Vs30 = 1,400 m/s).

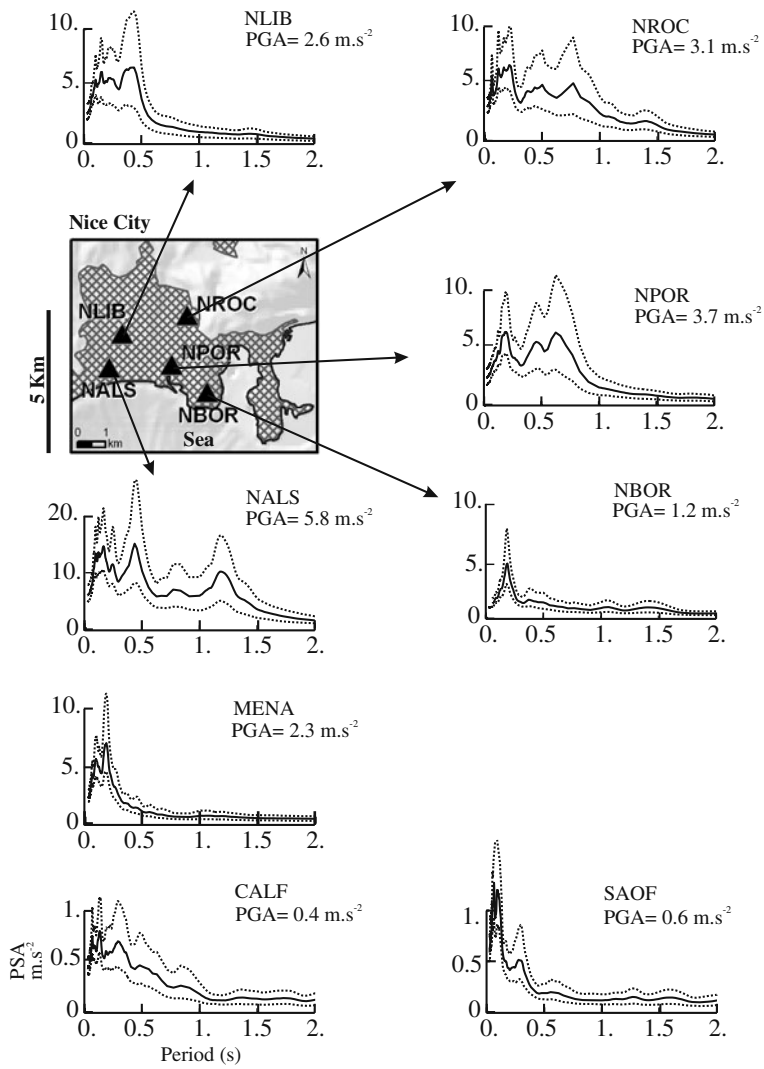


Fig. 9 Elastic acceleration response spectra at $C = 7.8$. The response spectra acceleration medians (*black lines*) and the 84th and 16th percentiles (*dotted lines*) are presented for the N–S component of the eight stations used in this study. A map recalls the location of the station within the city of Nice

Table 5 Median PGA value for a stress-drop ratio $C = 7$

	PGA ($m\,s^{-2}$) NS comp	PGA ($m\,s^{-2}$) EW comp	Distance (km)
NALS(s)	5.8 (4.6/7.5)	5.2 (4.2/6.7)	29.7
NPOR(s)	3.7 (2.7/4.8)	4 (3.2/5.2)	27.6
NROC(s)	3.1 (2.5/3.8)	2.9 (2.4/3.6)	28.4
NLIB(s)	2.6 (2.1/3.4)	2.3 (1.7/3.1)	30.1
MENA(r)	2.3 (1.9/2.9)	2.4 (1.8/3.2)	28.3
NBOR(r)	1.2 (0.95/1.7)	0.96 (0.77/1.2)	25.7
SAOF(r)	0.59 (0.5/0.73)	0.54 (0.46/0.67)	51.3
CALF(r)	0.43 (0.37/0.52)	0.36 (0.31/0.43)	63.5

The 16th and 84th percentiles are shown between brackets (*s*) sediment sites, (*r*) rock sites

Figure 8 shows the comparison of the spectral response between the selected GMPEs and the simulations. Though the GMPEs are scattered, we can easily exclude the simulation hypothesis of $C = 1$ and $C = 18.6$ that underestimates and overestimates the predicted spectral acceleration amplitudes, respectively. The simulation realized at $C = 7.8$ produces the ground motion that best fit with the GMPEs set at least below the natural period of 1 s. Above this period, the predicted spectral amplitude decreases with a greater slope than the ones from our simulations. Nevertheless, $C = 7.8$ can be taken as a reference to provide constrained ground motion in our study.

6.2 Final simulation results

From the GMPEs comparison at the reference rock site (NBOR), we chose the ground motion corresponding to a stress-drop ratio equal to 7.8, and we consider that this calibration leads into relevant ground motion prediction to the other sites, especially those affected by local site effects. The results of the simulation of the Mw 6.3 event are summarized in Fig. 9 (N–S horizontal component response spectrum) and Table 4 (horizontal PGAs). Figure 9 shows the acceleration spectrum median, 16th and 84th percentile that we obtain at each RAP station.

The PGA is almost similar on both horizontal components of the ground motion at each station (Table 5). It ranges from about 0.4 $m\,s^{-2}$ at station CALF to 5.8 $m\,s^{-2}$ at station NALS located on the quaternary deposits in the center of Nice. At the reference station in Nice (NBOR), the PGA reaches a value of 1.2 $m\,s^{-2}$. This acceleration is in good agreement with the one obtained in the RISK-UE project from the same earthquake scenario simulation (Bour et al. 2003). On the other hand, the PGAs deduced in this project from 1D site effect linear-equivalent modeling (Modaressi et al. 1997) exhibit significant smaller values in the valleys. Indeed, the maximum PGA given by the RISK-UE project reached only 1.8 $m\,s^{-2}$, whereas in this present study, we obtain PGAs of 2.6, 3.1, 4, and 5.8 $m\,s^{-2}$ for stations NLIB, NROC, NPOR, and NALS, respectively.

The acceleration response spectra are compared to those recommended by the French regulation (deduced from the EC8) for similar soils. According to Bertrand et al. (2007), the mean S-waves propagation velocity (Vs30) under NALS,

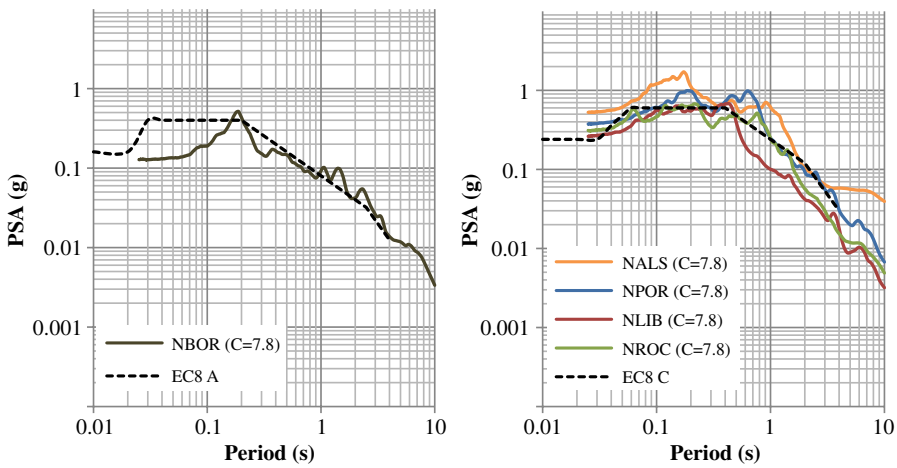


Fig. 10 Comparison of calibrated simulation acceleration response spectra (*thin lines*) to EC8 regulation (*dotted lines*). *Left* Comparison at NBOR rock site. *Right* Comparison at soil sites

NLIB, NPOR, and NROC is characteristic of the subsoil class *C*. The associated regulatory response spectrum is shown in Fig. 10. The shape of the response spectra simulated at NBOR is concordant with the one of the EC8 spectrum at rock site even if this latter spectrum slightly underestimates the amplitude for the natural period larger than 1 s. The simulated PGA at this station is somewhat smaller than the one prescribed for Nice in the French paraseismic rules for class II buildings—the current dwelling building. On the contrary, the PGA computed at NALS is much larger than the one taken from the regulation in Nice. At this station, the numerical response spectrum exhibits larger amplitudes than the one prescribed by the French paraseismic code over almost the whole range of natural periods. We observe the same trend for station NPOR, but for station NLIB and NROC, the EC8 class *C* response spectra seems to be quite adapted since the simulated response spectra are below the regulatory curve. The observed discrepancy at NALS and NPOR shows that the simple Vs30 subsoil classification seems to be insufficient for describing the amplification due to local site effect. A similar statement was suggested in Bragato (2008) regarding the use of this classification in the GMPEs including site effect estimation. It also confirms that amplification due to 3D geology certainly occurs in Nice in the center of the basin quaternary fillings.

7 Discussion

In this part, we address some issues regarding the relevance of the results, the assumptions made, and the parameters used in the different methods.

7.1 Nonlinearity

The EGF method is based on the assumption of soil response linearity. We do not account for the nonlinear soil behavior triggered by sufficiently strong ground motion that is known to occur particularly in soft soil. The actual ground motion and their maxima are controlled not only by the source and the travel paths accounted for in our method but also by the limits on the strongest motion that can be transmitted to the surface by shallow geological materials. It therefore implies that the ground motions are bounded at a given site (Bommer et al. 2004). In Hartzell et al. (2002), the study of the nonlinear effects shows that the assumption of linear soil response can lead to values unrealistically high and inconsistent with observed data for earthquakes. Assessment of the nonlinear effect at sediment sites has been performed by Régnier et al. (2008) with independent linear and nonlinear methods based on the soils mechanical properties. The nonlinear effect appears to be significant only for the site NALS with possible PGA deamplification of about 2 m s^{-2} compared to independent linear approach. This approach is nonetheless limited by the uncertainty on the soil mechanical parameters. Therefore, the acceleration values found in our study at sediment sites should be considered as upper bound estimations of expected ground motion related to the Mw 6.3 target earthquake.

7.2 Static stress-drop parameter

We show that the ground motion amplitudes of our simulations depend on the inferred stress-drop ratio between the large and the small event. The static stress drop represents the only parametric uncertainty in the source characteristics that is not easily set a priori in our procedure but it is a critical parameter. As previously described by Kohrs-Sansorny et al. (2005), our approach has the advantage of not requiring the static stress drop to be scale independent. So we explored relative static stress drops between 1 to about 20 and found that a value of *C* of about 8 gives the best fit to the a GMPEs predictions. Kanamori and Rivera (2004) suggest relative stress drops between small and large events as being in the range $1e^{-2}$ to 100.

In this study, we only assume a magnitude-increasing stress-drop ratio for the simulation although a magnitude-decreasing stress-drop ratio is also possible. This would allow longer equivalent source durations. Nevertheless, the simulations with $C < 1$, giving low amplitude acceleration response spectra, are not in agreement

with the GMPEs amplitudes. Thus, we only consider equivalent durations of the target earthquake ranging from 3 s ($C = 18.6$) to 8 s ($C = 1$). Our best choice for a static stress-drop ratio of 7.8 leads to an equivalent duration of 4 s implying a rather rapid energy release for a Mw 6.3 earthquake. Nevertheless, especially in the case of a bilateral rupture process, this duration seems to be realistic.

7.3 Far-field and point source approximations

Our method does not account properly for the complete description of the displacement field (Eq. 4.32; Aki and Richards 1980), i.e., the near-field terms. Nevertheless, according to Ichinose et al. (2000), given a distance of 25 km and a P-wave velocity of 5.8 km/s, the near-field terms contribution can be neglected for frequencies above 0.15 Hz. Therefore, our simulations are fully valid in the frequency range of engineering interest.

The point source approximation, intrinsic in this method, does not account for the fault finiteness. Is a single small event valid enough to represent the wave path for all the points of the fault? In this simulation, we assume that this is almost true because the geometry of the faulting is parallel to the main geological and tectonic structure of the area (see Larroque et al. 2008). Therefore, the ray paths are considered identical all along the fault.

In addition, the point source approach neglects the directivity effects. The source directivity of a Mw > 6 event can be important; nevertheless, the large variability of the ESTFs population in terms of duration and shape includes implicitly various directivity effects. In the case of our study, the fault orientation (parallel to the coast line) and the station site locations almost perpendicular to the fault strike angle present a configuration where directivity effects are limited.

7.4 Robustness of the GMPEs

In absence of local instrumented large earthquakes required to perform a local empirical attenuation relationship, the strong-motion simulation is constrained with GMPEs that are derived from data sets from different geographical regions. It is a strong assumption even if we reduce some epistemic uncertainty using several relationships. The simulations obtained in this study may not necessarily represent actual ground motion levels, e.g., the actual attenuation of waveforms with distance corresponding to the region and for the given magnitude. We just aimed at constraining our simulations with the more relevant available information. Nevertheless, such an approach seems to be confirmed in areas where large events are instrumented (Courboulex and Converset 2009).

7.5 Parametrization

Our study focuses on the influence of the stress-drop ratio parameter between a small earthquake taken as an EGF and a target event. In our method, it is the only parameter that cannot be deduced by a direct observation of the signals or inferred from the historical seismicity. Nevertheless, other parameters have an influence on the simulation such as, the EGF itself, the corner frequency of the EGF and its seismic moment (Pavic et al. 2000). Further studies should be lead to address the sensitivity of the simulation to the input parameters. Courboulex and Converset (2009) for instance compared ten EGFs used to reproduce the characteristics of the 2004, Mw 6.4, Les Saintes (Guadeloupe) earthquake.

8 Conclusion

The moderate seismicity, the topographic and the geologic heterogeneities of the southeastern part of France make a standard approach of the ground motion estimation rather difficult to perform using only the of GMPEs. In this study, we implement an accelerogram simulation method for a hypothetical, moderate earthquake based on the knowledge of a few parameters and on the use of a small event. It provides a population of synthetic accelerograms that can be used to estimate ground motion at instrumented sites. Nevertheless, our approach is limited by the unconstrained static stress-drop ratio between the targeted Mw 6.3 and the EGF events. In order to fix a static

stress-drop ratio, we used GMPEs at a rock site not affected by local site effects. The comparison between the acceleration response spectra issued from the GMPEs and the simulation allows setting a stress-drop ratio parameter in agreement with all the considered empirical relationships. We thus chose a static stress-drop ratio of 7.8. Under this condition, we find that the hypothetical Mw 6.3 earthquake occurring on the same location as the February 25th, 2001 event could produce noticeable ground motion in the city of Nice, up to a median PGA value of 4 m s^{-2} at station NPOR for which linear behavior is still valid. Nevertheless, our results have to be considered as an upper limit of expected ground motion at the studied sediment sites since our approach is based on the assumption of the soil seismic response linearity.

The comparison of the simulated acceleration response spectra to the EC8 regulation shows that the Vs30 subsoil classification seems to be limited to describe some local site effects, especially in areas where the waveform amplification is related to complex superficial geology such as a basin. Our method has the advantage to directly account for these local specificities.

This process complements well the empirical ground motion prediction equations by accounting for the regional and 3D local site effects in the high frequency domain at any instrumented site and by providing statistically realistic waveform data sets. Finally, some improvement should be addressed by considering the nonlinearity of the soil response in the method by accounting for the site dynamic properties.

Acknowledgements We thank the persons in charge of the seismological networks stations around Nice—Didier Brunel, Christophe Maron, and Sylvain Vidal—and the persons in charge of the RAP central data management center in Grenoble. We are very grateful to Jenny Trevisan for GIS maps and Bertrand Delouis for moment magnitude determination. We benefited from the helpful scientific input of Anne Deschamps, Celine Beauval, and Laetitia Honoré. We thank Julie Régnier for her additional scientific input contributing to the validation of this study. We are grateful to Anne-Marie Duval for her relevant comments on our work. We thank the reviewers for their important and relevant remarks. This research has been supported by the French Agency of Research "ANR" through the contract ANR-05-CATT-011-03 (Quantitative Seismic Hazard Assessment project).

References

Aki K (1967) Scaling law of seismic spectrum. J Geophys Res 72:1217–1231

Aki K, Richards P (1980) Quantitative seismology: theory and methods. Freeman and Co, San Francisco

Ambraseys NN, Douglas J, Sarma SK, Smit PM (2005) Equation for the estimation of strong ground motions from shallow crustal earthquakes using data from Europe and the Middle East: horizontal peak ground acceleration and spectral acceleration. Bull Earth Eng 3:1–53

Arroyo D, Ordaz M (2007) Inelastic-strength spectra in probabilistic seismic hazard analysis. Bull Seismol Soc Am 97(6):2171–2181

Bakun WH, Scotti O (2006) Regional intensity attenuation models for France and the estimation of magnitude and location of historical earthquakes. Geophys J Int 164:596–610

Bard P-Y, Duval A-M, Bertrand E, Vassiliadès J-F, Vidal S, Thibault C, Guyet B, Mèneroud J-P, Guéguen P, Foin P, Dunand F, Bonnefoy-Claudet S, Vettori G (2005) Le risque Sismique à Nice: apport méthodologique, résultats et perspectives opérationnelles. GEMGEP final report, 52 pages. www.equipement.gouv.fr/IMG/pdf/rapportfinalgemgep-part1_cle546382.pdf

Baroux E, Béthoux N, Bellier O (2001) Analyses of the stress field in the southeastern France from earthquake focal mechanisms. Geophys J Int 145:336–348

BCSF (1992) Observations sismologiques 1989–1992. Bureau Central Sismologique Français. In French. http://www.seisme.prd.fr/donnees/publi/1989–1992/obs_sismo_1989–92.pdf

BCSF (2006) Observations sismologiques 2000–2002. Bureau Central Sismologique Français. In French. http://www.seisme.prd.fr/donnees/publi/2000–2002/OBS_SISMO_2000–02ebook.pdf

Beauval C, Honoré L, Courboulex F (2009) Ground-motion variability and implementation of a probabilistic–deterministic hazard method. Bull Seismol Soc Am 99(5):2992–3002. doi:10.1785/0120080183

Beeler NM, Wong TF, Hickman SH (2003) On the expected relationships between apparent stress, static stress drop, effective shear fracture energy and seismic efficiency. Bull Seismol Soc Am 93:1381–1389

Berge-Thierry C, Cotton F, Scotti O, Griot-Pommera DA, Fukushima Y (2003) New empirical response spectral attenuation laws for moderate European earthquakes. J Earthqu Eng 7:193–222

Bertrand E, Duval A-M, Castan M, Vidal S (2007) 3D geotechnical soil model of Nice, France, inferred from seismic noise measurements, for seismic hazard assessment, paper number: NS11D-0798, American Geophysical Union Fall Meeting, San Francisco, CA, USA

Béthoux N, Cattaneo M, Delpech PY, Eva C, Réhault JP (1988) Mécanismes au foyer de séismes en mer Ligure et dans le Sud des Alpes occidentales: Résultats et interprétations. C R Acad Sci Paris 307(2):71–77

Béthoux N, Fréchet J, Guyoton F, Thouvenot F, Cattaneo M, Eva C, Nicolas M, Granet M (1992) A closing Ligurian sea? Pure Appl Geophys 139(2):179–194

Béthoux N, Tric E, Chery J, Beslier MO (2008) Why is the Ligurian basin (Mediterranean Sea) seismogenic? Thermomechanical modeling of a reactivated passive margin. Tectonics 27:TC5011. doi:10.1029/2007TC002232

Bommer JJ, Abrahamson NA, Strasser FO, Pecker A, Bard PY, Bungum H, Cotton F, Faeh D, Sabetta F, Scherbaum F, Studer J (2004) The challenge of determining upper limits on earthquake ground motions. Seismol Res Lett 75:82–95

Bour M, Bertrand E, Le Brun B, Mouroux P (2003) RISK-UE WP2: seismic hazard assessment for the city of Nice. Report to the EC, EVK4-CT-2000-00014, 86pp

Bragato PL (2008) Limits for the improvement of ground-motion relations in Europe and the Middle East by accounting for site effects. Bull Seismol Soc Am 98(4):2061–2065

Brune JN (1970) Tectonic stress and the spectra of seismic shear waves from earthquakes. J Geophys Res 75:4997–5009

Calais E, Nocquet JM, Jouanne F, Tardy M (2002) Current strain regime in the Western Alps form continuous global positioning system measurements, 1996–2001. Geology 30(7):651–654

Campbell KW, Bozorgnia Y (2008) NGA ground motion model for the geometric mean horizontal component of PGA, PGV, PGD and 5% damped linear elastic response spectra for periods ranging from 0.01 to 10 s. Earthq Spectra 24(1):139–172

Chiou B, Youngs RR (2008) A NGA model for the average horizontal component of peak ground motion and response spectra. Earthq Spectra 24(1):173–216

Cotton F, Scherbaum F, Bommer J, Bungum H, Sabetta F (2006) Criteria for selecting and adapting ground-motion models for specific target regions application to central Europe and rock sites. J Seismol 1:1–20. doi:10.1007/s10950-005-9006-7

Courboulex F, Converset J (2009) Ground motion simulations of a Mw 6.4 earthquake (Guadeloupe, 2004): test on 10 smaller events as empirical Green's functions. Bull Seismol Soc Am (in press)

Courboulex F, Larroque C, Deschamps A, Kohrs-Sansorny C, Gélis C, Got JL, Charreau J, Stéphan JF, Béthoux N, Virieux J, Brunel D, Maron C, Duval AM, Perez JL, Mondielli P (2007) Seismic hazard on the French Riviera: observations, interpretations and simulations. Geophys J Int 170:387–400. doi:10.1111/j.1365-246X.2007.03456.x

Delouis B, Legrand D (1999) Focal mechanism determination and identification of the fault plane of earthquakes using only one or two near-source seismic recordings. Bull Seismol Soc Am 89:1558–1574

Douglas J (2003) Earthquake ground motion estimation using strong-motion records: a review of equations for the estimation of peak ground acceleration and response spectral ordinates. Earth-Sci Rev 61(1–2): 43–104

Drouet S (2006) Analyse des données accélèrométriques pour la caractérisation de l'aléa sismique en France métropolitaine. PhD thesis, Toulouse III, Paul Sabatier University

Duval A-M (1996) Determination of the seismic site response with microtremors. Experimental analysis (in French). PhD thesis, University Paris VI, Etudes et Recherches des LPC, GT62, LCPC, Paris, 265 pp

Duval A-M, Bard PY, Lebrun B, Lacave-Lachet C, Riepl J, Hatzfeld D (2001) H/V techniques for site response analysis: synthesis of data from various surveys. Boll Geofis Teor Appl 42:267–280

Ferrari G (1991) The 1887 Ligurian earthquake: a detailed study from contemporary scientific observations. Tectonophysics 193:131–139

Gélis C, Bonilla L-F, Régnier J, Bertrand E, Duval A-M (2008) On the use of Saenger's finite difference stencil to model 2D P-SV non linear basin response: application to Nice, France. Proceed. Seismic Risk conf., Liège, Belgique

Hanks TC, McGuire RK (1981) The character of high frequency strong ground motion. Bull Seismol Soc Am 71:2071–2095

Hartzell SH (1978) Earthquake aftershocks as Green's functions. Geophys Res Lett 5:1–4

Hartzell S, Leeds A, Frankel A, Williams RA, Odum J, Stephenson W, Silva W (2002) Simulation of broadband ground motion including nonlinear soil effects for a magnitude 6.5 earthquake on the Seattle fault, Seattle, Washington. Bull Seismol Soc Am 92:831–853

Ichinose GA, Goldstein P, Rodgers AJ (2000) Relative importance of near-, intermediate- and far-field displacement terms in layered earth synthetic seismograms. Bull Seismol Soc Am 90:531–536

Idriss IM (2008) A NGA empirical model for estimating the horizontal spectral values generated by shallow crustal earthquakes. Earthq Spectra 24(1): 217–242

Joyner WB, Boore DM (1986) On simulating large earthquakes by Green's function addition of smaller earthquakes. In: Das S, Boatwright J, Scholtz CH (eds) Earthquake source mechanics, volume 37 of Maurice Ewing series 6. American Geophysical Union Monograph. American Geophysical Union, Washington, D.C., pp 269–274

Kanamori H, Rivera L (2004) Static and dynamic scaling relations for earthquakes and their implications for rupture speed and stress drop. Bull Seismol Soc Am 94:314–319

Kohrs-Sansorny C, Courboulex F, Bour M, Deschamps A (2005) A two-stage method for ground-motion simulation using stochastic summation of small earthquakes. Bull Seismol Soc Am 95:1387–1400

Lambert J, Moroni A, Stucchi M (1994) An intensity distribution for the 1564, Maritime Alps earthquake. In: Albini P, Moroni A (eds) Materials of the CEC project review of historical seismicity in Europe, vol 2. CNR, Milan, pp 143–152

Larroque C, Migeon S, Beslier MO, Mercier de Lépinay B, Sage F, Cattaneo A, Corradi N, Cuppari A,

Marsset B, Brosolo L (2006) Aléa sismique et aléa gravitaire sur la marge nord du bassin Ligure: Résultats préliminaires de la campagne MALISAR 1. Réunion des Sciences de la Terre, Dijon 04–08 Décembre 2006, Volume des résumés p 88

Larroque C, Delouis B, Godel B, Nocquet J-M (2008) Active deformation at the southwestern Alps–Ligurian basin junction (France–Italy boundary): evidence for recent change from compression to extension in the Argentera massif. Tectonophysics 467:22–34. doi:10.1016/j.tecto.2008.12.013

Madeddu B, Béthoux N, Stéphan JF (1996) Champ de contrainte post-pliocène et déformations récentes dans les Alpes sud-occidentales. Bull Soc Géol Fr 167(6):797–810

McClusky S, Reilinger R, Mahmoud S, Ben Sari D, Tealeb A (2003) GPS constraints on Africa (Nubia) and Arabia plate motions. Geophys J Int 155:126–138

Modaressi H, Foerster E, Mellal A (1997) Computer-aided seismic analysis of soils. In: Proceedings of the 6th Symp. On numerical models in Geomechanics, NUMOG VI, Montréal, Quebec, Canada

Mouroux P, Bertrand E, Le Brun B, Depinois S, the RISK-UE team (2004) The European RISK-UE project: an advanced approach to earthquake risk scenario. In: Proceed. 13th World Conference on Earthquake Engineering, Vancouver, BC, Canada

Nocquet JM, Calais E (2003) Crustal velocity field of western Europe from permanent GPS array solutions, 1996–2001. Geophys J Int 154:72–88

Nocquet JM, Calais E (2004) Geodetic measurements of crustal deformation in the Western Mediterranean and Europe. Pure Appl Geophys 161:661–681. doi:10.1007/s00024-003-2468-z

Ordaz M, Arboleda J, Singh SK (1995) A scheme of random summation of an empirical Green's function to estimate ground motions from future large earthquakes. Bull Seismol Soc Am 85:1635–1647

Pavic R, Koller MG, Bard PY, Lacave-Lachet C (2000) Ground motion prediction with the empirical Green's function technique: an assessment of uncertainties and confidence level. J Seismol 4:59–77

Pequegnat C, Gueguen P, Hatzfeld D, Langlais M (2008) The French Accelerometric Network (RAP) and National Data Centre (RAP-NDC). Seismol Res Lett 79(1):79–89

Power M, Chiou B, Abrahamson N, Bozorgnia Y, Shantz T, Roblee C (2008) An overview of the NGA Project. Earthq Spectra 24(N°1):3–21

Régnier J, Bonilla L-F, Bertrand E, Duval A-M, Beauval C, Scotti O, Douglas J, Gehl P (2008) Variability of one-dimensional soil amplification estimates at four sites of the French permanent accelerometer network (RAP). In: Proceed. 14th World Conference on Earthquake Engineering, Beijing, China

Ritz JF (1992) Tectonique récente et sismotectonique des Alpes du sud: analyses en termes de contraintes. Quaternaire 3:111–124

Scotti O, Larroque C, Courboulex F, Delouis B, Baumont D (2008) On the definition of realistic earthquake parameters along potential active faults in the French–Italian Riviera: a key step in Quantitative Seismic Hazard Assessment (QSHA)—a platform for strong ground motion modeling. EGU general assembly 2008. Geophys Res Abs 10:EGU2008-A-09004

Semblat JF, Duval A-M, Dangla P (2000) Numerical analysis of seismic wave amplification in Nice (France) and comparison with experiments. Soil Dyn Earthqu Eng 19:347–362

Serpelloni E, Vannucci G, Pondrelli S, Argnani A, Casula G, Anzidei M, Baldi P, Gasperini P (2007) Kinematics of the Western Africa–Eurasia plate boundary from focal mechanisms and GPS data. Geophys J Int 169(3):1180–1200. doi:10.1111/j.1365246X.2007.03367.x

Stieltjes L, Bour M, Monge O, Martin C, Mouroux P (1996) Projet GEMITIS Nice: evaluation de l'aléa sismique local sur la ville de Nice. Rapport BRGM n° R39082, 80pp, 22 fig., 9 tables, 8 pl. In French

Trifunac MD, Brady AG (1975) A study on the duration of strong earthquake ground motion. Bull Seismol Soc Am 65:581–626

Wennerberg L (1990) Stochastic summation of empirical Green's function. Bull Seismol Soc Am 80:1418–1432

3.6 Méthode hybride probabiliste-déterministe

Pour l'évaluation de l'aléa sismique d'une région, il existe principalement deux types d'approches : déterministe ou probabiliste. La méthodologie que nous avons cherché à proposer consiste à combiner ces deux approches en remplaçant les modèles de prédiction des mouvements du sol par des simulations dans le cadre d'une étude probabiliste. Cette méthodologie hybride est appliquée à l'estimation de l'aléa probabiliste lié à la faille à l'origine du séisme des Saintes de magnitude Mw 6.4 (Guadeloupe, 21/11/04). Les calculs probabilistes sont réalisés sur plusieurs sites en utilisant un très grand nombre d'accélérogrammes synthétiques générés par la méthode des fonctions de Green empiriques.

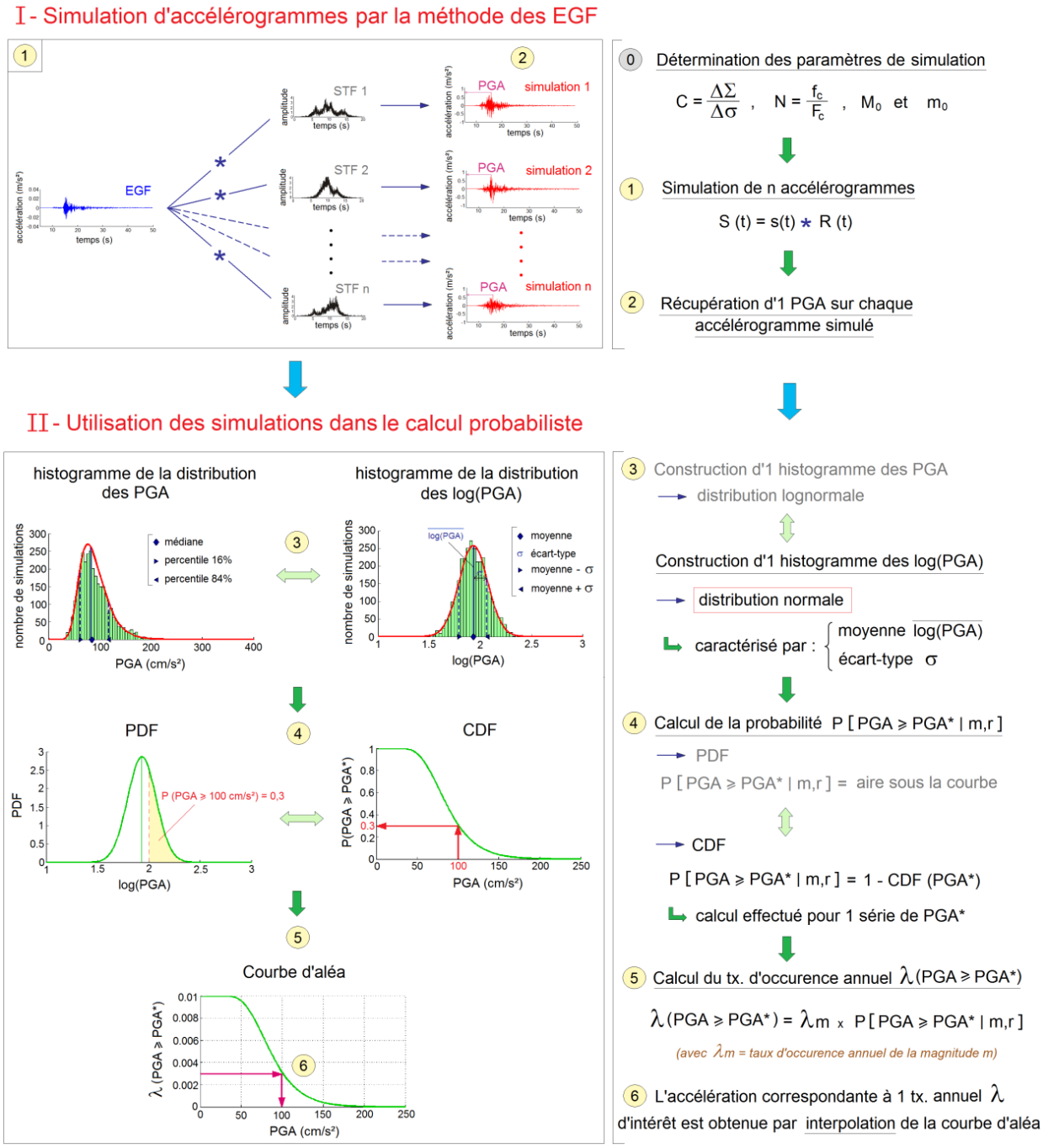


Figure 3. 9 : Représentation schématique des différentes étapes de la méthodologie hybride d'estimation de l'aléa sismique (figure extraite du rapport de Master de L. Honoré [*Honoré*, 2008]).

Les résultats obtenus pour l'étude du PGA (Peak Ground Acceleration) et du spectre de réponse à différences fréquences montrent que les simulations permettent de produire une courbe d'aléa spécifique à chaque site, grâce à une variabilité des mouvements du sol très différente d'un site à un autre. Contrairement à une relation d'atténuation qui considère la même variabilité des mouvements du sol quelque soit la station. Cette variabilité de la valeur de sigma en fonction de la distance et du type de site (variabilité plus forte sur les sites sédimentaires) est importante car elle pourrait être prise en compte dans les calculs probabilistes. Il nous faut néanmoins sur ce sujet travailler sur d'autres bases de données plus fournies pour tester si ce que nous observons sur les Saintes et sur nos simulations est réaliste.

Ce travail va se continuer dans le cadre de l'ANR « Andes du Nord » sur des données d'Equateur.

Bulletin of the Seismological Society of America, Vol. 99, No. 5, pp. 2992–3002, October 2009, doi: 10.1785/0120080183

Ground-Motion Variability and Implementation of a Probabilistic–Deterministic Hazard Method

by Céline Beauval,* Laetitia Honoré, and Françoise Courboulex

Abstract A key step in probabilistic seismic-hazard assessment is the prediction of expected ground motions produced by the seismic sources. Most probabilistic studies use a ground-motion prediction model to perform this estimation. The present study aims at testing the use of simulations in the probabilistic analysis instead of ground-motion models. The method used is the empirical Green's function method of Kohrs-Sansorny *et al.* (2005), which takes into account the characteristics of the source, propagation paths, and site effects. The recording of only one small event is needed for simulating a larger event. The small events considered here consist of aftershocks from the M 6.4 Les Saintes earthquake, which struck the Guadeloupe archipelago (French Antilles) in 2004. The variability of the simulated ground motions is studied in detail at the sites of the French Permanent Accelerometric Array. Intrinsic variability is quantified: ground motions follow lognormal distributions with standard deviations between 0.05 and 0.18 (log units) depending on the spectral frequency. One input parameter bearing large uncertainties is the ratio of the stress drop of the target event to the small event. Therefore, overall sigma values (and medians) are recomputed, varying stress drop ratio values between 1 and 15. Sigma values increase but remain in general lower or equal to the sigma values of current ground-motion prediction models. A simple application of this hybrid deterministic–probabilistic method is carried out at several sites in Guadeloupe for the estimation of the hazard posed by an M 6.4 occurring in the rupture zone of the Les Saintes event.

Introduction

A key step in probabilistic seismic-hazard assessment (PSHA) is the prediction of expected ground motions at a site of interest produced by the seismic sources identified around this site. Nearly all probabilistic seismic-hazard (PSH) studies use a ground-motion prediction model to perform this estimation. In the last few years, the expanding strong-motion databases enabled the development of more and more complex ground-motion prediction equations (see, for example, the recent models developed for western North America on the Next Generation of Ground-Motion Attenuation [NGA] models database; Boore and Atkinson, 2008; Idriss, 2008). Ground-motion equations present the great advantage of being able to predict ground motions at sites covering a broad range of site classifications and for a wide range of magnitudes and distances. However, they also have known shortcomings. Establishing a ground-motion prediction model requires a large strong-motion database. In low seismicity regions, strong-motion recordings are too few to constitute a database, and recordings from different regions must be gathered to develop the prediction model. In high seismicity regions, a ground-motion prediction model can be derived from recordings coming specifically from the region under study; however, the recordings always correspond to different strong-motion stations distributed throughout the region. Therefore, even in these high seismicity regions, the ground-motion prediction models inevitably predict average propagation paths and average site effects. Moreover, all ground-motion prediction models now provide a Gaussian probability density function for the logarithm of the ground motion, characterized by a mean and a standard deviation (sigma). This standard deviation plays a key role in PSH studies. Indeed, for a fixed mean value, the higher the standard deviation, the higher the ground motion for a given return period (considering return periods of interest in earthquake engineering, that is, longer than 100 yr, for example, Beauval and Scotti, 2004; Ordaz, 2004; Bommer and Abrahamson, 2006). Although strong-motion databases are expanding, the sigmas of increasingly complex ground-motion models do not decrease (Douglas, 2003). Some authors (e.g., Anderson *et al.*, 2000) believe that the standard deviations of empirical ground-motion models overestimate the actual variability

*Now at LGIT, IRD, UJF-CNRS, BP 53 Cedex 9, 38041 Grenoble, France.

in ground motions associated with a particular seismological scenario. Deriving an equation from data recorded at different stations distributed throughout a region might lead to an overestimation of the ground-motion variability for a specific couple source/site. However, up to now very few published studies have shown how to reduce this variability on realistic and sound grounds (Atkinson, 2006; Morikawa *et al.*, 2008).

Simulation methods present an alternative to ground-motion prediction models. Such methods can take into account the characteristics of the source, propagation paths, and site effects. The simulation method used here is the empirical Green's function (EGF) stochastic simulation method of Kohrs-Sansorny *et al.* (2005). This method presents great advantages for practical use in PSH studies: (1) The recording of only one small event is necessary to simulate the recording of a larger event at the same station. (2) Only four input parameters are needed: seismic moments of the small event and of the target event, corner frequency of the small event, and the ratio of the stress drop of the target event to the small event. The stress drop ratio is obviously the most difficult parameter to define, as the stress drop of the target event is not known in advance. However, the major shortcoming of this method for integration into a PSH study is the necessity to have at least one recording of a small event located in the vicinity of each fault to be taken into account and also the ability to simulate ground motions only at instrumented sites. Strong-motion networks have a short lifetime (maximum 40 yr, depending on the region of the world; Trifunac and Todorovska, 2001); however, in the future more and more sites will be instrumented and more and more earthquakes recorded, and this requirement might become less restrictive. In any case, it is already possible to study the potential of a hybrid probabilistic method integrating deterministic simulation techniques inside a probabilistic framework. The aim in the present study is to analyze the variability of ground motions predicted using the EGF simulation method in order to quantify the variability of the predictions. Deterministic studies have shown the potential of simulation methods for providing better ground-motion estimates than ground-motion prediction models. However, for PSH assessment purposes, both the median ground-motion levels and the uncertainties on these levels must be analyzed. Note that the present study focuses primarily on the aleatory variability of predicted ground motions.

This work builds on two published works. Convertito *et al.* (2005) introduced the numerical simulations of seismograms into the probabilistic seismic-hazard analysis, using the numerical simulation method of Zollo *et al.* (1997), whereas Hutchings *et al.* (2007) showed how to establish an empirical probabilistic hazard curve by simulating seismograms using a simulation method based on empirical Green's functions with a kinematic description of the rupture process. This study is one step further towards the establishment of a complete hybrid probabilistic methodology. The Kohrs-Sansorny *et al.* (2005) method, requiring much fewer input parameters than the Zollo *et al.* (1997) and Hutchings (1994) methods, is promising within the probabilistic seismic-hazard framework.

Data, Region of Interest, and Scope of the Study

The present study aims at testing the potential of a probabilistic hybrid methodology using data from Guadeloupe, an island of the French Antilles. In Guadeloupe, seismic hazard is posed both by close shallow crustal earthquakes (addressed here) and remote subduction earthquakes. In 2004, an M_W 6.4 earthquake occurred southeast of Les Saintes Island at 14.2 km depth (Delouis *et al.*, 2007), rupturing a 13 km long fault zone (Bertil *et al.*, 2005) and producing a long aftershock sequence. Aftershocks with magnitudes up to 5.1 were recorded in the area, yielding a unique strong-motion data set of shallow events with epicentral distances between 20 and 80 km. These earthquakes occurred within an active normal fault zone where previous tectonic studies had identified faults that could generate earthquakes with magnitudes higher or equal to 6 (Feuillet *et al.*, 2002).

There is no published peer-reviewed ground-motion equation for the prediction of strong motions based on data recorded in the Antilles (Douglas, 2006). Therefore, seismic-hazard studies have to use ground-motion models based on data from other regions of the world. Douglas *et al.* (2006) examined the available data, composed of 10 shallow earthquakes recorded between 1999 and 2005 by the strong-motion networks operating on Guadeloupe and Martinique (Bengoubou-Valerius *et al.*, 2008; Pequegnat *et al.*, 2008). Six of these events belong to the Les Saintes sequence. In order to determine which existing ground-motion model is adapted to the region, they applied the Scherbaum *et al.* (2004) method. They concluded that among the commonly used ground-motion models for shallow crustal earthquakes, none is predicting the data satisfactorily. However, the Ambraseys *et al.* (2005) model was found to be the most appropriate (capability class C; Scherbaum *et al.*, 2004). In the next two decades, it is possible that there will be sufficient data of engineering significance to develop a region-specific ground-motion model.

Because existing ground-motion prediction equations poorly estimate the observed ground motions, it is worth analyzing the integration of simulations for predicting ground motions in probabilistic hazard studies. Six aftershocks of the Les Saintes earthquake with magnitudes between 4.2 and 5.1 are used here as empirical Green's functions (Fig. 1 and Table 1). Stations belong to the French Permanent Accelerometric Array (Bengoubou-Valerius *et al.*, 2008) and are far enough from the fault zone to fulfill the point source approximation of the Kohrs-Sansorny *et al.* (2005) method. The variability of the simulations using the method of Kohrs-Sansorny *et al.* (2005) is tested here, for the first time, on a target event of M 6.4, the same magnitude as the 2004 mainshock. Simulating an M 6.4 enables (1) the comparison of the simulations with at least one observation in order to confirm the appropriateness of the method and (2) the ability to

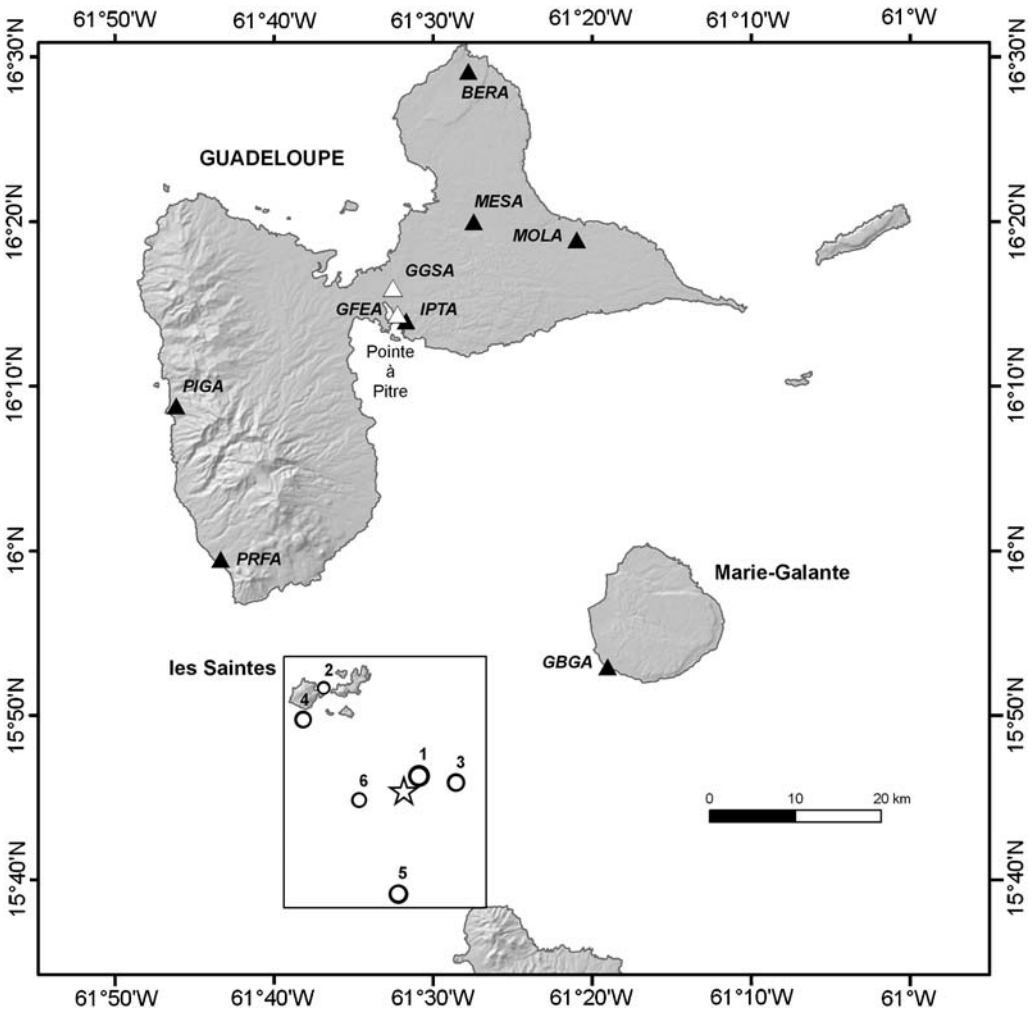


Figure 1. Guadeloupe archipelago. Triangles mark the strong-motion stations used in this study (RAP network). Black triangles, rock stations; white triangles, soil stations. Circles show the events used as empirical Green's functions (see Table 1). Star shows the mainshock M 6.4 of the 2004 Les Saintes sequence.

obtain one estimated value of the stress drop (determined from the Les Saintes mainshock). Note that the 2004 event is only one of many possible M 6.4 events that might occur in the considered normal fault zone.

Simulation Method Used, an Empirical Green's Function Approach

In the Kohrs-Sansorny *et al.* (2005) method, the ground motions produced by an earthquake are simulated by summing the recordings of a single small event taken as an empirical Green's function (Hartzell, 1978). For each realization, the target event records are obtained by the convolution between an equivalent source time function, representing the time history of the rupture over the fault and the small event record. A large number of equivalent source time functions are generated using a precise summation scheme (see details of the probability density functions used for the time delays in Kohrs-Sansorny *et al.* [2005] and Ordaz *et al.* [1995]). The synthetic time histories agree on average with the ω^{-2} Brune (1970) model in the whole frequency band. This approach, based on a point source representation of the fault, is easy to apply and relies only on two unknown parameters: the seismic moment of the target event and the ratio of the stress drop of the target event to the small event used as EGF. This stress drop ratio (C) is the crucial parameter. As shown by Kohrs-Sansorny *et al.* (2005), the method is able to generate a set of accelerograms that could realistically be generated by a given earthquake.

Quantifying the Intrinsic Variability of Ground-Motion Predictions

To begin with, the variability of simulated ground motions is analyzed at station IPTA, a rock station located near the main city Pointe à Pitre (Figs. 1 and 2). The east–west horizontal component is considered. The event used as EGF is the aftershock event 2 (M 4.2, Table 1), and the stress drop

Table 1
Characteristics of the Mainshock and Six Aftershocks of the Les Saintes Sequence

Event	Time (mm/dd/yy, hr:min)	Magnitude	Longitude	Latitude	Depth	f_c	C	N
Mainshock	11/21/04, 11:41	6.4 (M_w)	15.7573	−61.5305	14.2	-	-	-
1	11/21/04, 13:36	5.1 (M_D)	15.7720	−61.5148	12.4	0.62	2	5
2	11/21/04, 22:32	4.2 (m_b)	15.8613	−61.6142	14.6	0.87	5.81	7
3	11/21/04, 22:56	4.8 (m_b)	15.7653	−61.4758	9.9	0.62	2.77	5
4	11/22/04, 02:01	4.7 (M_D)	15.8293	−61.6358	12.4	0.5	5.54	4
5	12/02/04, 14:47	4.9 (M_D)	15.6522	−61.5363	13.7	0.37	6.58	3
6	12/26/04, 15:19	4.5 (m_b)	15.7477	−61.5773	10.5	0.5	11	4

Input parameters for the aftershocks used in the simulations as empirical Green's functions; f_C is the corner frequency, C is the stress drop ratio of the mainshock event to the small event, N[4] is the number of small events summed, C and N have been determined from the spectral ratios (Hough and Kanamori, 2002; Kohrs-Sansorny *et al.*, 2005).

of the target event is, within this section, assumed to be equal to the 2004 Les Saintes stress drop. The best value of C has been determined using the spectral ratio of the Les Saintes mainshock event to the small event used as EGF.

A large number of acceleration time histories are generated; they can be considered as different rupture processes that could happen if the earthquake occurred (Ordaz *et al.*, 1995). For each time history the response spectrum is calculated. Response spectra corresponding to a magnitude 6.4, occurring at the same location as the M 4.2 event, are superimposed in Figure 2 (left, light gray curves). For each frequency, a distribution of log spectral acceleration values is obtained. Figure 2b displays the distribution corresponding to 2 Hz; the logarithms of accelerations are revealed to be normally distributed, in the same way as residuals in real strong-motion databases. This hypothesis of a Gaussian behavior is not rejected when applying the Kolmogorov–Smirnov statistical test at each frequency (Massey, 1951). The distributions are, therefore, fully described by their means and standard deviations. For all frequencies, mean and standard deviations are calculated and superimposed to the response spectra in Figure 2a (black curves). Mean and standard deviations are calculated from 500 simulations, a number large enough to ensure a good statistical estimation.

In a previous study, Courboulex *et al.* (2007) showed that the EGF simulation method predicted quite well the observed M 6.4 Les Saintes mainshock by applying Anderson's (2004) method of quantifying the goodness-of-fit on 25 response spectra. This observation is confirmed here by superimposing the observed response spectrum on the mean and mean $\pm\,\sigma$ values. Figure 3 displays the results obtained at two example stations, the rock station MOLA and the station GGSA located on soil and prone to site effects. The mean and mean $\pm\,\sigma$ predicted by Ambraseys *et al.* (2005) model are also superimposed. Note that the predictions based on simulations are not as blind as the predictions of the ground-motion model; the stress drop of the target event used in the simulation is assumed equal to the stress drop of the observed Les Saintes event (in the following section this condition is removed). The main observation is that for the rock station the simulations are coherent both with the ground-motion model predictions and the observed spectrum whereas for the soil station the simulations are coherent with the observed spectrum but differ from the ground-motion

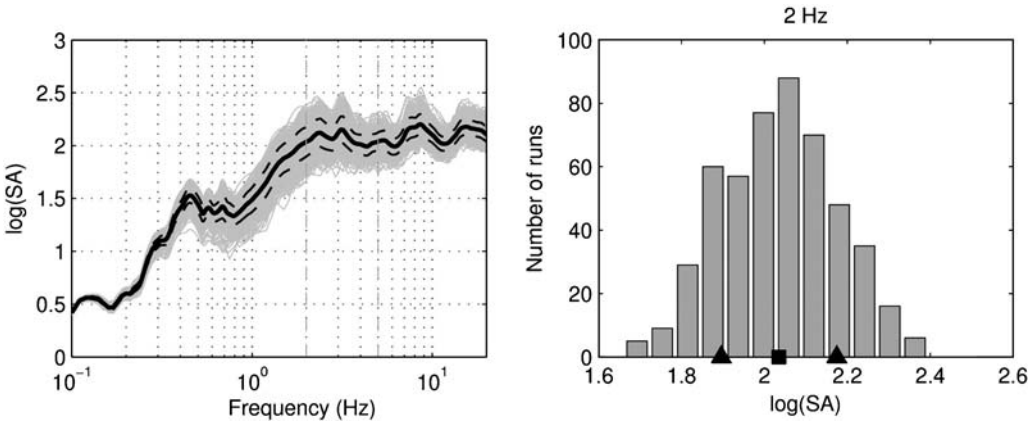


Figure 2. Quantification of the variability of the predictions, at station IPTA. Left, gray curves: response spectra of 500 simulations; black solid line: means of distributions for each frequency; dashed lines: means ±standard deviations(σ); spectral acceleration (SA) in cm.s^{-2}; east–west horizontal component. Right, example at 2 Hz, distribution of the 500 spectral accelerations simulated; square and triangles: mean and mean $\pm\sigma$.

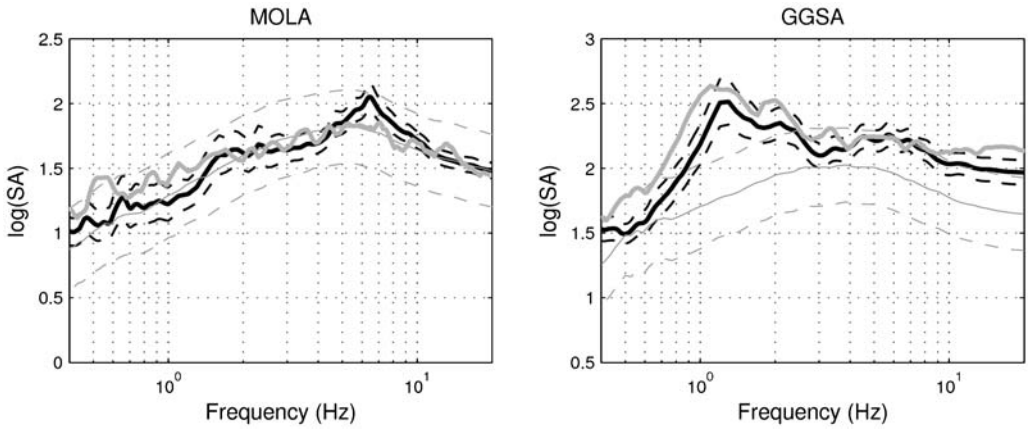


Figure 3. Comparisons of acceleration levels predicted by the EGF simulation technique for an M 6.4 event (black lines) with the observed spectrum corresponding to the 2004 Les Saintes mainshock (thick gray line) and with the acceleration levels predicted by the Ambraseys *et al.* (2005) ground-motion model (thin gray lines). Spectral accelerations in cm × sec^{-2}. Dashed lines correspond to mean $\pm\sigma$. MOLA is on rock and GGSA on soil. EGF used is aftershock event 6 (Table 1).

model predictions (for this soil class). As already observed in Courboulex *et al.* (2007), site amplifications are poorly predicted by the ground-motion model.

Moreover, the uncertainty on the values predicted by the ground-motion model (sigma) is much larger than the sigma based on the EGF simulations. The sigma has a key role in probabilistic hazard assessment and deserves careful analysis. Sigma represents the uncertainty in the ground motion produced by one magnitude at a given distance from the site. For fixed median levels, reducing the sigma leads to a reduction of hazard estimations for returns periods of interest in earthquake engineering. This key role of the sigma in PSH studies has made attempts to reduce the sigma or truncate the ground-motion probability distribution a current hot topic in the engineering seismology field (e.g., Bommer *et al.*, 2004; Strasser *et al.*, 2008).

The Gaussian distributions are calculated at all available stations and for the six EGF events (Table 1). Sigma values correspond to intrinsic uncertainties and are directly linked to the convolution of the EGF to a large number of different equivalent source time functions stochastically generated. Results show that the sigma values are roughly similar from one station to the other and from one EGF to the other (Fig. 4). Calculations were performed for all stations but results are displayed for six stations representative of rock stations. Three stations are located in the eastern part of the island (BERA, MESA, MOLA), two stations are situated in the western part (PIGA, PRFA), and the last one is on another small island west of Guadeloupe (GBGA). The sigma values globally increase from 0.4 to 1.0 Hz and then decrease from 1.0 Hz towards high frequencies, taking values between 0.05 and 0.18. These sigmas are source and site dependent. Therefore, as expected, these values are much lower than the sigmas of recent regional ground-motion prediction models in the range of 0.22 to 0.35 log units (Douglas, 2003; Atkinson, 2006). Note that Causse *et al.* (2008) calculated spectral accelerations distributions corresponding to an M 5.5 event at one rock station located at an epicentral distance of 15 km, using a kinematic EGF simulation method. They found a similar trend and values for the intrinsic standard deviations, over the frequency range 1–20 Hz. Furthermore, these sigmas can be compared to the single station, single source sigma evaluated by Atkinson (2006). Interestingly, Atkinson (2006) found a 0.18 value for the minimum sigma in the case of a single station and a single source of earthquake at a fixed azimuth, considering a range of magnitudes whereas Anderson *et al.* (2000) suggested that the maximum sigma corresponding to a single station, single source, and a characteristic earthquake on this source, is between 0.05 and 0.13, depending on the methods used (simulations or precarious rocks). Our results are coherent with these estimations. Here, only one magnitude is considered, 0.18 is the upper limit for our intrinsic sigmas and 0.05 the lower limit, depending on the spectral frequency. Moreover, Morikawa *et al.* (2008) applied source-area factors at individual observation stations, in order to reduce the uncertainty of source, path and site effect; the resulting standard deviations vary between 0.15 and 0.2. Douglas (2001) tested seven different methods for combining the two horizontal components and showed that the impact on the associated standard deviations is low, with the largest difference between two measures reaching 7%. In this study, different measures are not tested; however, applying this factor to the sigmas quantified here leads to adjusted values between 0.05 and 0.19.

Hence, as the prediction equations average different seismic sources, ground-motion propagation paths and sites, it is not surprising that the variability of these equations result higher than the intrinsic variability of the EGF method applied for one EGF at one site. The question posed is whether the EGF method used here catches the full range of uncertainties for a given couple site/source. The small event contains the information in the path and site effect, and only the variability in the source is explored by generating many different equivalent source time functions. The true

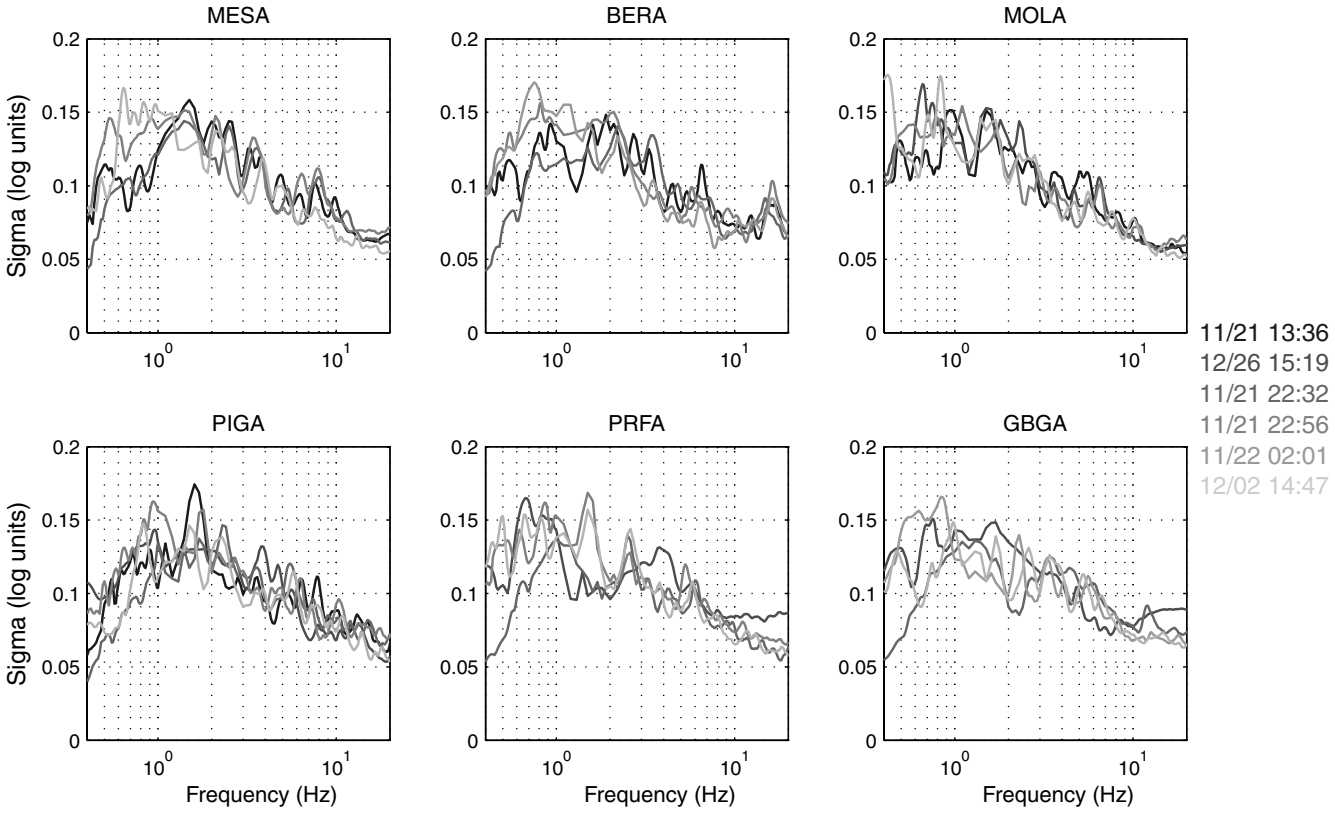


Figure 4. Standard deviations calculated from the spectral acceleration distributions (in log units) at 6 different strong-motion stations, and for the available EGF at each station (see Table 1).

ground-motion variability for a given couple site/source must be in between both estimations.

Variability of Predictions Including the Source Uncertainty

One of the input parameters for the simulation method bears large uncertainties: the *C* value, which is the ratio of the stress drop of the target event to the small event (EGF). In the previous section, calculations were performed using the *C* values determined from the ratios between the recordings of the Les Saintes mainshock event and the small events (varying between 2 and 11, Table 1). However, this event is only one of the possible *M* 6.4 events that could occur on the normal fault zone. Future events can be characterized by different stress drops, and this uncertainty must be included in the strong-motion prediction. Kohrs-Sansorny (2005) showed that *C* values can be as high as 15. Causse *et al.* (2008) explored a range of *C* values roughly in the interval 0–5. Here, the stress drop of the large target event is assumed to be higher than the stress drop of the small event (Kanamori and Riviera, 2004), as observed by Courboulex *et al.* (2007). In the following, *C* values between 1 and 15 are tested for each EGF (Table 2). Note that recent studies (e.g., Allmann and Shearer, 2009) show that no clear correlation between static stress drop and size of earthquakes can be demonstrated.

Figure 5 illustrates the calculation of the acceleration distributions including possible stress drop ratios between 1 and 15, on the example station BERA and using the EGF event 2 (Table 1). Seven *C* values are tested and the corresponding seven sets of spectral acceleration distributions are superimposed (Fig. 5a). Note that all *C* values are assumed equally likely. The median acceleration levels increase with increasing *C* values. As the overall distribution is still close to a Gaussian distribution (see at 2 Hz, Fig. 5b), overall means and standard deviations are calculated for each frequency. The overall sigmas are superimposed in Figure 5c, together with the individual sigmas. Overall sigmas vary between 0.15 and 0.24, over the frequency range 0.4–20 Hz. The sigmas predicted by the Ambraseys *et al.* (2005) ground-motion prediction model are also superimposed. They depend only on the magnitude of the earthquake; they decrease from 0.32 at 0.4 Hz to 0.28 at 20 Hz. These sigmas are representative values of other recent ground-motion models (e.g., Berge-Thierry *et al.*, 2003; Akkar and Bommer, 2007). The overall variability of the ground motion predicted by the EGF simulation method is still lower than the variability predicted by the ground-motion prediction model for the whole frequency range.

The variability including the *C* uncertainty is calculated for all EGF at all available stations in order to determine if this result can be generalized (Fig. 6, six example stations). The results show that for the same EGF, the sigmas calculated

Table 2

Stress Drop Ratios (C) Tested for the Computation of the Overall Acceleration Distributions Including the Uncertainty on the C Value

EGF Event	C						
1	1.16	2.0	3.9	9.27	-	-	-
2	1.16	1.5	2.0	2.74	3.9	5.83	9.25
3	1.0	1.6	2.77	5.41	12.81	-	-
4	1.03	1.64	2.84	5.55	13.16	-	-
5	1.42	2.78	6.58	-	-	-	-
6	1.38	2.06	3.27	5.66	11.06	-	-

All values contained in the interval [1 15] and in accordance with an N integer and the equation $M_0 = C \times N^3 \times m_0$ are tested (m_0 and M_0 seismic moments of the EGF and of the target event; see Kohrs-Sansorny *et al.*, 2005, equation 3).

from the overall acceleration distribution including the uncertainty on the C parameter, are very similar from one station to the other. However, differences appear from one EGF to the other. Sigma values vary between 0.15 and 0.3. Therefore, except for one EGF (event 3) slightly higher over 1–20 Hz, the sigmas remain lower or equal than the ground-motion model sigmas over the whole frequency range. These estimated sigmas take into account the uncertainty in the source, but they must still be considered as source- and site-dependent (they are valid only for an M 6.4 earthquake at a given location and for the recording site studied). As stressed before, the true sigma must be in between the sigma based on the EGF method (integrating the uncertainty in the source parameter) and the sigma of ground-motion prediction equations. The overall sigma calculated here does not take into account the uncertainty in the propagation path between the source and the site nor the uncertainty in the local site effect characterising the station. These results yield an estimate of the variability on the ground motions predicted by the Ordaz *et al.* (1995) and Kohrs-Sansorny (2005) simulation method. Once again, the source and site dependence of these results must not be forgotten, and the comparison with global ground-motion models' sigmas must be interpreted with great caution.

Experimental Probabilistic–Deterministic Seismic-Hazard Estimation

The probabilistic hazard study is carried out at the same strong-motion stations. This part of the study is purely an exercise to show how the hybrid method can be implemented. In a true hazard assessment study, all potential seismic sources posing a threat to the site under study should be taken into account. Here, the hazard is estimated for a magnitude 6.4 occurring in the rupture zone of the M 6.4 Les Saintes event. Moreover, very few events are reported in this normal fault region in the seismic catalog (Bertil *et al.*, 2005), and it is extremely difficult to evaluate recurrence times of earthquakes in this zone, even more for one magnitude only. Therefore, a fictitious recurrence interval of 100 yr for this characteristic M 6.4 earthquake is assumed, yielding an annual rate of 0.01 under the Poisson hypothesis.

To build the hazard curve at a site, annual rates of exceedance of different acceleration levels must be calculated (Cornell, 1968). For each acceleration level, this annual rate is obtained by summing the contributions of earthquakes. The contribution of one earthquake is obtained by multiplying the probability of this earthquake producing an acceleration higher than the target acceleration times the annual rate of occurrence of this earthquake. In classical PSHA studies, the probability of exceedance is calculated from the Gaussian probability density function provided by the ground-motion prediction model. Here this probability is calculated from the Gaussian probability density functions based on the EGF simulation method.

If only one empirical Green's function was available in the fault zone, the probability of exceedance of an acceleration level at a site would be obtained simply by multiplying the annual rate of the earthquake M 6.4 times the probability

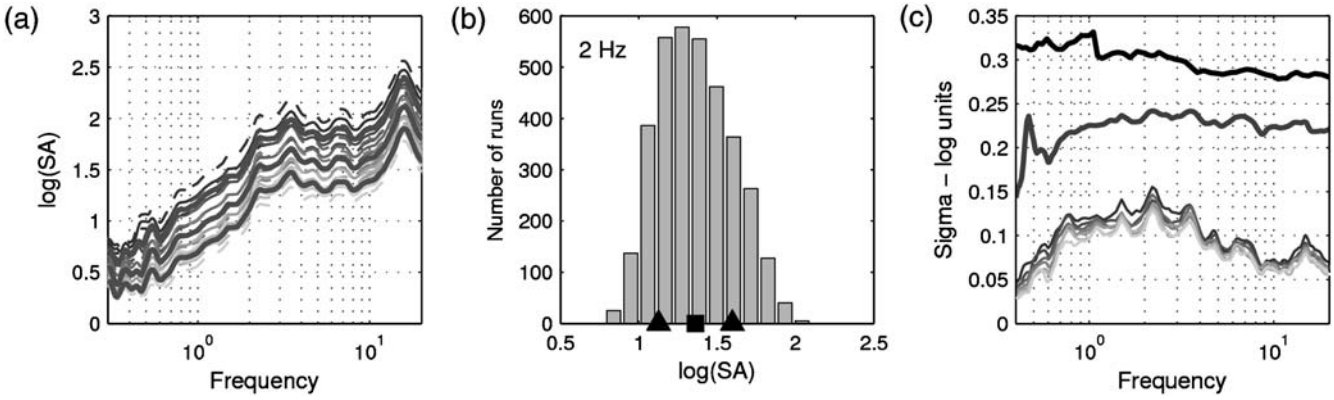


Figure 5. Variability in the prediction of accelerations including the uncertainty on the C parameter, at the example station BERA (EGF event 2): spectral accelerations in cm × sec^{-2}. (a) The overall mean and mean $\pm\sigma$ (thick solid lines) are superimposed on the values obtained from each C value (thin lines, means $\pm\sigma$); C values are increasing from light gray to dark. (b) Example at 2 Hz: the distribution of the logarithms of accelerations is still Gaussian. (c) The overall sigma (dark gray solid line) is larger than the intrinsic sigmas and lower than the sigma (dark solid line) predicted by Ambraseys *et al.* (2005).

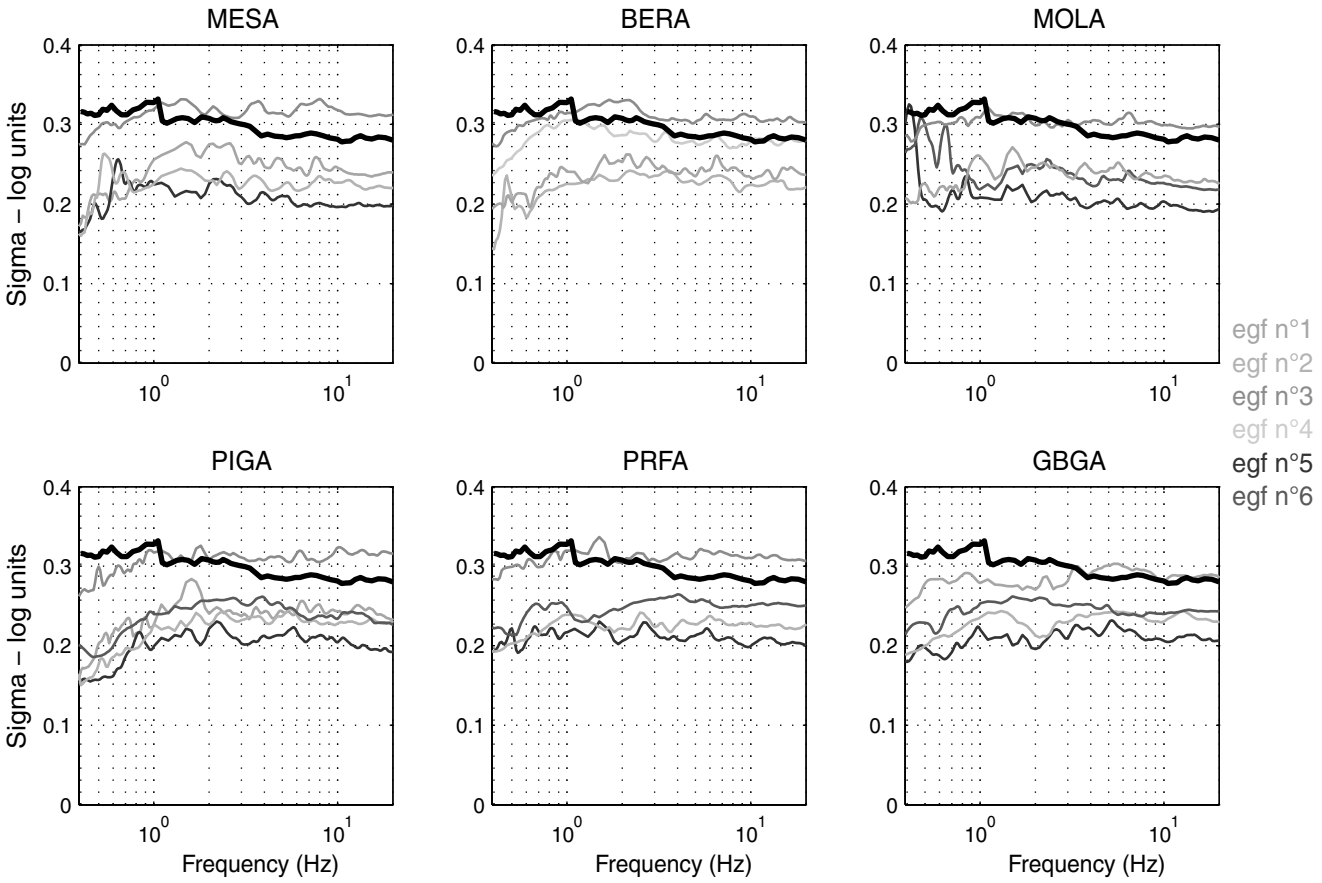


Figure 6. Standard deviations of acceleration distributions based on the EGF simulation technique including the uncertainty on the stress drop ratio (gray curves), compared to the sigmas predicted by the Ambraseys *et al.* (2005) ground-motion model (dark curves). For each station, the sigmas obtained from the different EGF event recorded are superimposed.

of exceedance obtained from the Gaussian predicted by this EGF. However, one can take advantage of the different EGF available, distributing the annual rate of the earthquake over the different EGF, in order to sample the fault zone and to allow the future M 6.4 fault plane to be at slightly different locations. The annual rate is distributed equally over the available small events used as EGF. The probabilities of exceedance are calculated from the probability density function including the uncertainty on the C parameter. Sampling different small events can be considered equivalent to taking into account the uncertainty in the propagation path and in the site effect; the influence of the number of available small events on the results should be tested in future studies.

Hazard curves obtained at different example sites are superimposed in Figure 7, for the spectral frequencies 1, 2, and 5 Hz. For a given annual exceedance rate, the sites closer to the fault rupture zone (PRFA and GBGA) yield the highest acceleration levels. Note that the truncation of ground-motion variability (e.g., Strasser *et al.*, 2008) is not addressed here as the aim is not to obtain absolute acceleration estimates but only to show a simple first implementation of the methodology. Moreover, hazard curves are calculated using a ground-motion prediction model (Ambraseys *et al.*, 2005) as in any classical PSH study. Figure 8 displays the hazard curves obtained for two stations, PRFA and MOLA, superimposed on the hazard curve based on the hybrid probabilistic method. For a given annual rate of exceedance, the hybrid method yields lower levels than the classical probabilistic methodology for both stations and for the three frequencies. This result is specific to the present exercise and cannot be generalized. Note that both the sigma and the median levels have an impact on the calculated probabilities of exceedance of ground motions. This comparison is made here for illustration purposes only because the Ambraseys *et al.* (2005) model has not proven to be well adapted to the region under study (Douglas *et al.*, 2006). The next step will be to take into account different magnitudes in order to implement an experiment closer to real probabilistic seismic-hazard studies.

Conclusions

A hybrid methodology for the computation of probabilistic seismic hazard using an empirical Green's function simulation technique is developed. The Kohrs-Sansorny *et al.* (2005) EGF simulation technique appears well adapted for a practical use in a probabilistic hazard study as the recording of only one small earthquake is required for the simulation of

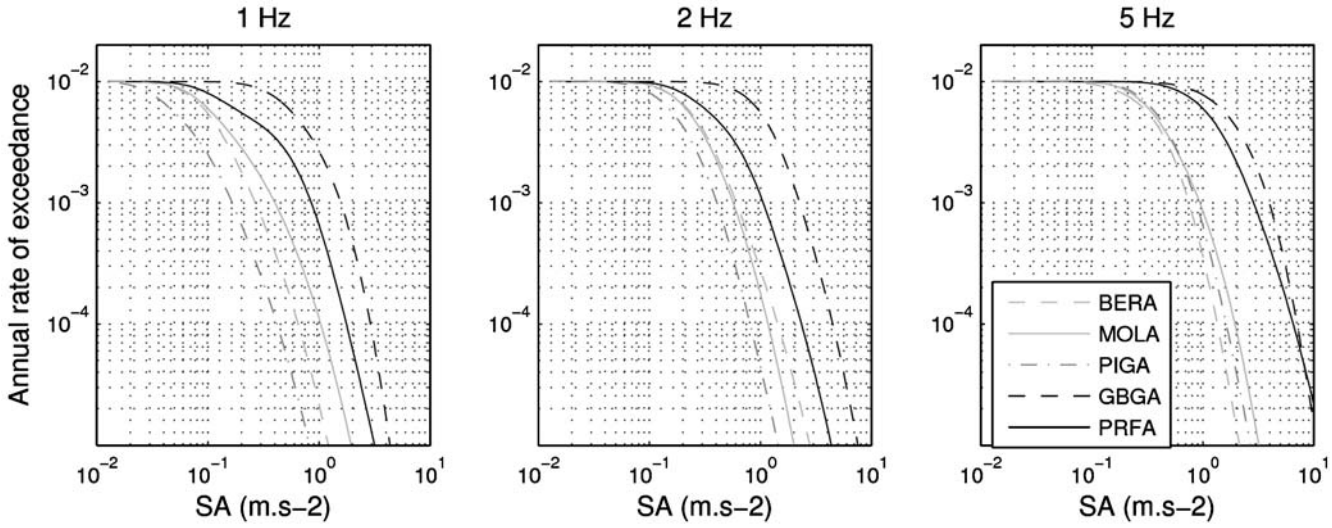


Figure 7. Hazard curves obtained at different strong-motion stations and for three spectral frequencies, using the hybrid methodology (see text for details). Note that this PSH study is purely an exercise as the annual rate of an earthquake of magnitude 6.4 in the fault zone cannot presently be determined and is assumed equal to 0.01.

a larger earthquake. The study focuses on the hazard posed by an M 6.4 event in the rupture zone of the Les Saintes mainshock event (M 6.4, 21 November 2004). For each EGF, the stochastic simulation method provides at each instrumented site of interest a distribution for the ground motion produced by a future M 6.4 event. Gaussian distribution characterized by means and sigmas are determined. These probability density functions are used in the probabilistic seismic calculation exactly in the same way as the Gaussian probability density functions predicted by a classical ground-motion prediction model. Therefore, once the probability density functions are calculated, the implementation of this hybrid deterministic–probabilistic methodology is straightforward. In the future, other summation techniques able to take into account extended sources should be tested. Moreover, the nonlinear issue will have to be addressed because an important shortcoming of this EGF simulation method is that potential nonlinear site effects cannot be taken into account.

The intrinsic variability of the predicted ground motions is quantified. The sigma values reveal themselves to be comparable to the findings of previous studies (Anderson *et al.*, 2000; Atkinson, 2006; Causse *et al.*, 2008), at least for rock stations. More work is required in order to understand the influence of site effects on the sigma values. Furthermore, the simulation method relies on the parameter C bearing large uncertainties: the ratio of the stress drop of the target event to the small event used as EGF. New sigma values (and new medians) are estimated on the ground-motion distributions

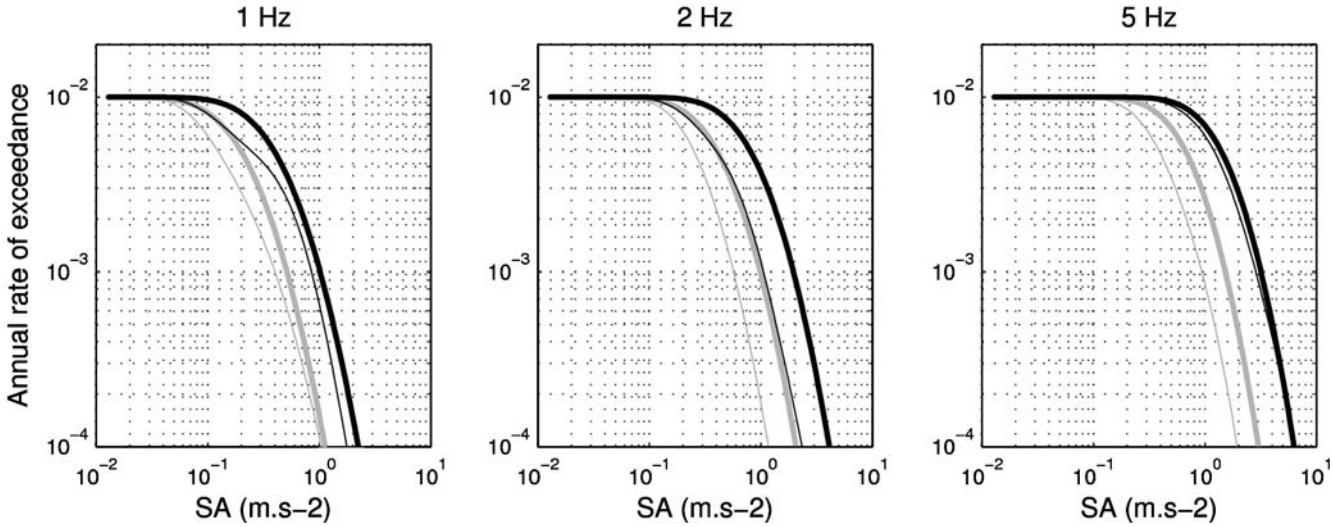


Figure 8. Comparison of hazard curves obtained at two different stations using the hybrid methodology and using the classical method based on the Ambraseys *et al.* (2005) ground-motion model. Gray curve, MOLA; dark curve, PRFA. Thin lines, hybrid method; thick line, classical method.

obtained from varying C between 1 and 15 and assuming that C values are equally likely. As expected, the dispersion is larger and all sigma values increase. However, these overall sigmas remain in general lower or equal than the sigmas of current ground-motion prediction equations for the whole frequency range. This result is expected as these equations average many different sources, paths, and site effects. The true sigma must be in between the sigma based on the EGF method and the sigma of ground-motion prediction equations. Note that the uncertainty interval for the C parameter would need to be more precisely defined, and this will be possible only when more studies are led on the estimation of the stress drop ratio between large and small earthquakes. Note also that a real PSHA study led in the Guadeloupe archipelago would require the use of a ground-motion model as classically done as all seismic sources posing a threat to the site must be taken into account in the probabilistic hazard estimation.

Hybrid methodologies taking advantage of ground-motion simulations (empirical, numerical methods) are promising. In a complete probabilistic seismic-hazard analysis, all seismic sources posing a threat to the site must be taken into account. At the moment, no simulation method is able to provide realistic and complex seismograms for the whole set of seismic sources and in the whole frequency range of engineering interest. However, the future might lie in the combination of different techniques for the prediction of ground motions within a PSH study, using ground-motion prediction models, empirical Green's functions, or synthetic Green's functions depending on the availability of strong-motion recordings at the site but also depending on information about the source, the propagation path, and the site effect.

Data and Resources

Seismograms used in this study were collected by the French Accelerometric Network (RAP). Data can be obtained from the RAP Data Center at www-rap.obs.ujf-grenoble.fr (last accessed March 2009).

Acknowledgments

Thanks to the comments and constructive criticisms of an anonymous reviewer and associate editors J. Bommer and P. Stafford, the content of this manuscript has been improved and its overall message clarified. Moreover, we are very grateful to the people in charge of operating and archiving data from the RAP stations in Guadeloupe at BRGM, IPGP, OVSG, and CDSA. We are also particularly thankful to J. Trévisan at Géoazur for her valuable help in handling data and maps and to A-G. Cox for careful proofreading of the manuscript. This work has been partially supported by the French Permanent Accelerometric Array and by two projects from the Agence Nationale de la Recherche: QSHA under the Contract Number ANR-05-CATT-011 and ADN under the Contract Number ANR-07-BLAN-143.

References

Akkar, S., and J.J. Bommer (2007). Prediction of elastic displacement response spectra in Europe and the Middle East, *Earthq. Eng. Struct. Dyn.* **36,** 1275–1301.

Allmann, B. B., and P. M. Shearer (2009). Global variations of stress drop for moderate to large earthquakes, *J. Geophys. Res.* **114,** doi 10.1029/2009JB005821.

Ambraseys, N. N., J. Douglas, S. K. Sarma, and P. M. Smit (2005). Equations for the estimation of strong ground motions from shallow crustal earthquakes using data from Europe and the Middle East: Horizontal peak ground acceleration and spectral acceleration, *Bull. Earthq. Eng.* **3,** no. 1, 1–53.

Anderson, J. G. (2004) Quantitative measure of the goodness-of-fit of synthetic seismograms, *Proc. of 13th World Conference on Earthquake Engineering*, paper no. 243.

Anderson, J., J. Brune, R. Anooshehpoor, and S. Ni (2000). New ground motion data and concepts in seismic hazard analysis, *Curr. Sci.* **79,** 1278–1290.

Atkinson, G. M. (2006). Single-station sigma, *Bull. Seismol. Soc. Am.* **96,** no. 2, 446–455.

Beauval, C., and O. Scotti (2004). Quantifying sensitivities of PSHA for France to earthquake catalog uncertainties, truncation of ground-motion variability, and magnitude limites, *Bull. Seismol. Soc. Am.* **94,** 1579–1594.

Bengoubou-Valerius, M., D. Bertil, S. Bazin, F. Beauducel, and A. Bosson (2008). CDSA: A new seismological data center for the French Lesser Antilles, *Seism. Res. Lett.* **79,** no. 1, 90–102.

Berge-Thierry, C., F. Cotton, O. Scotti, D. A. Griot-Pommera, and Y. Fukushima (2003). New empirical spectral attenuation laws for moderate European earthquakes, *J. Earthq. Eng.* **7,** no. 2, 193–222.

Bertil, D., S. Bes de Berc, and J. Douglas (2005). Synthèse de la crise sismique des Saintes (Guadeloupe) entre le 21 Novembre 2004 et le 30 Mars 2005, BRGM report, RP-54401-FR, 238 pp.

Bommer, J. J., and N. A. Abrahamson (2006). Why do modern probabilistic seismic-hazard analyses often lead to increased hazard estimates? *Bull. Seismol. Soc. Am.* **96,** no. 6, 1967–1977.

Bommer, J. J., N. A. Abrahamson, F. O. Strasser, A. Pecker, P.-Y. Bard, H. Bungum, F. Cotton, D. Fäh, F. Sabetta, F. Scherbaum, and J. Studer (2004). The challenge of defining upper bounds on earthquake ground motions, *Seism. Res. Lett.* **75,** no. 1, 82–95.

Boore, D. M., and G. M. Atkinson (2008). Ground-motion prediction equations for the average horizontal component of PGA, PGV, and 5%-damped PSA at spectral periods between 0.01 s and 10.0 s, *Earthq. Spectra* **24,** no. 1, 99–138.

Brune, J. N. (1970). Tectonic stress and the spectra of seismic shear waves from earthquakes, *J. Geophys. Res.* **75,** 4997–5009.

Causse, M., F. Cotton, C. Cornou, and P.-Y. Bard (2008). Calibrating median and uncertainty estimates for a practical use of empirical Green's functions technique, *Bull. Seismol. Soc. Am.* **98,** no. 1, 344–353.

Convertito, V., A. Emolo, and A. Zollo (2006). Seismic-hazard assessment for a characteristic earthquake scenario: An integrated probabilistic deterministic method, *Bull. Seismol. Soc. Am.* **96,** 377–391.

Cornell, C. A. (1968). Engineering seismic risk analysis, *Bull. Seismol. Soc. Am.* **58,** 1583–1606.

Courboulex, F., J. Converset, and C. Kohrs-Sansorny (2007). Simulation du séisme des Saintes (M_w 6.4, Guadeloupe, 2004) en utilisant une sommation stochastique de petits séismes, in *VIIth National Conference on Earthquake Engineering*, Chatenay-Malabry, France, 4–6 July 2007, Paper 84, 8 pp.

Delouis, B., M. Vallée, and V. Cruz-Atienza (2007). The $M_w = 6.3$ Saintes earthquake (West Indies): Source kinematics determination and uncertainties in a poorly known crustal structure, *Geophys. Res. Abstr.* **9,** 10050.

Douglas, J. (2001). A critical reappraisal of some problems in engineering seismology, *PhD Thesis*, University of London, London, United Kingdom.

Douglas, J., D. Bertil, A. Roullé, P. Dominique, and P. Jousset (2006). A preliminary investigation of strong-motion data from the french Antilles, *J. Seismol.* **10,** 271–299.

Feuillet, N., I. Manighetti, P. Tapponnier, and E. Jacques (2002). Arc parallel extension and localization of volcanic complexes in Guadeloupe,

Lesser Antilles, *J. Geophys. Res.* **107,** no. B12, 2331, doi 10.1029/2001JB000308.

Hartzell, S. H. (1978). Earthquake aftershocks as Green's functions, *Geophys. Res. Lett.* **5,** 1–4.

Hough, S., and H. Kanamori (2002). Source properties of earthquakes near the Salton Sea triggered by the 16 October 1999 *M* 7.1 Hector Mine earthquake, California, *Bull. Seismol. Soc. Am.* **92,** 1281–1289.

Hutchings, L. (1994). Kinematic earthquake models and synthesized ground motion using empirical Green's functions, *Bull. Seismol. Soc. Am.* **84,** 1028–1050.

Hutchings, L., E. Ioannidou, W. Foxall, N. Voulgaris, J. Savy, I. Kalogeras, L. Scognamiglio, and G. Stavrakakis (2007). A physically based strong ground-motion prediction methodology; application to PSHA and the 1999 $M_w = 6.0$ Athens earthquake, *Geophys. J. Int.* **168,** 659–680.

Idriss, I. M. (2008). An NGA empirical model for estimating the horizontal spectral values generated by shallow crustal earthquakes, *Earthq. Spectra* **24,** no. 1, 217–242.

Kanamori, H., and L. Rivera (2004). Static and dynamic scaling relations for earthquakes and their implications for rupture speed and stress drop, *Bull. Seismol. Soc. Am.* **94,** 314–319.

Kohrs-Sansorny, C., F. Courboulex, M. Bour, and A. Deschamps (2005). A two-stages method for strong ground-motion simulations using stochastic summation of small earthquakes, *Bull. Seismol. Soc. Am.* **95,** 4, 1387–1400.

Massey, F. J. (1951). The Kolmogorov-Smirnov test for goodness of fit, *J. Am. Stat. Assoc.* **253,** 68–78.

Morikawa, N., T. Kanno, A. Narita, H. Fujiwara, T. Okumura, Y. Fukushima, and A. Guerpinar (2008). Strong motion uncertainty determined from observed records by dense network in Japan, *J. Seism.* **12,** 529–546.

Ordaz, M. (2004). Some integrals useful in probabilistic seismic hazard analysis, *Bull. Seismol. Soc. Am.* **94,** 1510–1516.

Ordaz, M., J. Arboleda, and S. K. Singh (1995). A scheme of random summation of an empirical Green's Function to estimate ground motions from future large earthquakes, *Bull. Seismol. Soc. Am.* **85,** no. 6, 1635–1647.

Péquegnat, C., P. Guéguen, D. Hatzfeld, and M. Langlais (2008). The French Accelerometric Network (RAP) and National Data Center (RAPNDC), *Seism. Res. Lett.* **79,** no. 1, 79–89.

Scherbaum, F., F. Cotton, and P. Smit (2004). On the use of response spectral-reference data for the selection and ranking of ground-motion models for seismic-hazard analysis in regions of moderate seismicity: The case of rock motion, *Bull. Seismol. Soc. Am.* **94,** no. 6, 2164–2185.

Strasser, F. O., J. J. Bommer, and N. A. Abrahamson (2008). Truncation of the distribution of ground-motion residuals, *J. Seismol.* **12,** 79–105.

Trifunac, M. D., and M. I. Todorovska (2001). Evolution of accelerographs, data processing, strong motion arrays and amplitude and spatial resolution in recording strong earthquake motion, *Soil Dyn. Earthq. Eng.* **21,** 537–555.

Zollo, A., S. Martucci, G. Milana, and P. Capuano (1999). The 1997 Umbria-Marche (Central Italy) earthquake sequence: Insights on the main shock ruptures from near source strong motion records, *Geophys. Res. Lett.* **26,** 3165–3168.

Observatoire de la Côte d'Azur, Géoazur
IRD, CNRS, UNS
250 Rue Albert Einstein
Sophia Antipolis
06560 Valbonne, France
celine.beauval@obs.ujf-grenoble.fr

Manuscript received 11 July 2008

3.7 Conclusion

Nous avons proposé une approche stochastique en 2 étapes (programme SIMULSTOC) qui permet de produire un nombre important d'accélérogrammes susceptibles d'être générés par un séisme de magnitude donnée. Cette méthode permet de produire des fonctions source très différentes et donc de couvrir une variabilité importante des mouvements du sol. Elle a surtout un avantage précieux : elle ne nécessite que très peu de paramètres d'entrée. Le seul paramètre crucial et effectivement difficile à estimer reste le rapport des chutes de contrainte entre le petit séisme utilisé comme fonction de Green empirique et le séisme à simuler. En effet, la chute de contrainte est un paramètre pour le moment impossible à évaluer à l'avance [*Allmann and Shearer*, 2009; *Kanamori and Rivera*, 2004] et qui a une influence très grande sur les hautes fréquences du signal [*Causse et al.*, 2008].

Avant de proposer une méthode de calibration, nous avons travaillé sur des données venues de contextes différents où petits et gros séismes étaient enregistrés : Italie centrale, Mexique, Antilles. A chaque fois, nous avons remarqué que le rapport des chutes de contraintes entre les petits séismes (en général des répliques) et le choc principal pouvaient aller de 1 à 15. Certains auteurs trouvent une variation qui peut être légèrement plus importante, mais l'ordre de grandeur reste le même. Récemment, nos travaux sur les données des Pyrénées [*Honoré et al.*, 2009] ou sur le séisme de l'Aquila [*Honoré and Courboulex*, 2009] montrent au contraire des valeurs de C proches de 1, et même parfois inférieures.

Afin de réduire la gamme de valeurs de C possibles, nous proposons de nous appuyer sur les équations empiriques du mouvement du sol afin de ne garder que les valeurs de C les plus plausibles. Cette approche a l'avantage de nous permettre de ne plus supposer de rapport de proportionnalité entre les mouvements faibles et les mouvements forts. La forme spectrale est donnée par les petits séismes et le calage en amplitude est apporté par les équations empiriques bâties à partir de gros séismes. Cette approche a été testée sur les données des Saintes. Elle a ensuite été appliquée dans une simulation en aveugle sur les données de Nice. Une autre approche consiste à calibrer les valeurs plausibles de C en permettant une variation de la durée de rupture donnée. C'est cette approche que nous utilisons actuellement sur les données italiennes.

CHAPITRE 4 : DES SEISMES POUR PETITS ET GRANDS

4.1 Sismos à l'Ecole

Le domaine dans lequel j'ai la chance de faire de la recherche est si riche, varié et passionnant qu'il serait dommage de ne pas le faire connaitre et partager au plus grand nombre. J'ai toujours été partante et motivée pour entreprendre des actions vers les scolaires et le grand public, que ce soit à l'occasion de la fête de la science, d'interventions en milieu scolaire ou lors de conférences grand public. Depuis le départ de Jean Virieux pour le laboratoire de Grenoble en 2007, je me suis lancée dans une action de plus grande envergure : le suivi scientifique du programme « Sismos à l'Ecole ».



Figure 4. 1 : Réseau 'Sismos à l'Ecole' en début 2010 : 51 stations, une centaine d'enseignants, 20 référents scientifiques et des milliers d'élèves (cartes : Jenny Trévisan).

Ce projet né dans les Alpes maritimes il y a 13 ans grâce à la rencontre de Jean Virieux (professeur à l'université de Nice) et de Jean-Luc Bérenguer (professeur de Sciences de la vie et de la Terre au collège du Centre International de Valbonne) lors d'une fête de la science, s'est peu à peu développé. Ce concept de « Seismo at school » existait déjà aux états unis depuis quelques temps (Guust Nolet en a d'ailleurs été l'un des fondateurs).
Le réseau est rapidement devenu très actif dans les Alpes Maritimes grâce au dynamisme de ses fondateurs et à celui des enseignants impliqués. Ce projet a ensuite pris une dimension nationale en 2006 en intégrant le dispositif national « Sciences à l'Ecole » piloté par l'observatoire de Paris. Le réseau est devenu rapidement international avec plusieurs stations installées dans des lycées à l'étranger (Australie, Portugal, Turquie, Djibouti, république Dominicaine … et bien d'autres en projet).

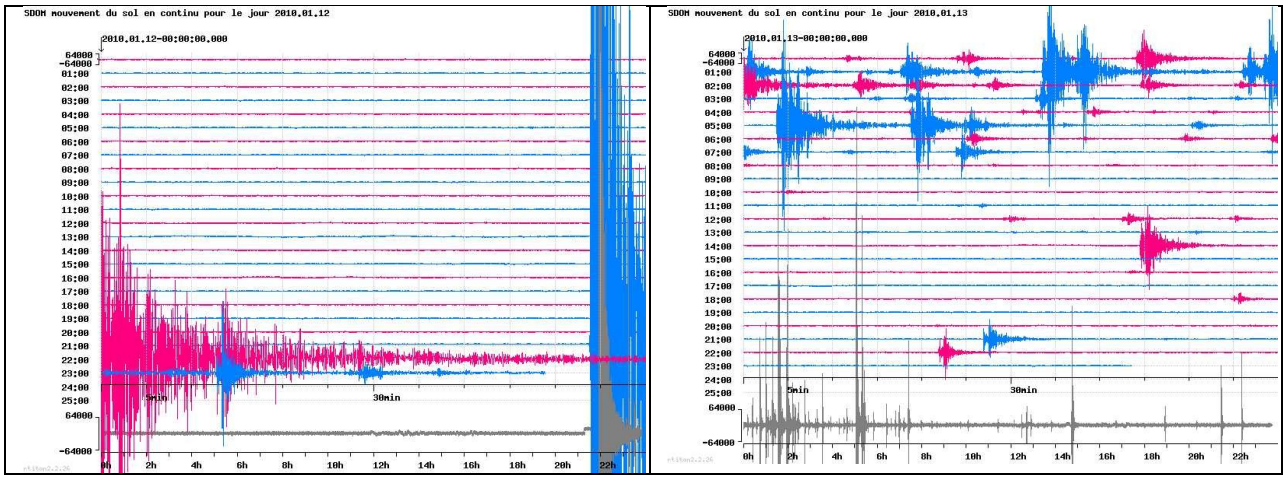


Figure 4. 2 : Dérouleur journalier du capteur vertical de la station SDOM du réseau 'Sismos à l'Ecole' située dans le lycée de Saint Domingue (république dominicaine). A gauche : Le très gros événement en bleu représente le tracé du séisme d'Haiti (2010). A droite : le nombre de répliques est impressionnant !

En tout un réseau de plus de 51 stations est opérationnel aujourd'hui (Figure 4. 1). Les données sont acquises grâce à des stations sismologiques de qualité (acquisition 24 bits, sismomètres 3 composantes large bande, liaison GPS pour le temps). Elles sont consultables et récupérables en temps réel via un site web ouvert à tous : www.edusismo.org. Il est ainsi très rapide d'aller vérifier directement sur une station si un séisme a été enregistré (cette fonctionnalité est utilisée également par les chercheurs !). La Figure 4. 2 montre par exemple les mouvements du générés par le séisme d'Haïti sur la station du lycée situé en république dominicaine.

Les données sont disponibles en temps réel sur la station mais elles sont également transmises au laboratoire Géoazur où une cellule « Sismos à l'école » gère les données en les classant dans une base de données relationnelle et en les mettant à disposition de façon conviviale et commentée (on indique les enregistrements les plus intéressants) sur le site web. Cette convivialité permet aux enseignants d'utiliser avec leurs élèves des données de leur station (s'ils en ont une dans leur collège) mais aussi de toutes les autres stations du réseau de façon transparente. Le site web est également très riche en échanges entre enseignants. Une rubrique leur permet en effet de mettre en ligne des activités qu'ils ont proposées à leurs élèves. Ces travaux pratiques sont « validés » par un comité scientifique.

L'efficacité de ce réseau tient au dynamisme des enseignants mais aussi au lien fort qui existe entre enseignement et recherche. A chaque équipe éducative en charge d'une station est en effet attaché un sismologue d'un laboratoire voisin. Ce sismologue appelé le « référent scientifique » a pour rôle de répondre aux questions scientifiques des enseignants, de les aider à différents niveaux et d'intervenir sur demande dans les classes.

En tant que coordinatrice scientifique du projet, je suis amenée à participer à des actions de formation des enseignants, à des réunions du groupe national regroupant enseignants et référents scientifiques, à discuter et proposer des pistes nouvelles pour l'avenir et à chercher des moyens de pérenniser ce réseau formidable.

4.2 Le projet européen O3E

Jean-Luc Berenguer, coordinateur du réseau 'Sismos à l'Ecole' a depuis quelques temps déjà à cœur d'exporter le succès de 'Sismo à l'Ecole' vers d'autres mesures environnementales. L'appel à projet européen INTERREG-ALCOTRA nous a donné l'opportunité de créer un réseau de stations multi-paramètres dans les établissements scolaires et d'étendre ce réseau à d'autres pays d'Europe. Les projets INTERREG concernent les territoires autour des frontières. Ce projet rassemble des italiens des régions Piemont et Ligurie, des Suisses et des français de la région PACA et Rhône Alpes. Son financement très conséquent nous permet de bénéficier d'un potentiel humain relativement important … mais il ne nous permet malheureusement pas de surmonter avec fluidité les contraintes administratives extrêmement lourdes de ce type de projet européen.

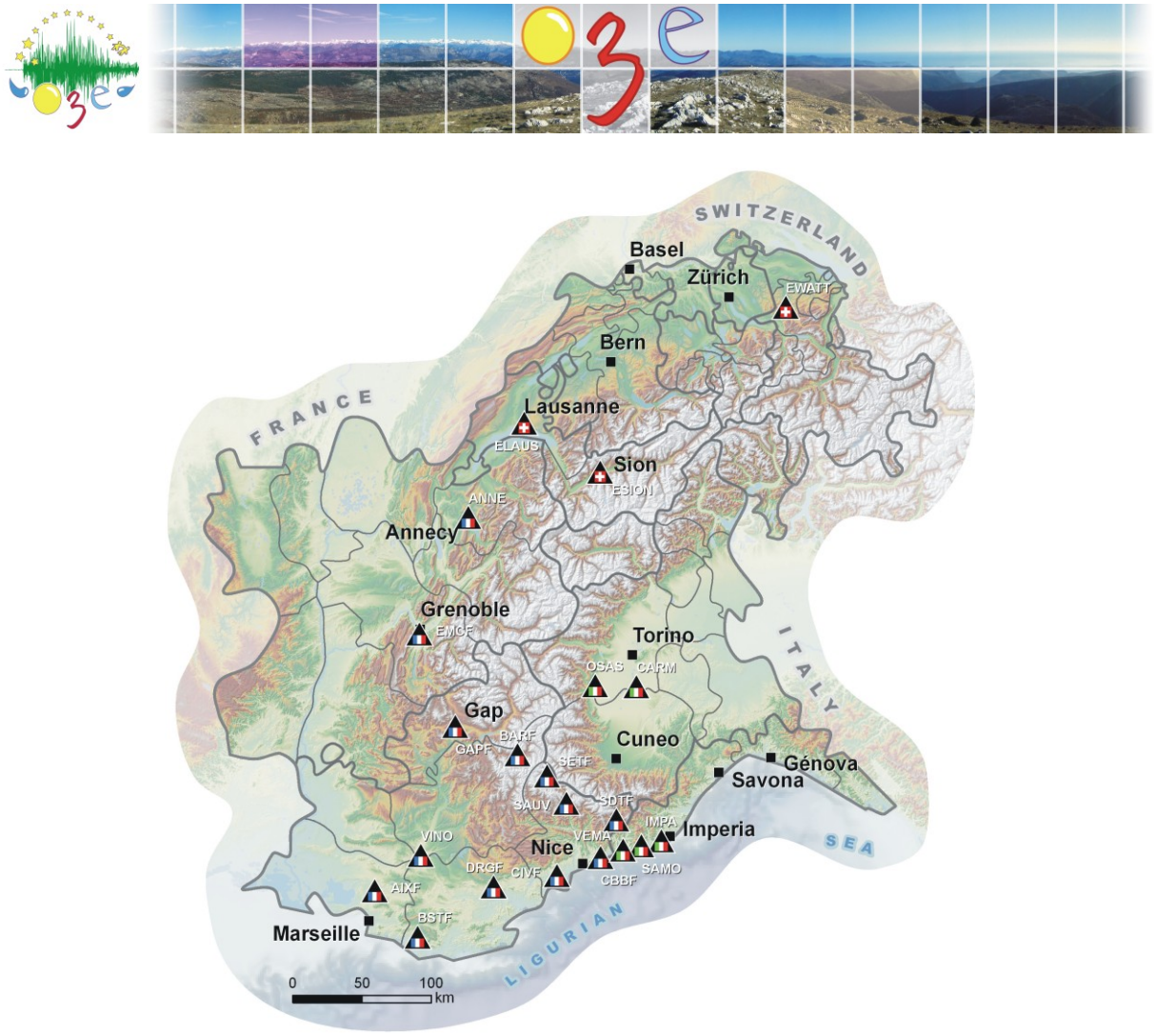


Figure 4. 3 : Localisations des stations sismologiques et météorologiques du programme éducatif O3E. Site web du projet, accès aux données : http://o3e.geoazur.eu

Comme pour le projet Sismo à l'Ecole, les mesures (Météo et sismo pour le moment) sont accessibles directement via un site web dédié au projet. Un séminaire de formation est prévu pour une cinquantaine d'enseignants des trois pays à la fin du mois de Mars 2010 (en même temps que ma soutenance d'HDR).

4.3 Et la suite ?

Le réseau de capteurs installés dans les établissements scolaires est à présent très important, le nombre d'enseignants et de chercheurs impliqués est impressionnant, les activités proposées sont nombreuses et de qualité, les outils mis à la disposition des professeurs sont de plus en plus performants.

Ce programme permet aux élèves de :

- Récolter des mesures environnementales réelles avec des instruments calibrés.
- Réaliser des expériences, émettre des hypothèses, obtenir des résultats, exercer leur esprit critique.
- Attiser leur envie de mieux comprendre le fonctionnement de notre Terre, les pousser à chercher et trouver des réponses par eux-mêmes. Continuer à s'émerveiller.
- Mieux connaitre les risques, les comprendre et les quantifier sans catastrophisme.
- Comprendre que la recherche n'est pas hors de leur portée. Devenir peut-être les scientifiques de demain dont notre monde a besoin.
- Devenir surement des citoyens mieux armés pour comprendre et appréhender notre monde complexe.
- Etre le vecteur de ces connaissances auprès de leur famille et de leurs amis.

Une question majeure se pose pourtant : **comment assurer la pérennité d'un tel dispositif ?**

Cette question est loin d'être élucidée. Pour l'instant, la coordination du projet par J.L Bérenguer n'est reconnue que par une décharge de quelques heures d'enseignement (et même ces heures ont été dures à obtenir). Le poste clé de Jessica Leputh, ingénieur, qui installe, maintient les stations dans les collèges, récupère les flux de données chaque soir pour les transmettre à une base de données est un poste en CDD, que nous cherchons chaque année à financer. Les données sont mises à disposition du site web grâce à un ingénieur du CRDP (Centre de recherches documentaires et pédagogiques) de Nice, mais nous ne savons pas jusqu'à quand. Enfin les chercheurs du CNRS ou de l'université qui participent au projet, le font en plus de leurs autres activités. Ceci est heureusement possible pour eux mais ils ne peuvent en aucun cas remplacer un enseignant à la tête du réseau. Il est donc indispensable de trouver une solution pour pérenniser un poste d'enseignant sur ces projets.

Je finirai en soulignant que les réseaux « Seismo at school » fleurissent en Europe et dans le monde. La *Newsletter* de décembre 2009 du CSEM (Centre Sismologique Euro Mediterranéen) le montre bien [*Bérenguer et al.*, 2009] ainsi que l'existence de « workpackage » dédiés aux réseaux éducatifs dans les récents projets (projet NERA soumis). Pour le moment la France est le leader européen dans ce domaine, mais jusqu'à quand ?

FEELING THE EARTH SHAKE... AT SCHOOL
EDUSISMO: THE FRENCH EDUCATIONAL SEISMOLOGICAL NETWORK

See authors list at the end of the article

Promotion of responsible behaviour of educated citizens is indispensable in response to the rapid evolution of our society, where scientific information must be correctly understood by the general public. One of the missions of the school, in this case through the teaching of geosciences, is to enable the students to better grasp sciences that were once confined to scientific laboratories. The educational programme "SISMOS à l'École" is a project that focuses on education on seismic risk through a scientific and technological approach. One could hope that this programme will lead the students towards scientific careers.

The programme « SISMOS à l'École » must be considered within the framework of teaching sciences and technologies at school and is a tool to better inform and sensitize the school community to natural risks.

A pilot experiment initiated in the French Riviera region

The innovative idea of the pilot experiment was to study the feasibility and the pedagogical interest of installing a seismometer in a school.

The project was implemented / tried out over a period of ten years (1996-2006) in the south of France. It involved a close partnership between the Conseil Général 06, the rectorat of the Nice district and the GeosciencesAzur research lab. After a two-year period of testing various materials at a pilot site (the Centre International de Valbonne), results from the deployment of five stations showed that it was possible to record high quality signals within a school (Fig. 1).



Fig. 1 : La Terre mise sur écoute... sismique au centre international de Valbonne.

Figure 1 - Feeling the Earth shake ... at school.

The main goal of this pedagogical programme was to make available for the school community an instrument measuring an environmental parameter and the related data.

Teachers took away a number of positive points from this experience : the students were enthusiastic to take measurements, the online database was easy to use, the experience encouraged the development of autonomy, the students took responsibility for the management of the seismic station, and the experience demonstrated the importance of regular contact with a reference scientist.

A seismological network with an educational purpose

The initial experiment has expanded. Since the beginning of the 2006 academic year the programme 'SISMOS à l'École', which is part of the broader project 'Sciences à l'Ecole', has extended the educational seismological network throughout the country.

Following a call to candidature, approximately thirty schools were selected according to the quality of their pedagogical projects in order to build this network (Fig. 2). In each school, a multidisciplinary team of teachers supported by a scientist is carrying out its project centred on a seismic station designed and realized for the school.

Seismological stations directly accessible online by everyone

Current seismicity and the associated signals recorded by the stations are registered online on a website dedicated to this school project. How is this database built?

Each seismological station records in continuous mode the ground motion with a sampling frequency of 50 Hz. Broad band seismometers ensure a high sensitivity and a good reproduction of a large frequency band, which enables to visualize correctly local and teleseismic earthquakes.

A GPS unit allows the data to be synchronized with universal time. As the data are viewable online, students can monitor ground motion in real time.

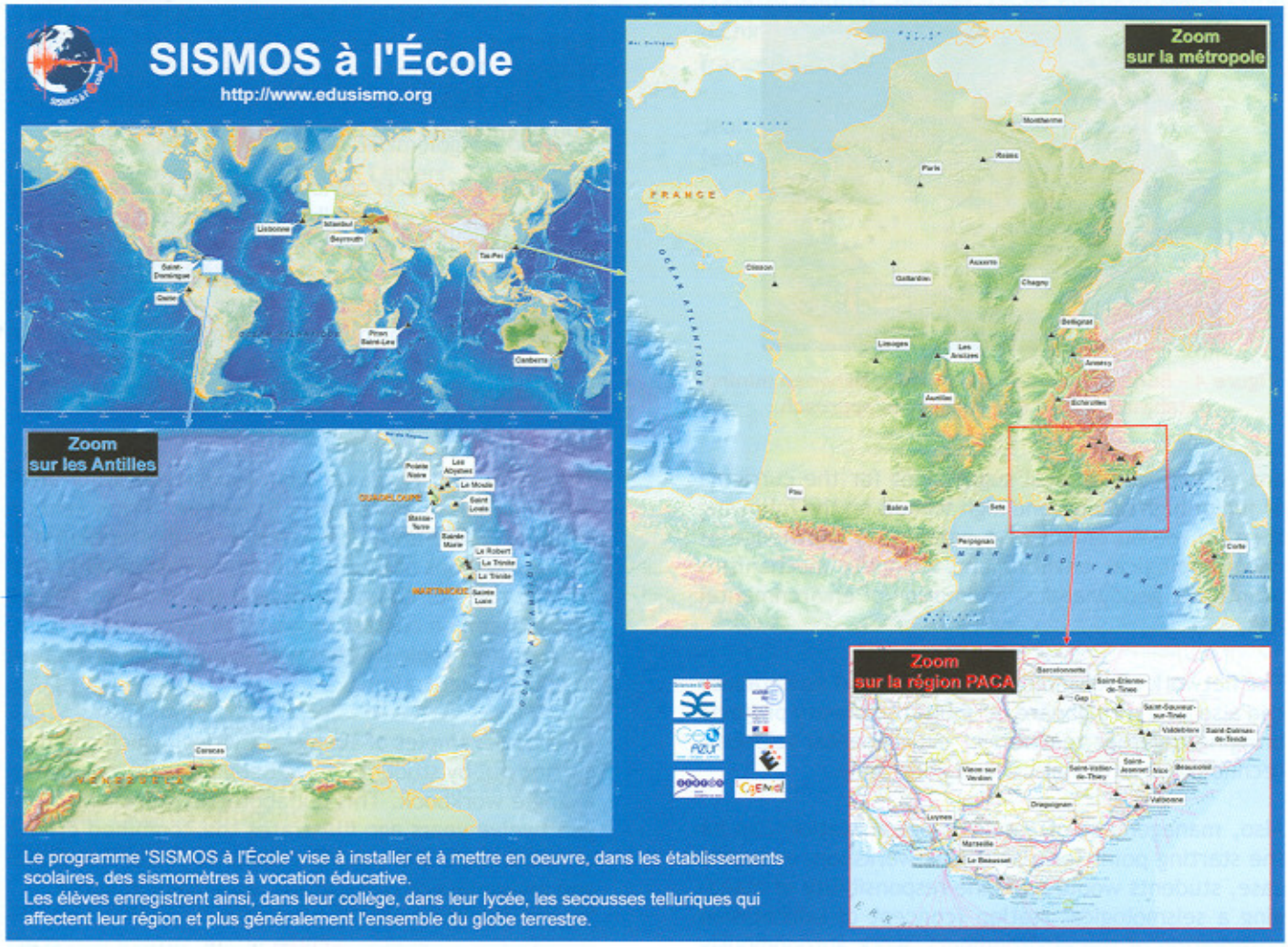


Figure 2 - A map of the "EduSismo" network (seismometers in schools).

They can identify the arrival of earth tremors and other vibrations, natural or generated by human activities (swell, quarry explosions).

Stations are queried daily to extract recordings related to seismic events.
In this way, a national server retrieves and archives seismic events identified by the seismological observatories and corresponding signals received from the stations. Selected events are at times earthquakes close to the station and at other times distant high-magnitude earthquakes. Signals from these events are then fed to an online database constituting a genuine seismic resource and a starting point for educational scientific activities (Fig. 3).

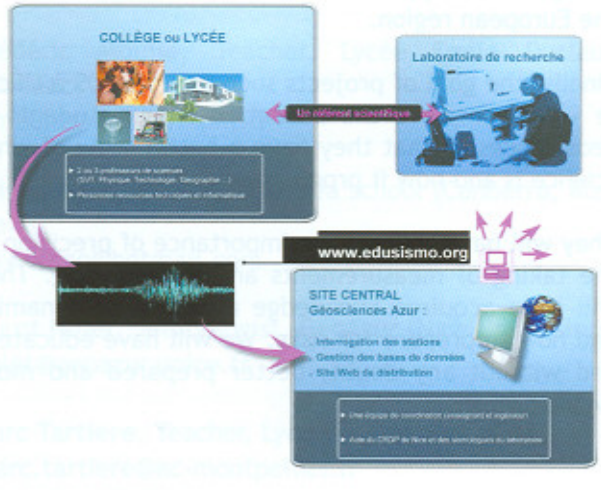


Figure 3 - The stations installed in the schools transmit their data to a central server.

The recorded data can be accessed by the entire educational community on a website.

Using a seismometer in the school

The school curriculum has several important aspects (placing large emphasis on new communication technologies): scientific content (instrumentation, geophysics, Earth sciences), educational dimension (sensitization to seismic risk), regional, national and international dimension (networking several schools). The team of teachers can follow various pedagogical suggestions.

What are the students doing? Observe, measure in order to understand better, compute and discover new parameters... then understand to act more appropriately (Fig. 4).
Within the framework of courses in Earth and Life Sciences, Physics, Technology and Geography, there



Figure 4 - Building scientific know-how, between mining databases and an investigational approach.

are various pedagogical suggestions for the curricula of junior high schools and high schools on the following themes: measurement of a parameter, knowledge of one's geological environment, complex mechanisms of internal geodynamics, and notion of environmental risk.

The network of seismological stations and its database can also be a springboard for multidisciplinary projects bringing together teachers of experimental sciences, technology, mathematicss and geography.

Also, management of a seismological station can be the starting point for a scientific workshop. In such a case, students would have the responsibility of managing a seismological station (concept of educational observation of the environment), work autonomously in teams and develop their skills in the **'Technologies of Information and Communication' (TIC)**.

In all these situations, transversal approaches are encouraged : measurement, observation, building of models, and investigative thinking to grasp scientific concepts related to geosciences and physics. This building of scientific know-how is essential to the education on environmental risk. Best practices all around the network have been shared by teachers of various schools and the following pedagogical suggestions attest to the richness of such sharing.

The «sensors» topic is an essential point. Measurements through a sensor (for example, measurement of ground motion in relation to universal time) could be explored, using sensors from the seismological station or sensors developed by students.
Various aspects of basic science are tackled, including frequency, bandwidth, fidelity, repeatability, and the robustness related to the often linear oscillator behind the sensor.

The «data» topic arises naturally. The analysis of recorded signals leads to various activities, including work on waves, a key notion in our society as radio, TV, and internet use them intensively. Travel times, wave speed, and localization through triangulation are typical concepts a student can easily master without getting into sophisticated mathematical tools.

The «tectonic» topic is also rich in possible activities. Numerous models have been proposed and realized by students. These practical exercises introduce abstract concepts, including seismic cycle, stress build-up, friction phenomena and energy release among others.

The «Earth» topic is obviously central to the teaching of natural sciences. Possible activities include geographical mapping through the presentation of data collected from various schools, the discussion of seismic hazard either on a global scale or a local scale, and the presentation of different seismic signatures such as Benioff planes or Moho discontinuity. These activities demonstrate how we discover the internal structure of the Earth.

The «risk» and «hazard» topics come naturally after these various speculations or analyses. From seismic records, students can illustrate through practical models the notions of intensity, building resonance, paraseismic rules of construction and the induced effects of a tsunami on coastal zones. With many national initiatives, this topic will become increasingly important in educational training.

All these examples of simple activities, which could be carried out by students, have been brought together in a single workbook. This collaborative work which began twelve years ago illustrates the combined efforts of researchers and teachers towards better education and awareness of risk culture, especially in youth.

«O3E»: towards a Euro-Mediterranean project

Students are encouraged to create contacts between schools while teachers share pedagogical ideas. The life of the network is based on exchanges between students, teachers and researchers. These networks now reach beyond France itself. The extension of the project into the Euro-Mediterranean region is underway. The "O3E" project (Observation of the Environment for an Educational purpose at School) unites the various experiments and skills of French, Italian, and Swiss Alps participants. It is a strong sign of the desire to expand this approach of education on natural risk in the European region.

Finally, the goal of projects such as « SISMOS à l'École » is to improve the education of our students in geosciences so that they have a better view of what science is and how it progresses.

They will have learned the importance of precision in the taking of measurements and in reasoning. They will have acquired knowledge about Earth dynamics and how to prepare for risks. We will have educated, and without any doubt, better prepared and more aware citizens.

Other readings...

J.-L. Berenguer, F. Pascucci, H. Ferry (2006) - Le cahier d'activités du SISMO, Scéren Nice, Septembre 2006.

J. Virieux (2000) - Educational Seismological project: EDUSEIS, Seismological Research Letters, 71, 530-535

«Sismos à l'Ecole», EduSismo network website: http://www.edusismo.org

«O3E», European Interreg project: O3E.geoazur.eu

"Eduseis", towards an european project: http://www.eduseis.net

Authors

Jean-Luc Berenguer, Centre international de Valbonne (Sophia Antipolis)
Jean-Luc.Berenguer@ac-nice.fr

Françoise Courboulex, CNRS Seismologist, GéoAzur (Sophia Antipolis)
courboulex@geoazur.unice.fr

Jessica Le Puth, Ingénieur d'études Laboratoire GéoAzur (Sophia Antipolis)
leputh@geoazur.unice.fr

Barbara Zodmi, Sciences à l'Ecole, Observatoire de Paris
barbara.zodmi@obspm.fr

Pascal **Bernard**, Seismologist, IPG (Paris)
bernard@ipgp.jussieu.fr

Christophe **Larroque**, Geologist, Champagne Ardennes University
christophe.larroque@univ-reims.fr

Luis **Matias**, Seismologist, Centro Geofisica (Universidade Lisboa)
lmmatias@fc.ul.pt

Frédéric **Moulié**, Teacher, Lycée Emile Duclaux (Aurillac)
jfmoulie@ac-clermont.fr

Olivier **Ngo**, Teacher, Teleopea school (Canberra, Australia)
olivierngo@hotmail.com

Guust **Nolet**, Seismologist, GéoAzur (Nice University)
nolet@geoazur.unice.fr

Marc **Tartiere**, Teacher, Lycée Paul Valery (Sète)
marc.tartiere@ac-montpellier.fr

François **Tilquin**, Teacher, Lycée Pierre et Marie Curie (Echirolles)
francois.tilquin@ac-grenoble.fr

Jean Virieux, **Seismologist**, LGIT (Grenoble)
jean.virieux@obs.ujf-grenoble.fr

ELEMENTS DE PERSPECTIVE

a. La simulation des mouvements du sol

La question principale qui se pose est la suivante : Peut-on simuler à l'avance les mouvements du sol qui seront engendrés par un séisme en réduisant les incertitudes inhérentes aux équations empiriques de prédiction des mouvements du sol ?
Pour y répondre, il est nécessaire de tenter de quantifier l'influence des différents paramètres sur le mouvement du sol. Je suis en particulier intéressée par l'influence des différents paramètres de la source sismique sur les mouvements du sol enregistrés en surface et sur les dégâts engendrés. Les paramètres de la source sont nombreux : moment sismique, vitesse de rupture, dimension de la rupture, directivité, effet du champ proche … ils peuvent aussi être simplifiés en regardant un paramètre clé : la chute de contrainte. Ce paramètre ne permet pas de prendre en compte tous ces effets (en particulier l'effet de directivité ou d'une propagation 'supershear'), mais il semble avoir un rôle prépondérant au moins sur la partie haute fréquence des enregistrements. Je souhaite travailler sur la variabilité possible de ce paramètre en fonction des contextes. Ce travail sera certainement lié à un travail sur les failles au sein de la future équipe « failles et séismes » de Géoazur.

Une question pratique importante est aussi d'estimer le degré de raffinement des modèles nécessaire pour obtenir une prédiction utile.
Pour cela il est nécessaire de tester si la variabilité de nos méthodes est suffisante pour simuler la variabilité observée dans les enregistrements réels, mais aussi de comparer nos résultats avec ceux d'autres méthodes plus lourdes à mettre en œuvre, mais où chaque paramètre peut être pris en compte individuellement.
Enfin, nous devons réfléchir sur la prise en compte des effets non linéaires, qui ont pour le moment été peu pris en compte dans mon travail.

Nous aborderons ces questions par l'approche combinée de l'observation et de la modélisation. Des simulations ont été réalisées par Laetitia Honoré dans le cadre de sa thèse pour produire des sismogrammes réalistes pour les séismes historique de 1660 à Lourdes à partir de séismes instrumentaux récents [Honoré et al., 2009]. Laetitia n'ayant pas fini sa thèse ni publié ce travail, je préfère n'inclure aucune figure sur ces résultats. Un nouvel apport de son travail est également de travailler sur les intensités macrosismiques et tenter de les comparer aux simulations. Elle travaille également sur le séisme de l'Aquila [Honoré and Courboulex, 2009]. Une collaboration avec David Baumont de l'IRSN et une équipe de l'INGV (Institut National de Géodésie et de Volcanologie) de Rome a d'ailleurs été initiée pour comparer ses résultats à ceux d'autres méthodes en champ proche.

Des simulations de séismes importants vont également être réalisées sur le tout nouveau réseau accélérométrique de Quito en Equateur dans le cadre du projet ADN (projet Andes du Nord financé par l'ANR). Un étudiant en Master 2 va d'ailleurs venir de Quito pour travailler avec nous sur ce sujet. Le travail entrepris avec Céline Beauval (LGIT, Grenoble) sur la mise au point d'une méthode probabiliste-déterministe sera également testé sur ces données.

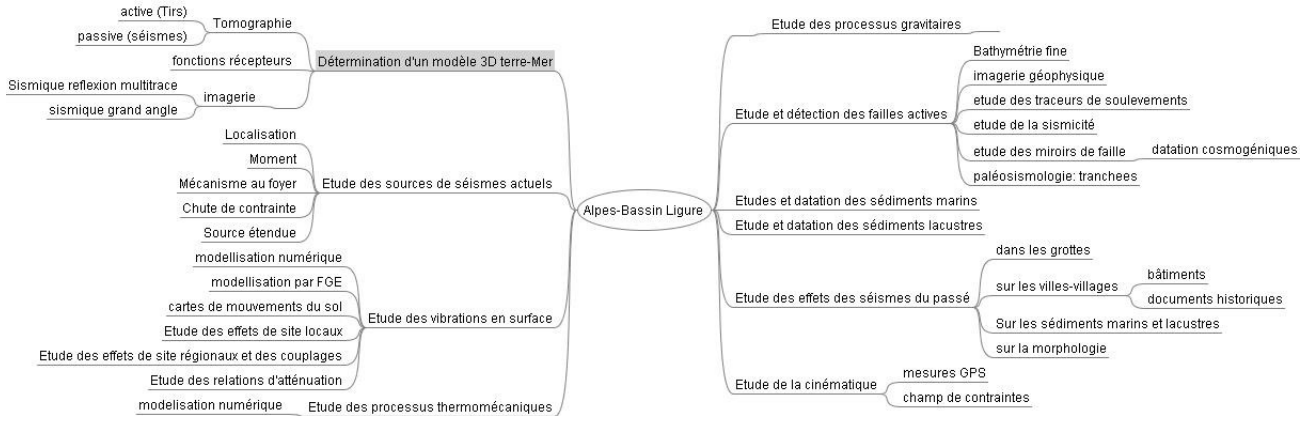
b. L'effet des ondes sismiques sur les déstabilisations de pentes en mer

Le milieu marin est un domaine que je connais peu. J'ai été amenée à initier une collaboration avec Didier Leynaud (IFREMER puis Université de Bordeaux) pour tenter de générer des accélérogrammes de séismes majeurs sur la pente de l'aéroport de Nice, ceci afin de tester son éventuelle déstabilisation lors de séismes.
Dans ce domaine, l'approche dynamique est importante car elle permet de prendre en compte la combinaison complexe de l'accélération, du contenu fréquentiel du signal et de sa durée totale (nombre de cycles). Seuls les séismes de forte magnitude produisent des cycles basse fréquence qui peuvent avoir un effet critique sur les sédiments ; ainsi, en l'absence d'enregistrement d'événements réels de forte magnitude, il est indispensable de pouvoir modéliser de telles accélérations.

Nous projetons de réaliser ces simulations à partir de données enregistrées sur des OBS disposés sur la pente de l'aéroport de Nice (projet MODALE soumis à l'ANR). Ce travail me permettra de tisser des liens plus étroits avec les chercheurs qui travaillent sur les glissements de terrain.

c. Le chantier Alpes-Bassin Ligure

Depuis deux ans, je suis co-animatrice de la thématique « chantier Alpes-Méditerranée » pour l'UMR en collaboration avec Françoise Sage et Yann Rolland. Notre rôle était de coordonner les actions sur ce vaste chantier et de stimuler des collaborations inter-équipes. Nous avons cherché à construire une base de documents accessibles sur le site intranet du laboratoire : publications, présentations orales, figures. Cette première étape est presque terminée. Des grands projets ont été menés comme la campagne GROSMARIN dont le but est de mieux connaitre le modèle de vitesse dans la région. Par contre, nous n'avons pas réussi jusqu'à présent à fédérer nos actions en proposant un projet pluridisciplinaire sur cette zone. Le schéma ci-dessous recense la plupart des champs d'action des membres de l'UMR concernant la déformation active et l'aléa sismique.



Perspectives, Figure 1 : Aléa sismique et chantier régional. Actions de l'UMR (organigramme non exhaustif)

Un tel projet ne verra le jour bien sur qu'avec des collaborations de chercheurs d'autres laboratoires ainsi que de nos collègues du CETE Méditerranée de Nice.

d. Autres sujets

Séismes lents et trémors. Des progrès considérables ont été réalisés ces dernières années dans les inversions de source sismique, en particulier en incluant des données de surface (géodésie , imagerie ou traces géologiques) mais aussi des données de plus en plus nombreuses d'accéléromètres proches des failles. Au sein du laboratoire, Martin Vallée et Bertrand Delouis s'occupent de près de ces aspects d'inversion multiparamètres de la source en interaction avec Mohamed Chlieh et Jean-Mathieu Nocquet pour la géodésie spatiale. Bien que les inversions de la source co et post-sismique soient de plus en plus précises, c'est bien la découverte des séismes lents qui a été la révolution de ces dernières années. Ils ont été détectés dans quelques zones de subduction (Cascades, Mexique, Japon) mais sont à présent observables à différents endroits du monde. Je suis pour le moment avec grand intérêt ce qui se passe dans ce domaine, et ne serais pas opposée à m'y investir si l'occasion se présentait.

Vulnérabilité des bâtiments. Le lien entre les mouvements du sol et la vulnérabilité des bâtiments me semble une étape incontournable si l'on cherche à étudier le risque sismique [*Gueguen*, 2009]. La possibilité d'utiliser les simulations de mouvements forts à partir de petits événements pourrait permettre de tester des structures dans des zones où les accélérogrammes réels n'existent pas … et, pourquoi pas, travailler également sur des accélérogrammes enregistrés directement dans les structures.

e. La divulgation scientifique

Mes ambitions dans ce domaine sont d'œuvrer pour :

- La pérennisation du réseau Sismos à l'Ecole, et l'extension de ce réseau à des établissements de quartiers défavorisés ;
- L'implication plus grande des référents scientifiques dans ce réseau ;
- La reconnaissance de ce réseau comme un réseau sismologique français qui peut être utilisé à la fois pour l'enseignement et la pour la recherche. Cette reconnaissance passera je l'espère par le programme RESSIF d'EPOS ;
- L'existence d'une cellule 'Education and Outreach' (proposée dans le prochain quadriennal par Jean-Luc Berenguer) au sein de Géoazur dans l'observatoire de la côte d'Azur.

BIBLIOGRAPHIE CITEE DANS LE TEXTE (HORS ARTICLES)

Aki, K., and P. G. Richards (Eds.) (1980), *Quantitative Seismology*, WH Freeman and Co.
, San Francisco, California.

Allmann, B. P., and P. M. Shearer (2009), Global variations of stress drop for moderate to large earthquakes, *J. Geophys. Res.*, *114*.

Ammon, C. J., A. A. Velasco, and T. Lay (1993), Rapid estimation of rupture directivity : application to the 1992 Landers (MS = 7.4) and Cape Mendocino (MS = 7.2), California earthquakes., *Geophys. Res. Lett.*, *20*.

Baumont, D., F. Courboulex, O. Scotti, N. S. Melis, and G. Stavrakakis (2002), Slip distribution of the Mw 5.9, 1999 Athens earthquake inverted from regional seismological data, *Geophys. Res. Lett.*, *29*.

Bengoubou-Valerius, M., S. Bazin, D. Bertil, F. Beauducel, and A. Bosson (2008), CDSA: a new seismological data center for the French Lesser Antilles, *Seismol. Res. Lett.*, *79*, 90-115.

Bérenguer, J. L., et al. (2009), Feeling the Earth Shake ... at school. EDUSISMO : the french educational Seismological Network., *CSEM/EMSC Newsletter*, *Dec 2009*.

Bernard, P., and R. Madariaga (1984), A new asymptotic method for the modeling of near-field accelerograms, *Bulletin of the Seismological Society of America*, *74*(2), 539-557.

Bertero, M., D. Bindi, P. Boccacci, M. Cattaneo, C. Eva, and V. Lanza (1997), Application of the projected Landweber method to the estimation of the source time function in seismology, *Inverse Problems*(2), 465.

Béthoux, N., J. Fréchet, F. Guyoton, F. Thouvenot, M. Cattaneo, C. Eva, M. Nicolas, and M. Granet (1992), A closing Ligurian Sea?, *Pure and Applied Geophysics*, *139*(2), 179-194.

Blundell, D., R. Freeman, and S. Mueller (1992), *A continent revealed : the European Geotraverse.*, 272 pp., Cambridge University Press.

Boatwright, J. (2007), The Persistence of Directivity in Small Earthquakes, *Bulletin of the Seismological Society of America*, *97*(6), 1850-1861.

Bonilla, F. (2007), Analyse des effets de site, estimation des mouvements forts et calcul probabiliste de l'aléa sismique, HDR thesis, 47 pp, Université Joseph Fourier, Grenoble.

Bouchon, M. (1973), Effect of topography on surface motion, *Bulletin of the Seismological Society of America*, *63*(2), 615-632.

Bour, M. (1993), Simulation de forts mouvements du sol à partir de petits séismes utilisés comme fonctions de Green empiriques, PhD thesis, 173 pp, Université de Strasbourg 1, France.

Bour, M., and M. Cara (1997), Test of a simple empirical Green's function method on moderate-sized earthquakes, *Bulletin of the Seismological Society of America*, *87*(3), 668-683.

Causse, M., F. Cotton, C. Cornou, and P. Y. Bard (2008), Calibrating Median and Uncertainty Estimates for a Practical Use of Empirical Green's Functions Technique, *Bulletin of the Seismological Society of America*, *98*(1), 344-353.

Chiaraluce, L., et al. (2004), Complex Normal Faulting in the Apennines Thrust-and-Fold Belt: The 1997 Seismic Sequence in Central Italy, *Bulletin of the Seismological Society of America*, *94*(1), 99-116.

Cocco, M., J. Pacheco, S. K. Singh, and F. Courboulex (1997), The Zihuatanejo, Mexico, earthquake of 1994 December 10 (M= 6.6): source characteristics and tectonic implications, *Geophysical Journal International*, *131*(1), 135-145.

Converset, J. (2007), Simulation du choc principal de la crise des Saintes (Mw 6.4, Guadeloupe, 2004), Master 2 thesis, 36 pp, Université de Nice Sophia Antipolis.

Corsini, M., G. Ruffet, and R. Caby (2004), Alpine and late-hercynian geochronological constraints in the Argentera Massif (Western Alps), *Eclogae Geologicae Helvetiae*, *97*(1), 3-15.

Cotton, F., G. Pousse, F. Bonilla, and F. Scherbaum (2008), On the Discrepancy of Recent European Ground-Motion Observations and Predictions from Empirical Models: Analysis of KiK-net Accelerometric Data and Point-Sources Stochastic Simulations, *Bulletin of the Seismological Society of America*, *98*(5), 2244-2261.

Courboulex, F., J. Virieux, and D. Gibert (1996a), On the use of simulated annealing method and cross-validation theory for deconvolution of seismograms, *Bulletin of the Seismological Society of America*, *86*(4), 1187-1193.

Courboulex, F., S. K. Singh, and J. Pacheco (1999), Ruoture sous l'altiplano, *La recherche*, *324*, 28-30.

Courboulex, F., S. K. Singh, J.-F. Pacheco, and C. J. Ammon (1996b), The 1995 Colima-Jalisco, Mexico, Earthquake (Mw 8): A Study of the Rupture Process, *Geophys. Res. Lett.*, *24*.

Courboulex, F., M. A. Santoyo, J. F. Pacheco, and S. K. Singh (1997), The 14 September 1995 (M = 7.3) Copala, Mexico, earthquake: A source study using teleseismic, regional, and local data, *Bulletin of the Seismological Society of America*, *87*(4), 999-1010.

Courboulex, F., J. Virieux, A. Deschamps, D. Gibert, and A. Zollo (1996c), Source investigation of a small event using empirical Green's functions and simulated annealing, *Geophysical Journal International*, *125*(3), 768-780.

Courboulex, F., A. M. Duval, A. Deschamps, A. Lomax, and C. Larroque (2001), Les enseignements du petit séisme de Peille (Alpes-Maritimes, France), *C. R. Acad. Sci.*, *333*, 105-112.

Courboulex, F., C. Larroque, A. Deschamps, C. Gélis, J. Charreau, and J. F. Stéphan (2003), An unknown active fault revealed by microseismicity in the south-east of France, *Geophys. Res. Lett.*, *30*.

Courboulex, F., A. Deschamps, M. Cattaneo, F. Costi, J. Déverchère, J. Virieux, P. Augliera, V. Lanza, and D. Spallarossa (1998), Source study and tectonic implications of the 1995 Ventimiglia (border of Italy and France) earthquake (ML=4.7), *Tectonophysics*, *290*(3-4), 245-257.

Deichmann, N. (1999), Empirical Green's functions: A comparison between pulse width measurements and deconvolution by spectral division, *Bulletin of the Seismological Society of America*, *89*(1), 178-189.

Dercourt, J., et al. (1986), Geological evolution of the Tethys belt from Atlantic to Pamirs since the Lias, *Tectonophysics*, *123*, 241-315.

Deschamps, A., et al. (2000), Spatio-temporal distribution of seismic activity during the Umbria-Marche crisis, 1997, *Journal of Seismology*, *4*(4), 377-386.

Douglas, J. (2003), Earthquake ground motion estimation using strong-motion records: a review of equations for the estimation of peak ground acceleration and response spectral ordinates, *Earth-Science Reviews*, *61*(1-2), 43-104.

Dreger, D. S. (1985), Empirical Green's function study of the January 17, 1994 Northridge, California earthquake, *Geophys. Res. Lett.*, *21*.

Drouet, S., A. Souriau, and F. Cotton (2005), Attenuation, Seismic Moments, and Site Effects for Weak-Motion Events: Application to the Pyrenees, *Bulletin of the Seismological Society of America*, *95*(5), 1731-1748.

Duval, A. M. (1994), Détermination de la réponse d'un site aux séismes à l'aide du bruit de fond : évaluation expérimentale., 265 pp, Université Pierre et Marie Curie.

Duval, A. M. (2007), Des effets de site aux scénarios de crise sismique: méthodes et applications, 176 pp, Université des Sciences et Technologies de Lille.

Fréchet, J. (1985), Sismogenese et doublets sismiques, Thèse d'état thesis, Univ. Sci. et Méd. de Grenoble.

Frez, J., F. A. Nava, and J. Acosta (2010), Source Rupture Plane Determination from Directivity Doppler Effect for Small Earthquakes Recorded by Local Networks, *Bulletin of the Seismological Society of America*, *100*(1), 289-297.

Fukuyama, E., and K. Irikura (1986), Rupture process of the 1983 Japan Sea (Akita-Oki) earthquake using a waveform inversion method, *Bulletin of the Seismological Society of America*, *76*(6), 1623-1640.

Fukuyama, E., W. L. Ellsworth, F. Waldhauser, and A. Kubo (2003), Detailed Fault Structure of the 2000 Western Tottori, Japan, Earthquake Sequence, *Bulletin of the Seismological Society of America*, *93*(4), 1468-1478.

Gaffet, S. (1995), Teleseismic waveform modeling including geometrical effects of superficial geological structures near to seismic sources, *Bulletin of the Seismological Society of America*, *85*(4), 1068-1079.

Gaffet, S., et al. (2000), A site effect study in the Verchiano valley during the 1997 Umbria-Marche (Central Italy) earthquakes, *Journal of Seismology*, *4*(4), 525-541.

Gélis, C. (2002), La crise sismique de Blausasc dans les Alpes Maritimes (2000) : Localisations absolue et relative, DEA thesis, Université de Nice-Sophia Antipolis.

Got, J. L., J. Fréchet, and F. W. Klein (1994), Deep fault plane geometry inferred from multiplet relative relocation beneath the south flank of Kilauea, *J. Geophys. Res.*, *99*.

Gueguen, P. (2009), Sismologie Urbaine: Aléa local, dynamique des structures, interaction site-ville et vulnérabilité urbaine, HDR thesis, 181 pp, Université Joseph-Fourier - Grenoble I.

Hartzell, S. (1989), Comparison of Seismic Waveform Inversion Results for the Rupture History of a Finite Fault: Application to the 1986 North Palm Springs, California, Earthquake, *J. Geophys. Res.*, *94*.

Hartzell, S. H. (1978), Earthquake Aftershocks as Green's Functions, *Geophys. Res. Lett.*, *5*.

Haskov, J., and L. Ottemöller (1999), SEISAN earthquake analysis software, *Seismol. Res. Lett.*, *70*, 532–534.

Helmberger, D., and R. A. Wiggins (1971), Upper Mantle Structure of Midwestern United States, *J. Geophys. Res.*, *76*.

Hernandez, B., M. Cocco, F. Cotton, S. Stramondo, O. Scotti, F. Courboulex, and M. Campillo (2004), Rupture history of the 1997 Umbria-Marche (Central Italy) main shocks from the inversion of GPS, DInSAR and near field strong motion data, *Annals of Geophysics*(47 (4)).

Honoré, L. (2008), Mise au point d'une méthodologie hybride d'évaluation de l'aléa sismique. Test sur la crise des Saintes (Guadeloupe, 2004-2005), Master 2 thesis, 35 pp, Université de Nice Sophia Antipolis.

Honoré, L., and F. Courboulex (2009), Ground-motion simulations of the L'Aquila earthquake Mw6.3 (April 6th, 2009) using aftershocks as empirical Green's functions, in *American Geophysical Union*, edited, San Francisco.

Honoré, L., F. Courboulex, and A. Souriau (2009), A major historical earthquake in the French Pyrenees revisited using actual moderate size earthquakes, in *American Geophysical Union*, edited, San Francisco.

Hough, S. E. (2001), Empirical Green's Function Analysis of Recent Moderate Events in California, *Bulletin of the Seismological Society of America*, *91*(3), 456-467.

Hutchings, L. (1991), "Prediction" of strong ground motion for the 1989 Loma Prieta earthquake using empirical Green's functions, *Bulletin of the Seismological Society of America*, *81*(5), 1813-1837.

Ihmlé, P. F. (1996), Frequency-dependent relocation of the 1992 Nicaragua slow earthquake: an empirical Green's function approach, *Geophysical Journal International*, *127*(1), 75-85.

Irikura, K. (1983), semi empirical estimation of strong ground motions during large earthqaukes, *Bull. Disas. Prev. Res. Inst.*, *33*, 66-104.

Irikura, K. (1986), Prediction of strong acceleration motion using empirical Green's functions, paper presented at 7th Japan Earthq. Eng. Symp., Tokyo.

Joyner, W. B., and D. M. Boore (1986), On simulating large earthquakes by Green's-function addition of smaller earthquakes, *Earthquake Source Mechanics, American Geophysical Union Monograph*, *37*, 269--274.

Kanamori, H., and L. Rivera (2004), Static and Dynamic Scaling Relations for Earthquakes and Their Implications for Rupture Speed and Stress Drop, *Bulletin of the Seismological Society of America*, *94*(1), 314-319.

Klein, F. W. (Ed.) (1978), *Hypocenter location program HYPOINVERSE*, US Geol. Surv. Open-File Rep. 78.

Kohrs-Sansorny, C. (2005), Modélisation de la source sismique et sommation de petits séismes pour l'évaluation des mouvements forts : application à une meilleure estimation de l'aléa sismique dans le sud est de la France, 182 pp, Université de Nice Sophia Antipolis.

Larroque, C. (2009), Aléa sismique dans une région intraplaque à sismicité modérée : la jonction Alpes - Bassin Ligure, HDR thesis, Université de Nice Sophia Antipolis.

Larroque, C., B. Delouis, B. Godel, and J.-M. Nocquet (2008), Active deformation at the southwestern Alps – Ligurian basin junction (France-Italy boundary) : Evidence for recent change from compression to extension in the Argentera massif., *Tectonophysics*.

Laurent, O., J. F. Stéphan, and M. Popoff (2000), Modalités de la structuration miocène de la branche sud de l'arc de Castellane (chaînes subalpines méridionales), *Géologie de la France*, *3*, 33-65.

Laurenti, A. (1998), *Les tremblements de terre des Alpes Maritimes, histoire et sensibilisation*.

Laurenti, A. (2006), *Les Alpes Maritimes à l'écoute des séismes*, 130 pp.

Lienert, B. R., E. Berg, and L. N. Frazer (1986), HYPOCENTER: An earthquake location method using centered, scaled, and adaptively damped least squares, *Bulletin of the Seismological Society of America*, *76*(3), 771-783.

Lomax, A., J. Virieux, P. Volant, and C. Berge (Eds.) (2000), *Probabilistic earthquake location in 3D and layered models: Introduction of a Metropolis-Gibbs method and comparison with linear locations*, Kluwer, Acad.

Mendoza, C., and S. Hartzell (2009), Source analysis using regional empirical Green's functions: The 2008 Wells, Nevada, earthquake, *Geophys. Res. Lett.*, *36*.

Michelini, A., and A. Lomax (2004), The effect of velocity structure errors on double-difference earthquake location, *Geophys. Res. Lett.*, *31*.

Mori, J. (1993), Fault Plane Determination of Three small earthquakes along the San Jacinto fault, California : Search fro cross faults, *J. Geophys. Res.*, *98*, 711-723.

Mori, J. (1996), Rupture directivity and slip distribution of the M 4.3 foreshock to the 1992 Joshua Tree earthquake, Southern California, *Bulletin of the Seismological Society of America*, *86*(3), 805-810.

Mueller, C. S. (1985), Source Pulse Enhancement by Deconvolution of an Empirical Green's Function, *Geophys. Res. Lett.*, *12*.

Nozu, A., and K. Irikura (2008), Strong-Motion Generation Areas of a Great Subduction-Zone Earthquake: Waveform Inversion with Empirical Green's Functions for the 2003 Tokachi-oki Earthquake, *Bulletin of the Seismological Society of America*, *98*(1), 180-197.

Ordaz, M., J. Arboleda, and S. K. Singh (1995), A scheme of random summation of an empirical Green's function to estimate ground motions from future large earthquakes, *Bulletin of the Seismological Society of America*, *85*(6), 1635-1647.

Pavic, R., M. G. Koller, P. Y. Bard, and C. Lacave-Lachet (2000), Ground motion prediction with the empirical Green's function technique: an assessment of uncertainties and confidence level, *Journal of Seismology*, *4*(1), 59-77.

Pillet, R., and J. Virieux (2007), The effects of seismic rotations on inertial sensors, *Geophysical Journal International*, *171*(3), 1314-1323.

Rubin, A. M., D. Gillard, and J.-L. Got (1999), Streaks of microearthquakes along creeping faults, *Nature*, *400*(6745), 635-641.

Sanchez, G., Y. Rolland, D. Schreiber, G. Giannerini, M. Corsini, and J. M. Lardeaux (2010a), The active fault system of SW Alps, *Journal of Geodynamics*, *In Press, Corrected Proof*.

Sanchez, G., Y. Rolland, M. Corsini, R. Braucher, D. Bourlès, M. Arnold, and G. Aumaître (2010b), Relationships between tectonics, slope instability and climate change: Cosmic ray exposure dating of active faults, landslides and glacial surfaces in the SW Alps, *Geomorphology*, *In Press, Corrected Proof*.

Scherbaum, F., and M.-P. Bouin (1997), FIR filter effects and nucleation phases, *Geophysical Journal International*, *130*(3), 661-668.

Scotti, O., D. Baumont, G. Quenet, and A. Levret (2004), The French microseismic database SISFRANCE – objectives, results and perspectives., *Annals of Geophysics*, *47*, 571-581.

Scotti, O., C. Larroque, F. Courboulex, B. Delouis, and D. Baumont (2008), On the Definition of realistic Earthquake Parameters along potential active Faults in the French-Italian Riviera: a key step in Quantitative Seismic Hazard Assessment (QSHA) -a Platform for strong Ground Motion Modeling, in *European Geophysical Union General assembly*, edited.

Scotti, O., et al. (2007), Définition de scénarii sismiques pour la région de Nice, paper presented at VIIème Colloque National de l'AFPS, Ecole Centrale de Paris, Chatenay-Malabry, 4-6 Juillet 2007.

Spudich, P., and L. N. Frazer (1984), Use of ray theory to calculate high-frequency radiation from earthquake sources having spatially variable rupture velocity and stress drop, *Bulletin of the Seismological Society of America*, *74*(6), 2061-2082.

Tahayt, A., et al. (2009), The Al Hoceima (Morocco) earthquake of 24 February 2004, analysis and interpretation of data from ENVISAT ASAR and SPOT5 validated by ground-based observations, *Remote Sensing of Environment*, *113-2*, 306-316.

Tapley, W. C., and J. E. Tull (1992), *SAC—Seismic Analysis Code USER'S MANUAL*, Regents of the University of California, CA.

Thouvenot, F., A. Paul, J. Fréchet, N. Béthoux, L. Jenatton, and R. Guiguet (2007), Are there really superposed Mohos in the southwestern Alps? New seismic data from fan-profiling reflections, *Geophysical Journal International*, *170*(3), 1180-1194.

Thouvenot, F., et al. (1998), The Ml 5.3 Epagny (French Alps) earthquake of 1996 July 15: a long-awaited event on the Vuache Fault, *Geophysical Journal International*, *135*(3), 876-892.

Turino, C., D. Scafidi, E. Eva, and S. Solarino (2009), Inferences on active faults at the Southern Alps–Liguria basin junction from accurate analysis of low energy seismicity, *Tectonophysics*, 470-479.

Vallée, M. (2004), Stabilizing the Empirical Green Function Analysis: Development of the Projected Landweber Method, *Bulletin of the Seismological Society of America*, *94*(2), 394-409.

Vallée, M. (2007), Rupture Properties of the Giant Sumatra Earthquake Imaged by Empirical Green's Function Analysis, *Bulletin of the Seismological Society of America*, *97*(1A), S103-114.

Velasco, A. A., C. J. Ammon, and T. Lay (1994), Empirical green function deconvolution of broadband surface waves: Rupture directivity of the 1992 Landers, California (Mw = 7.3), earthquake, *Bulletin of the Seismological Society of America*, *84*(3), 735-750.

Virieux, J., B. P.Y., F. Courboulex, E. Foerster, B. Hernandez, and J. F. Semblat (2009), Rapport final programme CATTELL

Projet QSHA, Projet ANR-05-CATT-011-04*Rep.*, LGIT, Géoazur, BRGM, CEA, IRSN, CETE.

Waldhauser, F. (2009), Near-Real-Time Double-Difference Event Location Using Long-Term Seismic Archives, with Application to Northern California, *Bulletin of the Seismological Society of America*, *99*(5), 2736-2748.

Waldhauser, F., and W. L. Ellsworth (2000), A Double-Difference Earthquake Location Algorithm: Method and Application to the Northern Hayward Fault, California, *Bulletin of the Seismological Society of America*, *90*(6), 1353-1368.

Wang, E., and A. M. Rubin (2009), Rupture directivity of micro-earthquakes along the San Andreas fault in *American Geophysical Union*, edited, San Francisco.

Wennerberg, L. (1990), Stochastic summation of empirical Green's functions, *Bulletin of the Seismological Society of America*, *80*(6A), 1418-1432.

Zollo, A., and P. Bernard (1991), Fault mechanisms from near-source data: joint inversion of S polarizations and P polarities, *Geophysical Journal International*, *104*(3), 441-451.

ANNEXE

A.1 Publications

Publications dans des revues internationales avec comité de lecture. :

P1. Courboulex F., J. Virieux, A. Deschamps, D. Gibert, and A. Zollo (1996) : Source investigation of small events using empirical Green functions and Simulated Annealing. Geophys. J. Int, 125, 768-780.
P2. Courboulex F., J. Virieux, and D. Gibert (1996) : On the use of cross-validation theory and simulated annealing for deconvolution. Bull. seism. Soc. Amer., 86, 1187-1193.
P3. Courboulex, F., S.K. Singh, J. Pacheco, and C. Ammon (1997) : The October 9, 1995, Colima-Jalisco, Mexico, earthquake (Mw 8): A study of the rupture process, Geophys. Res. Lett., 24-9, 1019-1022.
P4. Courboulex, F., M.A. Santoyo, J. Pacheco, and S.K. Singh (1997) : Source inversion of the September 14, 1995 Guerrero Mexico earthquake. Bull. Seism. Soc. Amer., 87,999-1010.
P5. Singh, S.K., J. Pacheco, F. Courboulex, and D. Novelo (1997): Source parameters of the Pinotepa National, Mexico, earthquake of 27 March, 1996 (Mw=5.5) estimated from near-field recordings of a single station, Journal of Seismology, 1, 39-45.
P6. Cocco, M., J. Pacheco, S.K. Singh, and F. Courboulex (1997): The Zihuatanejo, Mexico earthquake of December 10, 1994 (M=6.6): Source characteristics and tectonic implications, Geophys. J. Int, 131, 135-145.
P7. Bernard, P., P. Briole, B. Meyer, H. Lyon-Caen, J.M. Gomez, C. Tiberi, C. Berge, D. Hatzfeld, C. Lachet, B. Lebrun, A. Deschamps, F. Courboulex, C. Larroque, A. Rigo, D. Massonet, D. Papadimitriou, J. Kassaras, D. Diagourtas, K. Makropoulos, G. Veis, E. Papazisi, C. Mitsakaki, V. Karakostas, E. Papadimitriou, D. Papanastassiou (1997): The MS=6.2, June 15, 1995, AIGION earthquake (Greece): Results of a multidisciplinary study, J. Seismol. , 1,131-150.
P8. Amato, A. ; Azzara, R. ; Chiarabba, C. ; Cimini, G. B. ; Cocco, M. ; Di Bona, M. ; Margheriti, L. ; Mazza, S. ; Mele, F. ; Selvaggi, G. ; Basili, A. ; Boschi, E. ; Courboulex, F. ; Deschamps, A. ; Gaffet, S. ; Bittarelli, G. ; Chiaraluce, L. ; Piccinini, D. ; Ripepe, M. (1998) The 1997 Umbria-Marche, Italy, earthquake sequence: A first look at the main shocks and aftershocks, Geophys. Res. Lett., 25, 2861-2864.
P9. Larroque, C., S. Gaffet, C. Cornou, E. Schissele, E. Bertrand, N. Bethoux, M. Bouchon, M. Corrazi, F. Courboulex , A. Deschamps, A.M. Duval, C. Mar on, J.P.Glot, F. Janod, R. Guiguet, S. Vidal, J. Virieux : A multi array experim ent in Annot for site effect analysis, 1999, *C.R. Acad. Sci.*, 329, 167-1 74.
P10. Courboulex F., A. Deschamps, M. Cattaneo, F. Costi, J. Deverchere, J. Virieux, P. Augliera, V. Lanza and D . Spallarossa (1998): Source study and tectonic implications of the April 21, 1995 Ventimiglia (border of Italy and France) earthquake (Ml= 4.7), Tectonophysics, 290, 245-257.
P11. Courboulex, F., N. Deichmann, J.C. Gariel (1999): Rupture Complexity of a moderate intraplate earthquake in the Alps : the 1996 M5 Epagny-Annecy Earthquake, Geophys. J. Int, 139, 152-160.
P12. Singh, S.K., M. Ordaz, J.F. Pacheco, F. Courboulex (2000) : A simple source inversion scheme for displacement seismograms recorded at short distances, J. Seismol.,.4, 267-284.
P13. Bouchon, M., S. Gaffet, C. Cornou, M Dietrich, J.P. Glot, F Courboulex, A. Caserta, G. Cultrera, F. Mazza and R. Guiguet (2000): Evidence for vertical ground accelerations exceeding gravity during the 1997 Umbria-Marche (central Italy) earthquakes. J. Seismol, 4, 517-523.
P14. Deschamps A., Courboulex, F., Gafftet, S., Lomax A., Virieux, J., Amato, A. ; Azzara, R. ; Chiarabba, C. ; Cimini, G. B. ; Cocco, M. ; Di Bona, M. ; Margheriti, L. ; Mazza, S. ; Mele, F. ; Selvaggi, G. ; Basili, A. ; Boschi, E. (2000), Spatio-temporal distribution of seismic events during the 1997 Umbia-Marche crisis, J. Seismol, 4, 377-386.
P15. Gaffet, S., G. Cultrera, F. Courboulex, F. Marra, M. Dietrich, M. Bouchon, A. Caserta, C. Cornou, A. Deschamps, J.P. Glot, and R. Guiguet (2000), A site effect study during the 1997 Umbria-Marche (Central Italy) earthquakes : data analysis, J. Seismol., 4, 525-541.
P16. Larroque C, Béthoux N., Calais, E., Courboulex, F., Deschamps, A., Déverchère, J., Stéphan, J.F., Ritz, J.F. and Gill (2001), Joint Multidisciplinary studies of active faults and seismic hazard at the junction between southern French Alps and Ligurian basin. Abstract volume Paleosis, Han sur Lesse (Belgium), 13-17 march 2000, 89-92.
P17. Courboulex F, Duval A.M., Deschamps A., Lomax A., Larroque C.(2001), All the small Peille (Alpes Maritimes, France) earthquake can teach us, C. R. Acad. Sc., 333, 105-112.
P18. Baumont, D., Courboulex F, O. Scotti, N.S. Melis, G. Stavrakakis (2002) : Slip distribution of the Mw 5.9, 1999 Athens earthquake inverted from regional seismological data, Geophys. Res. Let., 29, 15.

P19. Courboulex, C. Larroque, A. Deschamps, C. Gelis, J. Charreau, J.F. Stephan (2003) : An unknown active fault revealed by microseismicity in the south-east of France, *Geophys. Res. Lett.* , 30 (15), 1792, 2003.
P20. Chiaraluce L., Amato A., Cocco, M., Chiarabba C., Selvaggi G., Di Bona M., Piccibibi D., Deschamps A., Margheriti L., Courboulex F. and Ripepe M. (2004) : Complex normal faulting in the Apennines thrust-and-fold belf : the 1997 seismic sequence in central italy, *Bull. Seismol. Soc. Am., 94, 99-116.*
P21. Baumont D., O. Scotti, F. Courboulex, and N. Melis (2004): Slip distribution of the Mw 5.9, 1999 Athens earthquake from a joint inversion of regional seismological and SAR data - Indirect evidence for non-coseismic slip, *Geophys. J. Int*, 158, 3, 1078-1087
P22. Hernandez B., Cotton F., Stramondo S., Scotti O., Courboulex F. and Campillo M (2004): Rupture History of the 1997 Umbria-Marche (Central Italy) main shocks from the inversion of GPS, DInsSAR and near field strong motion data, *Ann. Geophys.*, 2004, 47, 4, 1355-1376.
P23. Kohrs-Sansorny C., F. Courboulex, M. Bour and A. Deschamps (2005): A Two-Stage Method for Ground-Motion Simulation Using Stochastic Summation of Small Earthquakes, Bull. of the Seismological Society of Am. 95, 1387-1400.
P24. F. Courboulex, C. Larroque, A. Deschamps, C. Kohrs-Sansorny, C. Gélis, J.L. Got, J. Charreau, J.F. Stéphan, N. Béthoux, J. Virieux, D. Brunel, C. Maron, A.M. Duval, S. Vidal, and P. Mondielli (2007), Seismic hazard on the French Riviera: new data, interpretations and simulations, Geophys. J. Int, 170 (1), 387–400. doi:10.1111/j.1365-246X.2007.03456.x.
P25. Beauval C., Honoré L. and F. Courboulex, Ground-Motion Variability and Implementation of a Probabilistic-Deterministic Hazard Method (2009), *Bull. Seismol. Soc. Am*., 99, 2992-3002.
P26. Salichon J., Kohrs-Sansorny C, Bertrand E. and F. Courboulex (2010), A Mw 6.3 earthquake scenario in the city of Nice (South-East France): Ground motion simulations, J. Seismology in press. Doi: 10.1007/s10950-009-9180-0.
P27. Courboulex F., J. Converset, J. Balestra and B. Delouis (2010), Ground-Motion Simulations of the 2004 Mw 6.4 Les Saintes, Guadeloupe, Earthquake Using Ten Smaller Events, 100, 116-130, Bull. Seismol. Soc. Am., doi :10.1785/0120080372.

Publications dans d'autres revues, actes de colloques avec comité de lecture

PA1. Courboulex, F., N. Deichmann, O. sismiques (1999) : Le séisme d'Annecy : effets de la segmentation des failles sur la rupture, 5ème colloque de l'Association Française du génie Parasismique, 2, 339-347.
PA2. Courboulex F., Duval A.M., Lomax A., Deschamps, A., Larroque C. (2000), Les enseignements du petit séisme de Peille (M 3.3) du 1er novembre 1999 (Alpes Maritimes, France), actes du colloque Riviera 2000, 18-21 Oct. 2000, Villefranche sur Mer.
PA3. Larroque C., Béthoux N., Calais E., Courboulex F., Deschamps A., Deverchère J., Stéphan J.F., Ritz J.F., Gilli E., Joint Multidisciplinary studies of active faults and seismic hazard at the junction between southern French Alps and Ligurian basin. Abstract volume Paleosis, Han sur Lesse (Belgium), 13-17 March 2000, 89-92.
PA4. Courboulex F (2000), Evaluation de l'aléa sismique sur le littoral Méditerranéen, réseaux de surveillance sismique dans le sud-est de la France. : Actes du MICAM 2000, 4-15 Sept 2000, Nice
PA5. Sansorny C, .Courboulex F., Bour M, Deschamps A. :Validation d'un outil de simulation des mouvements sismiques basé sur la méthode des fonctions de Green empiriques (2003), actes du 6ème colloque de l'Association Française du génie Parasismique.
PA7. Berge−Thierry C., J−F. Fels, P. Dervin, P. Gueguen, S. Nechtschein, D. Hatfeld, P. Vollant, P−Y., Bard, F. Courboulex, P. Dominique, B. Feignier (2004): The french permanent accelerometric network: technological and parametrical choices, scientific goals and results, prooceedings of the "Invited Workshop on strong motion record procesing", convened by the Consortium of Organizations for strong motion observation systems (COSMOS), Richmond, May 2004.
PA8. Kohrs-Sansorny**, C.**, F. Courboulex, M. and A. Deschamps. (2006). Ground motion simulation of two moderate size earthquakes in the Grenoble area using summation of small earthquakes. Third International Symposium on the Effects of Surface Geology on Seismic Motion, volume II.
PA9. Courboulex F., Converset J and Kohrs-Sansorny C. (2007). Simulation du séisme des Saintes (Mw 6.4, Guadeloupe, 2004) en utilisant une sommation stochastique de petits sésimes, Actes du VIIème colloque de l'Association Française du génie Parasismique.
PA10. Scotti, O., Larroque C., Baumont D., Virieux J., Courboulex F., Delouis B., Deschamps A., Vallée M., Angelier J., Béthoux N. and Bellier O, Définition de scénarii sismiques pour la région de Nice, Actes du VIIème colloque de l'Association Française du génie Parasismique.

PA11. Duval A-M, Bertrand E., Vidal S., Bard P-Y., Guéguen P., Courboulex F. and Davi D. (2007). Transfert vers la société – Valorisation des recherches. Numéro spécial du BLPC sur les risques sismiques.

PA12. Beauval C., Honoré L., Courboulex F., Towards a Hybrid Probabilistic Seismic Hazard Assessment Methodology (2008), 14th World Conference on Earthquake Engineering, 12−17/09, Beijing, China,Paper 07−0095, 8 pages.

PA13. Bérenguer, J.L., Courboulex, F., Leputh, J., Zodmi, B., Bernard, P., Larroque, C., Matias, L, Moulié, F., Ngo, O., Nolet, G., Tartière, M., Tilquin, F., Virieux, J. Feeling the Earth Shake ... at school. EDUSISMO : the French educational Seismological Network. CSEM-EMSC Newsletter, Dec 2009.

A.2 Communications dans des congrès

- Courboulex F., Virieux J. et Gibert D. Cross Validation Theory and non-Linear Inversion Method for Deconvolution of Empirical Green Functions.American Geophysical Union}, Baltimore, May 1995.
- Courboulex, F. and S.K. Singh :Evidence of rupture directivity for the September 14, 1995 Guerrero earthquake using regional broad-band data.: Union Geofisica Mexicana, Puerto Vallarta (Mexico), Nov. 1995.
- Courboulex, F., A. Deschamps, J. Virieux, M. Cattaneo, F. Costi, N. Bethoux, S. Gaffet, J. Deverchère, and C. Eva : Application of the empirical Green function method to the 21 April 1995 earthquake near the border between Italy and France :American Geophysical Union, San Francisco, Dec. 1995.
- Courboulex, F., J. Pacheco, S.K. Singh and C.J. Ammon : Source study of the October 9, 1995, Colima-Jalisco (Mexico) earthquake (Mw 8).European Seismological Society}, Reykjavik, Sept. 1996.
- Singh, S.K., J. Pacheco, F. Courboulex, V. Kostoglodov, M.A. Santoyo : Source duration of mexican earthquakes.
- American Geophysical Union, San Francisco, Dec. 1996.
- Courboulex F.: Source study of small earthquakes : example of the Ligurian region. Thirty years of earthquakes in Italy, Erice, Italy 13-18 Juillet 1998.
- Calais E., Courboulex F., Cotton F. (1998).- SAR Interferometry study of the M80 Oct. 9. 1995 Jalisco earthquake (Mexico). EGS'98, Nice, France.
- Gaffet S., Courboulex F., Cornou C., Caserta I., Brouchon M., Cultera G., Dietrich M., Glot J.P., Guiguet R., Marra F. (1998).- A site effect study during the 1997 Umbria-Marche (Central Italy) earthquakes : preliminary results. EGS'98, Nice, France.
- Courboulex F., Deichmann N., Gariel J.C. (1998).- Rupture process of the 1996 Epagny-Annecy Earthquake (French Alps). EGS'98, Nice, France
- Castello, B.; Deschamps, A.; Courboulex, F.;Cattaneo, M. :Are aftershocks on individualized faults ? EGS, The Hague, Netherland, 1999.
- Amato, A.; Azzara, R.; Chiarabba, C.; Cimini, G.B.; Cocco, M.; Di Bona, M.; Margheriti, L.; Mazza, S.; Selvaggi, G.; Deschamps, A.; Courboulex, F.; Gaffet, S.; Chiaraluce, L.; Picc Inini, D.; Ripepe, M. Space and time evolution of the 1997-98 Umbria-Marche (Italy) earthquake sequence EGS, The Hague, Netherland, 1999.
- Singh, S.K.; Ordaz, M.; Pacheco, J.F.; Courboulex, F. : A simple source inversion scheme for displacement seismograms, recorded at short distances EGS, The Hague, Netherland, 1999.
- Courboulex, F.; Singh, S.K.; Hernandez, B.; Deschamps, A.; Castello, B.; Cocco, Source of moderate size events during the 1997 Umbria-Marche seismic crisis. EGS, The Hague, Netherland, 1999.
- Courboulex, F., N. Deichmann, O. sismiques (1999) : Le séisme d'Annecy : effets de la segmentation des failles sur la rupture, 5ème colloque de l'Association Française du génie Parasismique, Cachan, 1999.
- Courboulex F, Duval A.M., Lomax A., Deschamps, A., Regional and local Hazard investigation using a small earthquake near Nice (France). EGS, Nice, 2000.
- Larroque C., Béthoux N., Calais E., Courboulex F., Deschamps A., Déverchère J., Stéphan J.F., Ritz J.F. and E. Gilli, 2000. Joint Multidisciplinary studies of active faults and seismic hazard at the junction between southern French Alps and Ligurian basin. Abstract volume Paleosis, Han sur Lesse (Belgium), 13-17 march 2000, 89-92.
- Courboulex F., Duval A.M., Lomax A., Deschamps, A., Larroque C. (2000), Les enseignements du petit séisme de Peille (M 3.3) du 1er novembre 1999 (Alpes Maritimes, France). Colloque Riviera 2000, V illefranche sur Mer, 2000.
- Castello, B., Cataneo, M., Courboulex, F., Deschamps, A., Michelini, A., Selvaggi, G., Precise relocation of recent seismic sequences in the Appenines (Italy) using cross correlation procedures. EGS, Nice, 2001.
- Sansorny C, Courboulex, F., Pacheco, J., Singh, S.K., Study of the rupture process of a moderate size earthquake (Mexico, Mw 6.4) based on regional data. EGS, Nice, 2001.
- Courboulex F., Deschamps A., Béthoux N., Brunel, D., Calais E., Déverchère J., Gaffet S ., Hustedt B., Larroque C., Lomax A., Maron C., Monfret T., Pillet R., Sansorny C., Stéphan J.F., Virieux J., Duval A.M., Méneroud

J.P., Perez J.L., Vidal S., Mondielli P., 2001. Preliminary results of the SALAM (Sismologie et Aléas dans les Alpes maritimes) experiment. EGS, Nice, 2001.

- Deschamps, A., Bethoux, N., Courboulex, F., Duval, A.M., Hello, Y., Anglade, A., Brunel, D., Vidal, S. ; Study of the February 25th 2001 event (Ml=4.6) offshore of NICE and it's contribution to seismic hazard evaluation. EGS, Nice, France, 2002.
- Baumont, D., Scotti, O., Courboulex, F., Nostro, C., Melis, N. : To what extent the accuracy of slip models helps explain the aftershock distribution using CFF : The Mw 5.9 Athens earthquakes case study. EGS, Nice, France, 2002.
- Courboulex F., Deschamps A., Castello, B., Gélis, C., Larroque, C. Stéphan, J.F., Charreau, J. : New insights for active tectonics in Nice Area (South of France) from the results of the seismological SALAM experiment (2000-2001). EGS, Nice, France, 2002.
- Sansorny C., F. Courboulex, M. Bour, A. Deschamps : Simulation of a Mexican earthquake (Mw 6.4) using empirical Green's function summation, European Seismological Commission, Genova, Italy, 2002.
- Hatzfeld D., P.-Y. Bard, F. Beauducel, C. Berge, P. Bernard, P. Beys, F. Blarel, D. Brunel, F. Cotton, F. Courboulex, A. Deschamps, P. Dominique, M. Granet, Guéguen, B. Lebrun, M. Nicolas, T. Piquet, A. Souriau, S. Vidal, J-P Viodé : The French Accelerometric Network (RAP) : a free access to data, European Seismological Commission, Genova, Italy, 2002.
- Courboulex F., Deschamps A., Gélis, C., Larroque : Results of seismic experiments (2000-2001) in the South-East of France. European Seismological Commission, Genova, Italy, 2002.
- Sansorny C., Courboulex F., Bour M., Deschamps A.. Strong ground motions simulation using small earthquakes summation : validation and application, EGS-AGU-EUG Joint Assembly, Nice, France, 2003.
- Sansorny, C., F. Courboulex, M. Bour and A. Deschamps. Validation d'un outil de simulation des mouvements sismiques, basé sur la méthode des fonctions de Green empiriques. VI Colloque National AFPS, Palaiseau, Juillet 2003.
- Larroque C., Courboulex F., Charreau J., Deschamps A., Gélis C., Stéphan J.-F., Perez J.L.. Active tectonics in the southwestern Alps : hidden faulting revealed by microsismicity in the Nice area (France), *EGS-AGU-EUG Joint Assembly*, *Nice, France*, *2003.*
- Gélis C., Courboulex F., Deschamps A., Got J.-L., Duval A.-M., Larroque C.. How seismic activity reveals active faults in the south east of France, *EGS-AGU-EUG Joint Assembly*, *Nice, France*, *2003.*
- Regnier M., Deschamps A., Monfret T., Pelletier B., Pillet R., Lebellegard P., Courboulex F., Delouis B., Gaffet S.. Stress interaction during a seismic swarm at the southern termination of the New Hebrides trench, *EGU*, *Nice*, *France*, *2004.*
- Sansorny, C., Courboulex F., Bour M, Deschamps A., Bertrand E.. Simulation of two moderate size earthquakes earthquakes in the south east of France. EGU, Nice France, 2004.
- -Berge.T.C., Fels J-F., Dervin P., Guéguen P., Nechtschein S., Hatzfeld D., Volant P., Bard P-Y., Courboulex F., Dominique P.. The french permanent accelerometric network: technological and parametrical choices, scientific goals and results, *Invited Workshop on strong motion record proceesing*, *Richmond, EU.*, *2004.*
- Kohrs-Sansorny, C., F. Courboulex, M. Bour, A. Deschamps and E. Bertrand. Simulation of two moderate sized earthquakes in the south-east of France. 1st General Assembly of the European Geosciences Union, Nice, Avril 2004.
- Kohrs-Sansorny, C., F. Courboulex, M. Bour, A. Deschamps and E. Bertrand. Sommation de petits séismes pour la simulation des mouvements du sol : application à des données RAP dans la ville de Nice. Journées RAP, Carry le Rouet, Juin 2004.
- Larroque C., Courboulex F., Delouis B., Deverchère J., Migeon S. : Aléa sismique à la jonction Alpes-Bassin Ligure, Où sera le prochain séisme de 1887 ? Colloque sur les sciences et technologies marines du Futur, 18-18 Mai 2005, Marseille.
- Kohrs-Sansorny, C., F. Courboulex, E. Bertrand and A. Deschamps. Small earthquakes summation for a better estimation of the seismic hazard in the south-east of France. European Geosciences Union, Vienne, Autriche, Avril 2006.
- Courboulex F., Kohrs-Sansorny, C., Simulation de séismes de magnitude modérée dans la ville de Nice, journées scientifiques et Techniques du RAP, Les Houches, Mai 2006.
- Courboulex, F. Le projet PASSERELLE : un lien entre la recherche et la gestion du risque sismique et gravitaire dans les Alpes Maritimes, Séminaire RDT du MEDD, Mars 2006, Paris, France.
- Kohrs-Sansorny, C., F. Courboulex, M. and A. Deschamps. Ground motion simulation of two moderate size earthquakes in the Grenoble area using summation of small earthquakes. Third International Symposium on the Effects of Surface Geology on Seismic Motion, Grenoble, Aout 2006.
- Kohrs-Sansorny C., Courboulex F., Bertrand E. et Deschamps A., simulation de séismes de magnitude modérée dans le sud-est de la France à partir d'une méthode de sommation stochastique de petits séismes, Réunion des Sciences de la Terre (RST), Dijon, 4-8 dec 2006.

- Courboulex F., Kohrs-Sansorny C. and Converset J. , Variability of the ground motion generated by a stochastic summation of empirical Green's functions : Study of the Saintes crisis (2004, French Indies), IUGG, IASPEII, Perugia (Italy), Juil. 2007.
- Scotti, O., Larroque C., Baumont D., Virieux J., Courboulex F., Delouis B., Deschamps A., Vallée M., Angelier J., Béthoux N. and Bellier O, Définition de scénarii sismiques pour la région de Nice, VIIème Colloque National AFPS, Juil 2007, Paris.
- Courboulex F., Kohrs-Sansorny C. and Converset J, Simulation des deux chocs principaux de la crise des Saintes (Antilles, 2004-2005) en utilisant une sommation stochastique de petits séismes, VIIème Colloque National AFPS, Juil 2007, Paris.
- Courboulex F. and J. Converset, Ground Motions Simulations of the 2004 Les Saintes Earthquake (Mw 6.4) and its Largest Aftershock (Mw 5.9). American Geophysical Union, Dec. 2007, San Francisco, USA.
- Bérenguer J-L., Le Puth J., Courboulex F., Zodmi B. and M. Bonneff , Sismos à l'Ecole : a Seismic Educational Network (FRANCE) linked with research, AGU San Francsico, Dec 2007.
- O. Scotti O., C. Larroque, F. Courboulex , B. Delouis and D. Baumont, On the Definition of realistic Earthquake Parameters along potential active Faults in the French-Italian Riviera: a key step in Quantitative Seismic Hazard Assessment (QSHA) -a Platform for strong Ground Motion Modeling. European Geophysical Union General assembly, Vienna, May 2008.
- Beauval C., Honoré L., Courboulex F., Towards a Hybrid Probabilistic Seismic Hazard Assessment Methodology, 14th World Conference on Earthquake Engineering, sept 2008, Beijing, China.
- Honoré, L., Courboulex, F., Souriau, A., A major historical earthquake in the French Pyrenees revisited using actual moderate size earthquake, Colloque Lambesc-Provence 2009, Aix en Provence, Juil 2009.
- Salichon, J., Kohrs-Sansorny C., Bertrad E. and Courboulex F., Ground motion simulations of a Mw 6.3 earthquake in Southeastern France (Nice Region), Colloque Lambesc-Provence 2009, Aix en Provence, Juil 2009.
- Bérenguer J.L., S. Solarino, H., Bossert, R. Cremonini, F. Courboulex,C. Eva, E. Eva, G. Ferretti, J. Leputh, M. Ponzone, and A. Sornette, THE "O3E" PROGRAM: RAISING AWARENESS ON NATURAL HAZARDS, Colloque Lambesc-Provence 2009, Aix en Provence, Juil 2009.
- Larroque, C., Scotti O., Courboulex F., Delouis B., Deschamps A. and Nocquet J.M., Towards a new seismotectonic zonation of the south east of France., Colloque Lambesc-Provence 2009, Aix en Provence, Juil 2009.
- Honoré, L., and F. Courboulex, Ground-motion simulations of the L'Aquila earthquake Mw6.3 (April 6th, 2009) using aftershocks as empirical Green's functions, American Geophysical Union Fall meeting, 14-18 Dec 2009, San Francisco.
- J.L. Bérenguer; F. Courboulex; E. Baroux; R. Cremonini; G. Ferretti; C. Eva; D. Giardini; F. Haslinger; J. Leputh; M. Ponzone; S. Solarino; A. Sornette, American Geophysical Union Fall meeting, 14-18 Dec 2009, San Francisco.
- F. Courboulex; J. Berenguer; J. Leputh; B. Zodmi; F. Tilquin; M. Tartiere; O. Ngo; L. Mathias; F. Moulié; J. Virieux; C. Larroque; J. Douchain; G. Nolet; p. bernard; P. Arroucau; M. Chlieh; A. Deschamps; R. Pillet; M. Regnier, Feeling the Earth Shake… at School, American Geophysical Union Fall meeting, 14-18 Dec 2009, San Francisco.
- Courboulex F., L. Honoré and A. Souriau, A major historical earthquake in the French Pyrenees revisited using actual moderate size earthquakes, American Geophysical Union Fall meeting, 14-18 Dec 2009, San Francisco.

A.3 Pilotage et participation à des projets de recherche:

J'ai été responsable ou co-responsable de plusieurs projets de recherche de dimension nationale ou internationale. Voici un bref descriptif des principaux projets dans lesquels j'ai joué un rôle de pilotage ou d'animation

- Projet « **Etude de la séquence sismique d'Ombrie Marche en Italie** », Appel d'offres du Programme National sur les Risques Naturels, INSU-CNRS, 1999-2000 – ***Responsable***

  Ce projet a permis de travailler finement sur les enregistrements sismologiques de la crise sismique d'Ombrie-Marche de 1997 collectés lors d'une campagne post-sismique.

- Projet *« **Evaluation du potentiel sismogène dans une région à sismicité modérée et failles lentes II : études interdisciplinaires à la jonction Alpes-Bassin Ligure »***. Appel d'offres du Programme National sur les Risques Naturels, INSU-CNRS, 2001-2002.- Co-responsable avec C. Larroque.

  Ce projet a permis de mener une véritable étude pluridisciplinaire sur les failles actives de la jonction Alpes bassin Ligure, et de mettre en évidence une faille active méconnue.

- Projet européen PRESAP « **Towards pratical, real-time estimation of spatial aftershock probabilities: a feasibility study in earthquake hazard** » en collaboration avec l'IRSN (Institut de Recherche et de sûreté nucléaire): (financement d'un post-doc) de 2000 à 2003 - Responsable scientifique au niveau de Géosciences Azur. – Responsable d'un groupe de travail

  L'idée de ce projet était de tenter de prévoir dans un temps court où les répliques les plus fortes allaient se produire après un séisme. Ma contribution a concerné l'étude de la source du séisme d'Athènes de 1999 (Post doc : David Baumont).

- Projet **PASSERELLE** (RDT-Ministère de l'écologie) de 2004 à 2006 (Co-Responsables F. Courboulex, et A-M Duval). – Co- Responsable avec Anne-Marie Duval.

  Ce projet a permis de créer des liens entre les chercheurs et les opérationnels dans le domaine du risque sismique et gravitaire dans les Alpes maritimes. Les recherches menées durant ce projet se sont concentrées sur la vallée du Var (études de terrain, campagne de sismologie, imagerie géophysique d'une faille, effet de site, suivi temporel d'un glissement de terrain).

- Projet **RAP-Antilles** (financé par le GIS RAP) en 2007. – Responsable

  Nous avons travaillé sur la crise des Saintes de 2004 en utilisant les données accélérométriques du réseau RAP : détermination des paramètres de la source, simulation des mouvements forts par une sommation de petits séismes, élaboration et test d'une méthodologie hybride déterministe –probabiliste pour l'évaluation de l'aléa sismique.

- Projet **PYRSIM** (Simulation d'un séisme historique majeur dans les Pyrénées à partir de séismes instrumentaux) financé de 2008 à 2009 (AO RAP). – Responsable

  L'étude porte sur la simulation du séisme Bigorre de 1660 dans les Pyrénées en utilisant des séismes récents bien enregistrés par le réseau RAP comme fonctions de Green empiriques.

- Projet INTERREG **O3E** (Appel d'offre ALCOTRA) financé de 2009 à 2011. – Responsable

  Dans le cadre de ce projet européen qui rassemble les régions d'Italie de France et de Suisse proches de la frontière, nous proposons de mettre en place un réseau éducatif de mesure de paramètres environnementaux dans les établissements scolaires (Sismologie, météorologie, hydrologie).

J'ai également joué un rôle actif dans les projets suivants :

- **Evaluation du potentiel sismogène dans une région à sismicité modérée et failles lentes I : études interdisciplinaires à la jonction Alpes-Bassin Ligure.** (Appel d'offres du Programme National sur les Risques Naturels, INSU-CNRS, 1999-2000 (Co-Responsables : C. Larroque et N. Béthoux).

- **IRIS** (Imagerie, Risques, Instabilités et Sismologie en region PACA). Appel d'offres de l'Action Concertée Incitative Catastrophes Naturelles, M.E.N.R.T., 2004-2006 (Co-Responsables C. Larroque et N. Béthoux).

- **Estimation des mouvements du sol** - financé par le GIS Curare 2004-2006 (responsable S. Gaffet).

- **QSHA** (Quantitative Seismic Hazard Assesment), financé par l'Agence Nationale de la Recherche de 2004 à 2007 (Co-responsables : J. Virieux et P-Y Bard).

- **ADN** (Andes du Nord) , financé par l'Agence Nationale de la Recherche de 2007 à 2010 (responsable J-M. Nocquet).

A.4 Encadrement de travaux de recherche

Thèses de Doctorat :

Carine Kohrs-Sansorny (Directeur HDR Anne Deschamps)
Sujet : Simulation des mouvements du sol en utilisant de petits séismes comme fonctions de Green empiriques. Cette thèse était co-encadrée par le BRGM et financée par la région PACA. Ces travaux ont permis notamment de développer 2 codes de simulations de séismes. Thèse soutenue en Janvier 2005.

Laetitia Honoré (Directeur HDR Nicole Béthoux) Co-direction avec D. Baumont de l'IRSN)
Sujet : Simulation des mouvements forts du sol dus à un séisme : contribution à l'estimation de l'aléa sismique en Equateur. Cette thèse a débuté en Oct 2008.

Stages de recherche de Master 1 Master 2, DEA, maîtrise et licence:

- Frédérique Murcia : Direction (100 %) du stage de recherche de **maîtrise** 1998.
- Frédéric Vincent : Co-direction (50 % avec E. Calais) du stage de recherche de **DEA** 1998.
- Stéphane Fiorucci : Direction (100 %) du stage de recherche de **maîtrise** 1999.
- Marie Laurent : Co-direction (50 % avec A. Deschamps) du stage de recherche de **maîtrise** 2000.
- Nicolas Plusquelec : Direction (100 %) du stage de recherche de **maîtrise** 2001.
- Céline Gélis : Direction (100%) du stage de **DEA,** 2002.
- Julien Charreau : Co-direction (33.3% avec C. Larroque) du stage de **DEA,** 2002.
- Nicolas Clarins : Direction (100%) du stage de **DEUG**, 2003.
- Emilie Noel : Co-direction (50% avec Etienne Bertrand) du stage de **Master** 1, 2006.
- Stéphanie Pilone : Direction (100%) du stage de **Licence**, 2007.
- Chloée Arnéodo : direction (100%) du projet tutoré en **L3**, 2008.
- Julien Converset, direction (100%) du stage de **Master 2**, 2007.
- Emilie Ribeiro : (Co-direction 50% avec M. Vallée), stage de **Master 1**, 2008.
- Laetitia Honoré : (Co-direction 50% avec C. Beauval), stage de **Master 2**, 2008.

Encadrement de post-doctorants

- David Baumont : (projet européen PRESAP), 2001.
- Carine Kohrs-Sansorny, GIS Curare (2006-2007).
- Jérome Salichon, ANR QSHA, (2008-2009).

A.5 Enseignement

J'enseigne en troisième cycle depuis la première année de mon recrutement au CNRS. J'ai tout d'abord assuré pendant 4 ans un cours de sismologie de la source au sein du DEA « dynamique de la lithosphère » co-dirigé par les universités de Grenoble, Chambery, Marseille et Nice.

A l'occasion de la mise en place des Master sur Nice, il m'est apparu nécessaire de proposer un module centré sur le risque sismique qui puisse profiter à la fois aux étudiants des parcours « recherche » et à ceux qui préféraient un parcours « professionnalisant ». Ce module a été monté en étroite collaboration avec nos collègues du CETE Méditerranée Anne-Marie Duval et Etienne Bertrand. L'intitulé en était « risque sismiques et gravitaire », la part du risque sismique se réduisant à 15h de cours + TP.

Ce module optionnel ayant eu chaque année un succès important, nous avons demandé en 2007 un doublement des heures afin de proposer un module « risque sismique » plus complet (30 heures). Cette maquette a été acceptée et ce module a été proposé pour la première fois aux étudiants en 2008-2009.

Même si le nombre d'heure reste assez réduit face à l'ampleur du sujet, nous cherchons à aller de l'aspect fondamental (source sismique, répartition des séismes, mesure des phénomènes) jusqu'à l'aspect plus appliqué (détermination d'un SMH, calcul des effets de site 1D, utilisation des bases de données accélérométriques, effets sur les bâtiments, règlementation).

J'ai également participé au master PREFALC (Université de Nice – Université de Quito) : 20 heures de cours sur l'aléa sismique à Quito en 2008.

Je participe actuellement à la mise en place d'un Master international Erasmus mundus « Georisk » crée en partenariat avec les Universités de Nice-Sophia Antipolis, Athènes, Liège, Meknes, Quito et Paris6.

A.6 Animation scientifique

- Organisation des « midi Science et sandwich » qui sont des séances scientifiques informelles pour parler des travaux en cours, des difficultés rencontrées, des projets en gestation, de l'avancement des thèses … Ces séances d'une heure environ ont lieu le mardi midi à Sophia Antipolis à l'heure du repas. Le principe qui déplu à quelques uns au début (manger un sandwich en écoutant de la Science) est maintenant bien accepté et ces séances ont une audience assez constante.
- membre élue du conseil d'UMR de 2000 à 2004.
- Membre du Bureau national du GIS RAP de 2001 à 2004.
- Responsable au niveau de l'UMR de la thématique « Chantier Alpes Méditerranée » avec deux autres collègues (dernier quadriennal).
- Membre du comité INSU CT3 « Aléa et Risque » depuis 2009.